Segmentierung medizinischer Bilddaten und bildgestützte intraoperative Navigation

Habilitationsschrift
zur
Erlangung der Facultas Docendi
für Informatik
(Dr. rer. nat. habil.)

dem Fachbereich Mathematik und Informatik
der Philipps-Universität Marburg
vorgelegt von

Dr. Dr. Jan Egger
aus Diez / Lahn

Marburg an der Lahn
2016

Angenommen vom Fachbereich Mathematik und Informatik der Philipps-Universität Marburg am 09.11.2016

Gedruckt mit der Genehmigung des Fachbereichs.

Dekan:	Professor Dr. Ilka Agricola
Gutachter:	Professor Dr. Bernd Freisleben
	Professor Dr. Dieter Schmalstieg
	Professor Dr. Andreas Kolb
	Professor Dr. Bernhard Preim

Kurzfassung

Die Entwicklung von Algorithmen zur automatischen oder semi-automatischen Verarbeitung von medizinischen Bilddaten hat in den letzten Jahren mehr und mehr an Bedeutung gewonnen. Das liegt zum einen an den immer besser werdenden medizinischen Aufnahmemodalitäten, die den menschlichen Körper immer feiner virtuell abbilden können. Zum anderen liegt dies an der verbesserten Computerhardware, die eine algorithmische Verarbeitung der teilweise im Gigabyte-Bereich liegenden Datenmengen in einer vernünftigen Zeit erlaubt. Das Ziel dieser Habilitationsschrift ist die Entwicklung und Evaluation von Algorithmen für die medizinische Bildverarbeitung. Insgesamt besteht die Habilitationsschrift aus einer Reihe von Publikationen, die in drei übergreifende Themenbereiche gegliedert sind:

- **Segmentierung medizinischer Bilddaten anhand von vorlagenbasierten Algorithmen**

- **Experimentelle Evaluation quelloffener Segmentierungsmethoden unter medizinischen Einsatzbedingungen**

- **Navigation zur Unterstützung intraoperativer Therapien**

Im Bereich *Segmentierung medizinischer Bilddaten anhand von vorlagenbasierten Algorithmen* wurden verschiedene graphbasierte Algorithmen in 2D und 3D entwickelt, die einen gerichteten Graphen mittels einer Vorlage aufbauen. Dazu gehört die Bildung eines Algorithmus zur Segmentierung von Wirbeln in 2D und 3D. In 2D wird eine rechteckige und in 3D eine würfelförmige Vorlage genutzt, um den Graphen aufzubauen und das Segmentierungsergebnis zu berechnen. Außerdem wird eine graphbasierte Segmentierung von Prostatadrüsen durch eine Kugelvorlage zur automatischen Bestimmung der Grenzen zwischen Prostatadrüsen und umliegenden Organen vorgestellt. Auf den vorlagenbasierten Algorithmen aufbauend, wurde ein interaktiver Segmentierungsalgorithmus, der einem Benutzer in Echtzeit das Segmentierungsergebnis anzeigt, konzipiert und implementiert. Der Algorithmus nutzt zur Segmentierung die verschiedenen Vorlagen, benötigt allerdings nur einen Saatpunkt des Benutzers. In einem weiteren Ansatz kann der Benutzer die Segmentierung interaktiv durch zusätzliche Saatpunkte verfeinern. Dadurch wird es möglich, eine semi-automatische Segmentierung auch in schwierigen Fällen zu einem zufriedenstellenden Ergebnis zu führen.

Im Bereich *Evaluation quelloffener Segmentierungsmethoden unter medizinischen Einsatzbedingungen* wurden verschiedene frei verfügbare Segmentierungsalgorithmen anhand von Patientendaten aus der klinischen Routine getestet. Dazu gehörte die Evaluierung der semi-automatischen Segmentierung von Hirntumoren, zum Beispiel Hypophysenadenomen und Glioblastomen, mit der frei verfügbaren Open Source-Plattform 3D Slicer. Dadurch konnte gezeigt werden, wie eine rein

manuelle Schicht-für-Schicht-Vermessung des Tumorvolumens in der Praxis unterstützt und beschleunigt werden kann. Weiterhin wurde die Segmentierung von Sprachbahnen in medizinischen Aufnahmen von Hirntumorpatienten auf verschiedenen Plattformen evaluiert.

Im Bereich *Navigation zur Unterstützung intraoperativer Therapien* wurden Softwaremodule zum Begleiten von intra-operativen Eingriffen in verschiedenen Phasen einer Behandlung (Therapieplanung, Durchführung, Kontrolle) entwickelt. Dazu gehört die erstmalige Integration des OpenIGTLink-Netzwerkprotokolls in die medizinische Prototyping-Plattform MeVisLab, die anhand eines NDI-Navigationssystems evaluiert wurde. Außerdem wurde hier ebenfalls zum ersten Mal die Konzeption und Implementierung eines medizinischen Software-Prototypen zur Unterstützung der intraoperativen gynäkologischen Brachytherapie vorgestellt. Der Software-Prototyp enthielt auch ein Modul zur erweiterten Visualisierung bei der MR-gestützten interstitiellen gynäkologischen Brachytherapie, welches unter anderem die Registrierung eines gynäkologischen Brachytherapie-Instruments in einen intraoperativen Datensatz einer Patientin ermöglichte. Die einzelnen Module führten zur Vorstellung eines umfassenden bildgestützten Systems für die gynäkologische Brachytherapie in einem multimodalen Operationssaal. Dieses System deckt die prä-, intra- und postoperative Behandlungsphase bei einer interstitiellen gynäkologischen Brachytherapie ab.

Abstract

The development of algorithms for the automatic and semiautomatic processing of medical image data became more and more important in recent years. On the one hand, this depends on improved image techniques, which allow increasingly finer virtual representations of the human body. On the other hand, this depends on improved computer hardware, which enables an algorithmic processing of data in gigabyte range in a reasonable time. The aim of this habilitation thesis is the development and evaluation of algorithms for medical image processing. Overall, the habilitation thesis consist of a number of publications, which are structured in three comprehensive topics:

- **Segmentation of medical image data on the basis of template-based algorithms**
- **Experimental evaluation of open source segmentation algorithms under clinical conditions**
- **Navigation to support intraoperative therapies**

The topic *Segmentation of medical image data on the basis of template-based algorithms* includes the development of several graph-based algorithms in 2D and 3D, where directed graphs a constructed via templates. This involves algorithms for the segmentation of vertebra in 2D and 3D. In 2D a rectangle and in 3D a cubic shaped template is used to construct the graph and calculate the segmentation result. Moreover, a graph-based segmentation of prostate central glands (PCG) is performed with a spherical shaped template to determine the border between the PCG and the surrounding organs. Based on the template-based algorithms an interactive segmentation algorithm has been developed and implemented that provides the segmentation result in real-time to the user. The algorithm uses different templates, however, needs only one user-defined seed point to perform the segmentation. In a further approach, the user can interactively refine a segmentation results by additional seed points. Thus, enabling also satisficing semi-automatic segmentations in difficult cases.

The topic *Experimental evaluation of open source segmentation algorithms under clinical conditions* covers the intensive testing of freely available segmentation algorithms with patient data from the clinical routine. This includes the evaluation of the semi-automatic segmentation of brain tumors, like pituitary adenomas and glioblastomas with the freely available Open Source platform 3D Slicer. Thereby it could be shown how a pure manual slice-by-slice measurement of a tumor volume can be supported and speed-up in practice. Furthermore, the segmentation of language pathways in medical scans of brain tumor patients has been evaluated on different platforms.

The topic *Navigation to support intraoperative therapies* includes the development of software modules to guide intraoperative interventions in different treatment stages (therapy planning, execution, monitoring). This includes the integration of the OpenIGTLink network protocol into the medical prototyping platform MeVisLab, which has been evaluated with an NDI navigation system. Furthermore, the conception and development of a medical software prototype to support an intraoperative gynecological brachytherapy has been introduced. The software prototype contained also a module for the enhanced visualization during a MR-guided interstitial gynecological brachytherapy, which enabled the registration of a gynecological brachytherapy device into the intraoperative dataset of the patient. The single modules lead to a comprehensive image-guided system for the gynecological brachytherapy in a multimodal operation suite. Thereby, the system covers the pre, intra and postoperative treatment stages during an interstitial gynecological brachytherapy.

Danksagungen

An erster Stelle bedanke ich mich bei Professor Dr. Bernd Freisleben, der mich nicht nur bei der Abfassung meiner Habilitationsschrift, sondern auch während meiner zwei Doktorarbeiten stets hilfreich unterstützt hat.

Mein besonderer Dank gilt meinem Chef Professor Dr. Dieter Schmalstieg für die überaus interessante und spannende Arbeit an seinem Institut. Ich danke ihm, Professor Dr. Andreas Kolb und Professor Dr. Bernhard Preim für ihre bereitwillige Übernahme des Korreferates.

Den an den Forschungsprojekten beteiligten Medizinern danke ich für ihre klinischen Beiträge.

Mein Dank geht auch an die naturwissenschaftlichen Projektpartner und Studenten – Dr. Xiaojun Chen, Dr. Dženan Zukić, Robert Schwarzenberg und Tobias Lüddemann – für ihr Engagement und ihre technische Unterstützung.

Auch bei meinen Eltern, meinem Bruder, meinen Freunden und meiner chinesischen Frau Xixi bedanke ich mich herzlich!

für Yanli

Inhaltsverzeichnis

1. Einleitung

1.1. Motivation

Die medizinische Bildverarbeitung befasst sich mit der computergestützten Verarbeitung von medizinischen Bilddaten wie der Magnetresonanztomographie (MRT) oder der Computertomographie (CT). Dabei sollen Medizinern in verschiedenen Phasen einer Behandlung technische Mittel an die Hand geben werden, um Therapien erfolgreich zu gestalten. Das kann schon bei der Diagnose beginnen und bis zum Monitoring und der Therapieplanung auch die Durchführung und Kontrolle einschließen. Das Ziel dieser kumulativen Habilitationsschrift ist die Entwicklung und Evaluation von Algorithmen für die medizinische Behandlung unterschiedlichster schwerer Erkrankungen. Zu diesem Zweck ist die Habilitationsschrift in drei übergreifende Bereiche gegliedert: *Segmentierung medizinischer Bilddaten anhand von vorlagenbasierten Algorithmen*, *Experimentelle Evaluation quelloffener Segmentierungsmethoden unter medizinischen Einsatzbedingungen* und *Navigation zur Unterstützung intraoperativer Therapien*.

Im Bereich Segmentierung werden in dieser Arbeit mehrere skalierungsinvariante graphbasierte Algorithmen entwickelt, die auf geometrischen Vorlagen basieren. Dazu gehört unter anderem die semi-automatische Segmentierung von Wirbeln in zwei- und dreidimensionalen Patientenaufnahmen anhand eines Rechtecks bzw. Kubus. Die Segmentierungsalgorithmen beschleunigen die sehr zeitaufwendigen manuellen Schicht-für-Schicht-Segmentierungen erheblich; sie werden anhand von Patientenaufnahmen aus der Klinik für Neurochirurgie (Direktor Professor Dr. med. Christopher Nimsky) des Universitätsklinikums in Marburg evaluiert.

Im zweiten Teil dieser Arbeit werden Beiträge zur Evaluation von Segmentierungsalgorithmen wie dem GrowCut und einem Fibertracking unter der frei verfügbaren *Open Source*-Plattform 3D Slicer geleistet. GrowCut wird anhand der semiautomatischen Segmentierung von zerebralen Pathologien wie Glioblastomen und Hypophysenadenomen evaluiert. Größenänderungen bei diesen zerebralen Pathologien sind ein kritischer Faktor bei der Behandlungsentscheidung; heutzutage wird das Volumen einer Pathologie in der Regel immer noch rein manuell vermessen. Der Fibertracking-Algorithmus wird zur Segmentierung von Sprachbahnen bei Hirntumorpatienten angewendet, bei denen der Tumor in der Nähe einer Sprachbahn angesiedelt ist und operiert werden soll. Bei diesen neurochirurgischen Eingriffen ist eine genaue Segmentierung extrem wichtig, um eine Beschädigung gesunder Gehirnareale beim operativen Eingriff zu vermeiden. Die Evaluationsergebnisse und die gut strukturierte und einfache Benutzung zeigen, dass sich 3D Slicer in diesen Bereichen bereits heute für den klinischen Einsatz eignet und eine Alternative zu teuren, nicht in jeder Klinik zur Verfügung stehenden kommerziellen Produkten sein kann.

Die Beiträge zur Unterstützung von intraoperativen Therapien realisieren zum einen erstmals die erfolgreiche Integration eines offenen medizinischen Netzwerkprotokolls (OpenIGTLink) in die medizinische Plattform MeVisLab. Zum anderen wird die Konzeption und Implementierung eines medizinischen Software-Prototypen (*iGyne*) zur Unterstützung der intraoperativen gynäkologischen Brachytherapie

vorgestellt. Durch die Integration von OpenIGTLink ist es jetzt möglich, mit MeVisLab-Prototypen medizinische Hardware wie das magnetische Trackingsystem von NDI Aurora direkt anzusteuern. Der iGyne-Prototyp hilft den behandelnden Ärzten bei der Auswahl und besonders bei der Positionierung von Nadeln und wurde parallel zu intraoperativen gynäkologischen Brachytherapie-Eingriffen in einem multimodalen Operationssaal im Brigham & Women's Hospital der Harvard Medical School in Boston (USA) getestet.

1.2. Medizinische Grundlagen

In diesem Abschnitt werden die medizinischen Grundlagen der vorliegenden Arbeit präzise dargelegt. Dazu gehören neurochirurgische Erkrankungen im Bereich des Kopfes und der Wirbelsäule und die neurochirurgische Volumetrie zur Ermittlung des Tumorvolumens eines Patienten. Außerdem werden zwei medizinische Bildgebungsverfahren, die Computertomographie (CT) und die Magnetresonanztomographie (MRT), beschrieben. Abschließend wird in diesem Abschnitt die gynäkologische Brachytherapie vorgestellt, eine Behandlungsform für bösartige gynäkologische Tumore.

1.2.1. Neurochirurgische Erkrankungen

Die häufigsten hirneigenen Tumore sind Gliome, die von den Stützzellen des Gehirns ausgehen. Die Ursprungszelle bestimmt ihre Entität, d.h. Astrozytome entstehen aus Astrozyten, Oligodendrogliome aus Oligodendrozyten und Ependymome aus Ependymzellen. Außerdem kennt man Mischformen dieser histopathologischen Subtypen, zum Beispiel Oligoastrozytome; die häufigsten Gliome sind mit über 60% Astrozytome. Es werden vier Subtypen unterschieden (I-IV), deren Klassifikation nach Vorgaben der Weltgesundheitsorganisation (WHO, World Health Organisation) festgelegt wurde, wobei die am seltensten auftretenden Grad I-Tumore als wenig aggressiv und proliferativ einzustufen sind, aber über 70% zu den malignen Gliomen – WHO Grad III (anaplastisches Astrozytom) und den besonders bösartigen Grad IV-Gliomen (Glioblastoma multiforme) – zählen. Seine Bezeichnung Glioblastoma multiforme (GBM) verdankt der Grad IV-Tumor seiner histopathologischen Erscheinung. Das Glioblastom als häufigster maligner hirneigener Tumor zählt gleichzeitig zu den bösartigsten Neoplasien des menschlichen Organismus. Das interdisziplinäre Behandlungskonzept vereint heute die bestmögliche mikrochirurgische Resektion mit Strahlentherapie und Chemotherapie. Auch neueste Bestrahlungskonzepte sowie die Etablierung von Alkylanzien (besonders häufig wird Temozolomid eingesetzt) als erprobte Chemotherapeutika konnten die Überlebensrate von der Diagnose bis zum Tod des Patienten bisher auf nicht mehr als durchschnittlich 15 Monate steigern [3], [36], [44].

Auch beim Hypophysenadenom – einem Tumor der Hypophyse (Hirnanhangsdrüse) – werden, abhängig von seiner Ausdehnung, vier Grade unterschieden: Grad I - intrasellär (Mikroadenom), Grad II - intrasellär, ggf. suprasellär (Makroadenom), Grad III - invasiv lokalisiert und Grad IV - invasiv diffus. Der Hypophyse als einer Hormondrüse kommt eine zentrale übergeordnete Rolle bei der Regulation des neuroendokrinen Systems (Hormonsystems) im Körper zu. Sie befindet sich in einer

knöchernen Vertiefung der Schädelbasis auf Höhe der Nase und mitten im Schädel (Sella turcica) und setzt sich aus einem Vorder- (Adenohypophyse) und einem Hinterlappen (Neurohypophyse) zusammen, die sich entwicklungsgeschichtlich, histologisch und funktionell unterscheiden [36], [44].

Die veränderte Altersstruktur der Gesellschaft hat zu einem höheren Anteil älterer Menschen in der Bevölkerung geführt, die wiederum häufiger einen operativen Eingriff an der Wirbelsäule benötigen. Denn degenerative Erkrankungen der Wirbelsäule werden vor allem durch altersbedingte Veränderungen der ligamentären und ossären Strukturen und die gleichzeitige Zunahme von Spinalkanalstenosen verursacht. Zur Erkennung knöcherner Strukturen eignen sich Computertomographie (CT)-Scans besser als zum Beispiel Magnetresonanztomographie (MRT)-Aufnahmen, deshalb werden sie bevorzugt zur präoperativen Evaluation der spinalen Knochenstruktur angefertigt [1], [4].

1.2.2. Medizinische Bildgebung

Die Computertomographie (CT) und die Magnetresonanztomographie (MRT) sind die beiden medizinische Bildgebungsverfahren, die für diese Arbeit wesentlich sind. Die Magnetresonanztomographie ist genau wie die Computertomographie eine Methode, Schnittbilder des menschlichen Körpers zu erzeugen. Bereits 1972 wurde der erste Computertomograph als Röntgengerät konstruiert; ein Jahr später, 1973, entwickelten Paul C. Lauterbur und Sir Peter Mansfield die nicht-invasive Bildgebungstechnik der Magnetresonanztomographie. Diese arbeitet mit starken Magnetfeldern, im Gegensatz zur Computertomographie, die mit Hilfe einer Röntgenröhre und mehreren Blenden einen schmalen Fächerstrahl (Röntgenstrahl) erzeugt und damit Querschnittbilder von verschiedenen Körperabschnitten anfertigt. Bei beiden Verfahren erlauben die Schnittbilder die Betrachtung und Beurteilung von Organen und möglicher krankhafter Organveränderungen.

Die Magnetresonanztomographie arbeitet außer mit Magnetfeldern mit elektromagnetischen Wechselfeldern im Radiofrequenzbereich. Durch sie werden bestimmte Atomkerne (meistens die Wasserstoffkerne/Protonen) im Körper gezielt angeregt, um dann wieder in ihren Grundzustand zurückkehren (Relaxation). Die sogenannten Relaxationszeiten bilden die Basis für den Bildkontrast der einzelnen Gewebearten, zu dem auch noch der unterschiedliche Gehalt an Wasserstoffatomen in verschiedenen Geweben (z.B. Muskeln und Knochen) beiträgt. Die beiden T-Kontraste (T1 und T2) kennzeichnen unterschiedliche Relaxationszeiten. Im T1-Kontrast erscheint Liquor dunkel, im T2-Kontrast dagegen hell. Ein weiterer Aspekt ist die Stärke des MRT-Magnetfelds, die sich unmittelbar auf die Signalqualität der gemessenen Daten auswirkt. Standardstärke bei Magnetfeldern für diagnostische Zwecke sind inzwischen 1-1,5 Tesla, wobei zunehmend auch Hochfeldgeräte mit Feldstärken von 3 Tesla zum Einsatz kommen. Diese 3 Tesla sollten allerdings nicht überschritten werden, andernfalls erleiden die Patienten infolge der entstehenden Wirbelströme im Gehirn Schwindel und Übelkeit. Ultrahochfeld-Systeme mit Feldstärken jenseits der 3 Tesla-Grenze werden in der Humanmedizin zurzeit noch ausschließlich für Forschungszwecke, nicht aber für Routineuntersuchungen eingesetzt [17], [36].

Röntgenstrahlung oder andere ionisierende Strahlung wird im MRT-Gerät nicht

erzeugt oder genutzt. Im Gegensatz dazu werden bei der Computertomographie alle Untersuchungen mit Röntgenstrahlen durchgeführt. Dabei durchdringen die Strahlen einen bestimmten Körperabschnitt, wobei sie in den verschiedenen Strukturen (z.B. Knochen, Haut, Fett, Organe und Muskeln) unterschiedlich stark abgeschwächt werden. Detektoren, die sich genau gegenüber der Röntgenröhre befinden, dienen dazu, den abgeschwächten Röntgenstrahl als Signal zu empfangen, elektronisch aufzubereiten und an einen Computer zur Auswertung weiterzuleiten. Die Röntgenröhre und die Detektoren drehen sich langsam um den Patienten und erzeugen dabei verschiedene Projektionen derselben Schicht. Die Aufnahmen werden nach mehrmaligem Wiederholen im Computer zu einem räumlichen Graustufenbild rekonstruiert, das anschließend auf einem Bildschirm betrachtet und ausgewertet werden kann. Durch die guten Kontraste können auf diesen Bildern die verschiedenen Gewebearten ohne Schwierigkeiten unterschieden werden; das macht ein CT-Bild in seiner Qualität und Übersichtlichkeit einem einfachen Röntgenbild im Allgemeinen deutlich überlegen. Mit Hilfe eines Computers ist es auch möglich, ein dreidimensionales Bild zu erzeugen und eine Schichtebene abzubilden, die nicht von anderen Schichten überlagert wird. Die Spiral-Computertomographie (Spiral-CT) als erste von drei Weiterentwicklungen der konventionellen Computertomographie ermöglicht es, durch eine verbesserte Technik größere Körperabschnitte aufzunehmen und ein genaueres dreidimensionales Bild der Gewebe zu erhalten. Die zweite Verbesserung betrifft den Multislice CT-Scanner, bei dem der Detektor aus mehreren Zeilen besteht, die das gleichzeitige Aufnehmen (Scannen) mehrerer Schichten eines Körpers ermöglichen. Bei der dritten Weiterentwicklung, den Dual-Source-Computertomographen (DSCT), verfügen die Spiral-CT über zwei Röntgenstrahler und zwei Detektoren; sie ermöglichen unter anderem Aufnahmen vom rasch schlagenden Herzen in höchster Detailgenauigkeit und Qualität [17], [36].

1.2.3. Neurochirurgische Volumetrie

Für eine genaue Ermittlung des Tumorvolumens ist es nötig, Methoden zu entwickeln, die alle MR-Schichten aus einem Patientendatensatz nutzen, um die Tumorgrenzen zu berechnen. Da eine manuelle Schicht-für-Schicht-Segmentierung durch die behandelnden Ärzte in der klinischen Routine in der Regel zu zeitaufwendig ist, werden meistens einfachere Rechenmethoden, wie die sogenannten geometrischen Modelle, verwendet, um das Tumorvolumen zu bestimmen. Allerdings liefern diese geometrischen Modelle nur eine Approximation des Tumorvolumens. Geometrische Modelle nutzen lediglich einen oder mehrere benutzerdefinierte Durchmesser – die manuell im Gegensatz zu einer Schicht-für-Schicht-Segmentierung sehr schnell bestimmt werden können –, um das Tumorvolumen zu berechnen. Bei einem kugelförmigen Modell zum Beispiel ist das Volumen als $(1/6)\pi d^3$ definiert (d ist hierbei der Durchmesser der maximalen Querschnittsfläche der Pathologie). Bei einem elliptischen Modell dagegen wird das Volumen über $(1/6)\pi abc$ berechnet (a, b, c sind dabei die drei Achsen des Tumors). In einer anderen Methode werden die Radien x, y, und z jeweils in der axialen, sagittalen und koronalen Schicht gemessen. Anschließend wird, basierend auf der Annahme eines kugelförmigen Volu-

mens, die Formel $(4/3)\pi r^3$ für die Volumenberechnung genutzt, wobei r der Durchschnitt der drei Radien x, y und z ist. Bei einer weiteren Methode wird die Größe von Hypophysenadenomen anhand des größten Tumordurchmessers a und senkrecht dazu des größten Durchmessers b bestimmt $(1/6)\pi ab^2$. Zusammenfassend kann gesagt werden, dass die Volumetrie gegenüber der Messung von Durchmessern nach den Response Evaluation Criteria In Solid Tumors (RECIST)-Kriterien oder den verbreiteten Macdonald-Kriterien den Vorteil einer erhöhten Genauigkeit bietet, sie setzt aber ohne algorithmische Unterstützung eine sehr zeitaufwendige manuelle Segmentierung der Läsionen voraus und ist deshalb in der klinischen Routine in der Regel nicht praktikabel [36], [56].

1.2.4. Gynäkologische Brachytherapie

Bösartige gynäkologische Tumore, die Zervixkarzinome (Gebärmutterhalskrebs), Endometriumkarzinome (Krebserkrankung der Gebärmutterschleimhaut), Ovarialkarzinom (Eierstockkrebs), Vaginalkarzinom und Vulvakarzinome (bösartige Tumorerkrankungen der äußeren Geschlechtsteile der Frau) betreffen, tragen erheblich zur Sterblichkeit von Frauen weltweit bei. In den Vereinigten Staaten hat die Anzahl gynäkologischer Krebserkrankungen in den letzten Jahren zugenommen, während die Sterblichkeitsrate relativ stabil bei circa 35% aller Neuerkrankungen verharrte. Das derzeitige Behandlungskonzept für erstmalig auftretende oder wiederkehrende gynäkologische Tumorerkrankungen besteht in der Regel aus einer externen Bestrahlung, gefolgt von einer Brachytherapie. Im Gegensatz zur externen Bestrahlung des Tumors im Beckenbereich durch einen Linearbeschleuniger von außen werden bei der Brachytherapie radioaktive Strahlenquellen mit einer hohen Strahlendosis unmittelbar im Tumorgewebe platziert. Die Platzierung der Strahlenquellen wird in der Regel über interstitielle Applikatoren, zum Beispiel Katheter, vorgenommen. Hierbei ist die optimale Verteilung und Planung der radioaktiven Dosis der einzelnen Katheter besonders wichtig, damit der Tumor, bei gleichzeitiger Schonung der umliegenden gesunden Gewebe und strahlungskritischen Organe (wie Blase, Rektum, Kolon), zerstört werden kann. Je nach Tumorgröße kann die Anzahl der benötigten Katheter von einigen wenigen bis zu mehreren Dutzend reichen. Dabei ist es auch für erfahrene Mediziner nicht möglich, alle Katheter auf der Grundlage vorheriger Patientenaufnahmen ohne ständige Korrekturen zufriedenstellend zu platzieren. Deshalb wird meistens mit dem Setzen von Kathetern um den vaginalen Kanal herum begonnen. Nach weiteren Aufnahmen zur Überprüfung und eventuellen Korrektur der Position der Katheter werden weitere Katheter hinzugefügt. Bei manchen Patientinnen kann dies mehrere Stunden in Anspruch nehmen, eine sehr belastende Therapie [14].

1.3. Technische Grundlagen

1.3.1. Segmentierungsverfahren

Unter Segmentierung versteht man in der Informatik die Aufteilung von Daten in sinnvolle Bereiche. In der medizinischen Bildverarbeitung kann es sich zum Bei-

spiel um einen Tumor handeln, dessen Darstellung aus einer MRT-Aufnahme extrahiert wird. Ein Beispiel zur konkreten Anwendung in der Praxis liefert die Volumetrie: Wenn Mediziner wissen möchten, welches Volumen ein Tumor hat, muss dieser in einem Datensatz segmentiert werden. Diese Segmentierung kann zum einen rein manuell erfolgen, indem Ärzte alle Schichten (im Falle eines 3D-Datensatzes) durchgehen und die Tumorgrenzen Schicht für Schicht einzeichnen. Diese rein manuelle Vorgehensweise ist im Allgemeinen allerdings sehr zeitaufwendig. Eine Segmentierung kann andererseits auch computergestützt erfolgen, d.h., dass speziell entwickelte Algorithmen aus der Informatik zuerst eine automatische Segmentierung (in der Regel in wenigen Sekunden) durchführen. Anschließend überprüfen die Mediziner die Ergebnisse dieser automatischen Segmentierung und nehmen gegebenenfalls Korrekturen vor. In der Bildverarbeitung wurden in den letzten Jahren mehrere Grundprinzipien automatischer Segmentierungsalgorithmen erforscht. Dazu gehören unter anderem die sogenannten Snakes – oder Aktiven Konturen – im Zwei- und Dreidimensionalen. Aktive Konturen werden in der (medizinischen) Bildverarbeitung meistens zur Bestimmung von Objektkonturen oder Oberflächen verwendet und besitzen interne und externe Energien. Dabei regelt die interne Energie die Steifigkeit der Objektkontur bzw. Oberfläche. Die externe Energie dagegen setzt sich aus Bildinformationen – zum Beispiel aus einem Kantenfilter – zusammen. Eine weitere Klasse von Segmentierungsalgorithmen sind statistische Ansätze wie die Active Appearance Models (AAM). Bei diesen Ansätzen ist ein statistisches Modell der zu segmentierenden Struktur nötig. Dieses Modell wird anhand von manuell segmentierten Strukturen erstellt. Dabei soll das Modell möglichst die Vielgestalt der Struktur bzw. deren Konturen abdecken, um später neue, unbekannte Konturen automatisch zu segmentieren. Aus den Objekten fließen jeweils die Formen (Shapes) und die Texturen in das statistische Modell ein. Eine dritte Klasse von Bildsegmentierungsverfahren sind graphbasierte Ansätze. Bei graphbasierten Ansätzen wird das Bild als Graph repräsentiert. Dabei stellen einzelne Bildpunkte die Knoten im Graphen, und aus den Beziehungen zwischen den Bildpunkten ergeben sich die Kanten. Nachdem ein Graph aufgestellt ist, wird das gesuchte Objekt durch einen Min-Cut-Algorithmus vom Hintergrund getrennt [17], [36].

1.3.2. MeVisLab

Das MeVis Center für Medical Diagnostic Systems and Visualization in Bremen entwickelt wissenschaftliche Methoden und Software für Computerunterstützung in der Medizin und Radiologie. Dazu gehören unter anderem die computergestützte Diagnose, Therapieplanung, Therapieüberwachung, computergestütztes Lernen und computergestütztes Ausbilden. Es sollen vor allem praktikable Lösungen für klinisch relevante Probleme gefunden werden. Dabei wird das aktuelle Wissen von Naturwissenschaftlern, Informatikern und Mathematikern genutzt und vereinigt. MeVisLab, die medizinische Forschungs- und Prototyping Plattform von MeVis, ist als reine Entwicklungsumgebung für medizinische Bildverarbeitung und Visualisierung gedacht. Innerhalb von MeVisLab existiert inzwischen eine große Anzahl von Modulen aus der (medizinischen) Bildverarbeitung, die einem Entwickler viele einfache Aufgaben abnehmen. Dazu gehören zum Beispiel die Module zum Laden

und zur 2D- und 3D-Darstellung von Patientendaten; wobei MeVisLab das objektorientierte Toolkit Open Inventor von Silicon Graphics (SGI) zur Programmierung von dreidimensionalen Graphiken nutzt. Der Programmierer kann sich dadurch auf das eigentliche Problem konzentrieren und sein Projekt effizienter realisieren. Die drei unterschiedlichen MeVisLab-Modularten sind Inventor-Module (visualisierende Module, für die Darstellung von Daten zuständig); ML-Module (grundlegende Module für die reine Bildverarbeitung, die sich nur auf die Bilddatensätze beziehen); Macro-Module (zusammengesetzte Module, die als kleinste Einheiten ML-Module und OpenInventor-Module enthalten). Zusätzlich können eigene Algorithmen mit Hilfe von in C++ programmierten DLLs unter MeVisLab eingebunden werden. Alle diese Module können über einen oder mehrere Ein- und Ausgänge verfügen, wobei in MeVisLab drei verschiedene Ein- und Ausgangstypen vorhanden sind. Über die sogenannten ML-Anschlüsse – dargestellt als Dreieckssymbole – werden Bilddaten zwischen den Modulen ausgetauscht; über Halbkreissymbole werden sogenannte Inventor-Strukturen (wie Knoten oder polygonale Netze) empfangen und gesendet; Quadrat-Symbole werden bei Anschlüssen für abstrakte Datenstrukturen verwendet [17], [36].

1.3.3. 3D Slicer

Die Software 3D Slicer (oder kurz Slicer) ist genau wie MeVisLab eine plattformunabhängige Forschungs- und Prototyping-Umgebung für die medizinische Bildverarbeitung bzw. die Entwicklung von medizinischen Anwendungen. Im Gegensatz zu MeVisLab ist Slicer komplett kostenlos und *Open Source* und wird größtenteils über Gelder des National Institutes of Health (NIH) finanziert. Ursprünglich ist Slicer 1998 aus einer Masterarbeit im Surgical Planning Laboratory des Brigham and Women's Krankenhauses in Boston hervorgegangen. Ähnlich wie MeVisLab können eigene Algorithmen über C++-Module in Slicer integriert werden, und es stehen für beide Plattformen Toolkits und Bibliotheken wie ITK und VTK aus der (medizinischen) Bildverarbeitung zur Verfügung, genauso wie die Programmiersprache Python, die hauptsächlich für Oberflächengestaltung bzw. Interaktion genutzt wird. Allerdings ist Slicer gegenüber MeVisLab stärker anwendungsorientiert. Nach der Slicer-Installation kann jeder Benutzer unmittelbar medizinische Daten laden und verarbeiten. Unter MeVisLab muss im Allgemeinen erst ein Netzwerk aus Modulen erstellt werden, was gewisse Kenntnisse voraussetzt, dafür können hier sehr schnell und einfach die eigenen C++-Module integriert werden, was wiederum unter Slicer mehr Aufwand erfordert. Ein wichtiger Fokus liegt bei Slicer auf der Verbreitung von Algorithmen und Anwendungen, da diese nach einer Freigabe von jedem, der Slicer installiert hat, nachgeladen werden können und damit prinzipiell überall und jederzeit zur Verfügung stehen. Unter MeVisLab dagegen generiert man im Allgemeinen Software-Installer, die klinischen Partnern auf Anforderung zur Erprobung bereitgestellt werden [10], [11].

1.3.4. OpenIGTLink

OpenIGTLink ist ein offenes, einfaches und erweiterbares Netzwerkprotokoll für bildgestützte Therapien (Image-Guided Therapies (IGT)). Die erste Spezifikation

des Protokolls wurde während einer Zusammenarbeit zwischen akademischen, klinischen und industriellen Partnern zum Zweck eines integrierten Robotersystems für MR-gestützte Prostataeingriffe entwickelt. Das Protokoll wurde speziell für die Benutzung der Verarbeitungsschicht des TCP/IP-Stack konzipiert. Dies erlaubt es Forschern, Prototypensysteme zu entwickeln, um mehrere medizinische Geräte durch die Benutzung der Standardnetzwerkinfrastruktur zu vernetzen. Im Gegensatz zu anderen Kommunikationsstandards für medizinische Geräte beinhaltet das OpenIGTLink-Protokoll keinen Mechanismus zum Einrichten und Verwalten einer Session. Das Protokoll definiert lediglich eine Reihe von Nachrichten, um die Kommunikation zwischen den Geräten zu regeln. Dazu gehört die Übertragung von Koordinaten, Bildern und Statusmeldungen; alle Nachrichten enthalten gerade so viele Informationen, wie nötig sind, um vom Empfänger interpretiert zu werden. Eine Nachricht beginnt dabei immer mit einem 58-Byte Header, der für alle Nachrichtentypen gleich ist, gefolgt vom Nachrichten-Body. Der Nachrichten-Body variiert je nach Datentyp, der seinerseits im Header definiert ist. Da jeder kompatible Empfänger den Header interpretieren kann, der wiederum die Größe und den Datentyp des Bodys definiert, kann er auch jede Nachricht *verarbeiten*. Das gilt sogar für Nachrichten mit unbekanntem Datentyp, indem diese ignoriert werden, ohne das System zum Absturz zu bringen. Demzufolge können Entwickler eigene Datentypen definieren und gleichzeitig die Kompatibilität zu allen Empfängern aufrechterhalten, auch zu solchen, die diese neuen Datentypen (noch) nicht interpretieren können [13].

1.4. Eigene Publikationen

Während der Forschungsarbeit zu dieser Habilitation sind Ergebnisse in Form von begutachteten (peer-reviewed) Veröffentlichungen in Fachzeitschriften, auf Konferenzen und Kongressen publiziert und vorgestellt worden. Diese Publikationen sollen im Folgenden chronologisch aufgeführt werden:

- ***J. Egger**, T. Kapur, T. Dukatz, M. Kolodziej, D. Zukić, B. Freisleben, C. Nimsky. Square-Cut: A Segmentation Algorithm on the Basis of a Rectangle Shape. PLoS One, 2012; 7(2):e31064. Epub 2012 Feb 21.* Entwicklung eines Algorithmus zur Segmentierung von Wirbeln in 2D. Der Ansatz nutzt eine rechteckige Vorlage, um einen Graphen aufzubauen und das Segmentierungsergebnis zu berechnen [1].

- ***J. Egger**, J. Tokuda, L. Chauvin, B. Freisleben, C. Nimsky, T. Kapur, W. M. Wells. Integration of the OpenIGTLink Network Protocol for Image-Guided Therapy with the Medical Platform MeVisLab. Int J Med Robot. 2012 Sep; 8(3):282-90. doi: 10.1002/rcs.1415. Epub 2012 Feb 28.* In diesem Beitrag wurde die Integration des OpenIGTLink-Netzwerkprotokolls in die medizinische Prototyping-Plattform MeVisLab vorgestellt. Die Integration wurde u.a. anhand eines NDI-Navigationssystems getestet [13].

- ***J. Egger**, T. Dukatz, B. Freisleben, C. Nimsky. Ein semiautomatischer Ansatz zur Flächenbestimmung von Wirbeln in MRT-Aufnahmen. In: Proceedings of Bildver-*

arbeitung für die Medizin (BVM) – Algorithmen - Systeme - Anwendungen, Springer Press, pp. 274-279, Berlin, Germany, March 2012. Auf dieser Konferenz wurden die ersten Ergebnisse eines semiautomatischen Ansatzes zur Flächenbestimmung von Wirbeln in MRT-Aufnahmen vorgestellt [2].

- ***J. Egger**, B. Freisleben, C. Nimsky, T. Kapur. Template-Cut: A Pattern-Based Segmentation Paradigm. Sci Rep., Nature Publishing Group (NPG), 2012; 2:420. Epub 2012 May 24.* Vorstellung eines vorlagenbasierten Algorithmus zur Segmentierung von Objekten in 2D und 3D. In dem Beitrag wird gezeigt, wie Graphen anhand von unterschiedlichen Vorlagen aufgebaut und zur Segmentierung genutzt werden können [3].

- *T. Kapur, **J. Egger**, A. Damato, E. Schmidt, A. Viswanathan. 3-T MR-guided brachytherapy for gynecologic malignancies. Magn Reson Imaging. 2012 Nov; 30(9):1279-90. doi: 10.1016/j.mri.2012.06.003. Epub 2012 Aug 13.* In dieser Arbeit wurde erstmals die Konzeption und Implementierung eines medizinischen Software-Prototypen zur Unterstützung der intraoperativen gynäkologischen Brachytherapie vorgestellt. Dabei wurde die Integrierung der Software in das aktuelle klinische Protokoll aufgezeigt [14].

- ***J. Egger**, T. Kapur, C. Nimsky, R. Kikinis. Pituitary Adenoma Volumetry with 3D Slicer. PLoS One, 2012; 7(12):e51788. Epub 2012 Dec 11.* Evaluierung der semiautomatischen Segmentierung von Hypophysenadenomen mit der frei verfügbaren Open Source-Plattform 3D Slicer. Dadurch kann die rein manuelle Vermessung des Volumens unterstützt und beschleunigt werden [10].

- *D. Kuhnt, M. H. A. Bauer, **J. Egger**, D. Merhof, M. Richter, T. Kapur, J. Sommer, C. Nimsky. Fiber tractography based on diffusion tensor imaging (DTI) compared with High Angular Resolution Diffusion Imaging (HAR-DI) with compressed sensing (CS) – initial experience and clinical impact. Neurosurgery, Volume 72, pp. A165-A175, January 2013.* Segmentierung und Evaluierung von Sprachbahnen in Datensätzen von Hirntumorpatienten auf verschiedenen Plattformen. Dazu gehört auch der Algorithmus der kostenlosen und frei verfügbaren Plattform 3D Slicer [12].

- ***J. Egger**, T. Kapur, A. Fedorov, S. Pieper, J. V. Miller, H. Veeraraghavan, B. Freisleben, A. J. Golby, C. Nimsky, R. Kikinis. GBM Volumetry using the 3D Slicer Medical Image Computing Platform. Sci Rep., Nature Publishing Group (NPG), 2013; 3:1364. Epub 2013 March 4.* Evaluierung der semi-automatischen Segmentierung von Glioblastomen mit der frei verfügbaren Open Source-Plattform 3D Slicer. Dadurch kann eine rein manuelle Vermessung des Volumens unterstützt und beschleunigt werden [11].

- *R. Schwarzenberg, B. Freisleben, R. Kikinis, C. Nimsky, **J. Egger**. Ein kubusbasierter Ansatz zur Segmentierung von Wirbeln in MRT-Aufnahmen. In: Proceedings*

of Bildverarbeitung für die Medizin (BVM) – Algorithmen - Systeme - Anwendungen, Springer Press, pp. 69-74, Heidelberg, Germany, March 2013. Vorstellung der ersten Ergebnisse eines graphbasierten Ansatzes zur Wirbelsegmentierung im Dreidimensionalen, wobei der Graph anhand einer würfelförmigen Vorlage konstruiert wird [4].

- ***J. Egger**, Image-guided therapy system for interstitial gynecologic brachytherapy in a multimodality operating suite. SpringerPlus, 2:395, August 2013.* Vorstellung eines umfassenden bildgestützten Systems für die gynäkologische Brachytherapie in einem multimodalen Operationssaal. Das System deckt die prä-, intra- und postoperative Behandlungsphase bei einer interstitiellen gynäkologischen Brachytherapie ab [16].

- ***J. Egger**. PCG-Cut: Graph Driven Segmentation of the Prostate Central Gland. PLoS One, 2013; 8(10):e76645. Epub 2013 Oct 11.* Vorstellung einer graphbasierten Segmentierung von Prostatadrüsen anhand einer Kugelvorlage zur automatischen Bestimmung der Grenzen zwischen Prostatadrüsen und umliegenden Organen [6].

- ***J. Egger**, T. Lüddemann, R. Schwarzenberg, B. Freisleben, C. Nimsky. Interactive-Cut: Real-Time Feedback Segmentation for Translational Research. Comput Med Imaging Graph. Available online 11 February 2014.* Interaktiver Segmentierungsalgorithmus, der einem Benutzer in Echtzeit das Segmentierungsergebnis anzeigt. Der Algorithmus nutzt zur Segmentierung verschiedene Vorlagen und benötigt nur einen Saatpunkt vom Benutzer [7].

- ***J. Egger**. Semi-automatische Echtzeit-Konturierung – Ein vorlagenbasierter skalierungsinvarianter Ansatz. In: Proceedings of Bildverarbeitung für die Medizin (BVM) – Algorithmen - Systeme - Anwendungen, Springer Press, pp. 366-371, Aachen, Germany, March 2014.* Auf dieser Konferenz wurden die ersten Ergebnisse eines semi-automatischen und skalierungsinvarianten Segmentierungsalgorithmus zur Echtzeit-Konturierung vorgestellt [8].

- *X. Chen, **J. Egger**. Development of an Open Source Software Module for Enhanced Visualization during MR-Guided Interstitial Gynecologic Brachytherapy. SpringerPlus, 3:167, March 2014.* Detaillierte Vorstellung eines Software-Moduls zur erweiterten Visualisierung bei der MR-gestützten interstitiellen gynäkologischen Brachytherapie. Die Software ermöglicht u.a. die Registrierung eines gynäkologischen Brachytherapie-Instruments in einen intraoperativen Datensatz einer Patientin [15].

- *R. Schwarzenberg, B. Freisleben, C. Nimsky, **J. Egger**. Cube-Cut: Vertebral Body Segmentation in MRI-Data through Cubic-Shaped Divergences. PLoS One, 2014; 9(4):e93389. Epub 2014 Apr 04.* Detaillierte Darstellung und Evaluierung eines graphbasierten Ansatzes zur dreidimensionalen Wirbelsegmentierung in MRT-

Aufnahmen. Dabei wird der Graph anhand einer würfelförmigen Vorlage konstruiert, um einen Wirbelkörper bei der Segmentierung zu bevorzugen [5].

- ***J. Egger***. *Refinement-Cut: User-Guided Segmentation Algorithm for Translational Science. Sci Rep., Nature Publishing Group (NPG), 2014; 4:5164. Epub 2014 Jun 4.* In diesem Beitrag wird ein Echtzeit-Segmentierungsansatz vorgestellt, bei dem der Benutzer die Segmentierung interaktiv durch zusätzliche Saatpunkte verfeinern kann. Dadurch kann die semi-automatische Segmentierung auch in schwierigen Fällen zu einem zufriedenstellenden Ergebnis geführt werden [9].

Dabei gibt es bei den Publikationen dieser kumulativen Habilitationsschrift keine Übereinstimmungen mit den Publikationen aus den nachfolgend aufgeführten Dissertationen und mit sonstigen eigenen Publikationen:

- *Prä- und postoperative Segmentierung und virtuelles Stenting von Aneurysmen und Stenosen.* Dissertation (Dr. rer. nat.), Fachbereich Mathematik und Informatik, Philipps-Universität Marburg, 215 Seiten, Juli 2009 [17]-[35];

- *Intraoperative Visualisierung multimodaler Daten in der Neurochirurgie.* Dissertation (Dr. rer. physiol.), Fachbereich Medizin, Philipps-Universität Marburg, 223 Seiten, Juni 2012 [36]-[45];

- Weitere Publikationen: [46]-[77].

1.5. Struktur

Das erste Kapitel dieser Arbeit enthält neben der Auflistung und Kurzvorstellung eigener Publikationen die medizinischen und technischen Grundlagen, die für diese Habilitationsschrift wesentlich sind. Die nächsten drei Kapitel bilden den Kern der Arbeit und beginnen jeweils mit einer Einleitung, in der die Probleme der klinischen Praxis und die aktuelle technische Herangehensweise diskutiert werden. Im Anschluss an die Einleitungen werden die eigenen Ansätze dargelegt. Die drei Kapitel enden jeweils mit einer Zusammenfassung, in denen diskutiert wird, welche Forschungsfragen angegangen bzw. gelöst wurden. Es werden aber auch Einschränkungen der eigenen Ansätze erörtert und gezeigt, für welche klinischen Fragestellungen sich die Ansätze nicht eignen. Im Anhang sind die eigenen Publikationen dieser kumulativen Habilitationsschrift angefügt.

2. Segmentierung medizinischer Bilddaten anhand von vorlagenbasierten Algorithmen

2.1. Einleitung

Mit Hilfe der Segmentierung werden in der medizinischen Bildverarbeitung Objekte in Patientenaufnahmen extrahiert. Dabei kann es sich um gesunde Strukturen handeln, meistens werden aber krankhafte Veränderungen, z.B. Tumore, betrachtet. Zur automatischen Segmentierung existieren verschiedene Algorithmen, die wiederum in einzelne Klassen eingeteilt sind. Zu einer dieser Klassen gehören die graphbasierten Segmentierungsalgorithmen, die ein Bild als Graphen mit Knoten und Kanten interpretieren. Anschließend wird ein minimaler Schnitt berechnet, der die Knoten in disjunkte Mengen teilt. Ziel ist hierbei, dass jede Knotenmenge einen bestimmten Bereich im Bild beschreibt. Bei zwei disjunkten Mengen kann das zum einen eine zu segmentierende Pathologie (z.B. ein Tumor) sein und zum anderen alle Strukturen, die nicht zum Tumor gehören, im Allgemeinen als *Hintergrund* bezeichnet.

2.2. Flächenbestimmung von Wirbeln in MRT-Aufnahmen

In den Arbeiten [1], [2] wird ein graphbasierter Segmentierungsalgorithmus für Wirbel vorgestellt. Das Verfahren nutzt eine rechteckige Vorlage, um den Graphen aufzubauen. Bei dieser Vorgehensweise bevorzugt der s-t-Schnitt eine rechteckige Struktur. Dies ist das erste Mal, dass bei einem graphbasierten Verfahren die Knoten des Graphen nicht gleichmäßig und äquidistant auf einem Bild verteilt werden, sondern anhand einer rechteckigen Vorlage. Der präsentierte Ansatz kann auch zur Segmentierung anderer rechteckiger Objekte genutzt werden und eignet sich besonders, wenn Bereiche des Objekts nicht vom Hintergrund zu unterscheiden sind.

Das vorgestellte Verfahren lässt sich in zwei Schritte unterteilen: Zuerst wird von einem benutzerdefinierten Saatpunkt aus (der innerhalb des Wirbels liegt) ein gerichteter 2D-Graph aufgebaut. Dann wird der minimale s-t-Schnitt auf diesem Graphen berechnet und dadurch der Wirbel vom Hintergrund getrennt (Abbildung 1).

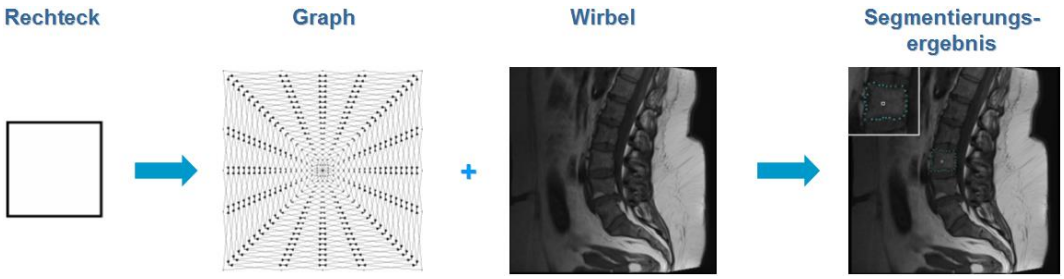

Abbildung 1 – Prinzipieller Ablauf des Verfahrens: Anhand einer rechteckigen Vorlage wird der Graph konstruiert und an der Position des benutzerdefinierten Saatpunktes im Bild positioniert. Anschließend liefert der s-t-Schnitt die Wirbelkontur bzw. Fläche zurück.

Die Knoten des Graphen werden durch Abtasten von Strahlen gewonnen, die durch die Kontur einer rechteckigen Vorlage verlaufen (Mittelpunkt der Vorlage ist der Saatpunkt). Die abgetasteten Punkte sind die Knoten $n \in V$ vom Graphen $G(V,E)$ und $e \in E$ ist ein Satz von Kanten. Es gibt zwei Arten von Kantentypen: Kanten, die den Graphen mit einer Quelle s und einer Senke t verbinden, und Kanten innerhalb des Graphen. Bei den Kanten innerhalb des Graphen gibt es wiederum mehrere Arten. Die Kanten $\langle v_i, v_j \rangle \in E$ des Graphen G verbinden immer zwei Knoten v_i, v_j innerhalb des Graphen. Es gibt unter anderem zwei ∞-gewichtete Kanten: z-Kanten A_z und r-Kanten A_r. Dabei ist Z die Anzahl der abgetasteten Punkte entlang eines Strahls $z = (0,...,Z-1)$ und R ist die Anzahl der Strahlen, die durch die Kontur des Rechtecks gesendet werden $r = (0,...,R-1)$, wobei $V(x_n, y_n)$ ein Nachbarpunkt von $V(x,y)$ ist (Abbildung 2):

$$A_z = \{\langle V(x,y), V(x,y-1)\rangle \mid y > 0\}$$
$$A_r = \{\langle V(x,y), V(x_n, \max(0, y-\Delta_r))\rangle\}$$

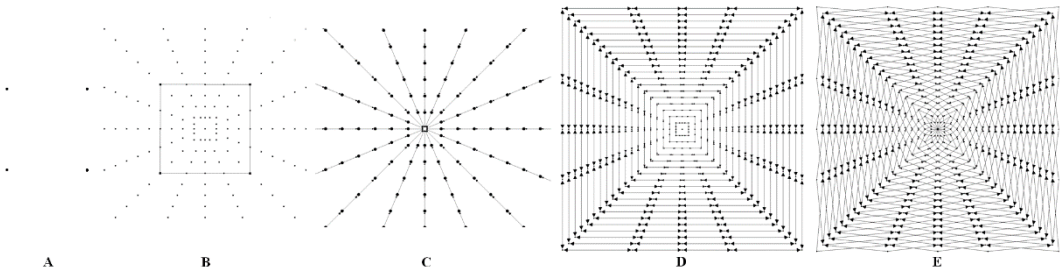

Abbildung 2 – A: rechteckige Vorlage, definiert durch vier Eckpunkte. B: Knoten, die anhand der Vorlage generiert wurden. C: z-Kanten A_z entlang der Strahlen. D: r-Kanten A_r zwischen benachbarten Strahlen mit $\Delta_r = 0$. E: r-Kanten A_r zwischen benachbarten Strahlen mit $\Delta_r = 1$.

Die Kanten zwischen zwei Knoten entlang eines Strahls A_z stellen sicher, dass alle Knoten unterhalb einer Kontur im Graphen in einem *closed set* enthalten sind. Die Kanten A_r zwischen den Knoten der unterschiedlichen Strahlen schränken die Anzahl der möglichen Segmentierungen ein und erzwingen eine Glätte der resultierenden Kontur mit Hilfe eines Parameters Δ_r. Je größer Δ_r ist, desto mehr mögliche Segmentierungen gibt es. Nach der Graphkonstruktion wird das *closed set* des Graphen mit minimalen Kosten anhand eines s-t-Schnittes berechnet. Dieser liefert eine optimale Segmentierung des Wirbels unter dem Einfluss des Parameters Δ_r, der die Steifigkeit der Kontur beeinflusst (Abbildung 3). Ein Deltawert von Null stellt sicher, dass das Segmentierungsergebnis ein Rechteck ist. Die Kosten $w(x, y)$ für die Kanten $v \in V$ zur Quelle und Senke werden folgendermaßen berechnet: Gewichte haben einen Wert von $c(x, y)$, wenn z Null oder maximal ist, ansonsten $c(x, y) - c(x, y-1)$, wobei $c(x, y)$ der Betrag der Differenz zwischen einem durchschnittlichen Grauwert des Wirbels und dem Grauwert des Voxels an Position (x, y) ist. Der durchschnittliche Grauwert zur Berechnung der Kosten ist essentiell für die Segmentierung. Basierend auf der Annahme, dass der benutzerdefinierte Saatpunkt innerhalb des Wirbels sitzt, kann der durchschnittliche Grauwert allerdings automatisch bestimmt werden. Dazu wird über eine Region der Dimension d (ca. 1 cm) um den benutzerdefinierten Saatpunkt (s_x, s_y) integriert:

$$\int_{-d/2}^{d/2} \int_{-d/2}^{d/2} T(s_x + x, s_y + y) dx dy$$

und anschließend durch die Voxelanzahl geteilt (Mittelwert).

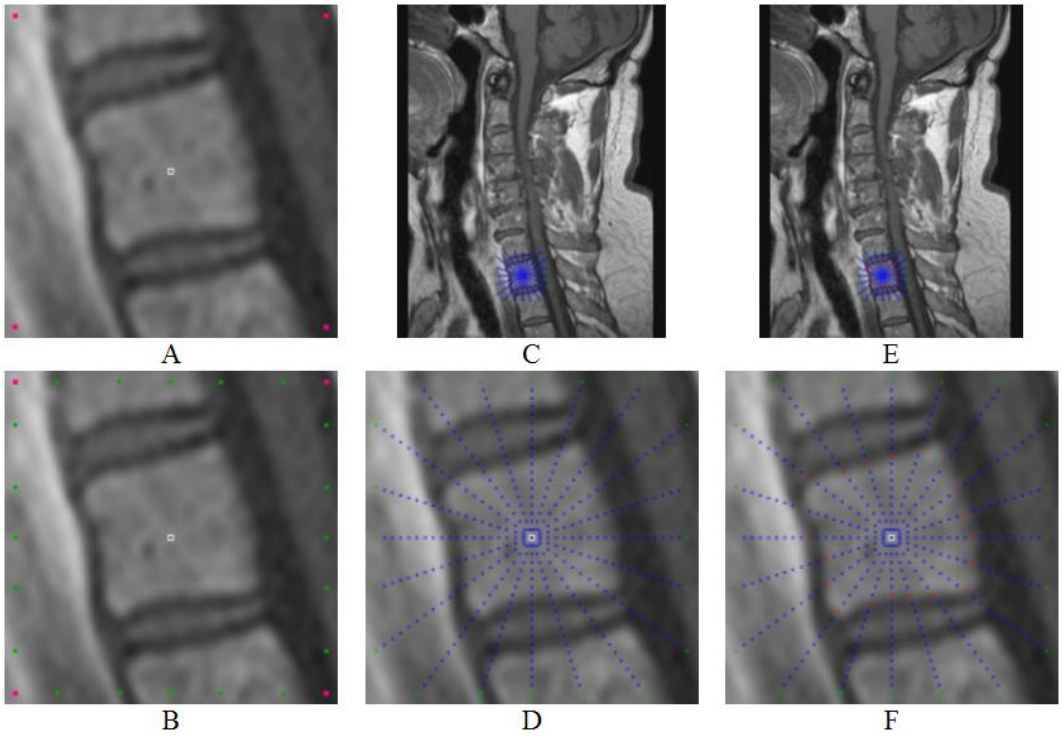

Abbildung 3 – Schritt-für-Schritt-Konstruktion eines Graphen und anschließende Segmentierung eines Wirbels. A: Saatpunkt (weiß) und die Ecken einer Vorlage (pink). B: Schnittpunkte der ausgesandten Strahlen mit der Vorlage (grün). C und D: Abgetastete Knoten für den Graphen (blau). E und F: Segmentierungsergebnis (rot).

Die Realisierung des Ansatzes erfolgte mit C++ innerhalb der medizinischen Plattform MeVisLab (http://www.mevislab.de). Die Graphkonstruktion und die Berechnung eines s-t-Schnitts benötigten in unserer Implementierung ca. eine Sekunde (gemessen auf einem Intel Core i5-750 CPU, 4x2.66 GHz, 8 GB RAM, Windows XP Professional x64 Version, 2003, SP 2). Dagegen nahm eine Segmentierung, von Ärzten manuell vorgenommen, ca. eine Minute in Anspruch. Zum Testen des Ansatzes standen vierzehn Datensätze von zwölf Patienten zur Verfügung, wobei nicht für alle Wirbel manuelle Expertensegmentierungen vorhanden waren. Tabelle 1 und Tabelle 2 listen detailliert die Evaluationsergebnisse für Segmentierungen des Verfahrens für neun Wirbel auf. Neben dem Volumen in Kubikmillimetern und der Anzahl der Voxel ist der Dice Similarity Coefficient (DSC) angegeben. Der DSC berechnet sich aus der Formel:

$$DSC = \frac{2 \cdot V(A \cap R)}{V(A) + V(R)}$$

wobei A die Binärmaske der automatischen Segmentierung und R die Binärmaske der Referenzsegmentierung ist. V ist das Volumen (in mm^3) der Voxel in einer Binärmaske. Dazu wird die Anzahl der Voxel in einer Binärmaske gezählt und mit

der Voxelgröße multipliziert (Abbildung 4). Der präsentierte Ansatz kann auch zur Segmentierung anderer rechteckiger Objekte genutzt werden und eignet sich besonders, wenn Bereiche des zu segmentierenden Objekts nicht vom Hintergrund zu unterscheiden sind (Abbildung 5).

Nr.	Volumen in mm^3		Anzahl der Voxel		DSC (%)
	manuell	automatisch	manuell	automatisch	
1	417,236	378,662	1709	1551	90,78
2	438,721	397,705	1797	1629	90,83
3	461,914	427,49	1892	1751	88,99
4	457,275	439,453	1873	1800	92,02
5	510,498	490,723	2091	2010	93,05
6	430,908	481,201	1765	1971	87,37
7	404,541	402,832	1657	1650	90,35
8	414,795	377,686	1699	1547	90,39
9	247,803	242,92	1015	995	94,93

Tabelle 1 – Direkter Vergleich der manuellen und der automatischen Segmentierungen für neun Wirbel anhand des Dice Similarity Koeffizienten (DSC).

	Volumen in mm^3		Anzahl der Voxel		DSC (%)
	manuell	automatisch	manuell	automatisch	
Min.	247,803	242,92	1015	995	87,37
Max.	510,498	490,723	2091	2010	94,93
$\mu \pm \sigma$	$420{,}41 \pm 72{,}22$	$404{,}30 \pm 72{,}98$	1722	1656	$90{,}97 \pm 2{,}2$

Tabelle 2 – Evaluationsergebnisse: Minimum (Min.), Maximum (Max.), Mittelwert μ und Standardabweichung σ für neun Wirbel.

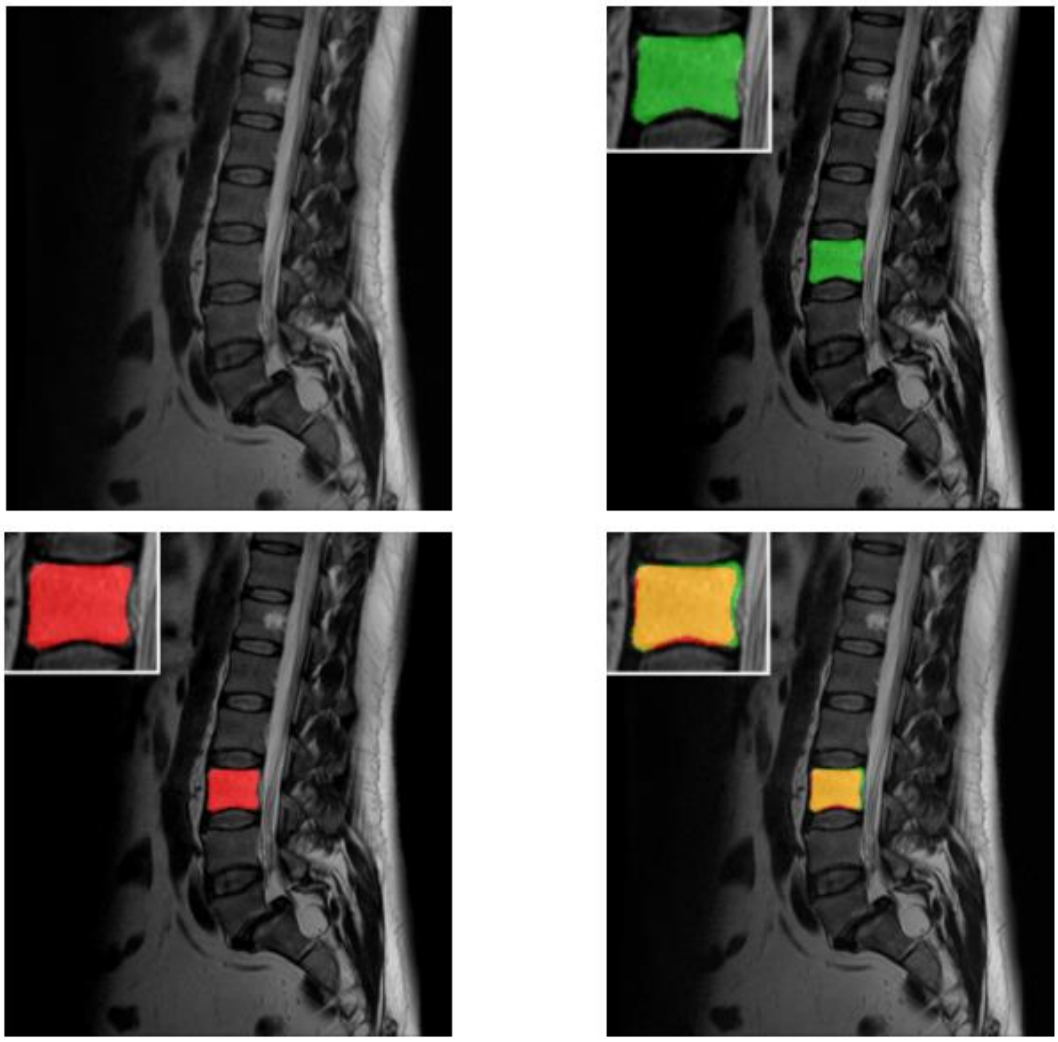

Abbildung 4 – Quantitative Evaluierung des Ansatzes anhand des Dice Similarity Koeffizienten (DSC): MRT-Datensatz (links oben), Fläche eines Wirbels (grün), die aus der manuellen Konturierung durch einen Neurochirurgen generiert wurde (rechts oben), Fläche des Wirbels (rot), berechnet mit dem vorgestellten Verfahren (links unten), und direkter Vergleich beider Segmentierungen (rechts unten).

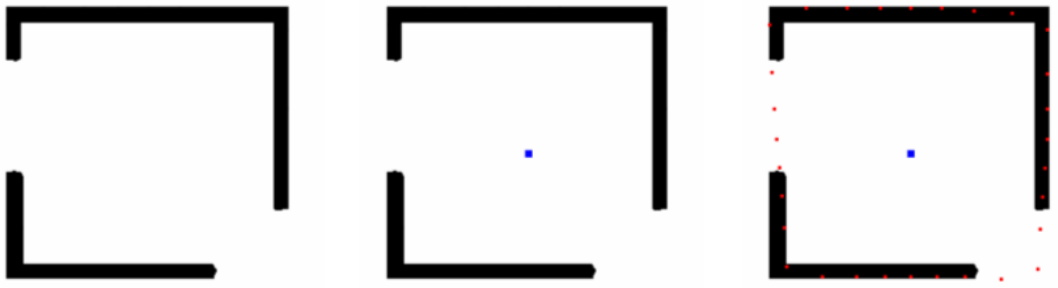

Abbildung 5 – Das vorgestellte Verfahren kann auch zur Segmentierung anderer rechteckiger Objekte genutzt werden, die subjektive Konturen aufweisen: Zu segmentierendes Objekt (schwarz), wobei nicht nur eine gerade Kante, sondern auch eine Ecke fehlt (links), benutzerdefinierter Saatpunkt (blau) innerhalb des Objektes (Mitte) und Segmentierungsergebnis (rot), bei dem die fehlende Ecke rechts unten rekonstruiert wurde (rechts).

2.3. Vorlagenbasierte Segmentierung von Pathologien in Patientendaten

In diesem Beitrag [3] wird ein skalierungsinvariantes und vorlagenbasiertes Segmentierungsparadigma vorgestellt, das einen Graphen konstruiert und einen minimalen s-t-Schnitt durchführt, um ein Objekt vom Hintergrund zu trennen. Normalerweise verteilen graphbasierte Ansätze die Knoten des Graphen gleichmäßig und äquidistant auf einem Bild und verwenden anschließend eine Kostenfunktion, damit der s-t-Schnitt eine bestimmte Struktur bevorzugt. Diese Strategie erlaubt es einem s-t-Schnitt aber im Allgemeinen nicht, komplexere Strukturen zu bevorzugen, insbesondere, wenn dabei Bereiche des Objekts nicht vom Hintergrund zu unterscheiden sind. Für diese Segmentierungsprobleme wird hier eine Lösung vorgestellt, bei der die Graphkonstruktion eine allgemeine Vorlage des zu segmentierenden Objekts nutzt. Dazu werden die Knoten auf dem Bild anhand der Objektvorlage ungleichmäßig und nicht äquidistant verteilt, damit der s-t-Schnitt schon durch die Knotenverteilung ein bestimmtes Objekt bevorzugt. Das Verfahren wird anhand von zweidimensionalen und dreidimensionalen (medizinischen) Bilddaten evaluiert, wobei teilweise große Bereiche des zu segmentierenden Objekts dem Hintergrund sehr ähnlich oder gleich waren. Während der Evaluation hat sich herausgestellt, dass das Segmentierungsergebnis auch von der Position des benutzerdefinierten Saatpunktes abhängt. Allgemein gilt: je zentrierter im Objekt, desto besser die Segmentierung.

Das vorgestellte Segmentierungsschema startet mit der Konstruktion eines gerichteten Graphen, ausgehend von einem benutzerdefinierten Saatpunkt innerhalb des zu segmentierenden Objekts. Für die Graphkonstruktion werden Punkte entlang von Strahlen abgetastet, die durch eine Kontur (2D) oder Oberfläche (3D) einer Objektvorlage verlaufen. Die abgetasteten Punkte sind die Knoten $n \in V$ eines Graphen $G(V,E)$ und $e \in E$ ist eine dazugehörige Menge von Kanten. Es gibt Kanten zwischen den Knoten und es gibt Kanten, die die Knoten mit einer Quelle s und einer Senke t verbinden, um die Berechnung eines s-t-Schnitts zu berechnen

(Anmerkung: die Quelle und die Senke $s,t \in V$ sind virtuelle Knoten). Per Notation verbindet die Kante $\langle v_i, v_j \rangle \in E$ aus dem Graphen die zwei Knoten v_i, v_j. Es gibt zwei Arten von ∞-gewichteten Kanten: p-Kanten A_p und r-Kanten A_r (P ist die Anzahl der abgetasteten Punkte entlang eines Strahls $p = (0,..., P-1)$) und R ist die Anzahl der Strahlen, die durch die Kontur oder die Oberfläche einer Objektvorlage geschickt werden, mit $r = (0,..., R-1)$, wobei $V(x_n, y_n)$ ein Nachbar von $V(x, y)$ ist oder – in anderen Worten – $V(x_n, y_n)$ und $V(x, y)$ gehören zu zwei benachbarten Strahlen. Für eine Oberfläche in 3D gilt das gleiche Prinzip, nur dass es eine zusätzliche Dimension für einen Knoten ($V(x, y, z)$) gibt:

$$A_p = \{\langle V(x,y), V(x,y-1)\rangle \mid y > 0\}$$
$$A_r = \{\langle V(x,y), V(x_n, \max(0, y-\Delta_r))\rangle\}$$

$$A_p = \{\langle V(x,y,z), V(x,y,z-1)\rangle \mid z > 0\}$$
$$A_r = \{\langle V(x,y,z), V(x_n, y_n, \max(0, z-\Delta_r))\rangle\}$$

Die Kanten zwischen zwei Knoten entlang eines Strahls A_p stellen sicher, dass alle Knoten unterhalb der Kontur bzw. der Oberfläche des Graphen ein *closed set* bilden (praktisch wird das Objekt vom Rest der Daten getrennt). Das Grundprinzip wird in Abbildung 6 auf der linken Seite (A) für zwei Strahlen einer kreisförmigen Vorlage aufgezeigt. Die Kanten A_r zwischen den Knoten unterschiedlicher Strahlen schränken die Anzahl der möglichen Segmentierungen ein und erzwingen eine bestimmte Glättung mit einem Parameter Δ_r – je größer dieser Parameter ist, desto größer ist auch die Anzahl der möglichen Segmentierungen. Das zugrundeliegende Prinzip der Konstruktion der Kanten zwischen den Knoten ist in Abbildung 6 auf der rechten Seite (B) verdeutlicht – wiederum für Strahlen einer kreisförmigen Vorlage und einem Deltawert von zwei ($\Delta_r = 2$). Die Kanten für unterschiedliche Deltawerte werden im unteren rechten Bereich der Abbildung 6 aufgezeigt: $\Delta_r = 0$ (links), $\Delta_r = 1$ (Mitte) und $\Delta_r = 2$ (rechts).

Nach der Konstruktion des Graphen wird das minimale *closed set* im Graphen anhand eines s-t-Schnittes in polynominaler Zeit berechnet. Der s-t-Schnitt erzeugt eine optimale Segmentierung des Objektes unter dem Einfluss des Parameters Δ_r, der die Steifigkeit der Oberfläche kontrolliert. Ein Deltawert von Null stellt sicher, dass das Segmentierungsergebnis exakt die Form der vordefinierten Vorlage hat – die Position und die Größe der Vorlage basieren auf der Position des benutzerdefinierten Saatpunktes und der besten Anpassung an die Farbverteilung im Bild. Die Gewichte $w(x, y)$ für alle Kanten zwischen $v \in V$ und der Quelle und der Senke werden nach folgender Vorschrift zugewiesen: Gewichte werden auf $c(x, y)$ gesetzt, wenn z Null ist; ansonsten werden sie auf $c(x, y) - c(x, y-1)$ gesetzt, wobei $c(x, y)$ der Absolutwert der Differenz zwischen einem mittleren Texturwert des zu

segmentierenden Objektes und dem Texturwert an der Position (x, y) ist. Der durchschnittliche Texturwert hat einen kritischen Einfluss auf das Segmentierungsergebnis. Basierend auf der Annahme, dass der benutzerdefinierte Saatpunkt im Objekt liegt, kann dieser durchschnittliche Grauwert (automatisch) abgeschätzt werden. Dazu wird über ein Quadrat (2D) oder einen Kubus (3D) der Dimension d um den benutzerdefinierten Saatpunkt (s_x, s_y) bzw. (s_x, s_y, s_z) herum integriert:

$$\int_{-d/2}^{d/2} \int_{-d/2}^{d/2} S(s_x + x, s_y + y) dx dy$$

$$\int_{-d/2}^{d/2} \int_{-d/2}^{d/2} \int_{-d/2}^{d/2} C(s_x + x, s_y + y, s_z + z) dx dy dz$$

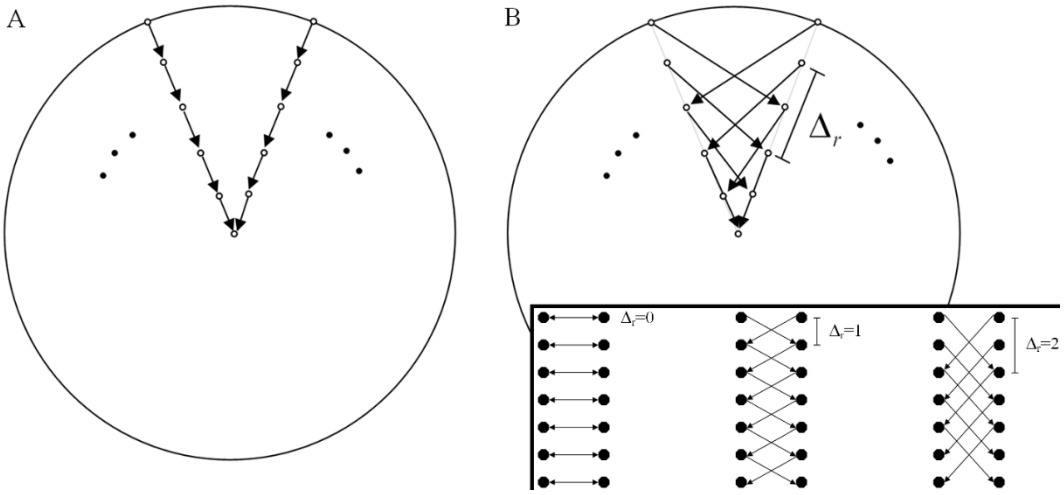

Abbildung 6 – Für den vorgestellten Segmentierungsansatz gibt es zwei unterschiedliche Arten von Kanten im Graphen, um kreisförmige Objekte zu segmentieren: A_p-Kanten (A) und A_r-Kanten (B). Unteres rechtes Bild: *Intercolumn*-Kanten für: $\Delta_r = 0$ (links), $\Delta_r = 1$ (Mitte) und $\Delta_r = 2$ (rechts).

Das Prinzip hinter der Graphkonstruktion für eine quadratische Vorlage wird in Abbildung 7 verdeutlicht. Bild A aus Abbildung 7 zeigt die Ecken einer quadratischen Vorlage, die dazu genutzt wird, um den Graphen aufzubauen. Bild B zeigt die Knoten, die entlang der Strahlen abgetastet wurden, die durch die Kontur der Vorlage geschickt wurden. Die Distanzen zwischen den Knoten entlang eines Strahls korrelieren dabei mit den Distanzen des Mittelpunktes der Vorlage (bzw. bei einer Segmentierung mit dem benutzerdefinierten Saatpunkt) und der Kontur der Vorlage. In anderen Worten: Entlang jedes Strahls wird die gleiche Anzahl von Knoten zwischen dem Mittelpunkt und der Objektkontur abgetastet, aber die Abstände zwischen den Knoten sind unterschiedlich groß. In den Bildern C, D und E

sind verschiedene ∞-gewichtete Kanten zu sehen, C: die p-Kanten entlang der einzelnen Strahlen, D: die r-Kanten A_r zwischen den Strahlen mit einem Deltawert von $\Delta_r = 0$. E: die r-Kanten A_r zwischen den Strahlen mit einem Deltawert von $\Delta_r = 1$.

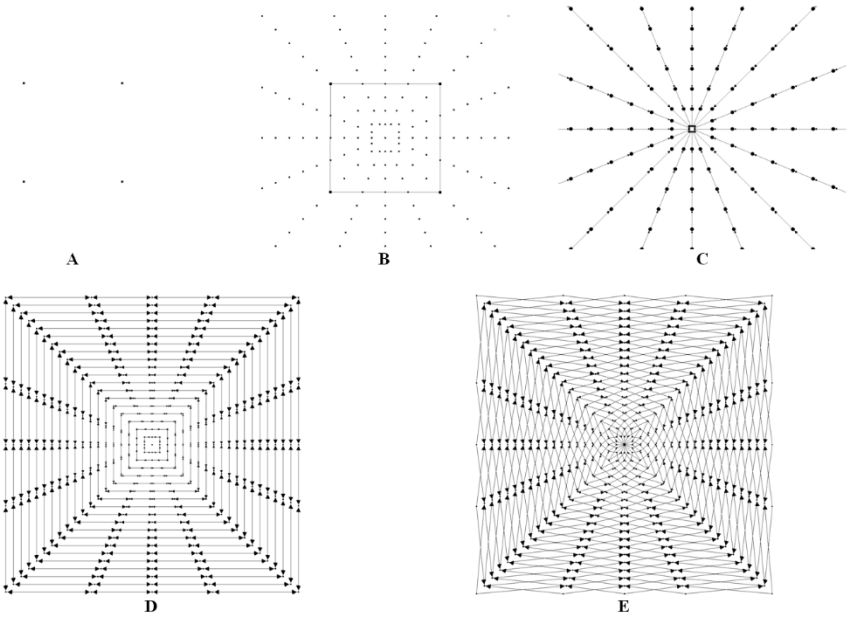

Abbildung 7 – (A) Definition einer rechteckigen Vorlage durch ihre Eckpunkte. (B) Knoten, die anhand dieser Vorlage generiert wurden. (C) p-Kanten A_p entlang der ausgesandten Strahlen. (D) r-Kanten A_r zwischen den Strahlen ($\Delta_r = 0$) und (E) r-Kanten A_r zwischen Strahlen ($\Delta_r = 1$).

Der gesamte Ablauf des vorgestellten Segmentierungsschemas ist in Abbildung 8 dargestellt. In der oberen Zeile wurde eine quadratische Vorlage zur Segmentierung von Wirbeln in 2D angewendet. In der unteren Zeile wurde eine kugelförmige Vorlage genutzt, um GBMs in 3D zu segmentieren.

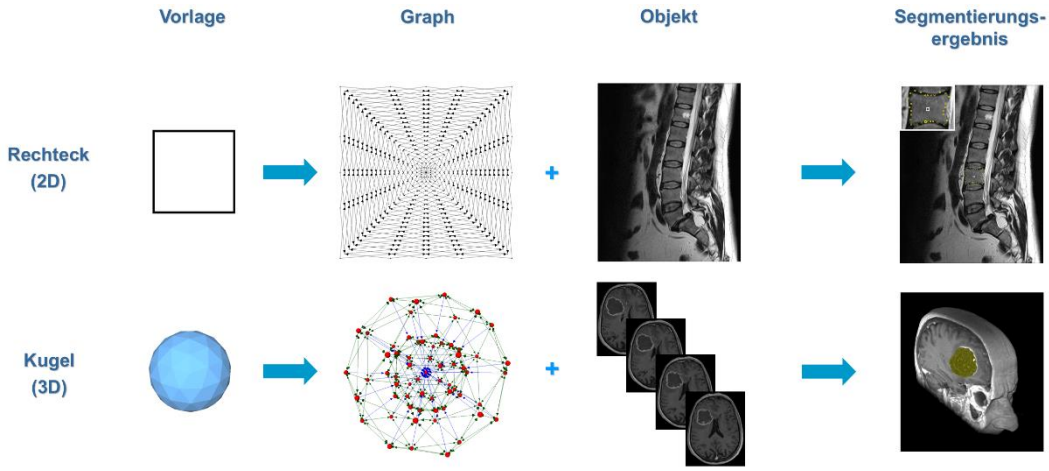

Abbildung 8 – Prinzipieller Ablauf des vorgestellten Segmentierungsschemas in 2D und 3D: In 2D wurde eine rechteckige Vorlage verwendet, um einen Wirbel zu konturieren. In 3D kam eine kugelförmige Vorlage zum Einsatz, um das Volumen eines Glioblastoms zu bestimmen.

Berechnung/Implementierung: Das Generieren der Knoten des Graphen anhand einer benutzerdefinierten Vorlage ist der schwierigste Schritt während der Berechnung des vorgestellten Algorithmus. Dagegen ist das Erzeugen der Kanten zwischen den Knoten und zwischen den Knoten und der Quelle s und Senke t recht unkompliziert: Es gibt die ∞-gewichteten Kanten, die zum einen von der Geometrie (*intracolumn arcs*) und dem Deltawert (*intercolumn arcs*) des Graphen abhängen. Die Kanten, die alle Knoten entweder mit der Quelle s oder der Senke t verbinden, basieren auf Texturwerten der Knoten bzw. der Texturdifferenz zum benachbarten Knoten. Um eine benutzerdefinierte Vorlage in die Konstruktion des Graphen einzubeziehen, werden Koordinaten in 2D oder 3D benötigt, die das Objekt beschreiben, das segmentiert werden soll (für ein Quadrat zum Beispiel die Ecken des Quadrates). Anhand dieser Koordinaten wird der Mittelpunkt des Objektes berechnet und anschließend wird das Objekt anhand des maximalen Durchmessers normalisiert bzw. anhand der Koordinate mit dem maximalen Abstand zum Mittelpunkt des Objektes. Nachdem der Benutzer einen Saatpunkt im Bild (2D) oder Volumen (3D) definiert hat, wird die normalisierte Vorlage mit ihrem Mittelpunkt an dieser benutzerdefinierten Position konstruiert. Danach werden die Strahlen radial (2D) oder kugelförmig (3D) vom Saatpunkt der normalisierten Vorlage durch die Kontur (2D) oder Oberfläche (3D) ausgesandt. Damit die Schnittpunkte der Strahlen mit der Vorlage berechnet werden können, muss ihre Kontur (2D) bzw. Oberfläche (3D) geschlossen sein. In dieser Implementierung gehen wir von der Annahme aus, dass der Benutzer die Kontur der Vorlage als 2D-Koordinaten im Uhrzeigersinn bereitstellt und der Algorithmus die Punkte einen nach dem anderen verbindet und am Ende den letzten mit dem ersten verbindet, um eine geschlossenen Kontur zu erhalten. Um in 3D eine geschlossene Oberfläche zu erhalten, kann diese trianguliert werden. Das ist allerdings nicht notwendig bei einer kugelförmigen oder elliptischen Segmentierung mit einer Kugel als Vorlage. Hier kann der Rechenaufwand

für die Triangulierung und die anschließende Strahl/Dreieck-Schnittpunktberechnung vermieden werden, wenn die Oberflächenpunkte eines Polyeders verwendet werden, da dessen Koordinaten schon die Positionen liefern, durch die die Strahlen gesendet werden.

Für die Implementierung des vorgestellten Segmentierungsschemas kam die MeVisLab-Plattform zum Einsatz, und der Algorithmus wurde als eigenes C++ Modul programmiert. Auch wenn die Prototyping Plattform MeVisLab auf medizinische Anwendungen abzielt, können damit doch auch Bilder aus anderen Bereichen verarbeitet werden. Auf einem Windows PC (Core i5-750 CPU, 4x2.66 GHz, 8 GB RAM, Windows XP Professional x64 Version, Version 2003, Service Pack 2) konnte eine Segmentierung einschließlich der Graphkonstruktion (bestehend aus mehreren hundert Strahlen und mehreren hundert abgetasteter Knoten entlang dieser Strahlen) in ein paar Sekunden erfolgen. Zur Evaluation in 2D wurden sowohl synthetische als auch „echte“ Bilder verwendet. Abbildung 9 zeigt einen Plattfisch (A), der sich seiner Umgebung anpassen kann, indem er seine Farbe verändert. Dadurch wird es für das menschliche Auge sehr schwer, ihn zu erkennen. In Bild B ist die benutzerdefinierte Vorlage dargestellt, die zur Graphkonstruktion verwendet wurde. Und Bild C zeigt die Knoten, die anhand dieser Vorlage generiert wurden. In Bild D werden die Knoten auf das Originalbild eingeblendet, wobei der Graph ungefähr doppelt so groß ist wie die Vorlage; dadurch spielt die Größe des Plattfischs keine Rolle (d.h. der Ansatz ist skalierungsinvariant) und die gleiche Vorlage kann für die Segmentierung von kleineren und größeren Plattfischen verwendet werden. Bild E präsentiert das Segmentierungsergebnis.

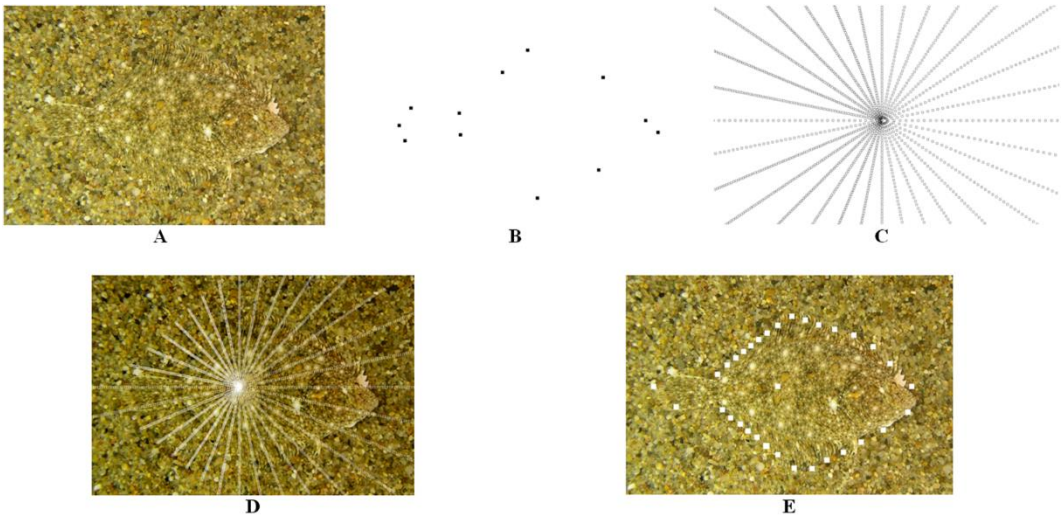

Abbildung 9 – (A) Plattfisch (Kareius bicoloratus). (B) Benutzerdefinierte Vorlage eines Plattfischs. (C) Knoten, die anhand der Vorlage generiert wurden. (D) Knoten eingeblendet in das Originalbild des Plattfischs. (E) Segmentierungsergebnis (weiße Punkte).

In 3D wurde der Algorithmus anhand der Segmentierung von Hirntumoren (GBM und Hypophysenadenomen) in MRT-Datensätzen aus der klinischen Routine evaluiert. Dabei hatten alle Hirntumore eine kugelförmige bzw. elliptische Form und es wurde die Oberfläche eines Polyeders genutzt, um die Graphen zu konstruieren. Als sogenannte "Ground Truth" oder als Goldstandard wurden die rein manuellen Segmentierungen dreier Neurochirurgen mit mehrjähriger Erfahrung in der Resektion von Hirntumoren verwendet, mit denen die Segmentierungsergebnisse des Algorithmus verglichen wurden. Hier ergab ein direkter Vergleich zwischen den automatischen und rein manuellen Segmentierungen einen DSC von ungefähr 80%.

Abbildung 10 zeigt einige Segmentierungsergebnisse für ein GBM, hierbei stellt (A) die 3D-Ansicht eines automatisch segmentierten Tumors (braun) dar. (B)-(D) präsentieren unterschiedliche 3D-Ansichten eines automatisch segmentierten Tumors (rot) und (E) die voxelisierte Tumormaske. (F)-(J) zeigen das Ergebnis einer automatischen Tumorsegmentierung mit einem DSC von 81,33%. Der gelbe Saatpunkt (innerhalb des Tumors) in Bild H ist der benutzerdefinierte Saatpunkt. Die rein manuelle Segmentierung dieses Datensatzes durch einen Neurochirurgen dauerte sechzehn Minuten. Wie in diesem Beispiel zu sehen ist, funktioniert der Algorithmus auch bei leicht elliptisch geformten Tumoren. Der Algorithmus setzt nur voraus, dass das zu segmentierende Objekt keine extrem tubuläre Form hat, wie etwa Blutgefäße oder der Spinalkanal. Auch muss der benutzerdefinierte Saatpunkt nicht exakt im Objekt zentriert sein, wie in Bild H zu sehen ist (gelb). Auch mit einem Saatpunkt etwas entfernter vom Mittelpunkt konnten die Tumorgrenzen (rot) noch mit einem DSC von über 80% segmentiert werden (Anmerkung: Die fünf axialen Schichten F-J zeigen nur einen Teil des Tumors, der gesamte Tumor erstreckte sich über sechzig Schichten).

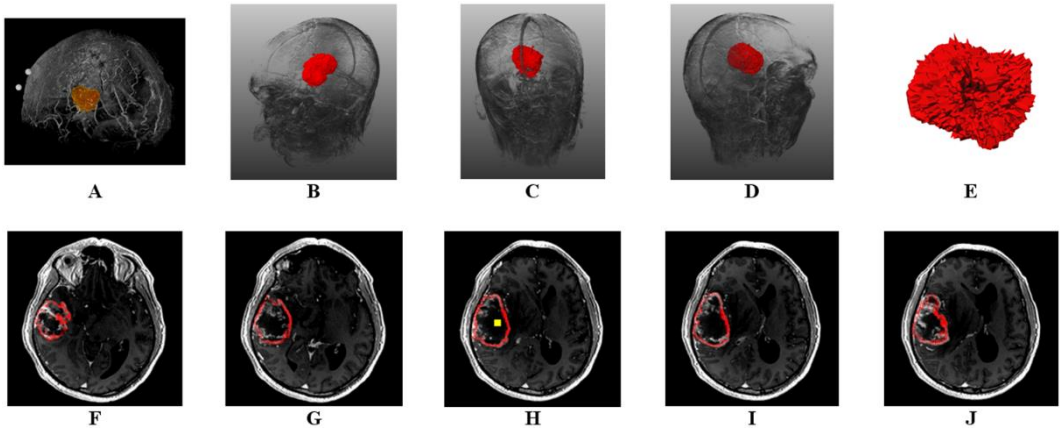

Abbildung 10 – (A) 3D-Ansicht eines automatisch segmentierten Tumors (braun). (B)-(D) Unterschiedliche 3D-Ansichten eines automatisch segmentierten Tumors (rot). (E) Voxelisierte Tumormaske. (F)-(J) Ergebnis einer automatischen Tumorsegmentierung (mit einem DSC von 81,33%). Der gelbe Saatpunkt (innerhalb des Tumors) in Bild H ist der benutzerdefinierte Saatpunkt. Die rein manuelle Segmentierung durch einen Neurochirurgen dauerte sechszehn Minuten bei diesem Datensatz.

In Bild A aus Abbildung 11 ist ein Graph (Knoten und Kanten) zu sehen, der anhand eines Polyeders konstruiert wurde. Der Graph wiederum dient der Segmentierung eines Hypophysenadenoms in einer MRT-Aufnahme aus der klinischen Routine. Bild B zeigt eine axiale Schicht des Hypophysenadenoms (H-Adenom) mit vergrößerter Darstellung (Rechteck links unten). Die Bilder C und D präsentieren verschiedene Ansichten von sagittalen Schichten eines automatisch segmentierten H-Adenoms (braun). Bild E stellt die 3D-Maske des automatisch segmentierten H-Adenoms dar (rot). Die Bilder F-J präsentieren das Segmentierungsergebnis in verschiedenen axialen Schichten mit dem benutzerdefinierten Saatpunkt (blau) in Bild H.

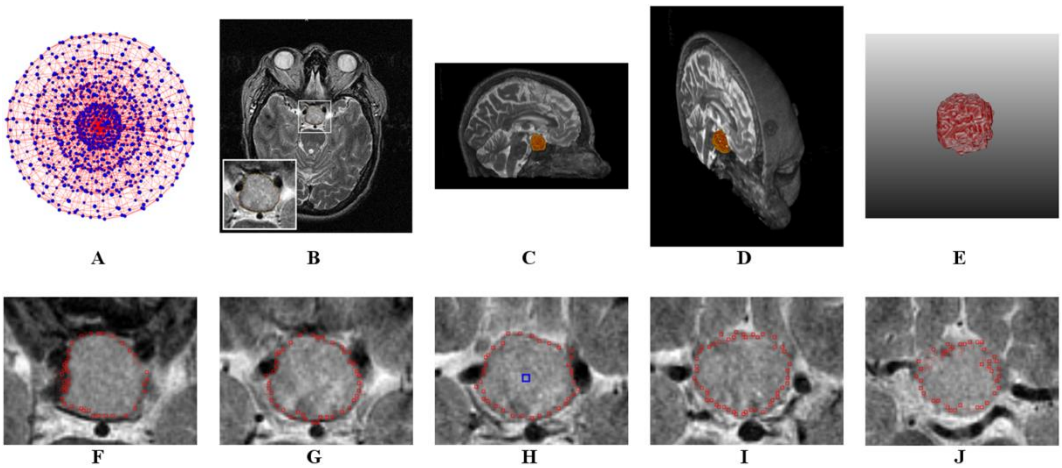

Abbildung 11 – (A) Graph (Knoten und Kanten) konstruiert anhand eines Polyeders. (B) Axiale Schicht eines Hypophysenadenoms (H-Adenom) mit vergrößerter Darstellung (Rechteck links unten). (C) und (D) Verschiedene Ansichten von sagittalen Schichten mit einem automatisch segmentierten H-Adenom (braun). (E) 3D-Maske eines automatisch segmentierten H-Adenoms (rot). (F)-(J) Das Segmentierungsergebnis in verschiedenen axialen Schichten. (H) Benutzerdefinierter Saatpunkt (blau).

Die Tabellen 3 bis 5 präsentieren die Ergebnisse (Minimum, Maximum, Mittelwert und Standardabweichung) aller GBMs, Hypophysenadenome und Wirbel, die mit dem vorgestellten Verfahren segmentiert und mit manuellen neurochirurgischen Schicht-für-Schicht-Segmentierungen verglichen wurden. Tabelle 3 verzeichnet die Evaluationsergebnisse der Tumorvolumen in cm^3, die Anzahl der Voxel und die DSCs von fünfzig Glioblastoma multiforme (GBM). Tabelle 4 zeigt die Evaluationsergebnisse der Tumorvolumen in cm^3, die Anzahl der Voxel und die DSCs für zehn Hypophysenadenome. Anmerkung: Eine rein manuelle Segmentierung dauerte im Schnitt knapp vier Minuten ($3{,}91 \pm 0{,}51$, Min. 3 Minuten und Max. 5 Minuten). Tabelle 5 zeigt die Evaluationsergebnisse von Wirbelvolumen in cm^3, die Anzahl der Voxel und die DSCs für neun Wirbel.

	GBM-Volumen in cm^3		Anzahl der Voxel		DSC (%)
	manuell	**automatisch**	**manuell**	**automatisch**	
Min.	0,47	0,46	524	783	46,33
Max.	119,28	102,98	1024615	884553	93,82
$\mu \pm \sigma$	$23{,}66 \pm 24{,}89$	$21{,}02 \pm 22{,}90$	145305,54	137687,24	$80{,}37 \pm 8{,}93$

Tabelle 3 – Evaluationsergebnisse: Minimum (Min.), Maximum (Max.), Mittelwert μ und Standardabweichung σ für fünfzig Glioblastoma multiforme (GBM).

	H-Adenom-Volumen in cm^3		Anzahl der Voxel		DSC (%)
	manuell	**automatisch**	**manuell**	**automatisch**	
Min.	0,84	1,18	4492	3461	71,07
Max.	15,57	14,94	106151	101902	84,67
$\mu \pm \sigma$	$6{,}30 \pm 4{,}07$	$6{,}22 \pm 4{,}08$	47462,7	47700,6	$77{,}49 \pm 4{,}52$

Tabelle 4 – Evaluationsergebnisse: Minimum (Min.), Maximum (Max.), Mittelwert μ und Standardabweichung σ für zehn Hypophysenadenome (H-Adenome). Eine rein manuelle Segmentierung dauerte im Schnitt knapp vier Minuten ($3{,}91 \pm 0{,}51$, Min. 3 Minuten und Max. 5 Minuten).

	Wirbelvolumen in cm^3		Anzahl der Voxel		DSC (%)
	manuell	**automatisch**	**manuell**	**automatisch**	
Min.	0,25	0,24	1015	995	87,37
Max.	0,51	0,49	2091	2010	94,93
$\mu \pm \sigma$	$0{,}42 \pm 0{,}072$	$0{,}40 \pm 0{,}073$	1722	1656	$90{,}97 \pm 2{,}2$

Tabelle 5 – Evaluationsergebnisse: Minimum (Min.), Maximum (Max.), Mittelwert μ und Standardabweichung σ für neun Wirbel.

In diesem Abschnitt wurde ein vorlagenbasiertes Segmentierungsschema für 2D- und 3D-Objekte vorgestellt. Dabei verteilt der graphbasierte Ansatz die Knoten für den Graphen nicht gleichmäßig auf einem Bild bzw. in einem Volumen sondern anhand einer definierten Vorlage. Durch diese neuartige Strategie ist es sogar möglich, fehlende Kanten und Ecken des Objektes während der Segmentierung zu rekonstruieren. Außerdem ist das Segmentierungsverfahren skalierungsinvariant.

Zusammengefasst wurden in diesem Abschnitt folgende Forschungsergebnisse erzielt:

- Ein vorlagenbasiertes Segmentierungsparadigma für 2D- und 3D-Objekte;
- Die Knoten für den graphbasierten Ansatz werden anhand einer vordefinierten Vorlage für die Segmentierung angeordnet;
- Der Ansatz repräsentiert einen neuen Typus von graphbasierten Algorithmen;
- Es ist möglich, fehlende Objektkanten und sogar Ecken zu rekonstruieren;
- Der Ansatz ist skalierungsinvariant.

2.4. Kubusbasierte Segmentierung von Wirbeln in MRT-Aufnahmen

In diesen Arbeiten [4], [5] wird ein graphbasierter Ansatz zur Wirbelsegmentierung in MRT-Aufnahmen vorgestellt, wobei der Graph anhand einer würfelförmigen Vorlage konstruiert wird und die Knoten des Graphen nicht gleich verteilt und nicht äquidistant innerhalb der MRT-Aufnahme gesampelt werden. Dadurch liefert ein anschließender minimaler s-t-Schnitt – in Abhängigkeit von einem benutzerdefinierten Smoothness-Term (Abweichung) – auch eine würfelförmige Segmentierung zurück. Dies das erste Mal, dass bei einem graphbasierten Ansatz die Knoten anhand einer würfelförmigen Vorlage verteilt werden und der minimale s-t-Schnitt deshalb auch ein würfelförmiges Segmentierungsergebnis bevorzugt. Das vorgestellte Verfahren kann auch zur Segmentierung anderer und vergleichbarer kubusförmiger Zielstrukturen genutzt werden und eignet sich besonders, um homogenen Objekt/Hintergrund-Übergängen zu begegnen, die eine automatische Segmentierung des Objekts erschweren.

Der hier vorgestellte Algorithmus konstruiert in einem ersten Schritt ein zweiterminales Flussnetzwerk $F = ((V(G), E(G), c, s, t)$, wobei $V(G) \setminus \{s,t\}$ eine Menge von Knoten bezeichnet, die wiederum einer Untermenge der Bildvoxel entspricht. $E(G)$ bezeichnet eine Menge von Kanten und c eine Funktion, die jeder Kante eine nicht-negative, reale Kapazität zuordnet. Außerdem besteht das Netzwerk aus einer Quelle $s \in V(G)$ und einer Senke $t \in V(G)$. Nach der Konstruktion des Netzwerks wird in polynomialer Zeit ein minimaler s-t-Schnitt (S,T) berechnet, aus dem anschließend das Segmentierungsergebnis wie folgt ermittelt wird:

- ein Knoten $v \in S$ wird dem Wirbelkörper zugeordnet und
- ein Knoten $v \in T$ wird dem Hintergrund zugeordnet.

Die betrachteten Voxel befinden sich entlang einer Menge von Strahlen, die ihren Ursprung alle in einem benutzerdefinierten Saatpunkt innerhalb des Wirbelkörpers haben. Hierbei besteht jeder Strahl aus der gleichen Menge von auf dem Strahl äquidistant verteilten Voxeln, und alle Voxel der gleichen Ebene – z.B. die Menge der zweiten Voxel auf allen Strahlen – bilden eine Würfelform (Abbildung 12, links).

Die terminalen Kanten des Netzwerks, die jeden Knoten mit s und t verbinden, repräsentieren die Grauwertunterschiede zwischen einem Voxel und seinem Vorgängervoxel auf demselben Strahl. Ist die Differenz klein (< 20), so wird davon ausgegangen, dass die beiden Voxel innerhalb einer homogenen Region des Bildes liegen (z.B. innerhalb des Wirbelkörpers), so dass die Kante, die den entsprechenden Knoten mit der Quelle verbindet, hoch gewichtet wird. Bei einer großen Differenz (> 20) kann von einem Objekt-Hintergrund-Übergang ausgegangen werden, so dass hier die entsprechende Kante zur Senke hoch gewichtet wird. Die terminalen Kantengewichtungen des ersten und des letzten Voxels auf jedem Strahl stellen außerdem sicher, dass der Saatpunkt dem Wirbelkörper und der letzte Voxel dem Hintergrund zugeordnet wird.

Um sicherzustellen, dass jeder Strahl nur genau einmal geschnitten wird, wird

eine Menge von nicht-terminalen, ∞-gewichteten Kanten eingeführt, die jeden Knoten $v_{i_r} \in V(G) \setminus \{s,t,v_1\}$ mit seinem Vorgänger $v_{(i-1)_r} \in V(G) \setminus \{s,t\}$ auf einem Strahl r verbinden (Abbildung 12, rechts)

$$A_z = \{(v_{i_r}, v_{(i-1)_r})\}$$

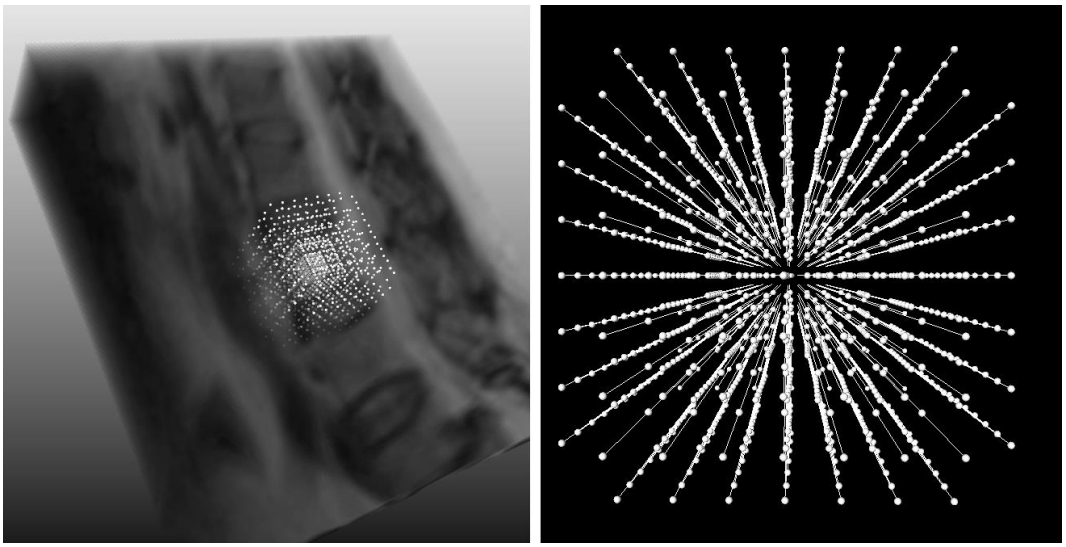

Abbildung 12 – Verteilung der Knoten eines Graphen (links) und Visualisierung der z -Kanten (rechts).

Einen Strahl r einmal zu schneiden verursacht aufgrund von A_z Kosten von mindestens ∞, da $(v_{i_r}, v_{(i+1)_r})$ geschnitten werden muss, genau dann, wenn $v_{(j \le i)_r} \in S$ und $v_{(j>i)_r} \in T$ ist. Einen Strahl zweimal zu schneiden, würde Kosten von mindestens $2 \cdot \infty$ verursachen. Da jedoch der Saatpunkt v_1 in S liegt, während der letzte Knoten auf jedem Strahl T zugeordnet ist, muss ein Strahl von einem minimalen s-t-Schnitt genau einmal geschnitten werden. Im Fall eines scharfen Objekt/Hintergrund-Überganges muss dieser Schnitt aufgrund der hohen Gewichtung der terminalen Kante zur Senke genau vor dem ersten Knoten im Hintergrund verlaufen.

Typische Herausforderungen im Kontext von graphbasierten Segmentierungen sind starke Abweichungen innerhalb der anatomischen Struktur, die einen zu frühen Schnitt zur Folge haben, sowie homogene Objekt/Hintergrund-Übergänge, die einen Überlauf des Segmentierungsergebnisses verursachen. Der Ansatz begegnet diesen Problemen, indem er dem Nutzer erlaubt, einen sogenannten *Smoothness*-Term zu definieren, der die Objekt/Hintergrund-Distanz $\Delta \in N_0$ zweier benachbarter Strahlen beschränkt. Hierzu wird eine weitere Menge von nichtterminalen, ∞-gewichteten Kanten eingeführt

$$A_{xy} = \{v_{i_r}, v_{\max\{i-\Delta,1\}_{r'}}\}$$

wobei r und r' aus einer Vierernachbarschaft stammen (Abbildung 13). Ein Δ-Wert von Null hat somit eine reguläre Würfelform zur Folge, bei einem Δ-Wert > Null sind entsprechende Abweichungen, abhängig von der Voxeldistanz auf den einzelnen Strahlen, möglich (Abbildung 14).

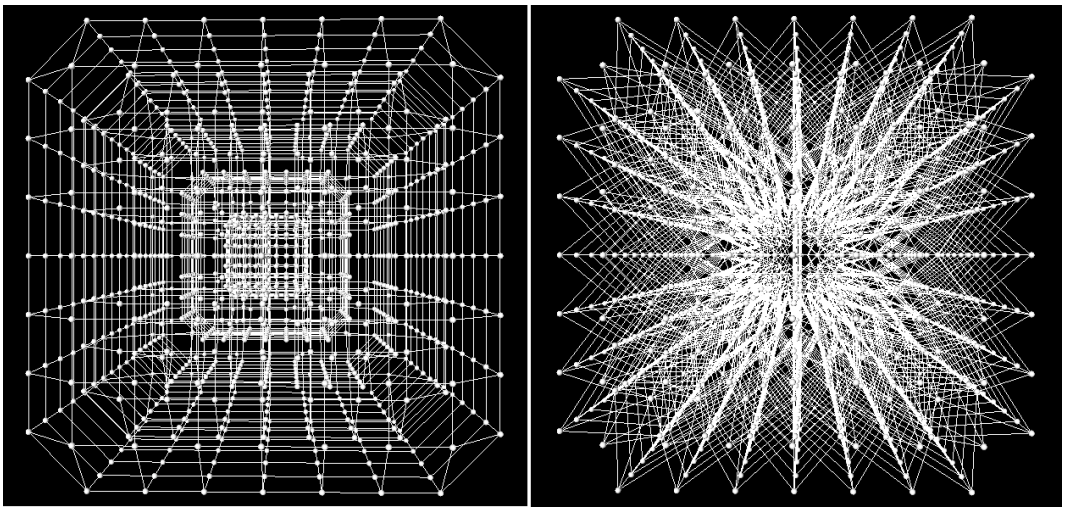

Abbildung 13 – Topologie der (x, y)-Kanten: $\Delta = 0$ (links) und $\Delta = 2$ (rechts).

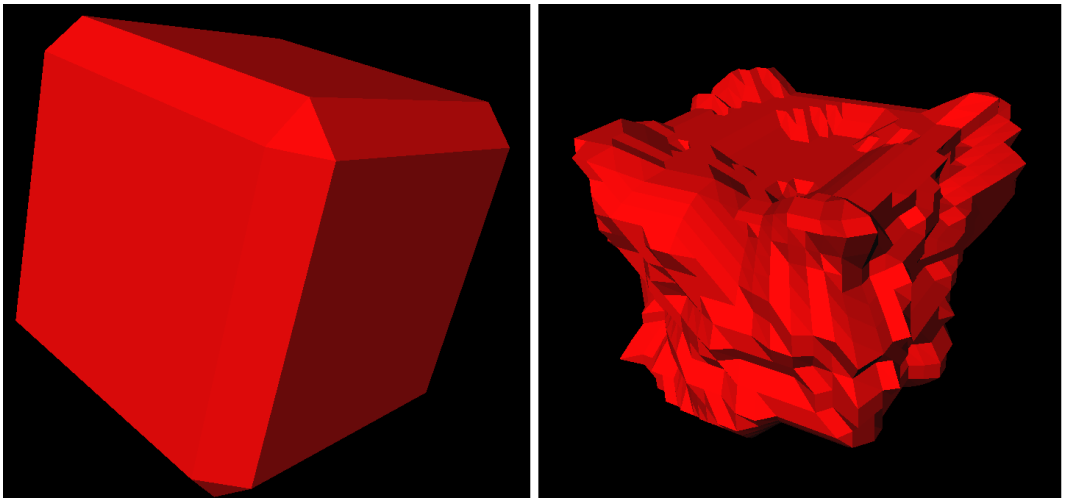

Abbildung 14 – Segmentierungsergebnis für $\Delta = 0$ (links) und $\Delta = 2$ (rechts).

Zur Evaluation des vorgestellten Segmentierungsverfahrens wurde eine C++ Implementierung innerhalb der medizinischen Bildverarbeitungsplattform MeVisLab (www.mevislab.de, Version 2.2.1) realisiert und anhand von zehn Wirbeln in zwei sagittalen, T2-gewichteten MRT-Datensätzen (160 × 160 × 35 und 160 × 160

× 23) getestet. Die Tests lieferten bei einem direkten Vergleich mit manuell vorgenommen Schicht-für-Schicht-Segmentierungen einen durchschnittlichen Dice Similarity Coefficient (DSC) von 81,33% (Tabelle 6). Abbildung 15 zeigt wiederum beispielhaft Segmentierungsergebnisse unseres Ansatzes (Cube-Cut): 3D-Segmentierungsergebnisse (links und Mitte) und 2D-Perspektive auf ein Segmentierungsergebnis mit benutzerdefiniertem Saatpunkt in Blau (rechtes Bild).

Dabei hatten die rechenaufwendigsten Parametereinstellungen eine maximale Terminierungszeit von unter einer Minute, mit Netzwerkkonstruktion, s-t-Schnitt und Triangulierung des Segmentierungsergebnisses (gemessen auf: 2,1 GHz, 4 GB RAM x64 PC, Windows 7 Home Premium (SP1)). Manuell erstellte Segmentierungen, für die Mediziner Schicht für Schicht die Außengrenzen eines Wirbelkörpers in den Aufnahmen einzeichneten, dauerten dagegen 6,65 bis 10 Minuten, so dass die automatische Segmentierung die präoperativen Evaluierungsmaßnahmen um 2,35 (Min.) bis 15,65 Minuten (Max.) verkürzte.

	Wirbelvolumen in cm^3		**Anzahl der Voxel**		**DSC (%)**
	manuell	**automatisch**	**manuell**	**automatisch**	
Min.	15,42	16,64	1892	2041	71,64
Max.	33,83	28,78	5240	4320	86,69
$\mu \pm \sigma$	$24{,}97 \pm 6{,}15$	$23{,}48 \pm 5{,}12$	3750	3152	$81{,}33 \pm 5{,}07$

Tabelle 6 – Evaluierungsergebnisse für zehn Wirbel in 3D: Minimum (Min.), Maximum (Max.), Mittelwert μ und Standardabweichung σ für die manuell und automatisch erzielten Segmentierungsvolumina, die dazugehörige manuelle und automatische Anzahl der Voxel und den Dice Similarity Koeffizienten zwischen den manuellen und automatischen Segmentierungen.

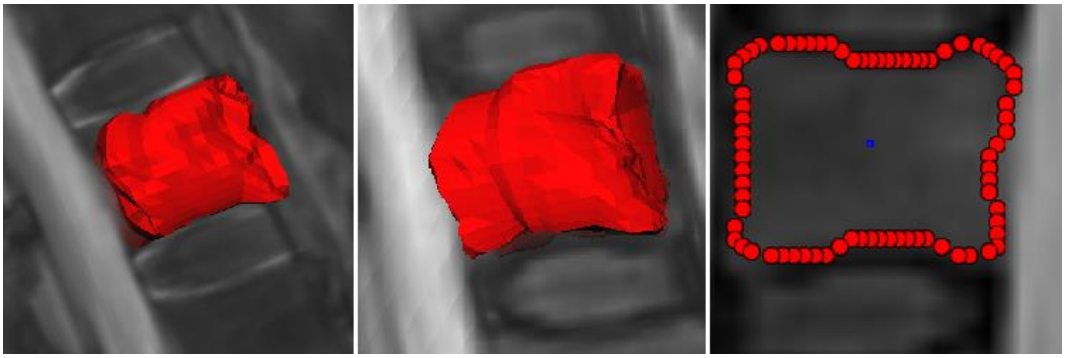

Abbildung 15 – 3D-Segmentierungsergebnisse (links und Mitte) und 2D-Perspektive auf ein Segmentierungsergebnis mit benutzerdefiniertem Saatpunkt in Blau (rechtes Bild).

In diesem Abschnitt wurde ein graphbasierter Ansatz zur Wirbelsegmentierung in MRT-Aufnahmen vorgestellt, wobei der Graph anhand einer würfelförmigen Vorlage konstruiert wurde und die Knoten des Graphen nicht gleichverteilt und nicht äquidistant innerhalb der MRT-Aufnahme gesampelt wurden. Dadurch liefert

ein anschließender minimaler s-t-Schnitt – in Abhängigkeit von einem benutzerdefinierten *Smoothness*-Term (Abweichung) – auch eine würfelförmige Segmentierung zurück.

Dies ist das erste Mal, dass bei einem graphbasierten Ansatz die Knoten anhand einer würfelförmigen Vorlage verteilt wurden und der minimale s-t-Schnitt deshalb auch ein würfelförmiges Segmentierungsergebnis bevorzugt. Das vorgestellte Verfahren kann auch zur Segmentierung anderer vergleichbarer kubusförmiger Zielstrukturen genutzt werden und eignet sich besonders, um homogenen Objekt/Hintergrund-Übergängen zu begegnen, die eine automatische Segmentierung des Objektes erschweren.

Bei den aktuellen Parametereinstellungen kam es allerdings auch vor, dass Ecken der Wirbel nicht genau segmentiert werden konnten. Abbildung 16 zeigt ein Beispiel, bei dem die Konturen zweier Ecken eines Wirbels (Kreise)" abgeschnitten" wurden. Dieser Ungenauigkeit kann durch eine Verdichtung der Strahlen, die eine Verdichtung der Knoten nach sich zieht, entgegengewirkt werden. Dies würde jedoch eine höhere Laufzeit zur Folge haben. Eine andere Möglichkeit wäre es, anstatt eines Kubus eine dem Wirbel besser angepasste Vorlage für den Aufbau des Graphen zu verwenden, zum Beispiel mit Würfelseiten, die leicht nach innen gewölbt sind.

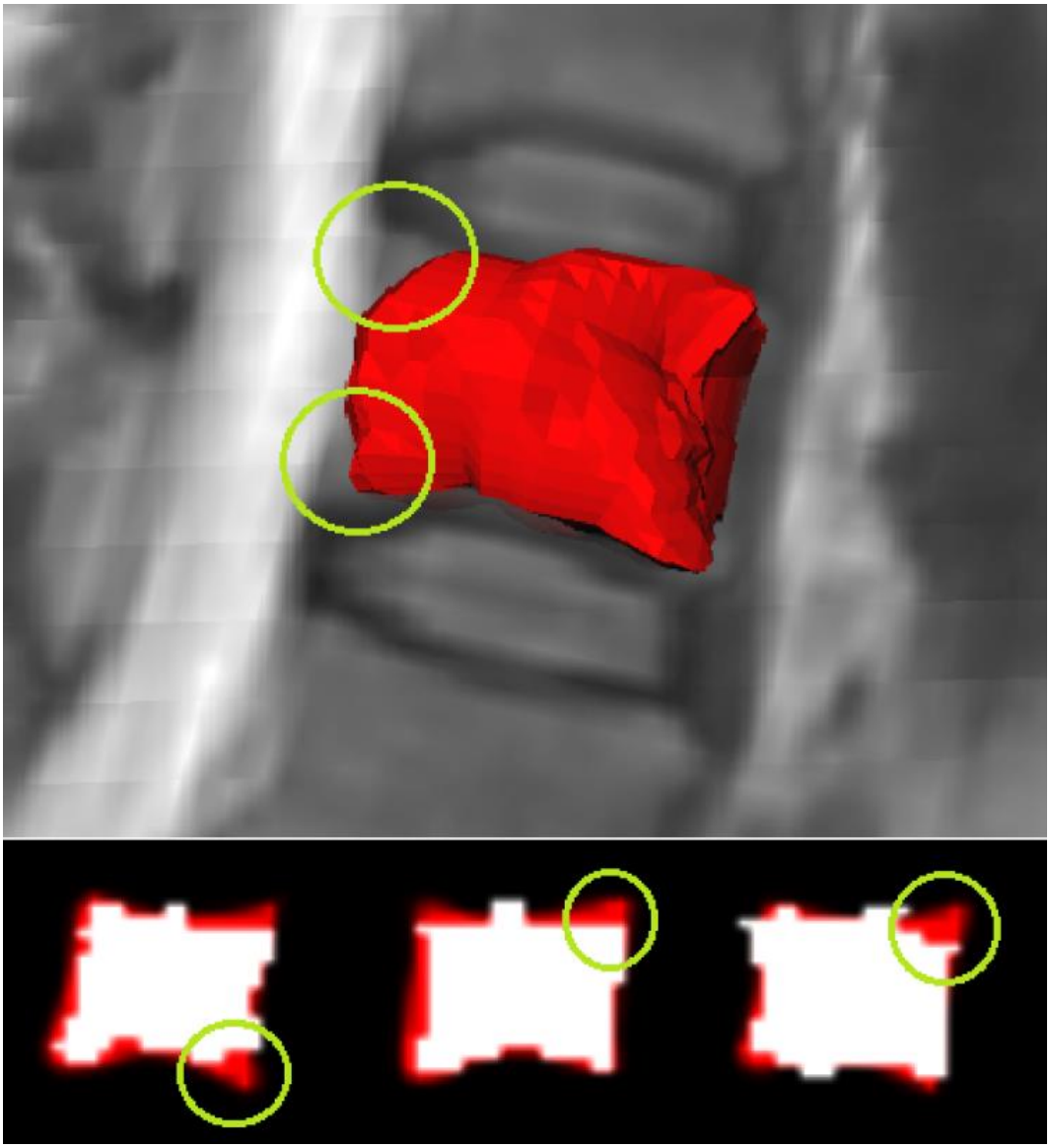

Abbildung 16 – Beispiel einer Segmentierung, bei der zwei Ecken des Wirbels (Kreise) nicht ausreichend segmentiert werden konnten. Im unteren Bildteil sind die manuellen Segmentierungen (rot) und die automatischen Segmentierungsergebnisse (weiß) in mehreren 2D-Schichten übereinandergelegt.

2.5. Segmentierung von Drüsen der Prostata anhand einer Kugelvorlage

Prostatakrebs ist die häufigste Krebserkrankung bei Männern mit über 200000 neuen Erkrankungen und ca. 28000 Toten alleine für das Jahr 2012 in den Vereinigten Staaten. In diesem Beitrag [6] wird die graphbasierte Segmentierung von Prostatadrüsen in MRT-Aufnahmen anhand einer Kugelvorlage vorgestellt. Damit können die Grenzen zwischen Prostatadrüsen und umliegenden Organen automatisch bestimmt werden. Ein weiteres Ziel dieser speziellen Segmentierung ist die

effiziente Unterstützung MR-gestützter Biopsien und Bestrahlungsplanungen. Zur Konstruktion des Graphen werden Strahlen durch die Oberfläche eines Polyeders gesandt, entlang derer die Knoten des Graphen abgetastet werden. Dazu benötigt der Ansatz nur einen benutzerdefinierten Saatpunkt innerhalb der Prostatadrüse. Anschließend wird ein minimaler s-t-Schnitt berechnet, der in der Kontur und in dem Volumen der Prostatadrüse resultiert. Der Ansatz wurde als eigenständiges C++ Modul innerhalb der MeVisLab-Plattform realisiert und anhand von intra-operativen T2-gewichteteten Aufnahmen aus MR-gestützten Biopsien evaluiert.

Zur Volumetrie der Prostatadrüsen wurde das sogenannte *Nugget-Cut*-Segmentierungsschema angewandt. Dabei wird ein gerichteter 3D-Graph $G(V,E)$ in zwei Schritten konstruiert: (I) Aussenden von Strahlen durch die Oberflächenpunkte eines Polyeders und (II) Abtasten der Knoten des Graphen $n \in V$ entlang jedes Strahls. Zusätzlich wird eine dazugehörige Menge von Kanten generiert, die aus Kanten zwischen den Knoten und Kanten, die die Knoten mit einer Quelle s und einer Senke t verbinden, bestehen. Nach der Konstruktion des Graphen – der Mittelpunkt des Polyeders wird durch den Benutzer vorgegeben und liegt innerhalb der Prostatadrüse – wird das *closed set* des Graphen mit minimalen Kosten anhand eines s-t-Schnittes berechnet, was wiederum in die Segmentierung der Kontur und des Volumens der Prostatadrüse mündet. Das gesamte Prinzip des *Nugget-Cut*-Segmentierungsschemas, das zur Segmentierung von Prostatadrüsen angewandt wurde, ist in Abbildung 17 präsentiert. Wie in der Abbildung dargestellt, wird eine kugelförmige Vorlage (links) als Grundstruktur zum Erstellen des Segmentierungsgraphen (Mitte) verwendet. Letztendlich wird der Graph innerhalb des Bildes konstruiert, wobei sein Mittelpunkt an der Stelle des benutzerdefinierten Saatpunktes liegt (rechts). Per Definition verbinden die Kanten/Knoten $\langle v_i, v_j \rangle \in E$ des Graphen G zwei Knoten v_i, v_j und es gibt zwei Typen von ∞-gewichteten Kanten: z-Kanten A_z und r-Kanten A_r. Dabei ist Z die Anzahl der abgetasteten Punkte (Knoten) entlang eines Strahls mit $z = (0,...,Z-1)$, und R ist die Anzahl der Strahlen, die durch die Oberflächenpunkte eines Polyeders gesandt wurden, mit $r = (0,...,R-1)$. Der Knoten $V(x_n, y_n, z_n)$ ist hierbei ein Nachbar des Knotens $V(x,y,z)$, bzw. der Knoten $V(x_n, y_n, z_n)$ und der Knoten $V(x,y,z)$ gehören zum selben Dreieck im Fall einer Triangulierung des Polyeders:

$$A_z = \{\langle V(x,y,z), V(x,y,z-1)\rangle \mid z > 0\}$$
$$A_r = \{\langle V(x,y,z), V(x_n, y_n, \max(0, z-\Delta_r))\rangle\}$$

Die ∞-gewichteten Kanten zwischen den Knoten entlang eines Strahls A_z stellen sicher, dass alle Knoten innerhalb einer Polyederoberfläche eines Graphen einen *closed set* ergeben, was wiederum gewährleistet, dass das Innere des Objekts (Prostatadrüse) vom Hintergrund innerhalb der Daten getrennt wird. Auf der anderen Seite enthalten die Kanten A_r zwischen Knoten von unterschiedlichen Strahlen eine Menge von möglichen Segmentierungen und stellen über einen Parameter Δ_r

eine bestimmte Glattheit sicher – je größer der Parameter ist, desto größer ist auch die Anzahl der möglichen Segmentierungen. Letztendlich erzeugt der s-t-Schnitt eine optimale Segmentierung einer Prostatadrüse unter dem Einfluss des Parameters Δ_r, der dabei die Steifigkeit der Grenze zum Hintergrund kontrolliert. Zum Beispiel stellt eine Deltawert von Null ($\Delta_r = 0$) sicher, dass das Segmentierungsergebnis in einer Kugel resultiert und die Größe und Position der Kugel innerhalb des Bildes auf den Kanten zwischen Quelle und Senke (s-t-Kanten) und dem benutzerdefinierten Saatpunkt basiert. Die Gewichte $w(x, y, z)$ für jede s-t-Kante werden nach folgender Vorschrift zugewiesen: Gewichte werden auf $c(x, y, z)$ gesetzt, wenn z Null ist, ansonsten auf $c(x, y, z) - c(x, y, z-1)$. Dabei ist $c(x, y, z)$ der Absolutwert der Differenz zwischen einem mittleren Grauwert der Prostatadrüse und dem Grauwert des Voxels an der Position (x, y, z). Der mittlere Grauwert der Prostatadrüse kann dabei automatisch im Bereich des benutzerdefinierten Saatpunktes innerhalb der Prostata berechnet werden.

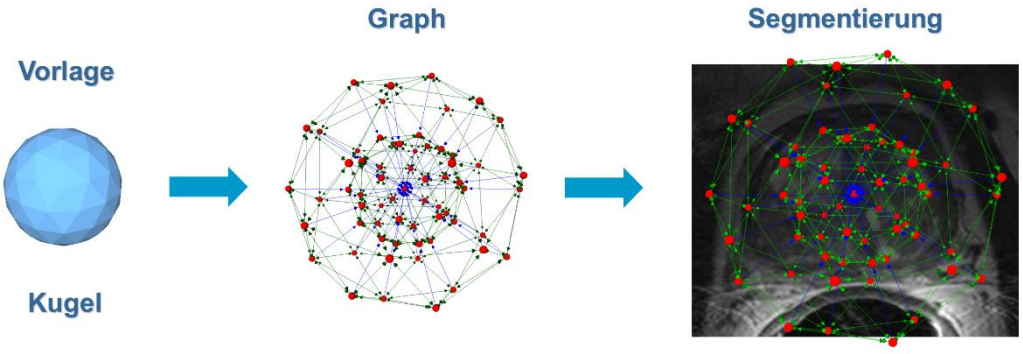

Abbildung 17 – Prinzip des *Nugget-Cut*-Segmentierungsschemas: Eine kugelförmige Vorlage (links) wird als Grundstruktur für den Segmentierungsgraphen (Mitte) verwendet, der innerhalb des Bildes konstruiert wird (rechts).

Zur Evaluierung wurde ein C++ Modul innerhalb der medizinischen Plattform MeVisLab implementiert. In dieser C++ Implementierung benötigte eine Segmentierung, bestehend aus: (1) Aussenden der Strahlen, (2) Konstruktion des Graphen und (3) *Min-Cut*-Berechnung, ungefähr eine Sekunde auf einem Macbook Pro Notebook mit einem Intel Core i7-2860QM CPU, 4 x 2.50 GHz, 8 GB RAM, Windows 7 Professional 64.

Abbildung 18 präsentiert Screenshots einer automatischen Segmentierung (rot) in einer axialen (links) und einer sagittalen (rechts) Schicht. Der blaue Pfeil im linken Bild zeigt auf die Position des benutzerdefinierten Saatpunktes. Abbildung 19 zeigt mehrere 3D-Visualisierungen von Segmentierungsergebnissen einer Prostatadrüse. Auf der linken Seite sind die Segmentierungsknoten (rot) und in der Mitte das triangulierte Segmentierungsergebnis (grün/gelb) mit umgebenden Strukturen zu sehen. Auf der rechten Seite ist die voxelisierte Maske der segmentierten Prostatadrüse (rot/grau) aufgezeigt, die auch für die Berechnung des DSC mit einer manuellen Schicht-für-Schicht-Segmentierung verwendet wurde.

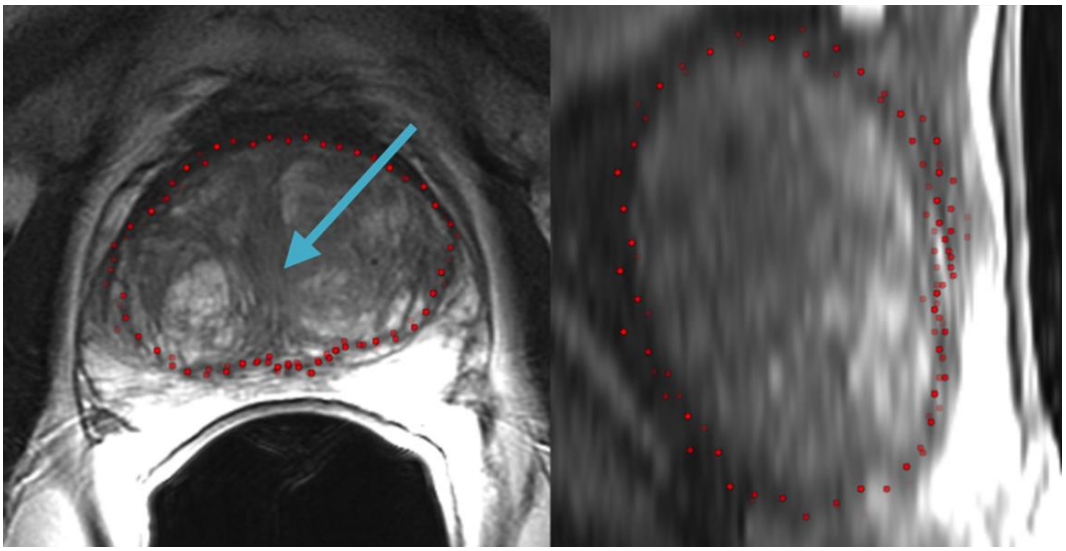

Abbildung 18 – Segmentierungsergebnis (rot) in einer axialen und einer sagittalen Schicht (blauer Pfeil: Position des Saatpunktes).

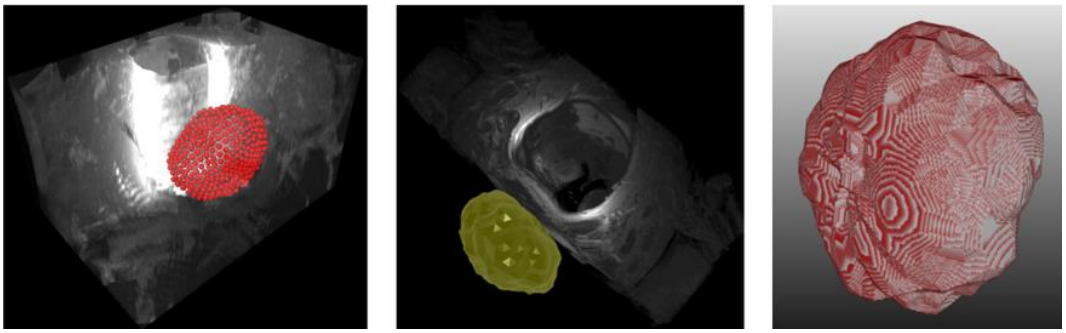

Abbildung 19 – 3D-Visualisierungen des Segmentierungsergebnisses: Segmentierungsknoten und trianguliertes Segmentierungsergebnis mit umgebenden Strukturen (links und Mitte), und voxelisierte Maske der segmentierten Prostatadrüse (rechts).

Segmentierungsergebnisse (rot) von drei unterschiedlichen Fällen für den vorgestellten Algorithmus – jeweils für die axiale Schicht, in der sich der benutzerdefinierte Saatpunkt (blau) befindet – sind in Abbildung 20 dargestellt. Ein direkter Vergleich der automatischen (rot) und manuellen (gelb) Segmentierungsergebnisse für einen bestimmten Fall sind in Abbildung 21 zu sehen. Das automatische Segmentierungsergebnis ist auf der linken Seite der Abbildung zu sehen, die manuelle Segmentierung in der Mitte und die überlagerte Visualisierung beider Segmentierungen auf der rechten Seite. Abbildung 22 wiederum zeigt mehrere axiale Schichten mit automatischen Segmentierungsergebnissen (rot). Die vierte Schicht von links enthält außerdem den benutzerdefinierten Saatpunkt, von dem aus der Graph für die Segmentierung konstruiert wurde.

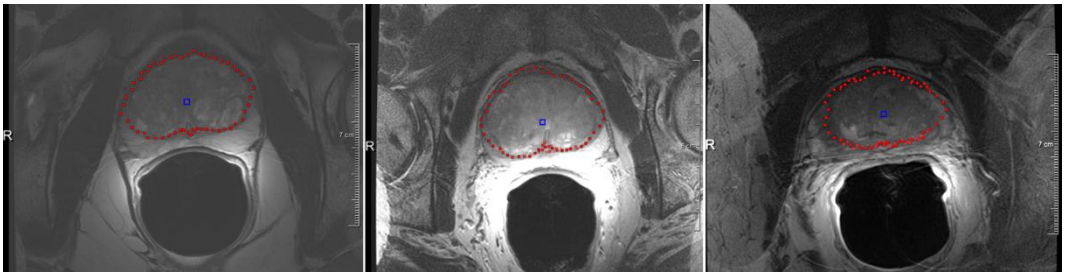

Abbildung 20 – Segmentierungsergebnisse (rot) dreier unterschiedlicher Fälle für den vorgestellten Algorithmus, jeweils für die axiale Schicht, in der sich der benutzerdefinierte Saatpunkt befindet (blau).

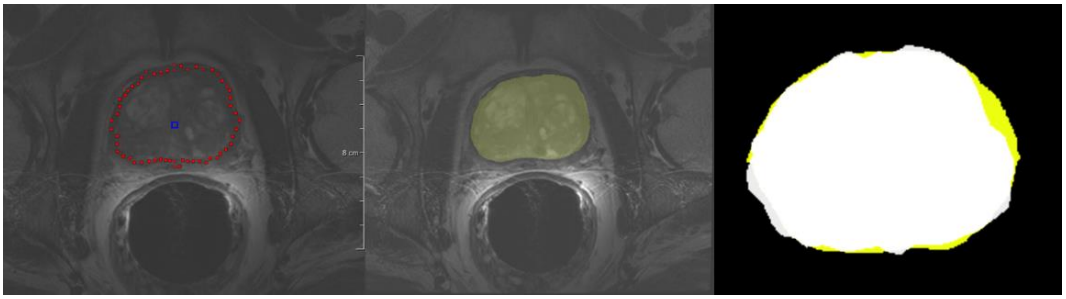

Abbildung 21 – Direkter Vergleich der automatischen (rot) und manuellen (gelb) Segmentierungsergebnisse für einen ausgesuchten Fall: automatisches Segmentierungsergebnis (links), manuelle Segmentierung (Mitte) und überlagerte Visualisierung beider Segmentierungen (rechts).

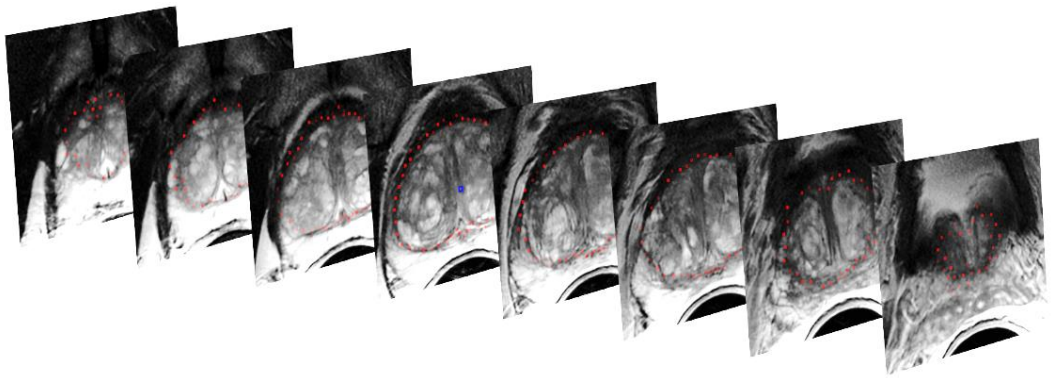

Abbildung 22 – Mehrere axiale Schichten mit automatischen Segmentierungsergebnissen (rot). Die vierte Schicht von links enthält außerdem den benutzerdefinierten Saatpunkt, von dem aus der Graph für die Segmentierung konstruiert wurde.

Tabelle 7 präsentiert den direkten Vergleich der manuellen mit den automatischen Segmentierungen von zehn Prostatadrüsen anhand des Dice Similarity Koeffizienten. Tabelle 8 präsentiert die Zusammenfassung der Evaluationsergebnisse aus Tabelle 7, einschließlich des Minimums (Min.), des Maximums (Max.), des Mittelwerts μ und der Standardabweichung σ der zehn Prostatadrüsen.

Nr.	PCG-Volumen in mm^3		Anzahl der Voxel		DSC (%)
	manuell	automatisch	manuell	automatisch	
1	20820,8	41692,1	682256	1366168	61,79
2	13670,3	16487,9	447949	540277	62,57
3	29006	31706,7	1419342	1551511	84,79
4	51418,2	56490,6	1684871	1851084	88,79
5	44258,4	40306	2165709	1972307	89,42
6	66161,6	67559,2	2167986	2213781	88,76
7	15317,8	13312,5	501932	436224	83,93
8	32826,1	38079,4	1075646	1247786	75
9	22047,6	13289,7	722456	435477	69,68
10	17718,1	16886	866648	825950	84,71

Tabelle 7 – Direkter Vergleich der manuellen mit den automatischen Segmentierungen von zehn Prostatadrüsen anhand des Dice Similarity Koeffizienten (DSC).

	PCG-Volumen in cm^3		Anzahl der Voxel		DSC (%)
	manuell	automatisch	manuell	automatisch	
Min.	13,67	13,29	447949	435477	61,79
Max.	66,16	67,56	2167986	2213781	89,42
$\mu \pm \sigma$	$31{,}32 \pm 17{,}45$	$33{,}58 \pm 18{,}88$	1173479,5	1244056,5	$78{,}94 \pm 10{,}85$

Tabelle 8 – Evaluationsergebnisse: Minimum (Min.), Maximum (Max.), Mittelwert μ und Standardabweichung σ von zehn Prostatadrüsen.

2.6. Semi-automatische Echtzeit-Konturierung

In den Beiträgen [7], [8] wird ein semi-automatischer und skalierungsinvarianter Segmentierungsalgorithmus zur Echtzeit-Konturierung vorgestellt. Dabei "verpackt" der Ansatz Parameter des Algorithmus in seiner Interaktivität für den Anwender. Dadurch wird vermieden, dass ein Anwender, um ein akzeptables Segmentierungsergebnis zu erzielen, ihm unbekannte Parametereinstellungen finden muss, die er im Gegensatz zum Entwickler des Algorithmus nicht ohne weiteres verstehen kann. Für die interaktive Segmentierung wurde ein spezieller graphbasierter Ansatz entwickelt, der sich insbesondere für eine interaktive Echtzeit-Konturierung eignet, da nur ein benutzerdefinierter Saatpunkt innerhalb der Zielstruktur benötigt wird und sich das Segmentierungsergebnis durch die besondere geometrische Konstruktion des Graphen sehr schnell berechnen lässt. Außerdem lassen sich die Grauwertinformationen, die für den Ansatz benötigt werden, automatisch aus dem Bereich um den benutzerdefinierten Saatpunkt herum extrahieren. Der Ansatz wurde über

feste Saatpunkte in medizinischen 2D- und 3D-Daten evaluiert. Ein direkter Vergleich mit wesentlich zeitintensiveren manuellen Segmentierungen hat die praktische Anwendbarkeit des Ansatzes erwiesen.

Der Segmentierungsansatz funktioniert mit 2D- und 3D-Daten und beginnt mit der Graphkonstruktion, ausgehend von einem benutzerdefinierten Saatpunkt innerhalb der zu segmentierenden Struktur. Die Knoten $n \in V$ des Graphen $G(V,E)$ werden entlang von Strahlen abgetastet, die radial vom Saatpunkt ausgesandt werden. Zusätzlich ist $e \in E$ eine Menge von Kanten, die aus Kanten zwischen den Knoten bestehen und aus Kanten, die die Knoten mit einer Quelle s und einer Senke t verbinden, um die Berechnung eines minimalen s-t-Schnitts zu ermöglichen. In Anlehnung an die Notation aus den vorherigen Abschnitten verbindet eine Kante $\langle v_i, v_j \rangle \in E$ zwei Knoten v_i, v_j. In der Kantenmenge gibt es zwei Arten von ∞-gewichteten Kanten: p-Kanten A_p und r-Kanten A_r. P ist die Anzahl der Knoten, die entlang eines Strahles $p = (0,..., P-1)$ abgetastet wurden, und R ist die Anzahl der Strahlen, die radial ausgesandt wurden, mit $r = (0,..., R-1)$. $V(x_n, y_n)$ ist als Nachbar von $V(x,y)$ definiert:

$$A_p = \{\langle V(x,y), V(x,y-1)\rangle \mid y > 0\}$$
$$A_r = \{\langle V(x,y), V(x_n, \max(0, y-\Delta_r))\rangle\}$$

Die ∞-gewichteten Kanten für eine Oberfläche in 3D werden äquivalent zu den ∞-gewichteten Kanten für eine Kontur in 2D definiert:

$$A_p = \{\langle V(x,y,z), V(x,y,z-1)\rangle \mid z > 0\}$$
$$A_r = \{\langle V(x,y,z), V(x_n, y_n, \max(0, z-\Delta_r))\rangle\}$$

Ist der Graph konstruiert, wird der minimale s-t-Schnitt für den Graphen berechnet, der wiederum dem Segmentierungsergebnis entspricht. In Abbildung 23 findet man verschiedene Beispiele für Vorlagen, mit denen unterschiedliche Pathologien in 2D und 3D segmentiert wurden. Bei allen Beispielen wurde der Graph von einem benutzerdefinierten Saatpunkt aus konstruiert, der innerhalb der Pathologie lag. Für die Segmentierung benötigt der Ansatz auch einen mittleren Grauwert der zu segmentierenden Struktur. Dieser mittlere Grauwert wird im Bereich des Saatpunktes automatisch bestimmt und jedes Mal neu berechnet, wenn der Benutzer ihn interaktiv auf dem Bild verschiebt. Das macht den Ansatz robuster gegen Segmentierungsfehler, wenn der Saatpunkt kurzfristig über Bereiche verschoben wird, die zwar innerhalb der zu segmentierenden Struktur liegen, aber nicht dem mittleren Grauwert der zu segmentierenden Struktur entsprechen, wie z.B. bei sehr hellen Kalzifikationen.

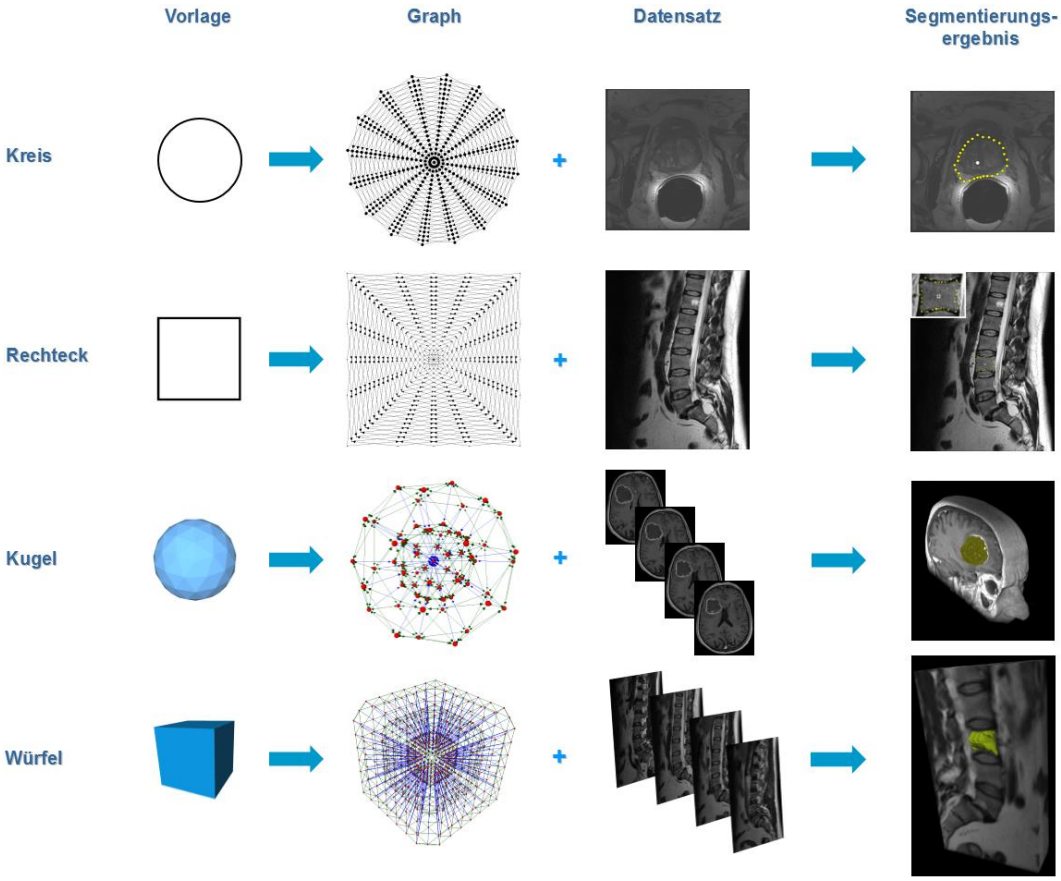

Abbildung 23 – Verschiedene Beispiele für Vorlagen, mit denen unterschiedliche Pathologien in 2D und 3D segmentiert wurden: Eine Kreisvorlage wurde dazu genutzt, einen Graphen aufzubauen und die Prostata zu segmentieren (erste Zeile); eine Rechteckvorlage wurde verwendet, um Wirbelkonturen in einzelnen 2D-Schichten zu bestimmen (zweite Zeile); eine Kugelvorlage diente dazu, Glioblastoma Multiforme (GBM) zu segmentieren (dritte Zeile); für die Bestimmung ganzer Wirbelkörper in 3D kam eine Würfelvorlage zum Einsatz (untere Zeile). Bei allen Beispielen wurde der Graph vom benutzerdefinierten Saatpunkt innerhalb der Pathologie aus konstruiert.

Der vorgestellte Ansatz wurde innerhalb der Plattform MeVisLab realisiert. Der spezielle Aufbau der Graphen ermöglichte eine Echtzeit-Konturierung auf einem Rechner mit Intel Core i5-750 CPU, 4x2.66 GHz, 8GB RAM. Die Evaluierung erfolgte über feste Saatpunkte in medizinischen 2D- und 3D-Daten (Tabelle 9). Abbildung 24 gibt mehrere Screenshots aus einem Video wider, die die interaktive Echtzeit-Konturierung von Wirbelkörpern und Bandscheiben in einer sagittalen Schicht einer MRT-Aufnahme zeigen. Der Mittelpunkt des Graphen ist in Weiß dargestellt und kann vom Benutzer interaktiv auf dem Bild verschoben werden, die roten Punkte stellen das Ergebnis der Segmentierung dar.

Pathologie	Min./Max. der Volumina (cm^3)		$\mu \pm \sigma$ der Volumina (cm^3)		$\mu \pm \sigma$ der DSCs (%)
	manuell	automatisch	manuell	automatisch	
GBM	0,47/119,28	0,46/102,98	23,66 ± 24,89	21,02 ± 22,90	80,37 ± 8,93
HA	0,84/15,57	1,18/14,94	6,30 ± 4,07	6,22 ± 4,08	77,49 ± 4,52
ZA	0,45/4,02	0,35/4,22	1,90 ± 1,88	2,02 ± 1,99	72,66 ± 10,71
PD	13,67/66,16	13,29/67,56	31,32 ± 17,45	33,58 ± 18,88	78,94 ± 10,85
WK 2D	0,25/0,51	0,24/0,49	0,42 ± 0,072	0,40 ± 0,073	90,97 ± 2,2
WK 3D	15,42/33,83	16,64/28,78	24,97 ± 6,15	23,48 ± 5,12	81,33 ± 5,07

Tabelle 9 – Evaluationsergebnisse: Minimum (Min.), Maximum (Max.), Mittelwert μ und Standardabweichung σ für die manuell und automatisch segmentierten Volumina (cm^3) der Pathologien und Mittelwert μ und Standardabweichung σ der Dice Similarity Koeffizienten (DSC) zwischen den manuellen und automatischen Segmentierungen. Abkürzungen: Glioblastoma Multiforme (GBM), Hypophysenadenome (HA), Zerebrale Aneurysmen (ZA), Prostatadrüsen (PD) und Wirbelkörper (WK).

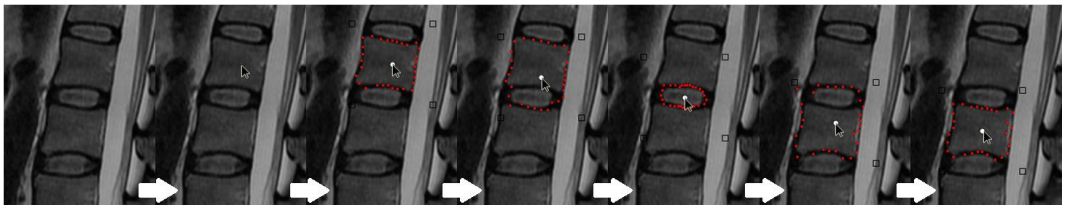

Abbildung 24 – Mehrere Screenshots aus einem Video, die die interaktive Echtzeit-Konturierung von Wirbelkörpern und Bandscheiben in einer sagittalen Schicht einer Magnetresonanztomographie (MRT)-Aufnahme zeigen (von links nach rechts). Der Mittelpunkt des Graphen ist in Weiß dargestellt und kann vom Benutzer interaktiv auf dem Bild verschoben werden, die kleinen schwarzen Boxen zeigen die Ecken der Rechteckvorlage an, und die roten Punkte stellen das Ergebnis der Segmentierung dar.

In Abbildung 25 sieht man eine interaktive Prostata-Segmentierung mit einer Kreisvorlage in einer MRT-Aufnahme. Die oberen vier Bilder zeigen die resultierende Kontur (rot), wenn der benutzerdefinierte Saatpunkt näher an den Rand der Prostata verschoben wurde. Im oberen linken Bild zum Beispiel befindet sich der Saatpunkt näher am linken Rand der Prostata, daher tendiert das Segmentierungsergebnis auch zu einer Übersegmentierung im linken Bereich der Prostata. Allerdings ermöglichen das interaktive Verhalten und die Echtzeit-Rückmeldung des Ansatzes es dem Benutzer, schnell ein zufriedenstellendes Segmentierungsergebnis zu finden (linkes unteres Bild). Zum visuellen Vergleich des Segmentierungsergebnisses aus dem linken unteren Bild ist im rechten unteren Bild die Maske (blau) einer rein manuellen Segmentierung auf derselben 2D-Schicht dargestellt.

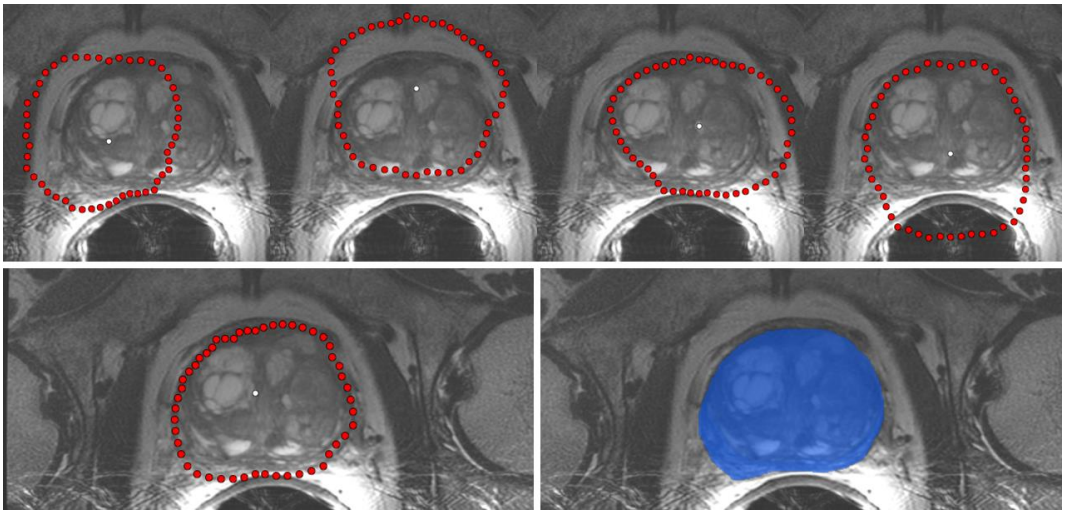

Abbildung 25 – Interaktive Prostata-Segmentierung mit einer Kreisvorlage in einer MRT-Aufnahme: Die oberen vier Bilder zeigen die resultierende Kontur (rot), wenn der benutzerdefinierte Saatpunkt näher an den Rand der Prostata verschoben wurde. Im oberen linken Bild z.B. befindet sich der Saatpunkt näher am linken Rand der Prostata, daher tendiert das Segmentierungsergebnis auch zu einer Übersegmentierung im linken Bereich der Prostata. Allerdings ermöglicht es die interaktive Echtzeit-Rückmeldung des Ansatzes dem Benutzer, schnell ein zufriedenstellendes Segmentierungsergebnis zu finden (linkes unteres Bild). Zum visuellen Vergleich des Segmentierungsergebnisses aus dem linken unteren Bild ist im rechten unteren Bild die Maske (blau) einer rein manuellen Segmentierung auf derselben 2D-Schicht dargestellt.

Der Fortschritt in diesem Beitrag besteht darin, dass Algorithmen (wie der Square-Cut) in einen echtzeitfähigen Ansatz transformiert und getestet wurden. Im Gegensatz zu anderen interaktiven Ansätzen, die meistens eine aufwändige Initialisierung benötigen, wird durch diesen Ansatz eine interaktive Echtzeit-Segmentierung ermöglicht, da nur ein benutzerdefinierter Saatpunkt innerhalb des zu segmentierenden Objektes benötigt wird. Außerdem kann durch die spezielle geometrische Konstruktion des Graphen die Echtzeitfähigkeit (insbesondere in 3D) je nach Rechnerausstattung sichergestellt werden, z.B. durch eine geringere Strahlen- und Knotendichte. Darüber hinaus können Grauwertinformationen im Bereich des Saatpunktes automatisch analysiert und für die Segmentierung genutzt werden. Damit "verpackt" der Ansatz in seinem interaktiven Verhalten Parameter und verhindert dadurch, dass der Benutzer diese definieren muss. Auch wenn die Evaluation gezeigt hat, dass der Ansatz mit (festen) Saatpunkten gute Ergebnisse liefert, ist es (im Gegensatz zu einer interaktiven Segmentierung in 2D) recht schwierig, ein Objekt in 3D interaktiv zu segmentieren. Das liegt daran, dass der Saatpunkt im Raum verschoben wird und dabei die Seiten eines 3D-Objekts für eine zufriedenstellende Segmentierung überwacht werden müssen. Das Verfahren kann dafür allerdings zu einer Art iterativem Ansatz erweitert werden. Dabei segmentiert der Benutzer (interaktiv) zuerst mehrere Konturen in 2D. Anschließend wird ein 3D-Graph zur in-

teraktiven Segmentierung aufgebaut, der allerdings in den drei vorher segmentierten 2D-Schichten bereits fixiert ist (Abbildung 26). Diese 2D-Fixierungen schränken die Anzahl der möglichen s-t-Schnitte massiv ein und unterstützen den Benutzer, auch in 3D einen geeigneten Saatpunkt interaktiv zu finden.

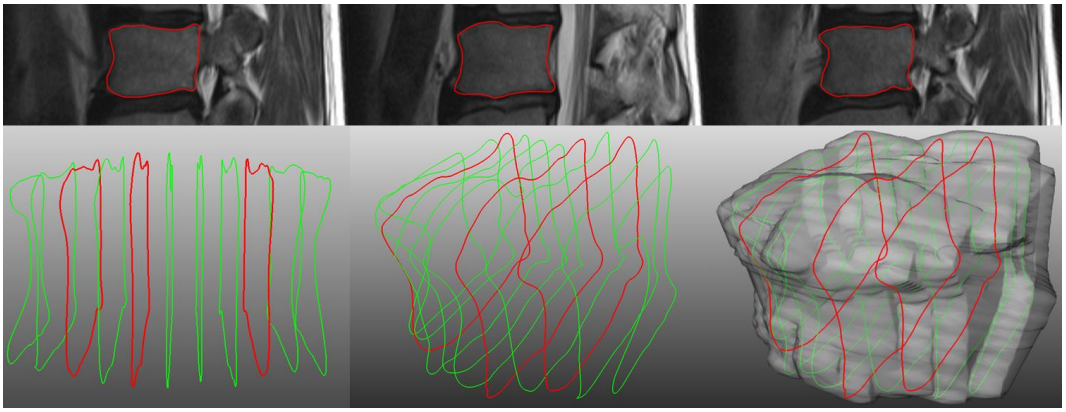

Abbildung 26 – Iterative Segmentierung: Zuerst werden mehrere Wirbelkonturen (obere Reihe, rot) mit einem interaktiven 2D-Ansatz wie aus Abbildung 24 segmentiert. Danach wird ein 3D-Graph zur Segmentierung des Wirbelkörpers in 3D konstruiert, bei dem die drei schon segmentierten 2D-Konturen im 3D-Graphen fixiert sind. Diese Restriktionen des 3D-Graphen beeinflussen und unterstützen die Segmentierung der restlichen Konturen des Wirbelkörpers (grüne Konturen in der unteren Reihe). Die roten Konturen aus den Bildern der unteren Reihe korrespondieren mit den roten Konturen der Bilder der oberen Reihe. Rechts unten ist die voxelisierte Maske (grau) des Wirbelkörpers eingeblendet.

2.7. Echtzeitsegmentierung mit interaktiver Verfeinerung

In dieser Arbeit [9] wird ein Algorithmus zur Echtzeitsegmentierung von medizinischen Bilddaten präsentiert, der es dem Benutzer erlaubt, die Segmentierung zusätzlich interaktiv zu verfeinern. Dadurch kann der Benutzer die semi-automatische Konturierung auch in schwierigen Fällen, bei denen zum Beispiel Objektkanten aufgrund von homogenen Grauwertübergängen fehlen, zu einem zufriedenstellenden Ergebnis führen. Der graphbasierte Ansatz baut auf den vorherigen Arbeiten aus diesem Kapitel auf und ermöglicht eine skalierungsinvariante und vorlagenbasierte Echtzeitkonturierung von Strukturen in medizinischen Bilddaten über einen einzigen Saatpunkt. Allerdings kann der Benutzer die Echtzeitkonturierung jetzt jederzeit unterbrechen und eine beliebige Anzahl von weiteren Saatpunkten auf dem Bild platzieren (optimaler Weise auf den Kanten des zu segmentierenden Objektes). Der Algorithmus erhält dadurch zusätzliche Informationen über das zu segmentierende Objekt und dessen genauen Kantenverlauf und wird sicherstellen, dass die Ergebniskontur durch die zusätzlichen Saatpunkte verläuft. Der Benutzer kann allerdings auch jederzeit wieder zur ursprünglichen interaktiven Segmentierung des

ersten (initialen) Saatpunktes zurückkehren, wobei die zusätzlichen Saatpunkte (auf den Objektkanten) erhalten bleiben und das Segmentierungsergebnis weiterhin beeinflussen. Genauso kann der Benutzer die zusätzlichen Saatpunkte auf den Objektkanten nochmal repositionieren, entfernen oder neu hinzufügen und so den Algorithmus iterativ zu einem für den Benutzer zufriedenstellenden Segmentierungsergebnis führen.

Der vorgestellte Ansatz wurde als eigenes C++ Modul innerhalb von MeVisLab (Version 2.3) auf einem 64 Bit Windows 7 Professional Rechner implementiert. Dabei wurden grundlegende Funktionen von MeVisLab, wie das Laden von medizinischen Daten im DICOM-Format (OpenImage-Modul), das Anzeigen und Navigieren durch 2D-Schichten (View2D-Modul), das Anzeigen von Daten und Ergebnissen in 3D (View3D-Modul) und das Platzieren von Saatpunkten (SoView2DMarkerEditor-Modul) verwendet.

Der Kernalgorithmus ist eine Kombination und Erweiterung der Template-Cut- und Interactive-Cut-Ansätze und einer Verfeinerungsmethode für das Segmentierungsergebnis. Der neue Algorithmus (genannt Refinement-Cut) wie auch die Vorgängermethoden, auf denen dieser aufbaut, gehören zu den graphbasierten Ansätzen. Dabei wird ein Bild als Graph $G(V,E)$ interpretiert, der aus Knoten $n \in V$, abgetastet im Bild, und Kanten $e \in E$, die Verbindungen zwischen Knoten herstellen, besteht. Nach der Graphkonstruktion wird ein minimaler s-t-Schnitt auf dem Graphen berechnet, der die Knoten in zwei disjunkte Mengen teilt, wobei eine Menge das segmentierte Objekt und eine Menge den Hintergrund repräsentiert – Hinweis: für die Berechnung des minimalen s-t-Schnittes werden zwei zusätzliche virtuelle Knoten $s \in V$ (genannt Quelle) und $t \in V$ (genannt Senke) verwendet. Der minimale s-t-Schnitt liefert das globale Optimum auf dem konstruierten Graphen zurück, im Gegensatz zu iterativen Ansätzen wie den Aktiven Konturen, die im Allgemeinen eine Lösung schrittweise finden und dabei in einem lokalen Minimum hängenbleiben können. Die direkte Berechnung eines globalen Minimums wie durch einen minimalen s-t-Schnitt machen graphbasierte Ansätze im Allgemeinen geeignet für interaktive Echtzeit-Anwendungen. Dazu werden zuerst die Knoten des Graphen $n \in V$ entlang der Strahlen abgetastet, die von einem einzigen Saatpunkt aus durch eine Vorlage gesendet werden. Diese Vorlage repräsentiert die grundlegende Form eines zu segmentierenden Objekts. Beispiele sind:

- Ein rechteckige Vorlage für eine Wirbelsegmentierung in 2D;
- Eine kreisförmige Vorlage für die Segmentierung von Prostatadrüsen in 2D;
- Eine würfelförmige Vorlage für die Segmentierung von Wirbeln in 3D;
- Eine kugelförmige Vorlage für die Segmentierung von Prostatadrüsen und Hirntumoren in 3D;
- Oder sogar benutzerdefinierte Vorlagen für Objekte, die zu sehr variieren, um durch eine einfache Vorlage vordefiniert zu werden.

Nachdem die Knoten und die dazugehörigen Texturwerte in einem Bild abgetastet wurden, werden die Kanten E des Graphen generiert, die die Verbindungen zwischen den (virtuellen) Knoten etablieren. Eine Kante $\langle v_i, v_j \rangle \in E$ definiert die

Verbindung zwischen den Knoten v_i und v_j. Dabei existieren zwei Arten von ∞-gewichteten Kanten:

- Intra-Kanten, die Knoten entlang desselben Strahls verbinden, die sicherstellen, dass der minimale s-t-Schnitt nur durch genau eine Kante innerhalb dieses Strahls verläuft;
- Inter-Kanten, die Knoten von verschiedenen Strahlen unter Berücksichtigung eines Steifigkeitswertes Δ_r verbinden, der die Anzahl der möglichen s-t-Schnitte und damit die Flexibilität der resultierenden Segmentierung beeinflusst.

Außerdem gibt es Kanten zwischen den abgetasteten Knoten und den virtuellen Knoten (s und t), die für die Graphkonstruktion eingeführt wurden und deren Kantengewichte von den abgetasteten Texturwerten im Bild und einer Kostenfunktion abhängen. Die spezielle Graphkonstruktion aus diesem Ansatz startet von einem einzigen Saatpunkt aus und ist daher besonders für eine interaktive Echtzeitsegmentierung geeignet, da ein Benutzer nur diesen einen Saatpunkt über das Bild verschieben muss. Dies steht im Gegensatz zu Ansätzen, bei denen mehr Input benötigt wird, zum Beispiel indem der Benutzer Teile des Objektes und des Hintergrunds als Information für den Ansatz markiert. Allerdings kann ein Benutzer des Refinement-Cut-Ansatzes relativ einfach neue Saatpunkte auf der Objektkontur hinzufügen, die den Graph modifizieren und den minimalen s-t-Schnitt zwingen, durch diese zusätzlichen Saatpunkte zu verlaufen. Dazu sucht der Algorithmus nach dem Knoten im Graphen, der dem zusätzlichen Saatpunkt des Benutzers am nächsten liegt (Hinweis: Im Allgemeinen wir ein zusätzlicher Saatpunkt nicht zu 100% mit der Position eines Knotens aus dem Graphen übereinstimmen, vor allem bei einer geringen Strahlen- und Knotendichte, vielmehr wird der nächstgelegene Knoten c aus dem Graphen genommen). Im nächsten Schritt wird der minimale s-t-Schnitt gezwungen, durch die Position des zusätzlichen Saatpunktes zu verlaufen. Um dieses Verhalten sicherzustellen, werden der Knoten c und alle seine Vorgänger auf demselben Strahl mit ∞-gewichteten Kanten mit der Quelle s und alle Nachfolger des Knoten c auf demselben Strahl mit ∞-gewichteten Kanten mit der Senke t verbunden. Zusätzlich wird die Intra-Kante zwischen dem Knoten c und seinem Nachfolgerknoten entfernt. Wird der initiale Saatpunkt vom Benutzer auf dem Bild verschoben, ändert sich im Allgemeinen auch der Knoten c und muss bei der Konstruktion des Graphen neu berechnet werden. Allerdings kann ein zusätzlicher Saatpunkt genauso wie der initiale Saatpunkt auf dem Bild verschoben werden und der Knoten c aus dem Graphen, der diesem am nächsten ist, wird dabei in Echtzeit berechnet, was wiederum den minimalen s-t-Schnitt beeinflusst. Außerdem beeinflusst ein zusätzlicher Saatpunkt auch die Positionen des minimalen s-t-Schnitts der benachbarten Strahlen. Dieser Einfluss wird sogar noch stärker bei kleineren Deltawerten, was wiederum die Flexibilität der resultierenden Segmentierung beeinflusst.

Für eine praktische Anwendung in der translatorischen Forschung wurde der Ansatz auf zwei- und dreidimensionalen Daten aus der medizinischen Routine ge-

testet. Dazu gehörten intraoperative gynäkologische MRT-Daten, MRT-Aufnahmen von der Wirbelsäule und prä- und intraoperative Daten von MR-gestützten Prostatabiopsien.

Abbildung 27 präsentiert die interaktive Verfeinerung einer Segmentierung einer Wirbelkontur in 2D aus einer MRT-Aufnahme. Das Bild auf der linken Seite zeigt die native Aufnahme, das zweite Bild von links zeigt den initialen Saatpunkt des Benutzers (weiß), der innerhalb des Wirbels zur interaktiven Segmentierung platziert wurde. Das dritte Bild von links zeigt das Segmentierungsergebnis der aktuellen Position des benutzerdefinierten Saatpunkts. Die helle Region innerhalb des Wirbels verfälscht die automatische Berechnung des durchschnittlichen Grauwertes im Bereich des benutzerdefinierten Saatpunktes. Dadurch stimmt die resultierende Kontur der Segmentierung (rot) im oberen Bereich und in der linken unteren Ecke nicht mit der Kontur des Wirbels überein (Anmerkung: Für die interaktive Segmentierung des Wirbels wurde eine rechteckige Vorlage zum Aufbau des Graphen genutzt. Dabei stimmt der Mittelpunkt der rechteckigen Vorlage mit der Position des benutzerdefinierten Saatpunkts überein und die gelben Kreuze in den beiden rechten Bildern markieren die Eckpunkte des Rechtecks). Das rechte Bild zeigt das Ergebnis der verfeinerten Segmentierung. Dabei hat der Benutzer drei zusätzliche Saatpunkte platziert (weiße Punkte auf der Kontur des Wirbels) und den Algorithmus dadurch gezwungen, den *Min-Cut* an diesen Positionen auszuführen – was wiederum auch die Schnitte entlang der benachbarten Strahlen beeinflusst. Außerdem können noch Grauwertinformationen aus den Bereichen der zusätzlichen Saatpunkte extrahiert werden, die der Benutzer auf der Kontur des Wirbels platziert hat.

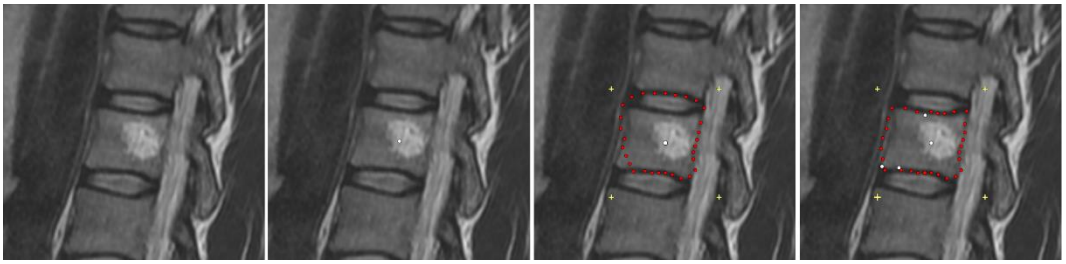

Abbildung 27 – Interaktive Verfeinerung einer Wirbelkontursegmentierung: Das linke Bild zeigt die native Aufnahme und das zweite Bild von links den initialen Saatpunkt des Benutzers (weiß). Das dritte Bild von links zeigt das Segmentierungsergebnis, wobei die resultierende Kontur der Segmentierung (rot) im oberen Bereich und in der linken unteren Ecke nicht mit der Kontur des Wirbels übereinstimmt (die gelben Kreuze markieren die Eckpunkte der Rechteckvorlage). Das rechte Bild zeigt das Ergebnis der verfeinerten Segmentierung. Dabei hat der Benutzer drei zusätzliche Saatpunkte platziert (weiße Punkte auf der Kontur des Wirbels).

Abbildung 28 zeigt die interaktiv verfeinerte Segmentierung eines Rektums aus einem intraoperativen gynäkologischen 3-Tesla MRT-Datensatz. Auf dem linken

Bild ist die native Aufnahme und auf dem zweiten Bild von links der initiale Saatpunkt (weiß) für die interaktive Segmentierung zu sehen, der vom Benutzer innerhalb des Rektums platziert wurde. Die roten Punkte präsentieren das Segmentierungsergebnis, das aus der aktuellen Saatpunktposition resultiert (Anmerkung: Zur interaktiven Segmentierung des Rektums wurde ein Dreieck als Vorlage für die Konstruktion des Graphen verwendet. Hierbei ist der Mittelpunkt des Dreiecks im benutzerdefinierten Saatpunkt lokalisiert und die drei gelben Kreuze geben die Positionen der Ecken des Dreiecks wieder). Im dritten Bild von links wurde ein zusätzlicher Saatpunkt (weiß) in der linken oberen Kontur des Rektums platziert. Dieser zusätzliche Saatpunkt zwingt den Algorithmus, den Min-Cut an dieser Position auszuführen. Im vierten Bild von links hat der Benutzer den initialen Saatpunkt interaktiv im Rektum repositioniert, um ein besseres Segmentierungsergebnis zu erzielen. Der zusätzliche Saatpunkt auf der Kontur bleibt während der Repositionierung des initialen Saatpunktes bestehen und zwingt den Algorithmus, weiterhin den Min-Cut an seiner Position in der linken oberen Kontur des Rektums auszuführen. Im rechten Bild hat der Benutzer die Segmentierung mit zwei weiteren Saatpunkten verfeinert.

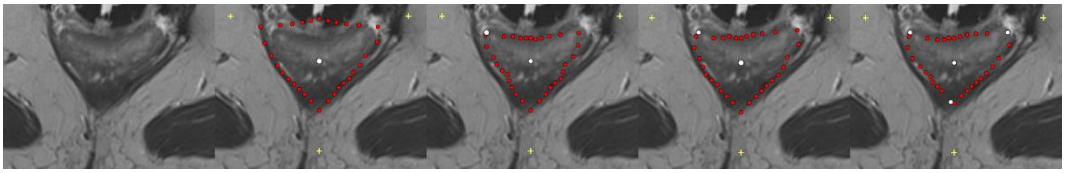

Abbildung 28 – Interaktiv verfeinerte Segmentierung eines Rektums aus einem intraoperativen gynäkologischen 3-Tesla MRT-Datensatz. Das linke Bild zeigt die native Aufnahme und das zweite Bild von links den initialen Saatpunkt (weiß) für die interaktive Segmentierung. Die roten Punkte präsentieren das Segmentierungsergebnis und die drei gelben Kreuze geben die Positionen der Ecken der Dreiecksvorlage wider. Im dritten Bild von links wurde ein zusätzlicher Saatpunkt (weiß) in der linken oberen Kontur des Rektums platziert. Im vierten Bild von links hat der Benutzer den initialen Saatpunkt interaktiv im Rektum repositioniert und im rechten Bild die Segmentierung mit zwei weiteren Saatpunkten verfeinert.

Abbildung 29 präsentiert die interaktive Segmentierung des Lumen und Thrombus einer postoperativen Computertomographie-Angiographie (CTA)-Aufnahme eines Patienten, dessen abdominales Aortenaneurysma (AAA) mit einem Stent behandelt wurde. Das linke Bild zeigt den originalen Scan und das zweite Bild von links die Segmentierung des gestenteten Lumen (rot) mit dem initialen benutzerdefinierten Saatpunkt (grün), der innerhalb des Lumen platziert wurde (Anmerkung: Zur interaktiven Segmentierung wurde ein Kreis als Vorlage für die Graphkonstruktion verwendet). Die folgenden drei Bilder zeigen, wie der Benutzer einen zweiten Saatpunkt platziert und diesen interaktiv zur Thrombuskontur verschiebt. Dabei wird der Graph weiter vom initialen Saatpunkt aus konstruiert, der innerhalb des Lumen liegt. Der zweite Saatpunkt zwingt den Algorithmus, den Min-Cut an

dieser Stelle auszuführen, und beeinflusst damit auch den Min-Cut der benachbarten Strahlen. Während der interaktiven Verschiebung des zweiten Saatpunktes innerhalb des Thrombus (Bilder drei und vier von links) versucht der Algorithmus sich an andere Strukturen im Thrombus anzupassen und diese zu segmentieren. In diesem Beispiel ist kontrastiertes Blut von einem Endoleak zu sehen (länglicher heller Bereich innerhalb des Thrombus) und die resultierende Kontur passt sich diesem Endoleak teilweise – im dritten und vierten Bild im unteren rechten Bereich – an; einmal an die linke Kontur des Endoleaks (drittes Bild) und einmal an die rechte Kontur des Endoleaks (viertes Bild). Im rechten Bild wurde das Segmentierungsergebnis durch einen weiteren Saatpunkt verfeinert, der vom Benutzer auf der Thrombuskontur im linken unteren Bereich platziert wurde.

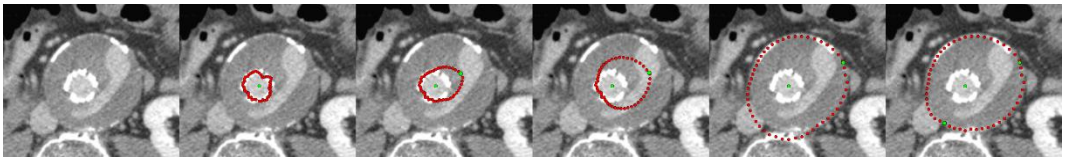

Abbildung 29 – Interaktive Segmentierung von Lumen und Thrombus in einer postoperativen Computertomographie-Angiographie (CTA)-Aufnahme mit gestentetem abdominalen Aortenaneurysma (AAA). Das linke Bild zeigt den originalen Scan und das zweite Bild von links die Segmentierung des gestenteten Lumen (rot) mit dem initialen benutzerdefinierten Saatpunkt (grün). Die folgenden drei Bilder zeigen, wie der Benutzer einen zweiten Saatpunkt platziert und diesen interaktiv zur Thrombuskontur verschiebt. Während der interaktiven Verschiebung des zweiten Saatpunktes (Bilder drei und vier von links) versucht der Algorithmus, sich an das kontrastierte Blut eines Endoleaks anzupassen. Im rechten Bild wurde das Segmentierungsergebnis durch einen weiteren Saatpunkt (links unten) verfeinert.

Abbildung 30 präsentiert die interaktive Segmentierung einer Prostatadrüse in 3D mit einer kugelförmigen Vorlage. Die linken Bilder zeigen die originale Aufnahme in axialer (oben), koronaler (Mitte) und sagittaler (unten) Ansicht. Das zweite Bild von rechts präsentiert das Segmentierungsergebnis (rot) eines benutzerdefinierten Saatpunktes (blau), der innerhalb der Prostata platziert wurde (Anmerkung. Der Saatpunkt wurde in der axialen Ansicht platziert, obwohl er auch in den koronalen und sagittalen Ansichten zu sehen ist). Für den direkten Vergleich mit einer manuellen Segmentierung zeigen die grünen Masken das Ergebnis einer Schicht-für-Schicht-Segmentierung durch einen Experten. Da der initiale Saatpunkt in der Nähe des rechten Prostatarandes platziert wurde, konnte der Algorithmus die Kontur auf der linken Seite der Prostatadrüse nicht ganz exakt segmentieren (axiale und koronale Ansichten). Allerdings macht es das Echtzeit-Verhalten des Ansatzes einfach, durch eine Repositionierung des initialen Saatpunktes ein gutes Segmentierungsergebnis für die axialen, koronalen und sagittalen Ansichten zu erzielen (drittes Bild von links). Im rechten Bild wurde das Segmentierungsergebnis durch einen zusätzlichen Saatpunkt, der durch den Benutzer im unteren rechten Bereich in der sagittalen Ansicht platziert wurde, weiter verfeinert.

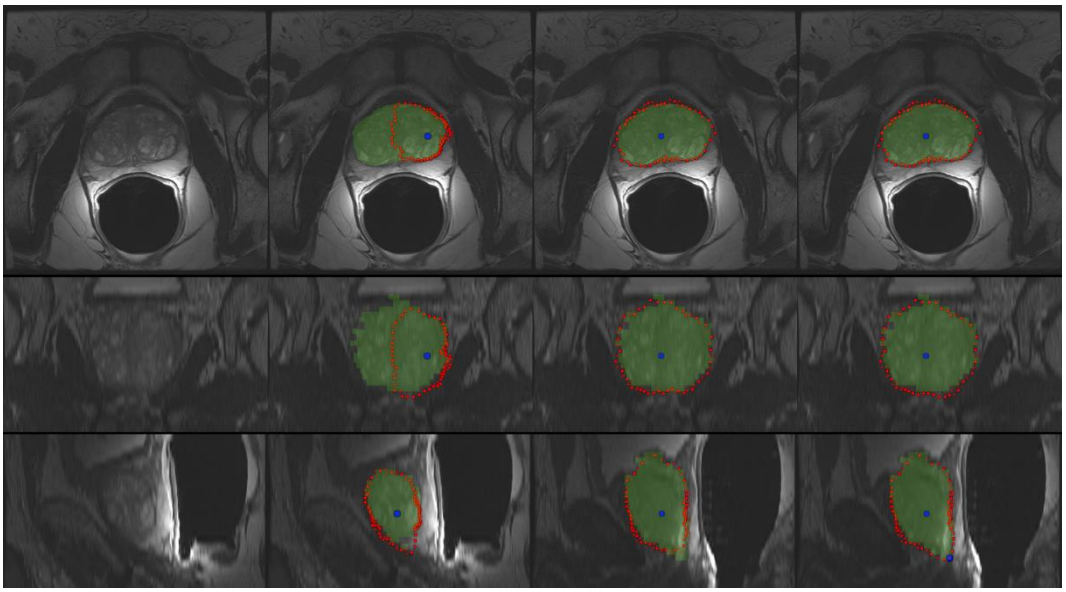

Abbildung 30 – Interaktive Segmentierung einer Prostatadrüse in 3D mit einer kugelförmigen Vorlage: Die linken Bilder zeigen die originale Aufnahme in axialer (oben), koronaler (Mitte) und sagittaler (unten) Ansicht. Das zweite Bild von rechts präsentiert das Segmentierungsergebnis (rot) zu einem benutzerdefinierten Saatpunkt (blau). Für einen direkten Vergleich mit einer manuellen Segmentierung zeigen die grünen Masken das Ergebnis einer Schicht-für-Schicht-Segmentierung durch einen Experten. Drittes Bild von links: Repositionierung des initialen Saatpunktes für ein besseres Segmentierungsergebnis. Im rechten sagittalen Bild wurde das Segmentierungsergebnis durch einen zusätzlichen Saatpunkt (unterer rechter Bereich) weiter verfeinert.

Abbildung 31 zeigt verschiedene Ansichten – axial (oben), koronal (Mitte) und sagittal (unten) – des Segmentierungsergebnisses aus Abbildung 30. Die linken Bilder zeigen die letzten Knoten (rot), die nach dem Min-Cut noch zum Vordergrund gehören und dadurch die Prostatadrüse definieren. In den Bildern der mittleren Spalte wurde zusätzlich die manuelle Schicht-für-Schicht-Expertensegmentierung (grün) eingeblendet. Die rechten Bilder stellen die geschlossene Oberfläche der Knoten aus den linken Bildern dar, die dazu genutzt werden kann, eine Maske des Segmentierungsergebnisses zur weiteren Verarbeitung zu generieren.

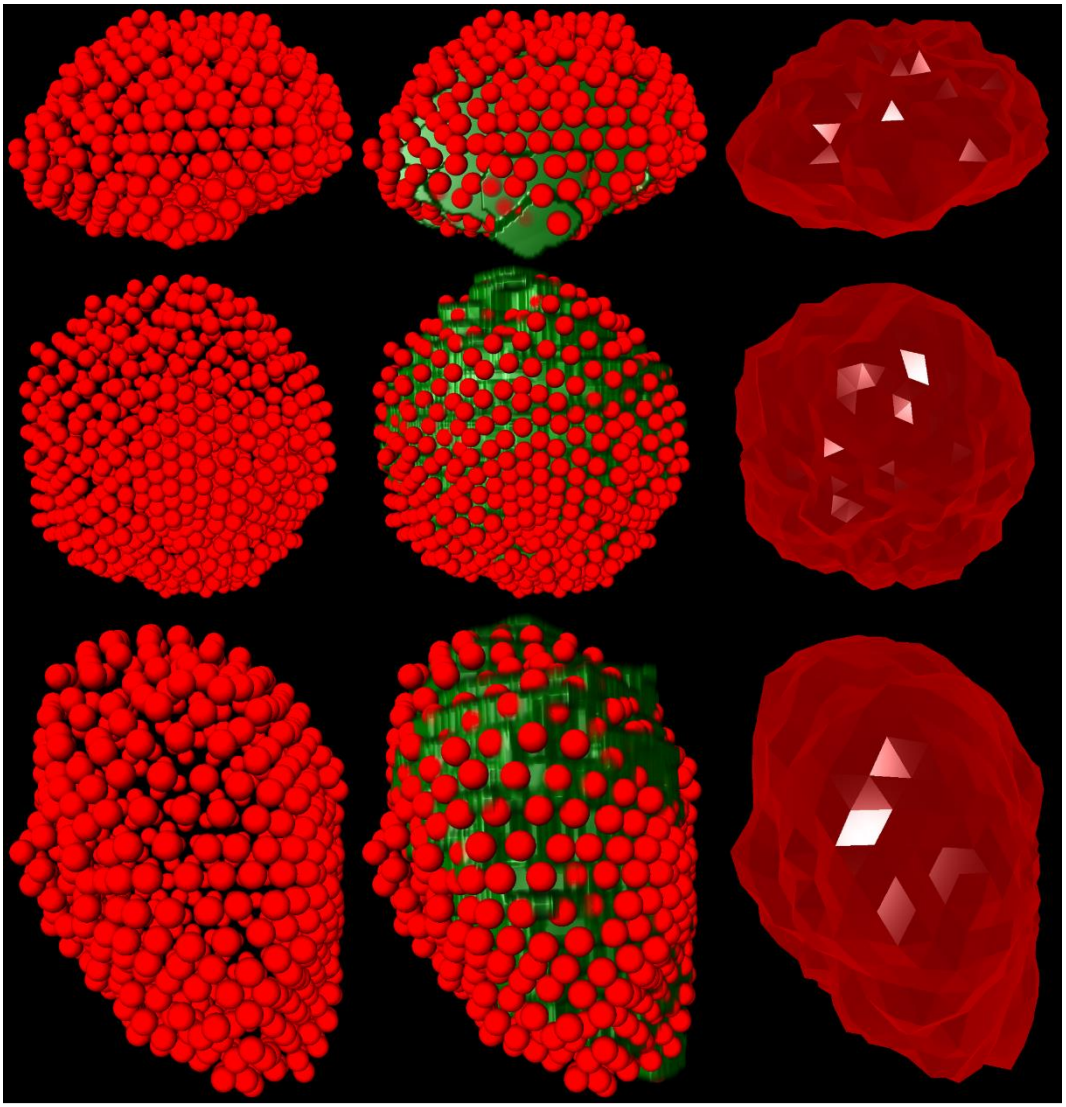

Abbildung 31 – Verschiedene Ansichten – axial (oben), koronal (Mitte) und sagittal (unten) – des Segmentierungsergebnisses aus Abbildung 30. Die linken Bilder zeigen die letzten Knoten (rot) nach dem Min-Cut. In den Bildern der mittleren Spalte wurde zusätzlich die manuelle Schicht-für-Schicht-Expertensegmentierung (grün) eingeblendet. Die rechten Bilder stellen die geschlossene Oberfläche der Knoten aus den linken Bildern dar, die dazu genutzt werden kann, eine Maske des Segmentierungsergebnisses zur weiteren Verarbeitung zu generieren.

Geschwindigkeitstests wurden anhand einer rechteckigen Vorlage zur Segmentierung von Wirbeln auf einem Laptop mit Intel Core i5-750 CPU, 4 x 2.66 GHz, 8 GB RAM auf dem Windows 7 Professional x64 läuft, durchgeführt. Dabei umfasste die Rechenzeit die Graphkonstruktion (Aussenden der Strahlen von einem benutzerdefinierten Saatpunkt, Abtasten der Knoten des Graphen entlang dieser Strahlen und Konstruktion der Kanten), Analysieren des durchschnittlichen Grauwertes im

Bereich des benutzerdefinierten Saatpunktes (was in die Kantengewichte einfließt) und die optimale Min-Cut-Berechnung, die den Hintergrund vom Vordergrund separiert. Der Durchmesser der rechteckigen Vorlage wurde auf 80 mm und der Deltawert auf zwei gesetzt. Für 900 Knoten (berechnet aus 30 Strahlen mit jeweils 30 Knoten) konnte eine durchschnittliche interaktive Segmentierungszeit von 30 Millisekunden (ms) erzielt werden. Für 9.000 Knoten (300 Strahlen, 30 Knoten per Strahl) war die Segmentierungszeit im Allgemeinen unter 100 ms, was für eine interaktive Segmentierung akzeptabel ist. Für 90.000 Knoten (3.000 Strahlen und 30 Knoten per Strahl oder 300 Strahlen und 300 Knoten per Strahl) lag die durchschnittliche Zeit schon im Bereich von 130 ms, wodurch eine kurze Verzögerung bei der interaktiven Segmentierung entstand. Das bedeutet, dass der Ansatz unter diesen Bedingungen streng genommen nicht mehr echtzeitfähig ist, allerdings aus Sicht eines Benutzers noch akzeptabel für eine interaktive Segmentierung. Im Gegensatz dazu waren 900.000 Knoten (30.000 Strahlen, 30 Knoten per Strahl) unter den gegebenen Hardwarevoraussetzungen zu viele für eine praktische interaktive Segmentierung, da die Segmentierungszeit bis zu einer Sekunde dauerte.

Das Segmentierungsergebnis für den interaktiven Ansatz hängt stark von der Position des benutzerdefinierten Saatpunktes ab. Allerdings kann ein Benutzer der “Ground Truth“ (rein manuelle Segmentierung) sehr nah kommen, wenn genügend zusätzliche manuelle Saatpunkte auf der Kontur des Objektes platziert werden. Abbildung 32 zeigt dazu das Beispiel einer Prostata, bei der mehrere Saatpunkte (weiß) platziert wurden, um ein Segmentierungsergebnis zu erhalten, das fast perfekt mit einer manuellen Segmentierung übereinstimmt (grün).

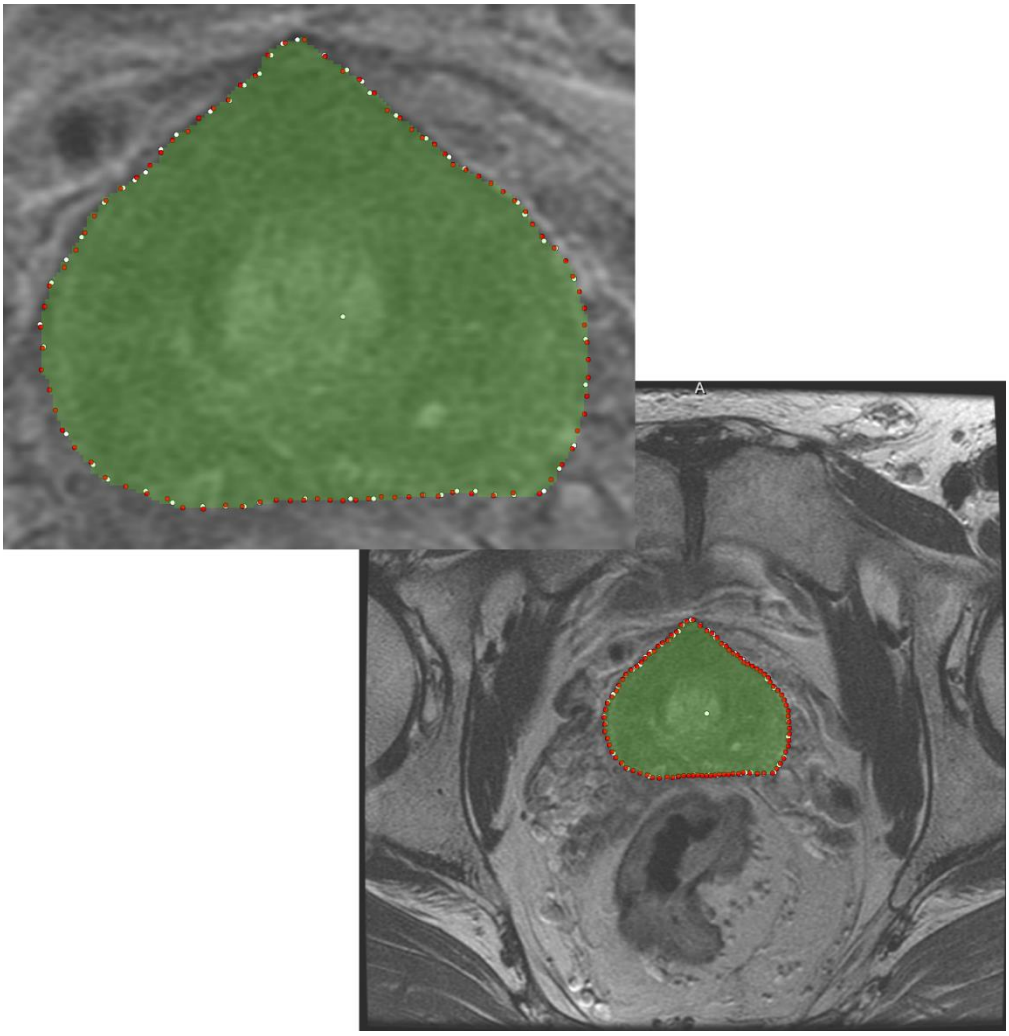

Abbildung 32 – Semiautomatische Segmentierung einer Prostata, bei der mehrere Saatpunkte (weiß) platziert wurden, um ein Segmentierungsergebnis (rot) zu erhalten, das fast perfekt mit einer manuellen Segmentierung übereinstimmt (grün).

2.8. Zusammenfassung

In diesem Kapitel wurden mehrere Segmentierungsalgorithmen für die semi-automatische Analyse von medizinischen Bilddaten vorgestellt. Dabei kamen vorwiegend MRT-Daten zum Einsatz, allerdings eignen sich die Algorithmen auch für andere Modalitäten wie CT oder auch nicht-medizinische Bilddaten. Die Algorithmen arbeiten mit vordefinierten Vorlagen (Templates) der Zielstruktur, was den Segmentierungsprozess erheblich unterstützt. Allen Algorithmen gemeinsam ist hierbei, dass diese nur einen einzigen benutzerdefinierten Saatpunkt innerhalb der zu segmentierenden Struktur benötigen. Diese Besonderheit ermöglicht allerdings auch eine interaktive Segmentierung, bei der ein Benutzer den Saatpunkt auf dem Bild verschiebt und das Segmentierungsergebnis in *Echtzeit* angezeigt bekommt.

Die Evaluierung der Algorithmen erfolgte über feste Saatpunkte, indem die resultierenden Segmentierungsergebnisse mit manuellen, von Ärzten vorgenommenen Schicht-für-Schicht-Segmentierungen verglichen wurden. Dadurch konnte gezeigt werden, dass die Algorithmen zufriedenstellende Ergebnisse liefern können. Zusammengefasst kann der Schluss gezogen werden, dass die Algorithmen die sehr zeitintensiven manuellen Schicht-für-Schicht-Konturierungen von Medizinern unterstützen können, wobei der Benutzer durch die Interaktivität direkt in den Segmentierungsprozess eingreift. Dieses steht im Gegensatz zu vollautomatischen Ansätzen, die es einem Benutzer nach dem Starten des Algorithmus nicht mehr erlauben, in die Segmentierung einzugreifen. Außerdem schlagen vollautomatische Ansätze heutzutage noch zu häufig fehl und haben deshalb auch noch nicht den Weg in die klinische Praxis gefunden. Semi-automatische Ansätze stellen solange einen Kompromiss dar, bis vollautomatische Segmentierungsalgorithmen zuverlässig funktionieren. Allerdings basieren auch semi-automatische Ansätze im Allgemeinen auf der Definition von Parametern. Für die vorgestellten Algorithmen sind das der Steifigkeitswert Delta und die Anzahl und die Verteilung der Knoten des Graphen auf dem Bild. Die vorgestellten Algorithmen eignen sich aber durch die benötigte Interaktivität nicht für alle Fragestellungen im Bereich der Segmentierung, wie beispielsweise für die Auswertung von großen Datenmengen in einer Stapelverarbeitung (Batch-Prozess) oder für die Segmentierung einer umfangreichen Struktur, wie sie der Gefäßbaum der Leber darstellt.

3. Experimentelle Evaluation quelloffener Segmentierungsmethoden unter medizinischen Einsatzbedingungen

3.1. Einleitung

Eine solide Evaluation von Algorithmen aus der medizinischen Bildverarbeitung ist extrem wichtig für die klinische Anwendung. Als sogenannter *Goldstandard*, mit dem sich automatisch erzeugte Resultate messen müssen, gelten immer noch die manuellen Berechnungen von Medizinern, die auf ihren jahrelangen praktischen Erfahrungen basieren. Leider stehen die meisten Algorithmen nur den lokalen Gruppen, in denen sie entwickelt werden, zur Verfügung. Dieser Nachteil wird in den letzten Jahren immer mehr durch medizinische Plattformen aufgehoben, die helfen, die neuen Algorithmen auch anderen Instituten zur Verfügung zu stellen, und damit den Austausch und die Zusammenarbeit von Forschungsgruppen ermöglichen.

3.2. Semi-automatische Segmentierung medizinischer Daten

In diesen Arbeiten [10], [11] wird die semi-automatische Segmentierung von Glioblastomen und Hypophysenadenomen mit der frei verfügbaren *Open Source*-Plattform 3D Slicer präsentiert. Größenänderungen von zerebralen Pathologien wie Hirntumoren sind ein kritischer Faktor bei der Behandlungsentscheidung; heutzutage wird das Volumen einer Pathologie fast immer noch rein manuell vermessen. Dazu müssen in der Regel die einzelnen Schichten der dreidimensionalen Patientenaufnahmen in regelmäßigen Zeitabständen manuell segmentiert werden, um daraus die einzelnen Volumina zu generieren. Die GrowCut-Implementierung unter 3D Slicer stellt dazu eine Alternative dar, die überall zur Verfügung steht und von jedem frei genutzt werden kann. GrowCut ist ein Regionenwachstumsverfahren, das zur interaktiven Segmentierung von n-dimensionalen Bildern verwendet werden kann. Als effektivste Initialisierung von GrowCut hat sich eine einfache Markierung der Pathologie und des Hintergrunds auf einer axialen, sagittalen und koronalen 2D-Schicht herausgestellt. Für die Evaluierung wurden mehrere Mediziner in der GrowCut-basierten Segmentierung anhand eines Pools von Trainingsdaten angeleitet. Anschließend segmentierten die Mediziner neue Datensätze selbstständig, und die Segmentierungsergebnisse wurden mit manuellen Schicht-für-Schicht-Segmentierungen verglichen. Die Auswertung der Ergebnisse hat gezeigt, dass mit GrowCut in wesentlich kürzerer Zeit Segmentierungen erzeugt werden können, die statistisch äquivalent zu den rein manuellen Segmentierungen sind.

Abbildung 33 zeigt einen Screenshot der (3D) Slicer-Oberfläche mit dem Slicer-Editor auf der linken Seite und einem geladenen Patientendatensatz mit Hypophysenadenom (heller, rundlicher Bereich in der Mitte) auf der rechten Seite. Dabei wird vom Patientendatensatz eine axiale Schicht im linken oberen Fenster, eine

sagittale Schicht im linken unteren Fenster, eine koronale Schicht im rechten unteren Fenster und eine 3D-Visualisierung der drei Schichten im rechten oberen Fenster angezeigt. Äquivalent zu Abbildung 33 zeigt Abbildung 34 einen Screenshot der 3D Slicer-Oberfläche mit dem Slicer-Editor auf der linken Seite und einem geladenen Patientendatensatz mit Glioblastom (heller Bereich in der Mitte) auf der rechten Seite. Wieder wird eine axiale Schicht im linken oberen Fenster, eine sagittale Schicht im linken unteren Fenster, eine koronale Schicht im rechten unteren Fenster und eine 3D-Visualisierung der drei Schichten im rechten oberen Fenster angezeigt. Anmerkung: im Allgemeinen bietet sich die Darstellung von drei 2D-Schichten (axial, sagittal und koronal) und einer 3D-Visualisierung des Datensatzes im medizinischen Bereich an. Die einzelnen Fenster auf der rechten Seite unter Slicer können allerdings auch vom Benutzer je nach Anwendung und Pathologie konfiguriert und angeordnet werden.

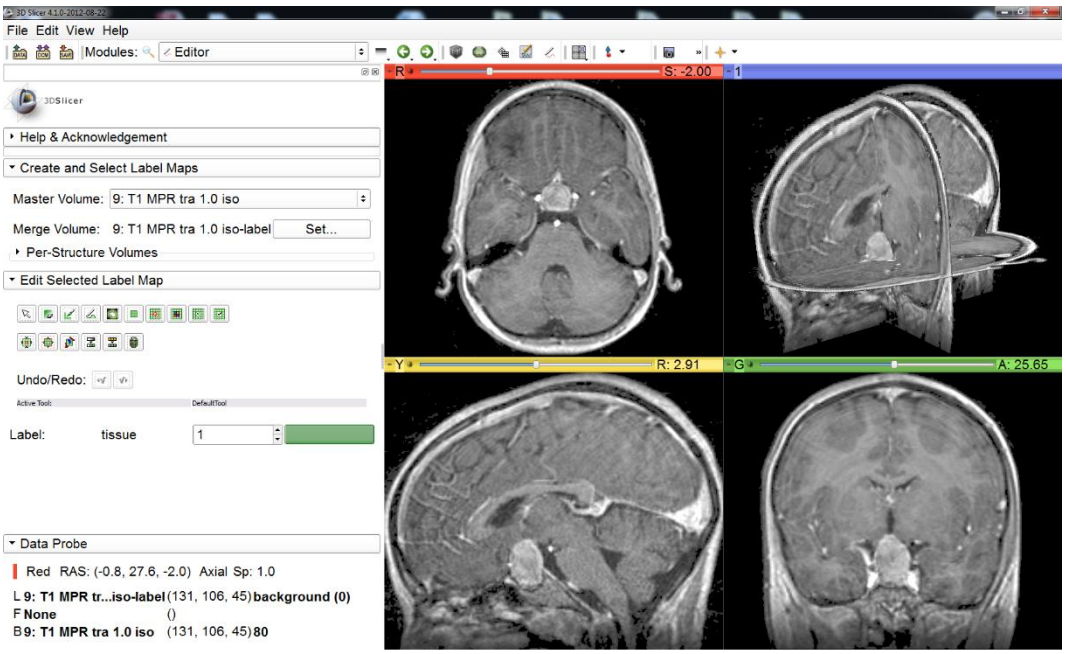

Abbildung 33 – 3D Slicer-Oberfläche mit dem Slicer-Editor auf der linken Seite und einem geladenen Patientendatensatz mit Hypophysenadenom (heller, rundlicher Bereich in der Mitte) auf der rechten Seite: axiale Schicht (linkes oberes Fenster), sagittale Schicht (linkes unteres Fenster), koronale Schicht (rechtes unteres Fenster) und den drei Schichten als 3D-Visualisierung (rechtes oberes Fenster).

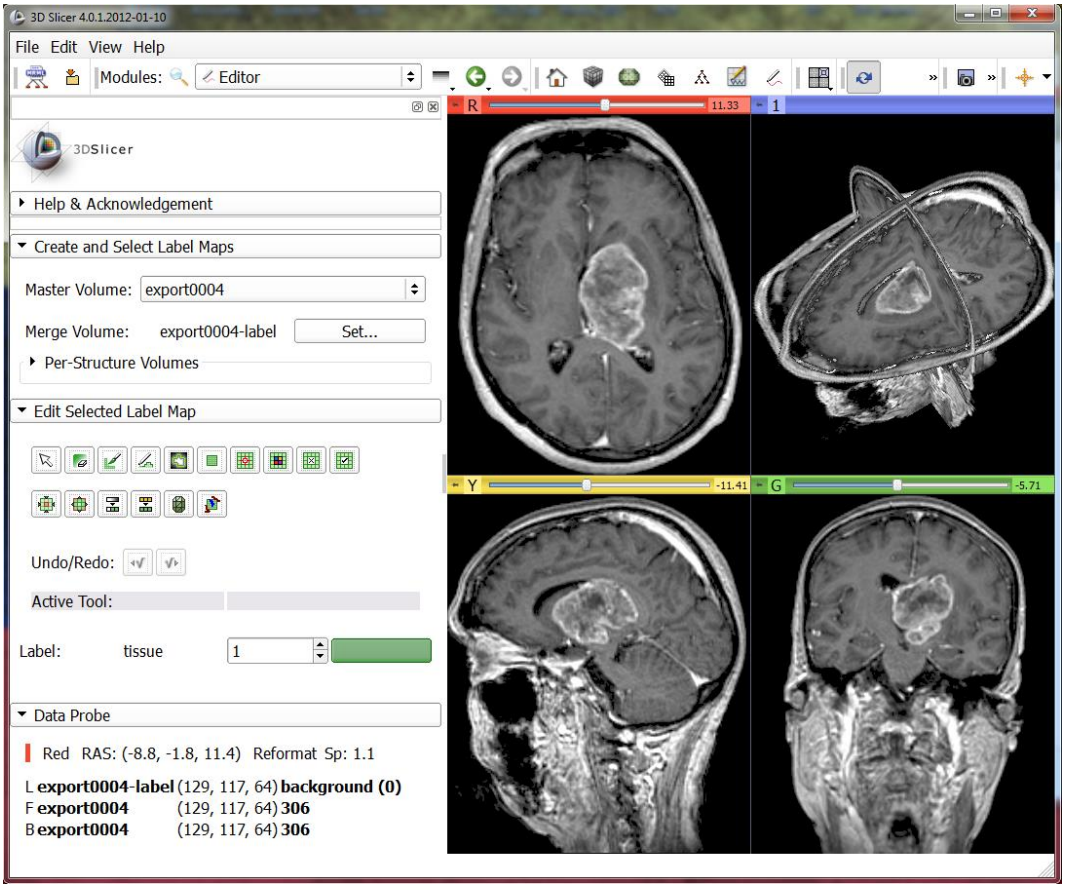

Abbildung 34 – 3D Slicer-Oberfläche mit dem Slicer-Editor auf der linken Seite und einem geladenen Patientendatensatz mit Glioblastom (heller Bereich in der Mitte) auf der rechten Seite: axiale Schicht (linkes oberes Fenster), sagittale Schicht (linkes unteres Fenster), koronale Schicht (rechtes unteres Fenster) und den drei Schichten als 3D Visualisierung (rechtes oberes Fenster).

Der GrowCut-Algorithmus ist ein interaktiver Segmentierungsansatz, dem ein konkurrierendes Regionenwachstumsverfahren zugrunde liegt. Dabei liefert GrowCut zuverlässige und schnelle Segmentierungen von moderat schwierigen Objekten in 2D und 3D. Die benutzerdefinierte Initialisierung von GrowCut besteht aus initialen Saatpunkten im Bild. Diese Saatpunkte werden vom Benutzer unter Slicer in einem geladenen Datensatz eingezeichnet. Dazu wählt der Benutzer im Editor zuerst eine Farbe für die zu segmentierende Pathologie aus und färbt damit Teile dieser Pathologie im Datensatz auf der rechten Seite ein. Anschießend wählt der Benutzer im Editor eine Farbe für den Hintergrund der Pathologie und färbt einige Bereiche mit ihr ein. Wie schon eingangs erwähnt, hat sich als effektivste Initialisierung von GrowCut unter Slicer eine einfache Markierung der Pathologie und des Hintergrunds auf einer axialen, sagittalen und koronalen 2D-Schicht herausgestellt. Abbildung 35 veranschaulicht eine solche Initialisierung des GrowCut-Algorithmus unter Slicer zur automatischen Segmentierung eines Hypophysenadenoms.

Der Tumor wurde in einer axialen Schicht (links), einer koronalen Schicht (Mitte) und einer sagittalen Schicht (rechts) mit der Farbe Grün initialisiert. Anschließend wurden Teile des Hintergrunds mit der Farbe Gelb auf den einzelnen 2D-Schichten initialisiert. Äquivalent zu dieser Initialisierung eines Hypophysenadenoms zeigt Abbildung 36 eine typische Initialisierung des GrowCut-Algorithmus unter Slicer zur automatischen Segmentierung eines Glioblastoms. Wieder wurden Teile des Tumors und des Hintergrunds in einer axialen Schicht (links), einer sagittalen Schicht (zweites Bild von links) und einer koronalen Schicht (drittes Bild von links) in den Farben Grün bzw. Gelb vom Benutzer markiert. Das rechte Bild zeigt zusätzlich noch eine 3D-Darstellung der drei initialisierten 2D-Schichten.

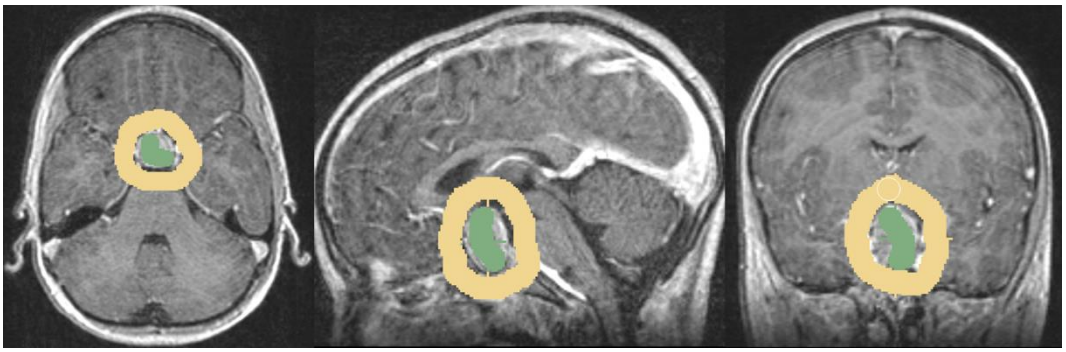

Abbildung 35 – Typische Initialisierung des GrowCut-Algorithmus unter Slicer zur automatischen Segmentierung eines Hypophysenadenoms in einer axialen Schicht (links), einer koronalen Schicht (Mitte) und einer sagittalen Schicht (rechts). Anmerkung: Der Tumor wurde in der Farbe Grün und der Hintergrund in der Farbe Gelb initialisiert.

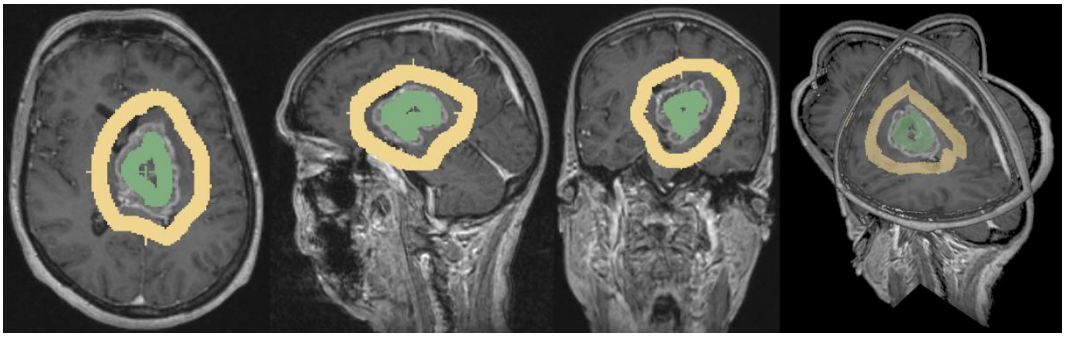

Abbildung 36 – Typische Initialisierung des GrowCut-Algorithmus unter Slicer zur automatischen Segmentierung eines Glioblastoms in einer axialen Schicht (links), einer sagittalen Schicht (zweite Abbildung von links) und einer koronalen Schicht (dritte Abbildung von links). Die rechte Abbildung zeigt eine 3D-Darstellung der drei initialisierten Schichten. Anmerkung: Der Tumor wurde in der Farbe Grün und der Hintergrund in der Farbe Gelb initialisiert.

Nach einer Initialisierung, wie sie in Abbildung 35 und in Abbildung 36 gezeigt wurden, kann der GrowCut-Algorithmus unter Slicer über einen Button im Editor gestartet werden. Der GrowCut-Algorithmus berechnet dann aus den Vorgaben bzw. der Initialisierung des Benutzers das komplette Volumen des Tumors und stellt es graphisch in den 2D- und 3D-Ansichten auf der rechten Seite unter Slicer dar. Vor der Evaluierung von GrowCut wurden mehrere Mediziner in der GrowCut-basierten Segmentierung anhand eines Pools von Trainingsdaten unterrichtet (Trainingsphase). Anschließend segmentierten die Mediziner neue Datensätze selbstständig, und die Segmentierungsergebnisse wurden mit manuellen Schicht-für-Schicht-Segmentierungen verglichen (Evaluierungsphase). Abbildung 37 zeigt im oberen Diagramm den detaillierten Ablauf des Segmentierungsprozesses, der sowohl für die Trainings- als auch für die Evaluierungsphase verwendet wurde. Der Segmentierungsprozess startet mit der Initialisierung des GrowCut-Algorithmus durch den Benutzer auf einer axialen, sagittalen und koronalen Schicht. Anschließend wird die automatische Segmentierung angestoßen und das Ergebnis durch den Benutzer überprüft. Dies resultiert in einem Verfeinerungsschritt, in der die Editor-Werkzeuge genutzt werden können, um das automatische Segmentierungsergebnis zu korrigieren. Während der Evaluierungsphase wurden die Zeiten für die Initialisierung und die Verfeinerung gemessen. Der gesamte Ablauf der Studie, der mit den Bilddaten startet und mit dem Trainings- bzw. dem Evaluierungsprozess endet, ist im unteren Diagramm dargestellt. Dabei wurden die Daten in Trainings- und Evaluierungsdatensätze unterteilt, wobei der Segmentierungsprozess für alle Daten-sätze gleich war. Für die Evaluierung wurde allerdings noch eine weitergehende Bildverarbeitung (bestehend aus einer Voxelisierung und einer anschließenden Volumenberechnung) für die Berechnung des DSC und der Hausdorff-Distanz benötigt.

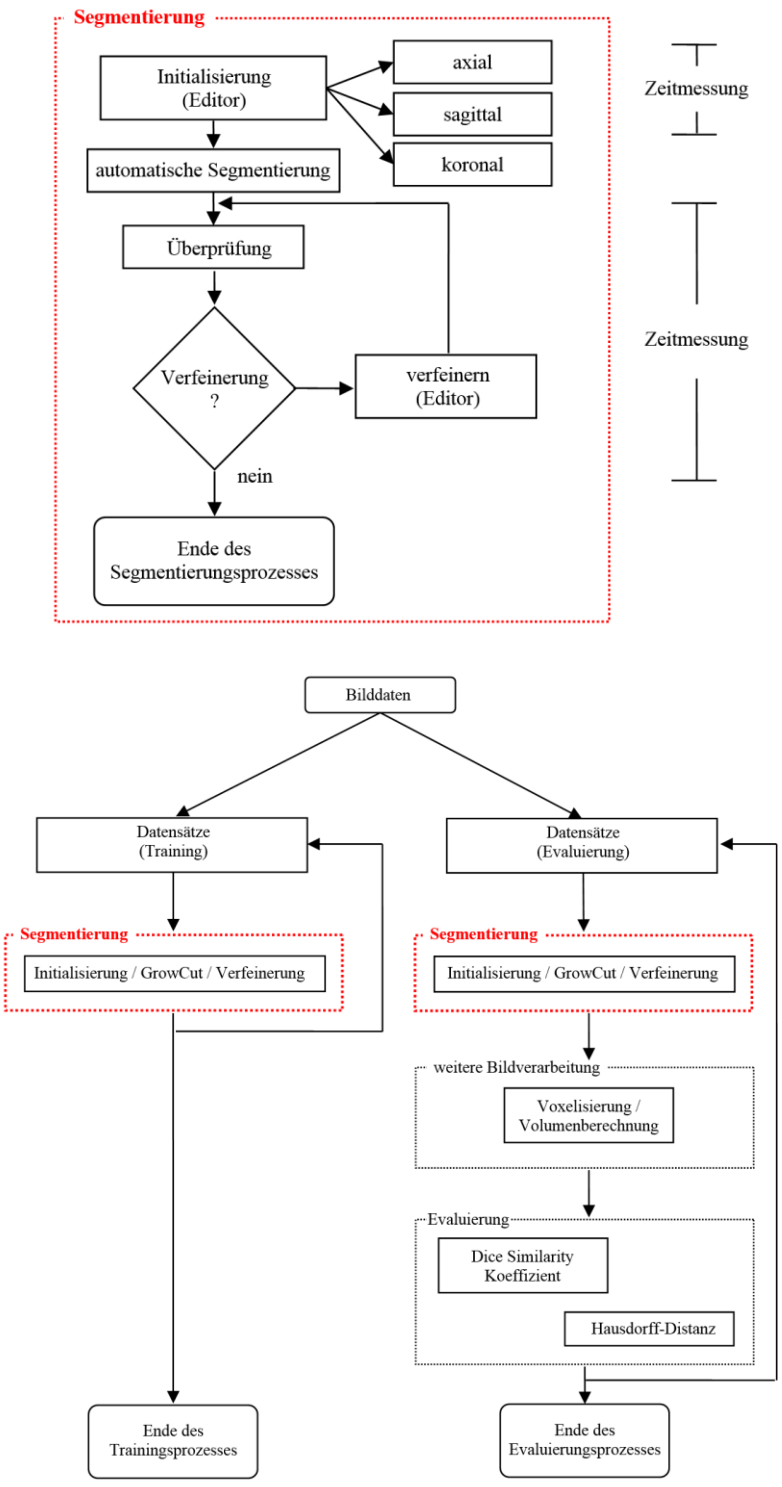

Abbildung 37 – Detaillierter Ablauf des Segmentierungsprozesses, der für die Trainings- und Evaluierungsphase angewandt wurde (oben): Der Segmentierungsprozess startet mit der Initialisierung des GrowCut-Algorithmus durch

den Benutzer auf einer axialen, sagittalen und koronalen Schicht. Anschließend wird die automatische Segmentierung angestoßen und das Ergebnis durch den Benutzer überprüft. Dies resultiert in der Verfeinerungsphase, in der die Editor-Werkzeuge genutzt werden, um das automatische Segmentierungsergebnis zu korrigieren. Während der Evaluierungsphase wurden die Zeiten für die Initialisierung und die Verfeinerung gemessen. Der gesamte Ablauf der Studie, der mit den Bilddaten startet und mit dem Trainings- bzw. dem Evaluierungsprozess endet, wird im unteren Diagramm gezeigt. Dabei wurden die Daten in Trainings- und Evaluierungsdatensätze unterteilt, wobei der Segmentierungsprozess in allen Datensätzen gleich war. Für die Evaluierung wird allerdings noch eine weitergehende Bildverarbeitung benötigt (Voxelisierung und Volumenberechnung), damit der DSC und die Hausdorff-Distanz berechnet werden können.

Abbildung 38 zeigt das GrowCut-Segmentierungsergebnis eines Hypophysenadenoms unter Slicer. Der automatisch segmentierte Tumor wird hierbei in der Farbe Grün in einer axialen Schicht auf der linken Seite, einer sagittalen Schicht in der Mitte und einer koronalen Schicht auf der rechten Seite in den originalen Datensatz eingeblendet.

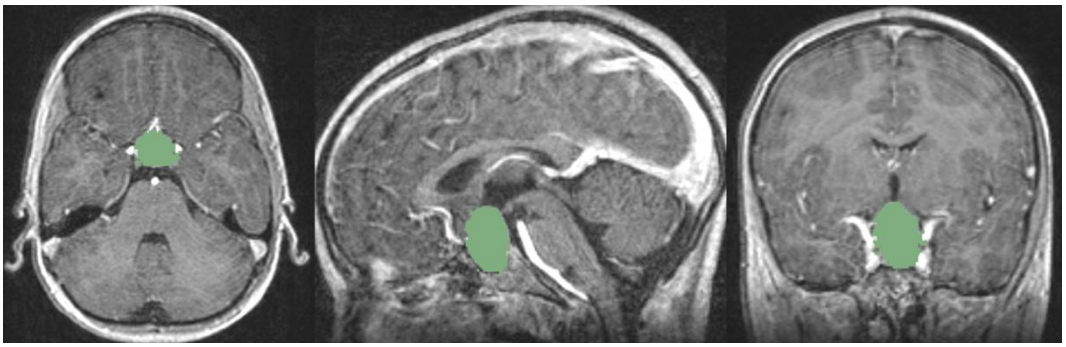

Abbildung 38 – GrowCut-Segmentierungsergebnis eines Hypophysenadenoms unter Slicer (grün) in einer axialen Schicht (links), einer sagittalen Schicht (Mitte) und einer koronalen Schicht (rechts).

Abbildung 39 veranschaulicht den direkten Vergleich zwischen einer GrowCut-basierten Segmentierung und einer rein manuellen Segmentierung in den Aufnahmen zweier Hypophysenadenomen. Dargestellt sind die Aufnahmen und Segmentierungsergebnisse in einer sagittalen Schicht in der oberen Reihe und in einer axialen Schicht in der unteren Reihe. Auf der linken Seite sind jeweils die originalen Schichten ohne Segmentierungen zu sehen. In den Bildern in der Mitte sind die manuellen Segmentierungen der Hypophysenadenome in Gelb in die originalen Datensätze eingeblendet. Die Bilder auf der rechten Seite wiederum zeigen die Ergebnisse der GrowCut-basierten Segmentierungen unter Slicer, eingeblendet in Magenta auf die originalen Schichten der beiden Hypophysenadenome.

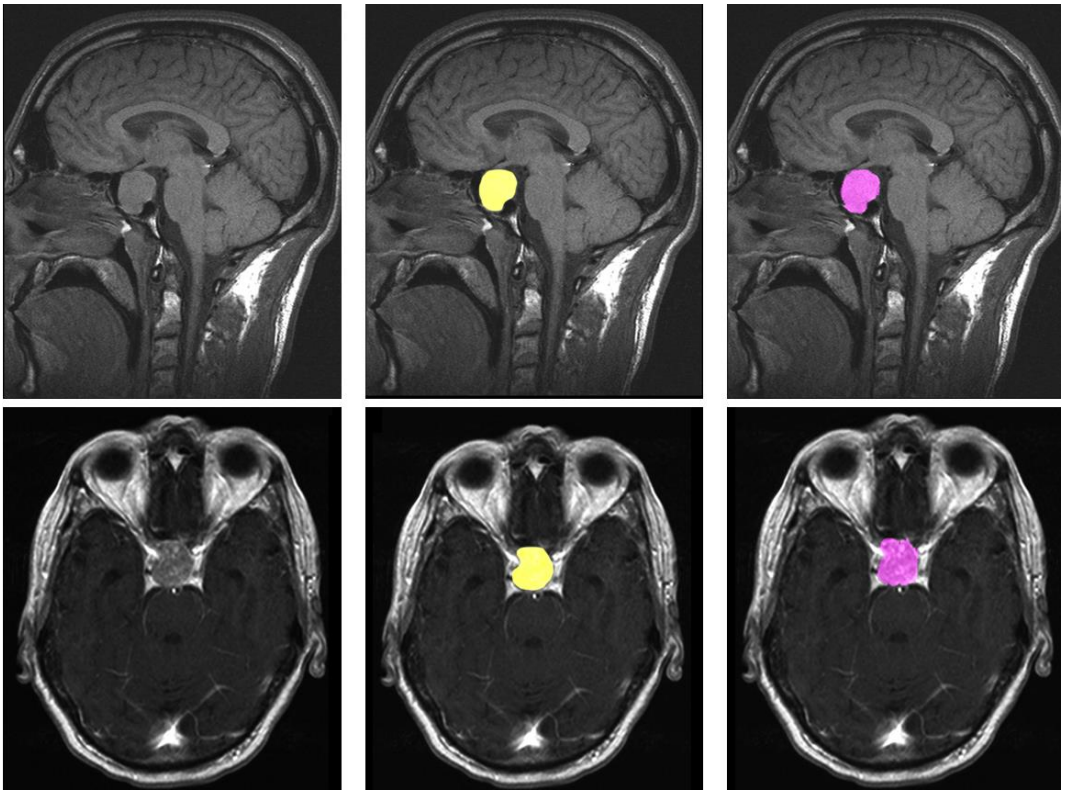

Abbildung 39 – Segmentierungsergebnisse für zwei Hypophysenadenome dargestellt in einer sagittalen Schicht (obere Reihe) und einer axialen Schicht (unteren Reihe); links die originale Schicht ohne Segmentierung, in der Mitte eine manuelle Segmentierung (gelb) und rechts das Ergebnis der GrowCut-Segmentierung unter Slicer (Magenta).

Abbildung 40 soll die die Dilatations- und Erosions-Optionen unter Slicer verdeutlichen, die für die Studie im Verfeinerungsschritt zum Einsatz kamen. Im Hintergrund der Abbildung ist eine axiale Schicht mit einem Glioblastom (umrandet durch ein weißes Rechteck) zu sehen. Auf der linken Seite ist das gezoomte Segmentierungsergebnis von GrowCut in Grün dargestellt. Dieses Segmentierungsergebnis ist allerdings nicht besonders glatt im Bereich des Tumorrandes. Dafür bietet Slicer in seinem Editor-Modul unter anderem Dilatations- und Erosions-Optionen zur Glättung an. Konkret wurden in diesem Beispiel eine Dilatation, eine Erosion und eine weitere Erosion auf das Segmentierungsergebnis angewandt. Das (geglättete) Resultat dieser Operationen ist auf der rechten Seite dargestellt.

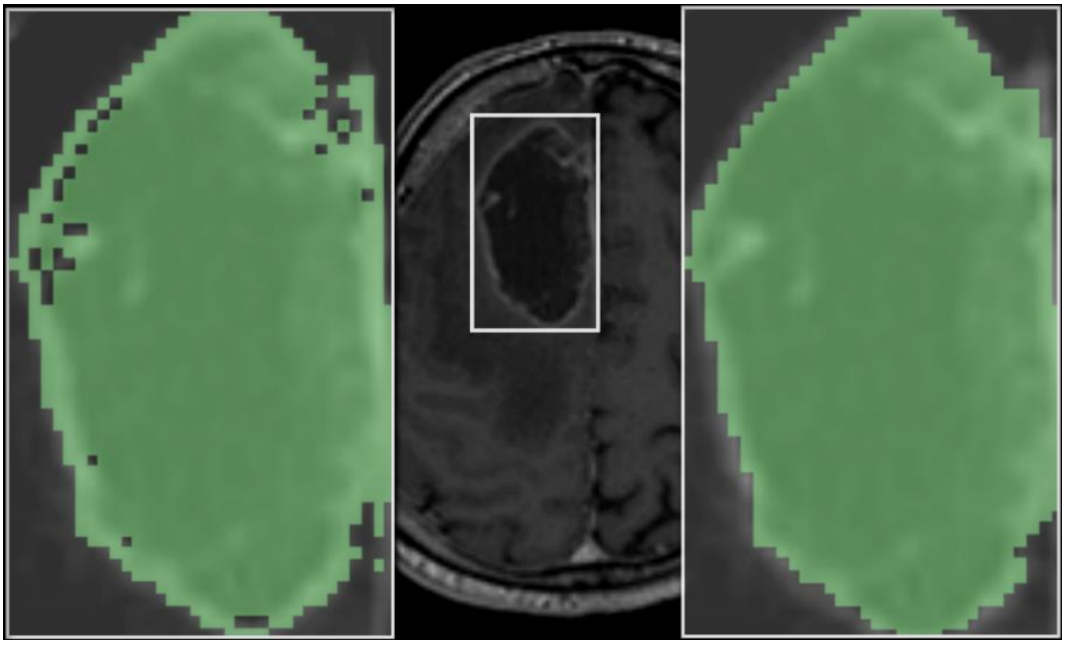

Abbildung 40 – Dieses Bild soll die Dilatations- und Erosions-Optionen unter Slicer verdeutlichen. Im Hintergrund ist eine axiale Schicht mit einem Glioblastom (weißes Rechteck) zu sehen. Auf der linken Seite ist das gezoomte Segmentierungsergebnis von GrowCut (grün) dargestellt. Allerdings ist das Segmentierungsergebnis nicht besonders glatt im Bereich des Tumorrandes. Für ein geglättetes Segmentierungsergebnis können die Dilatations- und Erosions-Optionen unter Slicer verwendet werden. In diesem Beispiel wurden eine Dilatation und zwei Erosionen ausgeführt. Das Ergebnis dieser Operationen ist auf der rechten Seite dargestellt.

In Abbildung 41 wird eine dreidimensionale Visualisierung eines Hypophysenadenoms unter Slicer in Grün gezeigt. Dabei wurde das Hypophysenadenom mit dem GrowCut-Algorithmus von Slicer – wie in den vorherigen Abschnitten beschrieben – segmentiert. In die dreidimensionale Visualisierung des segmentierten Hypophysenadenoms sind zusätzlich noch eine axiale Schicht, eine sagittale Schicht und eine koronale Schicht des originalen Datensatzes zur besseren Orientierung eingeblendet.

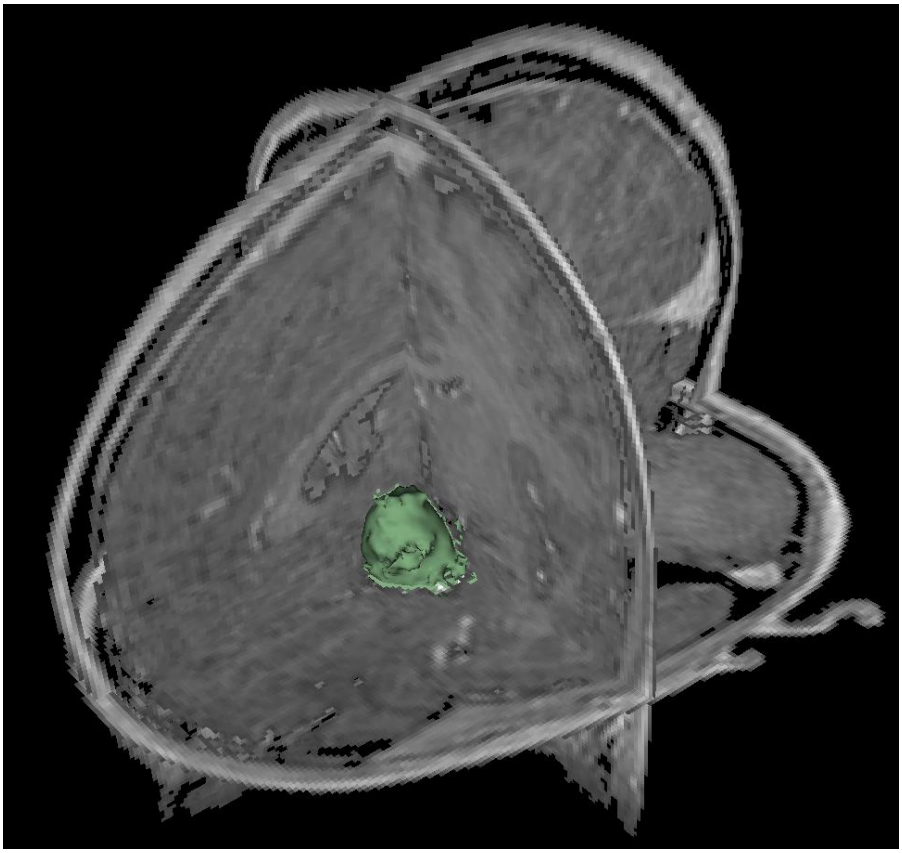

Abbildung 41 – GrowCut-Segmentierungsergebnis für ein Hypophysenadenom in einer 3D-Ansicht (grün). Zusätzlich sind eine axiale, eine sagittale und eine koronale Schicht des originalen Datensatzes dargestellt.

Abbildung 42 zeigt den direkten Vergleich zwischen einer manuellen und einer GrowCut-basierten Glioblastomsegmentierung unter Slicer für eine axiale 2D-Schicht. Zu sehen ist das Ergebnis einer semiautomatischen Segmentierung mit GrowCut unter Slicer in Grün auf der linken Seite und einer rein manuellen Segmentierung in Blau im mittleren Bild (jeweils mit einer Vergrößerung des Segmentierungsbereichs). Außerdem wird auf der rechten Seite noch eine fusionierte Visualisierung der dreidimensionalen Masken der manuellen und der Slicer-gestützten Segmentierung angezeigt.

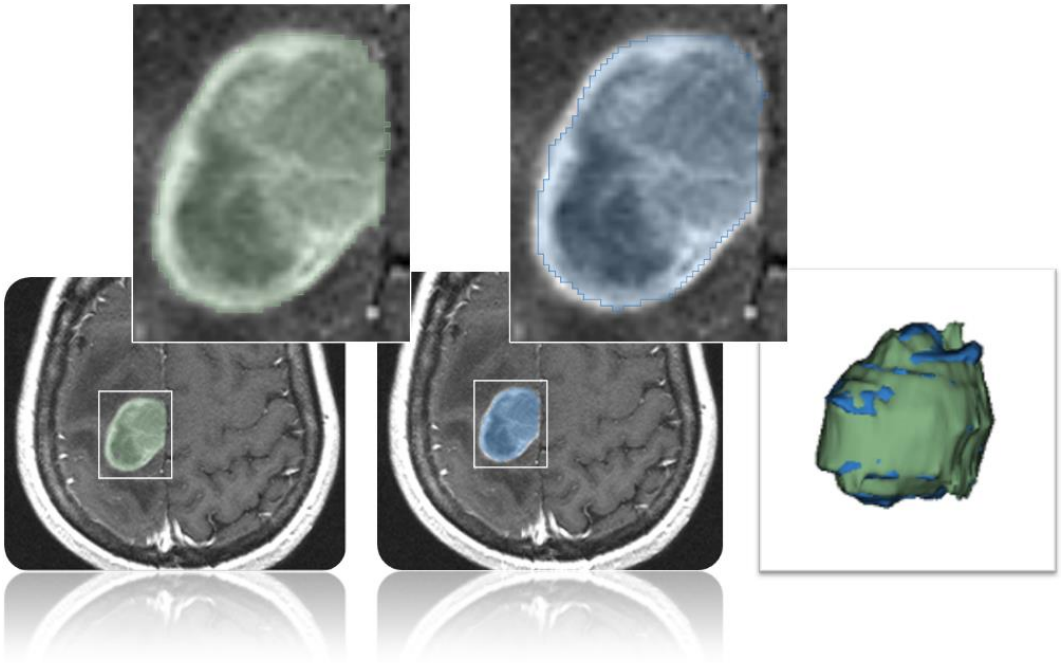

Abbildung 42 – Direkter Vergleich der Segmentierung eines Glioblastoms auf einer axialen Schicht; dargestellt ist das Ergebnis einer semiautomatischen Segmentierung unter Slicer (grün) auf der linken Seite und einer rein manuellen Segmentierung (blau) im mittleren Bild. Zusätzlich wird auf der rechten Seite eine fusionierte Visualisierung der 3D-Masken der manuellen und der Slicer gestützten Segmentierung präsentiert.

In Abbildung 43 ist eine dreidimensionale Visualisierung eines Glioblastoms unter Slicer in Grün dargestellt. Hierbei wurde das Glioblastom mit dem GrowCut-Algorithmus von Slicer – wie in den vorherigen Abschnitten beschrieben – segmentiert. In die dreidimensionale Visualisierung des segmentierten Glioblastoms sind zur besseren Orientierung noch eine axiale Schicht, eine sagittale Schicht und eine koronale Schicht des originalen Datensatzes eingeblendet.

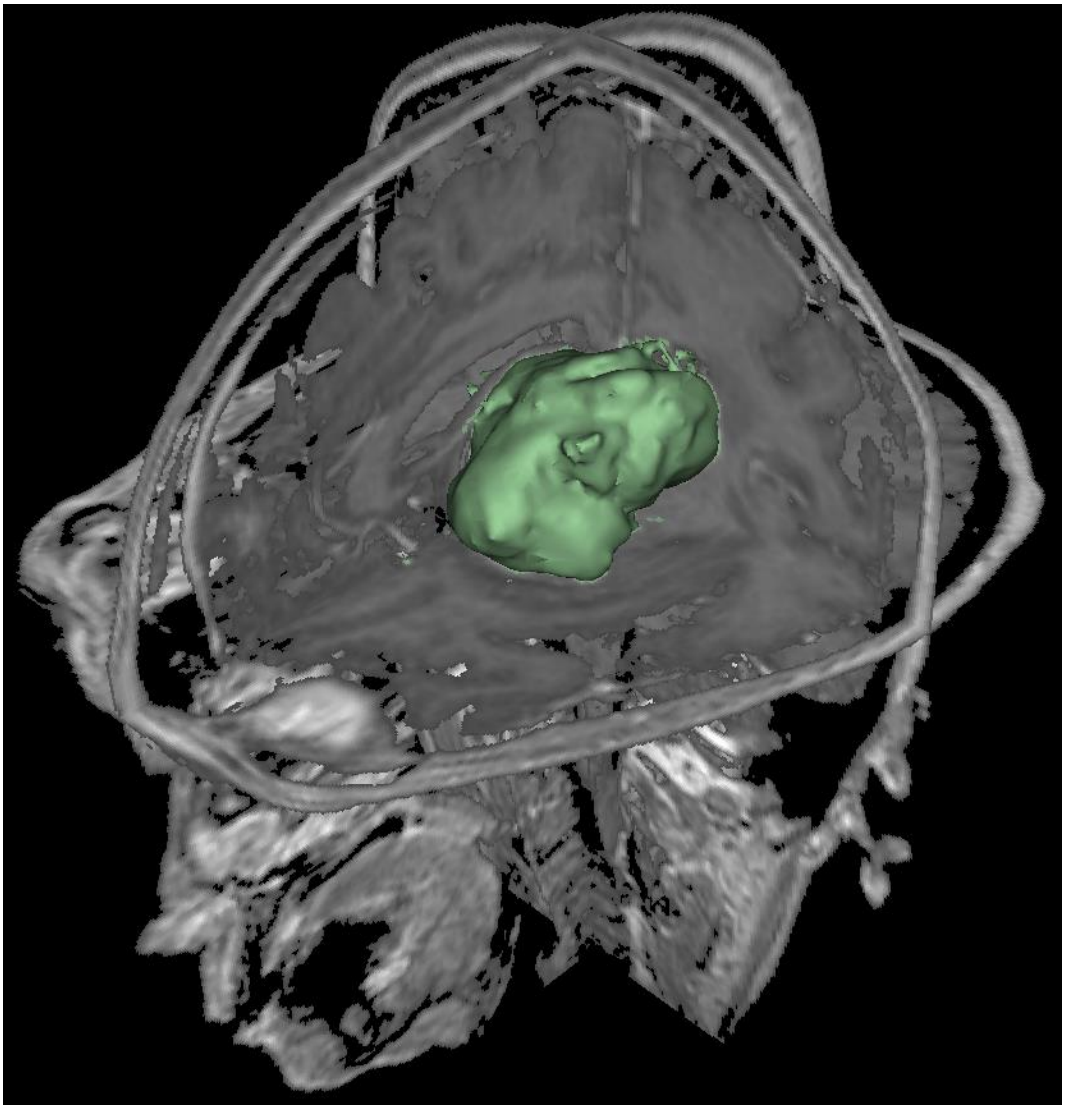

Abbildung 43 – GrowCut-Segmentierungsergebnis für ein Glioblastom in einer 3D-Ansicht (grün). Zusätzlich sind eine axiale, eine sagittale und eine koronale Schicht des originalen Datensatzes dargestellt.

Die folgenden Tabellen zeigen Übereinstimmungen und Laufzeiten für GrowCut-basierte Segmentierungen unter Slicer und rein manuelle Schicht-für-Schicht-Segmentierungen von Hypophysenadenomen und Glioblastomen. Tabelle 10 spiegelt den direkten Vergleich der manuellen mit den automatischen Segmentierungen von zehn Hypophysenadenomen (HA) anhand des Dice Similarity Koeffizienten (DSC) wider. Tabelle 11 fasst diese Evaluationsergebnisse nochmals zusammen und gibt das Minimum (Min.), das Maximum (Max.), den Mittelwert μ und die Standardabweichung σ für alle Hypophysenadenome an.

Nr.	HA-Volumen in mm^3		Anzahl der Voxel		DSC (%)
	manuell	automatisch	manuell	automatisch	
1	6568,69	7195	72461	79370	85,87
2	4150,91	5427,76	4457	5828	84,36
3	7180,44	6481,12	35701	32224	82,11
4	5538,25	5964,5	61094	65796	85,1
5	3230,26	2950,45	22027	20119	77,51
6	9858,4	10410,8	67224	70991	84,46
7	6111,79	5274,89	52500	45311	75,6
8	5082,1	4169,32	56062	45993	80,1
9	15271,1	15838,9	104133	108005	83,41
10	757,01	1016,58	5162	6932	81,21

Tabelle 10 – Direkter Vergleich der manuellen mit den automatischen Segmentierungen von zehn Hypophysenadenomen (HA) anhand des Dice Similarity Koeffizienten (DSC).

	HA-Volumen in cm^3		Anzahl der Voxel		DSC (%)
	manuell	automatisch	manuell	automatisch	
Min.	0,76	1,02	4457	5828	75,6
Max.	15,27	15,84	104133	108005	85.87
$\mu \pm \sigma$	$6{,}37 \pm 3{,}96$	$6{,}47 \pm 4{,}14$	48082,1	48056,9	$81{,}97 \pm 3{,}39$

Tabelle 11 – Evaluationsergebnisse: Minimum (Min.), Maximum (Max.), Mittelwert μ und Standardabweichung σ für zehn Hypophysenadenome (HA).

Tabelle 12 listet sowohl den zeitlichen Vergleich als auch die Übereinstimmungen zwischen manuellen und Slicer basierten Segmentierungen von zehn Glioblastomen auf. Dabei geben die ersten beiden Spalten (*man.* und *Slicer*) die Zeiten in Minuten an, die ein Arzt für eine rein manuelle Schicht-für-Schicht-Segmentierung und eine Slicer gestützte Segmentierung benötigte. Die Spalte *Schichten* gibt wiederum die Anzahl der Schichten an, über die sich der jeweilige Tumor im Datensatz erstreckte. In neun von zehn Fällen waren die Segmentierungszeiten mit GrowCut unter Slicer kürzer als die Zeiten der rein manuellen Segmentierungen; im Durchschnitt benötigte eine Slicer basierte Segmentierung nur 61% der Zeit im Vergleich zu einer manuellen Schicht-für-Schicht-Segmentierung. Die Spalten *DSC* (Dice Similarity Coefficient) und *HD* (Hausdorff-Distanz) zeigen schließlich die Übereinstimmungen zwischen den rein manuellen und den Slicer gestützten Segmentierungen.

Nr.	Zeit in Minuten		Schich -ten	Slicer/man. Minuten	DSC (%)	HD (mm)	Volumen in mm^3		Slicer/man. Volumen
	man.	Slicer					man.	Slicer	
1	9	4	36	0,44	0,85	2,80	33522	44694	1,33
2	19	7,5	51	0,39	0,91	3,68	28373	32383	1,14
3	6	4,5	42	0,75	0,92	1,71	42056	47752	1,14
4	16	6,5	60	0,41	0,91	3,00	69448	78776	1,13
5	3	2,5	10	0,83	0,81	2,00	1480	2016	1,36
6	14	6,25	43	0,45	0,94	2,00	39097	38905	1,00
7	13	8,5	36	0,65	0,87	2,23	22468	25331	1,13
8	7	9,25	42	1,32	0,92	2,12	27368	30648	1,12
9	5	3	11	0,60	0,79	2,39	2703	3908	1,45
10	11	2,5	16	0,23	0,92	1,31	10318	11720	1,14
μ	10,30	5,45	34,7	0,61	0,88	2,32	27683	31613	1,19
		Zeit				Übereinstimmung			

Tabelle 12 – Zeitlicher Vergleich und Übereinstimmung zwischen manuellen und Slicer basierten Segmentierungen von zehn Glioblastomen. Die ersten beiden Spalten (*man.* und *Slicer*) geben die Zeiten in Minuten an, die ein Arzt für eine rein manuelle Schicht-für-Schicht-Segmentierung und eine Slicer gestützte Segmentierung benötigte. Die Spalte *Schichten* gibt die Anzahl der Schichten an, über die sich der jeweilige Tumor erstreckte. In neun von zehn Fällen waren die Zeiten der Slicer-Segmentierungen kleiner als die der rein manuellen Segmentierungen. Im Durchschnitt benötigte eine Slicer basierte Segmentierung 61% der Zeit im Vergleich zu den zeitlichen Aufwendungen für eine manuelle Schicht-für-Schicht-Segmentierung. Die Spalten *DSC* und *HD* zeigen wiederum die Übereinstimmungen zwischen den rein manuellen und den Slicer gestützten Segmentierungen.

3.3. Tracking von Nervenfaserbahnen bei Patienten mit Hirntumoren

In diesem Beitrag [12] werden die Sprachbahnen in Datensätzen von Hirntumorpatienten auf verschiedenen Plattformen segmentiert. Dazu gehört unter anderem der Fibertracking-Algorithmus, der auf der 3D Slicer-Plattform frei zur Verfügung steht. Bei neurochirurgischen Eingriffen, bei denen ein Hirntumor in der Nähe einer Sprachbahn operiert werden soll, ist es extrem wichtig, dass diese genau segmentiert wird, um ihre Beschädigung beim Eingriff zu vermeiden. Die häufigste Erzeugung von Nervenfaserbahnen basiert auf Diffusion Tensor Imaging (DTI)-Aufnahmen, die aufgrund der relativ geringen räumlichen Auflösung aber Einschränkungen aufweisen, wenn Bahnen sich in der Nähe eines Tumors kreuzen oder sehr nah nebeneinander verlaufen. Durch eine spezielle MRT-Aufnahmetechnik HARDI+CS (High-Angular-Resolution Diffusion Imaging und Compressed Sensing) können diese Nachteile überwunden werden. Allerdings sind die Aufnahmezeiten bei HARDI wesentlich höher. Die DTI-Aufnahmen konnten unter anderem mit 3D Slicer zufriedenstellend ausgewertet werden. 3D Slicer eignet sich beim

Tracking von Nervenfaserbahnen für den klinischen Einsatz, auch wegen der gut strukturierten und einfachen Benutzung.

In Tabelle 13 ist das Patientenkollektiv für die durchgeführte klinische Studie mit Altersangabe der Patienten in Jahren, dem Geschlecht und der Art der Läsion angegeben. Weiterhin sind die histologischen Einteilungen nach der Weltgesundheitsorganisation WHO (World Health Organization) und die Lokalisationen der einzelnen Läsion im Kopf mit dazugehörigem Tumorvolumen in cm^3 aufgelistet. Das durchschnittliche Alter der sechs Patienten war 54,3±14,9 Jahre; das Patientenkollektiv setzte sich aus zwei Patientinnen und vier Patienten zusammen. Bei allen Studienteilnehmern handelte es sich um Rechtshänder. Das Patientenkollektiv wurde prospektiv am Universitätsklinikum in Marburg zusammengestellt, nachdem die Ethikkommission ihre Zustimmung zur Studie erteilt hatte. Außerdem mussten alle Patienten ihre schriftliche Einwilligungserklärung geben, um an der Studie teilnehmen zu können. Von allen Patienten wurden am Tag vor ihrem operativen Eingriff MRT-Aufnahmen mit einem 3-Telsa MRT (Tim Trio; Siemens, Erlangen) angefertigt.

Patient Nr.	Alter (Jahre)	Geschlecht	Läsion	Lokalisation	Tumorvolumen (cm^3)
1	73	M	anaplastisches Oligodendrogliom (WHO III)	temporal	35,2
2	65	F	Glioblastoma multiforme (WHO IV)	temporal	10,7
3	41	M	anaplastisches Astrozytom (WHO III)	temporal	15,7
4	52	M	Glioblastoma multiforme (WHO IV)	temporo-okzipital	30,2
5	34	M	diffuses Astrozytom (WHO II)	frontal	76,0
6	61	F	anaplastisches Astrozytom (WHO III)	temporal	41,8

Tabelle 13 – Patientenkollektiv der Studie mit Altersangabe in Jahren, Geschlecht, Art der Läsion mit WHO (World Health Organization)-Einteilung, Lokalisation der Läsion im Kopf und Tumorvolumen in cm^3.

Abbildung 44 zeigt die Segmentierungsergebnisse der Nervenfaserbahnen für alle sechs Patienten der Studie auf den unterschiedlichen medizinischen Plattformen. Alle sechs Patienten hatten einen Tumor im Bereich der Sprachbahn, die Ergebnisse der ersten drei Spalten basieren auf Diffusion Tensor Imaging (DTI)-Aufnahmen. Die DTI-Aufnahmen wurden mit der kommerziellen Planungssoftware iPlan Cranial von BrainLAB in Feldkirchen (erste Spalte), mit 3D Slicer (zweite Spalte) und mit dem MedAlyVis (Medical Analysis and Visualization)-Framework (dritte Spalte) erzielt. Die Ergebnisse der letzten Spalte basieren auf High-Angular-Resolution Diffusion Imaging und Compressed Sensing (HARDI+CS) und wurden innerhalb von MedAlyVis ausgewertet.

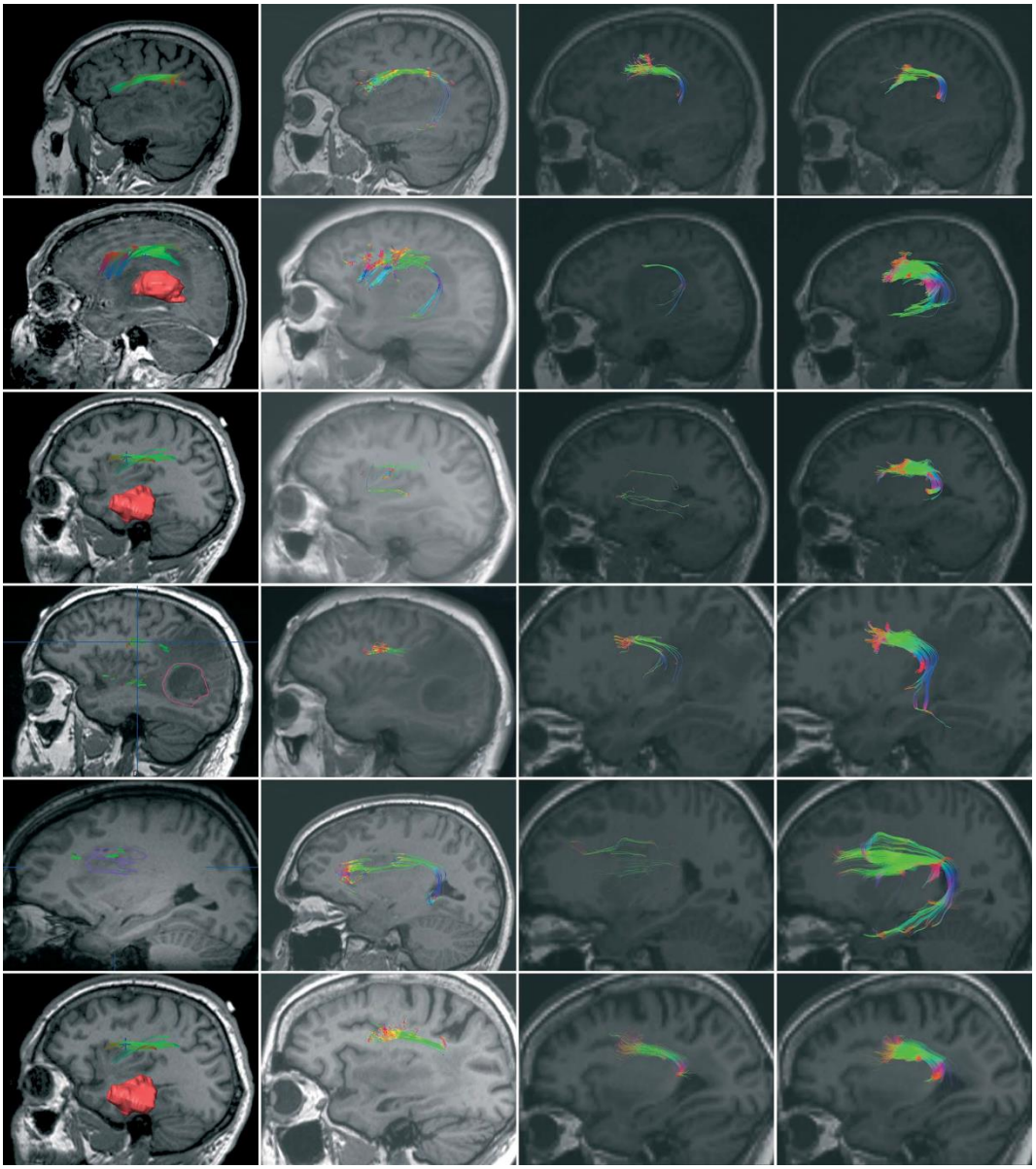

Abbildung 44 – Segmentierungsergebnisse der Nervenfaserbahnen aller sechs Patienten aus der Studie. Bei allen Patienten waren die Hirntumoren (Gliome) im Bereich der Sprachbahn lokalisiert (erste Spalte: 3D-Darstellungen der Tumore in Rot für die Patienten 2, 3 und 6; 2D-Darstellung in Rot für Patient 4; 2D-Darstellung in Lila für Patient 5). Die ersten drei Spalten basieren auf Diffusion Tensor Imaging (DTI)-Aufnahmen und wurden innerhalb von iPlan Cranial (erste Spalte), 3D Slicer (zweite Spalte) und MedAlyVis (dritte Spalte) ausgewertet. Die letzte Spalte basiert auf High-Angular-Resolution Diffusion Imaging und Compressed Sensing (HARDI+CS) und wurde innerhalb von MedAlyVis (Medical Analysis and Visualization) ausgewertet.

Die Abbildung 45 präsentiert den direkten Vergleich der Segmentierungsergebnisse der Nervenfaserbahnen bzw. Nervenfaserbündel innerhalb des MedAlyVis (Medical Analysis and Visualization)-Frameworks für alle sechs Patienten aus der durchgeführten Studie. Dabei sind die Segmentierungsergebnisse, basierend auf der Diffusion Tensor Imaging (DTI)-Traktographie, in der ersten Spalte in der Farbe Gelb aufgezeigt. Die Segmentierungsergebnisse dagegen, die auf der High-Angular-Resolution Diffusion Imaging und Compressed Sensing (HARDI+CS)-Traktographie basieren, sind in der zweiten Spalte in der Farbe Blau dargestellt. Die dritte Spalte wiederum präsentiert die mit DTI- und HARDI+CS visualisierten Faserbahnen bzw. Faserbündeln aus den ersten beiden Spalten in einer gemeinsamen überlagerten Ansicht.

Abbildung 46 präsentiert beispielhaft verschiedene (intraoperative) graphische Darstellungen und Screenshots des Patienten Nummer 5 aus dem Patientenkollektiv der Studie. In Abbildung (A) ist eine dreidimensionale Rekonstruktion des Tumors in der Farbe Gelb und der rekonstruierten Sprachbahn zu sehen. Dabei ist die Sprachbahn – wie auch schon in den vorherigen Abbildungen – in unterschiedlichen Farben kodiert, je nach Richtung der einzelnen Nervenfasern. Abbildung (B) zeigt die Ansicht des Operations (OP)-Mikroskops mit den Tumorkonturen in der Farbe Lila und der darunterliegenden Sprachbahn in der Farbe Gelb (eingeblendet im Heads-up-Display des Neurochirurgen). Die beiden Abbildungen (C) und (D) zeigen wiederum intraoperative MRT-Screenshots während der neurochirurgischen Navigation. Hierbei präsentiert Abbildung (C) eine axiale Ansicht und Abbildung (D) eine koronale Ansicht. Bei beiden Abbildungen (C und D) sind die Tumorkonturen jeweils in der Farbe Lila und die Sprachbahnen jeweils in der Farbe Grün in der MRT-Aufnahme dargestellt.

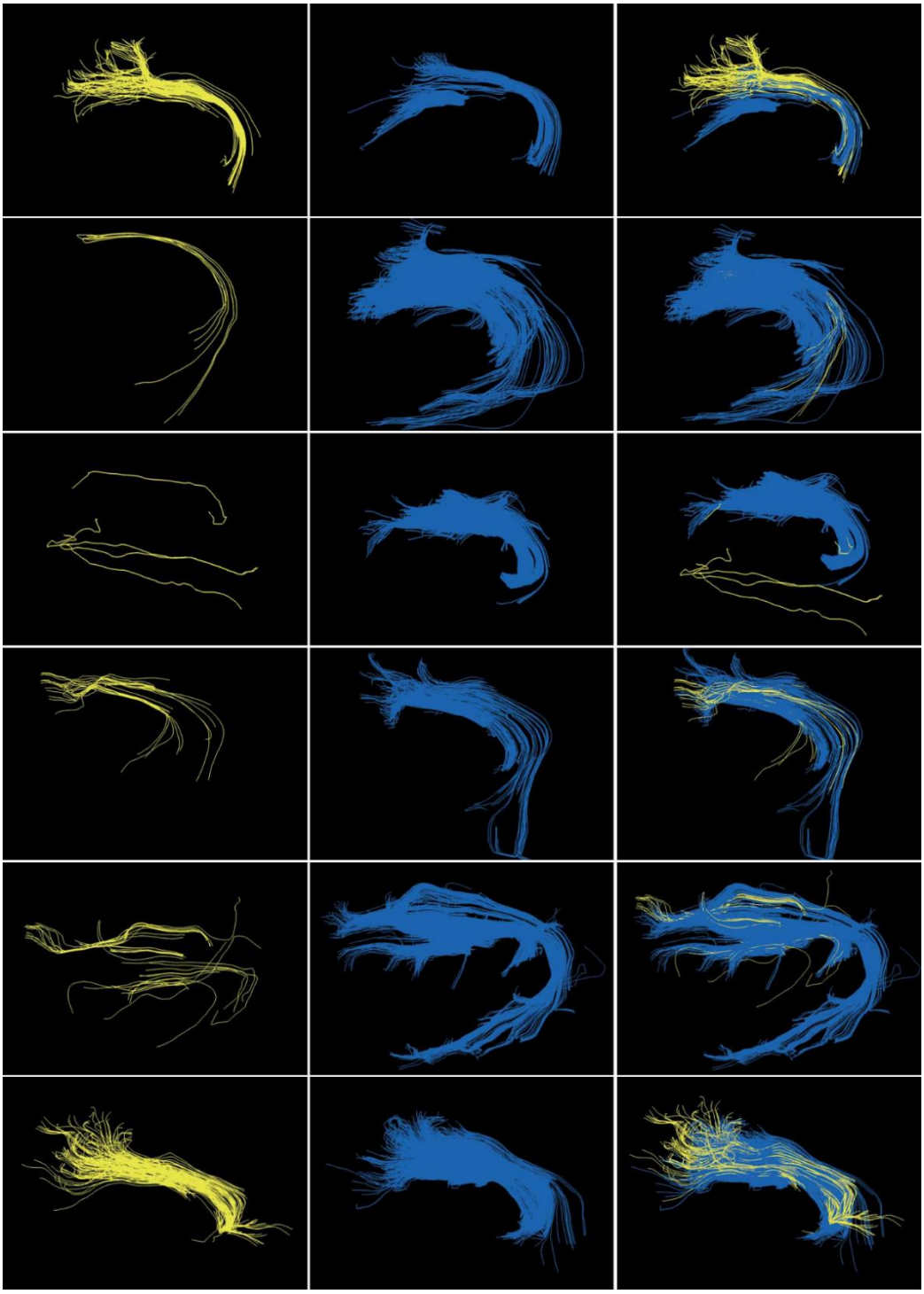

Abbildung 45 – Direkter Vergleich der Segmentierungsergebnisse der Nervenfaserbahnen innerhalb von MedAlyVis für sechs Patienten mit Hirntumoren: Diffusion Tensor Imaging (DTI)-basierte Traktographie (gelb, erste Spalte), High-Angular-Resolution Diffusion Imaging und Compressed Sensing (HARDI+CS)-basierte Traktographie (blau, zweite Spalte) und Überlagerung der DTI- und HARDI+CS-basierten Faserbahnen.

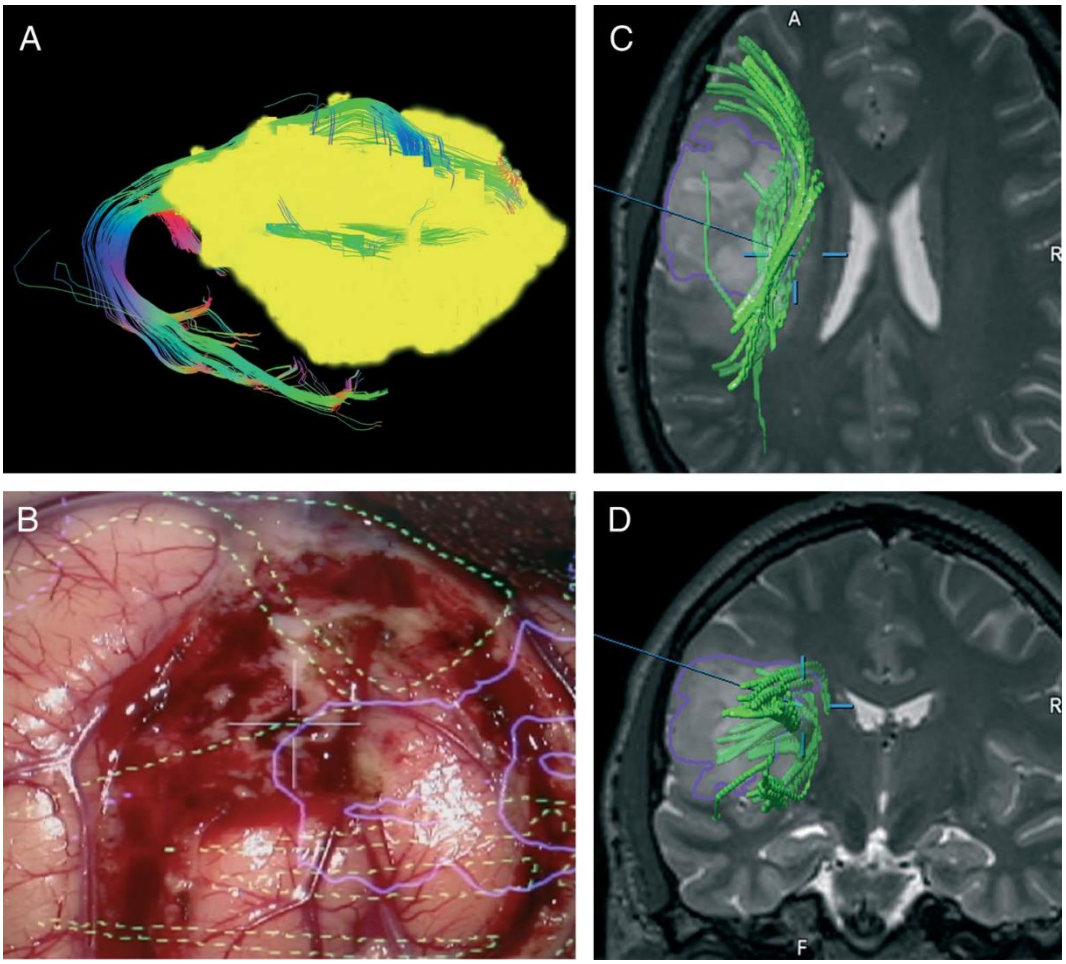

Abbildung 46 – Verschiedene (intraoperative) graphische Darstellungen von Patient 5 aus dem Patientenkollektiv der Studie. Dreidimensionale Rekonstruktion des Tumors (gelb) und der mehrfarbigen Sprachbahn (A). OP-Mikroskopsicht mit Tumorkonturen (lila) und darunterliegenden Sprachbahnen (gelb) im Heads-up-Display (B). Intraoperative Navigationsscreenshots in axialer Ansicht (C) und koronaler Ansicht (D) mit Tumorkontur in Lila und den Sprachbahnen in Grün.

Tabelle 14 präsentiert die Pre- und Postprocessing-Zeiten (in Minuten) zum direkten Vergleich zwischen Diffusion Tensor Imaging (DTI)-basierter Traktographie und High-Angular-Resolution Diffusion Imaging und Compressed Sensing (HARDI+CS)-basierter Traktographie innerhalb der drei medizinischen Plattformen (iPlan Cranial, 3D Slicer und MedAlyVis). Außerdem sind die Zeiten in Minuten zur Rekonstruktion der Faserbahnen (FT) in der Tabelle angegeben.

Patient Nr.	iPlan Cranial DTI			3D Slicer DTI			MedAlyVis DTI			MedAlyVis HARDI+CS		
	Pre	FT	Post	Pre	FT	Post	Pre	FT	Post	Pre	FT	Post
1	2	<1	3	2	1-2	5	2	1	4	25	18	13
2	2	<1	5	2	1-2	4	2	1	5	25	19	12
3	2	<1	11	2	1-2	10	2	1	12	25	18	14
4	2	<1	15	2	1-2	10	2	1	14	25	21	13
5	2	<1	15	2	1-2	13	2	1	14	25	20	15
6	2	<1	3	2	1-2	6	2	1	5	25	18	14

Tabelle 14 – Pre- und Postprocessing Zeiten (in Minuten) zum direkten Vergleich zwischen Diffusion Tensor Imaging (DTI)-basierter Traktographie und High-Angular-Resolution Diffusion Imaging und Compressed Sensing (HARDI+CS)-basierter Traktographie innerhalb von drei medizinischen Plattformen (iPlan Cranial von BrainLAB, 3D Slicer und MedAlyVis – Medical Analysis and Visualization). FT steht für die Zeit in Minuten zur Faserbahnrekonstruktion.

3.4. Zusammenfassung

In diesem Kapitel wurden frei verfügbare Segmentierungsalgorithmen anhand klinischer Daten gemeinsam mit Ärzten evaluiert. Diese Algorithmen sind als Open Source-Implementierungen unter 3D Slicer für jeden zugänglich, im Gegensatz zu vielen Ansätzen aus der Literatur, die nicht verfügbar oder nur lokal in den einzelnen Forschergruppen prototypisch vorhanden sind. Das wiederum macht eine unabhängige und intensive Evaluierung anhand eigener Daten nicht möglich, vor allem, wenn der dazugehörige Quellcode nicht öffentlich zugänglich ist. An der Evaluierung aus diesem Kapitel waren mehrere Kliniken beteiligt, und es wurden unterschiedliche Pathologien betrachtet. Dazu gehörten Hirntumore und Sprachbahnen, die mit den Algorithmen aus Slicer analysiert und segmentiert wurden. Dabei konnte zum Beispiel gezeigt werden, dass der sogenannte GrowCut-Algorithmus die sehr zeitaufwendigen Schicht-für-Schicht-Segmentierungen beschleunigen kann. Die GrowCut-Implementierung war sehr benutzerfreundlich, da keinerlei Parametereinstellungen für eine Segmentierung vorgenommen werden mussten, sie konnte von den an der Studie beteiligten Ärzten schnell erlernt werden. Auf der anderen Seite eignet sich eine solche parameterfreie und dadurch sehr leicht erlernbare und benutzerfreundliche Implementierung nur für einfache Segmentierungsprobleme, bei denen ein Objekt sehr gut vom umliegenden Hintergrund abgegrenzt ist. Für eine quantitative Evaluierung wurden die GrowCut-Ergebnisse mit manuellen Schicht-für-Schicht-Segmentierungen verglichen. Dies war allerdings bei den Sprachbahnen nicht möglich, da diese in den Aufnahmen nicht direkt erkennbar sind und es keine histologische “Ground Truth“ gibt. Die Segmentierungsergebnisse wurden in diesem Fall mit den Segmentierungen anderer Algorithmen verglichen. Insgesamt konnte gezeigt werden, dass die getesteten Algorithmen sich prinzipiell für die klinische Routine eignen. Es muss allerdings beachtet werden, dass

die vorgestellten Ergebnisse dieser Arbeit aus retrospektiven Studien hervorgegangen sind und die frei verfügbaren Algorithmen noch keine zertifizierten Medizinprodukte sind.

4. Navigation zur Unterstützung intraoperativer Therapien

4.1. Einleitung

Unter einer bildgestützten Therapie (Image-Guided Therapy) wird ein Konzept verstanden, bei dem Aufnahmemodalitäten, zum Beispiel die Magnetresonanztomographie oder die Computertomographie, medizinische Eingriffe unterstützen. Diese Unterstützung kann in ganz verschiedenen Phasen einer Behandlung (Therapieplanung, Durchführung, Kontrolle) erfolgen. Wegen der Vielzahl von bildgebenden Geräten unterschiedlicher Hersteller ist allerdings eine direkte Kommunikation zwischen Software und Hardware oft nicht möglich. Hier helfen offene und herstellerunabhängige Netzwerkprotokolle, die standardisierte Mechanismen zum Austausch von Koordinaten, Bildern und Statusmeldungen zwischen Software und Hardware bereitstellen. Prinzipiell ist die Entwicklung von praktischer Software zum Begleiten von intraoperativen Eingriffen nur möglich, wenn dabei mit den behandelnden Medizinern in den Krankenhäusern eng zusammengearbeitet wird.

4.2. Integration des OpenIGTLink-Protokolls in die Plattform MeVisLab

In diesem Beitrag [13] wird erstmals die erfolgreiche Integration des OpenIGTLink-Netzwerkprotokolls in die medizinische Plattform MeVisLab beschrieben. MeVisLab ist ein Framework zur Entwicklung von Bildverarbeitungsalgorithmen mit einem Fokus auf medizinischen Bilddaten; OpenIGTLink ist ein offenes Netzwerkprotokoll für bildgestützte Therapien. Das Protokoll erlaubt den Nutzern Transformationsoperationen, Bilddaten und Statusmeldungen standardisiert zu übertragen, um Software und Hardware von unterschiedlichen Herstellern zu verbinden. Durch die Integration von OpenIGTLink ist es jetzt möglich, mit MeVisLab-Prototypen medizinische Hardware wie das magnetische Trackingsystem von NDI Aurora direkt anzusteuern. OpenIGTLink erlaubt den Austausch von prä- und intraoperativen Bildern sowie das Verfolgen (Tracken) von Instrumenten zwischen zwei laufenden Systemen. Die Integration ermöglicht so auch die Kombination von zugelassenen und prototypischen Systemen, die noch in der Forschung sind. Dies bedeutet, dass Forscher neue Bildverarbeitungs- und Visualisierungstechniken unter MeVisLab in einem klinischen Umfeld erproben können, während die Operationsplanung und Durchführung mit einem kommerziellen System vorgenommen wird. Tatsächlich steht seit kurzem eine OpenIGTLink-Schnittstelle für Forschungszwecke an dem FDA-zugelassenen chirurgischen Navigationssystem von Brainlab zur Verfügung. Die Integration von OpenIGTLink in MeVisLab wird anhand von Tracker Clients und einem NDI-Navigationssystem evaluiert.

Abbildung 47 veranschaulicht das grundlegende Konzept von OpenIGTLink und die Interaktion von unterschiedlichen Geräten via OpenIGTLink. Bildgestützte Therapien basieren im Allgemeinen auf der Kommunikation zwischen Sensoren,

(medizinischen) Geräten und Computern. Ein Beispiel ist die Übertragung von intraoperativen MRT-Aufnahmen des Patienten (Abbildung 47 rechts oben) zu einer Navigationssoftware (Abbildung 47 links oben), um Medizinern die Überwachung eines Eingriffs in Echtzeit zu ermöglichen. Gleichzeitig können die Positionen von medizinischen Instrumenten beispielweise über einen optischen Sensor getrackt (Abbildung 47 links unten) und zur Navigationssoftware übertragen werden, um diese in den Patientenaufnahmen anzuzeigen. Zusätzlich kann ein interventioneller Roboter Anweisungen von der Navigationssoftware erhalten und gleichzeitig seine Position und den Status zurückliefern (Abbildung 47 rechts unten).

Der gesamte Workflow des vorgestellten Systems, der mit den Bilddaten (*Image data*) beginnt und mit dem Ende der bildgestützten Therapie (*End of Image Guided Therapy*) abschließt, ist als Diagramm in Abbildung 48 gezeigt. Dabei werden die Bilddaten für ein benutzerdefiniertes MeVisLab-Netzwerk bereitgestellt, was mit Hilfe eines der MeVisLab-Module zum Laden von Bilddaten wie *OpenImage* oder *ImageLoad* bewerkstelligt werden kann. Innerhalb des Netzwerkes können je nach Anwendung beliebige MeVisLab-Module zur Bildverarbeitung, Visualisierung oder anderen genutzt werden. Für die Integration von OpenIGTLink musste allerdings ein neues Modul entwickelt werden. Wie in Abbildung 48 zu sehen ist, übernimmt das OpenIGTLink-Modul die Kommunikation zwischen MeVisLab und einem externen Gerät, zum Beispiel einer Robotersteuerung oder einem Navigationssystem. Während der Kommunikation werden unterschiedliche Daten – Statusinformationen, Positionskoordinaten oder Bilder – via OpenIGTLink-Protokoll ausgetauscht.

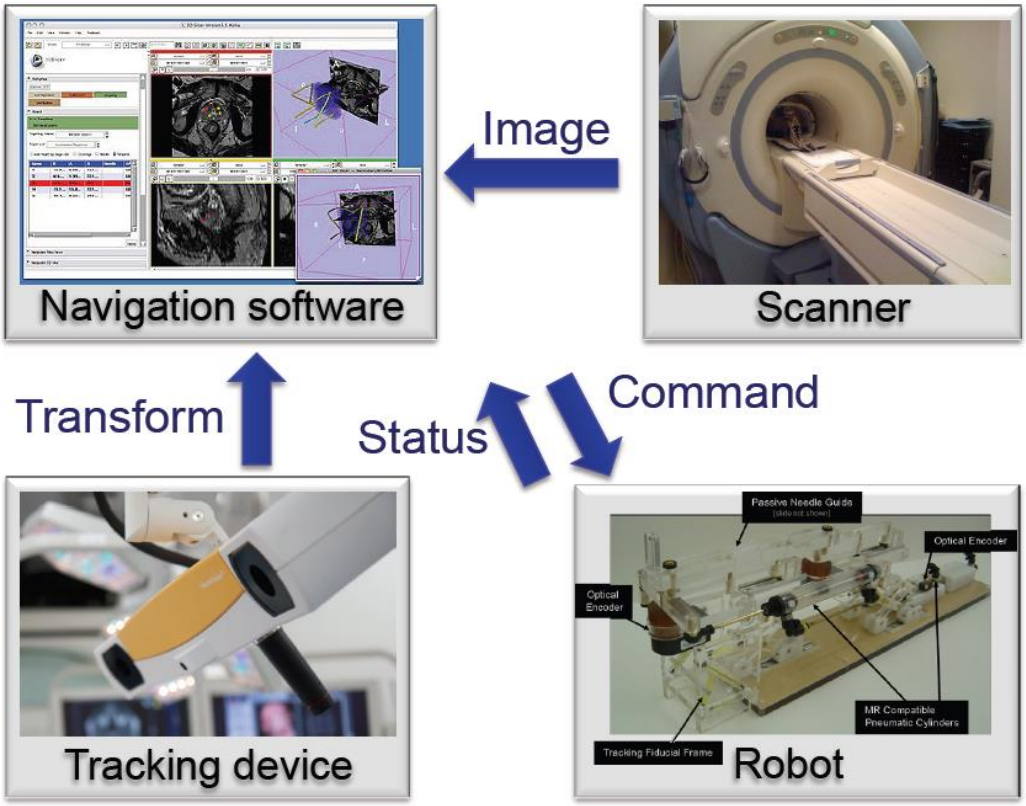

Abbildung 47 – Das grundlegende Konzept von OpenIGTLink (http://openigt-link.org/): Bildgestützte Therapien basieren im Allgemeinen auf der Kommunikation zwischen Sensoren, medizinischen Geräten und Computern. Ein Beispiel ist die Übertragung von intraoperativen MRT-Aufnahmen des Patienten (rechts oben) zu einer Navigationssoftware (links oben), um Medizinern die Überwachung eines Eingriffs in Echtzeit zu ermöglichen. Gleichzeitig können die Positionen von medizinischen Instrumenten beispielweise über einen optischen Sensor getrackt (links unten) und zur Navigationssoftware übertragen werden, um diese in den Patientenaufnahmen anzuzeigen. Zusätzlich kann ein interventioneller Roboter Anweisungen von der Navigationssoftware erhalten und gleichzeitig seine Position und den Status zurückliefern (rechts unten).

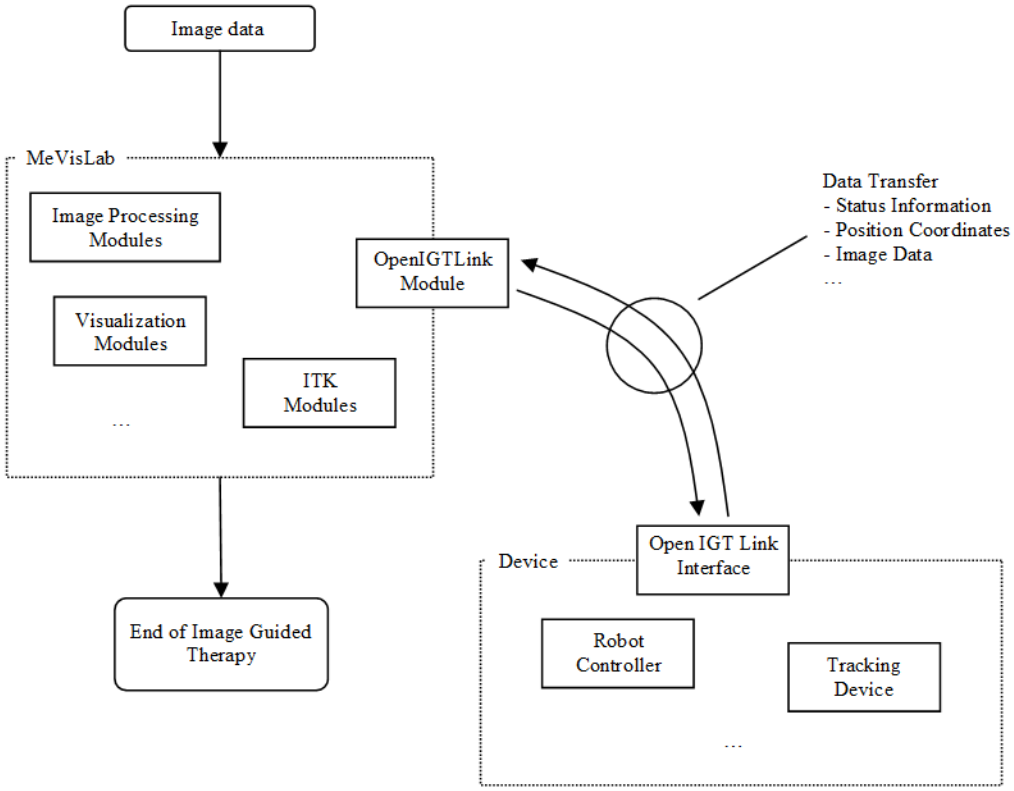

Abbildung 48 – Der gesamte Workflow des vorgestellten Systems, der mit den Bilddaten (*Image data*) beginnt und mit dem Ende der bildgestützten Therapie (*End of Image Guided Therapy*) abschließt. Das OpenIGTLink-Modul übernimmt die Kommunikation zwischen MeVisLab und einem externen Gerät wie einer Robotersteuerung oder einem Navigationssystem. Während der Kommunikation werden unterschiedliche Daten – zum Beispiel Statusinformationen, Positionskoordinaten oder Bilder – via OpenIGTLink-Protokoll ausgetauscht.

Die folgenden Abschnitte beschreiben die Implementierung eines OpenIGTLink-Moduls für MeVisLab. Das Modul wurde dabei als Bildverarbeitungs (ML)-Modul unter MeVisLab realisiert, das den ML-Modulen zu Grunde liegende Quellcodegerüst in C++ wurde mit dem sogenannten Projekt Wizard von MeVisLab generiert. Die Implementierung des Konstruktors eines OpenIGTLink-Moduls ist in Quellcode 1 angegeben. Die Initialisierung *Module(1,1)* des Konstruktors gibt die Anzahl der Ein- und Ausgänge für Bilddaten an. In diesem Beispiel gibt es einen Ein- und einen Ausgang für Bilddaten. ML_TRACE_IN ist ein Status Makro, das vom MeVisLab-Projekt Wizard per Default im Quellcodegerüst angelegt wird. Das OpenIGTLink-Modul stellt mehrere GUI-Komponenten bereit, unter anderem ein Eingabefeld für den Netzwerkport und einen Button, um auf einen Client zu warten und eine TCP-Verbindung aufzubauen. Um diese Komponenten zu implementieren, werden zuerst die Aufrufe der *handleNotification*-Methode

unterdrückt, um Seiteneffekte während der Initialisierung zu vermeiden. Anschließend wird eine Referenz zum Container der Komponenten bezogen und danach werden die unterschiedlichen Komponenten, wie ein Feld für den Netzwerkport und den Start Button, angelegt. Zur Visualisierung und weiteren Verarbeitung der erhaltenen Daten durch die OpenIGTLink-Verbindung wird zusätzlich noch ein Ausgabefeld für die Daten des Clients angelegt (in diesem Fall eine Transformation). Am Ende des Konstruktors werden die automatischen Aufrufe der *handleNotification*-Methode durch die einzelnen Felder bzw. GUI-Komponenten wieder reaktiviert.

```
// constructor
OpenIGTLink::OpenIGTLink()
  : Module(1, 1)
{
  ML_TRACE_IN("OpenIGTLink::OpenIGTLink()"); // status and tracing macro

  // suppress calls of handleNotification on field changes to avoid side effects
  // during initialization phase
  handleNotificationOff();

  // get a pointer to the container of all the module's fields
  FieldContainer *fields = getFieldContainer();
  ...

  // create different fields, e.g. for the port and a start button
  _port = fields->addInt("port");
  _start = fields->addNotify("start");

  // create and add an output field for the transformation data of the client
  _transformation = new SoTransform();
  (_outSoTransformation =
                        fields->addSoNode("outputTransformation"))->
setSoNodValue(_transformation);

  // reactivate calls of handleNotification on field changes
  handleNotificationOn();
}
```

Quellcode 1 – C++ Implementierung des OpenIGTLink-Konstruktors für ein ML-Modul unter MeVisLab.

Im folgenden Quellcodebeispiel (Quellcode 2) wird beschrieben, wie die wichtigsten Teile der *handleNotification*-Methode eines OpenIGTLink-Moduls implementiert werden können. Die *handleNotification*-Methode wird automatisch bei Benutzereingaben oder Interaktionen wie dem Start Button aufgerufen. Äquivalent

zum Konstruktor ist ML_TRACE_IN ein Status Makro, das vom MeVisLab-Projekt Wizard per Default im Quellcodegerüst angelegt wird. Wurde der Start Button vom Benutzer gedrückt, werden die Initialisierung einer Verbindung und der Datentransfer vorbereitet. Zum Beispiel wird der vom Benutzer angegebene Port verwendet, um einen socketbasierten Server zu erzeugen. Ist der Socket gültig und der Client verbunden, werden anschließend die unterschiedlichen Datentypen nach ankommenden Daten abgefragt. Die Vorgehensweise folgt hierbei der Standardbenutzung der OpenIGTLink-Bibliothek. Der Einfachheit halber und um den Codeschnipsel übersichtlich zu halten, wird hier nur die *if*-Bedingung für den TRANSFORM-Datentyp aufgezeigt. Wurde ein TRANSFORM-Datentyp vom Client empfangen, wird die *ReceiveTransform*-Methode mit dem Socket und dem Nachrichtenheader (headerMsg) als Parameter aufgerufen.

```
// handle changes of a field
void OpenIGTLink::handleNotification (Field *field)
{
  ML_TRACE_IN("OpenIGTLink::handleNotification ()"); // status and tracing
macro
  ...
  if (field == _start)
  {
    int port = _port->getIntValue();
    igtl::ServerSocket::Pointer serverSocket;
    serverSocket = igtl::ServerSocket::New();
    int r = serverSocket->CreateServer(port);
    ...
    igtl::Socket::Pointer socket;
    …
    if (socket.IsNotNull()) // if client connected
    {
      ...
      // check data type and receive data body
      if (strcmp(headerMsg->GetDeviceType(), "TRANSFORM") == 0)
      {
        ReceiveTransform(socket, headerMsg);
      }
      ...
    }
    ...
  }
  ...
}
```

Quellcode 2 – Implementierung der *handleNotification*-Methode des OpenIGTLink-Moduls.

Quellcode 3 präsentiert die Implementierung der *ReceiveTransform*-Methode, die aufgerufen wird, um den Datentyp TRANSFORM zu verarbeiten. Die Methode besitzt zwei Parameter: Den Socket und den Nachrichtenheader, die beide durch den Funktionsaufruf innerhalb der *handleNotification*-Methode übergeben wurden (siehe dazu den Codeschnipsel aus dem vorherigen Abschnitt). Als erstes wird ein Nachrichtenspeicher innerhalb der *ReceiveTransform*-Methode angelegt, um die Daten aus dem übertragenem TRANSFORM-Datentyp zu empfangen. Die Vorgehensweise folgt hierbei wieder der Standardbenutzung der OpenIGTLink-Bibliothek; Tutorials und komplette Quellcodebeispiele sind online verfügbar und frei zugänglich. Als nächstes wird die automatische Notifikation des *_transformation*-Feldes, das innerhalb des Konstruktors angelegt wurde, deaktiviert. Anschließend wird der vom Client empfangene *transformation*-Wert dem korrespondierenden Ausgang des OpenIGTLink-Moduls zugewiesen und die automatische Notifikation des *_transformation*-Feldes wird wieder reaktiviert. Dementsprechend werden alle Inventor-Sensoren getriggert, um die dazugehörigen Viewer zu aktualisieren. Ein Inventor-Sensor ist ein Inventor-Objekt, das auf verschiedene Typen von Ereignissen wartet und dann eine Callback-Methode aufruft, falls eines dieser Ereignisse auftritt. Zusätzlich wird das *transformation*-Feld als modifiziert markiert, um eine Änderung zu simulieren und alle Auditors der Instanz zu benachrichtigen.

```
// handle and process data type TRANSFORM
int OpenIGTLink::ReceiveTransform(igtl::Socket * socket, igtl::MessageHeader
* header)
{
  std::cerr << "Receiving TRANSFORM data type." << std::endl;

  // create a message buffer to receive transform data
  igtl::TransformMessage::Pointer transMsg;
  transMsg = igtl::TransformMessage::New();
  transMsg->SetMessageHeader(header);
  transMsg->AllocatePack();
  ...

  _transformation->enableNotify(false); // turning notification of this field off
  _transformation->setMatrix( SbMatrixValue ); // setting value
  _transformation->enableNotify(true); // turning notification of this field on

  // force all inventor sensors to be triggered and do a refresh on all viewers
  SoDB::getSensorManager()->processDelayQueue(false);

  // marks an instance as modified, simulating a change to it this will notify all
auditors of the instance
  _transformation->touch();
  ...
}
```

Quellcode 3 – Implementierung der *ReceiveTransform*-Methode des OpenIGTLink-Moduls.

Abbildung 49 zeigt die Module und Verbindungen eines Netzwerks, das zum Testen der Integration von OpenIGTLink innerhalb der medizinischen Prototyping Plattform MeVisLab verwendet wurde. Dabei findet der Daten- und Kommunikationsfluss von unten nach oben statt und beginnt mit dem Laden eines Bildes durch das *OpenImage*-Modul, zum Beispiel im medizinischen DICOM-Format. Nach dem Laden eines Bildes wird dieses automatisch über den Ausgang (rechtes Dreieck (1)) an das OpenIGTLink-Modul weitergegeben. Das Hauptmodul in diesem MeVisLab-Netzwerk ist das OpenIGTLink-Modul, das mehrere Eingänge (unterer Bereich) und Ausgänge (oberer Bereich (2)) besitzt. Ein Eingang des OpenIGTLink-Moduls (linkes unteres Dreieck (3)) wird für die Bilddaten verwendet, die durch das OpenImage-Modul bereitgestellt werden. Die Transformationsdaten wiederum, die vom Client empfangen wurden, werden über den dritten Ausgang von links (obere Reihe) des OpenIGTLink-Moduls an ein sogenanntes SoGroup-Modul weitergegeben. Die Transformationsdaten beeinflussen einen 3D-Zylinder (Rotation und Translation), der mit dem *SoGroup*-Modul verbunden ist. Das *SoExaminer*-Modul wiederum erhält den transformierten Zylinder und visua-

lisiert diesen in 3D in einem eigenen Fenster, in dem mehrere Benutzerinteraktionen und Einstellungen möglich sind. Ein zusätzliches *transform*-Feld wurde dazu genutzt, die vom Client übermittelten Transformationsdaten in weiteren Modulen (*SoDecomposeMatrix* und *DecomposeMatrix*) zu analysieren. Auf der rechten Seite des Screen-shots ist das Interface des OpenIGTLink-Moduls mit allen seinen Parametereinstellungen und Buttons zu sehen.

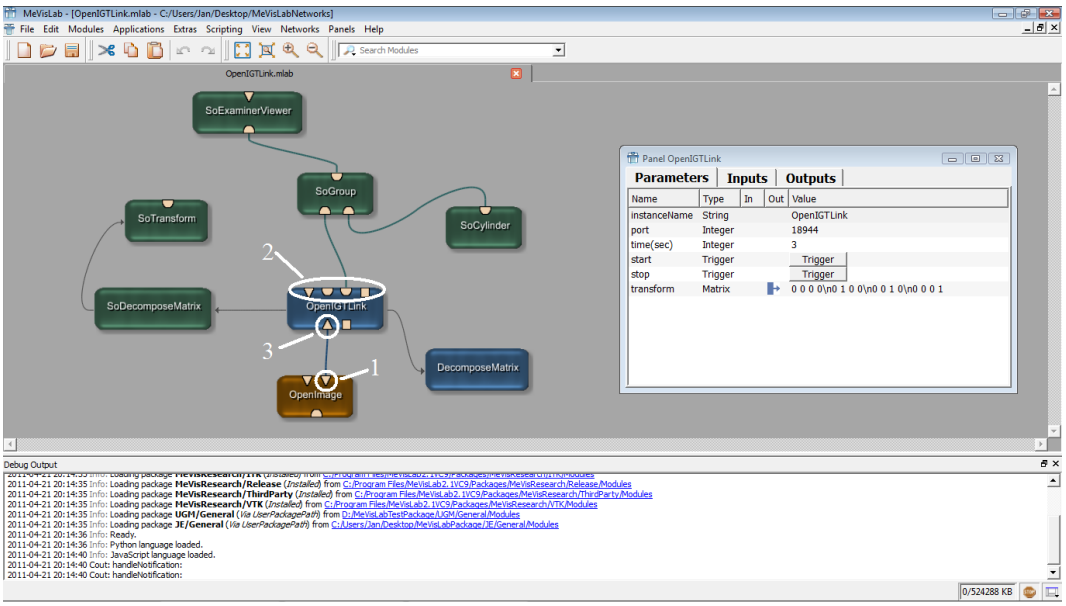

Abbildung 49 – Module und Verbindungen, die zur Realisierung von OpenIGTLink unter der medizinischen Prototyping Plattform MeVisLab verwendet wurden.

In Abbildung 50 ist nur das OpenIGTLink-Modul mit seinen Ein- (*inputs*) und Ausgängen (*outputs*), das unter MeVisLab als ML-Modul in C++ realisiert wurde, zu sehen. Für die vorgestellte Implementierung wurde sowohl ein Eingang für Bilddaten als auch ein Eingang für (abstrakte) Datenstrukturen realisiert. Über den Datenstrukturen-Eingang können zum Beispiel Markerlisten weitergebeben werden – eine Markerliste ist eine Liste von MeVisLab XMarker-Objekten, die aus einer 6D-Position, einem 3D-Vektor, einem Typ und einem Namen bestehen. Im oberen Bereich des OpenIGTLink-Moduls befinden sich vier Ausgänge. Der linke Ausgang zum Beispiel kann für die Ausgabe der Bilddaten verwendet werden, die vom Client über das OpenIGTLink-Protokoll empfangen wurden. Die nächsten zwei Ausgänge sind OpenInventor-Ausgänge, um nur die Rotation oder aber die gesamte Transformation des Trackers weiterzugeben, die vom Client über das OpenIGTLink-Protokoll empfangen wurden. Ganz rechts besitzt das OpenIGTLink-Modul letztendlich einen Ausgang für Datenstrukturen wie Markerlisten oder Saatpunkte.

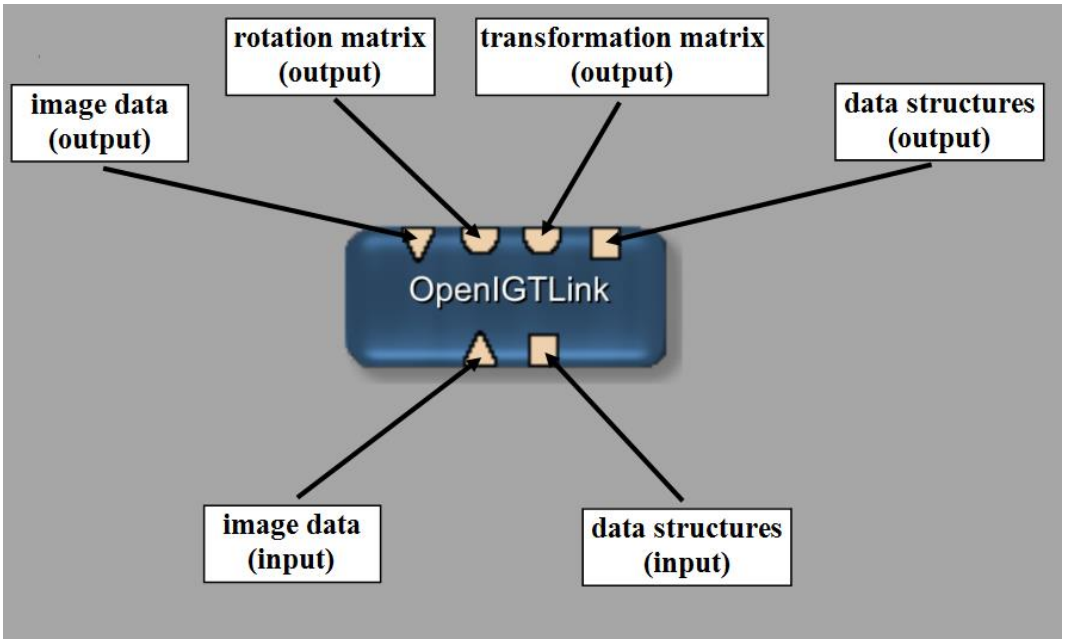

Abbildung 50 – Das OpenIGTLink-Modul mit seinen Ein- (*inputs*) und Ausgängen (*outputs*), das unter MeVisLab als ML-Modul in C++ realisiert wurde.

Abbildung 51 zeigt einen Screenshot eines MeVisLab-Prototypen mit OpenIGTLink-Modul und einem Client (Kommandofenster links), der Tracker-Koordinaten sendet, die die Position eines Zylinders im dreidimensionalen Raum vorgeben. In diesem Beispiel wurde ein Software-Client verwendet, der mit der OpenIGTLink-Bibliothek zur Verfügung steht. Diese beinhaltet unter anderem einen sogenannten TrackerClient, der als TCP-Client arbeitet und veranschaulicht, wie Tracking-Koordinaten zu einem Server gesendet werden können.

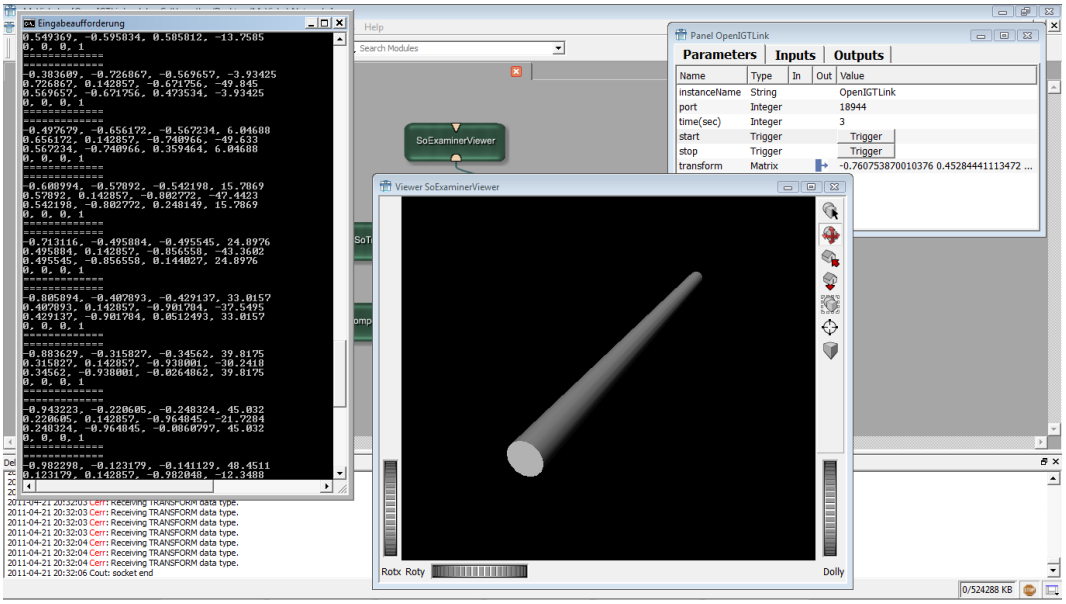

Abbildung 51 – Screenshot eines MeVisLab-Prototypen mit OpenIGTLink-Modul und einem Client (Kommandofenster links), der Tracker-Koordinaten sendet, die die Position eines Zylinders im dreidimensionalen Raum vorgeben.

Tabelle 15 präsentiert die Zeitangaben (Minimum, Maximum und Mittelwert μ) in Millisekunden für die Übertragung und Darstellung von hundert Datenpaketen (vom OpenIGTLink-Datentyp TRANSFORM) von einem Tracker-Client zu MeVisLab (insgesamt betrug der Mittelwert und die Standardabweichung 30,77±1,79 Millisekunden). Ähnliche Resultate konnten auch erzielt werden, wenn Daten vom Typ TRANSFORM vom MeVisLab-Prototypen zu einem Tracker-Server – NDI-Navigationssystem – via Netzwerk übermittelt wurden. Für die Übertragung und Visualisierung von hundert Paketen wurden 19,28±1,43 Millisekunden gemessen (Minimum 17,56 Millisekunden und Maximum 24,06 Millisekunden). Allerdings hängen diese Zeiten auch davon ab, welche Art von 3D-Objekt gerendert und visualisiert wird (in diesem Fall war es ein einfacher Zylinder). Ohne die Weitergabe der übermittelten Transformationsdaten an das Visualisierungsmodul wurden beispielsweise 1,48±0,22 Millisekunden gemessen (Minimum 1,35 Millisekunden und Maximum 2,86 Millisekunden).

Testlauf Nr.	**1**	**2**	**3**	**4**	**5**	**6**	**7**	**8**	**9**	**10**
Min.	9,34	10,76	9,39	8,15	9,71	8,39	8,25	9,69	9,46	6,66
Max.	51,86	41,76	43,28	52,15	43,43	39,34	56,93	45,19	67,72	85.96
μ	29,66	30,14	30,01	30,24	30,09	29,98	31,86	29,70	30,45	35,54

Tabelle 15 – Zeitangaben für das Minimum (Min.), das Maximum (Max.) und den Mittelwert μ in Millisekunden für die Übertragung und Darstellung von hundert Datenpaketen (mit dem Datentyp *TRANSFORM*) von einem Tracker-Client zu MeVisLab.

4.3. MR-gestützte Brachytherapie zur Behandlung bösartiger Tumoren

In diesen Arbeiten [14], [15] wird erstmals die Konzeption und Implementierung eines medizinischen Software-Prototypen (*iGyne*) zur Unterstützung der intraoperativen gynäkologischen Brachytherapie vorgestellt. Der Software-Prototyp ermöglicht die Registrierung des CAD-Modells eines gynäkologischen Brachytherapie-Instruments (ein sogenanntes Template) in einen intraoperativen Datensatz einer Patientin. Dies erlaubt eine präoperative Planung und Simulation von Hohlnadeln, die zur Tumorbehandlung optimal in einer Patientin platziert und verteilt werden müssen. Durch diese Hohlnadeln wird nach dem Eingriff radioaktives Material, meistens über mehrere Tage hinweg, in den Tumor eingeleitet. Der Tumor wird also von innen heraus bestrahlt. Zur Schonung von umliegendem gesundem Gewebe ist dabei eine exakte Dosisverteilung erforderlich. iGyne hilft den behandelnden Ärzten bei der Auswahl und besonders bei der Positionierung der Nadeln, was manchmal mehrere Stunden in Anspruch nehmen kann, da immer wieder einige Nadelpositionen anhand von Kontrollscans korrigiert werden müssen. Der iGyne-Prototyp wurde parallel zu intraoperativen gynäkologischen Brachytherapie-Eingriffen im multimodalen Operationssaal AMIGO (Advanced Multimodality Image Guided Operating Suite) des Brigham & Women's Hospital (BWH) der Harvard Medical School (HMS) in Boston (USA) getestet.

Abbildung 52 zeigt eine photographische Panoramaübersicht über den multimodalen Operationssaal AMIGO mit dem MRT-Raum (A) auf der linken Seite, dem Operationsraum (B) in der Mitte und dem Positronen-Emissions-Tomographie (PET) / CT-Raum (C) auf der rechten Seite. Passend dazu zeigt Abbildung 53 das Layout des AMIGO-Grundrisses mit dem MRT-Raum (MRI) und den MRT-Deckenschienen (MRI Ceiling Track, rot) auf der linken Seite, dem Operationsraum (OR) in der Mitte und dem PET/CT-Scanner-Raum auf der rechten Seite. Motorisierte Deckenschienen ermöglichen es, den MRT-Scanner zwischen MRT- und OP-Raum hin und her zu bewegen. Zusätzlich befinden sich im Operationsraum unter anderem noch ein Navigationssystem von Brainlab, ein Angiographie-System von Siemens (Artis zeego) und zwei 3D-Ultraschall-Bildgebungssysteme von Siemens (S2000) und von BK Medical (Pro Focus UltraView). Außerdem gibt es mehrere große LCD-Bildschirme, auf denen Patientendaten jederzeit abgerufen und großformatig angezeigt werden können.

Abbildung 52 – Multimodaler Operationssaal AMIGO (Advanced Multimodality Image Guided Operating Suite) des Brigham & Women's Hospital (BWH) der Harvard Medical School (HMS) in Boston (USA) mit MRT-Raum (A), Operationsraum (B) und Positronen-Emissions-Tomographie (PET) / CT-Raum (C).

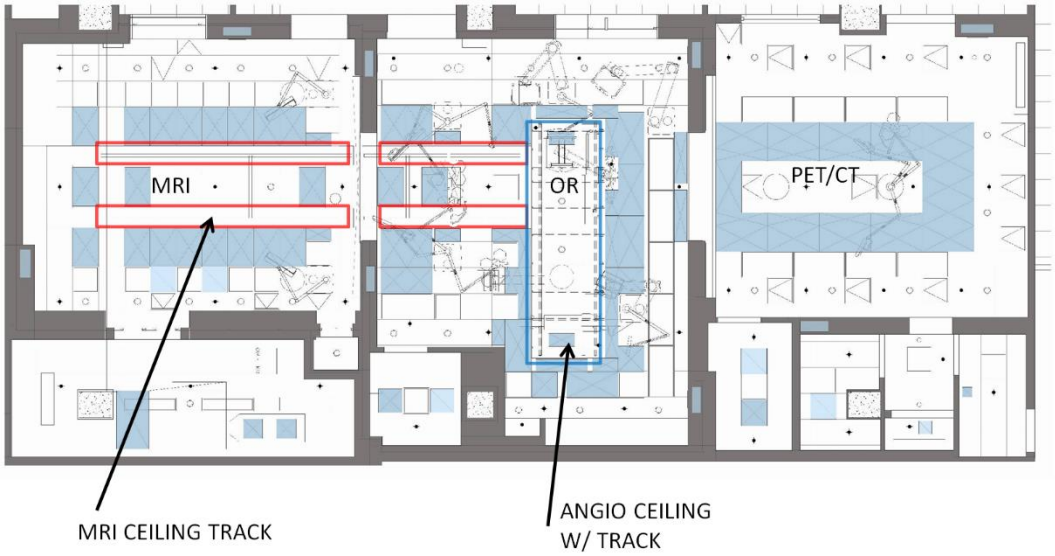

Abbildung 53 – Layout des AMIGO-Grundrisses mit dem MRT-Raum (MRI) und den MRT-Deckenschienen (MRI Ceiling Track, rot) auf der linken Seite, dem Operationsraum (OR) in der Mitte und dem PET/CT-Scanner-Raum auf der rechten Seite. Motorisierte Deckenschienen ermöglichen es, den MRT-Scanner zwischen MRT- und OP-Raum hin und her zu bewegen.

In Abbildung 54 sind zwei medizinische Instrumente, die in der interstitiellen gynäkologischen Brachytherapie zur Anwendung kommen, als CAD-Modelle dargestellt. Das sogenannte Template (blau) auf der linken Seite der Abbildung wird direkt an das Perineum der Patientin genäht und verbleibt dort für die Zeit der Behandlung/Bestrahlung, die sich auch über mehrere Tage erstrecken kann. Wurde das Template an das Perineum festgenäht, werden anschließend Hohlnadeln durch die Löcher des Templates in der Patientin platziert. Der Obturator (blau) auf der rechten Seite der Abbildung wird durch das große Loch in der Mitte des Templates

in den vaginalen Kanal der Patientin eingeführt. Dies dient unter anderem der Stabilisierung des Templates und dadurch gleichzeitig der Stabilisierung der einzelnen Hohlnadeln.

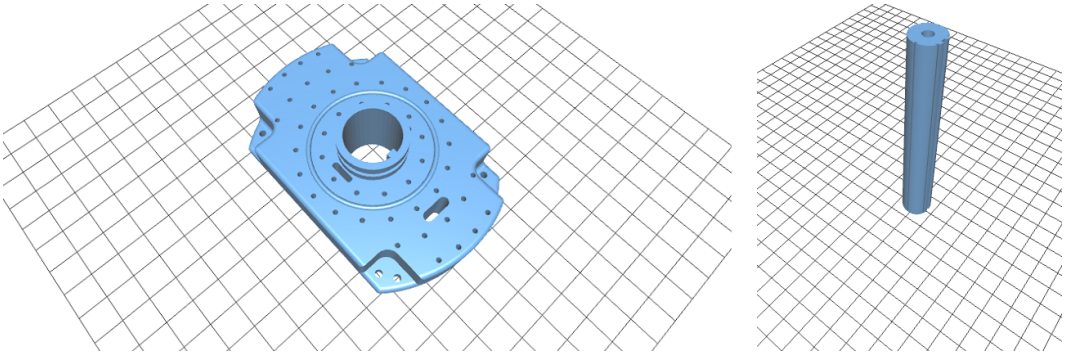

Abbildung 54 – Zwei medizinische Instrumente, die in der interstitiellen gynäkologischen Brachytherapie zur Anwendung kommen: Das sogenannte Template (links) wird an das Perineum der Patientin genäht. Anschließend werden Hohlnadeln durch die Löcher des Templates eingeführt und platziert. Der Obturator (rechts) wird durch das große Loch in der Mitte des Templates in den vaginalen Kanal eingeführt (unter anderem zur Stabilisierung des Templates).

Abbildung 55 stellt die übergreifende Infrastruktur des vorgestellten Softwaremoduls iGyne für 3D Slicer dar. Die beiden Komponenten GUI und Logic überwachen zum einen Änderungen in der Medical Reality Markup Language (MRML)-Szene und verarbeiten zum anderen unterschiedliche (benutzerdefinierte) Ereignisse, die bei der Anwendung des iGyne-Moduls eintreten können. Abbildung 56 zeigt wiederrum ein detaillierteres Diagramm des iGyne-Moduls für Slicer, bestehend aus dem Ablauf und der Funktionsweise für die verbesserte Visualisierung während der MR-gestützten interstitiellen gynäkologischen Brachytherapie (grün), den relevanten Slicer4-Modulen (blau) und den unterstützenden Algorithmen (orange). Der Arbeitsablauf startet mit dem Laden der MRT-Daten einer Patientin und der CAD-Modelle der medizinischen Instrumente (Template und Obturator) und endet mit der Auswahl der interstitiellen Nadeln, die virtuell in den Patientenaufnahmen geplant und gesetzt werden können.

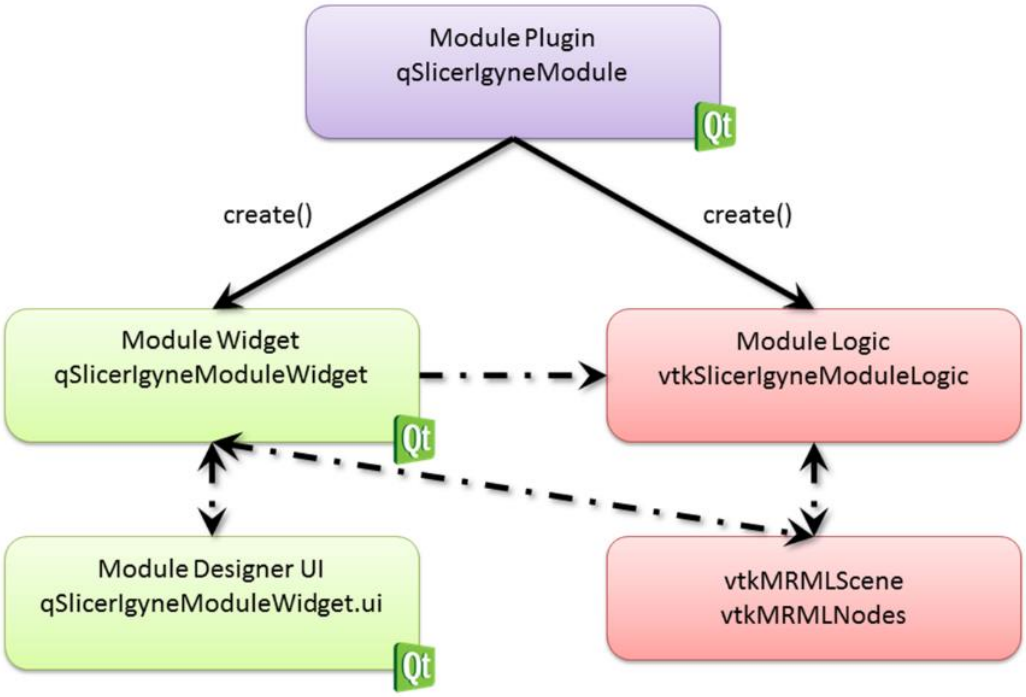

Abbildung 55 – Die übergreifende Infrastruktur des entwickelten iGyne-Softwaremoduls für 3D Slicer: Es wurden zwei Komponenten (GUI und Logic) implementiert, um zum einen Änderungen in der Medical Reality Markup Language (MRML)-Szene zu überwachen und zum anderen (benutzerdefinierte) Ereignisse zu verarbeiten.

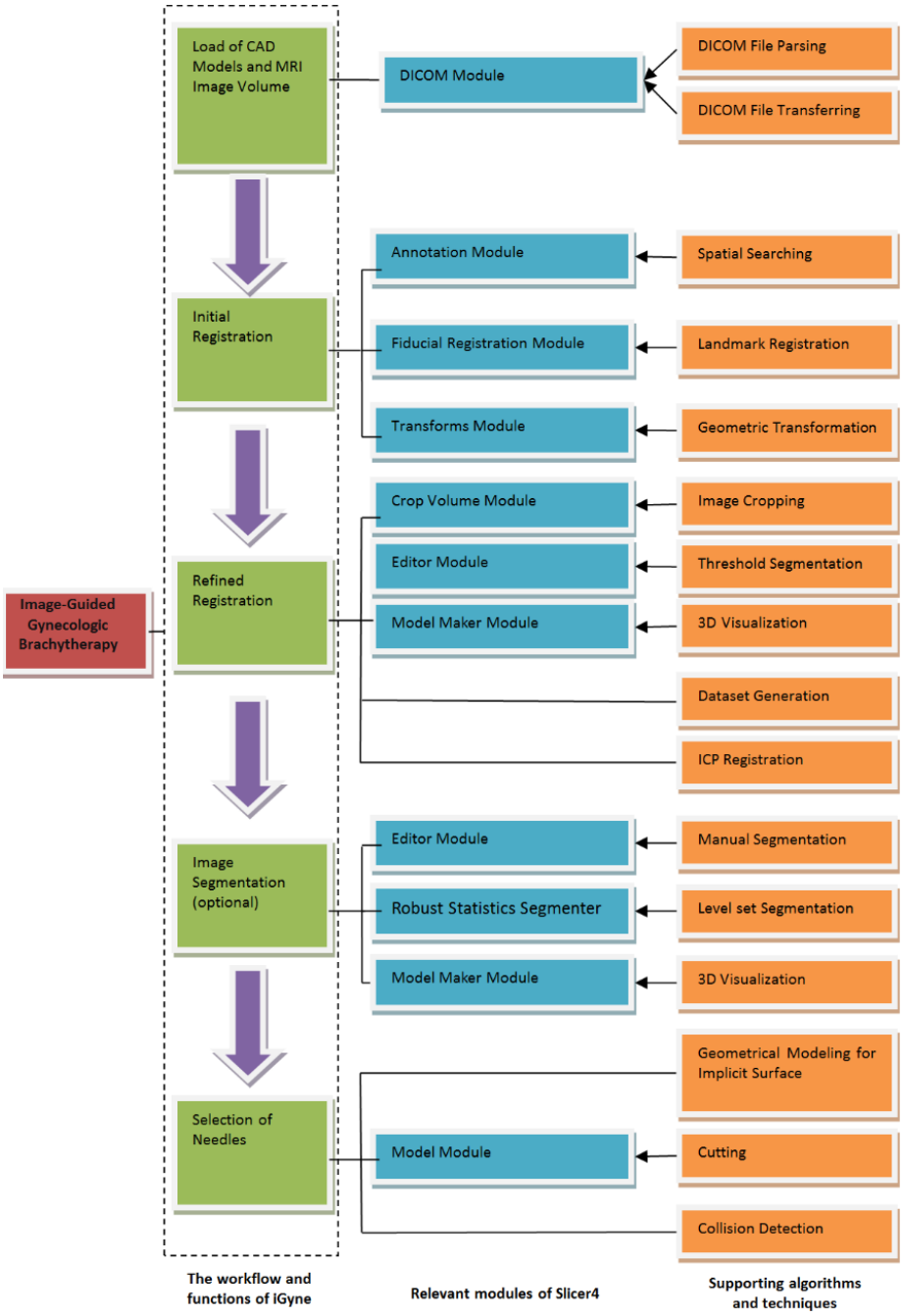

Abbildung 56 – Diagramm des entwickelten iGyne-Moduls, bestehend aus dem Ablauf und der Funktionsweise für die verbesserte Visualisierung während der MR-gestützten interstitiellen gynäkologischen Brachytherapie (grün), den relevanten Slicer4-Modulen (blau) und den unterstützenden Algorithmen (orange). Der Arbeitsablauf startet mit dem Laden der MRT-Daten und der CAD-Modelle der medizinischen Instrumente und endet mit der Auswahl der interstitiellen Nadeln.

Abbildung 57 soll die drei korrespondieren Punktepaare, die zur initialen Template-Registrierung unter iGyne genutzt werden, veranschaulichen. Dazu zeigt das linke Bild benutzerdefinierte Landmarken (F, F_4 und F_5, rot) für die Template-Registrierung in einer MRT-Aufnahme. Das rechte Bild wiederum zeigt die korrespondierenden Positionen (rot) in dem CAD-Modell des Templates (blau), das unter iGyne zur Verfügung steht.

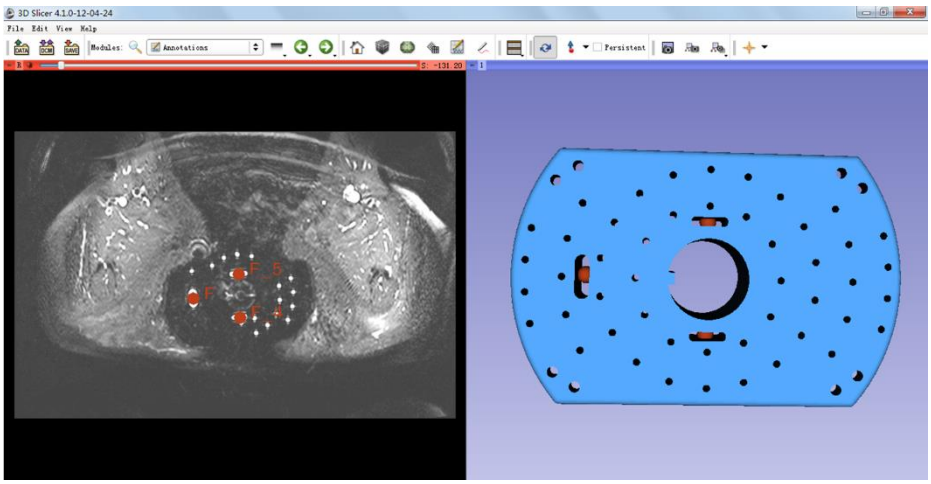

Abbildung 57 – Die drei korrespondieren Punktepaare (rot), die zur initialen Template-Registrierung unter iGyne genutzt werden: Das linke Bild zeigt benutzerdefinierte Landmarken in der MRT-Aufnahme einer Patientin, das rechte Bild wiederum zeigt die korrespondierenden Positionen in dem iGyne CAD-Modell des Templates (blau).

Abbildung 58 verdeutlicht den prinzipiellen Ablauf der Registrierung eines Templates für die gynäkologische Brachytherapie mit den initialen CT-Aufnahmen einer Patientin unter iGyne. In Bild A geben die drei roten Kreise die korrespondieren Nadellöcher im Template und der CT-Aufnahme an. Die Registrierung wiederum erfolgt danach über eine rigide Transformation zwischen diesen korrespondierenden Punktmengen. Die blauen Kreise zeigen an, dass die rechte und linke Seite der Patientenaufnahmen mit dem Template übereinstimmen. In Bild B sind ein virtuell registriertes Template der gynäkologischen Brachytherapie und die Auswahl einer interstitiellen Nadel (Ba, rote Kreise im Screenshot) dargestellt. Wie auf der linken Seite des Prototypeninterface zu sehen ist, kann das Einbringen von Nadeln anhand der Nadellänge und der Nadeltiefe individuell geplant werden. In Bild C ist die virtuelle Platzierung von mehreren Nadeln (Purpur) mit unterschiedlichen Längen und Eindringtiefen zu sehen (definiert im Menü auf der linken Seite). Dies erlaubt dem Radioonkologen, die Platzierung der Nadeln vor der Behandlung virtuell zu planen. In Bild D wird die Nadel (weiße Linie im oberen rechten Fenster) gezeigt, die zur Visualisierung der multiplanaren Rekonstruktionen (MPRs) entlang des Nadelpfads (linkes unteres Fenster) ausgewählt wurde. Die Position der MPR-Schicht im Bereich des Pfeils (Spitze des roten Pfeils im oberen rechten Fenster)

wird zur besseren Orientierung im unteren linken Fenster als 2D-Schicht dargestellt. Der Querschnitt der Nadel (weiß) ist in der MPR-Schicht des unteren linken Fensters durch einen roten Kreis angegeben.

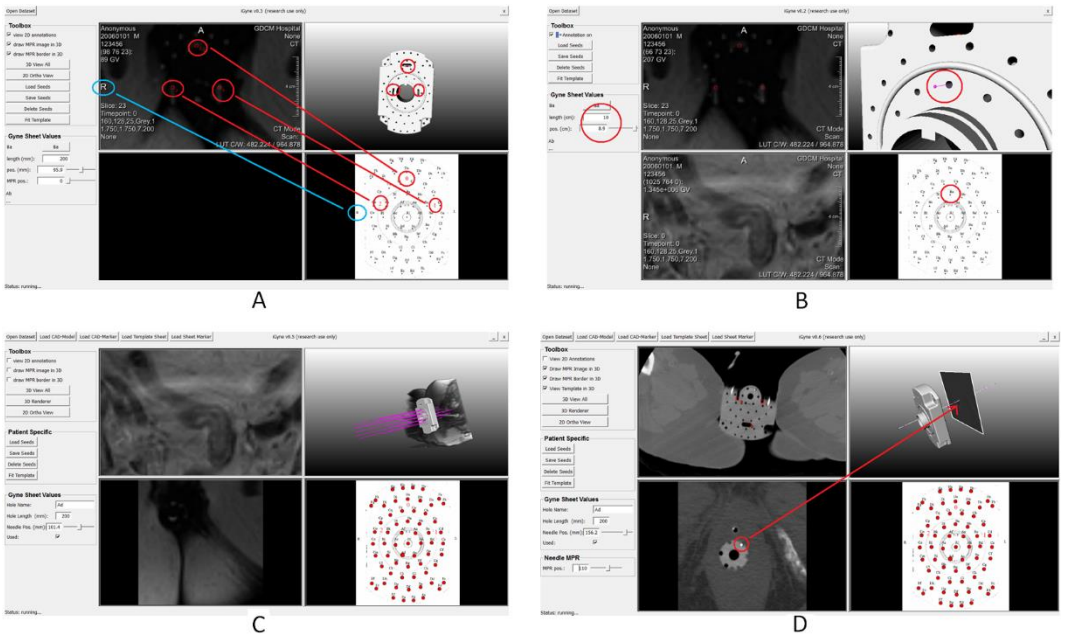

Abbildung 58 – Prinzipieller Ablauf der iGyne Template-Registrierung für die gynäkologische Brachytherapie mit den initialen CT-Aufnahmen einer Patientin: (A) Die drei roten Kreise geben die korrespondieren Nadellöcher im Template und der CT-Aufnahme an. Die Registrierung erfolgt über eine rigide Transformation zwischen diesen korrespondierenden Punktmengen. Die blauen Kreise zeigen an, dass die rechte und linke Seite der Patientenaufnahmen mit dem Template übereinstimmen; (B) virtuell registriertes Template der gynäkologischen Brachytherapie und Auswahl einer interstitiellen Nadel (Ba, rote Kreise im Screenshot). Wie auf der linken Seite des Prototypeninterface zu sehen ist, kann das Einbringen von Nadeln anhand der Nadellänge und der Nadeltiefe individuell geplant werden. (C) Virtuelle Platzierung von mehreren Nadeln (Purpur) mit unterschiedlichen Längen und Eindringtiefen. Dies erlaubt dem Radioonkologen die Platzierung der Nadeln präinterventionell zu planen. (D) Nadel (weiße Linie im oberen rechten Fenster), die zur Visualisierung der multiplanaren Rekonstruktionen (MPRs) entlang des Nadelpfads (linkes unteres Fenster) ausgewählt wurde. Die Position der MPR im Bereich des Pfeils (Spitze des roten Pfeils im oberen rechten Fenster) wird im unteren linken Fenster als 2D-Schicht dargestellt. In der MPR des unteren linken Fensters ist der Querschnitt der Nadel (weiß) durch einen roten Kreis angegeben.

Abbildung 59 und Abbildung 60 zeigen Screenshots von iGyne in der Anwendung unter 3D Slicer. Abbildung 59 stellt das Ergebnis einer verfeinerten Registrierung von Template (blau) und Obturator (grün) in einer axialen (oberes linkes Fenster), einer sagittalen (unteres linkes Fenster), einer koronalen (unteres rechtes

Fenster) und einer 3D-Ansicht (oberes rechtes Fenster) dar. Abbildung 60 wiederum präsentiert einen Screenshot der Visualisierung eines segmentierten Tumors (braun) mit ausgewählten Nadeln (pink und grün) in einer 3D-Ansicht. Zusätzlich ist es möglich, die geplanten interstitiellen Nadeln in unterschiedlichen 2D-Schichten zu rendern (rechte Fenster).

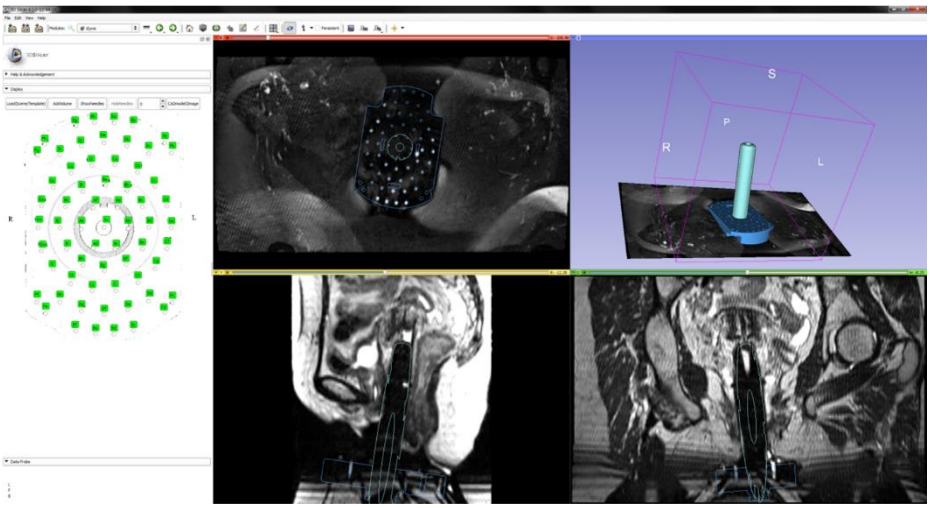

Abbildung 59 – Screenshot des Ergebnisses einer verfeinerten Registrierung von Template (blau) und Obturator (grün) in einer axialen (oberes linkes Fenster), einer sagittalen (unteres linkes Fenster), einer koronalen (unteres rechtes Fenster) und einer 3D-Ansicht (oberes rechtes Fenster).

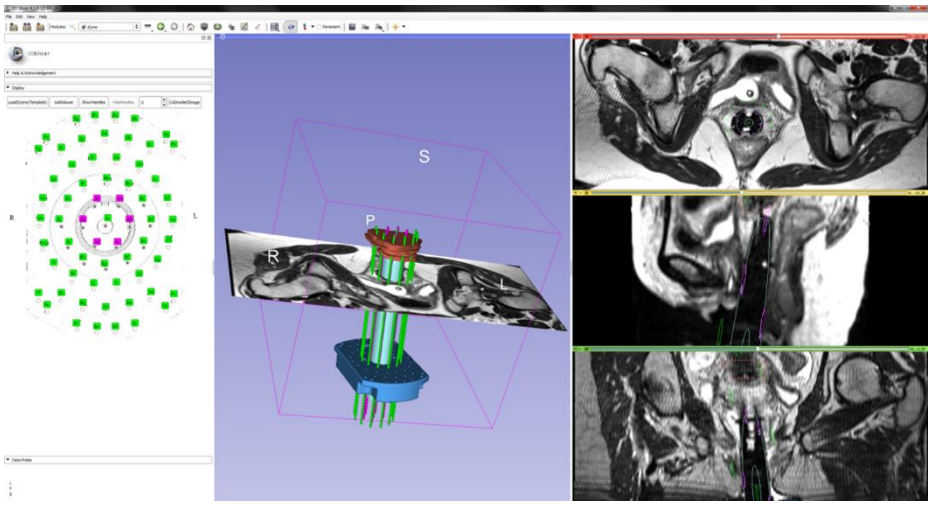

Abbildung 60 – Screenshot der Visualisierung eines segmentierten Tumors (braun) mit ausgewählten Nadeln (pink und grün) in einer 3D-Ansicht. Außerdem ist es möglich, die geplanten interstitiellen Nadeln in unterschiedlichen 2D-Schichten zu rendern (rechte Fenster).

4.4. Ein bildgestütztes System für die gynäkologische Brachytherapie

In diesem Beitrag [16] wird erstmals ein alle Operationsphasen umfassendes bildgestütztes System für die gynäkologische Brachytherapie in einem multimodalen Operationssaal präsentiert. Dieses komplexe System wurde von einem Informatiker mit Unterstützung durch ein interdisziplinäres Team aus Medizinern und Ingenieuren anhand des multimodalen Operationssaals AMIGO ausgearbeitet. Dabei besteht das vollständige Therapiesystem aus der prä-, intra- und postoperativen Behandlungsphase bei einer interstitiellen gynäkologischen Brachytherapie. Die präoperative Behandlungsphase beginnt mit der Ankunft einer Patientin und den Bildaufnahmen. Diese Patientenaufnahmen werden anschließend für die Diagnose und eine Begutachtung und Vermessung der Patientenanatomie für die gynäkologische Strahlentherapie genutzt. Dies führt zuerst zu der Entscheidung, ob die Patientin für eine Behandlung geeignet ist oder nicht. Kommt die Patientin für eine Behandlung in Frage, wird eine erste Auswahl des medizinischen Instrumentariums getroffen und bei der Bestandsdatenbank angefragt, eventuell auch bei einem Medizintechnikhersteller nachgeordert. Das ausgewählte Instrument (zum Beispiel Tandem und Ring/Ovoid +/− interstitielle Nadeln, Vienna Applikator, rein interstitielle Nadeln) wird in den präoperativen Patientenaufnahmen modelliert und visualisiert und von Medizinern begutachtet. Dabei ermöglicht das vorgestellte System die virtuelle Modellierung und Visualisierung mehrerer Instrumente in den präoperativen Patientenaufnahmen, was wiederum einen direkten Vergleich zwischen den unterschiedlichen Instrumenten erlaubt, um das optimale Instrument für die Behandlung und die notwendige Strahlendosis zu finden. Anschließend wird das ausgewählte Instrument aus dem Inventar geordert, und das dazugehörige Modell (zum Beispiel ein 3D CAD-Modell) wird in einem PACS-System für die intra- und postoperative Behandlungsphase abgespeichert. In der intraoperativen Behandlungsphase werden von der Patientin Aufnahmen mit einem intraoperativen MRT angefertigt, wobei das modellierte Instrument aus dem PACS-System zur Steuerung des realen Instruments verwendet wird. Um dem behandelnden Mediziner die optimale Position für eine spätere Bestrahlung anzuzeigen, wird das Instrument in den intraoperativen Patientenaufnahmen visualisiert. Das bildgestützte Therapiesystem endet in der postoperativen Phase mit einer Nachuntersuchung, bei der weitere Patientenaufnahmen mit einer Visualisierung des Instruments aus dem PACS-System angefertigt werden.

Abbildung 61 veranschaulicht den gesamten Ablauf des bildgestützten Systems für die gynäkologische Brachytherapie in einem multimodalen Operationssaal nochmals in einem Diagramm. Wie schon im vorherigen Abschnitt detailliert beschrieben, beginnt das umfassende System hierbei mit der Ankunft der Patientin in der präoperativen Phase und endet mit der Kontrolluntersuchung in der postoperativen Phase.

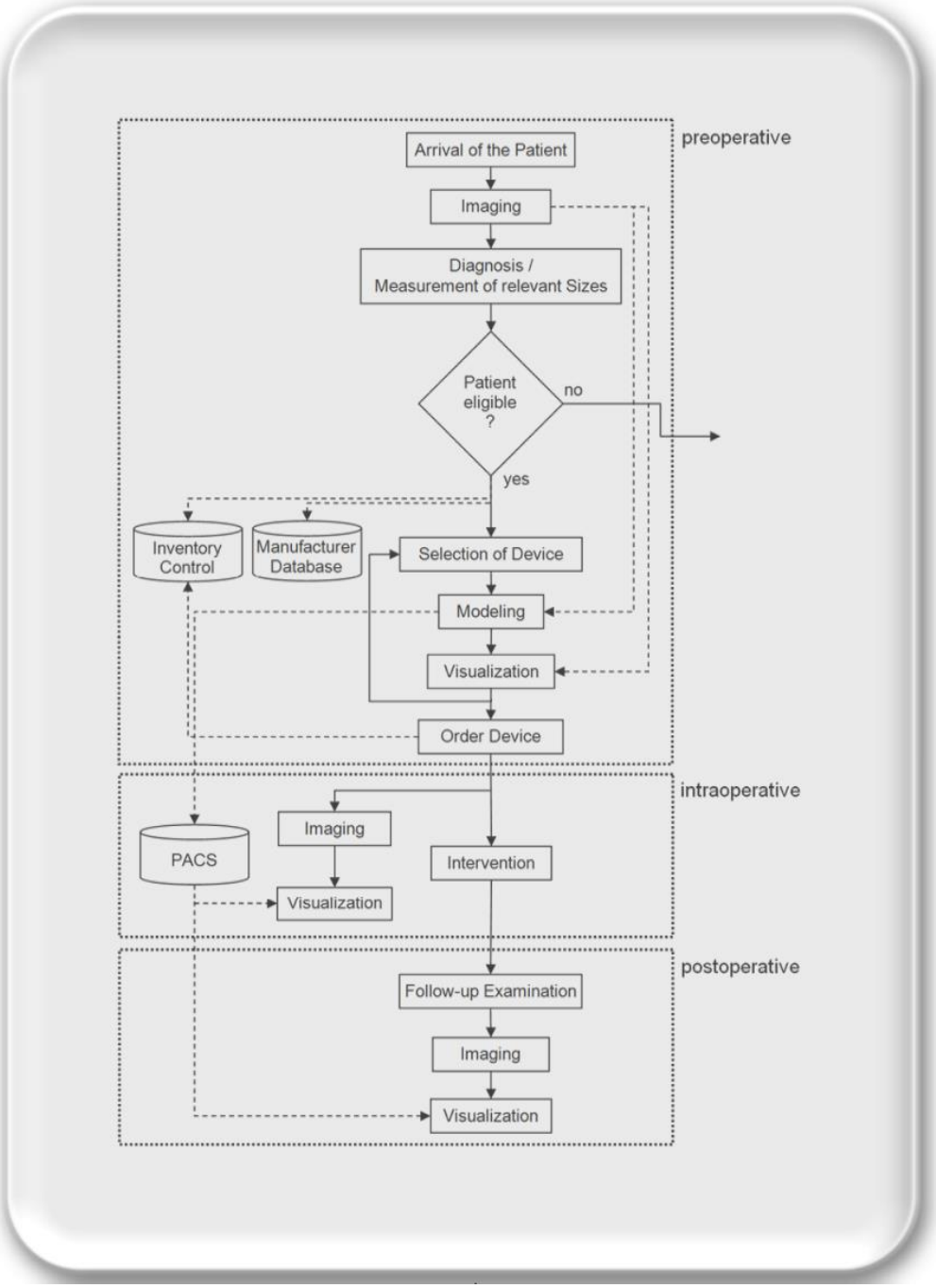

Abbildung 61 – Der gesamte Ablauf des bildgestützten Systems für die gynäkologische Brachytherapie in einem multimodalen Operationssaal. Das umfassende System beginnt mit der Ankunft der Patientin in der präoperativen Phase und endet mit der Kontrolluntersuchung in der postoperativen Phase.

In Abbildung 62 werden dreidimensionale CAD-Modelle von einem interstitiellen Template (oben links) und einem Obturator (oben Mitte) für die gynäkologischen Brachytherapie, einem modifizierten interstitiellen Template (oben rechts)

und einem sogenannten Tandem und Ring (unten rechts) gezeigt, die auch in der gynäkologischen Brachytherapie zum Einsatz kommen.

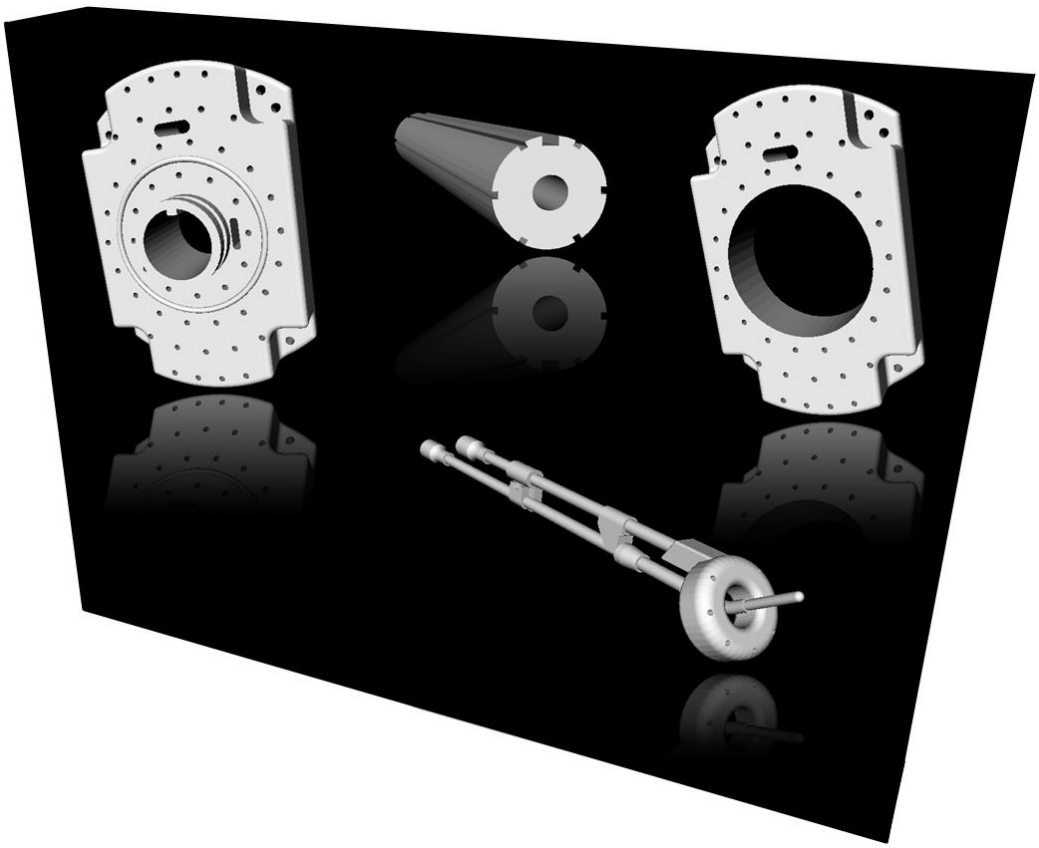

Abbildung 62 – 3D-CAD-Modelle von einem interstitiellen Template (oben links) und einem Obturator (oben Mitte) für die gynäkologischen Brachytherapie, einem modifizierten interstitiellen Template (oben rechts) und einem sogenannten Tandem und Ring (unten rechts), die auch in der gynäkologischen Brachytherapie zum Einsatz kommen.

Abbildung 63 präsentiert vier Screenshots der Forschungssoftware iGyne, die für das vorgestellte System in der gynäkologischen Brachytherapie als eigenes Modul für die medizinische Plattform 3D Slicer entwickelt und implementiert wurde. Zu sehen sind das Template (blau), der Obturator (türkis) und Hohlnadeln (mehrfarbig), die virtuell in der MRT-Aufnahme einer Patientin platziert wurden. Die Hohlnadeln können unter iGyne auf der rechten Seite in der 2D-Abbildung des Templates einzeln aktiviert/deaktiviert bzw. platziert werden. Bei der Aktivierung kann unter anderem auch die Eindringtiefe der Hohlnadel in den Körper eingestellt werden. Das mittlere Fenster präsentiert eine 3D-Darstellung des MRT-Datensatzes mit den CAD-Modellen der interstitiellen Instrumente (Template und Obturator) und den platzierten Hohlnadeln. Auf der rechten Seite sind eine axiale (rot), sagittale (gelb) und koronale (grün) 2D-Schicht dargestellt.

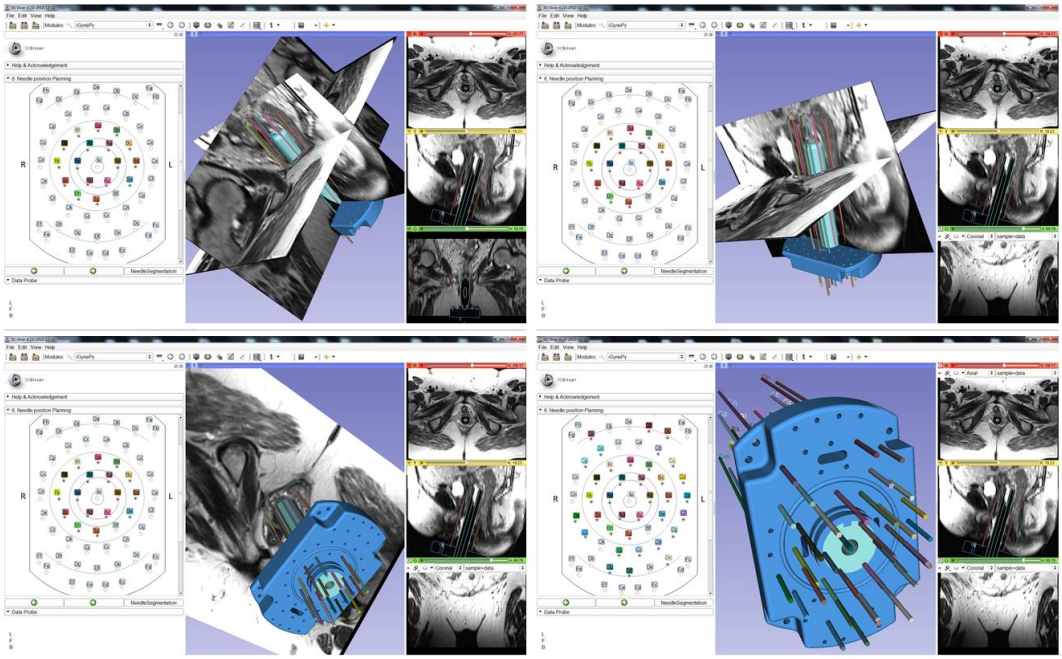

Abbildung 63 – Screenshots der Forschungssoftware iGyne, die für das vorgestellte System in der gynäkologischen Brachytherapie als eigenes Modul für die medizinische Plattform 3D Slicer entwickelt und implementiert wurde.

4.5. Zusammenfassung

In diesem Kapitel wurden Methoden und Module für intraoperative Therapien entwickelt. Dazu gehört die erstmalig erfolgreiche Integration des OpenIGTLink-Protokolls in die medizinische Prototypen-Plattform MeVisLab. Die Integration erlaubt es Forschern nicht nur, Geräte, die OpenIGTLink unterstützen, mit ihren MeVisLab-Prototypen anzusteuern, sondern auch mit anderen Plattformen – wie 3D Slicer – zu kommunizieren. Damit wird auch auf Plattformebene eine Zusammenarbeit zwischen verschiedenen Forschergruppen ermöglicht. Außerdem wurde in diesem Kapitel erstmalig ein Software-Prototyp zur Unterstützung der intraoperativen gynäkologischen Brachytherapie vorgestellt. Der Software-Prototyp wurde für intraoperative MRT-Daten entwickelt und anhand solcher Bilddaten getestet, kann aber auch auf andere Modalitäten wie CT übertragen werden. Zuletzt wurde in diesem Kapitel auch ein umfassendes bildgestütztes System für die gynäkologische Brachytherapie in einem multimodalen Operationssaal dargestellt. Das System integriert unter anderem den vorgestellten Software-Prototypen und kann für die Kommunikation zwischen den Software- und Hardwarekomponenten den OpenIGTLink-Standard nutzen. Das System könnte durch eine zusätzliche intraoperative Navigation beim Setzen der Hohlnadeln noch erweitert werden. Allerdings wird das intraoperative Navigieren während der gynäkologischen Brachytherapie nicht standardmäßig in der Praxis eingesetzt und ist bisher noch Gegenstand der Forschung – im Gegensatz zu neurochirurgischen Eingriffen, bei denen intraoperatives Navigieren in vielen Kliniken bereits zur Routine gehört. Der Unterschied liegt hierbei in der Registrierung, die in der Neurochirurgie über den Schädel rigide

erfolgen kann, was im abdominalen Bereich nicht ohne weiteres möglich ist. Insgesamt sind die vorgestellten Methoden und Module schon sehr nah an der Praxis und könnten prinzipiell nach einer Zertifizierung auch schon routinemäßig eingesetzt werden. Das liegt vor allem daran, dass die Forschungsergebnisse direkt in einer Klinik zusammen mit Ärzten in einem multimodalen Operationssaal erarbeitet wurden. Allerdings besitzen bisher nicht viele Kliniken multimodale Operationssäle mit intraoperativen MRTs (dies ist eine Kostenfrage).

Abbildungsverzeichnis

Tabellenverzeichnis

Quellcodeverzeichnis

Eigene Publikationen

[1] **J. Egger**, T. Kapur, T. Dukatz, M. Kolodziej, D. Zukić, B. Freisleben, C. Nimsky. Square-Cut: A Segmentation Algorithm on the Basis of a Rectangle Shape. PLoS One, 2012; 7(2):e31064. Epub 2012 Feb 21.

[2] **J. Egger**, T. Dukatz, B. Freisleben, C. Nimsky. Ein semiautomatischer Ansatz zur Flächenbestimmung von Wirbeln in MRT-Aufnahmen. Proceedings of Bildverarbeitung für die Medizin (BVM) – Algorithmen - Systeme - Anwendungen, Springer Press, pp. 274-279, Berlin, Germany, March 2012.

[3] **J. Egger**, B. Freisleben, C. Nimsky, T. Kapur. Template-Cut: A Pattern-Based Segmentation Paradigm. Sci Rep., Nature Publishing Group (NPG), 2012; 2:420. Epub 2012 May 24.

[4] R. Schwarzenberg, B. Freisleben, R. Kikinis, C. Nimsky, **J. Egger**. Ein kubusbasierter Ansatz zur Segmentierung von Wirbeln in MRT-Aufnahmen. Proceedings of Bildverarbeitung für die Medizin (BVM) – Algorithmen - Systeme - Anwendungen, Springer Press, pp. 69-74, Heidelberg, Germany, March 2013.

[5] R. Schwarzenberg, B. Freisleben, C. Nimsky, **J. Egger**. Cube-Cut: Vertebral Body Segmentation in MRI-Data through Cubic-Shaped Divergences. PLoS One, 2014; 9(4):e93389. Epub 2014 Apr 04.

[6] **J. Egger**. PCG-Cut: Graph Driven Segmentation of the Prostate Central Gland. PLoS One, 2013; 8(10):e76645. Epub 2013 Oct 11.

[7] **J. Egger**. T. Lüddemann, R. Schwarzenberg, B. Freisleben, C. Nimsky. Interactive-Cut: Real-Time Feedback Segmentation for Translational Research. Comput Med Imaging Graph. Available online 11 February 2014.

[8] **J. Egger**. Semi-automatische Echtzeit-Konturierung – Ein vorlagenbasierter skalierungsinvarianter Ansatz. Proceedings of Bildverarbeitung für die Medizin (BVM) – Algorithmen - Systeme - Anwendungen, Springer Press, pp. 366-371, Aachen, Germany, March 2014.

[9] **J. Egger**. Refinement-Cut: User-Guided Segmentation Algorithm for Translational Science. Sci Rep., Nature Publishing Group (NPG), 2014; 4:5164. Epub 2014 June 4.

[10] **J. Egger**, T. Kapur, C. Nimsky, R. Kikinis. Pituitary Adenoma Volumetry with 3D Slicer. PLoS One, 2012; 7(12):e51788. Epub 2012 Dec 11.

[11] **J. Egger**, T. Kapur, A. Fedorov, S. Pieper, J. V. Miller, H. Veeraraghavan, B. Freisleben, A. J. Golby, C. Nimsky, R. Kikinis. GBM Volumetry using the 3D Slicer Medical Image Computing Platform. Sci Rep., Nature Publishing Group (NPG), 2013; 3:1364. Epub 2013 March 4.

[12] D. Kuhnt, M. H. A. Bauer, **J. Egger**, D. Merhof, M. Richter, T. Kapur, J. Sommer, C. Nimsky. Fiber tractography based on diffusion tensor imaging (DTI) compared with High Angular Resolution Diffusion Imaging (HARDI) with compressed sensing (CS) – initial experience and clinical impact. Neurosurgery, Volume 72, pp. A165-A175, January 2013.

[13] **J. Egger**, J. Tokuda, L. Chauvin, B. Freisleben, C. Nimsky, T. Kapur, W. M. Wells. Integration of the OpenIGTLink Network Protocol for Image-Guided Therapy with the Medical Platform MeVisLab. Int J Med Robot. 2012 Sep; 8(3):282-90. doi: 10.1002/rcs.1415. Epub 2012 Feb 28.

[14] T. Kapur, **J. Egger**, A. Damato, E. Schmidt, A. Viswanathan. 3-T MR-guided brachytherapy for gynecologic malignancies. Magn Reson Imaging. 2012 Nov; 30(9):1279-90. doi: 10.1016/j.mri.2012.06.003. Epub 2012 Aug 13.

[15] X. Chen, **J. Egger**. Development of an Open Source Software Module for Enhanced Visualization during MR-Guided Interstitial Gynecologic Brachytherapy. SpringerPlus, 3:167, March 2014.

[16] **J. Egger**, Image-guided therapy system for interstitial gynecologic brachytherapy in a multimodality operating suite. SpringerPlus, 2:395, August 2013.

[17] **J. Egger**. Prä- und postoperative Segmentierung und virtuelles Stenting von Aneurysmen und Stenosen. Dissertation (Dr. rer. nat.), Fachbereich Mathematik und Informatik, Betreuer Prof. Dr.-Ing. Bernd Freisleben, Philipps-Universität Marburg, 215 Seiten, Juli 2009.

[18] **J. Egger**, S. Großkopf, B. Freisleben. Comparison of Two Methods for the Preoperative Visualization of Stent Grafts in CT-Data. Proceedings of the 5. Jahrestagung der Deutschen Gesellschaft für Computer- und Roboterassistierte Chirurgie (CURAC), Hanover, Germany, pp. 140-141, October 2006.

[19] **J. Egger**, S. Großkopf, B. Freisleben. Simulation of Bifurcated Stent Grafts to Treat Abdominal Aortic Aneurysms (AAA). Proceedings of SPIE Medical Imaging Conference, Vol. 6509, pp. 65091N(1-6), San Diego, California, USA, February 2007.

[20] **J. Egger**, S. Großkopf, B. Freisleben. Präoperative Simulation von Rohrprothesen und Y-Stents zur endovaskulären Behandlung von Stenosen und Aneurysmen. Proceedings of Bildverarbeitung für die Medizin (BVM), Munich, Germany, pp. 182-186, Springer Press, March 2007.

[21] **J. Egger**, Z. Mostarkić, S. Großkopf, B. Freisleben. Preoperative Measurement of Aneurysms and Stenosis and Stent-Simulation for Endovascular Treatment. IEEE International Symposium on Biomedical Imaging: From Nano to Macro, Washington (D.C.), USA, pp. 392-395, IEEE Press, April 2007.

[22] **J. Egger**, Z. Mostarkić, S. Großkopf, B. Freisleben. A Fast Vessel Centerline Extraction Algorithm for Catheter Simulation. 20th IEEE International Symposium on Computer-Based Medical Systems, Maribor, Slovenia, pp. 177-182, IEEE Press, June 2007.

[23] **J. Egger**, Z. Mostarkić, F. Maier, J. N. Kaftan, S. Großkopf, B. Freisleben. Fast Self-Collision Detection and Simulation of Bifurcated Stents to Treat Abdominal Aortic Aneurysms (AAA). 29th Annual International Conference of the IEEE Engineering in Medicine and Biology Society, Lyon, France, pp. 6231-6234, IEEE Press, August 2007.

[24] J. Lu, **J. Egger**, A. Wimmer, S. Großkopf, B. Freisleben. Segmentierung und Visualisierung von Lumen und Thrombus bei thorakalen Aortenaneurysmen. Proceedings of 6. Jahrestagung der Deutschen Gesellschaft für Computer- und Roboterassistierte Chirurgie (CURAC), Karlsruhe, Germany, pp. 251-254, October 2007.

[25] J. Lu, **J. Egger**, A. Wimmer, S. Großkopf, B. Freisleben. Detection and Visualization of Endoleaks in CT Data for Monitoring of Thoracic and Abdominal Aortic Aneurysm Stents. Proceedings of SPIE Medical Imaging Conference, Vol. 6918, pp. 69181F(1-7), San Diego, California, USA, February 2008.

[26] K. Greiner, **J. Egger**, S. Großkopf, J. N. Kaftan, R. Dörner, B. Freisleben. Segmentierung von Aortenaneurysmen in CTA-Bildern mit dem statistischen Verfahren der Active Appearance Models. Proceedings of Bildverarbeitung für die Medizin (BVM), Berlin, Germany, Springer Press, pp. 51-55, April 2008.

[27] **J. Egger**, S. Großkopf, B. Freisleben. Virtual Stenting for Carotid Stenosis with Elastic Artery Wall Modeling. Proceedings of 4th European Congress for Medical and Biomedical Engineering, Engineering for Health, Antwerp, Belgium, Springer Press, pp. 2499-2502, November 2008.

[28] **J. Egger**, T. O'Donnell, C. Hopfgartner, B. Freisleben. Graph-Based Tracking Method for Aortic Thrombus Segmentation. Proceedings of 4th European Congress for Medical and Biomedical Engineering (EMBEC), Engineering for Health, Antwerp, Belgium, Springer Press, pp. 584-587, November 2008.

[29] **J. Egger**, S. Großkopf, T. O'Donnell, B. Freisleben. A Software System for Stent Planning, Stent Simulation and Follow-Up Examinations in the Vascular Domain. 22nd IEEE International Symposium on Computer-Based Medical Systems, Albuquerque, New Mexico, USA, IEEE Press, ACM/SIGAPP, pp. 1-7, August 2009.

[30] **J. Egger**, B. Freisleben, R. Setser, R. Renapuraar, C. Biermann, T. O'Donnell. Aorta Segmentation for Stent Simulation. 12th International Conference on Medical Image Computing and Computer Assisted Intervention (MICCAI), Cardiovascular Interventional Imaging and Biophysical Modelling Workshop, pp. 1-10, London, UK, September 2009.

[31] **J. Egger**, C. Biermann, S. Großkopf, C. Hopfgartner, D. Fritz, B. Freisleben. Vollautomatische Stent-Planung und Stent-Simulation zur Unterstützung der minimal-invasiven Behandlung von abdominalen Bauchaortenaneurysmen. 39. Jahrestagung der Gesellschaft für Informatik, Lübeck, Lecture Notes in Informatics (LNI), pp. 1317-1327, October 2009.

[32] **J. Egger**, M. H. A. Bauer, B. Freisleben, C. Nimsky. Determination, Calculation and Representation of the Upper and Lower Sealing Zones During Virtual Stenting of Aneurysms. Proceedings of Computer Assisted Radiology and Surgery (CARS 2010), Geneva, Switzerland, Int J CARS, Vol. 5, Suppl. 1, pp. 13-14, Springer Press, June 2010.

[33] **J. Egger**, S.K. Zhou, S. Grosskopf, D. Liu, C. Hopfgartner, D. Bernhardt, C. Biermann, C. Nimsky, B. Freisleben. Body Landmark Detection for a Fully Automatic AAA Stent Graft Planning Software System. 23rd IEEE International Symposium on Computer-Based Medical Systems, IEEE Press, ACM, pp. 364-369 , Perth, Australia, October 2010.

[34] R. D. Renapurkar, R. M. Setser, T. P. O'Donnell, **J. Egger**, M. L. Lieber, M. Y. Desai, A. E. Stillman, P. Schoenhagen, S. D. Flamm. Aortic volume as an indicator of disease progression in patients with untreated infrarenal abdominal aneurysm. Eur J Radiol. 2012 Feb; 81(2):e87-93. Epub 2011 Feb 12.

[35] **J. Egger**, S. Grosskopf, C. Nimsky, T. Kapur, B. Freisleben. Modeling and Visualization Techniques for Virtual Stenting of Aneurysms and Stenoses. Comput Med Imaging Graph. 2012 Apr; 36(3):183-203. Epub 2012 Jan 9.

[36] **J. Egger**. Intraoperative Visualisierung multimodaler Daten in der Neurochirurgie. Dissertation (Dr. rer. physiol.), Fachbereich Medizin, Betreuer Prof. Dr. med. Christopher Nimsky, Philipps-Universität Marburg, 223 Seiten, Juni 2012.

[37] **J. Egger**, M. H. A. Bauer, D. Kuhnt, C. Kappus, B. Carl, B. Freisleben, C. Nimsky. A Flexible Semi-Automatic Approach for Glioblastoma multiforme Segmentation. Proceedings of International Biosignal Processing Conference, Kurths J, Penzel T, Malberg H, Wessel N (Hrsg), Berlin, Germany, Paper-ID: 060:1-4, July 2010.

[38] **J. Egger**, M. H. A. Bauer, D. Kuhnt, B. Freisleben, C. Nimsky. Pituitary Adenoma Segmentation. Proceedings of International Biosignal Processing Conference, Kurths J, Penzel T, Malberg H, Wessel N (Hrsg), Berlin, Germany, Paper-ID: 061:1-4, July 2010.

[39] **J. Egger**, M. H. A. Bauer, D. Kuhnt, B. Carl, C. Kappus, B. Freisleben, C. Nimsky. Nugget-Cut: A Segmentation Scheme for Spherically- and Elliptically-Shaped 3D Objects. 32nd Annual Symposium of the German Association for Pattern Recognition (DAGM), LNCS 6376, pp. 383-392, Springer Press, Darmstadt, Germany, September 2010.

[40] **J. Egger**, M. H. A. Bauer, D. Kuhnt, C. Kappus, B. Carl, B. Freisleben, C. Nimsky. Evaluation eines neuen Ansatzes zur automatischen Volumenbestimmung von Glioblastomen anhand von mehreren manuellen Expertensegmentierungen. Proceedings of 44. Jahrestagung der DGBMT, Biomedizinische Technik/Biomedical Engineering, Band 55, Heft s1, 119-122, de Gruyter Verlag, Rostock, Germany, Oct. 2010.

[41] D. Zukić, **J. Egger**, M. H. A. Bauer, D. Kuhnt, B. Carl, B. Freisleben, A. Kolb, C. Nimsky. Glioblastoma Multiforme Segmentation in MRI Data with a Balloon Inflation Approach. Proceedings of 6th Russian-Bavarian Conference on Bio-Medical Engineering, Editors A. Alexandrov et al., Publisher Bauman Moscow State Technical University (BMSTU), State Technical University, Moscow, Russia, pages 9-13, November 2010.

[42] **J. Egger**, D. Zukić, M. H. A. Bauer, D. Kuhnt, B. Carl, B. Freisleben, A. Kolb, C. Nimsky. A Comparison of Two Human Brain Tumor Segmentation Methods for MRI Data. Proceedings of 6th Russian-Bavarian Conference on Bio-Medical Engineering, Editors A. Alexandrov et al., Publisher Bauman Moscow State Technical University (BMSTU), State Technical University, Moscow, Russia, pages 40-44, November 2010.

[43] **J. Egger**, C. Kappus, B. Freisleben, C. Nimsky. Ein effizienter geometrischer Ansatz zur Unterstützung der Trajektoriebestimmung bei der Tiefenhirnstimulation. Proceedings of Bildverarbeitung für die Medizin (BVM) – Algorithmen - Systeme - Anwendungen, Springer Press, pp. 374-378, Lübeck, Germany, March 2011.

[44] **J. Egger**, C. Kappus, B. Freisleben, C. Nimsky. A Medical Software System for Volumetric Analysis of Cerebral Pathologies in Magnetic Resonance Imaging (MRI) Data. J Med Syst. 2012 Aug; 36(4):2097-109. Epub 2011 Mar 8.

[45] **J. Egger**, R. Colen, B. Freisleben, C. Nimsky. Manual Refinement System for Graph-Based Segmentation Results in the Medical Domain. J Med Syst. 2012 Oct; 36(5):2829-39. Epub 2011 Aug 9.

[46] D. Richter, F. La Torre, **J. Egger**, G. Straßmann. Tetraoptical Camera System for Medical Navigation. Proceedings of the 17th International EURASIP Conference BIOSIGNAL, Brno, Czech Republic, pp. 270-272, Vutium Press, Jun. 2004.

[47] D. Richter, **J. Egger**, G. Straßmann. Ein Algorithmus zur Positionsbestimmung von Patienten und Biopsienadeln mit einem Vierkamerasystem. Bildverarbeitung für die Medizin (BVM), Hamburg, Germany, pp. 316-320, Springer-Verlag, Mar. 2006.

[48] M. H. A. Bauer, S. Barbieri, J. Klein, **J. Egger**, D. Kuhnt, B. Freisleben, H. K. Hahn, C. Nimsky. A Ray-based Approach for Boundary Estimation of Fiber Bundles derived from Diffusion Tensor Imaging. Proceedings of Computer Assisted Radiology and Surgery (CARS 2010), Geneva, Switzerland, Int J CARS, Vol. 5, Suppl. 1, pp. 47-48, Springer Press, June 2010.

[49] M. H. A. Bauer, **J. Egger**, D. Kuhnt, S. Barbieri, J. Klein, H. K. Hahn, B. Freisleben, C. Nimsky. Ray-Based and Graph-Based Methods for Fiber Bundle Boundary Estimation. Proceedings of International Biosignal Processing Conference, Kurths J, Penzel T, Malberg H, Wessel N (Hrsg), Berlin, Germany, Paper-ID: 048:1-4, July 2010.

[50] M. H. A. Bauer, S. Barbieri, J. Klein, **J. Egger**, D. Kuhnt, B. Freisleben, H. K. Hahn, C. Nimsky. Boundary Estimation of Fiber Bundles derived from Diffusion Tensor Images. Int J Comput Assist Radiol Surg. 2011 Jan; 6(1):1-11. Epub 2010 Jun 19.

[51] M. H. A. Bauer, **J. Egger**, T. O'Donnell, B. Freisleben, S. Barbieri, J. Klein, H. K. Hahn, C. Nimsky. A Fast and Robust Graph-based Approach for Boundary Estimation of Fiber Bundles Relying on Fractional Anisotropy Maps. 20th International Conference on Pattern Recognition (ICPR), Istanbul, Turkey, IEEE Computer Society, pp. 4016-4019, August 2010.

[52] M. H. A. Bauer, **J. Egger**, D. Kuhnt, S. Barbieri, J. Klein, H. K. Hahn, B. Freisleben, C. Nimsky. Ein semi-automatischer graphbasierter Ansatz zur Bestimmung des Randes von eloquenten Faserverbindungen des Gehirns. Proceedings of 44. Jahrestagung der DGBMT, Biomedizinische Technik/Biomedical Engineering, Band 55, Heft s1, 123-126, de Gruyter Verlag, Rostock, Germany, October 2010.

[53] M. H. A. Bauer, S. Barbieri, **J. Egger**, D. Kuhnt, J. Klein, H. K. Hahn, B. Freisleben, C. Nimsky. Segmentierung von Faserbahnsystemen mit einem strahlenbasierten Ansatz und Glättung der FA- und Winkel-Karten. Proceedings of 9. Jahrestagung der Deutschen Gesellschaft für Computer- und Roboterassistierte Chirurgie (CURAC), MEDICA, Düsseldorf, Germany, pp. 1-4, November 2010.

[54] D. Zukić, **J. Egger**, M. H. A. Bauer, D. Kuhnt, B. Carl, B. Freisleben, A. Kolb, C. Nimsky. Preoperative Volume Determination for Pituitary Adenoma. Proceedings of SPIE Medical Imaging Conference, Orlando, Florida, USA, Feb. 2011.

[55] D. Zukić, A. Vlasak, T. Dukatz, **J. Egger**, D. Horinek, C. Nimsky, A. Kolb. Segmentation of Vertebral Bodies in MR Images. Vision, Modeling, and Visualization (VMV), The Eurographics Association, pp. 135-142, Nov. 2012.

[56] **J. Egger**, D. Zukić, B. Freisleben, A. Kolb, C. Nimsky. Segmentation of Pituitary Adenoma: A Graph-based Method vs. a Balloon Inflation Method. Computer Methods and Programs in Biomedicine (Comput Methods Programs Biomed), Elsevier, 2013 June; 110(3):268-78. doi: 10.1016/j.cmpb.2012.11.010. Epub 2012 December 23.

[57] J. Klein, S. Barbieri, H. Stuke, M. H. A. Bauer, **J. Egger**, C. Nimsky, H. K. Hahn. On the Reliability of Diffusion Neuroimaging. Neuroimaging, published by Sciyo, pages 1-24, ISBN 978-953-307-127-5, 2010.

[58] T. Kapur, **J. Egger**, J. Jayender, M. Toews, W. M. Wells III. Registration and Segmentation for Image Guided Therapy. Intraoperative Imaging and Image-Guided Therapy, Ferenc A. Jolesz (Editor), Springer, pp. 79-91, ISBN: 978-1-4614-7656-6 (Print) 978-1-4614-7657-3 (Online), January 2014.

[59] D. Zukić, A. Vlasák, **J. Egger**, D. Hořínek, C. Nimsky, A. Kolb. Robust Detection and Segmentation for Diagnosis of Vertebral Diseases using Routine MR Images. Computer Graphics Forum, Wiley Online Library, Volume 33, Issue 6, pages 190-204, September 2014, Article first published online: 4 March 2014.

[60] T. Lüddemann, **J. Egger**. Interaktive und skalierungsinvariante Segmentierung des Rektums/Sigmoid in intraoperativen MRT-Aufnahmen für die gynäkologische Brachytherapie. Proceedings of Bildverarbeitung für die Medizin (BVM) – Algorithmen - Systeme - Anwendungen, Springer Press, pp. 29-34, Lübeck, Germany, March 2015.

[61] **J. Egger**, H. Busse, M. Moche, P. Brandmaier, D. Seider, M. Gawlitza, S. Strocka, N. Garnov, J. Fuchs, P. Voigt, F. Dazinger, P. Voglreiter, M. Dokter, M. Hofmann, A. Hann, B. Freisleben, T. Kahn, D. Schmalstieg. Semiautomatische Segmentierung von Schädigungszonen in post-interventionellen CT-Daten. Proceedings of Bildverarbeitung für die Medizin (BVM) – Algorithmen - Systeme - Anwendungen, Springer Press, pp. 281-286, Lübeck, Germany, March 2015.

[62] X. Chen, L. Xu, Y. Wang, H. Wang, F. Wang, X. Zeng, Q. Wang, **J. Egger**. Development of a Surgical Navigation System based on Augmented Reality using an Optical see-through Head-mounted Display. Journal of Biomedical Informatics (JBI), Elsevier, 2015 Jun; 55:124-31. doi: 10.1016/j.jbi.2015.04.003. Epub 2015 April 13.

[63] B. Kainz, C. Malamateniou, G. Ferrazzi, M. Murgasova, **J. Egger**, K. Keraudren, M. Rutherford, J. V. Hajnal, D. Rueckert. Adaptive Scan Strategies for fetal MRI Imaging using Slice to Volume Techniques. Proceedings of The IEEE International Symposium on Biomedical Imaging (ISBI): From Nano to Macro, IEEE Press, Brooklyn, NY, United States, pp. 849-852, April 2015.

[64] **J. Egger**, H. Busse, P. Brandmaier, D. Seider, M. Gawlitza, S. Strocka, P. Voglreiter, M. Dokter, M. Hofmann, B. Kainz, X. Chen, A. Hann, P. Boechat, W. Yu, B. Freisleben, T. Alhonnoro, M. Pollari, M. Moche, D. Schmalstieg. RFA-Cut: Semi-automatic Segmentation of Radiofrequency Ablation Zones with and without Needles via Optimal s-t-Cuts. 37th Annual International Conference of the IEEE Engineering in Medicine and Biology Society, Milan, Italy, pp. 2423-2429, IEEE Press, August 2015.

[65] **J. Egger**, H. Busse, P. Brandmaier, D. Seider, M. Gawlitza, S. Strocka, P. Voglreiter, M. Dokter, M. Hofmann, B. Kainz, A. Hann, X. Chen, T. Alhonnoro, M. Pollari, D. Schmalstieg, M. Moche. Interactive Volumetry of Liver Ablation Zones. Sci. Rep. 5, 15373; Nature Publishing Group (NPG), doi: 10.1038/srep15373, 2015.

[66] X. Chen, L. Xu, Y. Yang, **J. Egger**. A semi-automatic computer-aided method for surgical template design. Sci. Rep. 6, 20280; Nature Publishing Group (NPG), doi: 10.1038/srep20280, 2016.

[67] **J. Egger**, P. Voglreiter, M. Dokter, M. Hofmann, X. Chen, B. Kainz, W. G. Zoller, D. Schmalstieg, A. Hann. US-Cut: interactive algorithm for rapid detection and segmentation of liver tumors in ultrasound acquisitions. Proceedings of SPIE Medical Imaging Conference, Ultrasound Image Analysis and Tissue Characterization, Paper 9790-47, San Diego, California, USA, February 2016.

[68] **J. Egger**, C. Nimsky. Cellular automata segmentation of the boundary between the compacta of vertebral bodies and surrounding structures. Proceedings of SPIE Medical Imaging Conference, Image Perception, Observer Performance, and Technology Assessment, Paper 9787-52, San Diego, California, USA, March 2016.

[69] T. Lüddemann, **J. Egger**. Interactive and scale invariant segmentation of the rectum/sigmoid via user-defined templates. Proceedings of SPIE Medical Imaging Conference, Image Perception, Shape and Model-based Image Analysis, Paper 9784-113, San Diego, California, USA, March 2016.

[70] T. Lüddemann, **J. Egger**. Iterative-cuts: longitudinal and scale-invariant segmentation via user-defined templates for rectosigmoid colon in gynecological brachytherapy. J Med Imaging (Bellingham). 2016 April; 3(2):024004.

[71] M. Gall, X. Li, X. Chen, D. Schmalstieg, **J. Egger**. Computer-Aided Planning and Reconstruction of Cranial 3D Implants. In Proc. IEEE Engineering in Medicine and Biology Society (EMBC'16), Orlando, FL, USA, pp. 1179-1183, August 2016.

[72] A. Hann, W. Bohle, **J. Egger**, W. Zoller. Improvement in advanced pancreatic cancer survival with novel chemotherapeutic strategies – experience of a community based hospital. Z Gastroenterol 54(10), 1138-1142, October 2016.

[73] X. Chen, X. Li, L. Xu, Y. Sun, C. Politis, **J. Egger**. Development of a computer-aided design software for dental splint in orthognathic surgery. Sci. Rep., Nature Publishing Group (NPG), 2016 (accepted).

[74] **J. Egger**, K. Hochegger, M. Gall, X. Chen, K. Reinbacher, K. Schwenzer-Zimmerer, D. Schmalstieg, J. Wallner. Algorithmic evaluation of lower jawbone segmentations. Proceedings of SPIE Medical Imaging Conference, Biomedical Applications in Molecular, Structural, and Functional Imaging, Paper 10137-11, Orlando, Florida, USA, February 2017 (accepted).

[75] M. Gall, K. Reinbacher, J. Wallner, J. Stanzel, X. Chen, K. Schwenzer-Zimmerer, D. Schmalstieg, **J. Egger**. Interactive planning of miniplates. Proceedings of SPIE Medical Imaging Conference, Image-Guided Procedures, Robotic Interventions, and Modeling, Paper 10135-93, Orlando, Florida, USA, February 2017 (accepted).

[76] **J. Egger**, M. Gall, J. Wallner, P. de Almeida Germano Boechat, A. Hann, X. Li, X. Chen, D. Schmalstieg. Integration of the HTC Vive into the medical platform MeVisLab. Proceedings of SPIE Medical Imaging Conference, Imaging Informatics for Healthcare, Research, and Applications, Paper 10138-41, Orlando, Florida, USA, February 2017 (accepted).

[77] **J. Egger**, M. Gall, J. Wallner, K. Reinbacher, K. Schwenzer-Zimmerer, D. Schmalstieg. Interaktive Planung von Gesichtsimplantaten. Proceedings of Bildverarbeitung für die Medizin (BVM) – Algorithmen - Systeme - Anwendungen, Springer Press, Heidelberg, Germany, March 2017 (accepted).

Abstractverzeichnis

Erste Ergebnisse zu den Publikationen aus dieser Habilitationsschrift wurden regelmäßig zuerst auf internationalen Kongressen in Form von Vorträgen und Postern vorgestellt. Es folgt eine chronologische Auflistung der Abstracts mit Datum und Ort des jeweiligen Kongresses. Im Anschluss daran sind die entsprechenden dort ausgestellten Poster abgebildet:

- R. Tibrewal, A. Viswanathan, K. Townamchai, J. Fairhurst, M. Baust, **J. Egger**, A. Damato, S.-E. Song, S. Pieper, C. Tempany, W. M. Wells, T. Kapur. Concept Development and Feasibility Study of Image-based Needle Guidance for MR-Guided Interstitial Gynecologic Brachytherapy in AMIGO. 4th National Center for Image Guided Therapy (NCIGT) and National Institutes of Health (NIH) Image Guided Therapy Workshop, Arlington, Virginia, USA, page 94, October 2011.

- **J. Egger**, A. Viswanathan, T. Kapur. Bladder Segmentation for Interstitial Gynecologic Brachytherapy with the Nugget-Cut Approach. 4th National Center for Image Guided Therapy (NCIGT) and National Institutes of Health (NIH) Image Guided Therapy Workshop, Arlington, Virginia, USA, page 97, October 2011.

- **J. Egger**, B. Freisleben, R. Tibrewal, C. Nimsky, T. Kapur. A Method for Solving the Correspondence Problem for an n-Camera Navigation System for Image Guided Therapy. 4th National Center for Image Guided Therapy (NCIGT) and National Institutes of Health (NIH) Image Guided Therapy Workshop, Arlington, Virginia, USA, page 99, October 2011.

- **J. Egger**, X. Chen, T. Kapur, A. Viswanathan. A novel computer program to support MR-guided gynecologic brachytherapy. World Congress of Brachytherapy, Barcelona, Spain, Volume 103, Supplement 2, Page S115, PO-288, May 2012.

- **J. Egger**, T. Kapur, C. Nimsky, R. Kikinis. Pituitary Adenoma Segmentation Using the Medical Image Computing Platform 3D Slicer. 5th National Center for Image Guided Therapy (NCIGT) and National Institutes of Health (NIH) Image Guided Therapy Workshop, Boston, page 38, September 2012.

- **J. Egger**, T. Kapur, A. Fedorov, S. Pieper, J. V. Miller, H. Veeraraghavan, B. Freisleben, A. J. Golby, C. Nimsky, R. Kikinis. Capability of the Medical Image Computing Platform 3D Slicer for Glioblastoma Multiforme Segmentation in Magnetic Resonance Imaging (MRI) Data. 5th National Center for Image Guided Therapy (NCIGT) and National Institutes of Health (NIH) Image Guided Therapy Workshop, Boston, page 39, September 2012.

- **J. Egger**, T. Penzkofer, T. Kapur, C. Tempany. Prostate Central Gland Segmentation Using a Spherical Template Driven Graph Approach. 5th National Center for Image Guided Therapy (NCIGT) and National Institutes of Health (NIH) Image Guided Therapy Workshop, Boston, page 43, September 2012.

- R. Schwarzenberg, T. Kapur, W. Wells, C. Nimsky, B. Freisleben, **J. Egger**. Graph-Based Vertebra Segmentation Using a Cubic Template. 5th National Center for Image Guided Therapy (NCIGT) and National Institutes of Health (NIH) Image Guided Therapy Workshop, Boston, page 44, September 2012.

- **J. Egger**, N. Agrawal, T. Blevins, N. Farhat, G. Pernelle, X. Chen, Y. Gao, W. Wells, T. Penzkofer, T. Kapur, A. Viswanathan. Segmentation of Pelvic Structures for Gynecologic Brachytherapy. 5th National Center for Image Guided Therapy (NCIGT) and National Institutes of Health (NIH) Image Guided Therapy Workshop, Boston, page 45, September 2012.

- Y. Gao, N. Farhat, N. Agrawal, G. Pernelle, X. Chen, **J. Egger**, S. Blevins, S. Bouix, A. Tannenbaum, W. Wells, R. Kikinis, E. Schmidt, A. Viswanathan, T. Kapur. Needle Labeling for Interstitial Gynecological Brachytherapy. 5th National Center for Image Guided Therapy (NCIGT) and National Institutes of Health (NIH) Image Guided Therapy Workshop, Boston, page 48, September 2012.

- **J. Egger**, T. Kapur, P. Bruners, T. Penzkofer. A Software Prototype for Real-time Ablation Zone Planning Using Distance Transformation Calculated Isosurfaces. 5th National Center for Image Guided Therapy (NCIGT) and National Institutes of Health (NIH) Image Guided Therapy Workshop, Boston, page 49, September 2012.

- X. Chen, **J. Egger**, A. Viswanathan, N. Agrawal, W. Wells, R. Kikinis, C. Tempany, F. Jolesz, T. Kapur. Image Processing for MR-guided Gynecologic Interstitial Brachytherapy in AMIGO. 9th Interventional MRI Symposium, Boston, page 69, September 2012.

- **J. Egger**, T. Kapur, B. Freisleben, C. Nimsky. Interactive Real-Time Segmentation for Vertebral Bodies and Intervertebral Discs in Sagittal Planes. 6th National Center for Image Guided Therapy (NCIGT) and National Institutes of Health (NIH) Image Guided Therapy Workshop, page 56, Doubletree by Hilton Washington DC in Crystal City, VA, March 2013.

- G. Pernelle, **J. Egger**, C. Vale, X. Chen, F. Irlinger, T. Lueth, W. Wells, R. Kikinis, A. Viswanathan, T. Kapur. Robust Applicator Registration for In-

terstitial Gynecologic Brachytherapy. Brachytherapy, Volume 12, Supplement 1, Page S53, March 2013.

- T. Lüddemann, **J. Egger**. Rectum Segmentation in MR-guided Gynecologic Brachytherapy Data. Proceedings of The British Gynaecological Cancer Society Annual Scientific Meeting (BGCS) in conjunction with the Irish Gynaecological Cancer Society (IRGCS), The Waterfront, Belfast, Northern Ireland, Abstract topic: Cervix, PO97, pp. 162-163, June 2013.

- **J. Egger**, C. Kappus, B. Carl, C. Nimsky. GrowCut-Based Vertebral Body Segmentation with 3D Slicer. Jahrestagung der Sektion Wirbelsäule der Deutschen Gesellschaft für Neurochirurgie (DGNC), Frankfurt am Main, Germany, Poster 24, September 2013.

Concept Development and Feasibility Study of Image-based Needle Guidance for MR-Guided Interstitial Gynecologic Brachytherapy in AMIGO

Radhika Tibrewal, BS, Akila Viswanathan, MD, MPH, Kanokpis Townamchai, MD, Janice Fairhurst, BS, RT, Maximillian Baust, MS, Jan Egger, PhD, Antonio Damato, PhD, Sang-Eun Song, PhD, Steve Pieper, PhD, Clare Tempany, MD, William M. Wells, PhD, Tina Kapur, PhD
Brigham and Women's Hospital, Dana Farber Cancer Center, Harvard Medical School, Boston, MA, USA

OVERVIEW

Interstitial gynecologic brachytherapy, the placement of radioactive isotopes directly into a cancer of the uterine cervix or vagina in order to eradicate the cancer, requires insertion of hollow catheters with introducers into the tumor. The catheters are guided into place through holes in a template sutured to the patient's perineum as shown on the right [1]. In the newly constructed Advanced Multimodality Image-Guided Operating (AMIGO) suite at Brigham and Women's Hospital and Dana Farber Cancer Institute, intra-procedural Magnetic Resonance (MR) images are acquired to visualize the catheters in relationship to the tumor. The goal of this project is to develop algorithmic, software, and hardware technology to aid catheter placement during MR guided interstitial gynecologic brachytherapy in AMIGO.

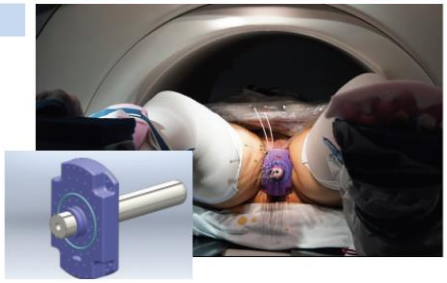

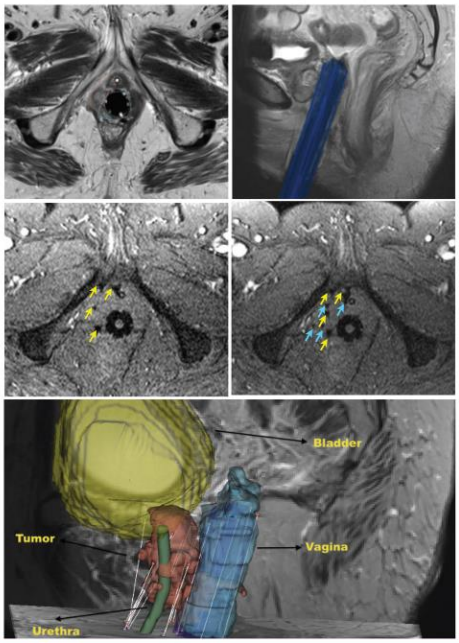

At the start of the procedure, an MRI series consisting of T2 Axial, Sagittal, and Coronal slices is acquired (TR 4000, TE 101, Flip Angle 150, Slice Thickness 4mm) with the obturator in place. The tumor, the organ of interest (OAR), the obturator and the template are segmented as shown on the left using the free and open source software platform 3D Slicer [2].

Alternating T2 and Gradient Echo (GRE) images (plane orthogonal to obturator) are acquired to show the advancing catheter and surrounding anatomy as shown on the left. Each of these MRI images is registered to the initial MRI, the catheters are marked, and rendered in relationship to the previous segmentations.

At the end of the insertion, a T2 weighted MRI series is obtained for confirmation. This series is registered to the initial MRI image and the catheter positioning validated.

This has been tested retrospectively, under IRB approval, on data obtained from the first AMIGO gynecologic brachytherapy procedure.

A CONCEPT FOR MODIFICATIONS TO TEMPLATE AND OBTURATOR

The figure on the right illustrates our concept model for a template and obturator to improve catheter access around the pubic arch area, as well as image based registration. To facilitate image based registration, MRI visible markers are embedded at all corners of the template as well as two on the obturator. These markers fully define catheter insertion position. Additional holes with upwards 30 degree angle have been created, for targeting areas superior ("behind") to the pubic bone.

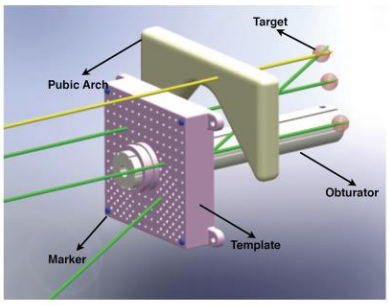

REFERENCES

1. Gynecologic Radiation Therapy: Novel Approaches to Image-Guidance and Management. Akila N. Viswanathan, Christian Kirisits, Beth E. Erickson, and Richard Pötter. Springer. ISBN-13: 978-3540689546
2. 3D Slicer software website http://www.slicer.org

This work was performed with partial support from NIH grants R03EB013792, P41RR019703, and P41RR013218.

National Center for Image Guided Therapy | Brigham and Women's Hospital | Harvard Medical School | Philipps Universität Marburg | Surgical Planning Laboratory

Bladder Segmentation for Interstitial Gynecologic Brachytherapy with the Nugget-Cut Approach

Jan Egger, Ph.D.[1,2,3], Akila Viswanathan, M.D., M.P.H.[1], Tina Kapur, Ph.D.[1]
[1] Brigham and Women's Hospital and Harvard Medical School, Boston, MA, USA
[2] Dept. of Math. and Computer Science, University of Marburg, Marburg, Germany
[3] Dept. of Neurosurgery, University of Marburg, Marburg, Germany
{ egger | tkapur }@bwh.harvard.edu, aviswanathan@lroc.harvard.edu

Purpose

Gynecologic malignancies, which include cervical, endometrial, and vaginal/vulvar cancers, are the 4th leading cause of death in women in the US, with 83,750 new cases in the US in 2010 and 26,930 deaths per year [1]. Treatment consists of concurrent chemotherapy and external beam radiation followed by brachytherapy. The clinical practice of brachytherapy is well characterized using five components: 1) Applicator Choice and Insertion Techniques 2) Imaging Protocol 3) Contouring Protocol 4) Treatment Planning 5) Dose and Fractionation. Details of each institutional experience are provided in the textbook of Viswanathan et al. [2] and its references. With this work we want to support the time consuming Contouring Protocol, more precise the segmentation of the bladder.

Methods

Our overall method starts by setting up a directed 3D graph from a user-defined seed point that is located inside the bladder. To set up the graph, the method samples along rays that are sent through the surface points of a polyhedron with the seed point as the center (Fig. 1).

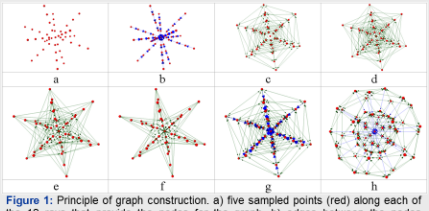

Figure 1: Principle of graph construction. a) five sampled points (red) along each of the 12 rays that provide the nodes for the graph. b) edges between the nodes belonging to the same ray. c) edges between nodes of different rays for Δ_s=0. d) Δ_s=1, e) Δ_s=2 and f) Δ_s=3. g) complete graph for Δ_s=0. h) complete graph with 32 surface points, 3 nodes per ray and Δ_s=0.

The sampled points are the nodes n ∈ V of the graph G(V,E) and e ∈ E is the corresponding set of edges. There are edges between the nodes and edges that connect the nodes to a source s and a sink t. After the graph has been constructed, the minimal cost closed set on the graph is computed via a polynomial time s-t cut [3], creating the segmentation of the object (Fig. 2).

Results

For testing the presented segmentation method we used a C++ implementation within the medical prototyping platform MeVisLab (see http://www.mevislab.de). The overall segmentation – sending rays, graph construction and mincut computation – in our implementation took about one second on an Intel Core i5-750 CPU, 4x2.66 GHz, 8 GB RAM, Windows XP Professional x64 Version, Version 2003, SP 2. The left image of Figure 3 shows the segmentation result of a bladder (red) on a 2D slice with the user-defined seed point (blue) located inside the bladder. The image in the middle visualizes a triangulated model of the segmented bladder (yellow/green) faded into the Computed Tomography (CT) dataset. The image on the right displays the 3D mask of the bladder (red).

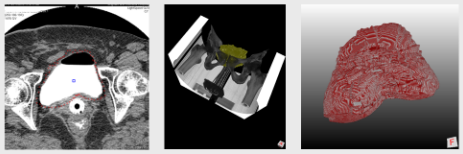

Figure 3: Left: segmentation result of a bladder (red) on a 2D slice with the user-defined seed point (blue) located inside the bladder. Middle: triangulated model of the segmented bladder (yellow/green) faded into the Computed Tomography (CT) dataset. Right: 3D mask of the bladder (red).

Conclusions

In this contribution, we present a segmentation method for the bladder. The method is based on an algorithm we developed recently in a previous work where the novel segmentation scheme was successfully used for segmentation of glioblastoma multiforme (GBM) and provided an average Dice Similarity Coefficient (DSC) of 80% [4]. For bladder segmentation, the original scheme was used, creating a directed 3D-graph within two steps: sending rays through the surface points of a polyhedron and sampling the graph's nodes along every ray. The center of the polyhedron was user-defined and located inside the bladder. Then, the minimal cost closed set on the graph is computed via a polynomial time s-t cut, creating an optimal segmentation of the bladder's boundary and volume.

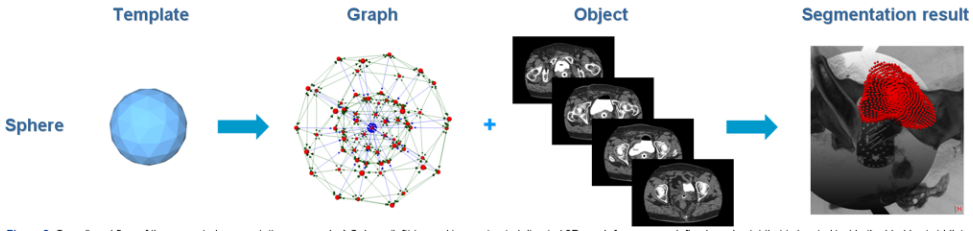

Figure 2: Overall workflow of the presented segmentation approach. A Sphere (left) is used to constructed directed 3D graph from a user-defined seed point that is located inside the bladder (middle). Then, the minimal cost closed set on the graph is computed via a polynomial time s-t cut, creating an optimal segmentation of the bladder's boundary and volume (right).

References

[1] American Cancer Society, Cancer Statistics 2010. http://www.cancer.org/acs/groups/content/@epidemiologysurveillance/documents/document/acspc-026238.pdf , accessed Oct. 4, 2011

[2] A.N. Viswanathan, C. Kirisits, B.E. Erickson, R. Pötter. *Gynecologic Radiation Therapy: Novel Approaches to Image-Guidance and Management*. Springer Press, ISBN-13: 978-3540689546, 2010.

[3] Y. Boykov, V. Kolmogorov. *An Experimental Comparison of Min-Cut/Max-Flow Algorithms for Energy Minimization in Vision*. IEEE Transactions on Pattern Analysis and Machine Intelligence, 26(9), pp. 1124-1137, 2004.

[4] J. Egger, M.H.A. Bauer, D. Kuhnt, B. Carl, C. Kappus, B. Freisleben, Ch. Nimsky. *Nugget-Cut: A Segmentation Scheme for Spherically- and Elliptically-Shaped 3D Objects*. In: 32nd Annual Symposium of the German Association for Pattern Recognition (DAGM), LNCS 6376, pp. 383–392, Springer Press, Darmstadt, Germany, Sep. 2010.

4th NCIGT and NIH Image Guided Therapy Workshop, October 12-13, 2011, Crown Plaza Hotel, Arlington, Virginia.

National Center for Image Guided Therapy | Brigham and Women's Hospital | Harvard Medical School | Philipps Universität Marburg | Surgical Planning Laboratory

A Method for Solving the Correspondence Problem for an n-Camera Navigation System for Image Guided Therapy

Jan Egger, Ph.D.[1,2,3], Bernd Freisleben, Ph.D.[2], Radhika Tibrewal, B.Sc.[1], Christopher Nimsky, M.D., Ph.D.[3], Tina Kapur, Ph.D.[1]

[1] Brigham and Women's Hospital and Harvard Medical School, Boston, MA, USA

[2] Dept. of Math. and Computer Science, University of Marburg, Marburg, Germany

[3] Dept. of Neurosurgery, University of Marburg, Marburg, Germany

{ egger | rtibrewa | tkapur }@bwh.harvard.edu, freisleb@informatik.uni-marburg.de, { egger | nimsky }@med.uni-marburg.de

Purpose

Precise navigation or tracking is a key component of image-guided procedures including biopsy, surgery, and radiation therapy. Users of optical navigation systems (that typically comprise of a pair of stereoscopic cameras) are well aware that having multiple cameras covering the field of view significantly facilitates workflow by minimizing the disruption of line of sight between the cameras and the tracked instruments. An algorithmic challenge in the use of an n-camera system for triangulation is the correspondence problem between the $n \cdot (n-1)/2$ resulting different binocular camera systems, and we describe a method for solving it.

Methods

We setup a tetra-optical camera system [1] and used five fiducial markers to localize an object (Fig. 1) or a patient in 3-space. If all fiducial markers are visible to all cameras, and correspondences between them are not known, up to 25 solutions are possible for a camera pair, and 125 for 6 camera pairs (or 4 cameras). Narrowing these to a single solution or knowledge of correspondences between the points leads to a unique solution and is the focus of this work.

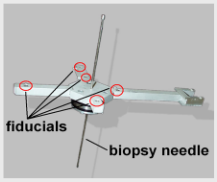

Figure 1.

In a pin-hole camera geometry all image points on one epipolar line correspond to points on a single epipolar line in the second image [2]. If a point in 3-space is visible in *m* images, then the intersection of the *m* resulting epipolar lines is used to reconstruct its 3D coordinates. Because of measurement errors, the lines often do not intersect in a point, and in our algorithm, we develop an efficient method for determining the approximate intersection points of these line clusters. In the case when $m=2$, we compute center point of the minimal distance between the lines. When $m > 3$, we compute the pairwise center points, and average the point cloud of centers thus obtained. The resulting points are matched with the (known) tracker or patient model via translation and rotation [3]. Therefore, we calculate the gravity center of a point cloud (Figure 2). The next images demonstrate step-by-step how a camera-detected model is matched with the tracker model. First the gravity center points for the patient (or instrument) model (Figure 3) and the detected model (Figure 4) are calculated and moved to the origin.

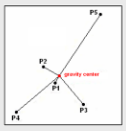

Figure 2.

Figure 3.

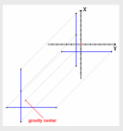

Figure 4.

Next, the point of the patient model with the largest distance to the gravity center is calculated (P_1^{ct}, Fig. 5). Equivalent, the point of the patient model with the largest distance to the gravity center is calculated (P_1^{vk}, Fig. 5). If such a point does not exists for the detected model (within tolerance), we can already skip this model and test the next point cloud. Otherwise the rotation axis and angle (Fig. 6) are determined to rotate P_1^{vk} on P_1^{ct} via the center of gravity (Fig. 7).

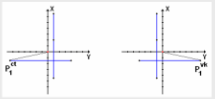

Figure 5.

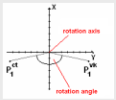

Figure 6.

Figure 7.

Then, a second point is calculated for the patient model (P_2^{ct}, Fig. 8) and the detected model (P_2^{vk}, Fig. 8) and the rotation axis (Fig. 9) and angle (Fig. 10 and 11) are determined to rotate P_2^{vk} on P_2^{ct} (Fig. 12).

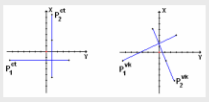

Figure 8.

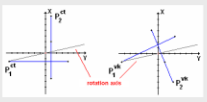

Figure 9.

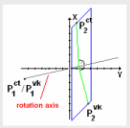

Figure 10.

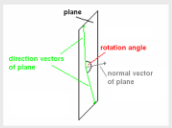

Figure 11.

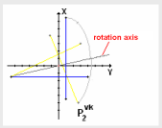

Figure 12.

After the second rotation, both models overlap on three points: the gravity center, P_1 and P_2. In 3-space the remaining three model points should also overlap if the detected model fits to the patient model. Otherwise this detected model can be skiped and the next point cloud is analyzed via translation and rotation.

Results

For evaluation we performed navigation in several scenarios using a tetra-optical camera system. We used standard CCD video cameras (Teli CS8320BC) and LEDs with wavelength of 890±45 nm. The correspondence algorithm was able to recover 3-space coordinates in all experiments, and repeated position measurements of the same position and orientation of the models could be reproduced within 0.5 mm. To accomplish the repeatability evaluation, we fixed the models to a robot (Mitsubishi RV-E2) with a positioning accuracy of ca. 0.4 mm [4]. Figure 13 shows an example for a two camera system where a patient could not be detected, because the patients body covered a fiducial F. Figure 14 presents an example for a four camera system where all fiducials are seen at leats with two of the four cameras. Therefore, the detection of the patient is possible when the correspondence problem is solved with our algorithm. We also measured the absolute deviation for our four camera system. Therefore, we fixed a LED to the Mitsubishi robot and drove the LED to the corners of a cube. Then, we detected the LED in every corner with every camera pair and plotted the resulting cubes into one diagram (Figure 15).

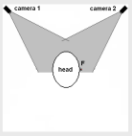

Figure 13.

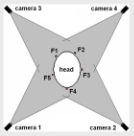

Figure 14.

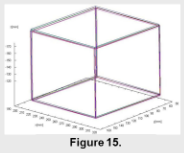

Figure 15.

Conclusions

We have introduced an algorithm for solving the correspondence problem for a multi-camera navigation system that can be used to track patient or instrument position in an operating or interventional suite. Compared to using a single stereo pair, a multi-camera navigation system allows a significantly larger field of view and is more robust to occlusions caused by breach of line of sight. Such a system is being planned for the ***A**dvanced **M**ultimodality **I**mage **G**uided **O**perating (AMIGO)* Suite of the ***N**ational **C**enter for **I**mage **G**uided **T**herapy (NCIGT)* funded in part by the NIH Grant P41RR019703 [5].

References

[1] D. Richter, F. La Torre, J. Egger, G. Straßmann. *Tetraoptical Camera System for Medical Navigation.* Proceedings of the 17th International EURASIP Conference BIOSIGNAL, Brno, Czech Republic, pp. 270-272, Vutium Press, June 2004.

[2] B.K.P. Horn. *Robot Vision.* The MIT Press McGraw-Hill Book Company, 1986.

[3] J. Egger. *Fractioned 3D Recognition of Landmarks with a Tetraoptical Camera System* (in German). Diploma thesis in Computer Science, University of Wiesbaden, Germany, 103 pp., 04.

[4] D. Richter, J. Egger, G. Straßmann. *An Algorithm to Determine the Position of Patients and Biopsy-Needles with a Tetraoptical Camera System* (in German). Proceedings of Bildverarbeitung für die Medizin (BVM), Hamburg, Germany, pp. 316-320, Springer Press, 2006.

[5] National Center for Image Guided Therapy (NCIGT), *Advanced Multimodality Image Guided Operating (AMIGO) Suite* funded by NIH Grant P41RR019703 (http://www.ncigt.org/pages/AMIGO)

4th NCIGT and NIH Image Guided Therapy Workshop, October 12-13, 2011, Crown Plaza Hotel, Arlington, Virginia.

A Novel Computer Program to Support MR-guided Gynecologic Brachytherapy

Jan Egger, Ph.D.[1], Xiaojun Chen, Ph.D.[1], Tina Kapur, Ph.D.[1], Akila Viswanathan, M.D., M.P.H.[2]

[1] *Department of Radiology, Brigham and Women's Hospital and Harvard Medical School, Boston, MA, USA*

[2] *Department of Radiation Oncology, Brigham and Women's Hospital and Harvard Medical School, Boston, MA, USA*

{ egger | xiaojun | tkapur }@bwh.harvard.edu, aviswanathan@lroc.harvard.edu

Purpose

To describe a novel computer program designed and implemented to provide an overall system for supporting MR-guided gynecologic brachytherapy

Material/Methods

From September 2011 to January 2012, 10 gynecologic-cancer patients requiring brachytherapy underwent image-guided applicator insertion in a multimodal operating suite with integrated MR scanner, ultrasound and PET/CT scanner. In order to increase the physician's speed and monitor the consequences of inserting interstitial catheters in real time, a novel computer program was designed and implemented and is described here.

Results

The overall system starts with pre-implant imaging and the integrated software permits measurement of relevant sizes for intervention leading to automatic inventory control and specific applicator request. Next, a device is selected (e.g., tandem and ring/ovoid +/- interstitial needles or interstitial needles alone) that is modeled in the preoperative images. Virtual modeling and visualization of several instruments for direct device comparison is enabled to identify the optimal one. In the intraoperative stage, the patient is imaged using 3 Tesla MRI with legs in the insertion position. The computer-visualized template allows guidance to an optimal position for dose delivery. Serial imaging examinations are superimposed on the visualization of the modeled device. With this interactive novel software program, the physician can select which interstitial needles may best benefit the patient, and at what depth they should be inserted, as determined by the MRI image viewed during the insertion process. The physician then inserts the correct interstitial needle into the necessary applicator hole based on the tumor location as visualized on intra-operative 3T MRI.

Conclusion

Novel software was developed that aids in the integration of preoperative assessment, intraoperative 3T imaging and applicator insertion. Novel features include 1) linking a diagnostic imaging set in real-time to a 3D CAD model of a medical device; 2) precise identification of catheter location in the 3D imaging model with real-time imaging feedback and 3) the ability to perform patient specific pre-implant evaluation by assessing in the computer the placement of interstitial needles prior to an intervention via virtual template matching with a diagnostic scan.

Figure 1 – 3D CAD models: Template (I), Obturator (II), Tandem&Ring and Template Cut-Out (IV)

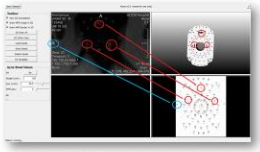

Figure 2a – Principle for fitting a gynecological template for brachytherapy with an initial CT image. The three red circles indicate corresponding needle holes in the template and the patient image. The fitting is realized via a rigid transformation between these corresponding point sets. The blue circles are used to ensure that the left and right sides of the patient and the template are matched correctly.

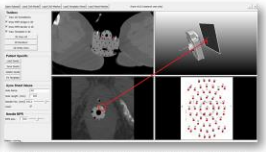

Figure 2b – Needle (white line in the upper right window) that has been selected for visualization of multiplanar reconstructions (MPR) along the needle path (lower left window). The MPR at the position of the arrow (tip of red arrow in the upper right image) is displayed in the lower left window as a 2D slice. In the MPR of the lower left window the needle cross section (white) is surrounded by a red circle.

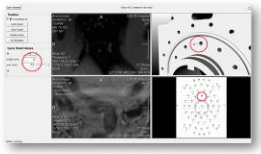

Figure 2c – Virtual fitted gynecological brachytherapy template and selection of a specific interstitial needle (Ba, red circles in the screenshot). As shown on the left side of the prototype interface, individual needle insertion can be planned by defining parameters such as the needle length and depth.

Figure 2d – Virtual placement of several interstitial needles (purple) with different lengths and depths as shown in the settings in the menu in the left column. This allows the radiation oncologist to plan the placement of needles.

Figure 3 – The Advanced Multimodality Image Guided Operating (AMIGO) Suite was launched in 2011 as a multimodal successor to the original 0.5T Signa SP (GE Healthcare) magnetic resonance therapy (MRT) unit at Brigham and Women's Hospital, in which interstitial gynecologic brachytherapy was performed from 2002 to 2006. AMIGO is an integrated operating suite in which multidisciplinary patient treatment may be guided by x-ray, ultrasound, intra-operative 3T MRI, and/or positron emission tomography/computed tomography (PET/CT).

Acknowledgments

The authors would like to acknowledge the support of the AMIGO clinical staff in enabling this clinical study, Sam Song, PhD for generating the CAD models of gynecologic devices and Junichi Tokuda, PhD for the AMIGO photo. We thank Prof. Dr. Horst K. Hahn and Fraunhofer MeVis in Bremen, Germany, for their support by providing an academic license for MeVislab software. The work was supported by NIH grant P41EB015898, P41RR019703, R03EB013792, and U54EB005149. Dr. Viswanathan receives support from NIH grant K07CA117979.

References

- American Cancer Society, Cancer Statistics 2010: http://www.cancer.org/acs/groups/content/@epidemiologysurveillance/documents/document/acspc-026238.pdf (accessed March 12, 2012)
- Viswanathan AN, Kirisits C, Erickson BE, Pötter R. *Gynecologic Radiation Therapy: Novel Approaches to Image-Guidance and Management*. Springer Press, ISBN-13: 978-3540689546, 2010.
- Kapur T, Egger J, Damato A, Schmidt EJ, Viswanathan AN. QIN: 3T MR-guided brachytherapy for gynecologic malignancies. Magnetic Resonance Imaging, Elsevier, *in Press*, 2012.
- Kapur T, Tempany CM, Jolesz FA. 4th NCIGT and NIH Image Guided Therapy Workshop, (4):1-121, Crown Plaza Hotel, Arlington, Virginia, October 12-13, 2011.

European Society for Radiotherapy and Oncology (ESTRO), World Congress of Brachytherapy (WCB), May 10-12, 2012, Barcelona, Spain.

Pituitary Adenoma Segmentation Using the Medical Image Computing Platform 3D Slicer

Jan Egger, Ph.D., Ph.D.[a,b,c], Tina Kapur, Ph.D.[a], Christopher Nimsky, M.D., Ph.D.[c], and Ron Kikinis, M.D.[a]
[a] Dept. of Radiology, Surgical Planning Lab, Brigham and Women's Hospital Boston, MA, USA
[b] Dept. of Mathematics and Computer Science, University of Marburg, Marburg, Germany
[c] Dept. of Neurosurgery, University of Marburg, Marburg, Germany

Purpose

Tumors of the sellar region, mainly pituitary adenomas, represent 10% to 25% of all intracranial neoplasms, with adenomas comprising the largest portion with an estimated prevalence of approximately 17% [1, 2]. These adenomas can be classified according to many criteria including size, histological characteristics, and hormone secretion (hormone active and hormone-inactive). Microadenomas are less than 1 cm in diameter, whereas macroadenomas measure more than 1 cm. Typically for macroadenomas with mass-effect, transsphenoidal surgery is the treatment of choice [3]. By contrast, hormone-inactive microadenomas are closely monitored using endocrine and ophthalmological evaluations as well as magnetic resonance imaging (MRI). Microsurgical excision is performed if the tumor volume increases over time. Image analysis that includes segmentation and registration of these successive scans is beneficial in the accurate measurement of tumor progression.

Methods

We performed segmentation of pituitary adenomas on T1- and T2-weighted images acquired on a MAGNETOM Sonata 1.5 T MRI scanner (Siemens Medical Solutions, Erlangen, Germany) equipped with a standard head coil. The segmentation method we used is the GrowCut implementation [4] in 3D Slicer (or Slicer) which is freely downloadable from the website http://www.slicer.org. GrowCut [5] is an interactive segmentation algorithm based on the idea of cellular automata. The algorithm achieves reliable and fast segmentation of moderately difficult objects in 2D and 3D using an iterative labeling procedure resembling competitive region growing. After trial of the various segmentation facilities available in Slicer, we determined that the use of GrowCut by initializing it on sagittal, axial, and coronal cross-sections provides the most efficient segmentations. In this initialization step, parts of the tumor and parts of the background are marked on the image with the Slicer brush tool. Figure 1 shows a typical initialization of a pituitary adenoma (blue) and the background (brown) on an axial slice.

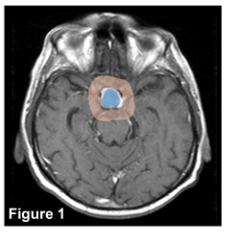
Figure 1

Results

The goal of this study was to evaluate the utility of Slicer for segmentation of pituitary adenomas. To evaluate the utility of Slicer, ground truth was provided by manual slice-by-slice segmentation of five pituitary adenomas by neurological surgeons with several years of experience in resection of pituitary adenomas. These manual segmentations were compared with the Slicer segmentation results of the proposed method via the Dice Similarity Coefficient (DSC) [6]. Briefly, the DSC measures the relative volume overlap between M and S, where M and S are the binary masks from the manual slice-by-slice (M) and the Slicer (S) segmentation. The average DSC for all data sets was 81.71%±4.78% and shows that the two are comparable. Figure 2 present segmentation results on a sagittal (upper row) and an axial (lower row) slice for the manual segmentation (middle images, yellow) and the Slicer segmentation (right images, magenta).

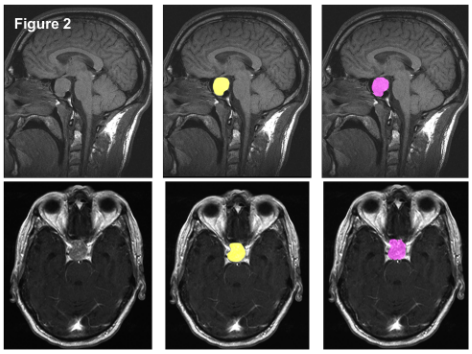
Figure 2

Conclusion

In this contribution, we present segmentation results for pituitary adenoma in MRI data using the medical platform 3D Slicer and showed that it is valuable to support the time-consuming process of volumetric assessment. The time and user effort required for GrowCut segmentation was on an average 50% compared to pure manual segmentation. There are several areas of future work including comparison with graph-based based segmentation methods such as [7, 8].

References

1. http://www.cancer.gov/cancertopics/pdq/treatment/pituitary/HealthProfessional/page1/AllPages#1 (last accessed: July 2012)
2. M.-A. Weber, et al., Sellar tumors (in German), Der Radiologe; 47(6):492-500. Springer Berlin / Heidelberg, 2007.
3. M. Buchfelder and S. Schlaffer, Surgical treatment of pituitary tumours, Best Pract Res Clin Endocrinol Metabol; 23(5):677-92, 2009.
4. GrowCut-Module under 3DSlicer http://www.slicer.org/slicerWiki/index.php/Modules:GrowCutSegmentation-Documentation-3.6
5. V. Vezhnevets and V. Konouchine, GrowCut - Interactive multi-label N-D image segmentation, in Proc. Graphicon, pp. 150-156, 2005.
6. K. H. Zou, et al., Statistical Validation of Image Segmentation Quality Based on a Spatial Overlap Index: Scientific Reports, Academic Radiology, 11(2):178-189, 04.
7. J. Egger, et al., Pituitary Adenoma Segmentation, Proc. of International Biosignal Processing Conference, Berlin, Germany, 1-4, 2010.
8. J. Egger, B. Freisleben, C. Nimsky, T. Kapur, Template-Cut: A Pattern-Based Segmentation Paradigm, Nature - Scientific Reports, Nature Publishing Group (NPG), 2(420), 2012.

Acknowledgements

We acknowledge the members of the Slicer Community and in particular Steve Pieper for their contributions, and moreover Harini Veeraraghavan and Jim Miller from GE for developing the GrowCut module in Slicer. Furthermore, the authors would like to thank the physicians Dr. med. Daniela Kuhnt, Dr. med. Barbara Carl, Christoph Kappus and Rivka Colen, M.D. for participating in this study. This work was supported by National Institutes of Health (NIH) grant P41EB015898.

5th NCIGT and NIH Image Guided Therapy Workshop • September 21, 2012 • Joseph B. Martin Conference Center, Harvard Medical School, Boston, Massachusetts

Capability of the Medical Image Computing Platform 3D Slicer for Glioblastoma Multiforme Segmentation in Magnetic Resonance Imaging (MRI) Data

Jan Egger, Ph.D., Ph.D.[a,b,c], Tina Kapur, Ph.D.[a], Andriy Fedorov, Ph.D.[a], Steve Pieper Ph.D.[a,d], James V. Miller, Ph.D.[e], Harini Veeraraghavan, Ph.D.[f], Bernd Freisleben, Ph.D.[c], Alexandra J. Golby, M.D.[a,g], Christopher Nimsky, M.D., Ph.D.[b] and Ron Kikinis, M.D.[a]

[a] Dept. of Radiology, Surgical Planning Lab, Brigham and Women's Hospital Boston, MA, USA, [b] Dept. of Neurosurgery, University of Marburg, Marburg, Germany, [c] Dept. of Mathematics and Computer Science, University of Marburg, Marburg, Germany, [d] Isomics, Inc., Cambridge, MA, USA, [e] Interventional and Therapy Lab, GE Research, Niskayuna, NY, USA, [f] Biomedical Image Analysis Lab, GE Research, Niskayuna, NY, USA, [g] Dept. of Neurosurgery, Brigham and Women's Hospital, Harvard Medical School, Boston, MA, USA

Purpose

Gliomas are the most common primary brain tumors, evolving from the cerebral supportive cells. The World Health Organization (WHO) grading system for gliomas defines grades I-IV, where grade I tumors are the least aggressive and IV are the most aggressive [1]. 70% belong to the group of malignant gliomas (anaplastic astrocytoma grade III, glioblastoma multiforme grade IV). The glioblastoma multiforme, named for its histopathological appearance, is the most frequent malignant primary tumor and is one of the most highly malignant human neoplasms. Volumetric change in grade IV tumors (glioblastoma multiforme (GBM)) over time is a critical factor in treatment decisions by physicians. Typically, the tumor volume is computed on a slice-by-slice basis using MRI patient scans obtained at regular intervals. In this contribution we investigated the capability of the medical image computing platform 3D Slicer for the segmentation of GBMs.

Methods

For this study, we used the GrowCut [2] software module in 3D Slicer [3], which is freely downloadable from the website http://www.slicer.org. The lower figure shows the 3D Slicer interface with the Editor on the left side and a loaded GBM data set on the right side: axial slice (upper left window), sagittal slice (lower left window), coronal slice (lower right window) and the three slices shown in a 3D visualization (upper right window). A typical user initialization of GrowCut under Slicer for the segmentation of a GBM is presented in Figure 2: axial (left image), sagittal (middle image) and coronal (right image). Note: the tumor has been initialized in green and the background has been initialized in yellow.

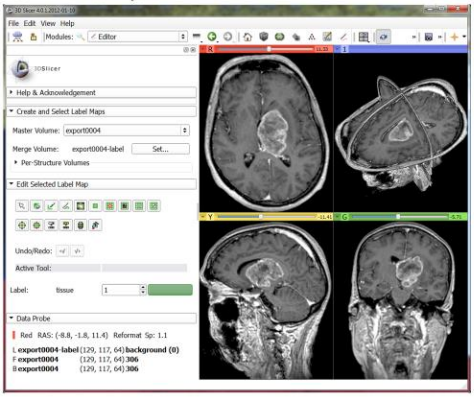

Figure 2

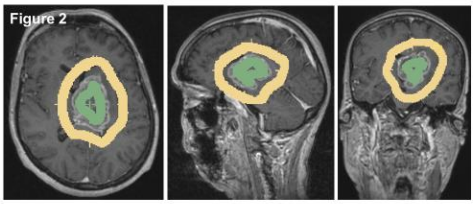

Results

In this study, four physicians segmented GBMs in ten patients, once using the competitive region-growing based GrowCut segmentation module of 3D Slicer, and once purely by drawing boundaries completely manually on a slice-by-slice basis. The time and user effort required for GrowCut segmentation was on an average 25% compared to pure manual segmentation. A comparison of Slicer based segmentation with manual slice-by-slice segmentation resulting in a Dice Similarity Coefficient [4] of 88.43±5.23% and a Hausdorff Distance of 2.32±5.23mm shows that the two are comparable. Figure 3 shows a comparison of GBM segmentation results on an axial slice: semi-automatic segmentation under Slicer (green, left image) and pure manual segmentation (blue, middle image). The right image presents a 3D segmentation result of GrowCut (green). After the initialization of the GrowCut algorithm under Slicer it took about ten seconds to get the segmentation result on an Intel Core i7-990 CPU, 12x3.47 GHz, 12 GB RAM, Windows 7 Home Premium x64 Version, Service Pack 1.

Figure 3

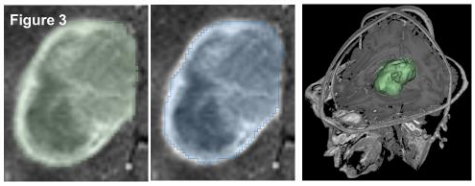

Conclusion

In this study we evaluated the capability of 3D Slicer for segmentation of GBMs compared to manual slice-by-slice segmentation. As a metric for our evaluation we used the agreement between slice-by-slice and Slicer segmentations to show that Slicer can be used to produce GBM segmentations that are statistically equivalent to what the physicians achieve manually in fraction of the time (0.25). Areas of future work include a direct comparison of the Slicer-based segmentation with a graph-based algorithm [5], and extension to multi-modal images.

References

1. P. Kleihues, et al., The WHO classification of tumors of the nervous system, Journal of Neuropathology & Experimental Neurology; 61(3):215-229, 2002.
2. V. Vezhnevets and V. Konouchine, GrowCut - Interactive multi-label N-D image segmentation, in Proc. Graphicon, pp. 150-156, 2005.
3. GrowCut-Module under 3DSlicer http://www.slicer.org/slicerWiki/index.php/Modules:GrowCutSegmentation-Documentation-3.6
4. K. H. Zou, et al., Statistical Validation of Image Segmentation Quality Based on a Spatial Overlap Index: Scientific Reports, Academic Radiology, 11(2):178-189, 04.
5. J. Egger, et al., Template-Cut: A Pattern-Based Segmentation Paradigm, Nature - Scientific Reports, Nature Publishing Group (NPG), 2(420), 2012.

Acknowledgements

The authors want to thank the members of the Slicer Community for their contributions and furthermore the physicians Dr. med. Daniela Kuhnt, Dr. med. Barbara Carl, Christoph Kappus and Rivka Colen, M.D. for participating in this study. This work was supported by National Institutes of Health (NIH) grant P41EB015898.

5th NCIGT and NIH Image Guided Therapy Workshop • September 21, 2012 • Joseph B. Martin Conference Center, Harvard Medical School, Boston, Massachusetts

Prostate Central Gland Segmentation Using a Spherical Template Driven Graph Approach

Jan Egger, Ph.D., Ph.D.[1,2,3], Tobias Penzkofer, M.D.[1,4], Tina Kapur, Ph.D.[1], Clare Tempany, M.D.[1]

[1] Dept. of Radiology, Surgical Planning Lab, Brigham and Women's Hospital Boston, MA, USA
[2] Dept. of Mathematics and Computer Science, University of Marburg, Marburg, Germany
[3] Dept. of Neurosurgery, University of Marburg, Marburg, Germany
[4] Dept. of Diagnostic and Interventional Radiology, RWTH Aachen University Hospital, Germany

Purpose

Prostate cancer is the most abundant cancer in men, with over 240,000 expected new cases and around 28,000 deaths in 2012 in the US alone [1]. Accurate risk stratification for each individual cancer is central to a successful treatment strategy, especially because of the high incidence rate of less aggressive prostate cancers, and the high complication rate of radical prostatectomy. Diagnostic prostate magnetic resonance imaging (MRI) and MRI guided prostate biopsies have demonstrated improved diagnostic discrimination rates of the different types of cancer [2]. Our goal is to enhance the state of the art in automated segmentation (i.e. delineation) of organ limits for the prostate, a step that has been shown to facilitate efficient MR-guided biopsy.

Methods

The Nugget-Cut scheme [3] was used for prostate center gland segmentation on 5 datasets [4]. It sets up a directed 3D-graph G(V,E) in two steps: (I) sending rays through the surface points of a polyhedron and (II) sampling the graph's nodes nϵV along every ray (Figure 1). Additionally, a corresponding set of edges eϵE is generated, which consists of edges between the nodes and edges that connect the nodes to a source s and a sink t. After graph construction – the center of the polyhedron was defined by the user and located inside the prostate center gland – the minimal cost closed set on the graph is computed via a polynomial time s-t-cut [5], which results in the segmentation of the prostate center gland's boundaries and volume. A C++ module was implemented within the medical prototyping platform MeVisLab (see http://www.mevislab.de) for evaluation. Results were compared to an expert segmentation using the Dice Similarity Coefficient (DSC).

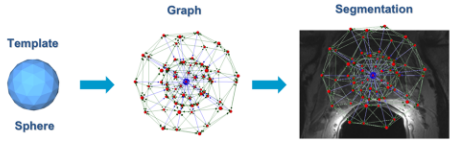

Fig 1. Nugget-Cut Scheme: A template is used as a basic structure for the segmentation graph

Results

A DSC of 85±6.0% overlap was achieved compared to expert segmentation. This is an improvement on recent 80% DSC reported in the literature [6]. In our C++ implementation the overall segmentation: (1) sending rays, (2) graph construction and (3) mincut computation, took about one second on an Intel Core i7 CPU, 4x2.50 GHz, 8 GB RAM. Figure 2 shows the segmentation result of a prostate central gland (red) on an axial and a sagittal 2D slice with the typical user-defined seed point position on the axial slice (blue arrow) located inside the organ.

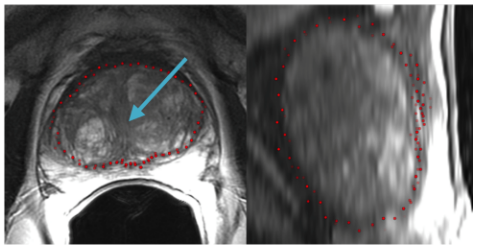

Fig 2. Segmentation results in axial and sagittal reformatting (blue arrow: seed point)

Conclusion

In this abstract, we present segmentation results for the prostate gland in MRI data using a recently developed method. A graph driven method has been used that is based on a spherical template. The algorithm prefers spherically- and elliptically-shaped 3D objects and has already been evaluated with glioblastoma multiforme, pituitary adenoma and cerebral aneurysm data [7]. There are several areas of future work including comparison with level-set based prostate segmentation methods such as [8], extensions for automatic segmentation of structures adjacent to the central prostate gland, such as the peripheral prostatic zone. An immediate next application for MR-guided biopsy is the generation of regions of interest towards automatic registration of preoperative to intraprocedural images.

References

1. National Institutes of Health Cancer Topics: Prostate, http://www.cancer.gov/cancertopics/types/prostate
2. D'Amico AV, Cormack RA & Tempany CM. MRI-Guided Diagnosis and Treatment of Prostate Cancer. N Engl J Med. 344:776-777, 2001.
3. Egger J, et al. Nugget-Cut: A Segmentation Scheme for Spherically- and Elliptically-Shaped 3D Objects. In: 32nd Annual Symposium of the German Association for Pattern Recognition (DAGM), LNCS 6376, pp. 383-392, Springer, 2010.
4. Fedorov A, et al. Image Registration for Targeted MRI-guided Prostate Transperineal Prostate Biopsy. J Magn Res Imag, 2012.
5. Boykov Y & Kolmogorov V. An Experimental Comparison of Min-Cut/Max-Flow Algorithms for Energy Minimization in Vision. IEEE Transactions on Pattern Analysis and Machine Intelligence, 26(9), pp. 1124-1137, 2004.
6. Yin Y, et al. Fully automated 3D prostate central gland segmentation in MR images: a LOGISMOS based approach. Proc. SPIE 8314, 83143B, 2012.
7. Egger J, et al. Template-Cut: A Pattern-Based Segmentation Paradigm. Nature - Scientific Reports, Nature Publishing Group, 2(420), 2012.
8. Tsai A, et al. A shape-based approach to the segmentation of medical imagery using level sets. IEEE TMI, 22(2), pp.137-154, 2003.

Acknowledgements

We acknowledge the help of Drs. Fedorov, Tuncali, Fennessy and Tempany for sharing the provided data collection. This work is supported by NIH 8P41EB015898-08 and 5P01CA067165-13. Its contents are solely the responsibility of the authors and do not necessarily represent the official views of the NIH.

National Center for Image Guided Therapy | BRIGHAM AND WOMEN'S HOSPITAL | HARVARD MEDICAL SCHOOL | Philipps Universität Marburg | Surgical Planning Laboratory

Graph-Based Vertebra Segmentation Using a Cubic Template

Robert Schwarzenberg[a,b], Tina Kapur, Ph.D.[a], William Wells, Ph.D.[a], Christopher Nimsky, M.D., Ph.D.[c], Bernd Freisleben, Ph.D.[b], Jan Egger, Ph.D., Ph.D.[a,b,c]

[a] Dept. of Radiology, Brigham and Women's Hospital, Harvard Medical School, Boston, MA, USA,
[b] Dept. of Mathematics and Computer Science, University of Marburg, Marburg, Germany,
[c] Dept. of Neurosurgery, University of Marburg, Marburg, Germany

{ rs | tkapur | sw | egger }@bwh.harvard.edu, { egger | nimsky }@med.uni-marburg.de, freisleb@informatik.uni-marburg.de

Purpose

The current development of the population's structure leads to a growing part of older patients with a more frequent insistence for surgical treatment like lumbar spinal stenosis (LS), which is the most common cause of spinal surgery in individuals older than 65 years of age [1]. For the assessment of spinal structures such as nerve roots, intervertebral discs and ligamentary constitution, Magnetic Resonance Imaging (MRI) is in general suitable. However, certain changes of the vertebra due to osteoporosis, fractures or osteophytes, require an evaluation of the bone structures via Computed Tomography (CT)-scans, which include radiation exposure [2]. In this contribution, we want to illustrate the capability of MRI-segmentation to reconstruct the vertebral body without x-ray examination, leading to less pre-operative examinations and therefore affecting radiation exposure costs and time-management.

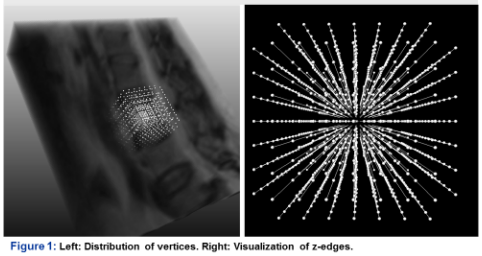

Figure 1: Left: Distribution of vertices. Right: Visualization of z-edges.

Methods

The presented approach is an extension of our previously introduced strategy [3, 4] to a third dimension. It starts by setting up a directed, weighted, two-terminal 3D-graph G = (V,E) (an s-t-network). After its construction, the minimal closed set on the graph is calculated via a polynomial time s-t-cut [5], creating a 3D segmentation of the vertebral body. The vertices $v \in V \setminus \{s,t\}$ are distributed along several rays that extend from a user-defined seed point inside the vertebra and intersect with the vertebral body's outer boundaries. All rays are made up of the same number of vertices and each layer forms a cube shape (see figure 1). There are two types of edges $e \in E$. *n-links* connect all vertices to a virtual source s and a virtual sink t and the n-links' capacities reflect a node's affiliation with either the source (vertebra) or the sink (background). A set of infinity-weighted *l-links* connects the vertices on the rays with each other. The l-links are further subdivided into *z-edges* (see figure 1) and *xy-edges* (see figure 2). The z-edges ensure that each ray is cut exactly one time, while the xy-edges allow the user to impose a smoothness constraint Δ on the segmentation result [6]. A Δ-value of zero results in a regular, cubic shape, whereas a Δ-value greater zero allows a corresponding deviation (see figure 3).

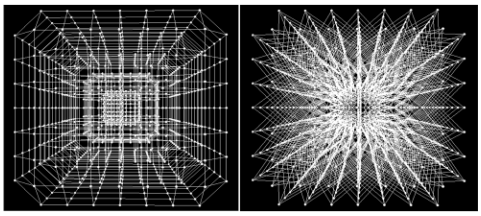

Figure 2: Topology of xy-edges. Left: Smoothness constraint $\Delta = 0$. Right: $\Delta = 1$.

Results

For testing the presented segmentation method we used a C++ implementation within the medical prototyping platform MeVisLab (see http://www.mevislab.de). The overall segmentation – sending rays, graph construction and mincut computation – in our implementation took about twenty seconds on an Intel 2.1 GHz CPU, 4 GB RAM, Windows 7 Home Premium x64 Version, SP 1. We carried out an initial evaluation, segmenting 5 vertebrae: The average DSC was 83%.

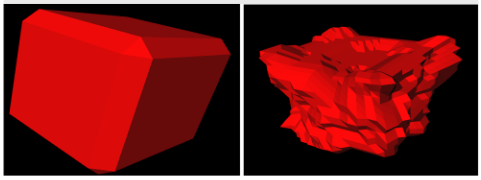

Figure 3: Left: Segmentation result for $\Delta = 0$. Right: Segmentation result for $\Delta = 2$.

Conclusions

In this contribution, we presented the initial results for a novel vertebra 3D segmentation method. The method enhances our recently developed algorithm to a third dimension. Whereas the previously introduced algorithm allowed the calculation of a vertebral area (2D), the method presented here determines the volume of a vertebra (3D) (see figure 4). It constructs an s-t-network within a cubic-shaped template and allows the user to impose a smoothness constraint on the segmentation result which determines the result's deviation from a regular cube shape. The segmentation result is computed by a polynomial s-t-cut, creating an optimal segmentation of the vertebra's outer boundaries. A first evaluation led to an average DSC of 83 %.

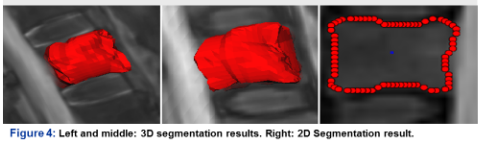

Figure 4: Left and middle: 3D segmentation results. Right: 2D Segmentation result.

References

[1] A.F. Joaquim, et al. Degenerative lumbar stenosis: update. Arq Neuropsiquiatr 67(2B): 553-8, 2009.
[2] P.J. Richards, et al. Spine computed tomography doses and cancer induction. Spine (Phila Pa 1976) 35(4): 430-3, 2010.
[3] J. Egger, T. Kapur, T. Dukatz, M. Kolodziej, D. Zukic, B. Freisleben, and C. Nimsky. Square-Cut: A Segmentation Algorithm on the Basis of a Rectangle Shape. In: PLoS ONE, 2012.
[4] J. Egger, B. Freisleben, C. Nimsky, and T. Kapur. Template-Cut: A Pattern-Based Segmentation Paradigm. In: Nature - Scientific Reports, Nature Publishing Group (NPG), 2(420), 2012.
[5] Y. Boykov and V. Kolmogorov. An Experimental Comparison of Min-Cut/Max-Flow Algorithms for Energy Minimization in Vision. IEEE Transactions on Pattern Analysis and Machine Intelligence, 26(9), pp. 1124-1137, 2004.
[6] K. Li, X. Wu, D.Z. Chen, and M. Sonka. Optimal Surface Segmentation in Volumetric Images – A Graph-Theoretic Approach. IEEE Transactions on Pattern Analysis and Machine Intelligence (PAMI) 28(1): 119-134, 2006.

5th NCIGT and NIH Image Guided Therapy Workshop, September 21, 2012, Joseph B. Martin Conference Center, Boston, MA.

Segmentation of Pelvic Structures for Gynecologic Brachytherapy

Jan Egger, Ph.D., Ph.D.[a], Neha Agrawal, M.D.[a], Tyler Blevins [a,b], Nabgha Farhat [a,c], Guillaume Pernelle [a], Xiaojun Chen, Ph.D.[a], Yi Gao, Ph.D.[a], William Wells [a], Tobias Penzkofer, M.D.[a], Tina Kapur, Ph.D.[a**] and Akila Viswanathan, M.D., M.P.H.[a**]
[a] Brigham and Women's Hospital, [b] University of Massachusetts, Amherst, [c] Rutgers University, **Joint Senior Authorship

Purpose

Gynecological cancers, which consist of cervical, endometrial, and vaginal/vulvar cancers, remain the 4th largest cause of death in women in the US since 2010, with reports of 88,750 (5.6% increase) new cases and 29,520 deaths per year in 2012 (6.5% increase) [1]. The standard treatment protocol for these malignancies consists of concurrent chemotherapy and external beam radiation directly followed by brachytherapy. Contouring the cancerous tissue, as well as adjacent organs at risk (OAR), is a routine clinical step. In this contribution, we report on the results of semi-automatic contouring of tumor, the bladder, and the rectosigmoid using the free and open source software package *3D Slicer* (http://www.slicer.org).

Methods

In this study we used six T2-weighted magnetic resonance imaging (MRI) datasets from a Siemens 3T scanner. A physician carefully manually segmented the tumor, the bladder, and the rectosigmoid in each dataset for reference. We used the *GrowCut* [2] algorithm in *3D Slicer* [3] which is an interactive segmentation algorithm based on the idea of cellular automata to segment each of the structures. In each case, the initialization of *GrowCut* was performed on sagittal, axial, and coronal cross-sections (Figure 1). The algorithm then automatically computed the contours for the structure.

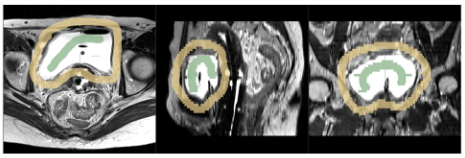

Figure 1: A typical initialization for the *GrowCut* algorithm. Parts of the structure to be segmented (green) and parts of the background (yellow) are marked on the image with the Slicer brush tool.

Results

Segmentation of the bladder was successfully performed in all cases, with a Dice Score of 91.94±5.4 compared to expert manual segmentation (Figure 2 / Figure 3). However, *GrowCut* was not able to achieve satisfactory segmentation results for the tumor and the rectosigmoid. This is attributable to the heterogeneity in appearance of these structures.

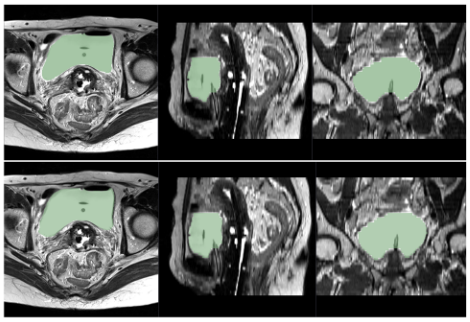

Figure 2: Comparison of segmentation achieved by *GrowCut* (top row) and manually by a physician (bottom row).

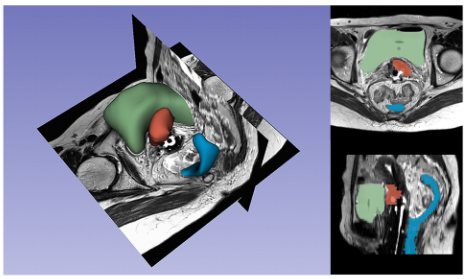

Figure 3: *GrowCut* segmentation of the bladder rendered together with manual segmentations of tumor and rectosigmoid.

Conclusion

In this contribution, we studied the segmentation of pelvic structures to support the process of automated contouring for gynecologic brachytherapy. Contouring of the bladder was achieved accurately using the *GrowCut* algorithm in *3D Slicer*. However, manual contouring was needed to achieve segmentation results for the tumor and the rectosigmoid. Future work will include the application of additional methods from the literature for these structures [4, 5].

References and Acknowledgements

1. American Cancer Society, *Cancer Statistics 2012*. http://www.cancer.org/acs/groups/content/@epidemiologysurveilance/documents/document/acspc-031941.pdf (accessed July 28, 2012)
2. V. Vezhnevets & V. Konouchine, GrowCut - Interactive multi-label N-D image segmentation, in Proc. Graphicon, 2005. pp. 150-156.
3. GrowCut-Module under 3DSlicer http://www.slicer.org/slicerWiki/index.php/Modules:GrowCutSegmentation-Documentation-3.6
4. J. Egger, et al., Manual Refinement System for Graph-Based Segmentation Results in the Medical Domain, Journal of Medical Systems, Springer Press, Aug. 2011.
5. J. Egger, B. Freisleben, C. Nimsky & T. Kapur, Template-Cut: A Pattern-Based Segmentation Paradigm, Nature - Scientific Reports, Nature Publishing Group (NPG), 2(420), 2012.

This work was supported by NIH grants R03EB013792, P41EB015898, U54EB005149, and members of the AMIGO and Slicer communities.

5th NCIGT and NIH Image Guided Therapy Workshop • September 21, 2012 • Joseph B. Martin Conference Center, Harvard Medical School, Boston, Massachusetts

Needle Labeling for Interstitial Gynecological Brachytherapy

Yi Gao[1], Nabgha Farhat[1], Neha Agrawal[1], Guillaume Pernelle[1], Xiaojun Chen[1], Jan Egger[1], Tyler Blevins[1], Sylvain Bouix[1], Allen Tannenbaum[2], William Wells[1], Ron Kikinis[1], Ehud Schmidt[1], Akila Viswanathan[1]** and Tina Kapur[1]**
[1]Brigham and Women's Hospital, [2]Boston University, **Joint Senior Authorship

Purpose

In interstitial brachytherapy for gynecological cancer, radioactive seeds are delivered to the target tissues using multiple hollow needles. However, due to tissue resistance, these needles may not follow a trajectory that can be accurately predicted using dead reckoning. In this work we provide a fast and accurate method to extract and display needles from MR images acquired during MR-guided gynecological cancer brachytherapy. Compared to CT, needle artifacts are less easily identifiable in T2w MR, the sequence of choice for visualizing gynecologic cancer. In previous work [1], we introduced the use of a customized SSFP MR sequence to enhance needle artifacts in these procedures, and in this work we provide a post-processing method that reliably and accurately extracts the needles from images acquired using these SSFP MR images.

Methods

The user is asked to provide two pieces of information in order to initiate the needle extraction tool (Figure 1). The algorithm then takes over to extract the needles in the image. Mathematically, denote the MR image as a function $I:\Omega \rightarrow R$ where Ω is the field of the view of the image. Accordingly, denote the voxel positions drawn by user for the template as $B = \{b_i \in \Omega;\ i = 1, \ldots, N\}$ and the voxel positions for the needles as $D = \{d_i \in \Omega;\ i = 1, \ldots, M\}$. Then, the Hessian image H: $\Omega \rightarrow S^{3\times 3}$ is computed. The eigen system of the 3×3 matrix defines a Conformal Euclidean metric on Ω [2]. A straight line is then computed from each needle label region among $d_{1,\ldots,M}$, to the template region B. By doing this, an optimal line is obtained for each needle, which is regarded as the needle. The algorithm is implemented in C++ language.

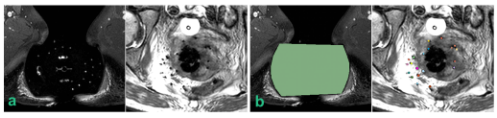

Figure 1: User Input
First, the user is asked to draw a region in one of the inferior most transverse slices through which all the needles pass. For example, when a Syed Neblett template is used and is visible in the scan, this region can be the approximate outer boundary of the template. Then, the user is asked to scroll to a superior transverse slice close to the tip of the needles, and identify the cross sections of the needles.
(a) Shows the unmarked scan and (b) shows a typical initiation marking.

Results

This needle extraction tool has been used to segment needles on 6 SSFP MR images. The running time, from user input to final results, is less than one minute to extract up to 20 needles. Results have been visually compared very favorably to manual needle extraction by a physician, and will be quantified in future work.

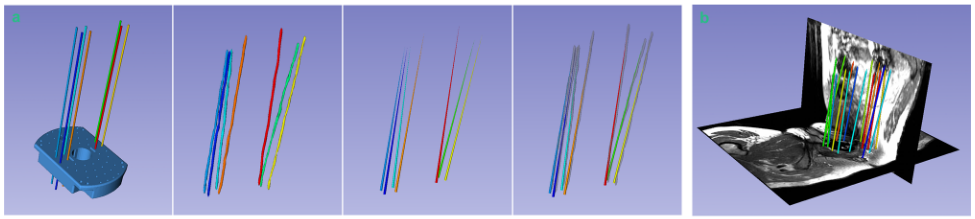

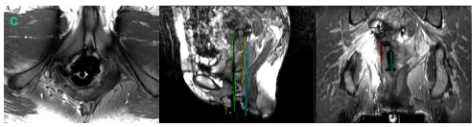

Figure 2: Results
(a) Left to right: CAD model of Syed Neblett template and ideal needle positions assuming no tissue resistance; Manual segmentation of needles from MR image; Automatic needle extraction from MR; Overlay manual and automatic.
(b) Results of needle extraction from Figure 1 rendered in 3D
(c) Results of needle extraction from Figure 1 in three cross-sections

Conclusion

In this work we have a novel algorithm to extract gynecologic brachytherapy needles from SSFP MR imagery. The algorithm requires simple inputs from the user based on which 3D models of the needles are constructed in a time frame that is acceptable for intra-procedural guidance. Future work includes (1) modeling the bending of needles (2) quantitative comparison of results to manual extraction of needles from MR, as well as to CT images.

References

[1] Kapur, T., Egger, J., Damato, A., Schmidt, E.J. & Viswanathan, A.N., 3-T MR-guided brachytherapy for gynecologic malignancies. Magnetic Resonance Imaging, Elsevier, in Press, 2012.
[2] Kichenassamy, S., *et al.*, Arch. Rational Mechanics and Analysis, 134(3):275–301, 1996.

This work was supported by NIH grants R03EB013792, P41EB015898, U54EB005149, and members of the AMIGO and Slicer communities.

5th NCIGT and NIH Image Guided Therapy Workshop • September 21, 2012 • Joseph B. Martin Conference Center, Harvard Medical School, Boston, Massachusetts

A Software Prototype for Real-time Ablation Zone Planning Using Distance Transformation Calculated Isosurfaces

Jan Egger, Ph.D., Ph.D.[1,2,3], Tina Kapur, Ph.D.[1], Philipp Bruners, M.D., Ph.D.[4], Tobias Penzkofer, M.D.[1,4]
1 Dept. of Radiology, Surgical Planning Lab, Brigham and Women's Hospital Boston, MA, USA,
2 Dept. of Mathematics and Computer Science, University of Marburg, Marburg, Germany,
3 Dept. of Neurosurgery, University of Marburg, Marburg, Germany,
4 Dept. of Diagnostic and Interventional Radiology, RWTH Aachen University Hospital, Germany

Purpose

Thermal or electrical ablative techniques are used in a variety of pathologies, such as local tumor control or local pain treatment. Additionally to cryoablation, microwave ablation and radiofrequency ablation, irreversible electroporation (IRE) was recently added to the toolbox of image guided therapy (IGT). For all aforementioned techniques planning and monitoring of the ablation areal is central to the procedure's success [1]. Many published methods include CPU-intensive simulations of ablation techniques [2,3]. We present a method to plan and monitor estimated ablation volumes in real-time.

Methods

A research software prototype was developed using MeVisLab (http://www.mevislab.de). In a showcase application the electrical field of irreversible electroporation was estimated using Euclidian distance transformations (DTF): a distinct inverse DTF around every manually determined (Figure 1) needle tip was calculated after manually segmenting the needle tips in an intraprocedural CT scan. Subsequently, summation of the distance fields was performed, isosurfaces at three distinct isovalues were calculated (Figure 2) and compared to postprocedural imaging (Figure 3).

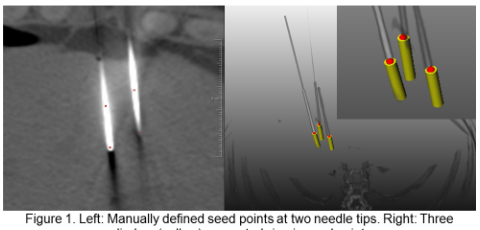

Figure 1. Left: Manually defined seed points at two needle tips. Right: Three cylinders (yellow) generated via six seed points.

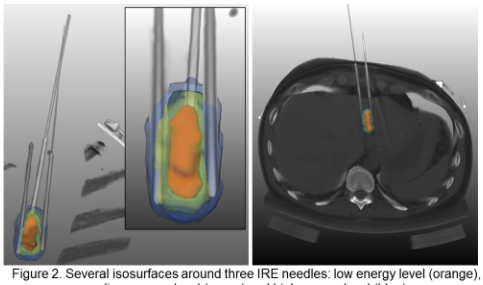

Figure 2. Several isosurfaces around three IRE needles: low energy level (orange), medium energy level (green) and high energy level (blue).

Results

The segmentation and isosurface calculation could be performed swiftly with minimal user interaction. A qualitative comparison of the generated isosurfaces with postprocedurally acquired MRI imaging showed reasonable concordance of the predicted and achieved ablation volume in the presented use case of irreversible electroporation (Figure 3).

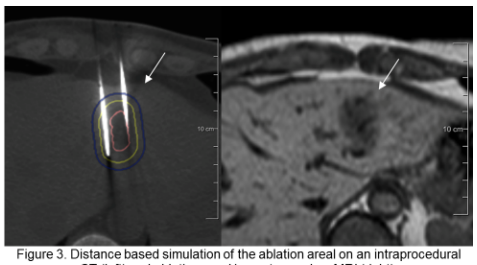

Figure 3. Distance based simulation of the ablation areal on an intraprocedural CT (left) and ablation areal in postprocedure MRI (right).

Conclusion

A software prototype was developed for preprocedural planning and intraoperative monitoring of ablative procedures such as IRE. The method needs to be validated against known ablative technologies and parameter sets for different ablation scenarios need to be determined [3,4]. Potential applications of the technique are real-time navigation based ablation volume calculation, real-time monitoring and adjustment of ablation volumes, especially in IRE, cryotherapy and microwave ablation. The value of the more tissue dependent and heat sink prone radiofrequency ablation is however questionable. The easy extensibility towards modified ablation volume calculations could be of further value.

Philipps Universität Marburg

Universitätsklinikum der Rheinisch-Westfälischen Technischen Hochschule Aachen
Klinik für Diagnostische und Interventionelle Radiologie

References

[1] Y. Zhang, et al. MR imaging to assess immediate response to irreversible electroporation for targeted ablation of liver tissues: preclinical feasibility studies in a rodent model. Radiology; 256(2):424-32, 2010.
[2] B. Rubinsky. Irreversible Electroporation in Medicine. Technol Cancer Res Treat; 6(4):255-60, 2007.
[3] J.F. Edd & R.V. Davalos. Mathematical modeling of irreversible electroporation for treatment planning. Technol Cancer Res Treat; 6(4):275-86, 2007.
[4] K.H. Zou, et al. Statistical Validation of Image Segmentation Quality Based on a Spatial Overlap Index: Scientific Reports. Academic Radiology, 11(2), pp. 178-189, 2004.

Acknowledgements

The authors would like to acknowledge Fraunhofer MeVis in Bremen, Germany, for their collaboration and especially Horst K. Hahn for his support. This work was supported by National Institutes of Health (NIH) grants R03EB013792 and P41EB015898.

5th NCIGT and NIH Image Guided Therapy Workshop • September 21, 2012 • Joseph B. Martin Conference Center, Harvard Medical School, Boston, Massachusetts

Image Processing for MR-guided Gynecologic Interstitial Brachytherapy in AMIGO

Xiaojun Chen, Jan Egger, Akila Viswanathan, William Wells, Ron Kikinis,
Clare Tempany, Ferenc Jolesz, Tina Kapur * (tkapur@bwh.harvard.edu)
Brigham and Women's Hospital and Harvard Medical School

Purpose

Interstitial brachytherapy, the delivery of planned radiation dose directly to the tissue via hollow needles inserted into the tumor and surrounding anatomy, is an effective treatment for gynecological cancer [1]. The purpose of the software module described here is to provide assistance to the physician in determining the optimal distribution and insertion depth of needles that provide maximal tumor coverage, while minimizing dose to the surrounding organs of interest such as the rectum, the bladder, and the sigmoid colon.

Methods and Materials

3D Slicer [2] is a free and open source software package for medical image analysis and visualization. iGyne(with its workflow shown in Fig.1) is a 3D Slicer module designed for MR-guided interstitial brachytherapy planning for gynecologic cancer in the Advanced Multimodality Image Guided Operating Suite (AMIGO) at Brigham and Women's Hospital. Use of the iGyne in AMIGO includes the following steps:

1) CAD models of the interstitial template and vaginal obturator are loaded;
2) MR scan of the patient with the template sutured to the perineum and the obturator placed in the vaginal canal is transferred to 3D Slicer using the DICOM protocol;
3) An initial rigid registration is computed from 3 corresponding point pairs provided by the user on the template holes(as shown in Fig.2);
4) The registration is refined using the Iterated Closest Point [3] algorithm for rigid registration (as shown in Fig.3);
5) Optionally, segmentation and visualization of 3D models of the tumor are obtained rapidly using editing capabilities of 3D Slicer,
6) Finally, virtual needles are selected on a schematic of the template and rendered in the 2D and 3D views, with the insertion depth independently adjustable for each needle. This allows for ease of visualization of spatial relationships among the needles, tumors, and surrounding anatomical structures can be clearly observed, and hence ease in determination of the optimal number and positions of the needles, as well as insertion depth (as shown in Fig.4)

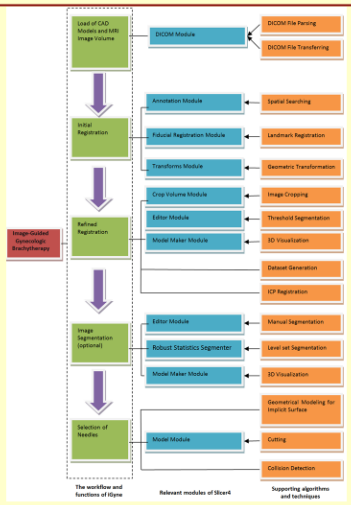

Figure_1. The workflow of the iGyne and its relevant algorithms

Results

A software module for MR-guided gynecologic brachytherapy has been developed for the established 3D slicer open source software platform using well-regarded toolkits in computer graphics and medical image processing such as VTK, ITK, CTK, and QT [4]. Furthermore, a multi-stage registration method is presented to register the CAD template model to the MRI image volume.

Conclusions

While the current version of iGyne address some important aspects of the planning task, including robust registration, needle visualization, user-friendly interface, it remains under active development for additional features such as integration with needle tracking hardware, which are essential in order to realize its full benefit for MR-guided needle guidance in AMIGO.

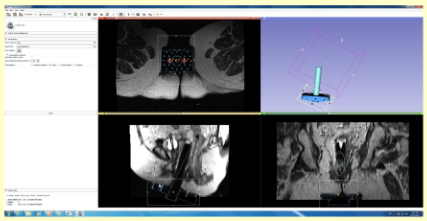

Figure_2. The screenshot of the initial registration result

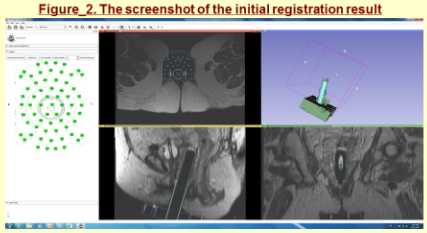

Figure_3. The screenshot of the refined registration result in iGyne

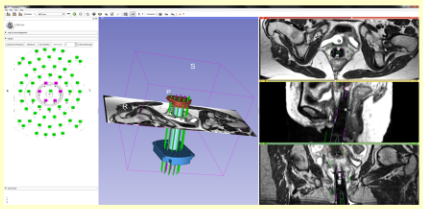

Figure_4. The visualization of the tumor and selected needles in iGyne

Acknowledgements

The authors would like to acknowledge the support of the *AMIGO* team in enabling this clinical study, Kanokpis Townamchai, M.D. for performing the manual segmentations of the medical images, members of the *Slicer Community*, especially Steve Pieper, Ph.D., for creating a platform that enabled iGyne. This work is supported by the *National Institutes of Health* (*NIH*) grants *P41EB015898*, *R03EB013792* and *U54EB005149*, and Dr. Viswanathan receives support from *NIH* grant *K07CA117979*.

References

1. A.N. Viswanathan, C. Kirisits, B.E. Erickson, and R. Pötter. Gynecologic Radiation Therapy: Novel Approaches to Image-Guidance and Management. Springer. 2010.
2. http://www.slicer.org
3. P. Besl and N. McKay. A method for Registration of 3-D Shapes. IEEE Transactions on Pattern Analysis and Machine Intelligence. 1992; 14(2):239 – 256
4. http://www.slicer.org/slicerWiki/index.php/Documentation/Nightly/Extensions/iGyne

9th Interventional MRI Symposium September 22-23, 2012 Joseph B. Martin Conference Center, Harvard Medical School, Boston, Massachusetts

Interactive *Real-Time* Segmentation for Vertebral Bodies and Intervertebral Discs in Sagittal Planes

Jan Egger, Ph.D., Ph.D.[a,b,c], Tina Kapur, Ph.D.[a], Bernd Freisleben, Ph.D.[b], Christopher Nimsky, M.D., Ph.D.[c]
[a] Dept. of Radiology, Surgical Planning Lab, Brigham and Women's Hospital Boston, MA, USA
[b] Dept. of Mathematics and Computer Science, University of Marburg, Marburg, Germany
[c] Dept. of Neurosurgery, University of Marburg, Marburg, Germany

Purpose

Interactive segmentation approaches like [1, 2] get more and more popular, because automatic segmentation methods are typically only suitable for a specific type of pathology in a specific imaging modality and still fail time-by-time. Moreover, most automatic approaches need precise parameter settings to provide good results. The state of the art or rather clinical practice is in the most medical departments still manual slice-by-slice segmentations which are very time consuming. In this contribution, we present the initial results of an interactive graph-based approach for vertebral bodies and intervertebral discs segmentation that provides *real-time* feedback to the user during the segmentation process. The speed and *real-time* behavior makes this approach even suitable for MR-guided biopsies of vertebral bodies where several planes are used in planning and executing the interventions [3].

Methods

The *Square-Cut* scheme [4] was used and extended for this study. Briefly, the *Square-Cut* algorithm sets up a directed 2D-graph G(V,E) in two steps: (I) sending rays through the surface points of a square template and (II) sampling the graph's nodes $n \epsilon V$ along every ray (Figure 1). In addition, a set of edges $e \epsilon E$ is generated, which consists of edges between the nodes and edges that connect the nodes to a source s and a sink t. After graph construction from a user defined seed in the image (which is the square's center), the minimal cost closed set on the graph is computed via a polynomial time s-t-cut [5], which results in the segmentation outcome. For an initial study we implemented a C++ module within the prototyping platform MeVisLab (http://www.mevislab.de).

Results

With our interactive segmentation technique the user gets real-time feedback of the segmentation result. To demonstrate our technique and for an initial feasibility study we implemented an interactive version to segment vertebrae (discs) in 2D. Therefore, we applied a graph-based method that uses a square template like presented in [4] and made it interactively by allowing the user to move the graph's center point over the image. This could be achieved in real-time for a graph consisting of 900 nodes, 870 z-edges and 900 (1800) xy-edges (template diameter was 35mm, 30 rays, 30 points-per-ray and a delta value of 5). Figure 2 below illustrates – from the left to the right – how the user can interactively move the graph's center point (white dot) to find satisfying segmentations (red dots) by getting on the same time *real-time* feedback.

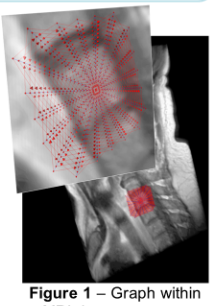

Figure 1 – Graph within a MRI dataset.

Conclusion

In this initial study, we showed that the *Square-Cut* scheme can be used as an interactive approach for vertebral body and intervertebral disc segmentation in sagittal planes. However, the presented principle can also be applied to other images and dimensions (e.g. non-medical, color-level, 3D) and potential application examples for different templates in 2D and 3D are presented in [6]. In a next step, we plan to extend the interactive approach to 3D for vertebral body segmentation based on a cubic template [7].

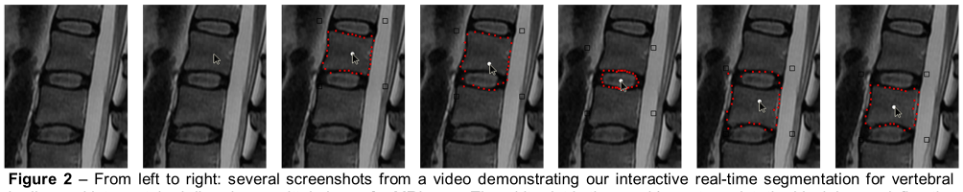

Figure 2 – From left to right: several screenshots from a video demonstrating our interactive real-time segmentation for vertebral bodies and intervertebral discs in a sagittal plane of a MRI scan. The white dot is the graph's center point, the black boxes define the corners of the square template and the red dots are the segmentation outcomes.

References

1. Y. Boykov, et al. Interactive Graph Cuts for Optimal Boundary & Region Segmentation of Objects in N-D Images. ICCV, 105-112, 2001.
2. S. Steger, G. Sakas. FIST: Fast interactive segmentation of tumors. Abdominal Imaging, Vol. 7029, Springer, pp. 125-132, 2011.
3. E. Salomonowitz. MR imaging-guided biopsy and therapeutic intervention in a closed-configuration magnet: single-center series of 361 punctures. AJR Am J Roentgenol. 2001 Jul;177(1):159-63.
4. J. Egger, et al. Square-Cut: A Segmentation Algorithm on the Basis of a Rectangle Shape. PLoS One. 2012; 7(2):e31064.
5. Y. Boykov, V. Kolmogorov. An Experimental Comparison of Min-Cut/Max-Flow Algorithms for Energy Minimization in Vision. IEEE Transactions on Pattern Analysis and Machine Intelligence, 26(9), pp. 1124-1137, 2004.
6. J. Egger, et al. Template-Cut: A Pattern-Based Segmentation Paradigm. Scientific Reports, Nature Publishing Group, 2(420), 2012.
7. R. Schwarzenberg, B. Freisleben, R. Kikinis, C. Nimsky, J. Egger. [A Cube-Based Approach to Segment Vertebrae in MRI-Acquisitions]. In: Proceedings of BVM, Springer Press, pp. 69-74, Heidelberg, Germany, March 2013.

Acknowledgements

The authors would like to thank Fraunhofer MeVis in Bremen, Germany, for their collaboration and especially Professor Dr. Horst K. Hahn for his support.

6th NCIGT and NIH Image Guided Therapy Workshop • March 21-23, 2013 • Doubletree by Hilton Washington DC in Crystal City, VA.

Robust Applicator Registration for Interstitial Gynaecologic Brachytherapy

Guillaume Pernelle [a,b*], Jan Egger, Ph.D., Ph.D.[b*], Carolina Vale [c], Xiaojun Chen, Ph.D.[b], Franz Irlinger, Ph.D.[a], Tim C. Lueth, Ph.D.[a], Ron Kikinis, M.D.[b], William Wells, Ph.D.[b], Akila Viswanathan, M.D., M.P.H.[b**], Tina Kapur, Ph.D.[b**]

[a] Technical University of Munich (TUM), [b] Brigham and Women's Hospital, Boston, [c] Faculty of Science, University of Lisbon *Joint First Authorship, **Joint Last Authorship

Purpose – We present a method for robust localization of the Syed-Neblett gynecologic brachytherapy applicator in intra-operative Magnetic Resonance (MR) imagery by alignment with its computer aided design (CAD) model. This alignment allows us to visualize "virtual needles" prior to the actual insertion.

Methods – Previously, we reported initial development of a software module named "iGyne" using the free and open source software platform *3D Slicer* (http://www.slicer.org). Within iGyne, we reported a registration method based on user-initialized correspondences between 3 points, followed by Iterative Closest Points surface registration of the Syed-Neblett template [2,5]. In this work, we provide additional information to the registration method by including the obturator in the process. Specifically, we have added to the iGyne software module a step that automatically segment the obturator from the rest of the image based on the difference of contrast between the obturator and its surrounding tissues. As an intermediate step, a 3D model is generated from the segmented label map of the obturator, and then an ICP registration (similar to [5]) is used to register the surfaces of both the template and obturator CAD models against their segmentations in the MR images.

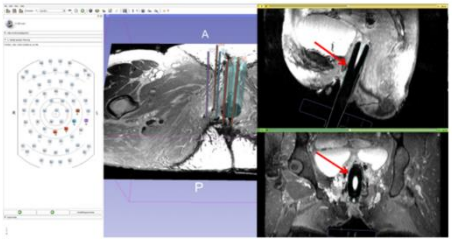

Figure 1. Interface of *iGyne* in *3D Slicer* allowing simulating insertion of needles (left image). Result of the refined ICP registration of the obturator and the template (right images).

Results – We applied this method to six T2-weighted MRI datasets acquired using a Siemens 3T scanner in the Advanced Multimodality Image Guided Operating (AMIGO) suite at Brigham and Women's Hospital.

We computed the quadratic mean distance (Root Mean Square error) between corresponding resulting points – of a manually obtained registration (ground truth) – and of both registration methods described above. We obtained a significant accuracy improvement compared to the previous (template-only) registration method. The RMS error dropped by more than 70% (from 14mm to 4mm). We also obtained a significant computation time improvement (eight times shorter) compared to the GrowCut method [3,4] which was previously used to segment the obturator by asking the user to apply roughly label on its inside and outside. Figure 1 illustrates a representative case. To support open science, all data sets used in this study have been anonymized and made available freely and publicly [6]. Potential users of this data are requested to cite article [2] that provides the overall vision of gynecological brachytherapy in AMIGO.

Case	Initial registration error (mm)	"Template only" error (mm)	"GrowCut" error (mm)	"Auto segmentation" error (mm)
1	21.08	2.01	1.45	3.57
2	18.24	24.61	7.96	6.70
3	7.98	8.46	2.92	7.31
4	8.51	12.17	0.84	6.10
5	17.60	16.75	7.11	0.71
6	22.58	19.74	3.00	1.38
Average	16.00±6.28	13.96±8.14	3.88±2.96	4.30±2.83
Computation Time (s)		32±7	235±124	27±4

Table 1. Evaluation of the RMS error and computation time of the methods named by the column header. The first column presents the evaluation results of the registration state after the first initial landmark registration. RMS error are in millimeters, computation times are in seconds.

Conclusions – In this contribution, we present a registration method for CAD models of the Syed-Neblett template and the obturator for interstitial gynecologic brachytherapy that is available in the iGyne module of the open source software package 3D Slicer. Areas of immediate future work include the further improvements to the accuracy of the method so that it is less than 2mm Root Mean Square error.

References

1. American Cancer Society, *Cancer Statistics 2012*. Accessed July 28, 2012. http://www.cancer.org/acs/groups/content/@epidemiologysurveilance/documents/document/acspc-031941.pdf
2. T. Kapur, et al., 3-T MR-guided brachytherapy for gynecologic malignancies, Magn Reson Imaging. 2012 Aug 13. [Epub]
3. V. Vezhnevets & V. Konouchine, GrowCut - Interactive multi-label N-D image segmentation, in Proc. Graphicon, 2005. pp. 150-156.
4. GrowCut-Module under 3DSlicer http://www.slicer.org/slicerWiki/index.php/Modules:GrowCutSegmentation-Documentation-3.6
5. X. Chen, et al., Image Processing for MR-guided Gynecologic Interstitial Brachytherapy in AMIGO, 9th iMRI Symposium, Boston, 2012.
6. BWH/DFCI Gynecological Brachytherapy Open Data Collection. http://www.spl.harvard.edu/publications/item/view/2227

Acknowledgements

This work was supported by NIH grants R03EB013792, P41EB015898, U54EB005149, and members of the AMIGO and Slicer communities.

Rectum Segmentation in MR-guided Gynecologic Brachytherapy Data

Tobias Lüddemann [a], Jan Egger [b]

[a] Technical University of Munich (TUM), Munich, Germany
[b] University Hospital of Marburg (UKGM), Marburg, Germany

Background

Among all cancer types, gynecological malignancies - including endometrial, vaginal/vulvar and cervical cancers - belong to the 4th most frequent type of cancer among women [1]. Besides chemotherapy and external beam radiation, brachytherapy is the standard procedure for the treatment of these malignancies. In the progress of treatment planning, segmentation of the tumor as the target volume as well as segmentation of adjacent organs of risks is crucial to accomplish an optimal radiation distribution to the tumor while simultaneously preserve healthy tissue. This contribution presents the initial results of contouring the rectum with a novel interactive graph-based segmentation method based on a user-defined template.

Methods

The proposed method uses a graph-based segmentation scheme [2] and extends it to an interactive approach (named *Interactive-Cut*) with a user-defined template. In summary, the scheme creates a directed 2D graph, followed by the minimal cost closed set computation on the graph [3], resulting in an optimal outlining of the rectum. Thereby, the graph's center can be interactively dragged to compute a further segmentation and optimize the result. Figure 1 demonstrates the interactive segmentation process: original dataset (A), interactive moving of the graph's center (B-E) with *real-time* feedback of the rectum contour (red) and resulting segmentation (F) after a satisficing outline of the rectum has been achieved.

Results

Six intraoperative T2-weighted magnetic resonance imaging (MRI) datasets acquired with a Siemens 3T scanner at the Brigham and Women's Hospital (BWH) have been used for this initial study [4, 5]. Segmentation of the rectum could successfully be performed in all cases. For visual side-by-side inspection Figure 2 presents three manual segmentations (A, C and E, blue) and the corresponding interactive segmentations (B, D and F, red). For all segmentations the same template has been used (blue dots in the right images) and no parameter definitions were required from the user. However, a satisficing rectum contour could always be found within seconds for every plane.

Conclusion

In this contribution, we tested a novel interactive graph-based approach – called *Interactive-Cut* – to segment the rectum with a user-defined template. Our long-term objective is to support the time-consuming process of manual rectum outlining for gynecologic brachytherapy and our initial 2D results show already promising results. Areas of future work include a comprehensive evaluation via the Dice Similarity Coefficient (DSC) and an extension of the algorithm to 3D.

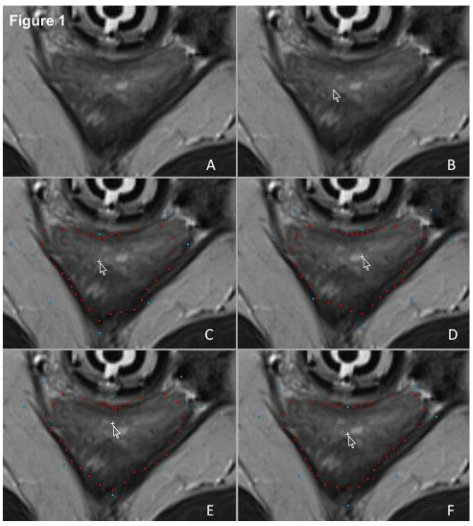

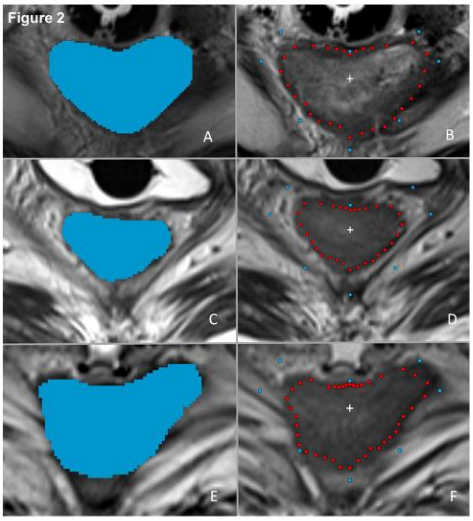

References

1. American Cancer Society, Cancer Statistics, 2012.
2. J. Egger, et al. Template-Cut: A Pattern-Based Segmentation Paradigm. Sci Rep., Nature Publishing Group (NPG), 2012;2:420. Epub 2012 May 24.
3. Y. Boykov & V. Kolmogorov. An Experimental Comparison of Min-Cut/Max-Flow Algorithms for Energy Minimization in Vision. IEEE Transactions on Pattern Analysis and Machine Intelligence, 26(9), pp. 1124-1137, 2004.
4. J. Egger, et al. GYN Data Collection. NCIGT, online available: http://www.spl.harvard.edu/publications/item/view/2227
5. T. Kapur, et al. 3-T MR-guided brachytherapy for gynecologic malignancies. Magn Reson Imaging., 2012 Aug 13. [Epub ahead of print]

Acknowledgements

The authors would like to thank Neha Agrawal for performing the manual segmentations. The authors would also like to thank Fraunhofer MeVis in Bremen, Germany, for their collaboration and especially Professor Hahn for his support.

The British Gynaecological Cancer Society Annual Scientific Meeting in conjunction with the Irish Gynaecological Cancer Society
The Waterfront, Belfast, Northern Ireland • 20th - 21st June, 2013.

GrowCut-Based Vertebral Body Segmentation with 3D Slicer

Dr. Dr. Jan Egger, Christoph Kappus, Dr. Barbara Carl,
Professor Dr. Christopher Nimsky

Clinic for Neurosurgery, University Hospital of Gießen and Marburg (UKGM), Marburg, Germany

UKGM UNIVERSITÄTSKLINIKUM GIESSEN UND MARBURG

Jahrestagung Sektion Wirbelsäule der Deutschen Gesellschaft für Neurochirurgie 27.–28. September 2013 FRANKFURT am Main

Introduction

Diseases of the spine are quite common, especially due to degenerative changes of the ligamentary and osseous structures. When making the decision for adequate procedure neuro-imaging plays a main role for estimating the dimension of surgical treatment [1]. Accurate and objective evaluation of vertebral deformations is of significant importance in clinical diagnostics and therapy of pathological conditions affecting the spine [2]. A Computer assisted diagnosis system aims to facilitate characterization and quantification of abnormalities. Our aim is to perform semi-automated segmentation of vertebral bodies derived from MRI acquisitions to speed-up a pure manually analysis.

Material and Methods

We used the GrowCut segmentation method of the 3D Slicer platform [3] to delineate vertebral bodies of 13 cases. GrowCut Segmentation is a competitive region growing algorithm using cellular automata [4]. The algorithm starts with a random number of seed points and automatically converges to a natural segmentation. This is useful when deriving classes from large image datasets for applications such as region-based image retrieval. The algorithm achieves reliable and fast segmentation of moderately difficult objects in 2D and 3D using an iterative labeling procedure resembling competitive region growing. After trial of the various segmentation facilities available in Slicer, we determined that the use of GrowCut by initializing it on sagittal, axial, and coronal cross-sections provides the most efficient segmentations of vertebral bodies (Figure 1).

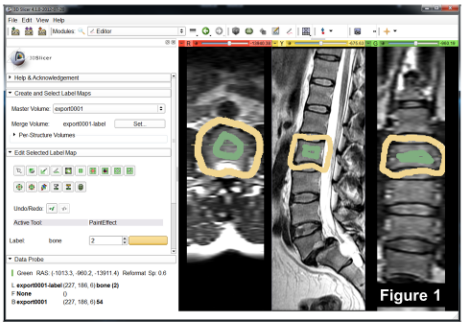

Figure 1

Results

For an evaluation of our study, the GrowCut results have been compared with manually slice-by-slice segmentations using the Dice Similarity Coefficient (DSC) [5]. The DSC measures the relative volume overlap between M and S, where M and S are the binary masks from the manual slice-by-slice (M) and the Slicer (S) segmentation. The average DSC for all data sets was 82.99±%±5.03% and shows that the two are comparable. We also found an average segmentation time for a GrowCut-based segmentation of less than 6 minutes (5.77±0.73). For visual inspection, Figure 2 presents a direct comparison of a manual (blue) and a GrowCut (yellow) segmentation on a sagittal slice, and a 3D visualization of the GrowCut segmentation result (green).

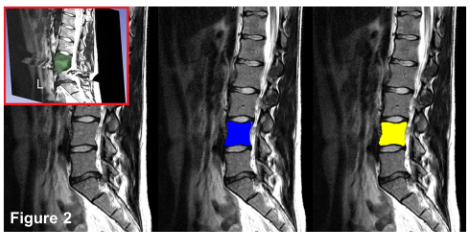

Figure 2

Discussion

In this initial study, we present segmentation results for vertebral bodies in T2-weighted MRI data using the 3D Slicer platform. We showed that a Slicer-based segmentation can be more efficient and thus a less time-consuming process compared to manually volumetric assessment. The time and user effort required for GrowCut segmentation was on an average about 50% compared to a manual segmentation. There are several areas of future work including the evaluation of a larger set of data and comparison with other segmentation methods, like [6-8].

Acknowledgements

We want to acknowledge the members of the Slicer Community and in particular Harini Veeraraghavan and Jim Miller from GE for developing the GrowCut module for 3D Slicer. Furthermore, the authors would like to thank Neha Agrawal for participating in this study. Finally, the authors would like to thank Fraunhofer MeVis in Bremen, Germany, for their collaboration and especially Professor Dr. Horst K. Hahn for his support.

References

1. A.F. Joaquim, et al. *Degenerative lumbar stenosis: update*. Arq Neuropsiquiatr., 67(2):553-8, 2009.
2. G.E. Hicks, et al. *Degenerative lumbar disc and facet disease in older adults: prevalence and clinical correlates*. Spine (Phila Pa 1976); 34(12):1301-6, 2009.
3. GrowCut-Module under 3D Slicer http://www.slicer.org/slicerWiki/index.php/Modules:GrowCutSegmentation-Documentation-3.6
4. V. Vezhnevets & V. Konouchine. *GrowCut - Interactive multi-label N-D image segmentation*. Proc. Graphicon, pp. 150-156, 2005.
5. K.H. Zou, et al. *Statistical Validation of Image Segmentation Quality Based on a Spatial Overlap Index: Scientific Reports*. Acad Radiol., 11(2), pp. 178-189, 2004.
6. J. Egger, T. Kapur, T. Dukatz, M. Kolodziej, D. Zukić, B. Freisleben, C. Nimsky. *Square-Cut: A Segmentation Algorithm on the Basis of a Rectangle Shape*. PLoS One. 2012; 7(2):e31064. Epub 2012 Feb 21.
7. J. Egger, B. Freisleben, C. Nimsky, T. Kapur. *Template-Cut: A Pattern-Based Segmentation Paradigm*. Sci Rep., Nature Publishing Group (NPG), 2(420), 2012.
8. R. Schwarzenberg, B. Freisleben, R. Kikinis, C. Nimsky, J. Egger. [*A Cube-Based Approach to Segment Vertebrae in MRI-Acquisitions*]. In: Proceedings of Bildverarbeitung für die Medizin (BVM), Springer Press, pp. 69-74, Heidelberg, Germany, March 2013.

Jan Egger

Christoph Kappus

Barbara Carl

Christopher Nimsky

Jahrestagung Sektion Wirbelsäule der Deutschen Gesellschaft für Neurochirurgie FRANKFURT 27.–28. September 2013

Weitere Abstracts:

- M. H. A. Bauer, **J. Egger**, D. Kuhnt, S. Barbieri, B. Freisleben, C. Nimsky. Evaluation of Several Cost Functions for Min-Cut-Segmentation of Tubular Fiber Bundles in the Human Brain. In: 61. Jahrestagung der Deutschen Gesellschaft für Neurochirurgie (DGNC), Mannheim, DocP 1821, DOI: 10.3205/10dgnc292, September 2010.

- **J. Egger**, M. H. A. Bauer, D. Kuhnt, B. Freisleben, C. Nimsky. Min-Cut-Segmentation of WHO Grade IV Gliomas Evaluated against Manual Segmentation. In: XIX Congress of the European Society for Stereotactic and Functional Neurosurgery, Athens, Greece, 2/OP64, September 2010.

- C. Kappus, **J. Egger**, B. Carl, M.H.A. Bauer, C. Nimsky. Investigation of an image-based tool for planning safe trajectories in deep-brain-stimulation. In: 63. Jahrestagung der Deutschen Gesellschaft für Neurochirurgie (DGNC), Leipzig, DocP 048, DOI: 10.3205/12dgnc435, June 2012.

- H. F. Busse, M. Moche, P. Brandmaier, M. Gawlitza, S. Strocka, T. K. Kahn, D. Schmalstieg, **J. Egger**. Novel Semiautomatic Real-time CT Segmentation Tool and Preliminary Clinical Evaluation on Thermally Induced Lesions in the Liver. In: 100th Annual Meeting of The Radiological Society of North America (RSNA), PHS 171, December 2014.

- P. Voglreiter, J. Wallner, K. Reinbacher, K. C. Schwenzer-Zimmerer, D. Schmalstieg, **J. Egger**. Global Illumination Rendering for High-Quality Volume Visualization in the Medical Domain. In: face 2 face - science meets art, Medical University of Graz, Hörsaalzentrum, Austria, October 2015.

- **J. Egger**, P. Voglreiter, M. Dokter, M. Hofmann, H. F. Busse, D. Seider, P. Brandmaier, R. Rautio, G. Zettel, B. Schmerböck, M. van Amerongen, S. Jenniskens, M. Kolesnik, B. Kainz, R. B. Sequeiros, H. Portugaller, P. Stiegler, J. Futterer, D. Schmalstieg, M. Moche. In-depth Multicenter Workflow Analysis of Liver Tumor Ablations for the Development of a Novel Computer-aided Software Tool. 101th Annual Meeting of The Radiological Society of North America (RSNA), December 2015.

- J. Wallner, K. Reinbacher, **J. Egger**, M. Pau, W. Zemann, T. Zrnc, D. Schmalstieg, K. Schwenzer-Zimmerer. Image-guided real-time-segmentation of the mandibular bone: Can a simple Segmentation approach provide a satisfying result for a practicable use?. 20. Jahreskongress der Österreichischen Gesellschaft für Mund-, Kiefer- und Gesichtschirurgie (ÖGMKG),

Kur- und Kongresszentrum, Bad Hofgastein, Salzburg, Jänner 2016.

- K. E. Reinbacher, J. Wallner, **J. Egger**, P. Voglreiter, M. Pau, T. Zrnc, M. Feichtinger, K. Schwenzer-Zimmerer. AR (augmented reality)-Paradigmenwechsel im Therapiedesign. 20. Jahreskongress der Österreichischen Gesellschaft für Mund-, Kiefer- und Gesichtschirurgie (ÖGMKG), Kur- und Kongresszentrum, Bad Hofgastein, Salzburg, Jänner 2016.

- M. Gall, X. Li, X. Chen, D. Schmalstieg, **J. Egger**. Computer-Aided Planning of Cranial 3D Implants. Proceedings of the 30th International Congress and Exhibition of Computer Assisted Radiology and Surgery (CARS) 11 (Suppl 1):S241, ISCAS Poster 067, Heidelberg, Germany, June 2016.

- X. Li, L. Xu, Y. Zhu, **J. Egger**, X. Chen. A semi-automatic implant design method for cranial defect restoration. Proceedings of the 30th International Congress and Exhibition of Computer Assisted Radiology and Surgery (CARS) 11 (Suppl 1):S241-S243, ISCAS Poster 068, Heidelberg, Germany, June 2016.

- **J. Egger**, J. Wallner, K. Hochegger, M. Gall, K. Reinbacher, K. Schwenzer-Zimmerer, D. Schmalstieg. Clinical Evaluation of Mandibular Bone Segmentation. IEEE Engineering in Medicine and Biology Society (EMBC'16), Poster, Orlando, FL, USA, August 2016.

- M. Gall, J. Wallner, K. Schwenzer-Zimmerer, D. Schmalstieg, K. Reinbacher, **J. Egger**. Computer-aided Reconstruction of Facial Defects. IEEE Engineering in Medicine and Biology Society (EMBC'16), Poster, Orlando, FL, USA, August 2016.

- **J. Egger**, M. Gall, J. Wallner, Z. Deng, P. Boechat de Almeida Germano, A. Hann, X. Li, X. Chen, K. Reinbacher, K. C. Schwenzer-Zimmerer, D. Schmalstieg. Virtual Reality in the Medical Domain. face 2 face - science meets art, Medical University of Graz, Hörsaalzentrum, Austria, September/October 2016.

- **J. Egger**, M. Gall, D. Schmalstieg. Translational Research (TR) Applications in Biomedical Engineering. 1st Field of Expertise (FoE) Day Human & Biotechnology, Lecture Hall, Petersgasse 12, TU Graz, Austria, November 2016.

Datenrepositorien

Im Rahmen dieser Arbeit sind zwei öffentliche Repositorien für medizinische Daten aus der klinischen Routine entstanden:

J. Egger, T. Kapur, A. Viswanathan A. *GYN Data Collection*. The National Center for Image Guided Therapy (NCIGT), August 2012.
http://www.spl.harvard.edu/publications/item/view/2227

D. Zukić, **J. Egger**, C, Nimsky, A, Kolb. *Spine Datasets and Segmentations*. Lehrstuhl für Computergraphik und Multimediasysteme, Universität Siegen, 2013.
http://www.cg.informatik.uni-siegen.de/de/spine-segmentation-and-analysis

Stand: Dezember 2016

Haftungsausschluss

Der Autor weist darauf hin, dass die in der Habilitationsschrift enthaltene externe Links nur bis zum Zeitpunkt der Veröffentlichung von ihm eingesehen werden konnten. Auf spätere Veränderungen hat der Autor keinen Einfluss. Eine Haftung des Autors für externe Links und deren Inhalt ist daher stets ausgeschlossen.

class **Lebenslauf** *{*

private:

Dr. Dr. Jan Egger, geboren am 8. Dezember 1975 in Diez

protected:

August 1982 – Januar 1986	Karl-von-Ibell-Grundschule Diez
Februar 1986 – Juli 1987	Pestalozzi-Grundschule Diez
August 1987 – Juli 1993	Sophie-Hedwig-Gymnasium Diez
August 1993 – Juni 1996	Peter-Paul-Cahensly-Gymnasium Limburg

public:

13.06.1996	**Abitur**
Juli 1996 – August 1997	Zivildienst am DRK-Krankenhaus Diez
Oktober 1997 – Juli 1999	Technische Universität Kaiserslautern, Studium der Informatik mit Nebenfach Wirtschaftswissenschaften
September 1999 – Februar 2004	Informatikstudent an der Fachhochschule Wiesbaden
März 2003 – August 2003	Berufspraktisches Semester bei Siemens Corp. Research, Princeton/New Jersey (USA)
19.02.2004	**Diplom in Informatik (FH)**
März 2004 – Juni 2006	Informatikstudent an der Hochschule Darmstadt
Januar 2006 – Juni 2006	Masterarbeit bei Siemens Medical Solutions, Forchheim (Bayern)
14.07.2006	**Master of Science in Informatik (M.Sc.)**
Juli 2006 – Juli 2009	Doktorand an der Philipps-Universität Marburg, Fachbereich Mathematik und Informatik in Kooperation mit Siemens Healthcare, Forchheim (Bayern)
Februar 2008 – Juli 2008	Forschungsaufenthalt bei Siemens Corp. Research, Princeton/New Jersey (USA)
09.07.2009	**Doktor der Informatik (Dr. rer. nat.)**
Juli 2009 – Oktober 2009	Forschung und Entwicklung in der Abteilung Computed Tomography, Siemens Healthcare, Forchheim (Bayern)
Dezember 2009 – August 2013	Wissenschaftlicher Mitarbeiter in der Klinik für Neurochirurgie, Universitätsklinikum Gießen und Marburg GmbH, Standort Marburg
Februar 2010 – Juni 2012	Doktorand an der Philipps-Universität Marburg, Fachbereich Medizin
März 2011 – Juni 2011	Forschungsaufenthalt am Brigham & Women's Hospital der Harvard Medical School, Boston/Massachusetts (USA)
Oktober 2011 – April 2013	Research Fellow am Brigham & Women's Hospital der Harvard Medical School, Boston/Massachusetts (USA)
06.06.2012	**Doktor der Humanbiologie (Dr. rer. physiol.)**

Juni 2014	Forschungsaufenthalt an der Aalto-Universität, School of Science, Department of Biomedical Engineering and Computational Science (BECS), Espoo (Finnland)
Juli 2012 – Dezember 2016	Habilitand an der Philipps-Universität Marburg, Fachbereich Mathematik und Informatik
14.12.2016	**Habilitation in Informatik (Dr. rer. nat. habil.)**
Januar 2014 – heute	Senior Researcher am Institut für Maschinelles Sehen und Darstellen, Technische Universität Graz, Fakultät für Informatik und Biomedizinische Technik, Graz (Österreich)

};

Anhang

Diese kumulative Habilitationsschrift setzt sich aus einer Reihe von Publikationen zusammen, die im Folgenden in chronologischer Reihenfolge angefügt sind. Dabei gelten die Copyrightbestimmungen der einzelnen Verleger. Zur besseren Übersicht hier eine zusammenfassende Gliederung der einzelnen Publikationen nach Themenbereichen:

Segmentierung medizinischer Bilddaten anhand von vorlagenbasierten Algorithmen:

- Square-Cut: A Segmentation Algorithm on the Basis of a Rectangle Shape [1]
- Ein semiautomatischer Ansatz zur Flächenbestimmung von Wirbeln in MRT-Aufnahmen [2]
- Template-Cut: A Pattern-Based Segmentation Paradigm [3]
- Ein kubusbasierter Ansatz zur Segmentierung von Wirbeln in MRT-Aufnahmen [4]
- Cube-Cut: Vertebral Body Segmentation in MRI-Data through Cubic-Shaped Divergences [5]
- PCG-Cut: Graph Driven Segmentation of the Prostate Central Gland [6]
- Interactive-Cut: Real-Time Feedback Segmentation for Translational Research [7]
- Semi-automatische Echtzeit-Konturierung – Ein vorlagenbasierter skalierungsinvarianter Ansatz [8]
- Refinement-Cut: User-Guided Segmentation Algorithm for Translational Science [9]

Experimentelle Evaluation quelloffener Segmentierungsmethoden unter medizinischen Einsatzbedingungen:

- Pituitary Adenoma Volumetry with 3D Slicer [10]
- GBM Volumetry using the 3D Slicer Medical Image Computing Platform [11]
- Fiber Tractography based on Diffusion Tensor Imaging (DTI) Compared with High Angular Resolution Diffusion Imaging (HARDI) with Compressed Sensing (CS) – Initial Experience and Clinical Impact [12]

Navigation zur Unterstützung intraoperativer Therapien:

- Integration of the OpenIGTLink Network Protocol for Image-Guided Therapy with the Medical Platform MeVisLab [13]
- 3-T MR-guided Brachytherapy for Gynecologic Malignancies [14]
- Development of an Open Source Software Module for Enhanced Visualization during MR-Guided Interstitial Gynecologic Brachytherapy [15]
- Image-guided Therapy System for Interstitial Gynecologic Brachytherapy in a Multimodality Operating Suite [16]

OPEN ACCESS Freely available online

PLoS one

Square-Cut: A Segmentation Algorithm on the Basis of a Rectangle Shape

Jan Egger[1,2,3]*, Tina Kapur[1], Thomas Dukatz[2], Malgorzata Kolodziej[2], Dženan Zukić[4], Bernd Freisleben[3], Christopher Nimsky[2]

1 Department of Radiology, Surgical Planning Laboratory, Brigham and Women's Hospital, Harvard Medical School, Boston, Massachusetts, United States of America, **2** Department of Neurosurgery, University of Marburg, Marburg, Germany, **3** Department of Mathematics and Computer Science, University of Marburg, Marburg, Germany, **4** Computer Graphics Group, University of Siegen, Siegen, Germany

Abstract

We present a rectangle-based segmentation algorithm that sets up a graph and performs a graph cut to separate an object from the background. However, graph-based algorithms distribute the graph's nodes uniformly and equidistantly on the image. Then, a smoothness term is added to force the cut to prefer a particular shape. This strategy does not allow the cut to prefer a certain structure, especially when areas of the object are indistinguishable from the background. We solve this problem by referring to a rectangle shape of the object when sampling the graph nodes, i.e., the nodes are distributed non-uniformly and non-equidistantly on the image. This strategy can be useful, when areas of the object are indistinguishable from the background. For evaluation, we focus on vertebrae images from Magnetic Resonance Imaging (MRI) datasets to support the time consuming manual slice-by-slice segmentation performed by physicians. The ground truth of the vertebrae boundaries were manually extracted by two clinical experts (neurological surgeons) with several years of experience in spine surgery and afterwards compared with the automatic segmentation results of the proposed scheme yielding an average Dice Similarity Coefficient (DSC) of 90.97±2.2%.

Citation: Egger J, Kapur T, Dukatz T, Kolodziej M, Zukić D, et al. (2012) Square-Cut: A Segmentation Algorithm on the Basis of a Rectangle Shape. PLoS ONE 7(2): e31064. doi:10.1371/journal.pone.0031064

Editor: Yong Fan, Institution of Automation, CAS, China

Received October 7, 2011; **Accepted** January 1, 2012; **Published** February 21, 2012

Funding: This work is supported by NIH P41RR19703 and R03EB013792. Its contents are solely the responsibility of the authors and do not necessarily represent the official views of the NIH. The funders had no role in study design, data collection and analysis, decision to publish, or preparation of the manuscript.

Competing Interests: The authors have declared that no competing interests exist.

* E-mail: egger@bwh.harvard.edu

Introduction

Template-based segmentation algorithms are suitable for medical image processing, because a patient's data – mostly in the DICOM (Digital Imaging and Communications in Medicine, available: http://medical.nema.org, accessed: 2012 Jan 2) format – already offers useful information, e.g. the patient's orientation. Combined with a body landmark detection algorithm [1] that provides a landmark inside a specific organ, it is possible to choose the organ's template automatically and even get rid of a user-defined seed point inside the organ that is possibly needed by the used segmentation method.

Graph-based approaches have become quite popular during the last years. In contrast to deformable models [2] and [3] that can get stuck in local minima during the iterative segmentation (expansion) process, a graph cut algorithm provides an optimal segmentation for the constructed graph [4]. In this contribution, we present a novel graph-based algorithm for segmenting 2D objects that are rectangle shaped. The algorithm sets up a graph and performs a graph cut to separate an object from the background. However, typical graph-based segmentation algorithms distribute the nodes of the graph uniformly and equidistantly on the image. Then, a smoothness term is added [5] and [6] to force the cut to prefer a particular shape [7]. This strategy does not allow the cut to prefer a certain structure, especially when areas of the object are indistinguishable from the background. We solve this problem by referring to a rectangle shape of the object when sampling the graph nodes, i.e., the nodes are distributed non-uniformly and non-equidistantly on the image. This strategy can be useful, when areas of the object are indistinguishable from the background. To evaluate our proposal, we focus on vertebrae images from Magnetic Resonance Imaging (MRI) datasets to support the time consuming manual slice-by-slice segmentation performed by physicians – we identified an average manual segmentation time for a single vertebra of 10.75±6.65 minutes for our spine datasets. The ground truth of the vertebrae boundaries were manually extracted by two clinical experts (neurological surgeons) with several years of experience in spine surgery and afterwards compared with the automatic segmentation results of the proposed scheme yielding an average Dice Similarity Coefficient (DSC) [8] and [9] of 90.97±2.2%.

Diseases of the spine are quite common, especially due to degenerative changes of the ligamentary and ossuary structures. With increasing stenosis of the spinal cord the limitations of the patients in all-day life worsen and the current development of the population's structure leads to a growing part of older patients with a more frequent insistence for surgical treatment [10], [11] and [12]. When making the decision for adequate procedure neuroimaging plays a main role for estimating the dimension of surgical treatment. MRI-imaging of course is particularly suitable for the assessment of spinal structures such as nerve roots, intervertebral discs and ligamentary constitution without radiation exposure. Nevertheless, certain changes of the vertebra due to osteoporosis,

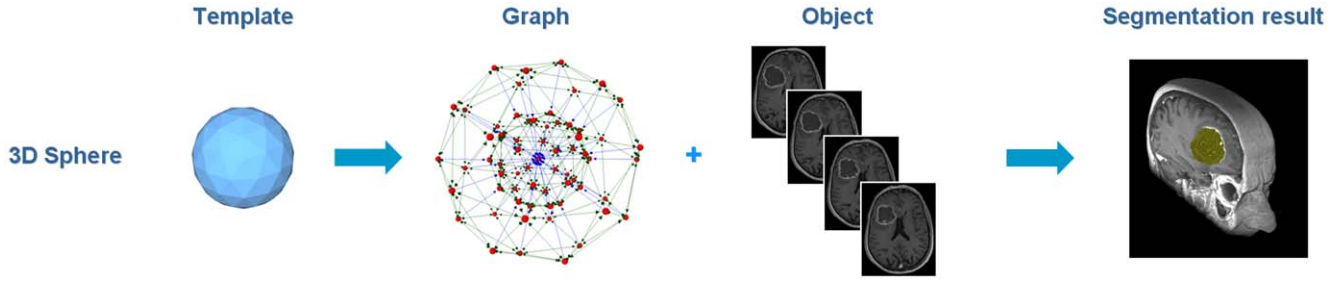

Figure 1. Principle workflow of a segmentation scheme for Glioblastoma multiforme (GBM) in 3D. A polyhedron (left) is used to set up a 3D graph. Then, the graph is used to segment the GBM in a Magnetic Resonance Imaging (MRI) dataset.
doi:10.1371/journal.pone.0031064.g001

fractures or osteophytes require an evaluation of the bone structures via Computed Tomography (CT)-scan including radiation exposure [13] and [14]. With our series of patient datasets we try to illustrate the capability of MRI-segmentation to reconstruct the vertebral body without x-ray examination. Consequently, the numbers of pre-operative examinations can be reduced affecting radiation exposure costs and time-management.

For vertebrae segmentation several algorithms have been proposed in the literature. 2D segmentation approaches are mostly applied to manually identified, best suitable cross-sections [15], [16], [17] and [18]. Automatic selection of best slice was done by Peng et al. [19] and independent segmentation of the vertebral bodies have been done by Michopoulou et al. [15] and Carballido-Gamio et al. [18]. Thereby, the approach from Huang et al. [18] uses normalized cut algorithm with Nyström approximation and achieves Dice Similarity Coefficients for six patients of about 93%–95%. The method from Michopoulou et al. [15] uses atlas registration of intervertebral disks, and provides DSC between 84% and 92%. The methods from Shi et al. [16] and Peng et al. [19] are both top-down approaches and Shi et al. use statistical pattern recognition for spinal cord extraction. A manually defined window is used as initialization for disk detection, and this window slides along the detected spinal cord. The authors report 96% detection rate. Peng et al. [19] do a fully automatic analysis of the whole-spine MR images. Disk clues are located by convolving a disk model with an entire MR image and a polynomial line is fit to those clues. The polynomial line has an intensity profile along which extrema indicate possible disks or vertebral bodies. It was tested on five datasets, with 100% vertebral body detection and about 95% vertebral body corner detection. Huang et al. [17] have performed the segmentation in three stages: AdaBoost-based vertebra detection, detection refinement via robust curve fitting, and vertebra segmentation by an iterative normalized cut algorithm. DSC was around 95%. This method could be called hybrid: it uses bottom-up approach for detecting vertebral body centers, but then it uses a top-down approach to segment vertebral bodies.

In contrast to the 2D approaches, 3D approaches mostly rely on user initialization. To extract the approximate spine position Yao et al. [20] use Hounsfield values and Klinder et al. [21] use CT rib cage segmentation method. The methods from Stern et al. [22], Weese et al. [23] and Hoad et al. [24] segment vertebrae independently. A very tedious initialization was used from Hoad et al., and manual corrections applied afterwards. The segmentation from Stern et al. is performed by optimizing the parameters of a 3D deterministic model of the vertebral body, aiming at the best alignment of the deterministic model and the actual vertebral body in the image. The authors estimated a 61% success rate for MRI and 84% for CT. Weese at al. use polygonal vertebra model and manual initialization. Internal energy reflects statistical shape, and external energy relies on image gradients. Method iterations consist of a surface detection step and a mesh reconfiguration step. The authors report 0.93 mm as the mean segmentation error. Top-down approaches are presented by Yao et al. [20], Ghebreab et al. [25] and Klinder et al. [21], i.e. they start from global position and approximate shape of the spine, and use that information to better fit segmentation surfaces to actual vertebrae in the images. Yao et al. focus on routine chest and abdominal CT images. The spinal canal is extracted using a watershed algorithm and directed acyclic graph search. The vertebrae are segmented by using a four-part vertebra model. The spinal column was correctly partitioned in 67 out of 69 cases. Ghebreab et al. use manual initialization for first vertebra and global spine shape. It uses B-spline surfaces with 12×12 control points for surface representation. It uses statistical spine shape for initializing segmentation of an adjacent vertebra. The mean shapes of four different lumber vertebrae are independently constructed. The method was tested on six CT images, but execution time and precision were not given. Klinder et al. initialized the global spine position by an automated rib cage segmentation method. A statistical constellation model for vertebrae is applied on a global

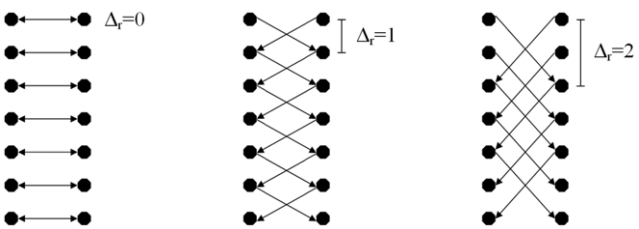

Figure 2. Intercolumn arcs that have been constructed with different delta values: $\Delta_r = 0$ (left), $\Delta_r = 1$ (middle) and $\Delta_r = 2$ (right).
doi:10.1371/journal.pone.0031064.g002

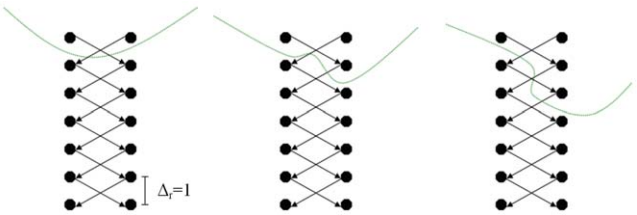

Figure 3. Basic concept of a cut (green) of intercolumn arcs between two rays for a delta value of one ($\Delta_r = 1$). Left and middle: same cost for a cut ($2\bullet\infty$). Right: higher cost for a cut ($4\bullet\infty$).
doi:10.1371/journal.pone.0031064.g003

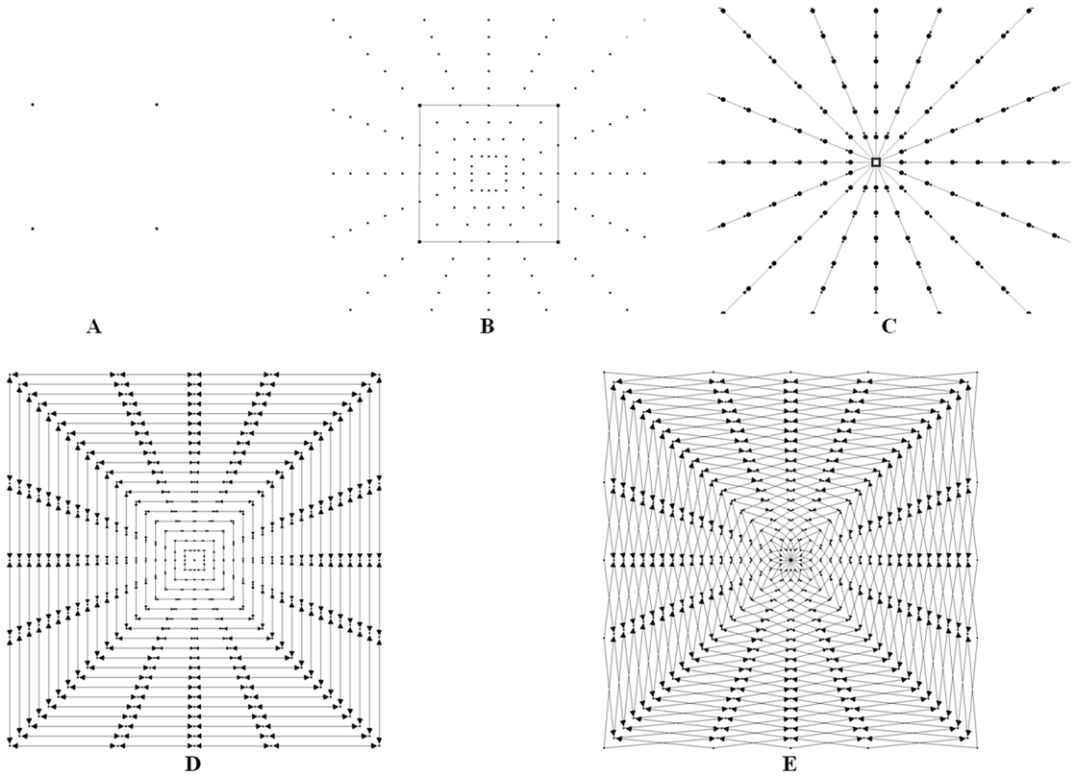

Figure 4. The principle graph construction for a square. A: square template defined by four corners. B: nodes set up with the square template. C: z-arcs A_z along the rays. D: r-arcs A_r between the rays ($\Delta_r = 0$). E: r-arcs A_r between the rays ($\Delta_r = 1$).
doi:10.1371/journal.pone.0031064.g004

scale to obtain an approximate position of individual vertebrae. Local adaptations of each vertebra are similar to the approach from Weese et al. The method was evaluated on ten thoracic CT datasets. The segmentation error was 1.0 ± 0.3 ($\mu \pm$s mm).

Some 2D methods avoid usage of computationally expensive operations and keep execution times within a few seconds [15] and [17]. Others have longer running times: forty seconds [16] and one minute [18]. Peng et al. [19] do not provide execution time. All existing 3D approaches have long running times: 1–15 minutes [22], 5–10 minutes [24], a few minutes [23] and for [21] similar to or more than [23] (not explicitly stated). Yao et al. [20] and Ghebreab et al. [25] do not provide execution time.

The paper is organized as follows. Section 2 presents the details of the proposed algorithm. Section 3 discusses the results of our experiments. Section 4 concludes the paper and outlines areas for future research.

Methods

The proposed segmentation algorithm starts by setting up a directed graph from a user-defined seed point that is located inside the object to be segmented. The basic principle was recently developed and used by the authors for a medical software system for volumetric analysis of different cerebral pathologies – glioblastoma multiforme (GBM) [26], pituitary adenomas [27] and cerebral aneurysms [28] – in MRI datasets [29]. However, these cerebral pathologies were spherical or elliptical shaped 3D objects [30] and therefore the segmentation scheme was not appropriate for our spine datasets. For better understanding of this paper the overall principle for GBM segmentation with a sphere template is presented in Figure 1: a polyhedron (left) is used to set up a 3D graph. Then, the graph is used to segment the GBM in a Magnetic Resonance Imaging (MRI) dataset.

To set up the graph, points are sampled along rays that are sent through the contour of a square template. The sampled points are the nodes $n \in V$ of the graph G(V, E) and $e \in E$ is the corresponding set of arcs. There are arcs between the nodes and arcs that connect the nodes to a source *s* and a sink *t* to allow the computation of a s-t cut (note: the source and the sink s, $t \in V$ are virtual nodes). The arcs $<v_i,v_j> \in E$ of the graph G connect two nodes v_i,v_j. There are two types of ∞-weighted arcs: z-arcs A_z and r-arcs A_r (Z is the number of sampled points along one ray $z = (0,\ldots,Z-1)$ and R is the number of rays sent out to the contour of an object template $r = (0,\ldots,R-1)$), where $V(x_n,y_n)$ is a neighbor of V(x,y) – in other words $V(x_n,y_n)$ and V(x,y) belong to two adjacent rays [31] and [32]:

$$\begin{aligned} A_z &= \{\langle V(x,y), V(x,y-1)\rangle \mid y > 0\} \\ A_r &= \{\langle V(x,y), V(x_n, \max(0, y-\Delta_r))\rangle\} \end{aligned} \quad (1)$$

The arcs between two nodes along a ray A_z ensure that all nodes below the contour in the graph are included to form a closed set (correspondingly, the interior of the object is separated from the exterior in the data). The arcs A_r between the nodes of different rays constrain the set of possible segmentations and enforce smoothness via the parameter Δ_r. The arcs for different delta values are presented in Figure 2: $\Delta_r = 0$ (left), $\Delta_r = 1$ (middle) and $\Delta_r = 2$ (right). The larger this parameter Δ_r is, the larger is the number of possible segmentations. In Figure 3 the basic concept of a cut (green) of intercolumn arcs between two rays for $\Delta_r = 1$ is presented. For the graphs on the left side and the middle the costs

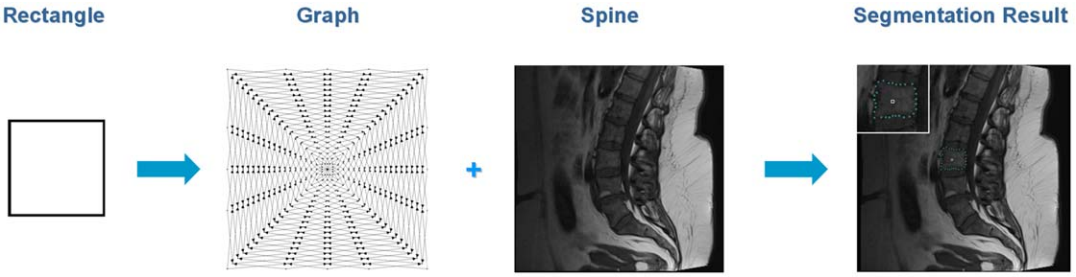

Figure 5. Overall workflow of the segmentation algorithm. A rectangle shape is used to set up a graph. The constructed graph is then used to segment the vertebrae in a Magnetic Resonance Imaging (MRI) scan.
doi:10.1371/journal.pone.0031064.g005

for a cut ($2 \bullet \infty$) are the same. However, for a cut like shown on the right side of Figure 3 the costs are higher ($4 \bullet \infty$).

After graph construction, the minimal cost closed set on the graph is computed via a polynomial time s-t cut [33]. The s-t cut creates an optimal segmentation of the object under influence of the parameter Δ_r that controls the stiffness of the resulting contour. A delta value of zero ensures that the segmentation result has exactly the form of the predefined template (square) – and the position of the template depends on the best fit to the image's texture. The weights w(x,y) for every arc between $v \in V$ and the sink or source are assigned in the following manner: weights are set to c(x,y) if z is zero; otherwise they are set to $c(x,y) - c(x,y-1)$, where c(x,y) is the absolute value of the intensity difference between an average texture value of the desired object and the texture value of the pixel at position (x,y) – for a detailed description, see [34], [35], [36] and [37]. The average grey value that is needed for the calculation of the costs and the graph's weights is essential for the segmentation result. Based on the assumption that the user-defined seed point is inside the object, the average gray value can be estimated automatically. Therefore, we integrate over a small square T of size d centered around the user-defined seed point (s_x, s_y):

$$\int_{-d/2}^{d/2} \int_{-d/2}^{d/2} T(s_x + x, s_y + y) dx dy \qquad (2)$$

Table 1. Comparison of manual and automatic segmentation results for nine vertebrae via the Dice Similarity Coefficient (DSC).

No.	Volume of vertebrae (mm^3)		Number of voxels		DSC (%)
	manual	automatic	manual	automatic	
1	417.236	378.662	1709	1551	90.78
2	438.721	397.705	1797	1629	90.83
3	461.914	427.49	1892	1751	88.99
4	457.275	439.453	1873	1800	92.02
5	510.498	490.723	2091	2010	93.05
6	430.908	481.201	1765	1971	87.37
7	404.541	402.832	1657	1650	90.35
8	414.795	377.686	1699	1547	90.39
9	247.803	242.92	1015	995	94.93

doi:10.1371/journal.pone.0031064.t001

The principle of the graph construction for a square is shown in Figure 4. Image A of Figure 4 shows the square template that is used to set up the graph. Image B presents the nodes that have been sampled along the rays that have been sent through the template's surface. Note that the distances between the nodes of one ray correlate with the distances between the template's center point (or for a later segmentation, the user-defined seed point) and the template surface. In other words, for every ray we have the same number of nodes between the center point and the object's border, but the length is different. In the images C, D and E, different ∞-weighted arcs are shown: C: the z-arcs A_z along the single rays, D: the r-arcs A_r between rays with a delta value of $\Delta_r = 0$. E: same as D only with a delta value of $\Delta_r = 1$.

Setting up the nodes of the graph with the user-defined template is the most difficult step of the proposed algorithm. Generating the arcs between the nodes and the source and the sink node is straightforward: there are the ∞-weighted arcs that depend on the geometry (intra column arcs) and the delta value (inter column arcs) used for the graph, and there are arcs that connect the nodes to the source s and the sink t. These arcs depend on the gray values of the nodes they connect – or rather they depend on the gray value difference to an adjacent node. To integrate the user-defined template into the construction of the graph, we need the coordinates in 2D describing the object that we want to segment (e.g. for a square the corner points of the square, see Figure 4 A). Using these coordinates, the center of gravity of the object is calculated, and the object is normalized with the maximum diameter, or rather with the coordinate that has the maximum distance to the center of gravity. After the user defines a seed point in the image, the normalized object is constructed with its center of gravity point located at the user-defined seed point. Then, rays are sent out radially from the seed point through the contour of the normalized object. To calculate the intersection points of the rays with the object, the object's contour has to be closed. In our implementation, the user has to provide the object's contour as 2D

Table 2. Summary of results: minimum, maximum, mean μ and standard deviation σ for manual and automatic spine segmentation.

	Volume of vertebrae (mm^3)		Number of voxels		DSC (%)
	manual	automatic	manual	automatic	
min	247.803	242.92	1015	995	87.37
max	510.498	490.723	2091	2010	94.93
$\mu \pm \sigma$	420.41 ± 72.22	404.3 ± 72.98	1722	1656	90.97 ± 2.2

doi:10.1371/journal.pone.0031064.t002

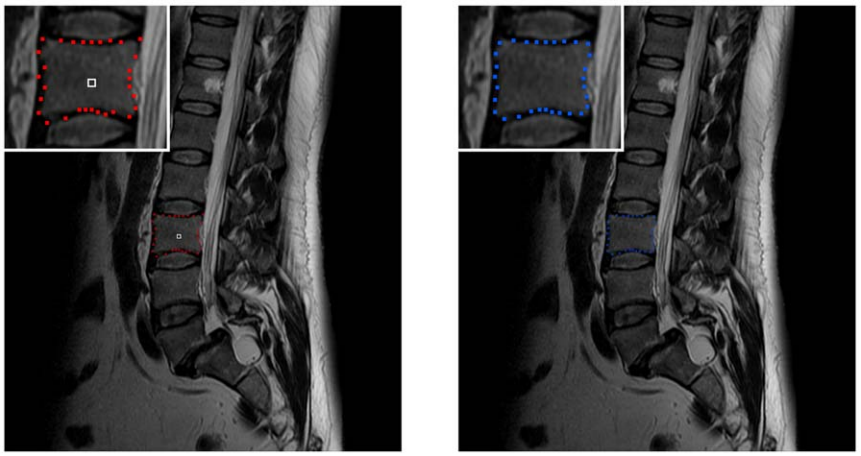

Figure 6. Example for smoothing a vertebra segmentation result. Left: 2D vertebra segmentation (red) of a Magnetic Resonance Imaging (MRI) dataset with a square template (number of rays = 30, number of nodes sampled per ray = 30 and delta value $\Delta_r = 4$). Right: nodes smoothed with a [0.25 0.5 0.25] kernel (one iteration).
doi:10.1371/journal.pone.0031064.g006

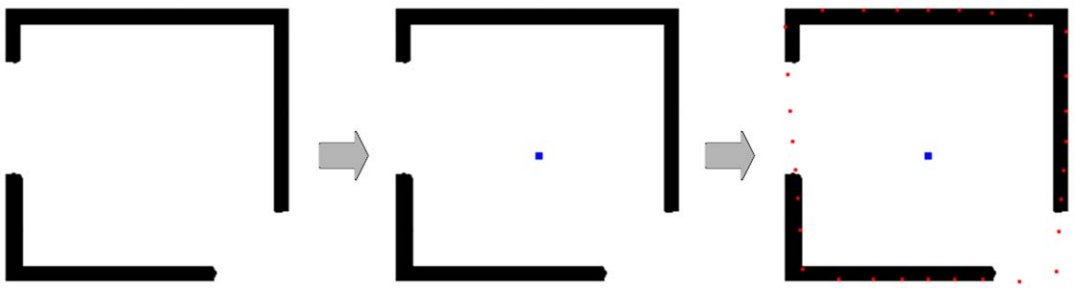

Figure 7. Segmentation of a rectangle where parts of the border are missing. Left: object to segment (black). Middle: user-defined seed point for the square-based segmentation (blue). Right: segmentation result (red). Note: even the missing corner in the lower right could be reconstructed.
doi:10.1371/journal.pone.0031064.g007

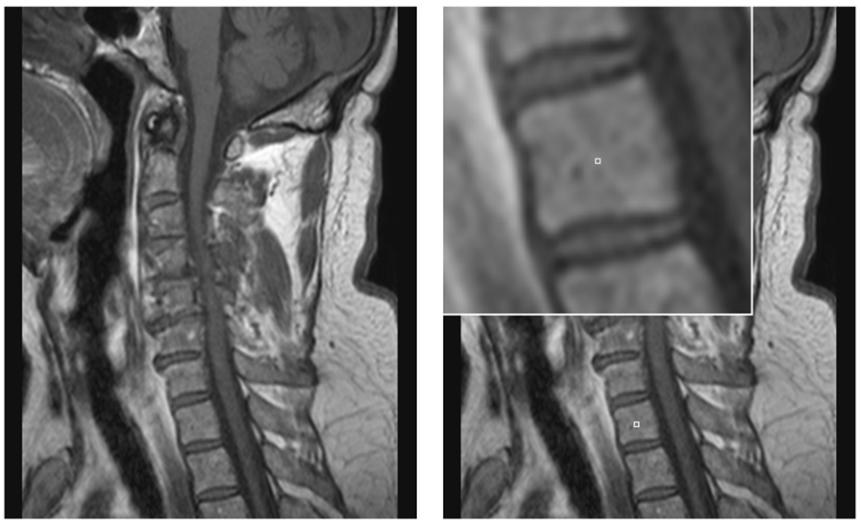

Figure 8. Example of a spine dataset and a user-defined seed point inside a vertebra of this dataset. Left: sagittal view of a Magnetic Resonance Imaging (MRI) spine dataset. Right: location of a user-defined seed point (white) inside a vertebra.
doi:10.1371/journal.pone.0031064.g008

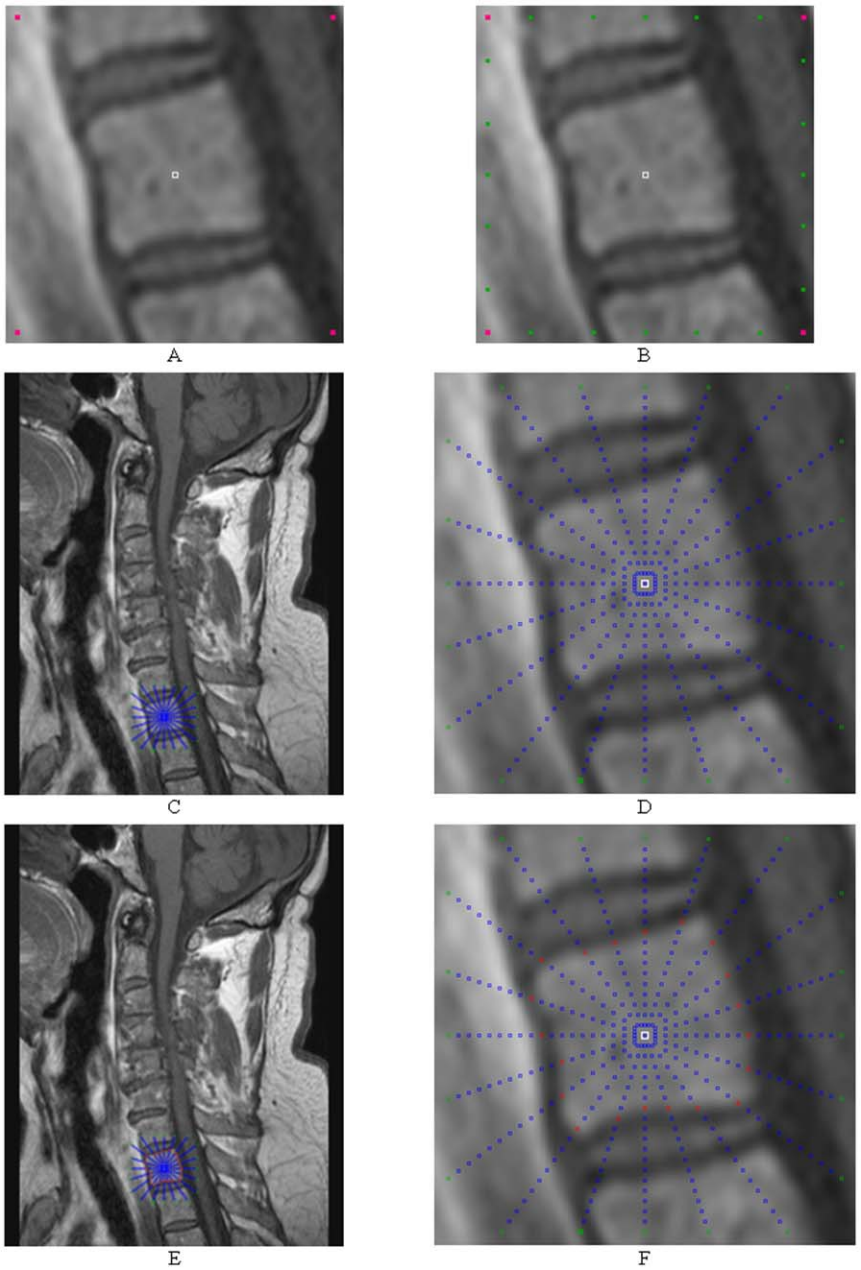

Figure 9. Step-by-step construction of a graph and the segmentation of a vertebra. A: seed point (white) and corners of a square template (magenta). B: intersection points where the send out rays cut the square template (green). C and D: sampled nodes for the graph (blue). E: segmentation results (red).
doi:10.1371/journal.pone.0031064.g009

coordinates ordered in clockwise direction, so we just have to connect the points one after the other and finally connect the last point with the first point to get a closed 2D contour.

The interception point of one ray with the object provides the distance between the nodes for this ray, because all rays have the same number of nodes from the center of gravity point to the intersection with the contour. For intersections that are located closer to the center of gravity point we get smaller distances, and for intersections that are located farer away from the center of gravity point we get larger distances. Calculating the intersection of a ray with a 2D object is straightforward, since it is simply a line-line intersection. One line is the actual ray and the other line is one straight line between two points of the predefined template.

Results

To implement the presented segmentation algorithm, the MeVisLab-Platform (available: http://www.mevislab.de, accessed: 2012 Jan 2) has been used; the algorithm has been implemented in C++ as an additional MeVisLab-module. Although the foci of the prototyping platform MeVisLab are medical applications, it is possible to process images from other fields. Even when the graph was set up with a few hundred rays and hundreds of nodes where

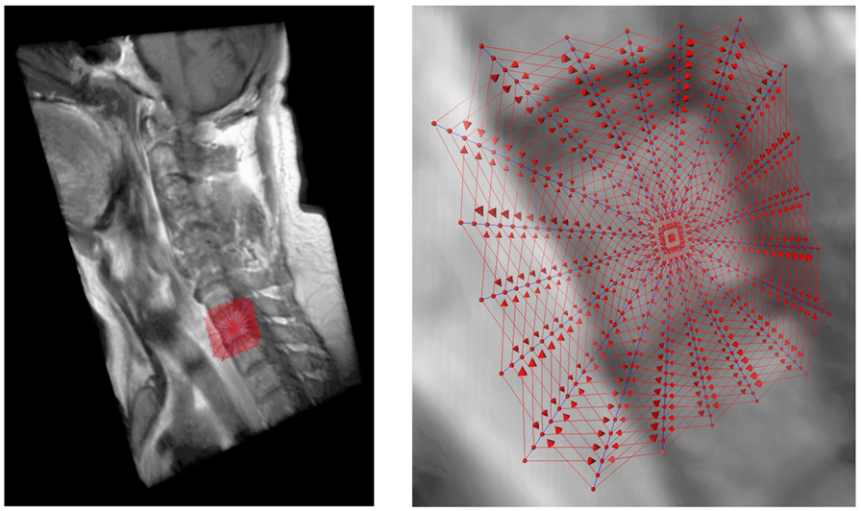

Figure 10. 3D visualization of a Magnetic Resonance Imaging (MRI) spine dataset with a graph that has been used to segment one vertebra: intracolumn arcs (blue) and intercolumn arcs (red) with 20 rays, 20 sampled nodes per ray and a delta value of two ($\Delta_r = 2$).
doi:10.1371/journal.pone.0031064.g010

sampled along each ray, the overall segmentation (sending rays, graph construction and mincut computation) for our implementation took only a few seconds on an Intel Core i5-750 CPU, 4×2.66 GHz, 8 GB RAM, Windows XP Professional x64 Version, Version 2003, Service Pack 2.

For 2D evaluation, we used several synthetic and real images. From the clinical routine we had more than 14 datasets from over 12 patients available for testing. The overall workflow of the introduced segmentation algorithm is presented in Figure 5 (from left to right): a rectangle shape is used to set up a graph and the constructed graph is used to segment the vertebrae in a Magnetic Resonance Imaging scan.

The ground truth of the vertebrae boundaries were manually extracted by two clinical experts (neurological surgeons) with several years of experience in spine surgery and afterwards compared with the automatic segmentation results of the proposed scheme yielding an average Dice Similarity Coefficient of 90.97±2.2% (Table 1 and Table 2). The Dice Similarity Coefficient is a measure for spatial overlap of different segmentation results and is commonly used in medical imaging studies to quantify the degree of overlap between two segmented objects A and R, given by:

$$DSC = \frac{2 \cdot V(A \cap R)}{V(A) + V(R)} \tag{3}$$

The Dice Similarity Coefficient is the relative volume overlap between A and R, where A and R are the binary masks from the automatic A and the reference R segmentation. $V(\cdot)$ is the volume (in mm^3) of voxels inside the binary mask, by means of counting the number of voxels, then multiplying with the voxel size. Tables 1 and Table 2 provide detailed results for several vertebrae areas of a MRI spine dataset that have been segmented with the presented algorithm. Table 1 shows the segmentation results for: volume of vertebrae (mm^3), number of

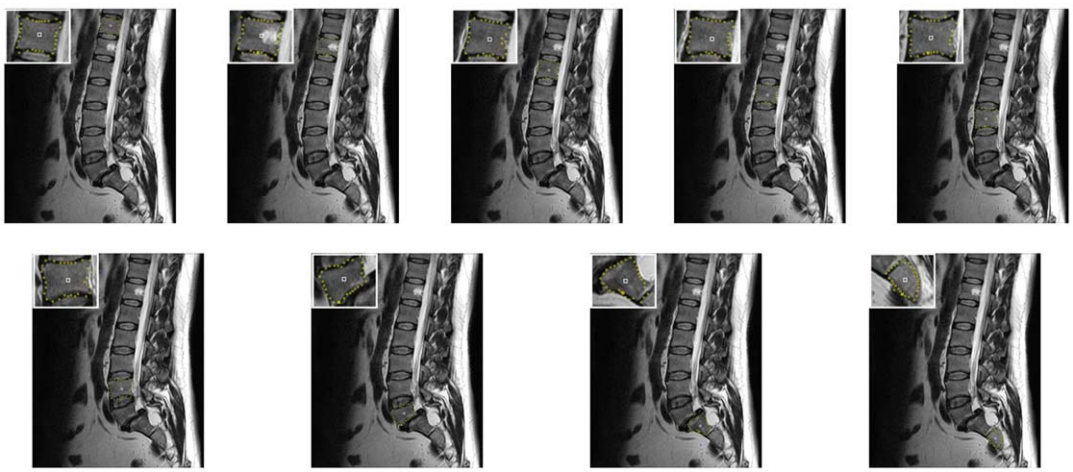

Figure 11. 2D vertebrae segmentation (yellow) of a Magnetic Resonance Imaging (MRI) dataset with a square template (number of rays = 30, number of nodes sampled per ray = 30 and delta value $\Delta_r = 4$).
doi:10.1371/journal.pone.0031064.g011

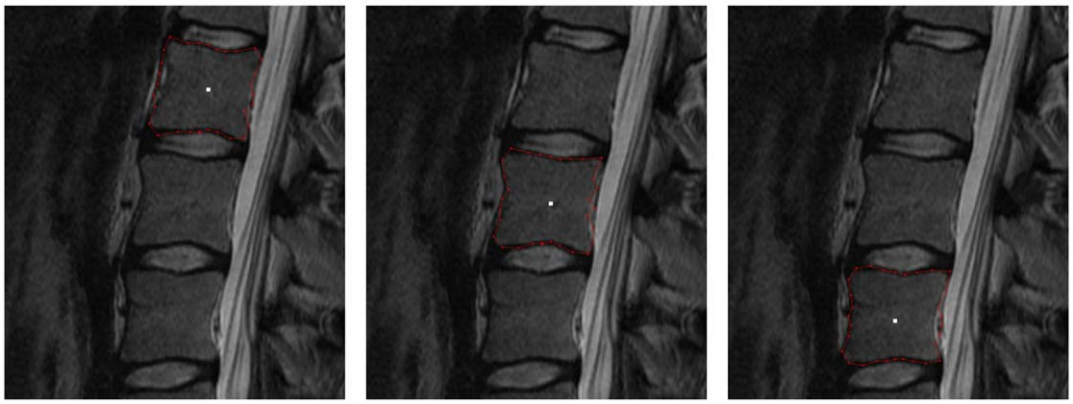

Figure 12. 2D vertebrae segmentation (red) of a Magnetic Resonance Imaging (MRI) dataset with a square template (number of rays = 30, number of nodes sampled per ray = 30 and delta value $\Delta_r = 4$).
doi:10.1371/journal.pone.0031064.g012

voxels and Dice Similarity Coefficient for nine vertebrae areas. In Table 2, the summary of results: minimum, maximum, mean μ and standard deviation σ for the nine vertebrae from Table 1 are provided. For the automatic segmentation we used the same parameter set for all vertebrae: 30 rays, 30 nodes sampled per ray and a delta value of four ($\Delta_r = 4$).The maximal length of the rays that have been sent out from the user-defined see point has been 35 mm. Furthermore we used a [0.25 0.5 0.25] kernel (one iteration) to smooth the resulting nodes that have been calculated (Figure 6).

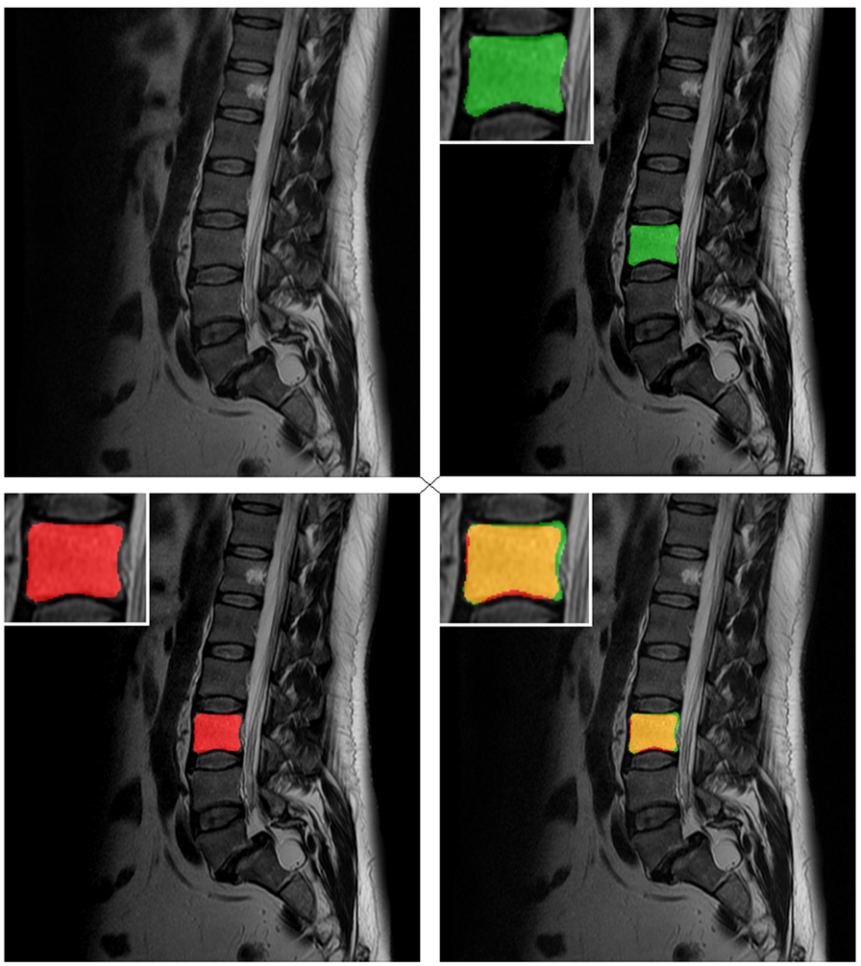

Figure 13. Direct comparison of an automatic segmentation with a manual segmentation. Upper right: manual segmentation mask of a vertebra (green). Lower left: automatic segmentation mask (red). Lower right: superimposed segmentation masks (manual and automatic).
doi:10.1371/journal.pone.0031064.g013

In Figure 7 the segmentation of a rectangle where parts of the border are missing is presented. On the left side of Figure 7 the object that has to be segmented (black) is shown. In the middle image the user-defined seed point (blue) for the square-based segmentation has been placed. The segmentation result (red) is shown in the rightmost image, whereby even the missing corner – in the lower right – has been reconstructed by the segmentation approach. For the segmentation we used the following parameter set: the number of rays was set to 30, the number of nodes sampled per ray was 100 and the delta value Δ_r was set to one.

Figure 8 shows on the left side a sagittal view of a MRI spine dataset. On the right side of the Figure 8 an user-defined seed point (white) has been set inside a vertebra. Figure 9 presents now step-by-step the construction of a graph and the segmentation of the vertebra of Figure 8:

A: seed point (white) and corners of a square template (magenta)

B: intersection points where the send out rays cut the square template (green)

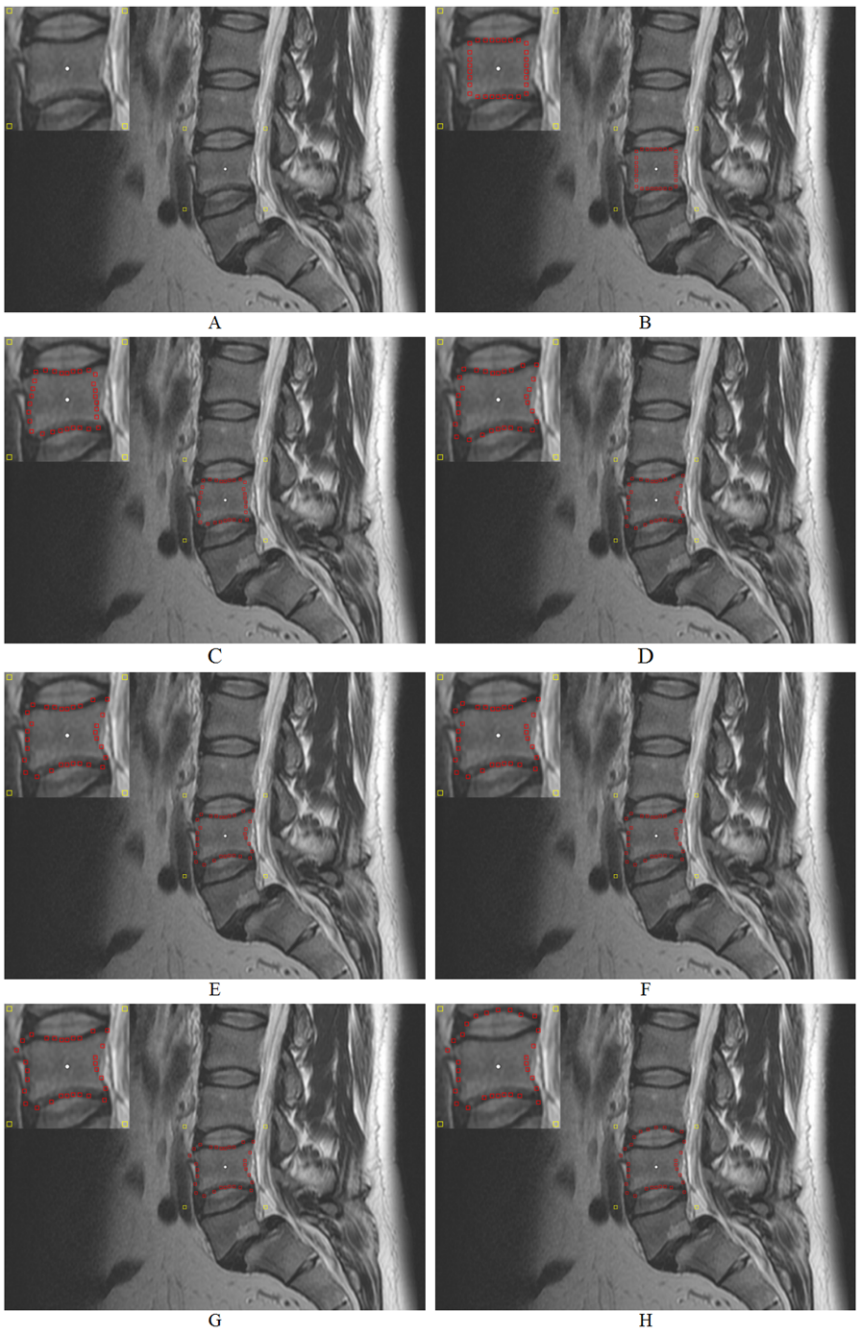

Figure 14. Example how the ∞-weighted arcs A_r (controlled via the delta value Δ_r) affect the segmentation performance. A: initial seed point (white) and corners of the square template (yellow). B–H: segmentation results (red) for different delta values $\Delta_r = 0,\ldots,\Delta_r = 6$ (number of rays = 30, number of nodes sampled per ray = 40 and diameter = 40 mm).
doi:10.1371/journal.pone.0031064.g014

C and **D**: sampled nodes for the graph (blue)

E: segmentation results (red)

A 3D visualization of a MRI spine dataset with a graph that has been used to segment one vertebra is displayed in Figure 10. The intracolumn arcs of the graph are drawn in blue and the intercolumn arcs are drawn in red. The following parameter settings have been used for graph construction: 20 rays, 20 sampled nodes per ray and $\Delta_r = 2$.

The segmentation results for several vertebrae of patients are shown in Figure 11 and Figure 12. The segmentations have been performed in 2D with a standard square template. Although most sides of the vertebrae are curved inwards and some vertebrae are rotated in Figure 11, the segmentation results for a square template are already reasonable. Furthermore, we have used the same parameter set for all vertebrae in Figure 11 and Figure 12, which means that the same number of rays (30), the same number of nodes sampled per ray (30) and the same delta value ($\Delta_r = 4$) for all segmentations have been used for both datasets.

Figure 13 shows the segmentation results in form of a mask for a vertebra. The original dataset is presented in the upper left of Figure 13. The manual segmentation mask of a vertebra (green) is shown in the upper right image. The lower left image presents the result of the automatic segmentation (red). Finally, the lower right image shows the superimposed manual and automatic segmentation masks.

Figure 14 shows an example how the ∞-weighted arcs A_r (controlled via the delta value Δ_r) affect the segmentation performance. Image A in Figure 14 presents the initial seed point in white inside a vertebra of a MRI spine dataset. Image A also presents the corners of the square template in yellow that has been set up with a diameter of 40 mm around the seed point. The images B-H of Figure 14 show the segmentation results in red for different delta values $\Delta_r = 0,\ldots,\Delta_r = 6$ whereby the number of rays (30) and the number of nodes sampled per ray (40) have not been changed.

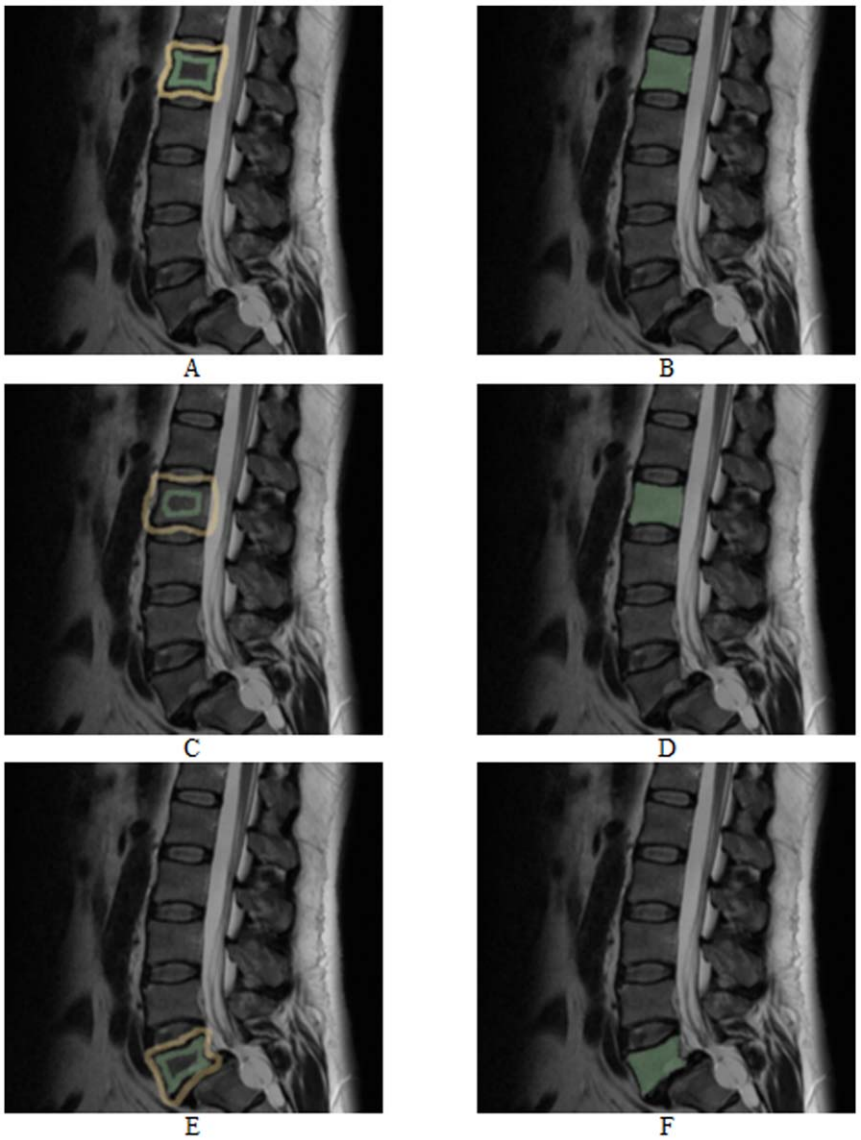

Figure 15. Vertebrae segmentation with the *GrowCut* approach. The images on the left side (A, C and E) show examples for a manual initialization of the algorithm: vertebra (green) and background (yellow). The images on the right side (B, D and F) present the corresponding segmentation results (green).
doi:10.1371/journal.pone.0031064.g015

In image B the delta value is zero ($\Delta_r = 0$) and therefore the resulting contour is a square, because the cut has to be on the same node level. The position of the square depends only on the gray values and edges of the image. The delta value in image C was set to one ($\Delta_r = 1$) and therefore the cut has more options and must not be on the same node level. As you can see in image C the resulting contour (red) already fits to the lower and upper border of the vertebra. However, the delta value is still too small – and therefore the possible resulting contours are to stiff – to segment the whole vertebra (see the left and right border of the vertebra). With a delta value of two ($\Delta_r = 2$) used to get the segmentation result in image D, the flexibility is high enough to segment also the left and right border of the vertebra. For the next three images E, F and G the delta values have even been increased: $\Delta_r = 3$ (E), $\Delta_r = 4$ (F) and $\Delta_r = 5$ (G). These higher delta values enables the cut to return a more "detailed" contour like the bulge in the upper left corner of image G. But higher delta values also increase the risk for an over-segmentation. That happened for a delta value of six ($\Delta_r = 6$) in the last image H, where the upper border of the segmentation result already returns the lower border of an adjacent vertebra.

As stated in the background paragraph, there have been published several methods – like deformable models and statistic approaches – for vertebra segmentation in the literature. All papers present detailed segmentation results and in almost all cases the computational time for their algorithms is also provided, which seem both – segmentation and time – to be similar to our results. Therefore, we decided to compare and discuss our approach with an interactive multi-label *N-D* image segmentation method called *GrowCut* from Vezhnevets and Konouchine [38]. To the best of our knowledge there has nothing been published about using *GrowCut* for spine segmentation. For testing *GrowCut* with our datasets we used an implementation that is freely available as an module for the medical platform *3DSlicer* [39] and [40]. *3DSlicer* – or *Slicer* – is a free, open source software package for visualization

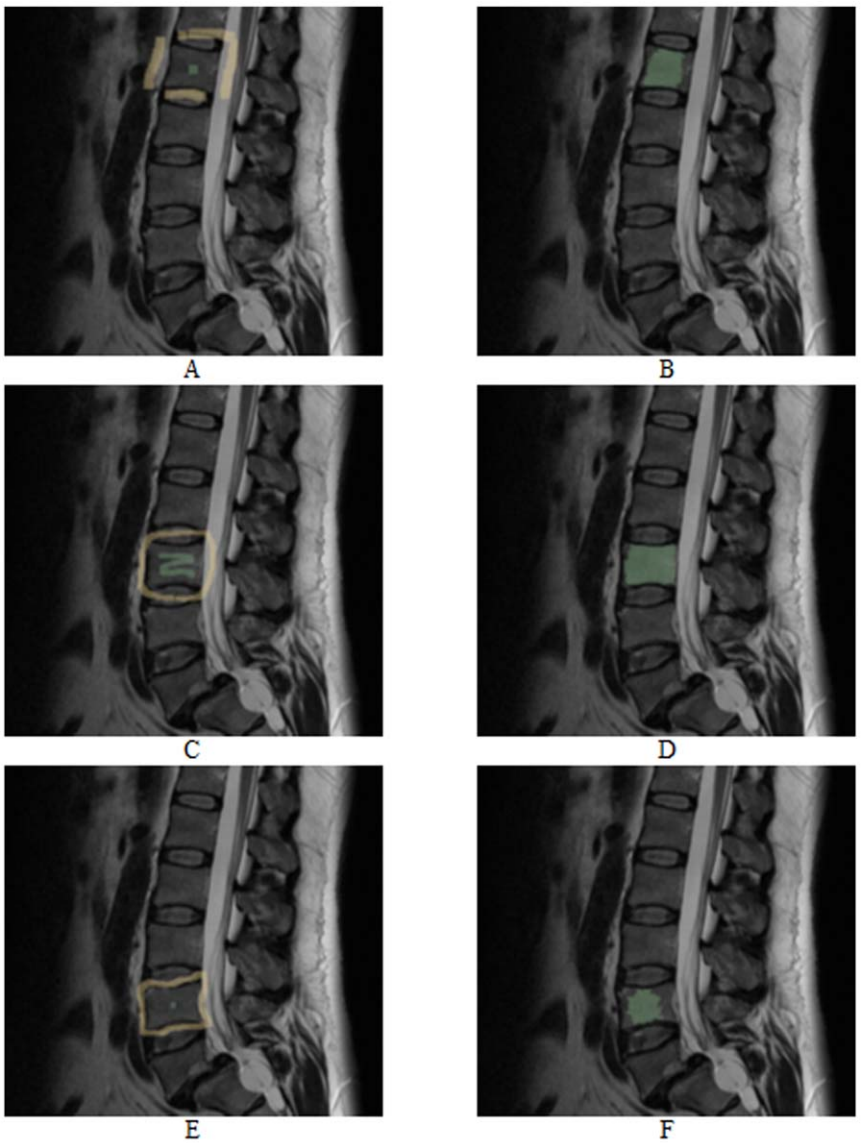

Figure 16. As for Figure 15, vertebrae segmentation with the *GrowCut* approach. The images on the left side (A, C and E) show examples for a manual initialization of the algorithm: vertebra (green) and background (yellow). The images on the right side (B, D and F) present the corresponding segmentation results (green).
doi:10.1371/journal.pone.0031064.g016

and image analysis primarily used in the medical domain and has been developed by the Surgical Planning Laboratory (SPL) of the Brigham and Women's Hospital in Boston. To use *GrowCut* for vertebra segmentation the user has to label a part of the vertebra and a part of the background with a simple brush tool.

Figure 15 and Figure 16 present vertebrae segmentations with the *GrowCut* approach. The images on the left side (A, C and E) show examples for a manual initialization of the algorithm with the vertebrae in green and the background in yellow. The images on the right side (B, D and F) present the corresponding segmentation results in green. As you can see in Figure 15 the *GrowCut* algorithm can provide very precise results for a careful initialization. However, for a rougher initialization it can provide not satisfactory results as you can see in Figure 16 – at least for Figure B and F. We did not do an exact evaluation with the *Dice Similarity Coefficient* for the *GrowCut*, because the segmentation results depend on the user initialization. But we can already tell that for someone who knows the algorithm and knows how to deal with the initialization, the *DSC* will be around ninety percent compared with a pure manual segmentation. A big advantage of the *GrowCut* – at least for the implementation we tested – is that a user doesn't have to define any parameters. In contrast, our approach has parameters which you have to deal with, but for someone who is used to the algorithm that can be handled. A disadvantage for the *GrowCut* is the time consuming and precise initialization you sometimes need to archive good results. In contrast, our approach only needs one centered seed point inside the vertebra.

Discussion

In this contribution, we have presented a template-based segmentation scheme for 2D objects. To the best of our knowledge, this is the first approach where the nodes of a graph-based algorithm have been arranged according to a predefined square template in a non-uniform and a non-equidistant manner on an image. Using this new type of segmentation algorithm, it is even possible to reconstruct missing corners in an object. In addition, the scaling of an object is irrelevant for the presented method. Experimental results for several 2D images based on Magnetic Resonance Imaging datasets consisting of vertebrae have indicated that the proposed algorithm requires very less computing time and gives already reasonable results even for a very simple cost function.

There are several areas of future work. For example, the cost function for the weights can be improved. Another possibility is to increase the sampling rate for the nodes near an object's border, because with an equidistant sampling rate (along the rays), there are more nodes near the user-defined seed point and less nodes going farther out. The user-defined seed point position that is located inside the object is also an issue that has to be analyzed in the future, e.g. for some images the seed point has to be chosen very carefully. In general, the presented approach provides better results if the seed point is located closer to the center of the vertebra and our method will fail or perform bad if the seed point is located very close to the border of the vertebra. One option to improve the presented algorithm is performing the whole segmentation iteratively: after segmentation has been performed, the center of gravity of the segmentation can be used as a new seed point for a new segmentation and so on. This might lead to more robustness with respect to the initialization. Furthermore, we plan to integrate our manual refinement method that takes advantage of the basic design of graph-based image segmentation algorithms [41] and [42]. Moreover, we want to enhance our segmentation algorithm to 3D. Possible is a cube template like shown in Figure 17.

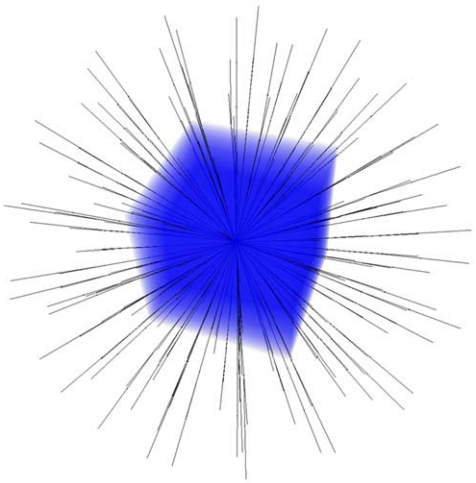

Figure 17. Principle enhancement of the introduced 2D segmentation algorithm with a cube shape to a 3D segmentation algorithm (Cube-Cut).
doi:10.1371/journal.pone.0031064.g017

Acknowledgments

First of all, the authors want to thank all reviewers for their thoughtful comments. The authors would also like to thank the members of the *Slicer Community* for their contributions and moreover Harini Veeraraghavan and Jim Miller from *GE* for developing the *GrowCut* segmentation module under *Slicer*. Moreover, the authors would like to thank the physicians Dr. med. Barbara Carl and Thomas Dukatz from the neurosurgery department of the university hospital of Marburg for performing the manual slice-by-slice segmentations of the spine images and therefore providing the ground truth for the evaluation. Furthermore, the authors would like to thank Fraunhofer MeVis in Bremen, Germany, for their collaboration and especially Horst K. Hahn for his support.

Author Contributions

Conceived and designed the experiments: JE. Performed the experiments: JE. Analyzed the data: JE TD MK. Contributed reagents/materials/analysis tools: CN. Wrote the paper: JE TK TD DZ BF.

References

1. Seifert S, Barbu A, Zhou K, Liu D, Feulner J, et al. (2009) Hierarchical parsing and semantic navigation of full body CT data. SPIE – Medical Imaging Conference, (7258):725902-725902-8.
2. Kass M, Witkin A, Terzopoulos D (1987) Snakes - Active Contour Models. International Journal of Computer Vision 1(4): 321–331.
3. McInerney T, Terzopoulos D (1996) Deformable models in medical image analysis: a survey. Medical Image Analysis 1(1): 91–108.
4. Li K, Wu X, Chen DZ, Sonka M (2006) Optimal Surface Segmentation in Volumetric Images – A Graph-Theoretic Approach. IEEE Transactions on Pattern Analysis and Machine Intelligence (PAMI) 28(1): 119–134.
5. Veksler O (2008) Star Shape Prior for Graph-Cut Image Segmentation. European Conference on Computer Vision (ECCV), Springer Press. pp 454–467.
6. Ishikawa H, Geiger D (1998) Segmentation by Grouping Junctions. IEEE Computer Society Conference on Computer Vision and Pattern Recognition (CVPR), IEEE Press. pp 125–131.
7. Grady L, Schwartz EL (2006) Isoperimetric Graph Partitioning for Image Segmentation. IEEE Transactions on Pattern Analysis and Machine Intelligence (PAMI) 28(3): 469–475.
8. Zou KH, Warfield SK, Bharatha A, Tempany CMC, Kaus MR, et al. (2004) Statistical Validation of Image Segmentation Quality Based on a Spatial Overlap Index: Scientific Reports. Academic Radiology 11(2): 178–189.
9. Sampat MP, Wang Z, Markey MK, Whitman GJ, Stephens TW, et al. (2006) Measuring intra- and inter-observer agreement in identifying and localizing structures in medical images. IEEE Inter Conf Image Processing, 4 pages.

10. Jeanneret B, Odstrcilik E, Forster T (1997) Degenerative spinal canal stenosis in lumbar spine: clinical view and treatment [Article in German]. Acta Chir Orthop Traumatol Cech 64(3): 133–43.
11. Joaquim AF, Sansur CA, Hamilton DK, Shaffrey CI (2009) Degenerative lumbar stenosis: update. Arq Neuropsiquiatr 67(2B): 553–8.
12. Hicks GE, Morone N, Weiner DK (2009) Degenerative lumbar disc and facet disease in older adults: prevalence and clinical correlates. Spine (Phila Pa 1976) 34(12): 1301–6.
13. Richards PJ, George J, Metelko M, Brown M (2010) Spine computed tomography doses and cancer induction. Spine (Phila Pa 1976) 35(4): 430–3.
14. Jackson RP, Cain JE, Jr., Jacobs RR, Cooper BR, McManus GE (1989) The neuroradiographic diagnosis of lumbar herniated nucleus pulposus: II. A comparison of computed tomography (CT), myelography, CT-myelography, and magnetic resonance imaging. Spine (Phila Pa 1976) 14(12): 1362–7.
15. Michopoulou SK, Costaridou L, Panagiotopoulos E, Speller R, Panayiotakis G, et al. (2009) Atlas-based segmentation of degenerated lumbar intervertebral discs from MR images of the spine. IEEE Trans Biomed Eng 56(9): 2225–31.
16. Shi R, Sun D, Qiu Z, Weiss KL (2007) An efficient method for segmentation of MRI spine images. IEEE/ICME International Conference on Complex Medical Engineering, CME, IEEE Press. pp 713–717.
17. Huang SH, Chu YH, Lai SH, Novak CL (2009) Learning-based vertebra detection and iterative normalized-cut segmentation for spinal MRI. IEEE Trans Med Imaging 28(10): 1595–605.
18. Carballido-Gamio J, Belongie SJ, Majumdar S (2004) Normalized cuts in 3-D for spinal MRI segmentation. IEEE Trans Med Imaging 23(1): 36–44.
19. Peng Z, Zhong J, Wee W, Lee JH (2005) Automated Vertebra Detection and Segmentation from the Whole Spine MR Images. Conf Proc IEEE Eng Med Biol Soc 3: 2527–30.
20. Yao J, O'Connor SD, Summers RM (2006) Automated spinal column extraction and partitioning. 3rd IEEE International Symposium on Biomedical Imaging: Nano to Macro, IEEE Press. pp 390–393.
21. Klinder T, Wolz R, Lorenz C, Franz A, Ostermann J (2008) Spine segmentation using articulated shape models. In Medical Image Computing and Computer-Assisted Intervention (MICCAI) Metaxas D, Axel L, Fichtinger G, Székely G, eds. vol. 5241 of Lecture Notes in Computer Science Springer Press. pp 227–234.
22. Stern D, Vrtovec T, Pernus F, Likar B (2011) Segmentation of vertebral bodies in CT and MR images based on 3D deterministic models. Proc SPIE Medical Imaging, Summers RM, van Ginneken B, eds. volume 7963.
23. Weese J, Kaus M, Lorenz C, Lobregt S, Truye R, et al. (2001) Shape constrained deformable models for 3D medical image segmentation. Information Processing in Medical Imaging, Insana M, Leahy R, eds. vol. 2082 of Lecture Notes in Computer Science, Springer Press. pp 380–387.
24. Hoad CL, Martel AL (2002) Segmentation of MR images for computer-assisted surgery of the lumbar spine. Physics in Medicine and Biology 47(19): 3503.
25. Ghebreab S, Smeulders AW (2004) Combining strings and necklaces for interactive three-dimensional segmentation of spinal images using an integral deformable spine model. IEEE Transactions on Biomedical Engineering 51(10): 1821–1829.
26. Kleihues P, Louis DN, Scheithauer BW, Rorke LB, Reifenberger G, et al. (2002) The WHO classification of tumors of the nervous system. J Neuropathol Exp Neurol 61(3): 215–229.
27. Weber MA, Zoubaa S, Politi M, Grunwald I, Essig M (2007) Sellar tumors [Article in German]. Der Radiologe, Springer Press 47(6): 492–500.
28. Molyneux AJ, Kerr RS, Yu LM, Clarke M, Sneade M, et al. (2002) International Subarachnoid Aneurysm Trial (ISAT) of neurosurgical clipping versus endovascular coiling in 2143 patients with unruptured intracranial aneurysms: a randomised trial. Lancet 360: 1267–1274.
29. Egger J, Kappus C, Freisleben B, Nimsky C (2011) A Medical Software System for Volumetric Analysis of Cerebral Pathologies in Magnetic Resonance Imaging (MRI) Data. Journal of Medical Systems (JOMS), Springer Press, 13 pages.
30. Egger J, Bauer MHA, Kuhnt D, Carl B, Kappus C, et al. (2010) Nugget-Cut: A Segmentation Scheme for Spherically- and Elliptically-Shaped 3D Objects. 32nd Annual Symposium of the German Association for Pattern Recognition (DAGM), LNCS 6376, Springer Press. pp 383–392.
31. Egger J, Dukatz T, Freisleben B, Nimsky C (2012) A Semiautomatic Approach to Determine the Area of Vertebrae in MRI-Scans (in German). Proceedings of Bildverarbeitung für die Medizin (BVM), Berlin, Germany, Springer Press, 6 pages (accepted for publication).
32. Egger J, Viswanathan AN, Kapur T (2011) Bladder Segmentation for Interstitial Gynecologic Brachytherapy with the Nugget-Cut Approach. 4th NCIGT and NIH Image Guided Therapy Workshop, Arlington, Virginia, USA.
33. Boykov Y, Kolmogorov V (2004) An Experimental Comparison of Min-Cut/Max-Flow Algorithms for Energy Minimization in Vision. IEEE Transactions on Pattern Analysis and Machine Intelligence 26(9): 1124–1137.
34. Egger J, O'Donnell T, Hopfgartner C, Freisleben B (2008) Graph-Based Tracking Method for Aortic Thrombus Segmentation. Proceedings of 4th European Congress for Medical and Biomedical Engineering, Engineering for Health, Springer Press. pp 584–587.
35. Egger J, Freisleben B, Setser R, Renapuraar R, Biermann C, et al. (2009) Aorta Segmentation for Stent Simulation. 12th International Conference on Medical Image Computing and Computer Assisted Intervention (MICCAI), Cardiovascular Interventional Imaging and Biophysical Modelling Workshop, 10 pages.
36. Bauer MHA, Egger J, O'Donnell T, Freisleben B, Barbieri S, et al. (2010) A Fast and Robust Graph-based Approach for Boundary Estimation of Fiber Bundles Relying on Fractional Anisotropy Maps. 20th International Conference on Pattern Recognition (ICPR), IEEE Press, 4 pages.
37. Egger J, Zukic D, Bauer MHA, Kuhnt D, Carl B, et al. (2010) A Comparison of Two Human Brain Tumor Segmentation Methods for MRI Data. Proceedings of 6th Russian-Bavarian Conference on Bio-Medical Engineering, State Technical University, Moscow, Russia, 4 pages.
38. Vezhnevets V, Konouchine V (2005) GrowCut - Interactive multi-label N-D image segmentation. Proceedings of Graphicon. pp 150–156.
39. DSlicer – a free, open source software package for visualization and image analysis. Surgical Planning Laboratory (SPL), Brigham and Women's Hospital, Harvard Medical School, Boston, Massachusetts, USA. Available: http://www.slicer.org/ Accessed 2012 Jan 2.
40. DSlicer Wiki, GrowCutSegmentation-Documentation-3.6 Available: http://www.slicer.org/slicerWiki/index.php/Modules:GrowCutSegmentation-Documentation-3.6 Accessed 2012 Jan 2.
41. Egger J, Colen RR, Freisleben B, Nimsky C (2011) Manual Refinement System for Graph-Based Segmentation Results in the Medical Domain. Journal of Medical Systems (JOMS), Springer Press, 11 pages.
42. Egger J, Bauer MHA, Kuhnt D, Kappus C, Carl B, et al. (2010) A Flexible Semi-Automatic Approach for Glioblastoma multiforme Segmentation. Biosignal Processing Conference, DGBMT, 4 pages.

The International Journal of **Medical Robotics** and **Computer Assisted Surgery**

THE INTERNATIONAL JOURNAL OF MEDICAL ROBOTICS AND COMPUTER ASSISTED SURGERY
Int J Med Robotics Comput Assist Surg (2012)
Published online in Wiley Online Library (wileyonlinelibrary.com) **DOI:** 10.1002/rcs.1415

ORIGINAL ARTICLE

Integration of the OpenIGTLink Network Protocol for image-guided therapy with the medical platform MeVisLab

Jan Egger[1,2,3]*
Junichi Tokuda[1]
Laurent Chauvin[1]
Bernd Freisleben[2]
Christopher Nimsky[3]
Tina Kapur[1]
William Wells[1]

[1]*Brigham and Women's Hospital and Harvard Medical School, Department of Radiology, Boston, Massachusetts 02115, USA*

[2]*University of Marburg, Math. and Computer Science, Marburg, Germany*

[3]*University of Marburg, Neurosurgery, Marburg, Germany*

*Correspondence to: J. Egger, Brigham and Women's Hospital and Harvard Medical School, Department of Radiology, Boston, Massachusetts 02115, USA.
E-mail: egger@bwh.harvard.edu, egger@med.uni-marburg.de

Received: 7 December 2011

Abstract

Background OpenIGTLink is a new, open, simple and extensible network communication protocol for image-guided therapy (IGT). The protocol provides a standardized mechanism to connect hardware and software by the transfer of coordinate transforms, images, and status messages. MeVisLab is a framework for the development of image processing algorithms and visualization and interaction methods, with a focus on medical imaging.

Methods The paper describes the integration of the OpenIGTLink network protocol for IGT with the medical prototyping platform MeVisLab. The integration of OpenIGTLink into MeVisLab has been realized by developing a software module using the C++ programming language.

Results The integration was evaluated with tracker clients that are available online. Furthermore, the integration was used to connect MeVisLab to Slicer and a NDI tracking system over the network. The latency time during navigation with a real instrument was measured to show that the integration can be used clinically.

Conclusions Researchers using MeVisLab can interface their software to hardware devices that already support the OpenIGTLink protocol, such as the NDI Aurora magnetic tracking system. In addition, the OpenIGTLink module can also be used to communicate directly with Slicer, a free, open source software package for visualization and image analysis. Copyright © 2012 John Wiley & Sons, Ltd.

Keywords OpenIGTLink; MeVisLab; image-guided therapy; surgical navigation; system; slicer

Introduction

Image-guided therapy (IGT) represents the use of medical images obtained either during or prior to a treatment, based on the assumption that knowledge of the location and orientation of a therapeutic process will allow a more specific therapy (1). In the past few years, image-guided therapy has been successfully applied to many different clinical applications including aneurysm surgery (2), deep brain stimulation (DBS) (3,4), robotic radiation delivery for the treatment of liver metastases (5), biopsy (6,7), and radiotherapy (IGRT) of prostate cancer (8). Locating surgical tools relative to the patient's body by using position and orientation tracking systems is now common. This can be achieved with optical (9), electromagnetic (10) or ultrasonic (11,12) sensors. Furthermore, this can also be achieved with image acquisition using real-time ultrasound, computed

tomography (CT) or magnetic resonance imaging (MRI). For visualization and guidance, this localization and image information is transferred from acquisition devices to navigation software. However, among the devices and the software in the operating room (OR) environment, standardization of communication is still a common issue in image-guided therapy (13). Furthermore, with the increasing number of medical software applications being developed by researchers worldwide under different medical (prototyping) environments, such as Slicer (14), MeVislab (15), OsiriX (16), the XIP-Builder (17) – and the previous version of the XIP-Builder, the Rad-Builder (18,19) – standardization of information and communication technology is of increasing importance in order for these research applications to robustly interact with the devices in the operating room. Such standardization will also enable communication and information exchange between applications that have been developed for different medical environments; it will allow different research teams to work together to collaboratively solve open image-guided therapy problems while using their individual software development platforms. Furthermore, there has been a strong demand for communication standards among devices and navigation software with increasing research on robotic devices that support image-guided interventions to allow sharing of information such as target positions, images and device status. In order to tackle this problem, Tokuda *et al*. (20) defined an open, simple and extensible peer-to-peer network protocol for IGT called OpenIGTLink.

The advantage of OpenIGTLink is its simple specification, initially developed through a collaboration of academic, clinical and industrial partners for developing an integrated robotic system for MRI-guided prostate interventions (21). It was designed for use in the application layer on the TCP/IP stack, allowing researchers to develop a prototype system that integrates multiple medical devices using the standard network infrastructure. Unlike existing interconnection standards for medical devices, e.g. ISO 11 073/IEEE 1073 Standard for Medical Device Communication (22), CANOpen (EN 50 325–4) (23), Controller-Area Network (CAN) (ISO 118 988) (24), and Medical Device Plug-and-Play (MD PnP) (25), the OpenIGTLink protocol itself does not include mechanisms to establish and manage a session. It only defines a set of messages, which is the minimum data unit of this protocol. An OpenIGTLink message contains all information necessary for interpretation by the receiver. The message begins with a 58-byte header section, which is common to all types of data, followed by a body section. The format of the body section varies by the data type that is specified in the header section. Since any compatible receiver can interpret the header section, which contains the size and the data type of the body, every receiver can gracefully handle any message, even those with an unknown data type, by ignoring incompatible messages without the system crashing. Hence, this two-section structure allows developers to define their own data types while maintaining compatibility with other software that cannot interpret their user-defined data types. This simple message mechanism eases the development of OpenIGTLink interfaces and improves compatibility, thus it is suitable for prototyping a clinical system consisting of multiple devices and software connected via standard TCP/IP network. For a detailed description of the standard data types, see the publication of Tokuda *et al.* (20). Further information is available on the web page provided by the National Alliance for Medical Image Computing (NA-MIC) (26).

In this paper, we present the integration of OpenIGTLink with the medical prototyping platform MeVisLab. MeVisLab is a framework for the development of image processing algorithms and visualization and interaction methods, with a focus on medical imaging. The integration of OpenIGTLink into MeVisLab has been realized by developing a software module in the C++ programming language. As a result, researchers using MeVisLab now have the possibility to connect to hardware devices that already support the OpenIGTLink protocol, such as the NDI Aurora magnetic tracking system. In addition, the OpenIGTLink module can also be used to communicate directly with Slicer, a free, open source software package for visualization and image analysis. The integration has been tested with tracker clients available online. Moreover, the integration was used to connect MeVisLab to Slicer and a commercial NDI tracking system over the network.

Material and Methods

This section describes our approach for integrating OpenIGTLink with MeVisLab.

Thereby, the integration has been realized as a client–server model. A client–server model is a distributed application where a resource or service is provided by a server to a resource or service requester which is called the client. The basic concept of OpenIGTLink and the interaction of OpenIGTLink with different devices is shown in Figure 1. Image-guided therapy often relies on communication among sensors, devices and computers. For example, an intraprocedural imaging scanner, e.g. MRI (see upper right image in Figure 1) transfers real-time images to navigation software (see upper left image in Figure 1) to allow the clinicians to monitor the progress of the procedure; positions of surgical instruments are tracked by an optical position sensor device (see lower left image in Figure 1) and transferred to navigation software to indicate where those instruments are with respect to pre-procedural images; a robotic interventional assistance device (see lower right image in Figure 1) receives commands from navigation software and returns the current position of its end-effector or the current status of the device as feedbacks. Keeping Figure 1 in mind, the overall workflow of the OpenIGTLink/MeVisLab integration starts with the image data (see Figure 2). The image data is provided to a user-defined MeVisLab network. To load image data into a user-defined MeVisLab network, several modules such as OpenImage or ImageLoad exist that allow us to process various image formats, including the standard format for

DOI: 10.1002/rcs

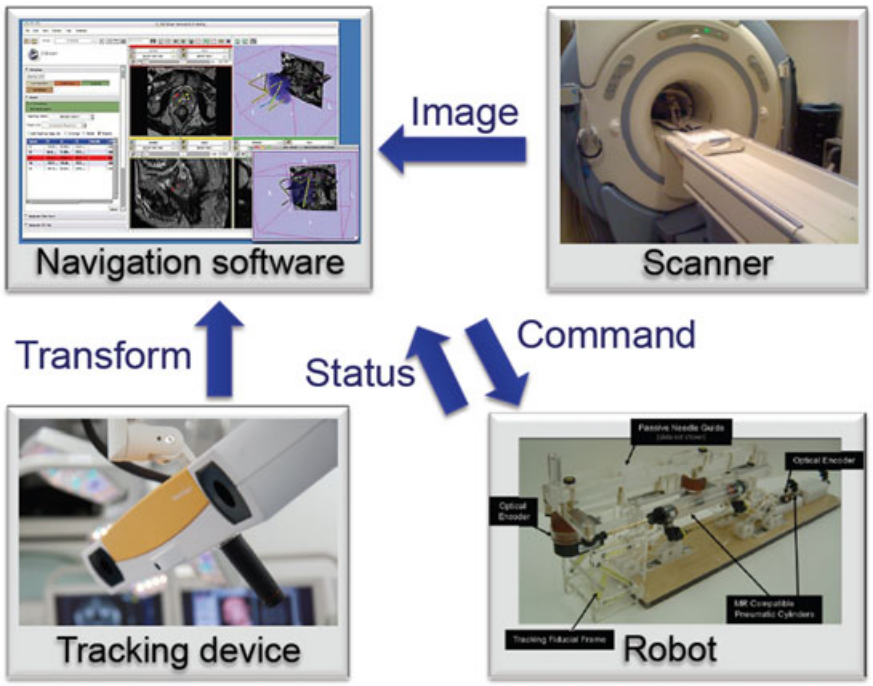

Figure 1. The basic concept of OpenIGTLink (see also http://www.na-mic.org/Wiki/index.php/OpenIGTLink)

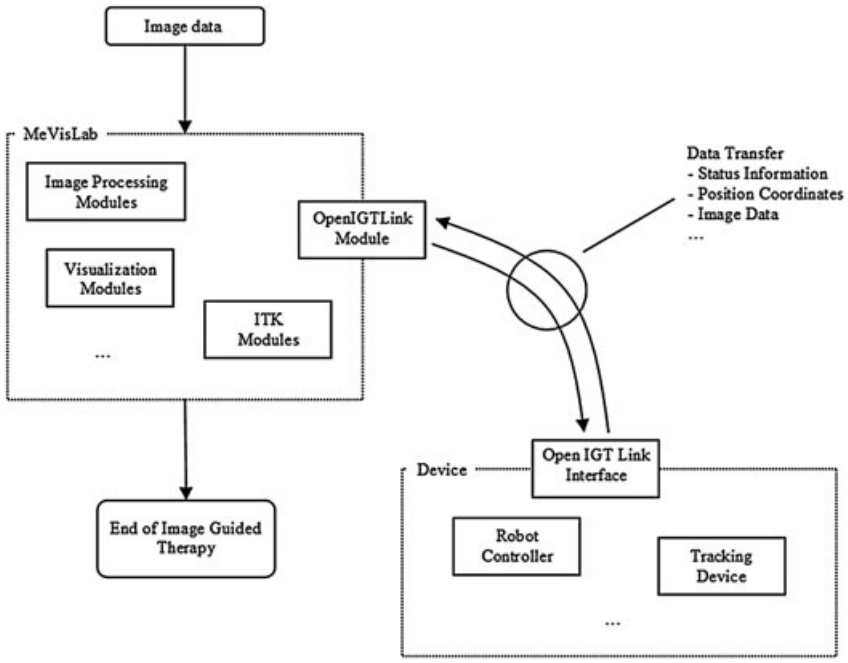

Figure 2. The overall workflow of the presented system, starting with the image data and finishing with the end of Image Guided-Therapy (IGT)

medical image data, called DICOM (Digital Imaging and Communications in Medicine, http://medical.nema.org). Besides the data fields (for example information about the images and diagnostic findings) DICOM also defines the syntax and semantic of commands and messages between DICOM compatible hardware. Nowadays, DICOM is the most widely used format for medical image data for communication between commercial software, open-source software, and devices/imaging systems. To continue processing the loaded image data, MeVisLab offers a collection of modules, such as image processing modules, visualization modules and also ITK (Insight Toolkit) (http://www.itk.org) modules (27). In addition, MeVisLab allows users to integrate their own modules, for example, under Microsoft

DOI: 10.1002/rcs

Visual Studio in C++. For integration of the OpenIGTLink protocol with MeVisLab, a new module has been developed. As shown in Figure 2, the OpenIGTLink module handles the data exchange between MeVisLab and an external device such as a robot controller or 6-DOF position and orientation tracker. During the data exchange, different types of information such as the status, the image data or the position coordinates are transferred via the OpenIGTLink protocol. The overall workflow of Figure 2 concludes with the end of the IGT procedure.

The following sections describe the implementation of the OpenIGTLink module under MeVisLab in detail. The module has been realized as an image processing module (ML) under MeVisLab and the basic source code has been created with the Project Wizard from MeVisLab.

Implementation of the Constructor

The following code example characterizes how the constructor of the OpenIGTLink module has been implemented. The initialization Module(1, 1) in the header of the constructor implementation indicates the number of input and output image connections for the OpenIGTLink module. In our example, we have one input and one output image connection. However, this is not a fixed number, and if a different number is required, the generation of more input and output connections is also possible. ML_TRACE_IN is a status and tracing macro that is set up by default if the Project Wizard of MeVisLab is used for generating the basic source code for a user's own module. The OpenIGTLink module provides several GUI components including an input field for the network port and a button to start listening to the client and setting up the TCP connection. To implement those components, we first suppress calls of the handleNotification function (see next code example) on field changes and to avoid side effects during the initialization phase, we obtain a pointer to the container of all the module's fields. Then, we create different fields, e.g. for the port and the start button. For visualization and further processing of the received data through the OpenIGTLink connection, we additionally create and add an output field for the data of the client (in this case the transformation data). Finally, the calls of the handleNotification function on field changes is reactivated again at the end of the constructor.

```
// constructor
OpenIGTLink::OpenIGTLink()
 : Module(1, 1)
{
 ML_TRACE_IN("OpenIGTLink::OpenIGTLink()"); //
status and tracing macro

 // suppress calls of handleNotification on field
changes to avoid side effects during initialization
phase
 handleNotificationOff();

 // get a pointer to the container of all the module's
fields
 FieldContainer *fields = getFieldContainer();
...

 // create different fields, e.g. for the port and a
start button
 _port = fields->addInt("port");
 _start = fields->addNotify("start");

 // create and add an output field for the transfor-
mation data of the client
 _transformation = new SoTransform();
 (_outSoTransformation =
                fields->addSoNode("outputTransfor-
mation"))->setSoNodeValue(_transformation);

 // reactivate calls of handleNotification on field
changes
 handleNotificationOn();
}
```

Handling Notifications of the OpenIGTLink Module

The next code example describes how the important parts of the handleNotification function for the OpenIGTLink module can be implemented. The handleNotification function is called on user interactions, e.g. the start button. However, the function is not called when new data is available through the OpenIGTLink mechanism, that is handled inside the handleNotification function when the start button has already been pressed. Just as with the constructor, ML_TRACE_IN is a status and tracing macro that is set up by default if the Project Wizard from MeVisLab is used for generating the basic source code for a user's own module. If the start button has been pressed by the user, the initialization for setting up the connection and the data transfer is prepared. For example, the user-defined port value is used to create the server socket. Afterwards, if the socket is valid – and therefore the client is connected – the different data types are checked for incoming data. This procedure follows the standard way of using the OpenIGTLink library; there are tutorials and a several code snippets available online (for example, see http://www.na-mic.org/Wiki/index.php/OpenIGTLink/Library/Tutorial). To keep the code snippet simple, we only list the *if*-condition for the TRANSFORM data type. If the TRANSFORM data type has been received from the client, the ReceiveTransform function is called with the socket und the message header (headerMsg) as parameters.

```
// handle changes of a field
void OpenIGTLink::handleNotification (Field *field)
{
 ML_TRACE_IN("OpenIGTLink::handleNotification
()"); // status and tracing macro
```


DOI: 10.1002/rcs

```
...

 if (field == _start)
 {
  int port = _port->getIntValue();
  igtl::ServerSocket::Pointer serverSocket;
  serverSocket = igtl::ServerSocket::New();
  int r = serverSocket->CreateServer(port);
...

  igtl::Socket::Pointer socket;
...

  if (socket.IsNotNull()) // if client connected
  {
...

   // check data type and receive data body
   if (strcmp(headerMsg->GetDeviceType(), "TRANS-
FORM") == 0)
   {
    ReceiveTransform(socket, headerMsg);
   }
...

  }
...
 }
...
}
```

```
// handle and process data type TRANSFORM
int OpenIGTLink::ReceiveTransform(igtl::Socket *
socket, igtl::MessageHeader * header)
{
 std::cerr << "Receiving TRANSFORM data type." <<
std::endl;

 // create a message buffer to receive transform
data
 igtl::TransformMessage::Pointer transMsg;
 transMsg = igtl::TransformMessage::New();
 transMsg->SetMessageHeader(header);
 transMsg->AllocatePack();
...

 _transformation->enableNotify(false); // turning
notification of this field off
 _transformation->setMatrix( SbMatrixValue ); //
setting value
 _transformation->enableNotify(true); // turning
notification of this field on

 // force all inventor sensors to be triggered and do
a refresh on all viewers
 SoDB::getSensorManager()->processDelayQueue
(false);

 // marks an instance as modified, simulating a change
to it this will notify all auditors of the instance
 _transformation->touch();
...
}
```

Processing the TRANSFORM Data Type

The third code example illustrates the implementation of the ReceiveTransform function that is called to handle and process the data type TRANSFORM. The function has two parameters: a socket and the message header that are passed by the function call inside the handleNotification function (see previous section and code example). First, a message buffer is created inside the ReceiveTransform function to receive the transform data. This procedure follows the standard method of using the OpenIGTLink library as is described in the tutorials and complete code examples available online. Next, the notification of the transformation field – that has been created inside the constructor – has to be turned off. Then, the transformation value received by the client is set to the corresponding output field of the OpenIGTLink module. Afterwards, the notification of the transformation field is turned on again. Accordingly, all inventor sensors are forced to be triggered and do a refresh on all viewers. An inventor sensor is an Inventor object that watches for various types of events and invokes a user-supplied callback function when these events occur. Additionally, the transformation field is marked as modified, simulating a change to notify all auditors of the instance.

Description of Modules and Connections

Figure 3 shows the modules and connections that have been used for realizing the OpenIGTLink protocol under the medical prototyping platform MeVisLab. Overall, the data and communication flow goes from the bottom to the top. It starts with the OpenImage module which can be applied by the user to load an image, for example, in the DICOM format. After the image is loaded it is automatic passed via an output (right triangle (1)) to the OpenIGTLink module. The main module in the MeVisLab network is the OpenIGTLink module that has several inputs (lower area) and outputs (upper area (2)). One input (the lower left one, triangle (3)) is used for the image data that is provided by an OpenImage module as previously described. The transformation data received from the client is passed on via the third output from the left (upper row) of the OpenIGTLink module to a so called SoGroup module. The transformation data influences a 3D cylinder that is also connected with the SoGroup module. The SoExaminerViewer module in turn gets the transformed cylinder and visualizes it in 3D in a window where several user interactions and settings are

DOI: 10.1002/rcs

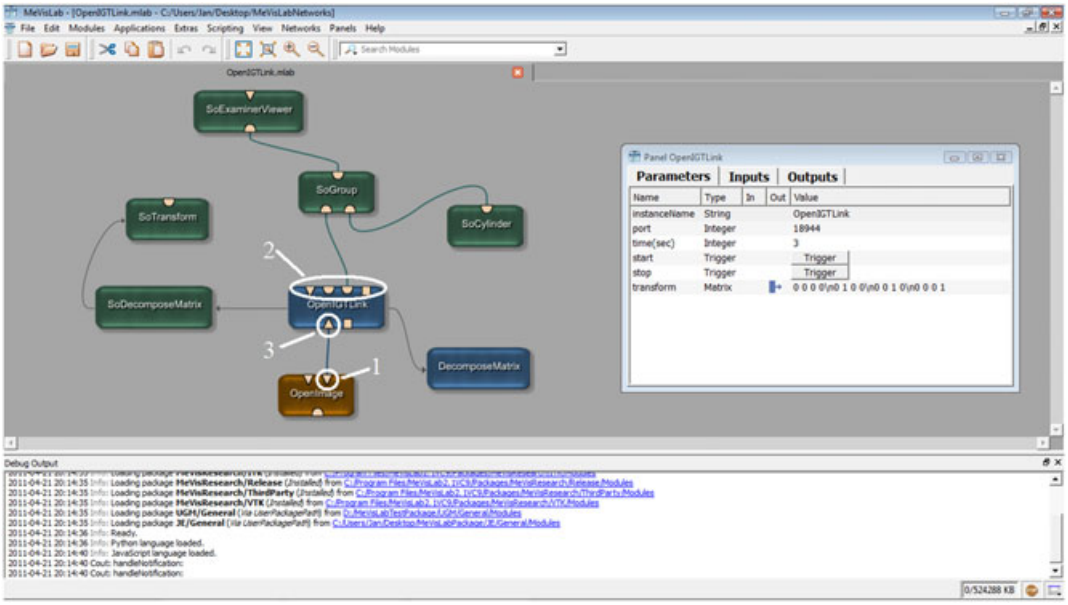

Figure 3. Modules and connections that have been used for realizing OpenIGTLink under the medical prototyping platform MeVisLab (see http://www.mevislab.de/)

possible. An additional transform field is used to analyze the transform data from the client with the decomposed matrices modules. However, these modules are not necessary for the processing of the client data, because it is directly available at one of the module's output. On the right side of the screenshot of Figure 3, the interface of the OpenIGTLink module with all its parameter settings and buttons is shown. The OpenIGTLink module with all its inputs and outputs is shown in detail in Figure 4, where the lower two connections are the inputs. For our implementation, we set up an input for image data and for data structures. The data structures can be used, for example, for marker lists – a marker list is a list of MeVisLab XMarker objects which consists of a 6D Position, a 3D Vector, a Type and a Name property. The upper four connections are the outputs of the OpenIGTLink module. One output, for example, can be used for the image data that has been received by the client via the OpenIGTLink protocol. The next two outputs are OpenInventor outputs that are used to provide only the rotation or the whole transformation for the tracker that has been provided by the client over the OpenIGTLink protocol. Finally, the OpenIGTLink module in the presented example also has an output connection for data structures like marker lists or seed points. Figure 3 shows the interface of the OpenIGTLink module with all its parameters and settings realized as a server, so the tracker clients could connect to it. We also realized our MeVisLab integration as a client. Therefore, the MeVisLab integration connects itself to a sever. We used this integration to connect to a real tracker system from NDI. However, for the realization as a client one more parameter has been used, which was the IP address of the server. For the IP address we set up an additional field in the interface of the OpenIGTLink module where the user can define it manually. After the user starts the client the IP address from the interface field is passed to the handleNotification function (see section Handling notifications of the OpenIGTLink module) and is then used to connect the client socket to the server.

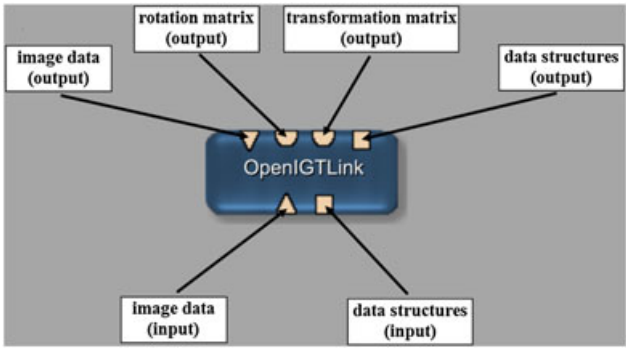

Figure 4. The OpenIGTLink module with its inputs and outputs realized as an ML module in C++ under MeVisLab

Specification of the Main Data Structures

As previous mentioned, we only list the *if*-condition for the TRANSFORM data type to keep the code snippet simple and clear. However, besides the TRANSFORM data type the OpenIGTLink protocol defines overall five default types: 'IMAGE', 'POSITION', 'STATUS' and 'CAPABILITY'. The main data structures are introduced in the following paragraph, for a detailed description see the publication of Tokuda *et al.* (20). The IMAGE format in the OpenIGTLink protocol supports 2D or 3D images with metric information, including image matrix size, voxel size, coordinate system type, position and orientation. The POSITION data type is used to transfer position and orientation information. The data are a combination of three-dimensional (3D) vector for the position and quaternion for the orientation.

DOI: 10.1002/rcs

Although equivalent position and orientation can be described with the TRANSFORM data type, the POSITION data type has the advantage of smaller data size. Therefore it is more suitable for pushing high frame-rate data from tracking devices. The STATUS data type is used to notify the receiver about the current status of the sender. The data consist of status code in a 16-bit unsigned integer, subcode in a 64-bit integer, error name in a 20 byte-length character string, and a status message. The CAPABILITY data type lists the names of message types that the receiver can interpret. Although the OpenIGTLink protocol guarantees that any receiver can at least skip messages with unknown type and continue to interpret the following messages, it is a good idea to get the capability information at system start-up to ensure application-level compatibility of the various devices (20). All these data structures can be used for the connection between the OpenIGTLink and MeVisLab and therefore transfer different information between a hardware device and MeVisLab based software.

Results

To use the OpenIGTLink library under the MeVisLab platform (Version 2.1, 2010-07-27 Release), we implemented an ML MeVisLab module in C++ with Microsoft Visual Studio 2008 (Version 9.0.21022.8 RTM). Figure 5 shows a screenshot of the MeVisLab prototype when a client provides tracker coordinates. The tracker coordinates from a tracker client are shown in the command window on the left side of Figure 5. The 3D visualization window in Figure 5 belongs to a SoExaminerViewer of MeVisLab that was used to visualize a cylinder whose location is connected with the tracker coordinates from a tracker client. In our evaluation, we used the simulator programs that come with the OpenIGTLink library. This includes, for example, a TrackerClient that works as a TCP client and is an example that illustrates how to send dummy tracking coordinates to a server. The tracker coordinates from the client could be displayed in real time with a laptop that has an Intel Atom Z530 CPU, 1.60 GHz, 2 GB RAM, Windows Vista Home Premium x32 Version, Version 2007, Service Pack 1. Note that even if Microsoft Windows Vista is not officially listed under the supported platforms of the OpenIGTLink library, we were able to successfully build, execute and use the simulator programs also under Windows Vista.

The frame rates for the SoExaminerViewer were measured with the SoShowFPS module from MeVisLab. The module was directly connected with the visualization module and superimposes the actual frame per second rate into the rotating tracker. With the introduced laptop configuration, we could achieve 35 fps on the average which is sufficient for the clinical requirements. The detailed times (min, max and mean) in milliseconds (ms) for the transfer and the visualization of 100 packets (via the data type TRANSFORM) from a tracker client to MeVisLab is presented in Table 1 (the overall mean and standard deviation was 30.77 ± 1.79 ms). Similar results could be achieved when we send TRANSFORM data types from the laptop to a tracker server – NDI tracking system – over a network. For the transfer and the visualization of 100 packets we measured 19.28 ± 1.43 ms (min = 17.56 ms and max = 24.06 ms). However, these time results also depend on the kind of 3D object that is rendered and visualized – as shown in Figure 5 we visualized a simple cylinder. Therefore, we also measured the time without transferring the data to the visualization module, which was 1.48 ± 0.22 ms (min = 1.35 ms and max = 2.86 ms).

Discussion

In this contribution, we have described the integration of the OpenIGTLink network protocol for image-guided

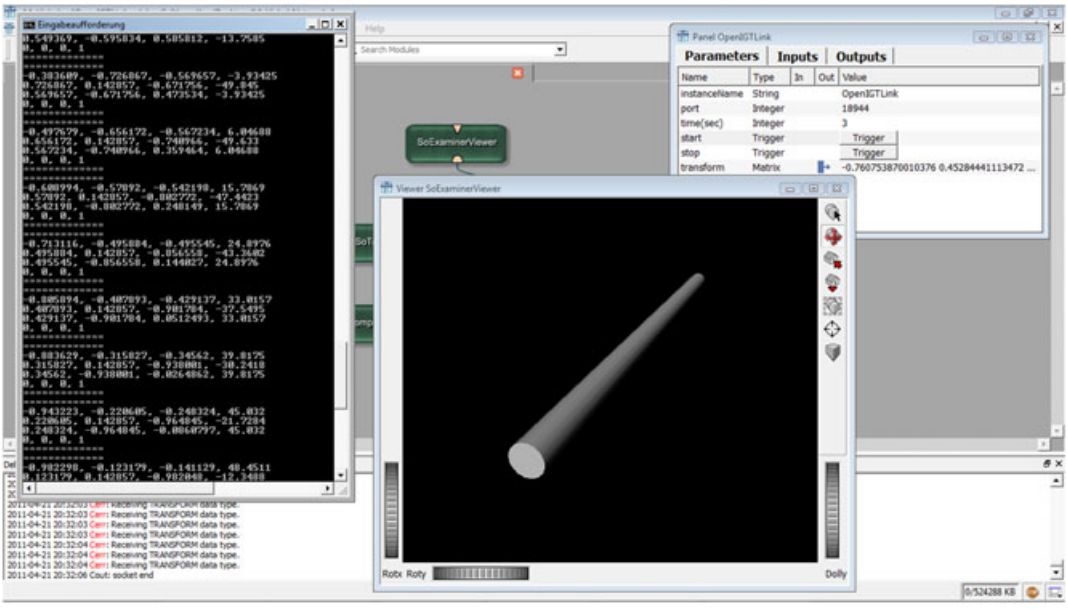

Figure 5. Screenshot of the MeVisLab prototype and a client that provides tracker coordinates

DOI: 10.1002/rcs

Table 1. Time (min, max and mean) in milliseconds (ms) for the transfer and visualization of 100 packets (via the data type TRANSFORM) from a tracker client to MeVisLab

Run No.	1	2	3	4	5	6	7	8	9	10
min	9.34	10.76	9.39	8.15	9.71	8.39	8.25	9.69	9.46	6.66
max	51.86	41.76	43.28	52.15	43.43	39.34	56.93	45.19	67.72	85.96
mean	29.66	30.14	30.01	30.24	30.09	29.98	31.86	29.70	30.45	35.54

therapy (IGT) with the medical prototyping platform MeVisLab. MeVisLab is a non open-source framework for the development of image processing algorithms and visualization and interaction methods, with a focus on medical imaging and the OpenIGTLink protocol is a new, open, simple and extensible network communication protocol for image-guided therapy. The protocol allows users to transfer transform, image and status messages as a standardized mechanism to connect software and hardware. To the best of our knowledge, the solution developed is the first approach to successfully integrate OpenIGTLink with MeVisLab. Researchers using MeVisLab now have the possibility to connect to hardware devices that already support the OpenIGTLink protocol, such as the NDI Aurora magnetic tracking system (28). The integration has been tested with tracker clients that are available online. Another possible application would be the integration of commercial FDA-approved surgical navigation system with research prototype software built on top of the MeVisLab platform (29). OpenIGTLink communication enables sharing pre- and intra-operative images as well as instrument tracking information between two systems online. The presented integration allows of combination of approved systems and prototype systems that are still under research. This means that researchers can explore new image processing and visualization techniques on MeVisLab in the clinical environment, while performing standard surgical planning and image guidance on the commercial system. In fact, an OpenIGTLink interface has become available as an option for research sites in a popular FDA-approved surgical navigation system provided by BrainLAB AG (30).

There are several areas of future work. For example, the latency and CPU load during image data transfers should be evaluated under MeVisLab by varying the data size of images. Moreover, several IGT applications apart from the already available IGT applications, such as the ultrasound navigation system, the tracking devices and navigation software and the MRI-compatible robot system for prostate intervention, will be available soon and therefore should be integrated and evaluated using the OpenIGTLink protocol. Finally, we plan to use the OpenIGTLink protocol for the communication between Slicer and MeVisLab and test the proposed solution under different operating systems such as Linux.

Acknowledgements

The authors would like to thank Fraunhofer MeVis in Bremen, Germany, for their collaboration and especially Professor Dr Horst K. Hahn for his support.

This work is supported by NIH 2R01CA111288-06, 5P41RR019703-07, 5P01CA067165-13, 5U54EB005149-07, 5R01CA138586-02, and Center for Integration of Medicine and Innovative Technology (CIMIT) 11–325. Its contents are solely the responsibility of the authors and do not necessarily represent the official views of the NIH.

Achievements

- The successful integration of OpenIGTLink with MeVisLab is presented
- The developed solution allows MeVisLab programs to connect to image-guided therapy (IGT) devices
- Real-time visualization of tracker client information is possible in MeVisLab
- Standardized communication to share target positions, images and device status is provided
- The solution developed enables direct communication between different medical (prototyping) environments, such as Slicer and MeVisLab

Conflict of interest

All authors in this paper have no potential conflict of interests.

References

1. Galloway R. New applications and continuing challenges in image-guided therapy. Medical Physics, Volume 32, Issue 6.In Joint Imaging, Therapy Symposium, Advances in Image-Guided Intervention, 2005.
2. RW K, CP H, Antoniadis G, *et al*. Image guided aneurysm surgery in a Brainsuite® ioMRI Miyabi 1.5T environment. *Acta Neurochirurgica Supp* 2011; **109**: 107–110.
3. Lanotte M, Cavallo M, Franzini A, *et al*. A computational model to compare different investment scenarios for mini-stereotactic frame approach to deep brain stimulation surgery. *J Neurosurg Sci* 2010; **54**(3): 91–97.
4. Egger J, Kappus C, Freisleben B, Nimsky Ch. An efficient, geometric approach to support the trajectory determination for the deep brain stimulation (in German). In *Proceedings of Bildverarbeitung für die Medizin (BVM)*, Berlin, Germany. Springer, 2011.
5. Vautravers-Dewas C, Dewas S, Bonodeau F, *et al*. Image-guided robotic stereotactic body radiation therapy for liver metastases: is there a dose response relationship? *Int J Radiat Oncol Biol Phys* 2011; **81**(3): e39–47.
6. Olaya W, Bae W, Wong J, *et al*. Accuracy and upgrade rates of percutaneous breast biopsy: the surgeon's role. *Am Surgeon* 2010; **76**(10): 1084–1087.
7. Xu H, Lasso A, Vikal S, *et al*. MRI-guided robotic prostate biopsy: a clinical accuracy validation. *Med Image Comput Comput-Assist Intervention* 2010; **13**(Pt 3): 383–391.

DOI: 10.1002/rcs

8. Deng J, Chen Z, JB Y, *et al*. Testicular doses in image-guided radiotherapy of prostate cancer. *Int J Radiat Oncol Biol Phys*, online April 2011; **82**(1): e39–47.
9. Bucholz RD, Smith KR, Henderson JM, McDurmont LL, Schulze DW. Intraoperative localization using a three-dimensional optical digitizer. *Proc. SPIE* 1993; **1894**(312). doi: 10.1117/12.154958
10. Birkfellner W, Watzinger F, Wanschitz F, *et al*. Calibration of tracking systems in a surgical environment. *Trans Med Imaging* 1998; **17**(5): 737–742.
11. Barnett GH, Kormos DW, Steiner CP, Weisenberger J. Intraoperative localization using an armless, frameless stereotactic wand, technical note. *J Neurosurg* 1993; **78**(3): 510–514.
12. Roberts DW, Strohbehn JW, Hatch JF, *et al*. A frameless stereotaxic integration of computerized tomographic imaging and the operating microscope. *J Neurosurg* 1986; **65**(4): 545–549.
13. Dimaio S, Kapur T, Cleary K, *et al*. Challenges in image-guided therapy system design. *Neuroimage* 2007; **37**: 144–S151.
14. Slicer – a free, open source software package for visualization and image analysis. Surgical Planning Laboratory (SPL), Brigham and Women's Hospital, Harvard Medical School, Boston, Massachusetts, USA. Available from: http://www.slicer.org/
15. MeVisLab – development environment for medical image processing and visualization. MeVis Medical Solutions AG and Fraunhofer MEVIS, Bremen, Germany. Available from: http://www.mevislab.de/
16. OsiriX – image processing software dedicated to DICOM images produced by imaging equipment (MRI, CT, PET, PET-CT, SPECT-CT, Ultrasounds, . . .). Available from: http://www.osirix-viewer.com/
17. XIP-Builder – the eXtensible Imaging Platform is a development tool to rapidly create applications for processing and visualizing medical image data Siemens Corporate Research, Princeton, New Jersey, USA. Available from: https://collab01a.scr.siemens.com/xipwiki/index.php/XipBuilder
18. Egger J, Großkopf S, O'Donnell T, Freisleben B. A software system for stent planning, stent simulation and follow-up examinations in the vascular domain. In *22nd IEEE International Symposium on Computer-based Medical Systems*. , Albuquerque, New Mexico, USA.IEEE Press, ACM/SIGAPP, , Aug.2009; 1–7.
19. Egger J, O'Donnell T, Hopfgartner C, Freisleben B. Graph-based tracking method for aortic thrombus segmentation. In *Proceedings of 4th European Congress for Medical and Biomedical Engineering, Engineering for Health*. , Antwerp, BelgiumSpringer, Nov. 2008; 584–587.
20. Tokuda J, Fischer GS, Papademetris X, *et al*. OpenIGTLink: an open network protocol for image-guided therapy environment. *Int J Med Robot Comput Assist Surg* 2009; **5**(4): 423–434. doi:10.1002/rcs.274.
21. Fischer GS, Iordachita I, Csoma C, *et al*. MRI-compatible pneumatic robot for transperineal prostate needle placement. *IEEE/ASME Trans Mechatronics* 2008; **13**(3): 295–305.
22. IEEE Standard for medical device communications – overview and framework. IEEE Standard No. 1073–1996. 1996.
23. EN 50325–4. 2002 Industrial communications subsystem based on ISO 11898 (CAN) for controller–device interfaces, Part 4: CANopen; 2002. p. 1995EN 50325–4.
24. ISO 11898–1. 2003. Road vehicles – interchange of digital information – controller area network (CAN) for high-speed communication; 2003. p. 2003ISO 11898–1.
25. Schrenker RA. Software engineering for future healthcare and clinical systems. *Computer* 2006; **39**(4): 26–32.
26. National Alliance for Medical Image Computing (NA-MIC). OpenIGTLink, 2008. Available from: http://www.na-mic.org/Wiki/index.php/OpenIGTLink
27. ITK software guide. Available from: http://www.itk.org/ItkSoftwareGuide.pdf
28. Pace D, Tokuda J, Liu H, Hata N. Image Guided Therapy in Slicer3: Advanced Tutorial on Navigation using OpenIGTLink. NCIGT-SNR Tutorial, June 2008.
29. Elhawary H, Liu H, Patel P, *et al*. Intraoperative real-time querying of white matter tracts during frameless stereotactic neuronavigation. *Neurosurgery* 2011; **68**(2): 506–516.
30. BrainLAB AG. Available from: http://www.brainlab.com

Ein semiautomatischer Ansatz zur Flächenbestimmung von Wirbeln in MRT-Aufnahmen

Jan Egger[1,2,3], Thomas Dukatz[2], Bernd Freisleben[3], Christopher Nimsky[2]

[1]SPL, Dept. of Radiology, BWH, Harvard Medical School, Boston, MA, USA
[2]Klinik für Neurochirurgie, Philipps-Universität Marburg
[3]Fachbereich Mathematik und Informatik, Philipps-Universität Marburg
egger@bwh.harvard.edu

Kurzfassung. Graphbasierte Verfahren verteilen die Knoten des Graphen gleichmäßig und äquidistant auf einem Bild. Hinzugefügt wird ein sog. Smoothness Term, um dem Segmentierungsergebnis eine gewisse Steifigkeit zu verleihen und es so zu beeinflussen. Diese Vorgehensweise erlaubt dem Cut (Trennung von Objekt und Hintergrund) allerdings nicht, eine bestimmte (komplexere) Struktur zu bevorzugen, insbesondere, wenn Bereiche des Objekts nicht vom Hintergrund zu unterscheiden sind. Zur Evaluierung unseres Ansatzes verwendeten wir Magnetresonanztomographie (MRT)-Aufnahmen der Wirbelsäule, um die zeitaufwendige Schicht-für-Schicht-Konturierung der Ärzte zu unterstützen. Die quantitative Auswertung erfolgte mit dem Dice Similarity Coefficient (DSC) und ergab bei einem direkten Vergleich mit manuellen Expertensegmentierungen einen Wert von 90,97±2,2% für neun Wirbel (bei einer Rechenzeit von ca. einer Sekunde).

1 Einleitung

Degenerative Erkrankungen der Wirbelsäule, insbesondere durch Veränderungen der ligamentären und ossären Strukturen, sind weit verbreitet. Die konsekutive Zunahme der Spinalkanalstenose hat vermehrt Einschränkungen der Patienten im Alltag zur Folge. Die demographische Entwicklung führt zu einem höheren Anteil älterer Patienten, die eine operative Maßnahme erfahren [1, 2]. Die bildgebende Diagnostik der spinalen Strukturen spielt für die Entscheidungsfindung der adäquaten Therapie und das Ausmaß der operativen Behandlung eine maßgebliche Rolle. Die MRT-Bildgebung ist für die Evaluation spinaler Erkrankungen besonders geeignet, da spinale Strukturen wie Bandscheibengewebe, Nervenwurzeln und Bandstrukturen ohne Strahlenbelastung in hoher Auflösung dargestellt werden können. Dennoch können bestimmte ossäre Veränderungen der Wirbelsäule besser über eine Computertomographie (CT)-Aufnahme diagnostiziert werden, wie es z.B. bei Osteoporose oder Frakturen im Wirbelsäulenbereich der Fall ist [3]. Mit diesem Beitrag soll die Möglichkeit der MRT-Segmentierung im Hinblick auf die Rekonstruktion der Wirbelkörper demonstriert werden. Dies

T. Tolxdorff et al. (Hrsg.), *Bildverarbeitung für die Medizin 2012,* Informatik aktuell,
DOI 10.1007/978-3-642-28502-8_48,

bedeutet eine reduzierte Anzahl von Untersuchungen vor operativen Eingriffen und Schonung der interdisziplinären Ressourcen bei Vermeidung einer potentiell gefährdenden Strahlenbelastung für den Patienten. In der Literatur finden sich mehrere 2D-Algorithmen für die (semi-)automatische Segmentierung von Wirbeln. Huang et al. [4] nutzten einen normierten Cut-Algorithmus mit Nyström-Approximation und erzielten einen DSC [5] von 93% bis 95% für sechs Patienten. Michopoulou et al. [6] registrierten Bandscheiben mit einem Atlas und erreichten einen DSC zwischen 84% und 92%. Das Verfahren von Shi et al. [7] ist ein top-down-Ansatz, der statistische Mustererkennung für die Rückenmarksextraktion verwendet. Ein manuell definiertes Fenster wird hierbei als Initialisierung für eine Bandscheibenerkennung eingesetzt, die Autoren berichten über eine 96%ige Detektionsrate. Huang et al. [4] und Michopoulou et al. [6] vermeiden aufwendige Rechenoperationen und brauchen für eine Segmentierung wenige Sekunden, der Ansatz von Shi et al. [7] dagegen benötigte ca. 40 Sekunden.

2 Material und Methoden

Das vorgestellte Verfahren lässt sich in zwei Schritte unterteilen: Zuerst wird von einem benutzerdefinierten Saatpunkt aus (der innerhalb des Wirbels liegt) ein gerichteter 2D-Graph aufgebaut. Dann wird der minimale s-t-Schnitt auf diesem Graphen berechnet und damit der Wirbel vom Hintergrund getrennt (Abb. 1). Die Knoten des Graphen werden durch Abtasten von Strahlen gewonnen, die durch die Kontur einer rechteckigen Vorlage verlaufen (Mittelpunkt der Vorlage ist der Saatpunkt). Die abgetasteten Punkte sind die Knoten $n \in V$ vom Graphen $G(V, E)$, und $e \in E$ ist ein Satz von Kanten. Es gibt zwei Arten von Kantentypen: Kanten, die den Graphen mit einer Quelle s und einer Senke t verbinden, und Kanten innerhalb des Graphen. Bei den Kanten innerhalb des Graphen gibt es wiederum mehrere Arten. Die Kanten $< v_\mathrm{i}, v_\mathrm{j} > \in E$ des Graphen G verbinden immer zwei Knoten $v_\mathrm{i}, v_\mathrm{j}$ innerhalb des Graphen. Dabei gibt es unter anderem zwei ∞-gewichtete Kanten: z-Kanten A_z und r-Kanten A_r. Dabei ist Z die Anzahl der abgetasteten Punkte entlang eines Strahls $z = (0, \ldots, Z-1)$ und R ist die Anzahl der Strahlen, die durch die Kontur des Rechtecks gesendet

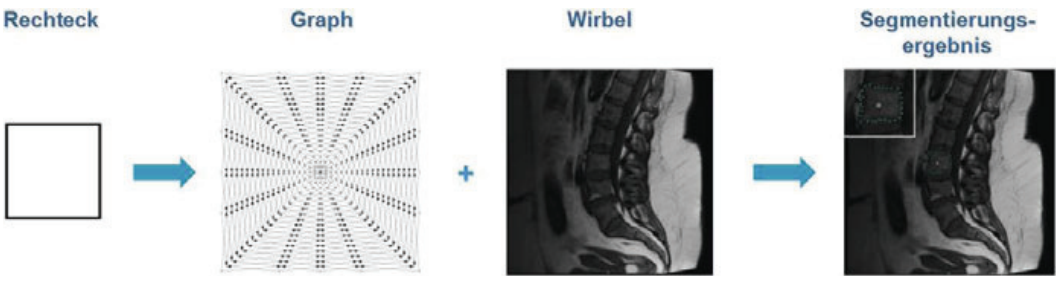

Abb. 1. Prinzipieller Ablauf des Verfahrens: Anhand einer rechteckigen Vorlage wird der Graph konstruiert und an der Position des benutzerdefinierten Saatpunktes im Bild positioniert. Anschließend liefert der s-t-Schnitt die Wirbelkontur bzw. Fläche zurück

werden $r = (0, \ldots, R-1)$, wobei $V(x_\mathrm{n}, y_\mathrm{n})$ ein Nachbarpunkt von $V(x, y)$ ist (Abb. 2)

$$A_\mathrm{z} = \{\langle V(x,y), V(x,y-1)\rangle \mid y > 0\} \tag{1}$$

$$A_\mathrm{r} = \{\langle V(x,y), V(x_\mathrm{n}, \max(0, y - \Delta_\mathrm{r}))\rangle\} \tag{2}$$

Die Kanten zwischen zwei Knoten entlang eines Strahls A_z stellen sicher, dass alle Knoten unterhalb einer Kontur im Graphen in einem closed set enthalten sind. Die Kanten A_r zwischen den Knoten der unterschiedlichen Strahlen schränken die Anzahl der möglichen Segmentierungen ein und erzwingen eine Glätte der resultierenden Kontur mit Hilfe eines Parameters Δ_r. Je größer Δ_r ist, desto mehr mögliche Segmentierungen gibt es. Nach der Graphkonstruktion wird das Closed Set des Graphen mit minimalen Kosten anhand eines s-t-Schnittes berechnet [8]. Dieser liefert eine optimale Segmentierung des Wirbels unter dem Einfluss des Parameters Δ_r, der die Steifigkeit der Kontur beeinflusst (Abb. 3). Ein Deltawert von 0 stellt sicher, dass das Segmentierungsergebnis ein Rechteck ist. Die Kosten $w(x, y)$ für die Kanten $v \in V$ zur Quelle und Senke werden folgendermaßen berechnet: Gewichte haben einen Wert von $c(x, y)$, wenn z Null oder maximal ist, ansonsten $c(x, y) - c(x, y-1)$, wobei $c(x, y)$ der Betrag der Differenz zwischen einem durchschnittlichen Grauwert (GW) des Wirbels und dem GW des Voxels an Position (x, y) ist [9]. Der durchschnittliche GW zur Berechnung der Kosten ist essentiell für die Segmentierung. Basierend auf der Annahme, dass der benutzerdefinierte Saatpunkt innerhalb des Wirbels sitzt, kann der durchschnittliche GW allerdings automatisch bestimmt werden. Dazu wird über eine Region der Dimension d (ca. 1 cm) um den Saatpunkt $(s_\mathrm{x}, s_\mathrm{y})$ integriert [10]

$$\int_{-d/2}^{d/2} \int_{-d/2}^{d/2} T(s_\mathrm{x} + x, s_\mathrm{y} + y)\,\mathrm{d}x\,\mathrm{d}y \tag{3}$$

und anschließend durch die Voxelanzahl geteilt (Mittelwert).

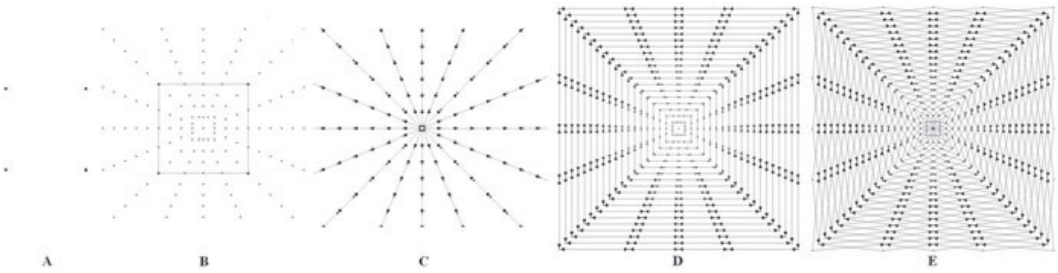

Abb. 2. A: rechteckige Vorlage, definiert durch vier Eckpunkte. B: Knoten die anhand der Vorlage generiert wurden. C: z-Kanten A_z entlang der Strahlen. D: r-Kanten A_r zwischen benachbarten Strahlen mit Δ_r=0. E: wie D nur mit Δ_r=1

3 Ergebnisse

Die Realisierung erfolgte mit C++ innerhalb von MeVisLab (www.mevislab.de). Die Graphkonstruktion und die Berechnung eines s-t-Schnitts benötigten in unserer Implementierung ca. eine Sekunde (Intel Intel Core i5-750 CPU, 4x2.66 GHz, 8 GB RAM, Win. XP Prof. x64, 2003, SP 2). Dagegen nahm eine Segmentierung, von Ärzten manuell vorgenommen, ca. eine Minute in Anspruch. Zum Testen des Ansatzes standen vierzehn Datensätze von zwölf Patienten zur Verfügung, wobei nicht für alle Wirbel manuelle Expertensegmentierungen vorhanden waren. Tab. 1 listet detailliert die Evaluationsergebnisse für Segmentierungen von neun Wirbeln auf. Neben dem Volumen in Kubikmillimetern und der Anzahl der Voxel ist der DSC [5] angegeben

$$DSC = \frac{2 \cdot V(A \cap B)}{V(A) + V(R)} \tag{4}$$

wobei A die Binärmaske der automatischen Segmentierung und R die Binärmaske der Referenzsegmentierung ist. V ist das Volumen (in mm^3) der Voxel in einer Binärmaske. Dazu wird die Anzahl der Voxel in einer Binärmaske gezählt und mit der Voxelgröße multipliziert (Abb. 4).

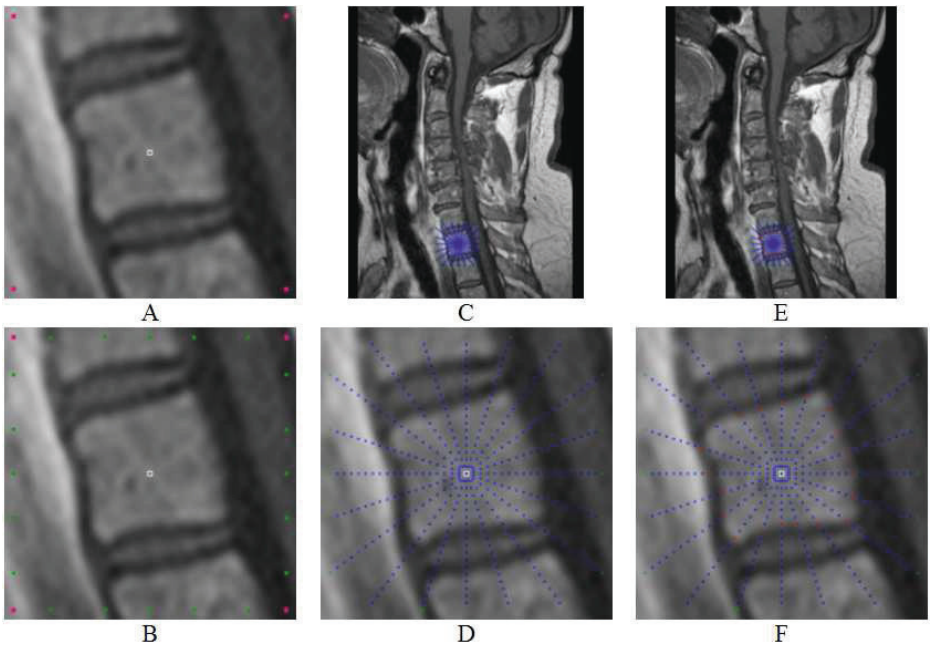

Abb. 3. Schritt-für-Schritt-Konstruktion eines Graphen und anschließende Segmentierung eines Wirbels. A: Saatpunkt (weiß) und die Ecken einer Vorlage (pink). B: Schnittpunkte der ausgesandten Strahlen mit der Vorlage (grün). C und D: abgetastete Knoten für den Graphen (blau). E und F: Segmentierungsergebnis (rot)

Tabelle 1. Evaluationsergebnisse: min., max., Mittelwert μ und Standardabw. σ

	Volumen in mm^3		Anzahl der Voxel		DSC (%)
	manuell	automatisch	manuell	automatisch	
min.	247,803	242,92	1015	995	87,37
max.	510,498	490,723	2091	2010	94,93
$\mu \pm \sigma$	420,41±72,22	404,30±72,98	1722	1656	90,97±2,2

4 Diskussion

In diesem Beitrag wurde ein graphbasierter Segmentierungsalgorithmus für Wirbel vorgestellt. Das Verfahren nutzt eine rechteckige Vorlage, um den Graphen aufzubauen. Bei dieser Vorgehensweise bevorzugt ein s-t-Schnitt eine rechteckige Struktur. Unseres Wissens nach ist dies das erste Mal, dass bei einem graphbasierten Verfahren die Knoten des Graphen nicht gleichmäßig und äquidistant auf einem Bild verteilt wurden, sondern anhand einer rechteckigen Vorlage. Der präsentierte Ansatz kann auch zur Segmentierung anderer rechteckiger Objekte genutzt werden und eignet sich besonders, wenn Bereiche des Objekts nicht vom Hintergrund zu unterscheiden sind (Abb. 5). Wie anhand der Evaluationsergebnisse zu erkennen ist, führt unser Verfahren eher zu einer Unterschätzung der Regionengröße. Diesem Trend kann durch eine höhere Gewichtung der Kanten zum "Hintergrund" entgegengewirkt werden. Das Segmentierungsergebnis hängt auch von der Position des benutzerdefinierten Saatpunktes ab. Allgemein gilt: je zentrierter im Objekt, desto besser die Segmentierung. Evtl. ist ein mehrstufiges Verfahren besser, indem das erste Segmentierungsergebnis genutzt wird, um einen zentrierteren Saatpunkt für einen weiteren Cut zu erhalten. Als nächstes ist geplant, das Verfahren auf einen Kubus zu erweitern, um Wirbel auch in

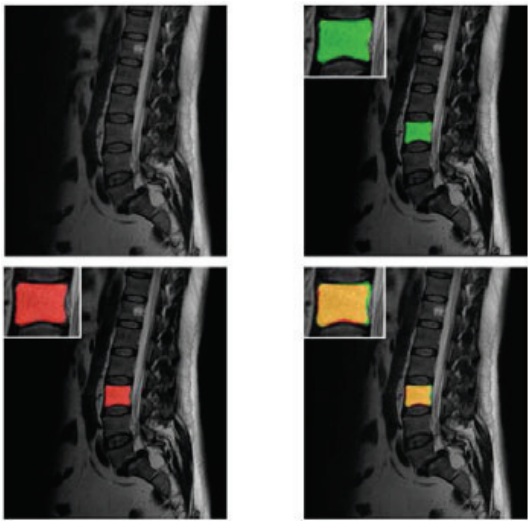

Abb. 4. Quantitative Evaluierung des Ansatzes anhand des Dice Similarity Coefficients (DSC): MRT-Datensatz (links oben), Fläche eines Wirbels (grün), die aus der manuellen Konturierung von einem Neurochirurgen generiert wurde (rechts oben), Fläche des Wirbels (rot), berechnet mit dem vorgestellten Verfahren (links unten), und direkter Vergleich beider Segmentierungen (rechts unten)

Abb. 5. Das vorgestellte Verfahren kann auch zur Segmentierung anderer rechteckiger Objekte genutzt werden, die subjektive Konturen aufweisen: zu segmentierendes Objekt (schwarz), wobei nicht nur eine gerade Kante, sondern auch eine Ecke fehlt (links), benutzerdefinierter Saatpunkt (blau) innerhalb des Objektes (Mitte) und Segmentierungsergebnis (rot), bei dem die fehlende Ecke rechts unten rekonstruiert wurde (rechts)

3D zu segmentieren. Dieser Ansatz soll anschließend aktuellen 3D-Verfahren zur Wirbelsegmentierung gegenübergestellt werden.

Literaturverzeichnis

1. Joaquim AF, et al. Degenerative lumbar stenosis: update. Arq Neuropsiquiatr. 2009;67(2):553–8.
2. Hicks GE, et al. Degenerative lumbar disc and facet disease in older adults: prevalence and clinical correlates. Spine (Phila Pa 1976). 2009;34(12):1301–6.
3. Richards PJ, et al. Spine computed tomography doses and cancer induction. Spine (Phila Pa 1976). 2010;35(4):430–3.
4. Huang SH, et al. Learning-based vertebra detection and iterative normalized-cut segmentation for spinal MRI. IEEE Trans Med Imaging. 2009;28(10):1595–605.
5. Zou KH, et al. Statistical validation of image segmentation quality based on a spatial overlap index. Sci Rep Acad Radiol. 2004;11(2):178–89.
6. Michopoulou SK, et al. Atlas-based segmentation of degenerated lumbar intervertebral discs from MR images of the spine. Trans Biomed Eng. 2009;56(9):2225–31.
7. Shi R, et al. An efficient method for segmentation of MRI spine images. IEEE ICME. 2007; p. 713–7.
8. Boykov Y, et al. An experimental comparison of min-cut/max-flow algorithms for energy minimization in vision. IEEE Trans Pattern Anal Mach Intell. 2004;26(9):1124–37.
9. Egger J, et al. Graph-based tracking method for aortic thrombus segmentation. Proc 4th Euro Congr MBEC, Engineering for Health. 2008; p. 584–7.
10. Egger J, et al. Nugget-Cut: a segmentation scheme for spherically- and elliptically-shaped 3D objects. Proc DAGM. 2010; p. 383–92.

SCIENTIFIC REPORTS

OPEN

Template-Cut: A Pattern-Based Segmentation Paradigm

Jan Egger[1,2,3], Bernd Freisleben[2], Christopher Nimsky[3] & Tina Kapur[1]

[1]Department of Radiology, Brigham and Women's Hospital, Harvard Medical School, Boston, MA, USA, [2]Department of Mathematics and Computer Science, University of Marburg, Marburg, Germany, [3]Department of Neurosurgery, University of Marburg, Marburg, Germany.

SUBJECT AREAS:
MATHEMATICS AND COMPUTING
METHODS
COMPUTATIONAL BIOLOGY
MODELLING

Received
23 January 2012

Accepted
10 May 2012

Published
24 May 2012

Correspondence and requests for materials should be addressed to J.E. (egger@bwh.harvard.edu)

We present a scale-invariant, template-based segmentation paradigm that sets up a graph and performs a graph cut to separate an object from the background. Typically graph-based schemes distribute the nodes of the graph uniformly and equidistantly on the image, and use a regularizer to bias the cut towards a particular shape. The strategy of uniform and equidistant nodes does not allow the cut to prefer more complex structures, especially when areas of the object are indistinguishable from the background. We propose a solution by introducing the concept of a "template shape" of the target object in which the nodes are sampled non-uniformly and non-equidistantly on the image. We evaluate it on 2D-images where the object's textures and backgrounds are similar, and large areas of the object have the same gray level appearance as the background. We also evaluate it in 3D on 60 brain tumor datasets for neurosurgical planning purposes.

Graph-based approaches to segmentation have gained popularity in recent years both in the general computer vision literature as well as in applied biomedical research[1–4] because of their ability to provide a globally optimal solution. This stands especially in contrast to another popular segmentation technique, deformable models[5,6], that can be easily confounded by local minima during the iterative segmentation (expansion) process. In this study, we present a novel graph-based algorithm for segmenting 2D and 3D objects. The algorithm sets up a graph and performs a graph cut to separate an object from the background. Typical graph-based segmentation algorithms distribute the nodes of the graph uniformly and equidistantly on the image. Then, a regularizer is added[7,8] to bias the cut towards a particular shape[9]. This strategy does not allow the cut to prefer more complex structures, especially when areas of the object are indistinguishable from the background. We solve this problem by introducing the concept of a "template" shape of the object when sampling the graph nodes, i.e., the nodes of the graph are distributed non-uniformly and non-equidistantly on the image. This type of template-based segmentation is particularly applicable to medical imagery, where it is easy to obtain initial landmarking[10,11] and patient orientation from the information stored in the image headers. To evaluate our method, we demonstrate results on 2D images where the gray level appearance of the objects and backgrounds are quite similar. In 3D, we demonstrate the results of the segmentation algorithm on 60 clinical Magnetic Resonance Imaging (MRI) datasets of brain tumor (glioblastoma multiforme and pituitary adenoma) patients to support the time-consuming manual slice-by-slice segmentation process typically performed by neurosurgeons.

Evolving from the cerebral supportive cells, gliomas are the most common primary brain tumors. The grading system for astrocytomas according to the *World Health Organization (WHO)* subdivides grades I–IV, where grade I tumors tend to be least aggressive[12]. Approximately 70% of the diagnosed tumors are malignant gliomas (anaplastic astrocytoma *WHO* grade III, glioblastoma multiforme *WHO* grade IV). Subject to its histopathological appearance, the grade IV tumor is given the name glioblastoma multiforme (GBM). The GBM is the most frequent malignant primary tumor and is one of the most malignant human neoplasms. Due to their biological behavior, surgery alone cannot cure this disease. Thus, current interdisciplinary therapeutic management combines maximum safe resection, percutaneous radiation and in most cases, chemotherapy. Despite new radiation strategies and the development of oral alkylating substances (for example Temozolomide), the survival rate is still only approximately 15 months[13]. Although in former years the surgical role was controversial, current literature shows maximum safe surgical resection as a positive predictor for extended patient survival[14]. Microsurgical resection is currently optimized with the technical development of neuronavigation[15] containing functional datasets such as diffusion tensor imaging (DTI), functional magnetic resonance imaging (fMRI), magnetoencephalography (MEG), magnetic resonance spectroscopy (MRS), or positron-emission-computed-tomography (PET). An early postoperative MRI with a contrast agent at the point of origin quantifies the tumor mass removal.

Then, the patient undergoes frequent MRI scans during the time of adjuvant therapy. Especially in case of a remnant tumor, the tumor volume has to be rigidly registered so a new tumor growth is not missed. For glioma segmentation in general (*WHO* grade I–IV), several MRI-based algorithms have been introduced in the literature.

A good overview of deterministic and statistical segmentation approaches is given by Angelini [16]. Most of these are region-based while the more recent ones are based on deformable models and include edge information. Segmentation based on outlier detection in T2-weighted MR data has been proposed by Prastawa *et al.*[17], whereby the image data is registered on a normal brain atlas to detect the abnormal tumor region. Sieg *et al.*[18] have introduced an approach to segment contrast-enhanced, intracranial tumors and anatomical structures of registered, multispectral MRI data. Using intensity-based pixel probabilities for tumor tissue, Droske *et al.*[19] have presented a deformable model, using a *level set*[20] formulation, to divide the MRI data into regions of similar image properties for tumor segmentation. An interactive method for segmentation of full-enhancing, ring-enhancing and non-enhancing tumors has been proposed by Letteboer *et al.*[21]. Clark *et al.*[22] introduced a knowledge-based automated segmentation method for multispectral data in order to partition glioblastomas. Gibbs *et al.*[23] introduced a combination of region growing and morphological edge detection for segmenting enhancing tumors in T1-weighted MRI data.

In the following, we describe studies that are more closely related to our contribution. For example, Song *et al.*[24] introduced a novel framework for automatic brain MRI tissue segmentation that overcomes inherent difficulties associated with this particular segmentation problem. They use a graph cut/atlas-based registration methodology that is iteratively optimized and incorporates probabilistic atlas priors and intensity-inhomogeneity correction for image segmentation. The usage of prior knowledge to guide the segmentation has been presented in a publication of Zhang *et al.*[25]. In a first step, they use the continuity among adjacent frames to generate a motion template according to the Displaced Frame Difference's (DFD) higher character and a color template is established by using k-means clustering. Afterwards (based upon the information derived from motion and the color templates), the segmentation image is defined as foreground, background and boundary regions. Finally, the segmentation problem is formulated as an energy minimization problem. Datteri *et al.*[26] proposed a combination of two segmentation methods: atlas based segmentation and spectral gradient graph cuts. To combine these two methods they first use the atlas-based segmentation method to segment the image. Then, they generate a third image used in the spectral gradient method as well as the source and sink points needed to initialize the graph cut algorithm.

This article is organized as follows. In Section 2, the experimental results are presented. Section 3 discusses our study and outlines areas for prospective tasks. Section 4 describes the details of the used material and the newly proposed approach. In part two of Section 4 (Calculation), a practical development from a theoretical basis is presented. Part three of Section 4 (Theory) extends the background of the contribution and lays the foundation for further work.

Results

To implement the presented segmentation scheme, the *MeVisLab*-Platform (see http://www.mevislab.de) has been used and the algorithm has been implemented in C++ as an additional *MeVisLab*-module. Although the prototyping platform *MeVisLab* especially targets medical applications, it is possible to process images from other fields. Even when the graph was set up with a few hundred rays and hundreds of nodes were sampled along each ray, the overall segmentation (sending rays, graph construction and mincut computation) for our implementation took only a few seconds on an *Intel Core i5-750 CPU, 4x2.66 GHz, 8 GB RAM, Windows XP Professional x64 Version, Version 2003, Service Pack 2*.

For 2D evaluation, we used several synthetic and real images. Figure 1 shows a stone flounder (A). Stone flounders can blend into their environment by changing their color, and therefore it is difficult for the human eyes to detect them. In image B, the user-defined template of a stone flounder is shown that has been used for setting up the graph, and image C shows the nodes that have been generated with this template. In image D, the nodes are superimposed on the original image; the graph is twice as large as the template, therefore, the scaling of the stone flounder does not play a role (i.e. it is *scale invariant*), and the same template can be used for segmentation of smaller or larger stone flounders. Finally, image E presents the segmentation result.

In 3D, the algorithm has been evaluated on segmentation of brain tumors (glioblastoma multiforme and pituitary adenoma) from 60 clinical Magnetic Resonance Imaging datasets from an active neurosurgical practice (see also Supplementary Information). All brain tumors were somewhat spherically or elliptically shaped; therefore, we used the surface of a polyhedron to construct the graph. Segmentations performed by three neurosurgeons with several years of experience in the resection of brain tumors are considered the "gold standard" or "ground truth" against which we evaluate the results of our algorithm. A comparison yields an average Dice Similarity

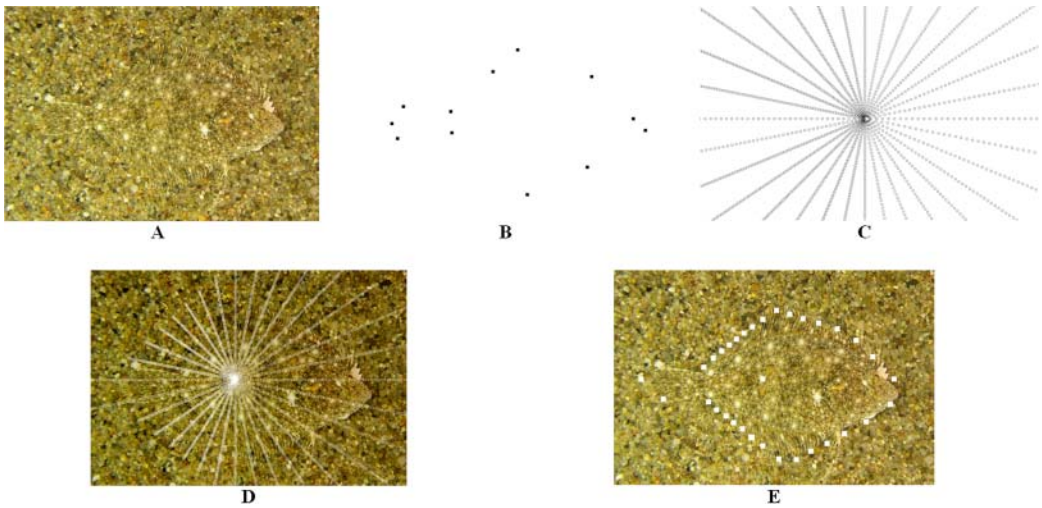

Figure 1 | (A) Kareius bicoloratus (stone flounder). (B) User-defined template of the stone flounder. (C) Nodes set up with the template. (D) Nodes superimposed in the original image. (E) Segmentation result (white seed points).

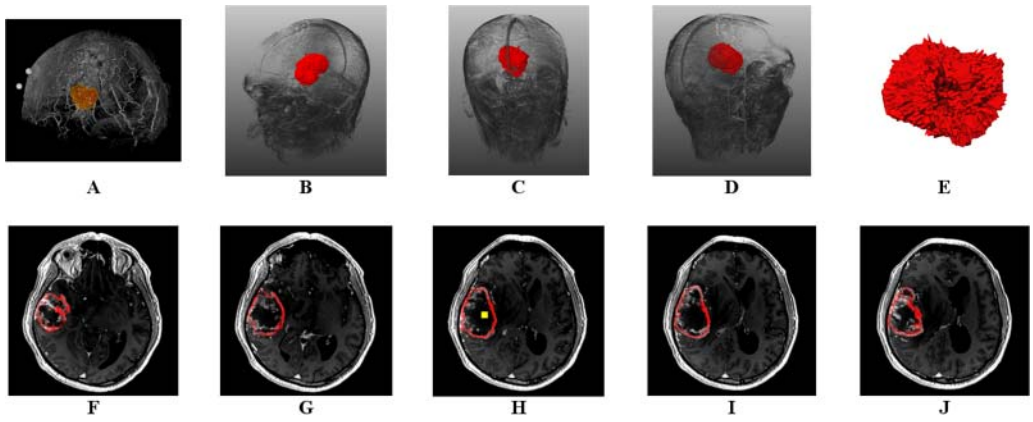

Figure 2 | (A) 3D view of an automatically segmented tumor (brown). (B)–(D) Different 3D views of an automatically segmented tumor (red). (E) voxelized tumor mask. (F)–(J) Result of automatic tumor segmentation (DSC=81.33%). The yellow point (inside the tumor) in image H is the user-defined seed point. Manual segmentation performed by a neurological surgeon took 16 minutes for this dataset.

Coefficient (DSC)[27,28] of about 80%. The Dice Similarity Coefficient is a measure for spatial overlap of different segmentation results and is commonly used in medical imaging studies to quantify the degree of overlap between two segmented objects A and R, given by:

$$DSC = \frac{2 \cdot V(A \cap R)}{V(A) + V(R)} \quad (1)$$

The Dice Similarity Coefficient is the relative volume overlap between A and R, where A and R are the binary masks from the automatic A and the reference R segmentation. $V(\cdot)$ is the volume (in cm^3) of voxels inside the binary mask, by means of counting the number of voxels, then multiplying with the voxel size.

Figure 2 shows some segmentation results for glioblastoma multiforme. In image A, a 3D view of an automatically segmented tumor (brown) is shown. The images B-D display different 3D views of an automatically segmented tumor (red), and the voxelized tumor mask is presented in image E. The images F-J show axial slices where the result of the automatic tumor segmentation is superimposed. The DSC for this segmentation is 81.33%, and the yellow point (inside the tumor) in image H is the user-defined seed point. Manual segmentation performed by a neurosurgeon took 16 minutes for this dataset. As shown in Figure 2, the segmentation works also with more elliptically shaped tumors. The algorithm only assumes that the object of interest is not extremely tubular, like vessels or the spinal cord. Also, the user-defined seed point does not have to be exactly in the center of the tumor, as shown in image H of Figure 2 (yellow). Even with a seed point that is located far from the center, the border of the tumor in Figure 2 (red) could still be recovered with a DSC of over 80% (note: the five axial slices F-J show only a small part of the tumor, the whole tumor was spread across 60 slices).

Image A of Figure 3 shows a graph (nodes and edges) constructed with a polyhedral surface to illustrate the dimensions of a typical graph used for pituitary adenoma segmentation. Image B of Figure 3 presents an axial slice of a pituitary adenoma with the segmented border superimposed and a zoomed-in view of the pituitary adenoma area for better illustration. The images C and D show different sagittal cross-sections with an automatically segmented pituitary adenoma (brown). Image E shows a 3D mask of an automatically segmented pituitary adenoma (red). Five axial slices with the superimposed border of the segmentation result (red) are presented in the images F-J where the user-defined seed point is located in image H (blue).

Table 1, Table 2 and Table 3 provide the results (minimum, maximum, mean μ and standard deviation σ) for all GBMs, pituitary adenomas and vertebrae that have been segmented with the presented algorithm and compared with manual slice-by-slice segmentations from the neurosurgeons. Table 1 provides results for fifty glioblastoma multiforme: volume of tumor (cm^3), number of voxels and Dice Similarity Coefficient. In Table 2, the results for ten pituitary adenomas are presented: volume of tumor (cm^3), number of

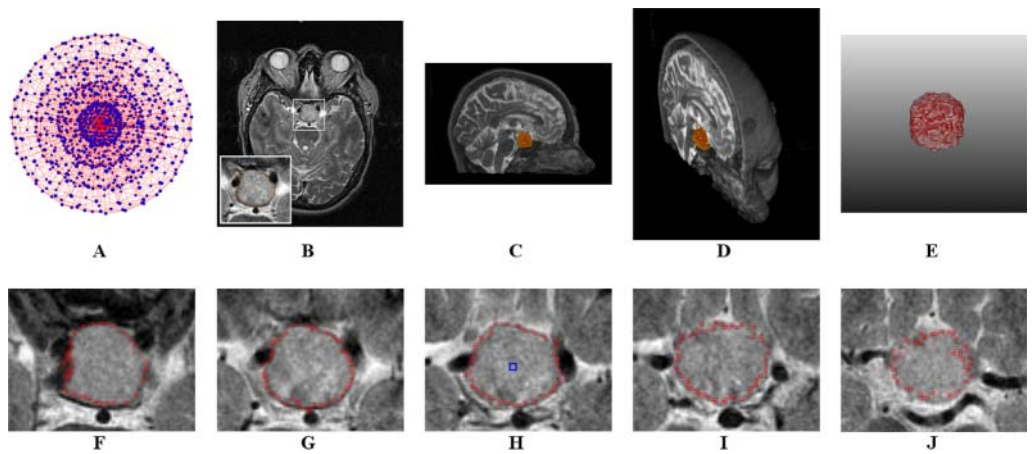

Figure 3 | (A) Graph (nodes and edges) constructed with a polyhedron surface. (B) Axial slice of a pituitary adenoma. (C) (D) Different views of sagittal slices with an automatic segmented pituitary adenoma. (E) 3D mask of an automatically segmented pituitary adenoma. (F)–(J) Segmentation results for a pituitary adenoma dataset. (H) user-defined seed point (blue).

Table 1 | Summary of results: min., max., mean μ and standard deviation σ for fifty glioblastoma multiforme (GBM)

	Tumor Volume (cm^3)		Voxel Number		
	manual	automatic	manual	automatic	DSC (%)
min	0.47	0.46	524	783	46.33
max	119.28	102.98	1024615	884553	93.82
$\mu \pm \sigma$	23.66±24.89	21.02±22.90	145305.54	137687.24	80.37±8.93

voxels, Dice Similarity Coefficient and the manual segmentation times (minutes). Finally, Table 3 shows the results for vertebrae segmentation: volume of vertebra (cm^3), number of voxels and Dice Similarity Coefficient. For a direct comparison and discussion of our method with other methods from the literature we refer the reader to previous publications[29,30]. In the first contribution[29], the results of vertebral segmentation – based on a rectangle shape – are compared with an interactive multi-label N-D image segmentation method called *GrowCut* from Vezhnevets and Konouchine[31]. In the other contribution[30], our method – based on a spherical template – is directly compared with a balloon inflation approach[32] for *WHO* grade IV glioma segmentation. Finally, we refer the reader to an additional publication where our template-based approach has been used to segment the bladder for MR-guided brachytherapy for gynecologic malignancies[33].

Discussion

In this contribution, we have presented a template-based segmentation scheme for 2D and 3D objects. To the best of our knowledge, this is the first approach where the nodes of a graph-based algorithm have been arranged according to a predefined template in a non-uniform and a non-equidistant manner on an image. Using this new type of segmentation algorithm, it is possible to reconstruct missing arcs and kinks in an object. In addition, the presented method is scale invariant. Experimental results for several 2D and 3D images based on 60 Magnetic Resonance Imaging datasets consisting of two types of brain tumors, glioblastoma multiforme and pituitary adenoma, indicate that the proposed algorithm requires less computing time and gives results comparable to human experts using a simple cost function. The presented work is a generalization of recent work by the authors[29,34] to arbitrary user-defined shapes in 2D and 3D. In previous work[34], a system for volumetric analysis of cerebral pathologies was introduced that used a sphere template for the segmentation process and therefore was limited to spherically-shaped objects. In[29] a rectangle-based segmentation algorithm for vertebrae MR images was introduced. As stated in the background section of the Introduction, there are proposed approaches from Song *et al.*[24], Zhang *et al.*[25] and Datteri *et al.*[26] that use prior knowledge like motion and color templates and shape information in graph based approaches. However, these approaches do not distribute the graphs nodes non-uniformly and non-equidistantly on the image. Instead they work on a regular grid, and compensate by adding complexity to the objective function. In summary, the achieved research highlights of the presented work are:

- A template-based segmentation paradigm for 2D and 3D objects
- Nodes are arranged according to a predefined template
- The approach represents a new type of graph-based algorithms
- It is possible to reconstruct missing arcs and kinks in an object
- The method is scale invariant

In our experience, and that of most applied researchers, automatic segmentation methods are served well by companion editing tools that can be used to efficiently "clean up" the results when needed. Therefore, we developed a manual refinement method that takes advantage of the basic design of graph-based image segmentation algorithms[35]. The manual refinement method can also be used for any graph-based image segmentation algorithms and therefore also for the template-based segmentation scheme. For twelve GBM cases, the Wilcoxon signed-rank test[36,37] verified a significant improvement ($p=0.016$) for our manual refinement method for a significance level of 0.05. However, the results presented in this study are not based on the use of manual refinement after the initial segmentations.

There are several areas of future work. For example, the cost function for the weights can be customized. Another possibility is to increase the sampling rate (for the nodes) near an object's border, because – with an equidistant sampling rate (along the rays) – there are more nodes near the user-defined seed point and less nodes going farther out. Moreover, the user-defined seed point position that is located inside the object is also an issue that can be analyzed in the future, e.g. for the stone flounder, the seed point has to be chosen carefully. One option to improve the presented algorithm is to perform the segmentation iteratively: After segmentation has been performed, the center of gravity of the segmentation can be used as a new seed point for a new segmentation and so on. This may lead to increased robustness with respect to the initialization.

Finally, we point the interested reader to publications from Sharon *et al.*[38] and Corso *et al.*[39] that are based on algebraic multigrid methods and graph cuts (normalized cuts) in which they introduced methods that adaptively build a graph and approximate cuts at varying resolutions and scales. A combination of their proposed method with our approach would result in an interesting template-based graph at every level.

Methods

The proposed segmentation scheme starts by setting up a directed graph from a user-defined seed point that is located inside the object to be segmented. To set up the graph, points are sampled along rays cast through the contour (2D) or surface (3D) of an object template. The sampled points are the nodes $n \in V$ of the graph $G(V, E)$ and $e \in E$ is the corresponding set of edges. There are edges between the nodes and edges that connect the nodes to a source s and a sink t to allow the computation of an s-t cut (note: the source and the sink $s, t \in V$ are virtual nodes). Similar to the notation introduced by Li *et al.*[4], the arcs $<v_i,v_j> \in E$ of the graph G connect two nodes v_i,v_j. There are two types of ∞-weighted arcs: p-arcs A_p and r-arcs A_r (P is the number of sampled points along one ray $p=(0,\ldots,P-1)$ and R is the number of rays cast to the contour or surface of an object template $r=(0,\ldots,R-1)$), where $V(x_n,y_n)$ is a neighbor

Table 2 | Summary of results: min., max., mean μ and standard deviation σ for ten pituitary adenomas

	PA Volume (cm^3)		Voxel Number			
	manual	automatic	manual	automatic	DSC (%)	Manual seg. time (minutes)
min	0.84	1.18	4492	3461	71.07	3
max	15.57	14.94	106151	101902	84.67	5
$\mu \pm \sigma$	6.30±4.07	6.22±4.08	47462.7	47700.6	77.49±4.52	3.91±0.54

Table 3 | Summary of results: min., max., mean μ and standard deviation σ for nine vertebrae.

	Vertebrae Volume (cm³)		Voxel Number		
	manual	automatic	manual	automatic	DSC (%)
min	0.25	0.24	1015	995	87.37
max	0.51	0.49	2091	2010	94.93
$\mu \pm \sigma$	0.42±0.072	0.40±0.073	1722	1656	90.97±2.2

of V(x,y) – in other words $V(x_n,y_n)$ and V(x,y) belong to two adjacent rays. For a surface in 3D, the principle is the same, except that there is an additional dimension for a node (V(x,y,z)):

$$\begin{aligned} A_p &= \{\langle V(x,\,y), V(x,\,y-1)\rangle | y>0\} \\ A_r &= \{\langle V(x,\,y), V(x_n, \max(0,\,y-\Delta_r))\rangle\} \end{aligned} \tag{2}$$

$$\begin{aligned} A_p &= \{\langle V(x,\,y,\,z), V(x,\,y,\,z-1)\rangle | z>0\} \\ A_r &= \{\langle V(x,\,y,\,z), V(x_n,\,y_n, \max(0,\,z-\Delta_r))\rangle\} \end{aligned} \tag{3}$$

The arcs between two nodes along a ray Ap ensure that all nodes below the contour or surface in the graph are included to form a closed set (correspondingly, the interior of the object is separated from the exterior in the data). This principle is shown in Figure 4 on the left side (A) for two rays of a circular template. The arcs A_r between the nodes of different rays constrain the set of possible segmentations and enforce smoothness via the regularization parameter Δ_r – the larger this parameter is, the larger is the number of possible segmentations. The principle underlying the construction of arcs between the nodes is shown in Figure 4 on the right side (B) – for rays of a circular template and a delta value of two (Δ_r=2). The arcs for different delta values are presented in the lower right of Figure 4: Δ_r=0 (left), Δ_r=1 (middle) and Δ_r=2 (right).

After graph construction, the minimal cost closed set on the graph is computed via a polynomial time s-t cut[40]. The s-t cut creates an optimal segmentation of the object under the influence of the regularizing parameter Δ_r that controls the stiffness of the surface. A delta value of zero ensures that the segmentation result has exactly the form of the predefined template – and the position of the template depends on the best fit to the gray levels or appearance of the image. The weights w(x,y) for every edge between $v \in V$ and the sink or source are assigned in the following manner: weights are set to c(x,y) if z is zero; otherwise they are set to c(x,y)-c(x,y-1), where c(x,y) is the absolute value of the difference between an average texture value of the desired object and the texture value of the pixel at position (x,y) – for a detailed description see[41–43]. The average texture value in this case, or the cost function in the general case, as well as the weights, critically influence the segmentation result. Based on the assumption that the user-defined seed point is inside the object, the average gray value can be estimated automatically. Therefore, we integrate over a small square S (2D) or cube C (3D) of dimension d centered on the user-defined seed point (s_x, s_y) in the 2D case and (s_x, s_y, s_z) in the 3D case:

$$\int_{-d/2}^{d/2}\int_{-d/2}^{d/2} S(s_x+x,\,s_y+y)\,dxdy \tag{4}$$

$$\int_{-d/2}^{d/2}\int_{-d/2}^{d/2}\int_{-d/2}^{d/2} C(s_x+x,\,s_y+y,\,s_z+z)\,dxdydz \tag{5}$$

The principle underlying the graph construction for a square is shown in Figure 5. Image A of Figure 5 shows the corners of a square template that are used to set up the graph. Image B shows the nodes that have been sampled along the rays that have been sent through the template's surface. Note that the distances between the nodes of one ray correlate with the distances between the template's center point (or for a later segmentation, the user-defined seed point) and the template surface. In other words, for every ray we have the same number of nodes between the center point and the object's border, but the length is different. In images C, D and E, different ∞-weighted arcs are shown: C: the p-arcs A_p along the single rays, D: the r-arcs A_r between rays with a delta value of Δ_r=0. E: same as D only with a delta value of Δ_r=1.

For the 3D case, both, the automatic segmentation method and a manual slice-by-slice segmentation performed by a domain expert (for a later evaluation of the automatic segmentation result) are post-processed in an identical manner. The resulting contours (given as point clouds) of the object's boundaries are triangulated to get a closed surface. This closed surface is used to generate a solid 3D mask (representing the segmented object), which is achieved by voxelization of the triangulated mesh[44].

The overall workflow of the introduced segmentation scheme is presented in Figure 6. In the upper row, a 2D square template is used for vertebral segmentation. In the lower row, a 3D sphere template is used to segment a GBM.

Calculation. Setting up the nodes of the graph with the user-defined template is the step that requires the most ingenuity in the proposed algorithm. Generating the arcs between the nodes and the source and the sink node is straightforward: there are the ∞-weighted arcs that depend on the geometry (intracolumn arcs) and the delta value (intercolumn arcs) used for the graph, and there are arcs that connect the nodes to the source *s* and the sink *t*. These arcs depend on the gray values of the nodes they connect – or rather they depend on the gray value difference to an adjacent node. To integrate the user-defined template into the construction of the graph, we need the coordinates in 2D or 3D describing the object that we want to segment (e.g. for a square the edges of the square, see Figure 5 A). Using these coordinates, the center of gravity of the object is calculated, and the object is normalized with the maximum diameter, or rather with the coordinate that has the maximum distance to the center of gravity. After the user defines a seed point in the image (2D) or volume (3D), the normalized object is constructed with its center of gravity point located at the user-defined seed point. Then, rays are drawn radially (2D) or spherically (3D) out from the seed point through the contour (2D) or surface (3D) of the normalized object. To

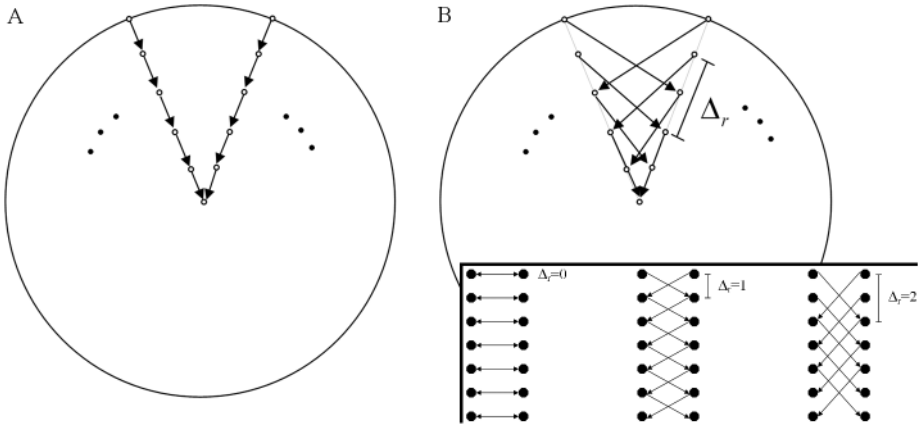

Figure 4 | The two different types of arcs for a graph that is used to segment circular shaped objects: A_p arcs (A) and A_r arcs (B). Lower right: Intercolumn edges for: Δ_r=0 (left), Δ_r=1 (middle) and Δ_r=2 (right).

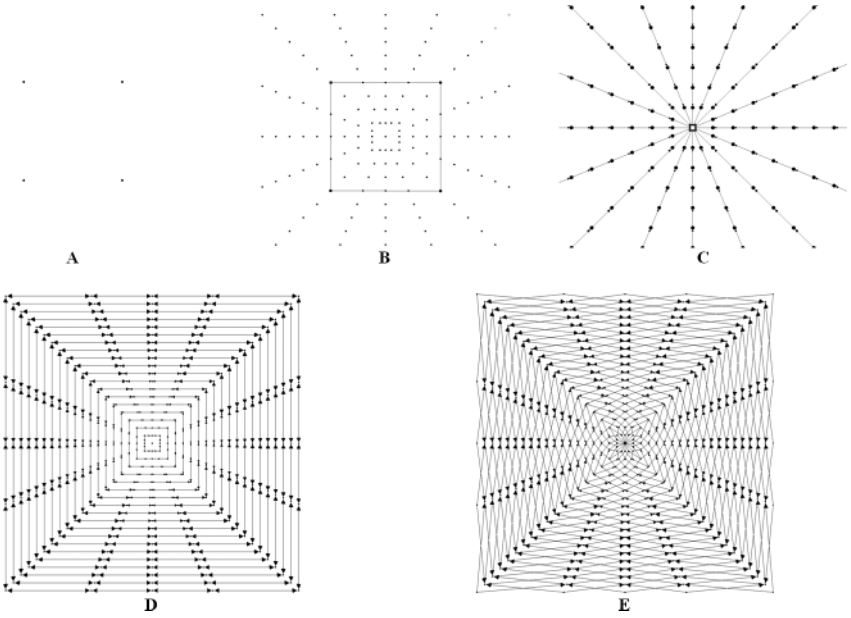

Figure 5 | (A) Square template given by its corners. (B) Nodes set up with the template. (C) p-arcs A_p along the rays. (D) r-arcs A_r between rays ($\Delta_r=0$). (E) r-arcs A_r between rays ($\Delta_r=1$).

calculate the intersection points of the rays with the object, its contour (in 2D) or surface (in 3D) has to be closed. In our implementation, we assume that the user provides the object's contour as 2D coordinates ordered in the clockwise direction, and we connect the points one after the other and finally connect the last point with the first point to get a closed 2D contour. To get a closed surface of the 3D objects, the object is triangulated[45]. However, this is not necessary for a spherical or elliptical segmentation where a sphere is used as a template. Thus, the computing time for the triangulation and the following ray-triangle intersection calculation can be avoided by using the surface points of a polyhedron. Their surface coordinates already provide the locations where the rays have to be sent through.

The intersection point of a ray with the object provides the distance between the nodes for this ray, because all rays have the same number of nodes from the center of gravity point to the intersection with the contour or surface. For intersections that are located closer to the center of gravity point we get smaller distances, and for intersections that are located farther away from the center of gravity point we get larger distances. Calculating the intersection of a ray with a 2D object is straightforward, since it is simply a line-line intersection. One line is the actual ray and the other line is one straight line between two adjacent points of the predefined template. Since triangulated objects are used for 3D segmentation, ray-triangle intersections for the 3D template segmentation have to be calculated. To implement ray-triangle intersections, there are several fast algorithms, such as the algorithms proposed by Möller and Trumbore[46] and by Badouel[47]. Given that the calculations of the ray-triangle intersections require the largest fraction of computing power, a GPU realization of these calculations[48] is used for objects with complex shapes.

Theory. The procedure of setting up the nodes of the graph based on the template biases the cut towards a particular shape, and the delta value Δ_r is a regularizer that influences the variations of the results. In other words, the delta value Δ_r specifies how much the segmentation results are allowed to deviate from the user-defined template. For example, a delta value of zero ($\Delta_r=0$) forces the segmentation result to have the exact shape of the template, which is optimal for problems where the shape but not the scale of the object is known. As is the case with regularizers in general, the delta value has to be chosen carefully corresponding to the segmentation problem. On the one hand, the segmentation results should not be too "stiff" with respect to the template, such that the algorithm is not flexible enough to handle some variations of the object and miss them during the segmentation process. On the other hand, if the delta value is too large, one risks obtaining results with shapes that do not correspond to the predefined template anymore. We studied this tradeoff for vertebral segmentation with a square template for different delta values[29]. Principal component analysis (PCA), also known as Karhunen-Loeve transform[49] can potentially be used as an interesting mechanism for incorporating additional domain knowledge about the shape of the target object into our algorithm, and also better informing the selection of the value for the delta regularizing parameter. This concept of using PCA for characterizing shapes is well developed in Active Shape Models (ASM)[50] and the shape model formulation of the Active Appearance Models (AAM)[51]. AAMs model the variability of shapes within an object class by removing variation introduced by rotational, translational and scaling effects from the training shapes, and all shapes need to be aligned to each other with respect to the mentioned transformations before a statistical analysis can be done. After the principal modes of variation (and corresponding eigenvalues) are computed from training data, legal shape instance *s*

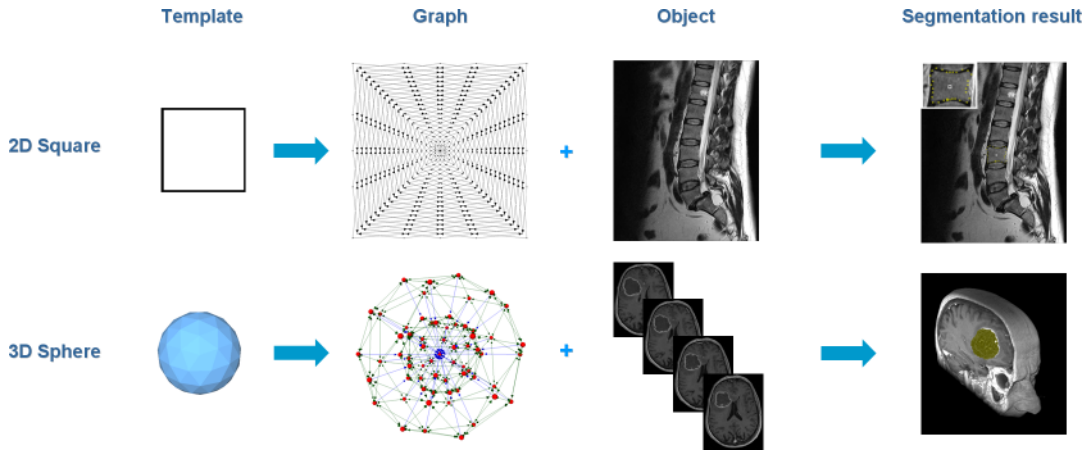

Figure 6 | **Principle workflow of the presented segmentation scheme in 2D and 3D.** In 2D a square template is used to segment a vertebra. In 3D a sphere template is used to segment a glioblastoma multiforme (GBM).

contained in the distribution derived from the training set can be generated from the model by deforming the *mean shape* $\bar{s}$ by a linear combination of eigenvectors. Thus, the shape model is described by

$$s = \bar{s} + \Phi_s b_s \quad (6)$$

where b_s is a vector containing the model parameters weighting the contribution of each eigenvector to the deformation, and Φ_s are the eigenvectors. To incorporate this shape model formulation into the template-based approach introduced in this contribution, first, a *mean shape* of the target object can be computed from several registered, manual segmentations using standard PCA. This *mean shape* $\bar{s}$ can then be input as the template or the distribution of the graph's nodes for our method. The next step is to establish a relationship between the variations of the object from the mean shape (as are obtained in standard PCA), and the delta regularizer of our algorithm. We believe that a reasonable scalar estimate of the delta value Δ_r can be computed proportional to the quantity $\max(\Phi_s b_s)$.

1. Shi, J. & Malik, J. Normalized cuts and image segmentation. *IEEE Transactions on Pattern Analysis and Machine Intelligence* **22**, 888–905 (2000).
2. Boykov, Y. Y. & Jolly, M.-P. Interactive graph cuts for optimal boundary & region segmentation of objects in N-D images. *International Conference on Computer Vision (ICCV)* **1**, 105–112 (2001).
3. Felzenszwalb, P. F. & Huttenlocher, D. P. Efficient graph-based image segmentation. *International Journal of Computer* **59**, 167–181 (2004).
4. Li, K., Wu, X., Chen, D. Z. & Sonka, M. Optimal surface segmentation in volumetric images – a graph-theoretic approach. *IEEE Transactions on Pattern Analysis and Machine Intelligence (PAMI)* **28**, 119–134 (2006).
5. Kass, M., Witkin, A. & Terzopoulos, D. Snakes - Active Contour Models. *International Journal of Computer Vision* **1**, 321–331 (1987).
6. McInerney, T. & Terzopoulos, D. Deformable models in medical image analysis: a survey. *Medical Image Analysis* **1**, 91–108 (1996).
7. Veksler, O. Star shape orior for graph-cut image segmentation. *European Conference on Computer Vision (ECCV)*, 454–467 (2008).
8. Ishikawa, H. & Geiger, D. Segmentation by grouping junctions. *IEEE Computer Society Conference on Computer Vision and Pattern Recognition (CVPR)*, 125–131 (1998).
9. Grady, L. & Schwartz, E. L. Isoperimetric graph partitioning for image segmentation. *IEEE Transactions on Pattern Analysis and Machine Intelligence (PAMI)* **28**, 469–475 (2006).
10. Seifert, S. *et al.* Hierarchical parsing and semantic navigation of full body CT data. *SPIE – Medical Imaging Conference* **7258**, 725902–725902-8 (2009).
11. Criminisi, A., Shotton, J., Robertson, D. & Konukoglu, E. Regression forests for efficient anatomy detection and localization in CT studies. *Medical Computer Vision, Recognition Techniques and Applications in Medical Imaging, Lecture Notes in Computer Science* **6533**, 106–117 (2011).
12. Kleihues, P. *et al.* The WHO classification of tumors of the nervous system. *Journal of Neuropathology & Experimental Neurology* **61**, 215–229 (2002).
13. Kortmann, R. D., Jeremic, B., Weller, M., Plasswilm, L. & Bamberg, M. Radiochemotherapy of malignant gliom in adults. Clinical experiences. *Strahlenther. Onkol.* **179**, 219–232 (2003).
14. Abi-Said, M. *et al.* A multivariate analysis of 416 patients with glioblastoma multiforme: Prognosis, extent of resection and survival. *J Neurosurg* **95**, 190–198 (2001).
15. Nimsky, C., Ganslandt, O., Kober, H., Buchfelder, M. & Fahlbusch, R. Intraoperative magnetic resonance imaging combined with neuronavigation: a new concept. *Neurosurgery* **48**, 1082–1091 (2001).
16. Angelini, E. D. *et al.* Glioma dynamics and computational models: a review of segmentation, registration, and in silico growth Algorithms and their Clinical Applications. *Current Medical Imaging Reviews* **3**, 262–276 (2007).
17. Prastawa, M., Bullitt, E., Ho, S. & Gerig, G. A brain tumor segmentation framework based on outlier detection. *Medical Image Analysis* **8**, 275–283 (2004).
18. Sieg, C., Handels, H. & Pöppl, S. J. Automatic segmentation of contrast-enhanced brain tumors in multispectral MR-images with backpropagation-networks (in German). *Bildverarbeitung für die Medizin (BVM)*, 347–351 (2001).
19. Droske, M., Meyer, B., Rumpf, M. & Schaller C. An adaptive level set method for interactive segmentation of intracranial tumors. *Neurol Res.* **27**, 363–70 (2005).
20. Malladi, R., Sethian, J. A. & Vemuri, B. C. Shape modeling with front propagation: a level set approach. *IEEE Transactions on Pattern Analysis and Machine Intelligence (PAMI)* **17**, 158–175 (1995).
21. Letteboer, M. M. L. *et al.* Segmentation of tumors in magnetic resonance brain images using an interactive multiscale watershed algorithm. *Academic Radiology* **11**, 1125–1138 (2004).
22. Clark, M. *et al.* Automatic tumor segmentation using knowledge-based techniques. *IEEE TMI* **17**, 187–201 (1998).
23. Gibbs, P., Buckley, D. L., Blackband, S. J. & Horsman, A. Tumour volume determination from MR images by morphological segmentation. *Physics in Med. & Biology* **41**, 2437–46 (1996).
24. Song, Z., Tustison, N., Avants, B. & Gee, J. Adaptive graph cuts with tissue priors for brain MRI segmentation. *3rd IEEE International Symposium on In Biomedical Imaging: Nano to Macro*, 762–76 (2006).
25. Zhang, H., Zuo, W. & Mu, Y. Auto-segmentation based on graphcut and template. *Proc. of SPIE*, **6786**, 67864W (2007).
26. Datteri, R., Barillot, C., Dawant, B. & Lecoeur, J. Segmentation of the thalamus in multi-spectral MR images using a combination of atlas-based and gradient graph cut methods. *Proc. of SPIE*, 9 pages (2010).
27. Zou, K. H. *et al.* Statistical validation of image segmentation quality based on a spatial overlap index: scientific reports. *Academic Radiology* **11**, 178–189 (2004).
28. Sampat, M. P. *et al.* Measuring intra- and inter-observer agreement in identifying and localizing structures in medical images. *IEEE International Conference on Image Processing*, 1–4 (2006).
29. Egger, J. *et al.* Square-Cut: a segmentation algorithm on the basis of a rectangle shape. *PLoS ONE* **7**(2), e31064 (2012).
30. Egger, J. *et al.* A Comparison of two human brain tumor segmentation Methods for MRI data. *Proceedings of 6th RBC on Bio-Medical Engineering*, 1–4 (2010).
31. Vezhnevets, V. & Konouchine, V. GrowCut - Interactive multi-label N-D image segmentation. *Proceedings of Graphicon*, 150–156 (2005).
32. Cohen, L. D. On active contour models and balloons. *CVGIP: Image Underst.* **53**, 211–218 (1991).
33. Kapur, T., Egger, J., Damato, A., Schmidt, E. J. & Viswanathan, A. N. QIN: 3T MR-guided brachytherapy for gynecologic malignancies. *Magnetic Resonance Imaging*, Elsevier, *in Press* (2012).
34. Egger, J., Kappus, C., Freisleben, B. & Nimsky, C. A medical software system for volumetric analysis of cerebral pathologies in magnetic resonance imaging (MRI) data. *Journal of Medical Systems*, 1–13 (2011).
35. Egger, J., Colen, R. R., Freisleben, B. & Nimsky, C. Manual refinement system for graph-based segmentation results in the medical domain. *Journal of Medical Systems*, 1–11 (2011).
36. Wilcoxon, F. Individual comparisons by ranking methods. *Biometrics Bulletin* **1**, 80–83 (1945).
37. Marascuilo, L. A. & McSweeney, M. Nonparametric and distribution-free methods for the social sciences. *Brooks/Cole Publishing Co*, ISBN-13:978-0818502026, 1–556 (1977).
38. Sharon, E., Galun, M., Sharon, D., Basri, R. & Brandt, A. Hierarchy and adaptivity in segmenting visual scenes. *Nature* **442**, 810–813 (2006).
39. Corso, J. J. *et al.* Efficient multilevel brain tumor segmentation with integrated Bayesian model classification. *IEEE Transactions on Medical Imaging (TMI)* **27**, 629–640 (2008).
40. Boykov, Y. & Kolmogorov, V. An experimental comparison of min-cut/max-flow algorithms for energy minimization in vision. *IEEE Transactions on Pattern Analysis and Machine Intelligence (PAMI)* **26**, 1124–1137 (2004).
41. Egger, J., O'Donnell, T., Hopfgartner, C. & Freisleben, B. Graph-based tracking method for aortic thrombus segmentation. *Proceedings of 4th European Congress for Medical and Biomedical Engineering, Engineering for Health*, 584–587 (2008).
42. Egger, J. *et al.* Aorta segmentation for stent simulation. *12th International Conference on Medical Image Computing and Computer Assisted Intervention (MICCAI), Cardiovascular Interventional Imaging and Biophysical Modelling Workshop*, 1–10 (2009).
43. Egger, J. *et al.* Nugget-cut: a segmentation scheme for spherically- and elliptically-shaped 3D objects. *32nd Annual Symposium of the German Association for Pattern Recognition (DAGM)* **6376**, 383–392 (2010).
44. Dachille, F. & Kaufman, A. Incremental triangle voxelization. *Proceedings of Graphics Interface*, 205–212 (2000).
45. Neugebauer, P. J. & Klein, K. Adaptive triangulation of objects reconstructed from multiple range images. *Proceedings of IEEE Visualization 97*, 41–44 (1997).
46. Möller, T. & Trumbore, B. Fast, minimum storage ray-triangle intersection. *Journal of Graphics Tools* **2**, 21–28 (1997).
47. Badouel, D. An efficient ray-polygon intersection. *Graphics gems*, 390–393 (1990).
48. Robert, P. C. D. & Schweri, D. GPU-based ray-triangle intersection testing. *Technical Report, University of Bern*, 1–14 (2004).
49. Pearson, K. On lines and planes of closest fit to system of points in space. *Philosophical Magazine* **2**, 559–572 (1901).
50. Cootes, T. F. & Taylor, C. J. Active Shape Models - 'Smart Snakes'. *Proceedings of the British Machine Vision Conference*, 266–275 (1992).
51. Cootes, T. F. & Taylor, C. J. Statistical models of appearance for computer vision. *Technical report, University of Manchester*, 1–125 (2004).

Acknowledgements

First of all, the authors would like to thank the physicians Dr. med. Barbara Carl, Thomas Dukatz, Christoph Kappus and Dr. med. Daniela Kuhnt from the neurosurgery department of the university hospital in Marburg for performing the manual slice-by-slice segmentations of the medical images, therefore, providing the ground truth for the evaluation. In addition, the authors would like to thank Brandon Greene from the Institute for Medical Biometry and Epidemiology (IMBE) of the University of Marburg for helping with the statistics. Moreover, the authors would like to thank Fraunhofer MeVis in Bremen, Germany, for their collaboration and especially Horst K. Hahn for his support.

This project was supported by the *National Center for Research Resources (P41RR019703)* and the *National Institute of Biomedical Imaging and Bioengineering (P41EB015898, U54EB005149, R03EB013792)* of the *National Institutes of Health (NIH)*. Its contents are solely the responsibility of the authors and do not necessarily represent the official views of the *NIH*.

Author contribution

Conceived and designed the experiments: JE. Performed the experiments: JE. Analyzed the data: JE CN. Contributed reagents/materials/analysis tools: CN BF JE TK. Wrote the paper: JE TK BF.

Additional information

Supplementary information accompanies this paper at http://www.nature.com/scientificreports

Competing financial interest: All authors in this paper have no competing financial interests.

How to cite this article: Egger, J., Freisleben, B., Nimsky, C. & Kapur, T. Template-Cut: A Pattern-Based Segmentation Paradigm. *Sci. Rep.* **2**, 420; DOI:10.1038/srep00420 (2012).

Available online at www.sciencedirect.com

SciVerse ScienceDirect

Magnetic Resonance Imaging xx (2012) xxx–xxx

MAGNETIC RESONANCE IMAGING

3-T MR-guided brachytherapy for gynecologic malignancies☆

Tina Kapur[a], Jan Egger[a], Antonio Damato[b], Ehud J. Schmidt[a], Akila N. Viswanathan[b,*]

[a]Department of Radiology, Brigham and Women's Hospital, Harvard Medical School, Boston, MA 02115, USA

[b]Department of Radiation Oncology, Brigham and Women's Hospital and Dana-Farber Cancer Institute, Harvard Medical School, Boston, MA 02115, USA

Received 6 February 2012; revised 31 May 2012; accepted 7 June 2012

Abstract

Gynecologic malignancies are a leading cause of death in women worldwide. Standard treatment for many primary and recurrent gynecologic cancer cases includes external-beam radiation followed by brachytherapy. Magnetic resonance (MR) imaging is beneficial in diagnostic evaluation, in mapping the tumor location to tailor radiation dose and in monitoring the tumor response to treatment. Initial studies of MR guidance in gynecologic brachytherapy demonstrate the ability to optimize tumor coverage and reduce radiation dose to normal tissues, resulting in improved outcomes for patients.

In this article, we describe a methodology to aid applicator placement and treatment planning for 3 Tesla (3-T) MR-guided brachytherapy that was developed specifically for gynecologic cancers. This methodology has been used in 18 cases from September 2011 to May 2012 in the Advanced Multimodality Image Guided Operating (AMIGO) suite at Brigham and Women's Hospital. AMIGO comprises state-of-the-art tools for MR imaging, image analysis and treatment planning. An MR sequence using three-dimensional (3D)-balanced steady-state free precession in a 3-T MR scanner was identified as the best sequence for catheter identification with ballooning artifact at the tip. 3D treatment planning was performed using MR images. Items in development include software designed to support virtual needle trajectory planning that uses probabilistic bias correction, graph-based segmentation and image registration algorithms. The results demonstrate that 3-T MR image guidance has a role in gynecologic brachytherapy. These novel developments have the potential to improve targeted treatment to the tumor while sparing the normal tissues.

Keywords: Brachytherapy; Segmentation; Bias correction; MR susceptibility artifact; Visualization; Registration

1. Introduction

Gynecologic malignancies, which include cervical, endometrial, ovarian, vaginal and vulvar cancers, cause significant mortality in women worldwide. In the United States, the number of gynecologic cancers has been increasing in recent years, while the death rate has remained relatively steady at about 35% of incidence [1]. The standard-of-care treatment for many primary and recurrent gynecologic cancers consists of external-beam radiation followed by brachytherapy [2]. In contrast to external-beam radiation treatment, in which a linear accelerator aims radiation beams at the pelvis from outside the body, in brachytherapy, radioactive sources that deliver very high doses of radiation are placed directly inside the cancerous tissue using intracavitary or interstitial applicators. The focus of our research is on gynecologic brachytherapy, a procedure in which the use of magnetic resonance (MR) guidance holds great promise.

The use of imaging to assist with gynecologic brachytherapy treatment planning and dose delivery has evolved from two-dimensional (2D) plain X-ray radiographs to three-dimensional (3D) volumes, including those created by computed tomography (CT) and magnetic resonance imaging (MRI) [3]. With plain X-ray imaging, the exact dose administered to the tumor is unknown. Therefore, in 2D imaging, proper positioning of the applicator is critical so that dose is delivered in as symmetric a fashion as possible; proper applicator position has been shown to impact disease-free survival [4]. With 3D imaging, in addition to noting applicator position, the tumor may be visualized and contoured, permitting accurate tailoring of the radiation dose.

☆ Conflict of interest notification: The authors have no conflicts of interest to report.

* Corresponding author. Tel.: +1 617 732 6331; fax: +1 617 732 7347.
E-mail address: aviswanathan@lroc.harvard.edu (A.N. Viswanathan).

0730-725X/$ – see front matter © 2012 Elsevier Inc. All rights reserved.
doi:10.1016/j.mri.2012.06.003

MRI is used routinely in the diagnosis of cervical cancer due to its increased sensitivity compared to CT [5], and its use in gynecologic brachytherapy planning is also gradually increasing [6,7]. Our previous studies using MRI in gynecologic brachytherapy demonstrated the feasibility of guidance for applicator placement using a low-field 0.5-T open-configuration scanner [8,9].

In this article, we present a combined diagnostic, guidance and treatment planning approach with imaging from a single high-field 3-T closed-bore MR scanner. We describe our developments to aid applicator placement and treatment planning for 3-T MR-guided brachytherapy specifically for gynecologic cancers and report on our experience implementing this system in the Advanced Multimodality Image Guided Operating (AMIGO) suite at Brigham and Women's Hospital (BWH).

2. Materials and methods

2.1. The AMIGO suite

AMIGO was launched in 2011 as a multimodal successor to the original 0.5-T Signa SP (GE Healthcare) magnetic resonance therapy unit at BWH, in which interstitial gynecologic brachytherapy was performed from 2002 to 2006. AMIGO is an integrated operating suite in which multidisciplinary patient treatment may be guided by X-ray, ultrasound, intraoperative 3-T MRI and/or positron emission tomography (PET)/CT (Fig. 1) imaging. A layout of the AMIGO unit is shown in Fig. 2. The goal of AMIGO is to better define anatomic tumor boundaries and the relationship of tumor to normal tissues using available imaging and to integrate this with more complete tumor treatment via excision, ablation or irradiation.

The MRI room of AMIGO (Fig. 1A) is centered on a ceiling-mounted Siemens Verio MRI scanner. This is a high-field (3-T) wide-bore (70-cm) MRI scanner integrated with video monitors, surgical lights, therapy-delivery equipment, an MRI-compatible anesthesia machine and vital-signs monitor. The ceiling-mounted MRI scanner can be moved out of the MR room and into the operating room (OR) (Fig. 1B). With this innovation, the patient does not need to be transferred from the OR table for MRI. The familiar "in–out" paradigm can also be used, in which the patient is imaged and then withdrawn from the bore of the scanner for intervention. In some procedures, the physician can reach into the scanner's bore to access the patient. These features enable flexibility in workflow to tailor procedures to the needs of the patient.

The OR in AMIGO is located between the MR and the PET/CT rooms (Fig. 1C). It is outfitted with an electronically controlled patient table surrounded by imaging modalities and therapy devices, including a ceiling-integrated Brainlab (Brainlab AG, Feldkirchen, Germany) navigation system, a Siemens (Siemens AG, Erlangen, Germany) Artis Zee angiography unit and two 3D ultrasound imaging systems — the Siemens S2000 and the BK (Analogic Corporation, Peabody, MA, USA) Profocus Ultraview. The table top can be changed to optimize the procedure for surgery or angiography. All images and data pertinent to the procedure are collected using video-integration technology, prioritized and then displayed on large LCD monitors at points of use in all three rooms in the suite.

2.2. Clinical approach

Patients with gynecologic malignancies are evaluated at the Department of Radiation Oncology at BWH. Most patients receive external-beam radiation prior to brachytherapy, whereas those who previously received external-beam irradiation to the pelvis are considered possible candidates for interstitial brachytherapy alone. From September 2011 to May 2012, 18 patients underwent gynecologic brachytherapy in the AMIGO suite. All patients were enrolled in an institutional-review-board-approved prospective clinical trial for gynecologic brachytherapy in the AMIGO suite, listed on the National Institutes of Health (NIH) Web site at www.clinicaltrials.gov.

Three categories of gynecologic procedures have been performed in the AMIGO suite: intracavitary procedures, used in six patients to date, which involve the insertion of an MR-compatible tandem coupled with ovoids (T&O) or a ring (T&R); procedures involving hybrid applicators in three patients, that is, a T&O with needle-bearing ovoids

Fig. 1. AMIGO Suite with (A) MR room, (B) operating room (OR) and (C) PET/CT room.

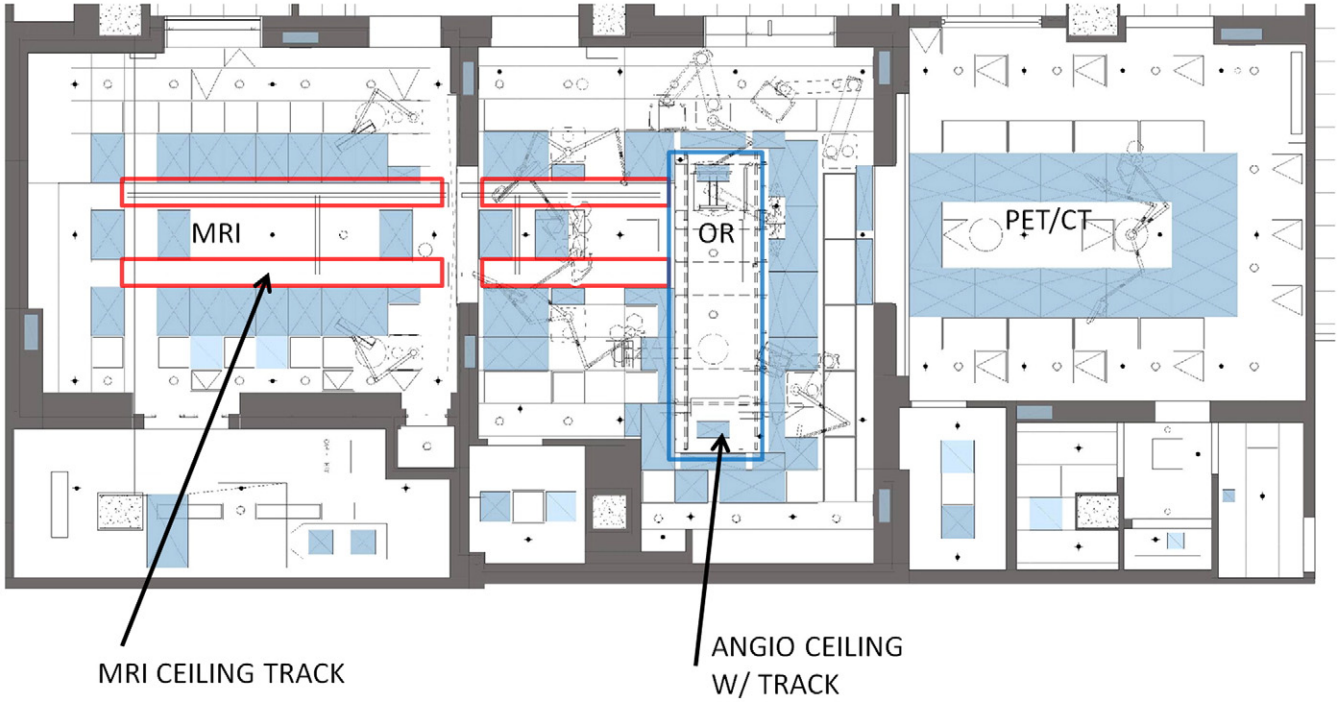

Fig. 2. Layout of the AMIGO floor plan with the MRI room and the MRI ceiling track (left), the operating room (OR) (middle) and the PET/CT scanner room (right), corresponding to Fig. 1. Motorized ceiling-mounted tracks allow the MRI scanner to move between the MRI and OR rooms.

(Utrecht Applicator) or T&R with needle-bearing ring (interstitial ring or Vienna Applicator); and interstitial procedures in nine patients, where plastic needles are inserted into a patient either through a Syed-Neblett template or freehand, sometimes in conjunction with a tandem but without ovoids or a ring. The interstitial needles consist of a plastic sharp-tipped outer catheter (ProGuide Needles, Nucletron Co., Veenendaal, the Netherlands) with a tungsten alloy obturator that fits through the center of the needle for stabilization and identification on imaging (Fig. 3A). Tandem-based applicators (Fig. 3B and C) are made of plastic (Nucletron Co.). All patients to date received high-dose-rate (HDR) brachytherapy.

Preimplantation procedures follow the standard recommendations for gynecologic brachytherapy as outlined by the American Brachytherapy Society [2,10,11]. The choice of applicator is determined by the physician based on clinical examination at the time of diagnosis, during external beam and during the immediate preimplantation assessment of disease extension. A rectovaginal clinical examination assesses the size of the tumor and cervix if present, the location of the uterus, the presence and extent of any vaginal disease, and whether the tumor extends into the parametrial or uterosacral tissues or to the pelvic sidewall.

2.3. Workflows for MR-guided gynecologic brachytherapy in AMIGO

2.3.1. Diagnostic MR (3-T) Protocol

Prior to receiving external beam radiation, a diagnostic MR protocol is performed on all patients. This protocol includes T2-weighted fast spin echo (Siemens turbo spin echo or TSE); T1-weighted fast spin echo (Siemens TSE) pre- and post-contrast-injection; single-shot half-Fourier fast spin echo (Siemens HASTE); fat-suppressed 3D gradient echo (Siemens VIBE), diffusion-weighted echo-planar imaging; as well as RF-spoiled gradient echo (GRE) sequences. After completing external-beam radia-

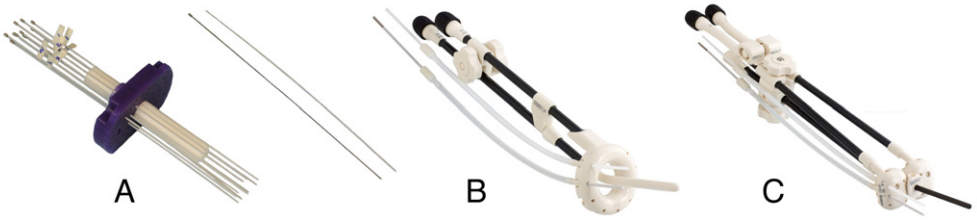

Fig. 3. Applicators used in gynecologic brachytherapy include (A) interstitial catheters with central tungsten alloy obturators placed through a central vaginal obturator (white) and through a disposable template, (B) tandem and ring, and (C) tandem and ovoids. B and C may be used with or without interstitial catheters.

tion, patients then undergo an AMIGO-based brachytherapy implant.

The AMIGO gynecologic brachytherapy workflow differs depending on whether patients undergo a tandem and ovoid/ring procedure or whether interstitial needles alone are required.

2.3.2. Tandem and ovoid or tandem and ring implant

2.3.2.1. Preimplantation 3-T MR (MR room, Fig. 1A). An eight-channel spine coil is placed under the patient, and a second eight-channel body matrix coil is placed on top of the patient to provide coverage of the entire pelvic area. Patients may be placed in a modified dorsal lithotomy position for imaging. Unless necessary due to patient anxiety, patients are not placed under anesthesia until after this preinsertion MRI. Similar sequences to those outlined in Section 2.3.1 are obtained, including the T2-weighted TSE, diffusion-weighted echo-planar imaging and GRE sequences in the sagittal, axial and coronal planes. The MR coils are removed. The patient is transferred to the main OR onto a movable table top with attached stirrups (Diacor, Inc. Salt Lake City, UT).

2.3.2.2. Anesthesia (OR, Fig. 1B). General anesthesia alone is used for all intracavitary patients treated as outpatients (this step is performed in the OR shown in Fig. 1B).

2.3.2.3. Applicator insertion (OR). A sterile speculum is inserted into the vagina to allow adequate visualization of the cervical os, the vagina and the tumor. For patients with an intact cervix, cervical dilators are inserted serially into the cervical os, often with ultrasound guidance, and a tandem is inserted into the uterus. Due to the use of ultrasound and the need to raise the legs in the lithotomy position, tandem insertion is performed in the OR. For intracavitary cases, the ring or ovoids are positioned over the tandem and pushed against the surface of the cervix. The patient is then transferred to the MR room and coils are again placed.

2.3.2.4. Guidance MR (MR Room). Patients may be positioned in a modified dorsal lithotomy setup using an MR table top designed at BWH with stirrups suitable for MRI. T2-weighted, diffusion-weighted and fat-suppressed images in the sagittal, axial and coronal planes are acquired. The T2-weighted 3D-SPACE (3D fast spin echo) images for postimplantation imaging include the following parameters: slice width=1.6 mm; field of view of 320×208 mm; the number of slices, depending on the region of interest; 1.4 averages; repetition time (TR)/echo time (TE)=2500/238 ms in most cases and bandwidth=521 Hz/pixel. A 1-mm slice thickness 3D axial SPACE scan is also performed. Treatment planning follows as described in Section 3.2.

2.3.3. Interstitial implant (MR Room, Fig. 1A)

2.3.3.1. Anesthesia. Epidural with general anesthesia is used for all interstitial cases, and the epidural is continued throughout the inpatient hospitalization.

2.3.3.2. Preimplantation 3-T MR. See Section 2.3.1 for details of the MR sequence obtained prior to applicator insertion.

2.3.3.3. Applicator insertion. A sterile speculum is inserted into the vagina to allow adequate visualization of the vagina and the tumor. A single suture is threaded into the vaginal apex. This suture is used to retract the apex as far inferiorly as possible. A vaginal obturator is inserted over the suture and against the vaginal apex. The template is placed over the plastic obturator (Fig. 3A). Prior to placement, the holes in the template are filled with sterile surgical lubricant to enhance visibility in subsequent MR scans. The template is sutured to the patient's perineal skin in the four corners of the template. An initial three-plane (sagittal, axial and coronal) T2-weighted MR localizer is performed with the applicator in situ. ProGuide (Nucletron Co.) hollow plastic catheters, 24–29 cm long, with metal central obturators, are inserted in the holes surrounding the plastic intravaginal obturator. After insertion of the first needles, a 3D-balanced steady-state free precession (bSSFP) sagittal image (Fig. 4) is obtained to localize the most superior aspect of the catheters. Adjustments to the most superior position are made to ensure no inadvertent insertion of a catheter into the bowel and adequate superior tumor coverage. Additional interstitial catheters are inserted, with the insertion depths intended to completely surround the visualized areas of the tumor and avoid normal tissues. A series of quick-monitoring, approximately 1 min, T2-weighted MR scans are acquired periodically as the needles are inserted and advanced to the tumor region. Confirmation MR scans, consisting of T2-weighted sagittal, axial and coronal images with slice thicknesses of 1.6 mm, are acquired at the end of applicator/needle placement. Diffusion-weighted echo-planar imaging is obtained in the axial, sagittal and coronal planes.

2.3.4. Radiation treatment planning and administration (Radiation Oncology Clinic)

MR images are transferred via the hospital network to the treatment-planning system (Oncentra Brachy, Nucletron Co.), where contouring of tumor and surrounding bladder, rectum and sigmoid and dosimetric calculations are performed. For interstitial cases, a confirmatory CT scan may be obtained to ensure accurate catheter identification. After appropriate safety and quality assurance checks [2,10–12], HDR brachytherapy is delivered based on the treatment plan in a room designated for radiation treatment with appropriate shielding.

Patients undergoing intracavitary treatment are discharged at the end of the day, while those undergoing interstitial

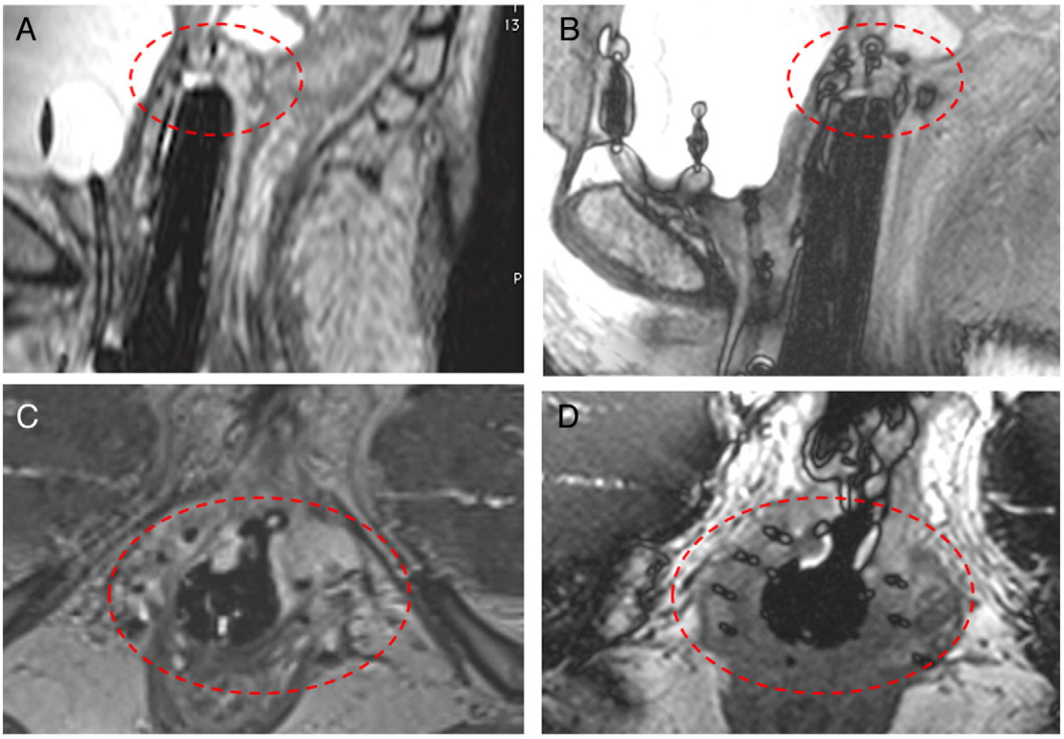

Fig. 4. Ballooning articfact created at the catheter tips using the 3D-SPACE and 3D-bSSFP sequence. (A) A sagittal image using the fat-suppressed 3D-FSE with 1.2-mm slice width, acquired in approximately 5 min, shows the difficulty in identifying catheter tips, whereas the (B) 3D fat-suppressed bSSFP, with 1.6-mm slice width, acquired over approximately 1.2 min, allows rapid identification of the catheter tip. This determines the deepest point of insertion, which is essential in order to avoid bowel insertion, and covers the length of the tumor. All subsequent needles are inserted to a similar depth based on tumor location. Similar results are seen on axial images (C) 3D-FSE and (D) 3D-bSSFP, where, instead of the ballooning artifact configuration seen on the sagittal image, a figure-eight centered on each catheter can be visualized.

treatment are admitted as an inpatient with epidural anesthesia to continue over the next 5–6 days while they receive HDR fractions twice a day throughout the week.

3. Results

3.1. Catheter identification

To more precisely locate the catheters during the insertion process, we reviewed 3D-FSE (Fig. 4A, 4C), 3D-GRE and 3D-bSSFP series and preliminarily found that the 3D-bSSFP sequence provides the best visual information for catheter identification utilizing the susceptibility-induced ballooning artifact at the tip on a sagittal image (Fig. 4B). On an axial scan, 3D-bSSFP produces a needle artifact that results in a cross shape at the center of the catheter (Fig. 4D). After a series of modifications to reduce the ballooning artifact size at the needle tip by changing the 3D-bSSFP bandwidth and TR, an optimized sequence was incorporated into the workflow with TR/TE/θ=4.6 ms/2.3 ms/30°, bandwidth=600 Hz/pixel, 0.9×0.9×1.6-mm^3 resolution, 160-mm superior–inferior coverage and 1.2 min/acquisition. The most accurate identification was confirmed with this optimized 3D-bSSFPP series. In contrast, the 3D T1-weighted GRE (TR/TE/θ=20 ms/7–9 ms/30°, bandwidth=800 Hz/pixel, 0.9×0.9×1.2-mm^3 resolution, 160-mm superior–inferior coverage, 3 min/acquisition) signal-to-noise ratio was lower, and an equivalent-resolution 3D-FSE (Siemens SPACE TR/TE=2500 ms/140 ms, bandwidth=800 Hz/pixel, 0.9×0.9×1.2-mm^3 resolution, 160-mm superior–inferior coverage, using a Generalized Autocalibrating Partially Parrallel Acquisitions (GRAPPA) acceleration factor of 2) required 5-min scans in contrast to the 1.2 min required for 3D-bSSFP. Accurate identification of the catheter tip during the insertion process allows proper placement and ensures that catheters are not unintentionally inserted into the normal-tissue structures.

3.2. Treatment planning

We define treatment planning as the process of designing the delivery of radiation through the implant and the calculation of the dose given to the patient. This definition is not inclusive: the concept of treatment planning can be expanded to embrace the choice of applicator and the specifics of the implantation (e.g., where the interstitial needles are positioned). The separation of the implantation planning from the treatment planning was dictated by the different role that the MR plays in these two phases of treatment management. Fig. 5 shows the typical workflow of the planning process from the end of the implantation to the optimized plan.

The concept of 3D treatment planning refers to the digitization of the location of the implant, optimization of

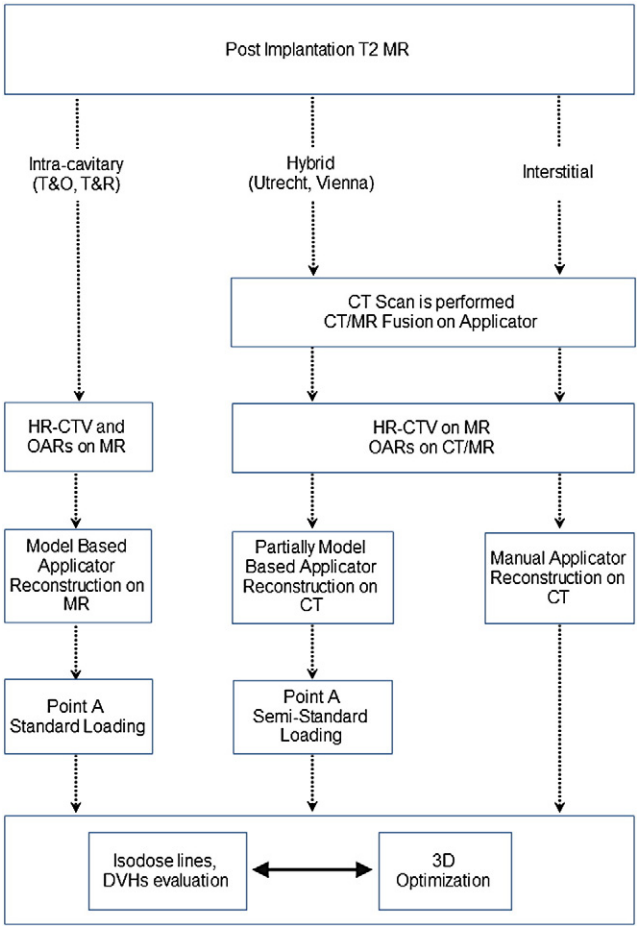

Fig. 5. Workflow of the treatment planning process for AMIGO procedures.

the dose distribution and calculation of a dose–volume histogram (DVH) to the organs at risk (OARs). 3D dose optimization is not commonly practiced yet [3], even though 3D imaging to guide and evaluate implantations is widely available. 3D planning based on MR is fairly recent, with some clinics reporting good results when an MR-based clinical target volume (CTV) was used for optimization [14–16].

3.2.1. Postimplantation MR

As described in the workflow, all patients receive an axial, sagittal and coronal T2-weighted MR scan with a slice thickness of less than 3 mm immediately after applicator insertion. Since March 2012, patients have undergone MR-based treatment planning using an axial T2-weighted MR with a slice thickness of 1.6 mm. The field of view of the planning MR should include the entire length of the applicator, with inferior and superior margins of at least 1 cm for correct evaluation of the clinical significance of the dose fall-off and calculation of the DVH for the OARs. When a template is used in interstitial applications, it should be included in the scan. For interstitial applications, axial b-SSFP images, as described in Section 3.1, are also acquired, and they include the needle tips but do not necessarily extend inferiorly to the template. The axial 1.6-mm T2-weighted MR and the b-SSFP should be performed back to back, with no patient movement in between if possible, to facilitate the registration between the two image sets. All MRI is performed without MR-specific dummies.

3.2.2. Additional imaging and registration

Additional imaging is only performed for interstitial, not intracavitary, insertions. From September 2011 to March 2012, prior to planning, all interstitial cases had a CT scan with 1.25 mm slice thickness in the Department of Radiation Oncology. This assures proper applicator localization. Since March 2012, the axial 1.6-mm T2-weighted MR and the b-SSFP are registered to localize of the needle tips if a CT scan is not available at the time of planning. For patients undergoing CT simulation after MR-guided insertion, copper radio-opaque markers are inserted in the needles. Commercially available markers are inserted into the T&O or T&R for ease of identification on CT. Registration of CT to MR is performed based on the rigid fusion of the applicator. The applicator is used as a proxy for the CTV soft tissue, which is not easily distinguishable on CT.

3.2.3. Tumor and normal-tissue contouring

Clinical contouring (manual segmentation) is performed on the available image sets. This is purely MR based for intracavitary cases. For other procedures, MR is used for all tumor contouring. Normal-tissue structure contouring is performed on the CT/MR fusion with comparison of the normal-tissue outlines. MR may be used for OAR contouring when CT cannot distinguish OAR borders, for example, when segments of bowel rest close to the cervix. With interstitial cases, CT may be preferable to ensure quick and accurate digitization of the needles. The CTV is contoured on MR, following published guidelines for cervical cancer [17,18]. A CTV encompassing the primary tumor volume and adjacent at-risk areas is contoured. An intermediate-risk vaginal structure is contoured if required based on tumor location.

MR scanning in gynecologic applications allows for clearer identification of the CTV as compared to CT-based imaging. This translates into two advantages: during implantation, the applicator and the needles can be located in closer proximity to their optimal position in relation to the tumor for radiation delivery, and contouring may be faster as the region of interest may be more clearly visualized [15].

3.2.4. Applicator reconstruction

Applicator reconstruction refers to the digitization of all possible locations of the source in the applicator. Due to the sharp dose gradients present in brachytherapy, applicator reconstruction is a critical part of treatment planning and has the potential for introducing large uncertainties into the dose delivery [19]. Two methodologies of applicator reconstruction are available: manual and model-based.

Manual reconstruction requires the manual digitization of the path available to the source along a catheter. We

manually digitize all needles on the CT images when available at the time of planning. CT scans are performed with dummy markers inserted inside the needle. These copper markers are radio-opaque along the path and have a 1-cm radiotransparent section before the last 0.5-cm radio-opaque tip. This configuration allows for easy digitization of the needle and easy identification of the needle tips.

Model-based reconstruction allows the planner to superimpose a model on the applicator that is visible on the scan. As long as the shape of the applicator contains enough details for correct registration of the model to the image, it is not necessary to visualize in detail the path available to the source inside the applicator. We use model-based reconstruction for T&R and T&O applicators.

All our patients are implanted under general anesthesia, so it is a priority to minimize both anesthesia time and X-ray dose. Avoiding CT imaging after MR is therefore advantageous. We performed three successful tests of T&O/T&R plastic-applicator reconstruction on MR in patients treated in AMIGO, as compared with reconstruction on a CT scan acquired immediately after implantation. We concluded that reconstruction of these applicators was possible directly on the T2-weighted axial MR image, aided by fusion with the concomitant T2 sagittal MR scan. This result is in line with the literature [20,21]. We observed a high degree of uncertainty in needle reconstruction on T2-weighted MR prior to development and implementation of the bSSFP series. Other clinics have reported good results with direct MR reconstruction of applicators including needles [22]. These results typically apply to needles anchored to ovoids, with an average insertion depth of 2.5 cm inside the patient from their anchorage on the applicator and also a maximum of 10 needles. For interstitial procedures performed recently in our clinic, a median of 15 needles was used with a depth typically exceeding 10 cm. The visibility of the needles degraded with the number of needles and with the depth of insertion as visualized on T2 images, making the needles in interstitial procedures particularly difficult to reconstruct on MR. The use of an axial T2-weighted MR with a slice thickness of 1.6 mm registered with the b-SSFP images as described in Section 3.1 represents a significant advance in MR-based needle reconstruction. The b-SSFP MR enhances the visibility of the needle tip locations and can be used to better distinguish needles that are close together. Our clinical practice is to obtain CT scans for the majority of patients in whom needles have been implanted, to verify accurate needle reconstruction. The CT scans can be acquired while the patient is awake, thus reducing anesthesia time. In the cases where the CT scans were available at the time of reconstruction, needle digitization was completed on CT because this is the fastest way to ensure accurate digitization of the needles.

3.2.5. Treatment planning

3D planning is an iterative process. The starting point of a T&O/T&R treatment plan is a preliminary 2D plan normalized to Point A, with a standard loading pattern of the applicator that provides a dose distribution commonly referred to as pear shaped (Fig. 6A). For hybrid applicators, the 2D plan is modified so that needles are loaded from the tip down to 1 cm away from the needle-bearing ovoid or ring, and dwell times are adjusted so that overall loading time is distributed 85% in the intracavitary applicator and 15% in the needles (Fig. 6B). For interstitial implants, the preliminary plan consists of a uniform loading of all needles, and Point A is not defined (Fig. 7A). These standard plans are not in general satisfactory. In the example in Figs. 6A–B and 7A, coverage of the CTV is inadequate. In other cases, the prescription dose might cover areas beyond the CTV into the OARs.

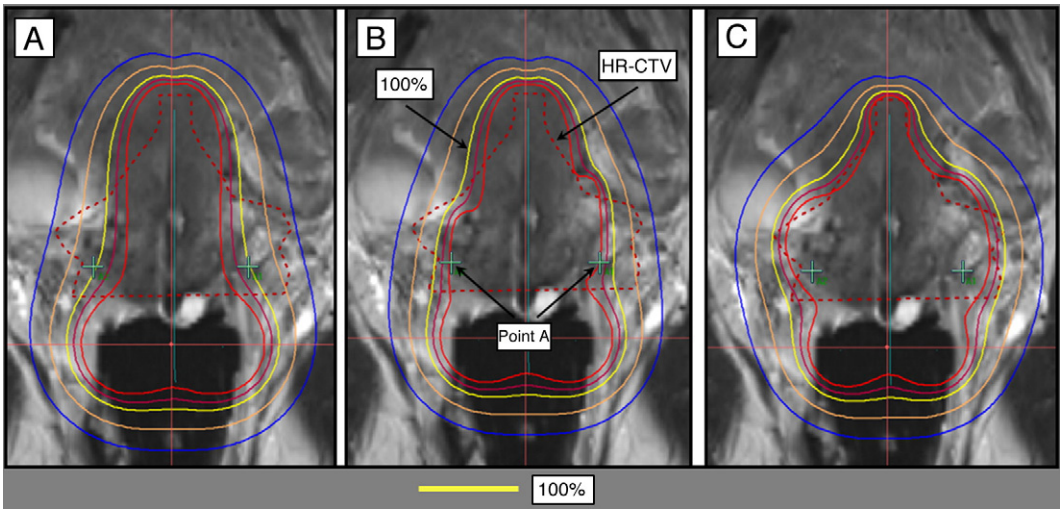

Fig. 6. T&R with interstitial needles. (A) The preliminary plan consists of a standard loading to the T&R, resulting in a pear-shaped distribution with prescription dose (100% isodose line in yellow) to the A points. (B) Interstitial needles are uniformly loaded, with dwell times amounting to 15% of the total dwell loading time. (C) 3D optimization of T&R and interstitial needles results in increased CTV coverage and sparing of the OARs.

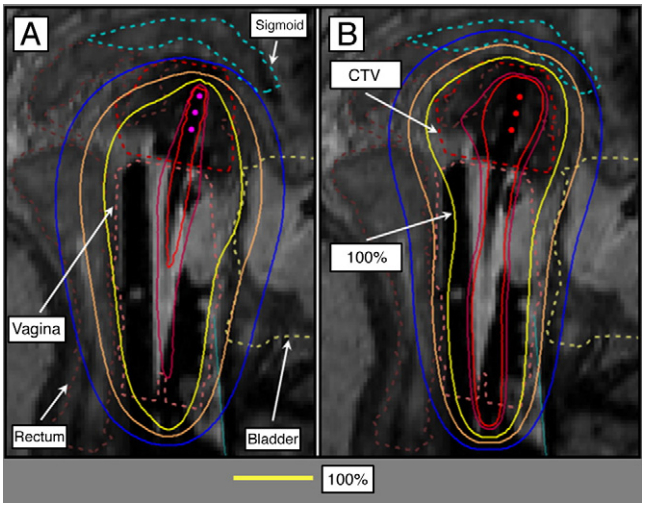

Fig. 7. Interstitial treatment planning with the 100% isodose line marked in yellow. (A) The preliminary plan consists of a uniform loading of all dwell positions. (B) 3D optimization of the dwell loading results in increased coverage to the CTV and sparing of the OARs.

3D optimization is the process of adjusting the standard plan to a specific case, based on the segmentation of the CT or MR scan. The dose distribution is optimized by manually adjusting the dwell times in specific locations to maximize coverage of the CTV, while dose to the OARs is minimized. An effort is made to minimize deviations from the standard pear-shaped distribution. Needles, if present, are loaded lightly, although no policy is in place on a maximum acceptable loading of a needle in hybrid applicators (Fig. 6C). For interstitial implants, a mix of manual and graphic optimization is at times performed, depending on the size of the implant and the planning time constraint (Fig. 7B). A final review of dwell times is always manually performed. This minimizes the variation of dwell times the length of the treatment.

The attending radiation oncologist and the planner make final adjustments by iteratively adjusting dwell times and checking the distribution of isodose lines and DVH. Optimization focuses on achieving an acceptable compromise between two goals: providing coverage to the tumor and sparing the OARs.

The coverage goal is quantitatively evaluated by the CTV D90, which ideally should exceed 100% of prescription dose. Qualitatively, it is evaluated by verifying, slice by slice, the overlap between prescription dose and CTV, and the location and extent of other dose levels, in particular, 200%, 150% and 60% of the prescription dose. Sparing of the OARs is monitored through the total dose received by the most irradiated 2cc volume of an organ (D2cc) which is the plan D2cc dose summed with previous irradiation using the Equivalent Dose in 2 Gy per fraction (EQD2) formalism. Total D2cc limits per organ have been previously published [16]. Our methodology and our results are in line with the 3D optimization experience reported by other clinics [14,23].

In summary, 3D planning increases coverage to the CTV and reduces the dose to the OARs. T&O and T&R applications can be planned directly on MR. If needles are inserted, a T2-weighted MR with 1.6-mm slice thickness and a b-SSFP MR may be sufficient for needle identification. A CT scan may be acquired and registered to the MR scan to verify the reconstruction and expedite the digitization process.

3.3. Future directions

3.3.1. Interleaving dose planning and needle guidance

We recognize that less-than-ideal needle placements can often be compensated for by the degrees of freedom available in the needle afterloading step. Early work from our group demonstrates a method for incorporating the observed needle positions from a 0.5-T intraoperative MR scanner into the treatment plan for prostate brachytherapy using permanent implants [24]. Our goal is to build upon that method in the development of treatment-planning software for gynecologic brachytherapy.

3.3.2. Needle trajectory planning

An image-guided navigation system, using pre- or intra-operative images, aids in the precise placement of needles, catheters and other instruments at prescribed locations in the patient's body and monitors their trajectory through the course of the intervention [13]. Navigation products are available commercially for brain-tumor resection, cardiac electrophysiology ablation, spine surgery and, more recently, abdominal ablation and lung bronchoscopy. In the pelvis, there are indications of progress in permanent seed implant prostate brachytherapy navigation products, but none that we are aware of for gynecologic brachytherapy. We have designed a navigation software application, *iGyne*, specifically for gynecologic brachytherapy procedures. In the future, critical feedback from dose planning will be incorporated. The needle-trajectory planning method focuses on Syed–Neblett template-based interstitial HDR brachytherapy; extensions to cover different applicators are in development.

3.3.3. iGyne software application

The *iGyne* software now in development, may, in the future, be utilized as part of the process outlined in Section 2.3.3.3 of the MR-guided brachytherapy workflow. After the template is sutured to the patient's perineum, the *iGyne* software may be used to perform a rigid registration of a Computer Aided Design (CAD) model of the template to its image in the MRI scan using corresponding markers that are clearly visible in the MR image. Fig. 8 presents the basic principle for fitting a Syed–Neblett template to a patient data set using *iGyne*. This further illustrates the principle of needle planning with the *iGyne* software prototype. The user can move a multiplanar reconstruction (MPR) along the needle path that is visualized in the 3D view, while the MPR itself is visualized as a 2D slice in the lower left window. Though this software may in the future assist with preplanning, it will be necessary to modify the program to

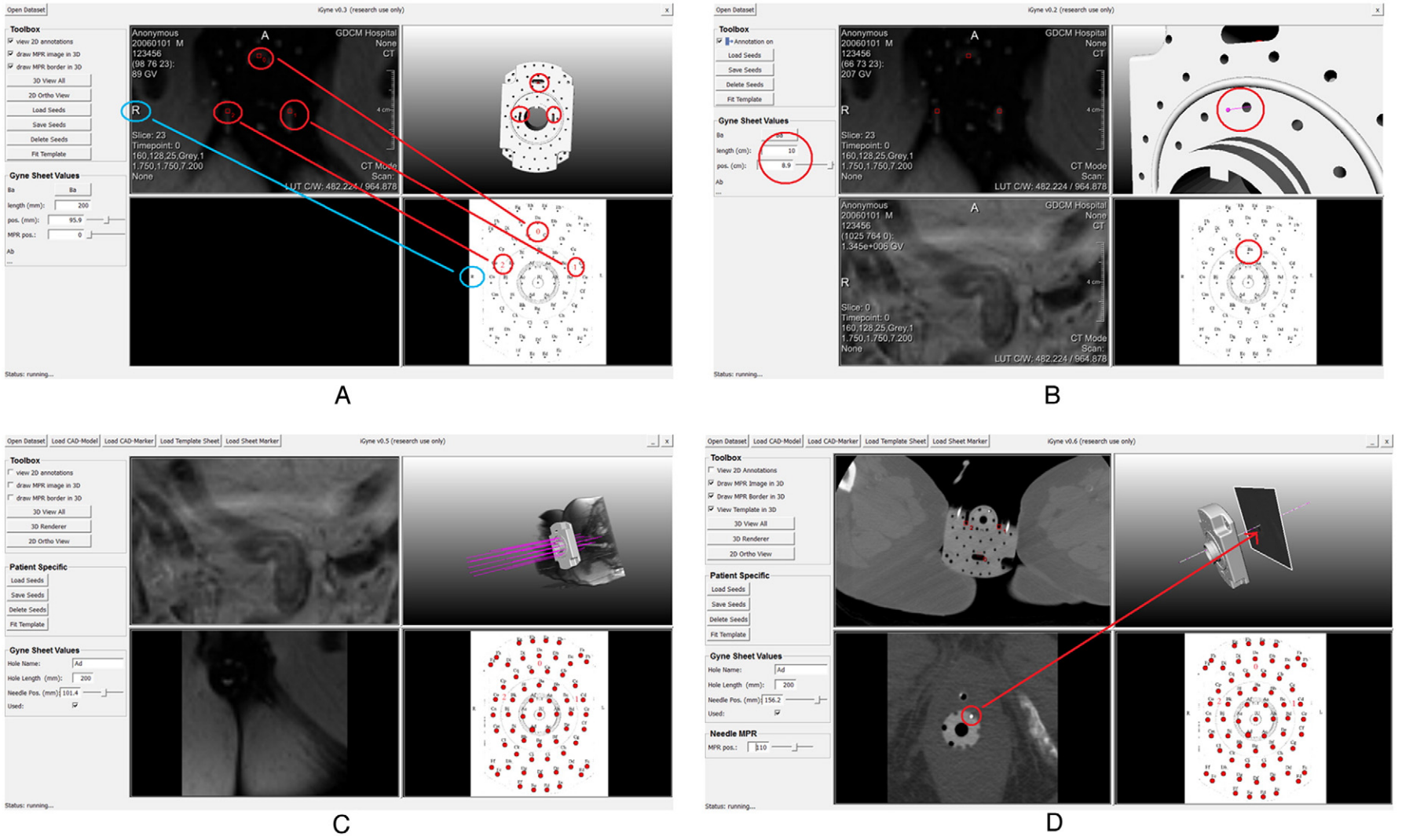

Fig. 8. Principle for registering a template for gynecologic brachytherapy with the initial MRI image. (A) The three red circles indicate corresponding needle holes in the template and the MRI image. The registration is realized via a rigid transformation between these corresponding point sets. The blue circles are used to ensure that the left and right sides of the patient and the template are matched correctly. (B) Virtual fitted gynecologic brachytherapy template and selection of a specific interstitial needle (Ba, red circles in the screen shot). As shown on the left side of the prototype interface, individual needle insertion can be planned by defining parameters, such as the needle length and depth. (C) Virtual placement of several interstitial needles (purple) with different lengths and depths as shown in the settings in the menu in the left column. This allows the radiation oncologist to plan the placement of needles. (D) Needle (white line in the upper right window) that has been selected for visualization of MPRs along the needle path (lower left window). The MPR at the position of the arrow (tip of red arrow in the upper right image) is displayed in the lower left window as a 2D slice. In the MPR of the lower left window, the needle cross section (white) is surrounded by a red circle.

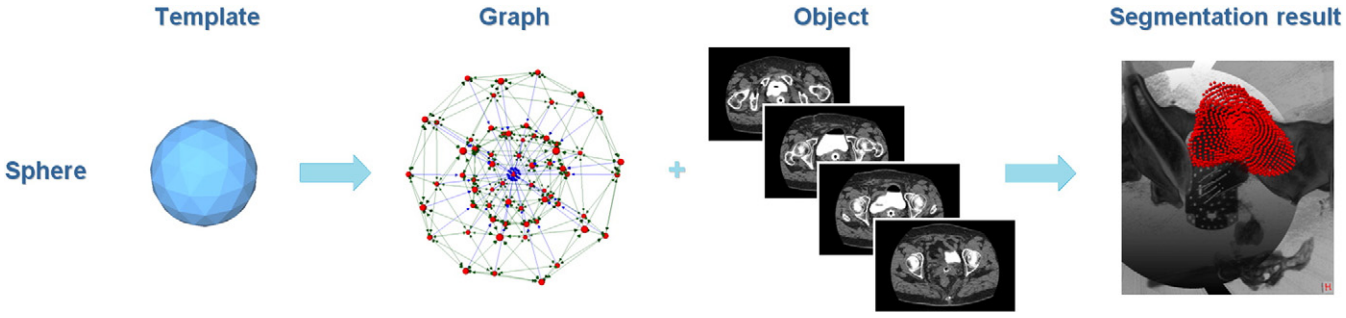

Fig. 9. Segmentation principle of the bladder with the Nugget–Cut approach: a spherical template (left image) is used to construct a directed graph (second image from the left). The graph is fused with the data set of a patient (third image from the left), and the algorithm provides the segmented bladder (red, rightmost image).

allow for needle deflection. Therefore, *iGyne* has not yet been used clinically but has potential for future implementation.

3.3.4. Image analysis: probabilistic bias correction of MRI spatial signal inhomogeneity

We plan to test the use of a probabilistic bias correction method. We will explicitly model and correct for the corrupting field in MR images. This corrupting field is due to spatial inhomogeneities in the radiofrequency field produced by the surface coils placed above and below the patient. Wells et al. introduced this Bayesian method [25] which has been further developed [26–28] based on the expectation–maximization algorithm. This is an estimation method used to find the parameters of a model that maximizes the likelihood of the data when some of the data are observable and some are hidden or unobserved [29].

3.3.5. Image analysis: segmentation of organs at risk

As a first step toward an overall segmentation of anatomy structures for gynecologic brachytherapy, we attempted segmentation of the bladder with the Nugget–Cut approach [30] [31], though many alternative approaches exist. We used a spherical template to construct a directed graph. This graph was fused with the CT data set; The segmented bladder that the algorithm provided is shown in Fig. 9.

4. Discussion

In this overview, we have described our ongoing work in gynecologic brachytherapy in the recently opened AMIGO suite at BWH. We have described the integration of the available imaging modalities as used to date. Prior to the development of the AMIGO suite, in a clinical trial from 2002 to 2006, we demonstrated the benefit of intraprocedural MR images in 25 patients both in identification of parametrial tissue involvement [9] and in optimized radiation delivery. That study included interstitial needle placement in a “double-doughnut” open-configuration 0.5-T MR scanner (Signa SP, GE Healthcare, Waukesha, WI, USA). Between 2005 and 2011, two dedicated CT-based brachytherapy suites were constructed in the Department of Radiation Oncology. In these suites, intraprocedural CT scans, in contrast to plain-film X-ray only, increased the precision of placement of intracavitary applicators for gynecologic brachytherapy. In parallel, the discovery and optimization of MR image sequences improved in diagnostic MRI, allowing translation of these MR findings to gynecologic brachytherapy [32,33].

Over the past months, we have begun to assess several technologies, including accurate interstitial catheter identification, MR bias correction and bladder segmentation, and have developed a novel software program to assist with accurate catheter placement. Ongoing areas of focus are the following: active tracking of the tips of interstitial needles in the MR scanner; fabrication of customized needles that generate a more distinct artifact in MRI and, in particular, a unique artifact at the needle tip; MR pulse sequences to enhance needle artifacts; a model-to-image registration method which aligns the geometric model of the template to its MRI image; improved image-based needle detection algorithms to precisely demarcate the inserted needles; extension of the Nugget–Cut algorithm to segment additional organs at risk and development of real-time iterative treatment planning modules available in the AMIGO suite. We expect to be able to make rapid strides in each of these areas, in some cases by translating advances from prostate cancer brachytherapy [34–36], MRI physics [37], active MRI tracking of cardiac catheters [38,39], and image processing for brain tumors and prostate cancer [40,41]. We also anticipate developing unique and novel strategies for gynecologic brachytherapy that may be translated to other fields in the future.

5. Conclusion

MR image guidance for brachytherapy of gynecologic malignancies permits accurate placement of the applicator and analysis of tumor location in relation to surrounding normal tissues. Advances in areas of MR bias correction, image-applicator identification, tracking, organ segmentation and radiation treatment planning provide unique opportunities to improve the process, increase speed and ideally improve outcomes for patients.

Acknowledgments

The authors would like to acknowledge the support of the AMIGO clinical staff in enabling this clinical study; Brendan Whalen and Dan Kacher for providing AMIGO architectural plans; Sam Song, PhD, for generating the CAD models of gynecologic devices; Jorgen Hansen for providing photos of the applicators; and Junichi Tokuda, PhD, for the AMIGO photo. We thank Prof. Dr. Horst K. Hahn and Fraunhofer MeVis in Bremen, Germany, for their support by providing an academic license for MeVisLab software. We thank Barbara Silver for proofreading the manuscript. The work was supported by NIH grants P41EB015898, P41RR019703, R03EB013792 and U54EB005149. Dr. Viswanathan has received support from NIH grant K07CA117979.

References

[1] Cancer facts & figures 2012 [http://www.cancer.org/Research/CancerFactsFigures/CancerFactsFigures/cancer-facts-figures-2012].
[2] Viswanathan AN, Thomadsen B. American Brachytherapy Society consensus guidelines for locally advanced carcinoma of the cervix. Part I: general principles. Brachytherapy 2012;11(1):33–46.
[3] Viswanathan AN, Kirisits C, Erickson B, Pötter R. Gynecologic radiation therapy: novel approaches to image-guidance and management. Berlin; London: Springer; 2011.
[4] Viswanathan AN, Moughan J, Small Jr W, Levenback C, Iyer R, Hymes S, et al. The quality of cervical cancer brachytherapy implantation and the impact on local recurrence and disease-free survival in radiation therapy oncology group prospective trials 0116 and 0128. Int J Gynecol Cancer 2012;22(1):123–31.
[5] Hricak H, Gatsonis C, Coakley FV, Snyder B, Reinhold C, Schwartz LH, et al. Early invasive cervical cancer: CT and MR imaging in preoperative evaluation — ACRIN/GOG comparative study of diagnostic performance and interobserver variability. Radiology 2007;245(2):491–8.
[6] Viswanathan AN, Erickson BA. Three-dimensional imaging in gynecologic brachytherapy: a survey of the American Brachytherapy Society. Int J Radiat Oncol Biol Phys 2010;76(1):104–9.
[7] Viswanathan AN, Creutzberg CL, Craighead P, McCormack M, Toita T, Narayan K, et al. International brachytherapy practice patterns: a survey of the Gynecologic Cancer Intergroup (GCIG). Int J Radiat Oncol Biol Phys 2012;82(1):250–5.
[8] Viswanathan AN, Cormack R, Holloway CL, Tanaka C, O'Farrell D, Devlin PM, et al. Magnetic resonance-guided interstitial therapy for vaginal recurrence of endometrial cancer. Int J Radiat Oncol Biol Phys 2006;66(1):91–9.
[9] Viswanathan AN, Szymonifka J, Tempany-Afdhal C, Cormack RA. A prospective trial of real-time magnetic resonance-guided catheter placement in interstitial gynecologic brachytherapy. Submitted 2012.
[10] Viswanathan AN, Beriwal S, De Los Santos JF, Demanes DJ, Gaffney D, Hansen J, et al. American Brachytherapy Society consensus guidelines for locally advanced carcinoma of the cervix. Part II: high-dose-rate brachytherapy. Brachytherapy 2012;11(1):47–52.
[11] Beriwal S, Demanes DJ, Erickson B, Jones E, De Los Santos JF, Cormack RA, et al. American Brachytherapy Society consensus guidelines for interstitial brachytherapy for vaginal cancer. Brachytherapy 2012;11(1):68–75.
[12] Lee LJ, Das IJ, Higgins SA, Jhingran A, Small Jr W, Thomadsen B, et al. American Brachytherapy Society consensus guidelines for locally advanced carcinoma of the cervix. Part III: low-dose-rate and pulsed-dose-rate brachytherapy. Brachytherapy 2012;11(1):53–7.
[13] Cleary K, Peters TM. Image-guided interventions: technology review and clinical applications. Annu Rev Biomed Eng 2010;12:119–42.
[14] Jurgenliemk-Schulz IM, Lang S, Tanderup K, de Leeuw A, Kirisits C, Lindegaard J, et al. Variation of treatment planning parameters (D90 CTV, D 2cc for OAR) for cervical cancer tandem ring brachytherapy in a multicentre setting: comparison of standard planning and 3D image guided optimisation based on a joint protocol for dose–volume constraints. Radiother Oncol: J Eur Soc Ther Radiol Oncol 2010;94(3):339–45.
[15] Viswanathan AN, Dimopoulos J, Kirisits C, Berger D, Potter R. Computed tomography versus magnetic resonance imaging-based contouring in cervical cancer brachytherapy: results of a prospective trial and preliminary guidelines for standardized contours. Int J Radiat Oncol Biol Phys 2007;68(2):491–8.
[16] Kirisits C, Potter R, Lang S, Dimopoulos J, Wachter-Gerstner N, Georg D. Dose and volume parameters for MRI-based treatment planning in intracavitary brachytherapy for cervical cancer. Int J Radiat Oncol Biol Phys 2005;62(3):901–11.
[17] Potter R, Haie-Meder C, Van Limbergen E, Barillot I, De Brabandere M, Dimopoulos J, et al. Recommendations from gynaecological (GYN) GEC ESTRO working group (II): concepts and terms in 3D image-based treatment planning in cervix cancer brachytherapy-3D dose volume parameters and aspects of 3D image-based anatomy, radiation physics, radiobiology. Radiother Oncol: J Eur Soc Ther Radiol Oncol 2006;78(1):67–77.
[18] Haie-Meder C, Potter R, Van Limbergen E, Briot E, De Brabandere M, Dimopoulos J, et al. Recommendations from Gynaecological (GYN) GEC-ESTRO Working Group (I): concepts and terms in 3D image based 3D treatment planning in cervix cancer brachytherapy with emphasis on MRI assessment of GTV and CTV. Radiother Oncol: J Eur Soc Ther Radiol Oncol 2005;74(3):235–45.
[19] Tanderup K, Hellebust TP, Lang S, Granfeldt J, Potter R, Lindegaard JC, et al. Consequences of random and systematic reconstruction uncertainties in 3D image based brachytherapy in cervical cancer. Radiother Oncol: J Eur Soc Ther Radiol Oncol 2008;89(2):156–63.
[20] Berger D, Dimopoulos J, Potter R, Kirisits C. Direct reconstruction of the Vienna applicator on MR images. Radiother Oncol: J Eur Soc Ther Radiol Oncol 2009;93(2):347–51.
[21] Haack S, Nielsen SK, Lindegaard JC, Gelineck J, Tanderup K. Applicator reconstruction in MRI 3D image-based dose planning of brachytherapy for cervical cancer. Radiother Oncol: J Eur Soc Ther Radiol Oncol 2009;91(2):187–93.
[22] De Leeuw AA, Moerland MA, Nomden C, Tersteeg RH, Roesink JM, Jurgenliemk-Schulz IM. Applicator reconstruction and applicator shifts in 3D MR-based PDR brachytherapy of cervical cancer. Radiother Oncol: J Eur Soc Ther Radiol Oncol 2009;93(2):341–6.
[23] Tanderup K, Nielsen SK, Nyvang GB, Pedersen EM, Rohl L, Aagaard T, et al. From point A to the sculpted pear: MR image guidance significantly improves tumour dose and sparing of organs at risk in brachytherapy of cervical cancer. Radiother Oncol: J Eur Soc Ther Radiol Oncol 2010;94(2):173–80.
[24] Cormack RA, Tempany CM, D'Amico AV. Optimizing target coverage by dosimetric feedback during prostate brachytherapy. Int J Radiat Oncol Biol Phys 2000;48(4):1245–9.
[25] Wells WM, Grimson WL, Kikinis R, Jolesz FA. Adaptive segmentation of MRI data. IEEE Trans Med Imaging 1996;15(4):429–42.
[26] Kapur T, Grimson WE, Wells III WM, Kikinis R. Segmentation of brain tissue from magnetic resonance images. Med Image Anal 1996;1(2):109–27.
[27] Pham DL, Prince JL. A generalized EM algorithm for robust segmentation of magnetic resonance images. Conference on Information Sciences and Systems, CISS; 1999. p. 558–63.
[28] Pohl KM, Fisher J, Levitt JJ, Shenton ME, Kikinis R, Grimson WE, et al. A unifying approach to registration, segmentation, and intensity correction. MICCAI International Conference on Medical Image Computing and Computer-Assisted Intervention 2005, 8(Pt 1):310–318.
[29] Dempster A, Laird N, Rubin D. Maximal likelihood from incomplete data via the EM algorithm. Royal Statistical Society 1977;B(39):1–38.

[30] Egger J, Bauer M, Kuhnt D, Carl B, Kappus C, Freisleben B, et al. Nugget–Cut: a segmentation scheme for spherically-and elliptically-shaped 3D objects. 32nd Annual Symposium of the German Association for Pattern Recognition (DAGM). Darmstadt, Germany: Springer; 2010. p. 373–82.

[31] Egger J, Viswanathan AN, Kapur T. Bladder segmentation for interstitial gynecologic brachytherapy with the Nugget–Cut approach. 4th NCIGT and NIH image guided therapy workshop; 2011. Arlington, VA.

[32] Mulkern RV, Barnes AS, Haker SJ, Hung YP, Rybicki FJ, Maier SE, et al. Biexponential characterization of prostate tissue water diffusion decay curves over an extended b-factor range. Magn Reson Imaging 2006;24(5):563–8.

[33] Roebuck JR, Haker SJ, Mitsouras D, Rybicki FJ, Tempany CM, Mulkern RV. Carr–Purcell–Meiboom–Gill imaging of prostate cancer: quantitative T2 values for cancer discrimination. Magn Reson Imaging 2009;27(4):497–502.

[34] DiMaio SP, Samset E, Fischer G, Iordachita I, Fichtinger G, Jolesz F, et al. Dynamic MRI scan plane control for passive tracking of instruments and devices. MICCAI International Conference on Medical Image Computing and Computer-Assisted Intervention 2007, 10(Pt 2):50–58.

[35] DiMaio SP, Kacher DF, Ellis RE, Fichtinger G, Hata N, Zientara GP, et al. Needle artifact localization in 3T MR images. Stud Health Technol Inform 2006;119:120–5.

[36] Goksel O, Salcudean SE, Dimaio SP. 3D simulation of needle-tissue interaction with application to prostate brachytherapy. Comput Aided Surg: Official J Int Soc Comput Aided Surg 2006;11(6):279–88.

[37] Cukur T, Yamada M, Overall WR, Yang P, Nishimura DG. Positive contrast with alternating repetition time SSFP (PARTS): a fast imaging technique for SPIO-labeled cells. Magn Reson Medicine: Official J Soc Magn Reson Med/Soc Magn Reson Med 2010;63(2):427–37.

[38] Dumoulin CL, Mallozzi RP, Darrow RD, Schmidt EJ. Phase-field dithering for active catheter tracking. Magn Reson Med: Official J Soc Magn Reson Med/Soc Magn Reson Med 2010;63(5):1398–403.

[39] Schmidt EJ. MRI catheter guidance and steering of vascular procedures with a reduced heating risk. Acad Radiol 2011;18(3):267–9.

[40] Gao Y, Sandhu R, Fichtinger G, Tannenbaum AR. A coupled global registration and segmentation framework with application to magnetic resonance prostate imagery. IEEE Trans Med Imaging 2010;29(10):1781–94.

[41] Han Q, Merck D, Levy J, Villarruel C, Damon JN, Chaney EL, et al. Geometrically proper models in statistical training. Inf Process Med Imaging: Proc Conf 2007;20:751–62.

OPEN ACCESS Freely available online

PLOS ONE

Pituitary Adenoma Volumetry with 3D Slicer

Jan Egger[1,2,3]*, Tina Kapur[1], Christopher Nimsky[2], Ron Kikinis[1]

1 Department of Radiology, Brigham and Women's Hospital, Harvard Medical School, Boston, Massachusetts, United States of America, **2** Department of Neurosurgery, University Hospital of Marburg, Marburg, Germany, **3** Department of Mathematics and Computer Science, The Philipps-University of Marburg, Marburg, Germany

Abstract

In this study, we present pituitary adenoma volumetry using the free and open source medical image computing platform for biomedical research: (3D) Slicer. Volumetric changes in cerebral pathologies like pituitary adenomas are a critical factor in treatment decisions by physicians and in general the volume is acquired manually. Therefore, manual slice-by-slice segmentations in magnetic resonance imaging (MRI) data, which have been obtained at regular intervals, are performed. In contrast to this manual time consuming slice-by-slice segmentation process Slicer is an alternative which can be significantly faster and less user intensive. In this contribution, we compare pure manual segmentations of ten pituitary adenomas with semi-automatic segmentations under Slicer. Thus, physicians drew the boundaries completely manually on a slice-by-slice basis and performed a Slicer-enhanced segmentation using the competitive region-growing based module of Slicer named GrowCut. Results showed that the time and user effort required for GrowCut-based segmentations were on average about thirty percent less than the pure manual segmentations. Furthermore, we calculated the Dice Similarity Coefficient (DSC) between the manual and the Slicer-based segmentations to proof that the two are comparable yielding an average DSC of 81.97±3.39%.

Citation: Egger J, Kapur T, Nimsky C, Kikinis R (2012) Pituitary Adenoma Volumetry with 3D Slicer. PLoS ONE 7(12): e51788. doi:10.1371/journal.pone.0051788

Editor: Arrate Muñoz-Barrutia, University of Navarra, Spain

Received September 20, 2012; **Accepted** November 8, 2012; **Published** December 11, 2012

Funding: This work was supported by National Institutes of Health (NIH) grant P41EB015898. Its contents are solely the responsibility of the authors and do not necessarily represent the official views of the NIH. The funders had no role in study design, data collection and analysis, decision to publish, or preparation of the manuscript.

Competing Interests: The authors have declared that no competing interests exist.

* E-mail: egger@bwh.harvard.edu

These authors contributed equally to this work.

Introduction

Tumors of the sellar region – primarily pituitary adenomas – represent 10% to 25% of all intracranial neoplasms and adenomas comprising the largest portion with an estimated prevalence of approximately 17% [1] and [2]. Adenomas can be classified according to several criteria including the size or the hormone secretion, like secreted hormones include cortisol (Cushing's disease) and treatment is in general followed by a decrease of prolactine levels and tumor volume, whereas the first choice of treatment for Cushing's disease remains surgery [3] and [4]. However, for hormone-inactive mircroadenomas, which are less than 1 cm in diameter, there is no need for a direct surgical resection and the follow-up examinations contain endocrine and ophthalmological evaluation, and magnetic resonance imaging mainly performed in one year intervals. In contrast to a wait-and-scan strategy which is no longer indicated, the microsurgical removal becomes the treatment of choice, in the case of continuous tumor volume progress, which has to be evaluated each time. Therefore, image analysis that includes segmentation and registration of these successive scans is useful in the accurate measurement of tumor progression.

In this section, related work in the field of supporting pituitary adenoma surgery is summarized. Other authors working in this field are Neubauer et al. [5] and [6] and Wolfsberger et al. [7] who investigated a virtual endoscopy system called STEPS. STEPS is designed to aid surgeons performing pituitary surgery, thereby using a semi-automatic segmentation approach which is based on the so-called watershed-from-markers method. This segmentation method technique uses manually defined markers in the object of interest – in this case the pituitary adenoma – and the background. The watershed-from-markers method is very computationally intensive, but Felkel et al. [8] introduced a memory efficient and fast implementation which can also be extended to 3D. Zukic et al. [9] developed a deformable model based approach that uses balloon inflation forces [10] for the segmentation of pituitary adenomas. The balloon inflation forces are used to expand a mesh iteratively incorporating different features for the vertex movement calculation: Vertices with lower curvature are moved outwards by a larger amount, thus stimulating smoother meshes. Vertices with high angle between normal and center vertex- vector are inflated by a smaller amount, in order to penalize protrusions. A recently introduced graph-based method for pituitary adenoma segmentation starts by setting up a directed and weighted 3D graph from a user-defined seed point that is located inside the pituitary adenoma [11]. Accordingly graph construction, the minimal cost closed set on the graph is computed via a polynomial time s-t cut [12]. The graph-based approach samples along rays that are sent through the surface points of a polyhedron [13] to generate the graph (note: the center of the polyhedral user-defined seed point that is located inside the pituitary adenoma). A novel multi-scale sheet enhancement measure that has been applied to paranasal sinus bone segmentation has been presented by Descoteaux et al. [14]. For the simulation of pituitary surgery, this measure has essential properties, which should be incorporated in the computation of anatomical models. However, if the volume of pituitary adenomas is analyzed over a long time of

period for clinical studies, this is in general done via manual slice-by-slice segmentation, or sometimes semi-automatically supported by a software tool. Then, the three-dimensional tumor volume is calculated out of the single 2D contours, the amount of slices and the slice thickness [15], [16] and [17]. The growth of on-functioning pituitary adenomas in patients referred for surgery for example, has been studied by Honegger et al. [18], by calculating the three-dimensional tumor volume from the two-dimensional contours that have been manually outlined on each slice. Pituitary adenoma volume changes after gamma knife radiosurgery (GKRS) have been studied by Pamir et al. [19]. Therefore, the magnetic resonance imaging (MRI)-based volumetric analysis of the pituitary adenomas was done by using GammaPlan software from Elekta Instruments (Atlanta, GA) for tumor volume at the time of treatment. For the tumor volume on the follow-up MRI scans software from Imaging Inc. (Waterloo, Canada) was used. However, no further details have been provided how time-consuming and precise this procedure is by comparing it with ground truth segmentations from experts, e.g. manual slice-by-slice segmentations. Jones and Keogh [20] introduced a simple technique of estimating the size of large pituitary adenomas. To measure the size of a large pituitary tumor they apply a method on computed tomography (CT) scan slices of known thickness. Thus, the edge of the pituitary tumor – seen on hard copy films of the CT scan – is traced using an outlining routine on a computer and associated digitising slab. Afterwards, the measured area of the tumor is scaled and multiplied by the slice thickness in order to obtain the tumor volume for this CT slice. Finally, the overall tumor volume is obtained by calculating and summing up all volumes of the CT slices where the tumor volume is visible.

Volumetric change in pituitary adenomas over time is a critical factor in treatment decisions by physicians. Typically, the tumor volume is computed on a slice-by-slice basis using MRI patient scans obtained at regular intervals. (3D) Slicer – a free open source software platform for biomedical research – provides an alternative to this manual slice-by-slice segmentation process, which is significantly faster and less user intensive. In this study, four physicians segmented pituitary adenomas in ten patients, once using the competitive region-growing based GrowCut segmentation module of Slicer, and once purely by drawing boundaries completely manually on a slice-by-slice basis. We show and evaluate the utility of 3D Slicer in simplifying the time-consuming manual slice-by-slice segmentation while achieving a comparable accuracy. To the best of our knowledge, this is the first time the evaluation of pituitary adenoma segmentation with the free and open source medical image analysis software Slicer has been presented. Because Slicer can be downloaded and used for free, our study could be useful in clinical practice for centers different from our in which the research has been performed. Moreover, the presented GrowCut segmentation study is not limited to pituitary adenomas. GrowCut could also be used to support the segmentations of other pathologies, e.g. glioblastoma multiforme where even more time-consuming volumetry is required.

The rest of this contribution is organized as follows: *Section 2* presents the material and the methods. *Section 3* presents the results

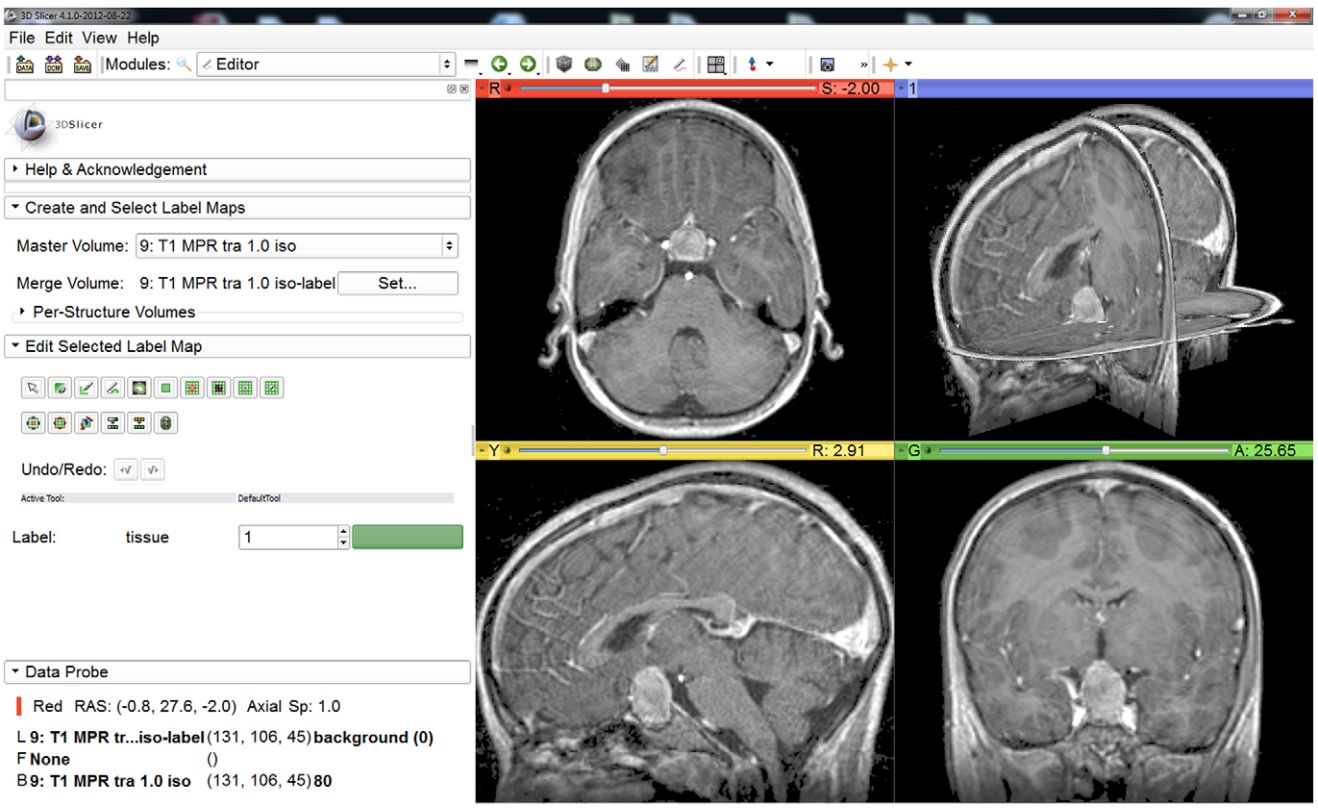

Figure 1. 3D Slicer interface with the Slicer-Editor on the left side and a loaded pituitary adenoma data set on the right side: axial slice (upper left window), sagittal slice (lower left window), coronal slice (lower right window) and the three slices shown in a 3D visualization (upper right window).
doi:10.1371/journal.pone.0051788.g001

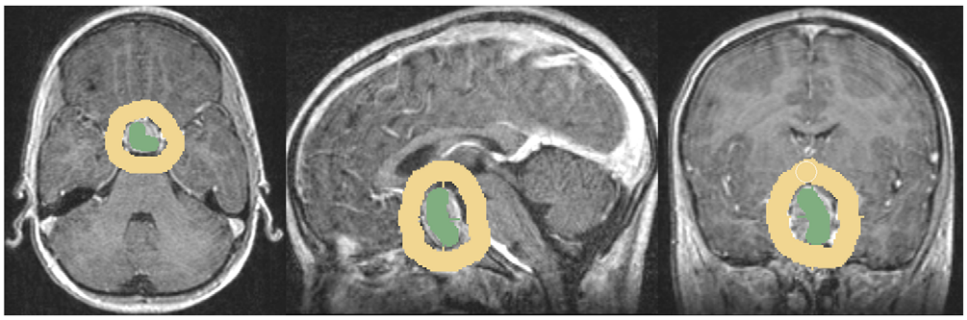

Figure 2. These images present a typical user initialization for pituitary adenoma segmentation under Slicer with for the GrowCut algorithm: axial (left image), sagittal (middle image) and coronal (right image). Note: the tumor has been initialized in green and the background has been initialized in yellow.
doi:10.1371/journal.pone.0051788.g002

of our experiments, and *Section 4* concludes and discusses the study and outlines areas for future work.

Materials and Methods

Data

Ten diagnostic T1- and T2- weighted magnetic resonance imaging scans of pituitary adenomas were used for segmentation. These were acquired on a 1.5 Tesla MRI scanner (Siemens MAGNETOM Sonata, Siemens Medical Solutions, Erlangen, Germany) using a standard head coil. Scan parameters were: TR/TE 4240/84.59 msec, 3850/11 msec, 2090/4.38 msec, 690/17 msec, 480/12 msec, 479/17 msec and 450/12 msec, isotropic matrix, 1 mm; FOV, 250×250 mm; 160 sections. The segmentations have been performed mainly in coronal but for some cases also in axial slices using the homogenously contrast-enhancing structures of the pituitary adenomas in the T1/T2 scans.

Software

The Software used in this study or the semi-automatic segmentation work was (3D) Slicer. Slicer is an open source medical image computing platform for biomedical research and freely downloadable (3D Slicer, available: http://www.slicer.org, accessed: 2012 Nov 13). To acquire the ground truth for our study, manual slice-by-slice segmentations of every data set have been performed by neurosurgeons at the *University Hospital of Marburg in Germany* (Chairman: Professor Dr. Christopher Nimsky). The physicians have several years of experience in the resection of pituitary adenomas. However, if the borders of pituitary adenomas have been very similar between consecutive slices, the physicians were allowed to skip manual segmentation for these slices. For the overall volume calculation the software interpolated the boundaries in these areas. The manual segmentation tool used for pituitary adenoma outlining provided simple contouring capabilities, and has been set-up with the medical prototyping platform MeVisLab (MeVisLab, available: http://www.mevislab.de/, accessed: 2012 Nov 13). As hardware platform we used an computer with Intel Core i5-750 CPU, 4×2.66 GHz, 8 GB RAM, with Windows XP Professional ×64 Version, Version 2003, Service Pack 2.

GrowCut Segmentation in Slicer

GrowCut is an interactive segmentation approach that bases on the idea of cellular automaton. Using an iterative labeling procedure resembling competitive region growing, the GrowCut approach achieves reliable and reasonably fast segmentation of moderately difficult objects in 2D and in 3D. The user's initialization of GrowCut results in a set of initial seed pixels. These seed pixels in turn try to assign their labels to their pixel neighborhood which happens when the similarity measure of the two pixels weighted by the neighboring pixel's weight or "strength" exceeds its current weight. A label assignment results in an actualization of the pixel's weight as well. This labeling procedure continues iteratively until modification of the pixel labels is no longer feasible and a stable configuration has been reached. Besides the initial seed pixels – in general painted strokes on the apparent foreground and background – the GrowCut approach requires no additional inputs from the user. However, by adding additional labels in the image, the user can modify the

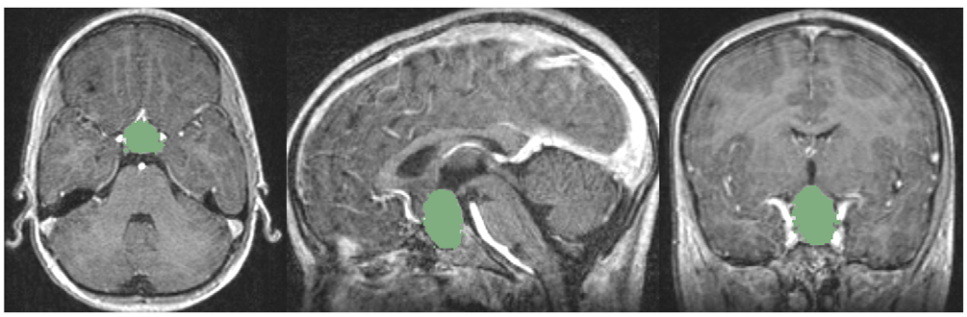

Figure 3. These images present the segmentation result (green) of the GrowCut algorithm of Slicer: axial (left image), sagittal (middle image) and coronal (right image). Note: the pituitary adenoma and background initialization for this segmentation result is presented in of Figure 2.
doi:10.1371/journal.pone.0051788.g003

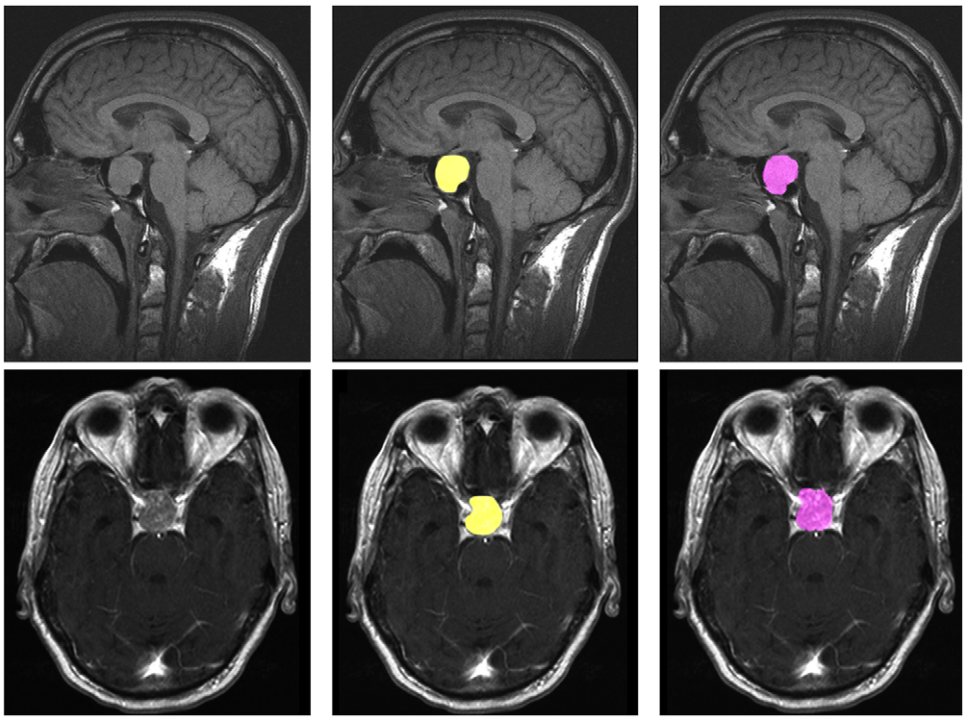

Figure 4. These screenshots present segmentation results on a sagittal (upper row) and an axial (lower row) slice for the manual segmentation (middle images, yellow) and the Slicer-based GrowCut segmentation (right images, magenta).
doi:10.1371/journal.pone.0051788.g004

segmentation, enabling personalization of the approach to the user. The current implementation of the GrowCut algorithm in Slicer consists of a GUI front-end to enable interactions of the user with the image and an algorithm back-end where the segmentation is computed. The GUI front-end consists of a simple to use interface which enables the user to paint directly on the image. GrowCut requires paints with at least two different colors: one for the foreground and one for the background label class. The naïve implementation of the GrowCut approach would require every single pixel to be visited within every iteration. Additionally, a pixel would need to "visit" every neighbor pixel and update the pixel's labels and strengths. Especially for large 3D images such an implementation would be computationally very expensive. Therefore, our implementation uses the following techniques for speeding up the automatic segmentation process:

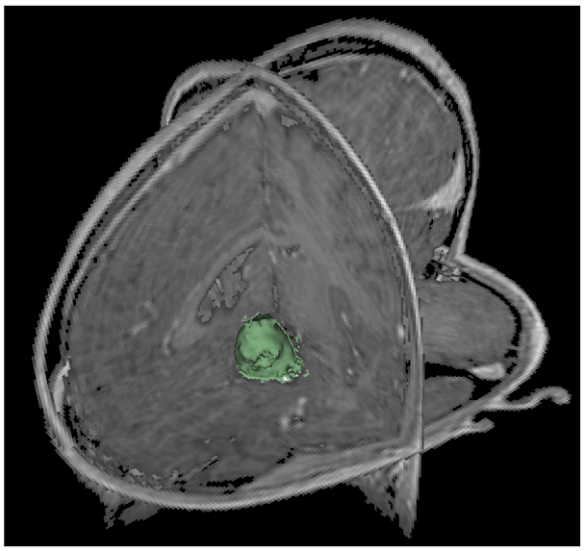

Figure 5. This image presents the 3D segmentation result of GrowCut (green) for the tumor and background initialization of Figure 2. After the initialization of the GrowCut algorithm under Slicer it took about three seconds to get the segmentation result on an Intel Core i7 CPU, 4×2.50 GHz, 8 GB RAM, Windows 7 Professional ×64 Version, Service Pack 1.
doi:10.1371/journal.pone.0051788.g005

- The algorithm computes the segmentation only within a small region of interest (ROI), because the user is typically interested only in segmenting out a small area in the image. This *ROI* is computed as a convex hull of all user labeled pixels with an additional margin.
- Several small regions of the image are updated simultaneously, by executing iterations involving the image in multiple threads.
- In addition, the similarity distance between the pixels are all pre-computed once and then reused.
- Moreover, the algorithm keeps track of "saturated" pixels – for "saturated" pixels the weights and therefore the labels can no longer be updated. This, on the other hand avoids the expensive neighborhood computation on those pixels. Finally, keeping track of such "saturated" pixels helps to determine when to terminate the algorithm.

Slicer-based Pituitary Adenoma Segmentation

After testing various segmentation facilities available in Slicer, we identified that the use of GrowCut followed by additional morphological operations (like erosion, dilation, and island removal) provides the most efficient segmentation method for

Table 1. Direct comparison of manual slice-by-slice and Slicer-based GrowCut segmentation results for ten pituitary adenomas via the Dice Similarity Coefficient (DSC).

Case No.	volume of pituitary adenomas (mm^3)		number of voxels		DSC (%)
	manual	automatic	manual	automatic	
1	6568.69	7195	72461	79370	85.87
2	4150.91	5427.76	4457	5828	84.36
3	7180.44	6481.12	35701	32224	82.11
4	5538.25	5964.5	61094	65796	85.1
5	3230.26	2950.45	22027	20119	77.51
6	9858.4	10410.8	67224	70991	84.46
7	6111.79	5274.89	52500	45311	75.6
8	5082.1	4169.32	56062	45993	80.1
9	15271.1	15838.9	104133	108005	83.41
10	757.007	1016.58	5162	6932	81.21

doi:10.1371/journal.pone.0051788.t001

pituitary adenomas for our MRI images. Therefore, the following workflow to perform pituitary adenoma segmentation has been used:

- loading the patient data set into Slicer
- initialize foreground and background for GrowCut, by drawing an area inside the pituitary adenoma and a stroke outside the tumor
- starting the automatic competing region-growing in Slicer
- after visual inspection of the results, use morphological operations like dilation, erosion, and island removal for post-editing.

The Slicer Editor module user interface, which has been used for the initialization of GrowCut is shown in Figure 1 on the left side. The right side of Figure 1 shows a pituitary adenoma after the data set is loaded into Slicer. A typical user initialization for GrowCut on the axial, sagittal and coronal cross-sections is presented in Figure 2. Finally, Figure 3 shows the results of the current Slicer GrowCut method for the initialization of Figure 2. As hardware platform for the GrowCut segmentation we used an Apple MacBook Pro with 4 Intel Core i7, 2.3 GHz, 8 GB RAM, AMD Radeon HD 6750M, Mac OS X 10.6 Snow Leopard.

Comparison Metrics

The Dice Similarity Coefficient (DSC) [21] and [22] was used to compare the agreement between the slice-by-slice segmentations (A) and the Slicer-based segmentations (B). Therefore, we saved the segmentation results from both methods as binary volumes and calculated the relative volume overlap between the two binary volumes A and B.

Results

The aim of this study was to evaluate the usability of Slicer for the segmentation of pituitary adenomas compared to manual slice-by-slice segmentation. Therefore, we used two metrics for an evaluation:

- The time it took for physicians to segment pituitary adenomas manually vs. using Slicer and
- the agreement between the two segmentations calculated via the Dice Similarity Coefficient.

By evaluating our results with these metrics, our assumption is that if Slicer can be used to produce pituitary adenoma segmentations that are statistically equivalent to the pure manual segmentations from physicians, and in substantially less time, then the tool is helpful for volumetric follow-ups of pituitary adenoma patients. The results of our study are presented in detail in Table 1 and Table 2, the primary conclusion of which is that Slicer-based pituitary adenoma segmentation can be performed in about two third of the time, and with acceptable DSC agreement of $81.97 \pm 3.39\%$ to slice-by-slice segmentations of physicians. Table 1 presents the segmentation results for: volume of tumor in mm^3, number of voxels and Dice Similarity Coefficient for ten pituitary adenomas. Moreover, in Table 2, the summary of results: minimum, maximum, mean μ and standard deviation σ for the ten pituitary adenomas from Table 1 are provided (note: volume is

Table 2. Summary of results: min, max, mean μ and standard deviation σ for ten pituitary adenomas.

	volume of pituitary adenomas (cm^3)		number of voxels		DSC (%)
	manual	automatic	manual	automatic	
min	0.76	1.02	4457	5828	75.60
max	15.27	15.84	104133	108005	85.87
$\mu \pm \sigma$	6.37 ± 3.96	6.47 ± 4.14	48082.1	48056.9	81.97 ± 3.39

doi:10.1371/journal.pone.0051788.t002

presented in cm^3 in Table 2). Additionally to these quantitative results, we present sample pituitary adenoma segmentation results in Figures 3, 4 and 5 for visual inspection. Figure 3 shows the results of the Slicer-based GrowCut segmentation for the tumor and background initialization of Figure 2. Figure 4 presents the direct comparison for two cases of a Slicer-based vs. the manual slice-by-slice segmentation on a sagittal (upper row) and an axial (lower row) slice. The semi-automatic Slicer-based segmentation (magenta) is shown on the right side of Figure 4 and the pure manual segmentation (yellow) is shown in the middle images of Figure 4. Finally, a 3D rendered pituitary adenoma segmentation (green) is superimposed on three orthogonal cross-sections of the data in Figure 5.

Discussion

For accurate volumetry of cerebral pathologies like pituitary adenomas it is necessary to investigate methods that calculate the boundaries on the basis of all slices. In contrast, simpler methods – such as geometric models – provide only a rough approximation of the volume of the pathology. Especially, when accurate determination of size is of upmost importance in order to draw safe conclusions in oncology, these should not be used. Instead of all slices, geometric models use only one or several user-defined diameters, which can be achieved manually very quickly, to approximate the volume. Thereby, the volume is defined as $1/6\ \pi d^3$ and the ellipsoid model defines the volume as $\frac{1}{6\pi abc}$, according to the spherical model. With d as the diameter of the maximum cross-sectional area and a, b, c represent the diameters in the three axes of the tumor [17]. Nobels et al. [23] measured the x, y and z radii in the frontal, sagittal and coronal planes, respectively, and assuming a spherical volume, the formula $\frac{4}{3\pi r^3}$ was afterwards used for the calculation of the volume – with r being the mean of the x, y and z radii. Korsisaari et al. [24] estimated the size of pituitary adenoma transplants with a caliper tool from *Fred V. Fowler Co., Inc.*, by measuring the largest tumor diameter and the diameter perpendicular to this diameter (with a the largest tumor diameter and b the perpendicular diameter). Then, the tumor volume was calculated using $V = \frac{\pi ab^2}{6}$. Though, the clinical standard for measuring brain tumors is the Macdonald criteria [25]. These adopt uniform, rigorous response criteria similar to those in general oncology where response is defined as a $\geq$50% reduction of the tumor size. In general, the measure of "size" is the largest cross-sectional area (the largest cross-sectional diameter multiplied by the largest diameter perpendicular to it). Even though the semi-automatic segmentation results achieved with the GrowCut module of Slicer were reasonably good, additional editing on some slices was always required. However, these edits could be accomplished quite quickly because the GrowCut results were in close proximity of the desired pituitary adenoma boundary. Moreover, the manual segmentations by the neurosurgeons took in average about four minutes. In contrast the semi-automatic segmentation with the GrowCut implementation under Slicer took in average under three minutes, including the time needed for the post-editing of the GrowCut results.

In this study, the evaluation of pituitary adenoma segmentation with the free and open source medical image analysis software Slicer has been presented. Slicer provides a semi-automatic, 3D segmentation algorithm called GrowCut, which is a feasible alternative to the time-consuming process of volume calculation during monitoring of a patient, for which slice-by-slice contouring has been the best demonstrated practice. In addition, Slicer offers Editing tools for a manual refinement of the results upon completion of the automatic GrowCut segmentation. Afterwards, the 3D volume of the pituitary adenomas is automatically computed and stored as an aide for the surgeon in decision making for comparison with follow-up scans. The segmentation results have been evaluated on ten pituitary adenoma data sets against manual slice-by-slice expert segmentations via the common Dice Similarity Coefficient. Summing up, the accomplished research highlights of the presented work are:

- Manual slice-by-slice segmentations of pituitary adenomas have been performed by clinical experts resulting in ground truth of tumor boundaries and estimates of rater variability.
- Physicians have been trained in segmenting pituitary adenomas with GrowCut and the Editor tools available in Slicer.
- Trained physicians segmented a pituitary adenoma evaluation set with Slicer.
- Segmentation times have been measured for the GrowCut-based segmentation under Slicer.
- The quality of the segmentations have been evaluated with the Dice Similarity Coefficient.

There are several areas of future work: For example, we plan to automate some steps of the segmentation workflow under Slicer for pituitary adenoma. For example the initialization of GrowCut could be more automated. Instead of initializing the foreground on three single 2D slices, a single 3D initialization could be used by means of generating a sphere around at the position of the user-defined seed point. In addition, the GrowCut algorithm can be enhanced with statistical information about the shape [26] and [27] and the texture [28] and [29] of pituitary adenomas to improve the automatic segmentation result. Moreover, we want to study how a Slicer-based GrowCut segmentation can be used to enhance the segmentation process of other cerebral pathologies [30], like glioblastoma multiforme. Furthermore, we are considering improving the algorithm by running the whole segmentation iteratively: After the segmentation has been performed, the result of the segmentation can be used as a new initialization for a new segmentation run and so on.

Acknowledgments

We want to acknowledge the members of the Slicer Community and in particular Steve Pieper for their contributions, and moreover Harini Veeraraghavan and Jim Miller from GE for developing the GrowCut module for Slicer. Furthermore, the authors would like to thank the physicians Dr. med. Barbara Carl, Christoph Kappus, Dr. med. Daniela Kuhnt and Rivka Colen, M.D. for participating in this study. Finally, the authors would like to thank Fraunhofer MeVis in Bremen, Germany, for their collaboration and especially Professor Dr. Horst K. Hahn for his support.

Author Contributions

Conceived and designed the experiments: JE. Performed the experiments: JE. Analyzed the data: JE. Contributed reagents/materials/analysis tools: JE TK CN RK. Wrote the paper: JE TK.

References

1. National Cancer Institute – Pituitary Tumors Treatment. Available: http://www.cancer.gov/cancertopics/pdq/treatment/pituitary/HealthProfessional/page1/AllPages#1. Accessed 2012 Nov 13.
2. Weber M-A, Zoubaa S, Politi M, Grunwald I, Essig M (2007) [Sellar tumors] Der Radiologe; Springer Berlin/Heidelberg, 47(6): 492–500.
3. Biller BMK, Colao A, Petersenn S, Bonert VS, Boscaro M (2010) Prolactinomas, Cushing's disease and acromegaly: debating the role of medical therapy for secretory pituitary adenomas. BMC Endocrine Disorders 10(1): 10.
4. Buchfelder M, Schlaffer S (2009) Surgical treatment of pituitary tumours. Best Pract. Res., Clin. Endocrinol. Metab 23(5): 677–692.
5. Neubauer A, Wolfsberger S, Forster MT, Mroz L, Wegenkittl R, et al. (2005) Advanced virtual endoscopic pituitary surgery. IEEE Trans. Vis. Comput. Graph. (TVCG) 11(5): 497–507.
6. Neubauer A (2005) Virtual Endoscopy for Preoperative Planning and Training of Endonasal Transsphenoidal Pituitary Surgery. Dissertation in Computer Science, Vienna University of Technology, 1–152.
7. Wolfsberger S, Neubauer A, Bühler K, Wegenkittl R, Czech T, et al. (2006) Advanced virtual endoscopy for endoscopic transsphenoidal pituitary surgery. Neurosurgery 59(5): 1001–1010.
8. Felkel P, Wegenkittl R, Bruckschwaiger M (2001) Implementation and complexity of the watershed-from-markers algorithm computed as a minimal cost forest. Proceedings of Eurographics'01, 26–35.
9. Zukic D, Egger J, Bauer MHA, Kuhnt D, Carl B, et al. (2011) Preoperative Volume Determination for Pituitary Adenoma. In: Proceedings of SPIE Medical Imaging Conference, Orlando, Florida, USA, Vol. 7963, 79632T-79632T-7.
10. Cohen LD (1991) On active contour models and balloons. CVGIP: Image Underst., 53(2), 211–218.
11. Egger J, Bauer MHA, Kuhnt D, Freisleben B, Nimsky C (2010) Pituitary Adenoma Segmentation. Proceedings of International Biosignal Processing Conference. Kurths J, Penzel T, Malberg H, Wessel N (Hrsg), Berlin, Germany, Paper-ID: 061: 1–4.
12. Boykov Y, Kolmogorov V (2004) An Experimental Comparison of Min-Cut/Max-Flow Algorithms for Energy Minimization in Vision. IEEE Transactions on Pattern Analysis and Machine Intelligence 26(9), 1124–1137.
13. Egger J, Mostarkić Z, Großkopf S, Freisleben B (2007) A Fast Vessel Centerline Extraction Algorithm for Catheter Simulation. In: 20th IEEE International Symposium on Computer-Based Medical Systems (CBMS). Maribor, Slovenia, IEEE Press, 177–182.
14. Descoteaux M, Audette M, Chinzei K, Siddiqi K (2006) Bone enhancement filtering: application to sinus bone segmentation and simulation of pituitary surgery. Comput Aided Surg 11(5): 247–255.
15. Buhk J-H, Jung S, Psychogios MN, Göricke S, Hartz S (2010) Tumor volume of growth hormone-secreting pituitary adenomas during treatment with pegvisomant: a prospective multicenter study. J Clin Endocrinol Metab 95 (2): 552–558.
16. Gondim AJ, Tella OI Jr, Schops M (2006) Intrasellar pressure and tumor volume in pituitary tumor. Arq Neuropsiquiatr 64(4): 971–975.
17. Jimenez C, Burman P, Abs R, Clemmons DR, Drake WM, et al. (2008) Follow-up of pituitary tumor volume in patients with acromegaly treated with pegvisomant in clinical trials. Eur J Endocrinol 159: 517–523.
18. Honegger J, Zimmermann S, Psaras T, Petrick M, Mittelbronn M, et al. (2008) Growth modelling of non-functioning pituitary adenomas in patients referred for surgery. Eur J Endocrinol 158: 287–294.
19. Pamir MN, Kiliç T, Belirgen M, Abacioğlu U, Karabekiroğlu N (2007) Pituitary adenomas treated with gamma knife radiosurgery: volumetric analysis of 100 cases with minimum 3 year follow-up. Neurosurgery 61(2): 270–80, discussion 280.
20. Jones AP, Keogh AJA (1990) simple method of estimating the size of large pituitary adenomas, Acta Neurochir (Wien), Springer Press, 107: 61–62.
21. Zou KH, Warfield SK, Bharatha A, Tempany CMC, Kaus MR, et al. (2004) Statistical validation of image segmentation quality based on a spatial overlap index: scientific reports. Acad Radiol 11(2): 178–189.
22. Sampat MP, Wang Z, Markey MK, Whitman GJ, Stephens TW, et al. (2006) Measuring intra- and inter-observer Agreement in Identifying and Localizing Structures in Medical Images. IEEE Inter. Conf. Image Processing, 81–84.
23. Nobels FRE, de Herder WW, van den Brink WM, Kwekkeboom DJ, Hofland LJ, et al. (2000) Long-term treatment with the dopamine agonist quinagolide of patients with clinically non-functioning pituitary adenoma. European Journal of Endocrinology, 143: 615–621.
24. Korsisaari N, Ross J, Wu X, Kowanetz M, Pal N, et al. (2008) Blocking Vascular Endothelial Growth Factor-A Inhibits the Growth of Pituitary Adenomas and Lowers Serum Prolactin Level in a Mouse Model of Multiple Endocrine Neoplasia Type 1, Clinical Cancer Research, January 1; 14(1): 249–258.
25. Macdonald DR, Cascino TL, Schold SC Jr, Cairncross JG (1990) Response criteria for phase II studies of supratentorial malignant glioma. J Clin Oncol.; 8(7): 1277–80.
26. Cootes TF, Taylor CJ (1992) Active Shape Models – 'Smart Snakes', Proceedings of the British Machine Vision Conference, 266–275.
27. Egger J, Freisleben B, Nimsky C, Kapur T (2012) Template-Cut: A Pattern-Based Segmentation Paradigm. Sci Rep., Nature Publishing Group (NPG), 2012;2: 420. Epub 2012 May 24.
28. Cootes TF, Taylor CJ (2004) Statistical Models of Appearance for Computer Vision. Technical report, University of Manchester.
29. Greiner K, Egger J, Großkopf S, Kaftan JN, Dörner R, et al. (2008) Segmentation of Aortic Aneurysms in CTA Images with the Statistic Approach of the Active Appearance Models (in German). In: Proceedings of Bildverarbeitung für die Medizin (BVM), Berlin, Germany, Springer Press, 51–55.
30. Egger J, Kappus C, Freisleben B, Nimsky (2011) C. A Medical Software System for Volumetric Analysis of Cerebral Pathologies in Magnetic Resonance Imaging (MRI) Data. In: Journal of Medical Systems, Springer, 6(4): 2097–109.

Fiber Tractography Based on Diffusion Tensor Imaging Compared With High-Angular-Resolution Diffusion Imaging With Compressed Sensing: Initial Experience

Daniela Kuhnt, MD*
Miriam H.A. Bauer, MSc*‡
Jan Egger, PhD*§
Mirco Richter, MSc¶
Tina Kapur, PhD§
Jens Sommer, PhD||
Dorit Merhof, PhD¶
Christopher Nimsky, MD, PhD*

*Department of Neurosurgery and; ||Department of Psychiatry and Psychotherapy, University of Marburg, Marburg, Germany; ‡International Clinical Research Center, St. Anne's University Hospital Brno, Brno, Czech Republic; §Department of Radiology, Brigham and Women's Hospital and Harvard Medical School, Boston, Massachusetts; ¶Visual Computing, University of Konstanz, Konstanz, Germany

The first 2 authors contributed equally to this manuscript.

Correspondence:
Christopher Nimsky, MD, PhD,
Department of Neurosurgery,
University of Marburg, Baldingerstraße,
35043 Marburg, Germany.
E-mail: nimsky@med.uni-marburg.de

Received, June 1, 2012.
Accepted, July 17, 2012.

BACKGROUND: The most frequently used method for fiber tractography based on diffusion tensor imaging (DTI) is associated with restrictions in the resolution of crossing or kissing fibers and in the vicinity of tumor or edema. Tractography based on high-angular-resolution diffusion imaging (HARDI) is capable of overcoming this restriction. With compressed sensing (CS) techniques, HARDI acquisitions with a smaller number of directional measurements can be used, thus enabling the use of HARDI-based fiber tractography in clinical practice.

OBJECTIVE: To investigate whether HARDI+CS-based fiber tractography improves the display of neuroanatomically complex pathways and in areas of disturbed diffusion properties.

METHODS: Six patients with gliomas in the vicinity of language-related areas underwent 3-T magnetic resonance imaging including a diffusion-weighted data set with 30 gradient directions. Additionally, functional magnetic resonance imaging for cortical language sites was obtained. Fiber tractography was performed with deterministic streamline algorithms based on DTI using 3 different software platforms. Additionally, tractography based on reconstructed diffusion signals using HARDI+CS was performed.

RESULTS: HARDI+CS-based tractography displayed more compact fiber bundles compared with the DTI-based results in all cases. In 3 cases, neuroanatomically plausible fiber bundles were displayed in the vicinity of tumor and peritumoral edema, which could not be traced on the basis of DTI. The curvature around the sylvian fissure was displayed properly in 6 cases and in only 2 cases with DTI-based tractography.

CONCLUSION: HARDI+CS seems to be a promising approach for fiber tractography in clinical practice for neuroanatomically complex fiber pathways and in areas of disturbed diffusion, overcoming the problem of long acquisition times.

KEY WORDS: Compressed sensing, Diffusion tensor imaging, Fiber tractography, Glioma, High-angular-resolution diffusion imaging, Multimodality navigation

Neurosurgery 72:A165–A175, 2013 DOI: 10.1227/NEU.0b013e318270d9fb www.neurosurgery-online.com

The aim to achieve best possible tumor resection with minimum postoperative morbidity, which has been shown to be associated with extended survival time[1-3] in glioma surgery, is still challenging. Despite microscope enhancement, as a result of their infiltrative nature, margins of high-grade gliomas generally remain difficult to distinguish from the surrounding brain parenchyma. This is of particular relevance for lesions near eloquent cortical areas or major white matter tracts. Thus, there is rising interest in navigation guidance and intraoperative imaging methods.[4,5] Conventional navigation guidance has become a routinely used tool during glioma surgery. However, with the so-called multimodality navigation, besides anatomic image data, functional

ABBREVIATIONS: AABT, Aachen Aphasia Bedside Test; **CS,** compressed sending; **DTI,** diffusion tensor imaging; **FA,** fractional anisotropy; **fMRI,** functional magnetic resonance imaging; **HARDI,** high-angular-resolution diffusion imaging; **WHO,** World Health Organization

information like eloquent cortical areas, metabolic activity, or fiber tracts can also be integrated.

Fiber tractography as a noninvasive method to estimate the course and location of white matter tracts integrated in the navigation system has been shown to contribute to minimizing postoperative morbidity.[6,7] For reasons of practicability and feasibility, until today, fiber tractography in clinical practice was based mostly on diffusion tensor imaging (DTI). DTI, as first described by Basser et al,[8] is based on a set of diffusion-weighted magnetic resonance images (MRIs). To obtain the diffusion properties within 1 voxel, a second-order tensor, describing the local diffusion characteristic within, is calculated with the Stejskal-Tanner equation. In anisotropic tensors, the main eigenvector encodes the longitudinal direction of axons in major white matter tracts.

So far, there are several different algorithms for fiber reconstruction,[9-12] which can generally be separated into deterministic and probabilistic methods. However, because of the restricted second-order tensor in each voxel, assuming gaussian-distributed diffusion, multifiber populations cannot be resolved adequately, resulting in the disability to reconstruct crossing or kissing fibers. Similarly, fanning fibers and fibers in the vicinity of tumor or edema[13,14] can hardly be reconstructed with this assumption.[15] In clinical practice, this becomes relevant for the reconstruction of neuroanatomically complex fiber structures like the language-associated tracts curving around the sylvian fissure. Even for healthy subjects, their reconstruction is challenging with the most commonly used deterministic tracking algorithms based on DTI; however, it becomes even more complex for patients with intracerebral pathology such as gliomas and their associated peritumoral edema, both affecting diffusion properties.

To overcome this drawback, particularly because about one-third of voxels in the brain contain $>$ 1 fiber population,[16] research focuses on alternative diffusion models such as those based on high-angular-resolution diffusion imaging (HARDI). Advanced diffusion models based on HARDI data sets are capable of overcoming the second-order tensor restriction.[17-20]

To represent a 3-dimensional (3-D) distribution of diffusivities as measured by HARDI, spherical harmonics are frequently used. However, because they do not provide a sparse representation of HARDI signals, clinical use is limited owing to a larger number of diffusion-encoding gradients (ranging from 60 to 100), resulting in long acquisition times. Based on spherical ridgelets, HARDI signals can be represented using a relatively small number of diffusion-encoding gradients,[21-24] thus enhancing the feasibility of HARDI-based fiber tractography in clinical practice.

To the best of our knowledge, there is no description of the application of HARDI with compressed sensing (CS) and accordingly tractography in clinical practice. This article compares DTI-based fiber tractography, performed on 3 different software platforms (iPlan[25] Cranial, Slicer4,[26-28] and MedAlyVis[29]), with HARDI+CS-based fiber tractography. Furthermore, DTI- and HARDI+CS-based fiber reconstruction performed on the same platform (MedAlyVis) was displayed and analyzed side by side.

MATERIALS AND METHODS

Patients

Patient collection was performed prospectively at the University Hospital Marburg (Marburg, Germany) from May 2011 to March 2012 after approval was given by the local ethics committee. All patients gave their written informed consent to participate in the study.

Six patients with left-sided gliomas were included in our study. Mean patient age was 54.3 ± 14.9 years. Two female patients and 4 male patients were included.

All patients were right handed with left dominant hemisphere according to functional MRI (fMRI). For all patients, the Aachen Aphasia Bedside Test (AABT)[30] was obtained preoperatively and 2 months after surgery. The following items were evaluated:

1. Request for visual and head movement (minimum, 0 points; maximum, 50 points)
2. Request for mouth movement (minimum, 0 points; maximum, 50 points)
3. Singing and speaking rows and empty phrases (minimum, 0 points; maximum, 50 points)
4. Identifying objects (minimum, 0 points; maximum, 50 points)
5. Naming objects (minimum, 0 points; maximum, 50 points)

The tumor localization is given in Table 1 and illustrated in Figure 1, in which all tumors are displayed in a physiological brain model. A detailed description of the patients' medical history, including AABT, tumor biology, and clinical course is given in the case presentation and Tables 1 and 2.

TABLE 1. Patient Collective[a]

Patient	Age, y	Sex	Lesion	Localization	Tumor Volume, cm^3
1	73	M	Anaplastic oligodendroglioma WHO III	Temporal	35.2
2	65	F	Glioblastoma multiforme WHO IV	Temporal	10.7
3	41	M	Anaplastic astrocytoma WHO III	Temporal	15.7
4	52	M	Glioblastoma multiforme WHO IV	Temporo-occipital	30.2
5	34	M	Diffuse astrocytoma WHO II	Frontal	76.0
6	61	F	Anaplastic astrocytoma WHO III	Temporal	41.8

[a]WHO, World Health Organization.

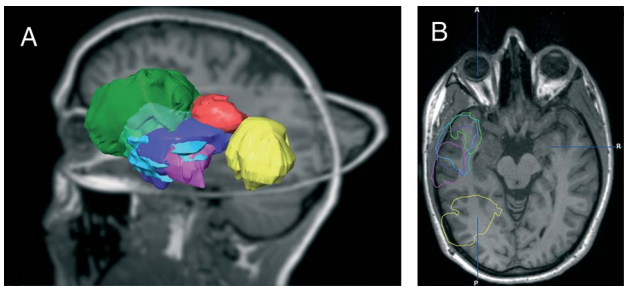

FIGURE 1. *Schematic of tumor localization with segmented tumor objects projected on a T1-weighted magnetic resonance imaging data set of a healthy volunteer.* **A**, *3-dimensional overview.* **B**, *axial view. Patient 1, blue; patient 2, red; patient 3, pink; patient 4, yellow; patient 5, green; and patient 6, purple.*

MRI Studies

For all patients, MRIs were acquired at on a 3-T MRI (Tim Trio; Siemens, Erlangen, Germany) on the preoperative day, including T1-weighted 3-D images (3-D magnetization-prepared rapid gradient echo; repetition time, 1900 milliseconds; echo time, 2.26 milliseconds; field of view, 256 mm; matrix, 256 × 256; slice thickness, 1 mm; 176 slices, sagittal), blood oxygen level-dependent fMRI using a single-shot echo-planar imaging sequence (repetition time, 2000 milliseconds; echo time, 30 milliseconds; field of view, 230 mm; matrix, 64 × 64; slice thickness, 3.6 mm; 33 slices, axial) for localization of cortical language areas using a word generation task, and diffusion-weighted images also using a single-shot echo-planar imaging sequence (repetition time, 7800 milliseconds; echo time, 90 milliseconds; field of view, 256 mm; matrix, 128 × 128; slice thickness, 2 mm; numbers of excitations, 1; b = 1000 s/mm^2; 30 noncollinear diffusion-encoding gradients; voxel size, 2 × 2 × 2 mm^3). This same diffusion-weighted image set was the base for both DTI-based fiber tractography and HARDI+CS-based fiber tractography. Acquisition of all data sets took 15 minutes per patient.

fMRI Analysis

The applied word generation task, as described by Jansen et al,[31] consisted of a block design task with displayed alternating letters and nonletters, 20 seconds each. Patients are asked to think of words starting with the displayed letter (activation) and to stop thinking of words when a nonletter is displayed (baseline).

fMRI analysis was performed within the iPlan Cranial planning software preoperatively for each patient, delivering adequate activation results for all patients. Segmented areas were then expanded with a 3-mm margin and manually transcribed into Slicer4 and MedAlyVis.

TABLE 2. Aachen Aphasia Bedside Test Results of the Patient Collective[a]

Patient	Preoperative AABT Score	Postoperative AABT Score
1	50-50-50-50-50	50-50-50-50-50
2	49-48-50-47-40	49-48-50-50-45
3	50-50-50-50-48	50-50-50-50-48
4	50-50-42-50-45	50-50-48-50-48
5	50-50-50-50-50	50-50-50-50-50
6	50-50-50-50-50	50-50-50-50-50

[a]AABT, Aachen Aphasia Bedside Test. First score, request for visual and head movement; second score, request for mouth movement; third score, singing and speaking rows and empty phrases; fourth score, identifying objects; and fifth score, naming objects.

Fiber Tractography

Evaluation was performed with 3 different platforms: the iPlan Cranial planning software (Brainlab, Feldkirchen, Germany),[25] Slicer4 (www.slicer.org [26-28]) for DTI-based fiber tractography, and the imaging platform MedAlyVis (Medical Analysis and Visualization)[29] for DTI-based and advanced tractography using HARDI signals derived from sparsely sampled diffusion data.

DTI-Based Fiber Tractography in iPlan Cranial, Slicer4, and MedAlyVis

Fiber tractography using the tensor deflection approach was performed routinely in iPlan Cranial planning software, with the defined activation area used as seed, with fractional anisotropy (FA) thresholds ranging between 0.16 and 0.20, depending on the proximity of the fiber to tumor and peritumoral edema. The fiber-tracking results were then reduced by application of exclude regions.

In Slicer4, the tractography algorithm described by Basser et al[9] is routinely used for basic fiber tractography. Similar to the procedure within iPlan Cranial planning software, fiber tracking was applied using the same FA thresholds for each patient.

Within MedAlyVis, fiber tractography was also performed using a tensor deflection approach with the same range of FA thresholds for each patient.

Multidirectional Deterministic Fiber Tractography Based on HARDI+CS

Tractography algorithms based on reconstructed diffusion signals using HARDI+CS[23] can be applied to reconstruct complex fibers within a single voxel, modeled as a probability distribution on a sphere, assigning the probability of diffusion for each direction. Using a higher number of gradients, HARDI requires longer acquisition times and thus is not yet suitable for clinical use. As proposed by Michailovich and Rathi[24,32] and Michailovich et al,[33] spherical ridgelets can be used to interpolate the diffusion signal, allowing a sparse representation of the signal.

Within the MedAlyVis platform, spherical ridgelets are calculated from the given diffusion data set.[24,32,33] For fiber reconstruction, a deterministic multidirectional orientation distribution function tracking is used, proposed by Descoteaux et al,[15] with the L index[34] as the anisotropy measure, ranging from 0.05 to 0.07.

RESULTS: CASE SERIES

The results of fiber tractography based on DTI performed on the 3 different platforms and of fiber tractography relying on HARDI+CS are described for each patient separately. Evaluation of tractography results was performed on the basis of neuroanatomical knowledge. Hereafter, DTI- and HARDI+CS-based fiber tractography results are compared side by side, and the workflow on the different software platforms is described.

Patient 1

A 73-year-old male patient presented after an episode of slight, completely recurrent motor aphasia and cognitive impairment. MRI showed a left temporal to temporodorsal intra-axial lesion with weak contrast enhancement infiltrating the superior temporal gyrus and directly neighboring the angular gyrus. The contrast-enhancing areas of the lesion, which histologically was an anaplastic oligodendroglioma (World Health Organization [WHO] III), were gross-totally resected, and the postoperative course was uneventful. The AABT was normal preoperatively and 2 months after surgery (50-50-50-50-50).

DTI-based tractography in iPlan Cranial resulted in a slender arc reaching from BA 44, 45, terminating in the angular and supramarginal gyrus. Despite gradual reduction of the FA threshold to 0.16, temporal fibers could not be displayed. DTI-based fiber tracking on Slicer4 platform resulted in a slender tract but this time terminating in the temporal lobe (inferior temporal gyrus). In contrast, DTI-based tracking on the MedAlyVis platform suggested frontal fibers terminating in BA 22 with few branches, which was supported by HARDI+CS-based tracking results, displaying a more solid bundle interconnecting BA 44, 45 and terminating in BA 22. The tractography results are displayed in Figure 2. Direct comparison of DTI- and HARDI+CS-based tractography on the MedAlyVis platform displays 2 anatomically similar fiber bundles; however, the whole bundle, particularly the arc surrounding the sylvian fissure, is traced more firmly relying on HARDI+CS (Figure 3).

Patient 2

A female 65-year-old patient presented with progressive aphasia and a marginally contrast-enhancing lesion with peritumoral edema in the left temporodorsal area, suggesting a glioblastoma multiforme. The AABT revealed aphasia preoperatively (AABT, 49-48-50-47-40) compared with an AABT of 49-48-50-50-45 postoperatively. The contrast-enhancing areas of the tumor were gross-totally resected. Histopathology secured the diagnosis of glioblastoma multiforme (WHO IV).

On iPlan Cranial and Slicer4 platforms, DTI-based tractography managed to display a frontal fiber compound from BA 44 and 45 merging to the dislocated supramarginal gyrus; the fibers were even displayed slightly within the tumor edema. Even a slight temporal fiber bundle was displayed here within the Slicer4 and MedAlyVis platforms. Still, HARDI+CS-based tractography represented a solid compound of frontotemporally arching fibers (connecting BA 44, 45 and BA 22), well displayed within the tumor and the peritumoral edema (see Figure 2). This difference of fiber complexity is also presented in Figure 3 (DTI- vs HARDI+CS-based tractography on MedAlyVis).

Patient 3

A 41-year-old patient was admitted in our clinic with cognitive impairment and mnestic deficits. The AABT furthermore revealed slight aphasia (AABT, 50-50-50-50-48), which was unchanged postoperatively (AABT, 50-50-50-50-48). These were based on an MRI morphologically nonenhancing intra-axial lesion in the left temporal lobe, which was gross-totally resected according to the T2-hyperintense signal alterations. Histopathology revealed an anaplastic astrocytoma (WHO III).

Tractography results based on DTI showed only sparse frontally located fibers on all platforms, not entirely reliable on Slicer4 and MedAlyVis platforms. No temporal fibers were displayed. With HARDI+CS-based fiber tractography on MedAlyVis, a compound frontal fiber bundle and a temporally curving part connecting to BA 22 was displayed (Figure 2). This bundle terminates in the posterior part of the superior temporal gyrus. Direct comparison of DTI- and HARDI+CS-based tractography results within the MedAlyVis platform shows solitary fibers of DTI-based reconstruction and the far more solid fiber bundle of HARDI+CS-based reconstruction (Figure 3).

Patient 4

A 52-year-old male patient was admitted with aphasic episodes and homonymous hemianopia caused by a left temporo-occipital lesion marginally contrast enhancing with significant perifocal edema. The AABT preoperatively was 50-50-42-50-45 but recurrent postoperatively (50-50-48-50-48). The lesion was gross-totally resected, which histologically was a glioblastoma multiforme (WHO IV).

DTI-based fiber tractography on the iPlan Cranial platform resulted in diffuse and slight fibers but with frontal and temporal extension as accepted by neuroanatomical knowledge. In the vicinity of the tumor in the posterior superior temporal gyrus, most fibers cannot be traced safely. Tracking with Slicer4 displayed merely a slender frontal fiber bundle, which terminated directly in front of the tumor edema before the supramarginal gyrus. A temporal extension cannot be displayed here. On MedAlyVis, DTI- and HARDI+CS-based fiber tracking managed to present a frontotemporal arc, interconnecting BA 44, 45 and BA 22. However, it can be clearly seen that HARDI+CS-based tractography displayed a significantly firmer and more solid fiber bundle, particularly also displaying the arc around the sylvian fissure (Figure 2, Figure 3).

Patient 5

A 34-year-old patient presented with general seizure without any further neurological deficits (preoperative and postoperative AABT, 50-50-50-50-50). A large left frontal lesion was detected on MRI, not showing contrast enhancement. He underwent subtotal tumor resection to prevent a neurological deterioration, which was secured in the postoperative neurological examination. Histologically, the lesion proved to be a diffuse astrocytoma (WHO II).

Tractography results are shown in Figure 2. DTI-based tractography on all platforms displayed a frontal fiber bundle; however, the temporal fibers were not traced safely. Furthermore, fiber results were obtained with an FA threshold < 0.16. HARDI+CS-based tractography displayed a neuroanatomically reliable and solid fiber object, representing frontally and

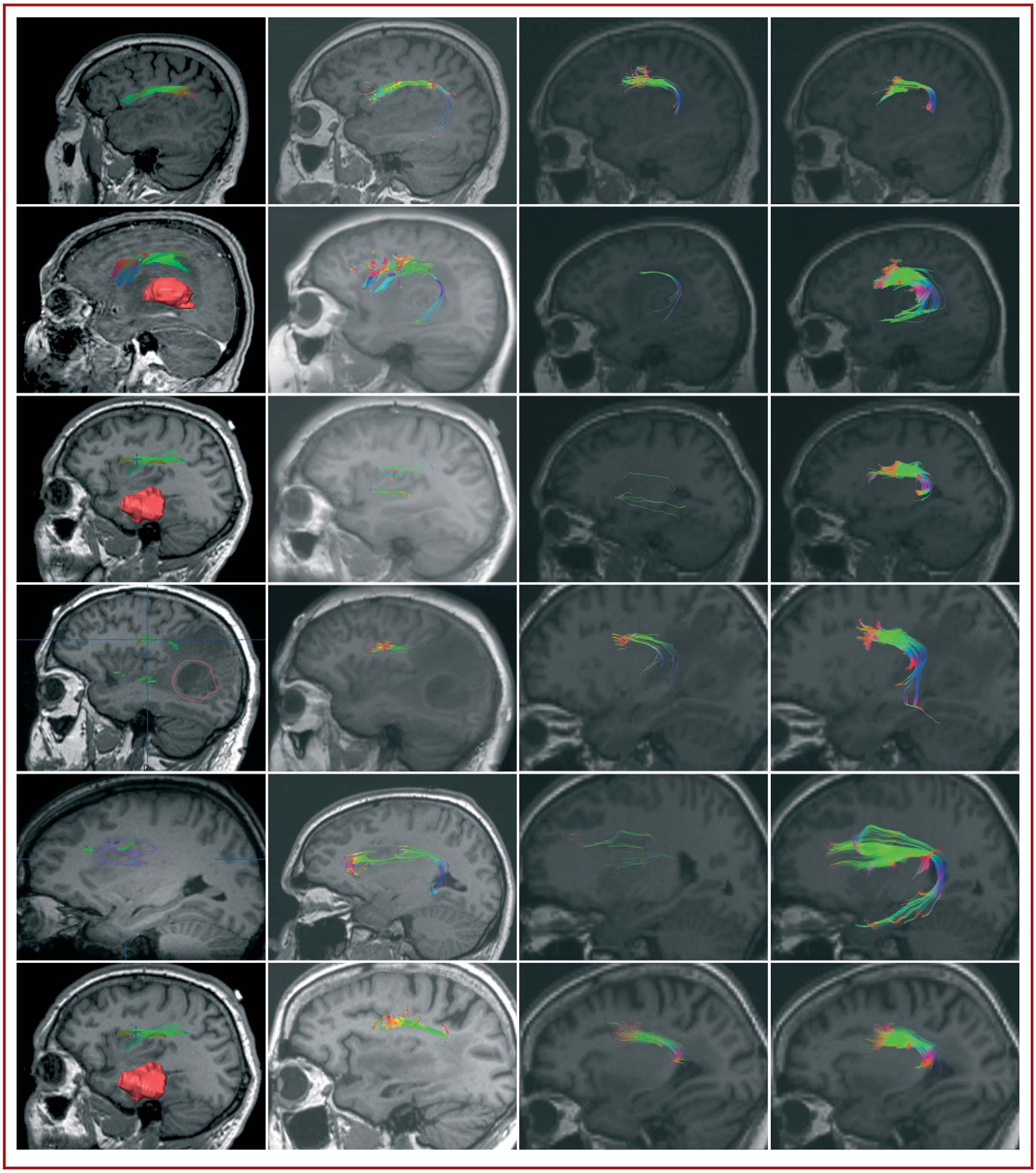

FIGURE 2. *Fiber tractography results presented for each patient based on diffusion tensor imaging within iPlan Cranial (column 1), Slicer4 (column 2), and MedAlyVis (column 3) and based on high-angular-resolution diffusion imaging with compressed sensing within MedAlyVis (column 4). Row 1: patient 1, a 73-year-old male patient with left temporal anaplastic oligodendroglioma. T1-weighted sagittal magnetic resonance imaging (MRI). Row 2: patient 2, a 65-year-old female patient with left temporal glioblastoma multiforme (3-dimensional [3-D] segmentation [red] in* **A***). T1-weighted sagittal MRI (***A***, with contrast agent;* **B**-**D***, without contrast agent). Row 3: patient 3, a 41-year-old male patient with temporal anaplastic astrocytoma (3-D segmentation [red] in* **A***). T1-weighted sagittal MRI. Row 4: patient 4, a 52-year-old male patient with left temporo-occipital glioblastoma multiforme (2-dimensional [2-D] segmentation [red] in* **A***). T1-weighted sagittal MRI. Row 5: patient 5, a 34-year-old male patient with left frontal diffuse astrocytoma (2-D segmentation [purple] in* **A***). T1-weighted sagittal MRI. Row 6: patient 6, a 61-year-old female patient with temporal anaplastic astrocytoma. T1-weighted axial MRI.*

temporally located fibers (Figure 3). Figure 4 illustrates the reconstructed fiber object in a 3-D model compared with the intraoperative navigation screenshot, here with fiber tractography based on DTI.

Patient 6

A 61-year-old woman with symptomatic seizures underwent subtotal resection of a large anaplastic astrocytoma (WHO III) in the left temporal lobe with infiltration of insula and only diffuse central contrast enhancement. She did not suffer from any focal neurological deficits preoperatively and postoperatively (AABT, 50-50-50-50-50).

Fibers displayed by DTI-based tractography showed a frontal fiber bundle on the iPlan Cranial platform that terminated in the angular gyrus without expanding into the temporal lobe and was not influenced by reduced FA thresholds or expanded seed region. A slight temporal fiber expansion could be seen with DTI-based fiber tracking on the MedAlyVis and Slicer4 platforms. The termination of these fibers was in the region of BA 22 for DTI- and HARDI+CS-based reconstruction. However, the most remarkable difference here is seen in the more compound HARDI+CS-based fiber bundle reconstruction, as demonstrated in Figure 2. In addition, the direct comparison of reconstructed fiber bundles derived from both approaches within MedAlyVis displays the contrast of firmly traced fibers in Figure 3.

Figure 3 presents DTI- and HARDI+CS-based fiber tractography results on MedAlyVis for each patient in side-by-side display and overlay. It can be seen that HARDI+CS-based reconstruction results in a more compound fiber bundle in all cases. In 4 cases, DTI-based tractography resulted in sparse fibers, whereby HARDI+CS-based fiber tracking displayed a solid object (rows 2-5). However, fiber tracking relying on DTI displayed acceptable tracking results comparing DTI- and HARDI+CS-based tractography results for patients 1 and 6. In DTI-based reconstruction objects, the reconstruction frequently failed to follow the curve of the fiber around the sylvian fissure. In contrast, the curvature or at least the beginning of the curve could be displayed with HARDI+CS-based tractography. This contrast can best be seen in rows 1, 3, 4, and 5.

The procedure for DTI-based fiber tractography, including preprocessing, postprocessing, and fiber tracking, took approximately 5 to 20 minutes on all 3 platforms. There were no significant differences in time regarding image preprocessing and basic fiber reconstruction process. Postprocessing times in between the platforms varied only slightly (Table 3).

In contrast, performing all necessary steps for HARDI+CS-based tractography took about 50 minutes for each data set, including the calculation of spherical ridgelets (preprocessing) and basic fiber tractography. In addition, postprocessing workflow was more time consuming, although the fibers were processed accordingly, restricting the objects with additional seed regions to exclude nonpertinent additional fibers (Table 3).

DISCUSSION

Intraoperative navigation systems are widely used among neurosurgical operating theaters, showing segmented risk structures and targets in the microscope heads-up display after a registration process of physical space and image space.[35] Besides mere anatomic MRIs, in recent years, functional data have been integrated into the navigation. The multimodality concept includes the display of eloquent cortical sites (given by fMRI),[36] metabolic data (given, for example, by magnetic resonance spectroscoptic imaging or single-photon emission computed tomography[37]), or major white matter tracts.

DTI is validated, challenged, and developed according to acquisition schemes, image processing, analysis, and interpretation of its results.[38] Early experiments showed that diffusion is faster along white matter tracts than perpendicular to the fiber bundle direction. This principle is the basis for the DTI-based tractography.[8] For tensor calculation, the needed data set includes 1 b0 image and at least 6 diffusion-weighted images, each applied with a noncollinear diffusion gradient. However, today, a total of 30 gradient directions has been proposed for the reconstruction of language pathways.[39]

DTI-based fiber tractography relies on the mathematical reconstruction of 1 second-order tensor in each voxel, not capable of resolving spatial locations in case of crossing, kissing, or diverging fibers in the voxel. This is of special interest for tractography results of anatomically complex fiber bundles like language pathways or the optic tract. However, until today, promising tracking results have already been achieved on the basis of DTI that have been shown to contribute to a low postoperative morbidity when integrated into the navigation system,[6] comparable to electrostimulation methods.[40,41] The most commonly used algorithm is the deterministic tensor deflection algorithm, which has been proven to be feasible for reconstruction of fiber

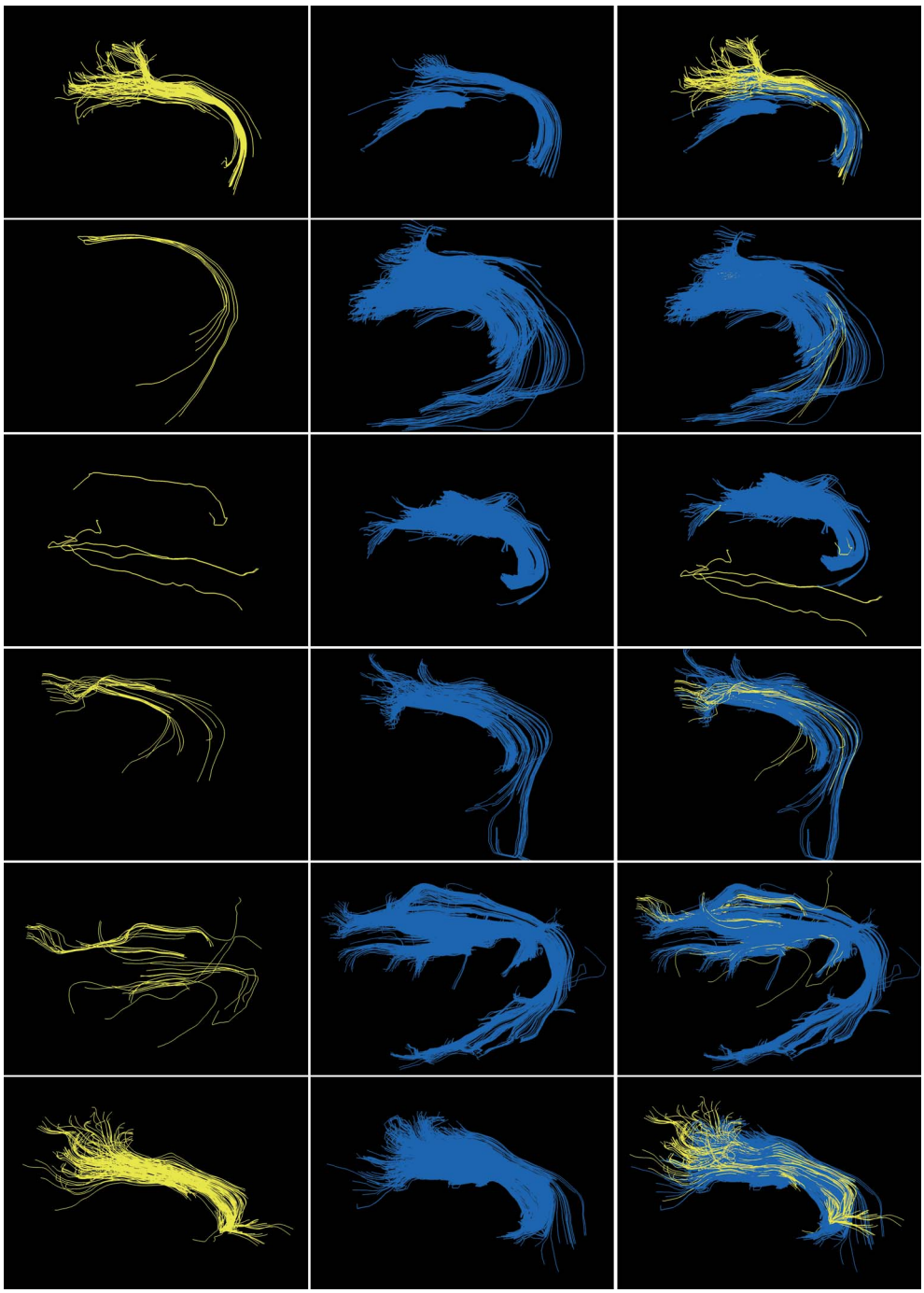

FIGURE 3. *Direct comparison of fiber tractography results in MedAlyVis (rows 1-6 correspond to patient numbers).* **Column 1**, *diffusion tensor imaging (DTI)-based tractography (yellow).* **Column 2**, *high-angular-resolution diffusion imaging with compressed sensing (HARDI+CS)-based tractography (blue).* **Column 3**, *overlay of DTI-, and HARDI+CS-based fiber bundles.*

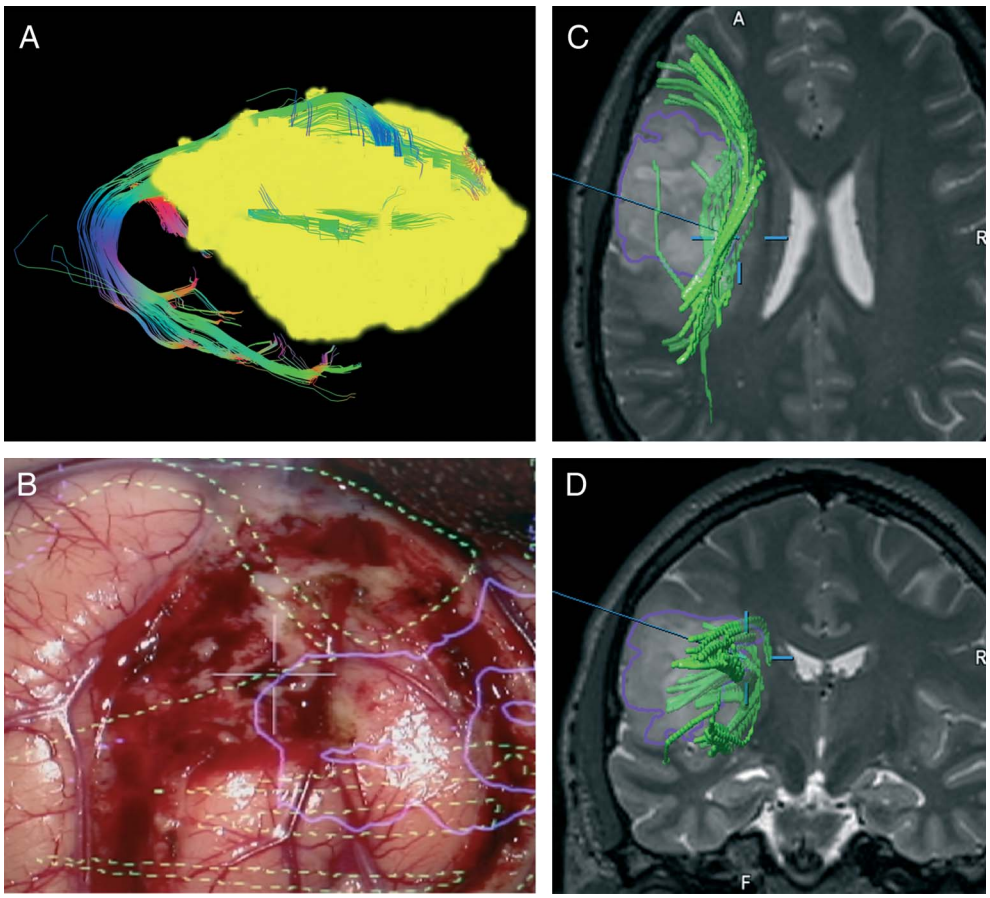

FIGURE 4. *Case illustration of patient 5.* **A**, *3-dimensional (3-D) reconstruction of tumor and language pathway view from lateral right.* **B**, *microscope view with outlines in heads-up display (purple, tumor; yellow, subjacent language pathways).* **C** *and* **D**, *intraoperative navigation screenshots, T2-weighted axial (***C***) and coronal (***D***) views. Tumor outlines segmented in purple; 3-D reconstruction of fiber bundle, in green.*

tracts without fanning fibers, curvatures or crossing, and kissing fibers. For anatomically complex fiber pathways like the language-associated tracts or the optic tract, probabilistic algorithms such as connectivity analysis[42] or bayesian approaches[10] have already shown success for more reliable tractography results based on DTI. Another method, which has been established for patient safety, is the placement of flexible hulls around the reconstructed fiber object.[43] Thus, an additional safety margin of a 5-mm surface hull around the intraoperatively displayed object has been shown to avoid postoperative neurological deficits.[7] Furthermore, the application of intraoperative high-field MRI has provided the possibility to obtain DTI intraoperatively. Fiber tractography with intraoperative DTI image data has shown to compensate for the effects of brain shift, also contributing to low postoperative morbidity.[44]

Despite enhanced patient safety as a result of these innovations in the field of DTI, the mentioned intrinsic drawbacks of this method cannot be overcome. Thus, there was a rising demand for alternative approaches. One of these was found using advanced diffusion models based on HARDI data sets. Multiple intravoxel fiber orientations are frequently reconstructed using analytical reconstruction based on spherical harmonics, or q-ball imaging,[45] in which the diffusion signal is sampled directly on a sphere using the Funk Radon transform. This improvement of high angular resolution is associated with 1 significant drawback. Acquisition of HARDI data sets requires a significantly higher number of diffusion gradients, ranging from 60 to 100. Associated data acquisition times are up to 25 minutes (on a 3-T MRI system) as opposed to approximately 4 minutes for DTI (on a 3-T MRI system). However, frequently used for theoretical neuroimaging, for example, by Frey et al,[46] clinical applications of HARDI are still rare. Thus, to the best of our knowledge, there is still no clinical study assessing HARDI in a neurosurgical patient collective. However, there seems to be particular impact of the method in cases of gliomas and perifocal edema with their associated more complex white matter architecture.

TABLE 3. Tractography Preprocessing and Postprocessing Times Comparing Diffusion Tensor Imaging and High-Angular-Resolution Diffusion Imaging[a]

	iPlan Cranial DTI, min			Slicer4 DTI, min			MedAlyVis DTI, min			MedAlyVis HARDI+CS, min		
Patient	Pre	FT	Post	Pre	FT	Post	Pre	FT	Post	Pre	FT	Post
1	2	< 1	3	2	1-2	5	2	1	4	25	18	13
2	2	< 1	5	2	1-2	4	2	1	5	25	19	12
3	2	< 1	11	2	1-2	10	2	1	12	25	18	14
4	2	< 1	15	2	1-2	10	2	1	14	25	21	13
5	2	< 1	15	2	1-2	13	2	1	14	25	20	15
6	2	< 1	3	2	1-2	6	2	1	5	25	18	14

[a]DTI, diffusion tensor imaging; FT, time for fiber reconstruction process; HARDI+CS, high-angular-resolution diffusion imaging with compressed sensing; Post, postprocessing time for fiber tracking; Pre, preprocessing time for fiber tracking.

So far, several frameworks have been presented to achieve a higher practicability for HARDI-based fiber reconstruction, eg, Prckovska et al[47] with a fused DTI/HARDI visualization or Reisert et al.[48] Among these techniques, with the mathematical model CS, based on the theory of sparse representation, the particular drawback of the long image acquisition time of HARDI can be overcome. In this way, CS potentially enables the reconstruction of HARDI signals from as low as 20 diffusion gradients, although with a low reconstruction error of approximately 1%.[24]

With the following interpretation comparing the tracking results, we can support the described theoretical advantages of HARDI+CS-based over DTI-based tractography. Analysis of the reconstructed language-associated fiber tracts was performed on the basis of current standard of neuroanatomical knowledge, whereby the complex anatomy of language-associated cortical areas and their connecting fiber bundles is not fully understood. Based on the Geschwind[49] model of the temporofrontal arc "arcuate fasciculus" connecting the Broca and Wernicke areas, there are new insights into the language-associated fiber structures, some of them based on diffusion studies. In this way, a "ventral pathway" is suggested, connecting the 2 cortical areas via the uncinate fasciculus, the external and extreme capsules.[50-52] A study from Frey et al[46] based on q-ball imaging[45] suggests that Brodmann area 45 in particular interconnects via the extreme capsule. Specific inferior temporal areas, including the parahippocampal gyrus and the fusiform gyrus, are part of semantic processing and interconnect BA 44, 45 and posterior BA 22.[53] However, other cortical sites like BA 6, 9, 21, 37, 40, or 39 and their associated interconnecting fibers are also involved in the cortical processing of language.[54]

Interpreting the tractography results indicates that the most obvious advantage of fiber tractography based on multidirectional diffusion patterns is the significantly higher compound and solid representation of the resulting fiber objects (Figures 2 and 3). This can be seen in all performed reconstructions, comparing results of HARDI+CS-based tractography with DTI-based results on the 3 different platforms, although DTI-based reconstructions also vary between platforms. It can be seen that with bigger tumor diameter, closer localization to the language pathways, or larger peritumoral edema, the tracking results differ more regarding the solidity of the fiber object, suggesting a higher rate of uncertainty (best seen in patient 5). In DTI-based fiber tracking objects, the fibers frequently fail to follow the curve around the sylvian fissure. This is the case on all 3 platforms, with very similar results seen for patients 1, 3, 4, and 5 (Figures 2 and 3). In contrast, the curvature or at least the beginning of the curve could be displayed with HARDI+CS-based tractography in these cases.

There also seems to be the expected advantage concerning the desired fiber reconstruction in near-tumor areas or in vasogenic edema. As can be seen in the HARDI+CS-based tractography results of patients 2, 4, and 5 (Figure 2), a solid fiber bundle can also be displayed in peritumoral edema. However, DTI-based fiber tractography displayed acceptable results consistently on all platforms for patients 1 and 6. This can be explained by the low peritumoral edema and localization of the oligodendroglioma and low-grade astrocytoma (Figure 2). DTI-based tractography fibers are rather displaced by tumor of peritumoral edema, or the tracking even terminates. This phenomenon is seen for patient 1 in iPlan Cranial and Slicer4 or patient 4 on Slicer4.

Despite these obvious advantages regarding image morphology, tractography results are not assessed quantitatively or compared with electrostimulation methods. Both methods have to be seen as in vivo estimation of course and localization of the fiber bundle. However, in our opinion, HARDI+CS-based fiber reconstruction is worth its effort in cases of large tumors with significant peritumoral edema. DTI tractography remains a feasible tool for tractography of pathways like the corticospinal tract or in proximity of smaller tumors with less peritumoral edema.

Despite these obvious advantages, certain drawbacks of the HARDI+CS-based fiber reconstruction have to be mentioned. Although using the same diffusion data set with 30 noncollinear gradients as the basis for DTI and HARDI+CS fiber reconstruction, the time for calculating orientation distribution functions and the fiber tracking procedure itself is significantly prolonged for HARDI+CS at 45 minutes compared with 5 minutes for DTI-based tractography. Although there are no drawbacks for the patient, this prolonged reconstruction process reduces practicability owing to larger effort in time and personnel. Time for DTI-based fiber tractography is almost consistent

for iPlan Cranial, MedAlyVis, and Slicer4. In our opinion, the open-source platform Slicer4 and iPlan Cranial are orientated for clinical use, with a well-structured and easily manageable workflow. In contrast, the MedAlyVis platform emphasizes science applications and requires a longer teach-in period. As mentioned previously, intraoperative application of DTI-based fiber tractography has provided new insights into the phenomenon of brain shift with a shown clinical impact. HARDI+CS-based tractography is, in our opinion, not yet feasible for intraoperative use because of the long processing times that would lengthen surgery significantly. Alternatively, preoperative HARDI+CS-based fiber tractography can be combined with nonlinear registration techniques or sophisticated techniques from pattern recognition, allowing the matching of preoperative data sets, including functional data with intraoperative MRIs.[55] Further registration techniques propose nonlinear registration of image space directly with the brain, not with the head. These techniques can also be applied for other intraoperative imaging modalities providing 3-D information such as ultrasound. Thus, intraoperative images can be nonlinearly registered to the preoperative data, providing the multimodal information.[56,57]

Outlook

Regarding image quality, future perspectives include the comparison of conventional HARDI- and HARDI+CS-based fiber objects. Furthermore, HARDI+CS will be obtained with varied MRI parameters such as voxel size, gantry tilt, or number of repetitions and number of diffusion gradients to compare the resulting fiber objects for optimization purposes. To assess accuracy, this can be done with a software phantom, offering the possibility to compare the resulting objects with a defined ground truth.

For clinically orientated future investigations, the most important steps will be the routine integration of HARDI+CS-based fiber reconstruction in the navigation system besides conventional DTI-based tractography results to support our hypothesis. This can be obtained, for instance, by using the binary mask derived from resulting fiber sets and visualized in a routinely used navigation software. To actually assess the clinical impact regarding accuracy and patient morbidity compared with DTI tractography, the intraoperative display of HARDI+CS fiber objects will be combined with subcortical stimulation methods. Furthermore, other tracking algorithms will be applied on the HARDI diffusion model and compared with the tensor deflection algorithm. The implementation of multidirectional diffusion models in open-source navigation planning software should also be an aim of future investigations, offering a user-friendly software interface that can be used by clinical physicians during daily business.

CONCLUSION

With our prospectively conducted case series on 6 patients, we show that HARDI+CS fulfills the requirement of adequately low data acquisition times, which are required for use in clinical practice. Furthermore, according to the DTI-based reconstruction of language pathways with 3 different platforms (iPlan Cranial, Slicer4, and MedAlyVis) compared with HARDI+CS-based reconstruction on MedAlyVis, we show that HARDI+CS-based reconstruction seems to have potential not only in the more compound display of reconstructed fibers but also in areas of locally disturbed diffusion (tumor and peritumoral edema).

Thus, HARDI+CS seems to be a new approach that combines the advantages of the estimation of multiple intravoxel fiber populations of HARDI with the clinical feasibility of routinely used DTI image data acquisition in presurgical practice. Despite longer preprocessing times and thus presurgical planning, there is no disadvantage for the patient regarding the presurgical workflow.

Disclosures

This work was supported in part by von Behring Roentgen Foundation, Germany (58-004), and European Regional Development Fund, project FNUSA-ICRC (No. CZ.1.05/1.1.00/02.0123). Prof Nimsky is scientific consultant for intraoperative imaging for BrainLab (Feldkirchen, Germany). The other authors have no personal financial or institutional interest in any of the drugs, materials, or devices described in this article.

REFERENCES

1. Lacroix M, Abi-Said D, Fourney DR, et al. A multivariate analysis of 416 patients with glioblastoma multiforme: prognosis, extent of resection, and survival. *J Neurosurg.* 2001;95(2):190-198.
2. McGirt MJ, Chaichana KL, Gathinji M, et al. Independent association of extent of resection with survival in patients with malignant brain astrocytoma. *J Neurosurg.* 2009;110(1):156-162.
3. Sanai N, Polley MY, McDermott MW, Parsa AT, Berger MS. An extent of resection threshold for newly diagnosed glioblastomas. *J Neurosurg.* 2011;115(1):3-8.
4. Kuhnt D, Becker A, Ganslandt O, Bauer M, Buchfelder M, Nimsky C. Correlation of the extent of tumor volume resection and patient survival in surgery of glioblastoma multiforme with high-field intraoperative MRI guidance. *Neuro Oncol* 2011;13(12):1339-1348.
5. Senft C, Bink A, Franz K, Vatter H, Gasser T, Seifert V. Intraoperative MRI guidance and extent of resection in glioma surgery: a randomised, controlled trial. *Lancet Oncol.* 2011;12(11):997-1003.
6. Kuhnt D, Bauer MH, Becker A, et al. Intraoperative visualization of fiber tracking based reconstruction of language pathways in glioma surgery. *Neurosurgery*. 2012; 70(4):911-919; discussion 919-920.
7. Nimsky C, Ganslandt O, Merhof D, Sorensen AG, Fahlbusch R. Intraoperative visualization of the pyramidal tract by diffusion-tensor-imaging-based fiber tracking. *Neuroimage*. 2006;30(4):1219-1229.
8. Basser PJ, Mattiello J, LeBihan D. MR diffusion tensor spectroscopy and imaging. *Biophys J.* 1994;66(1):259-267.
9. Basser PJ, Pajevic S, Pierpaoli C, Duda J, Aldroubi A. In vivo fiber tractography using DT-MRI data. *Magn Reson Med.* 2000;44(4):625-632.
10. Friman O, Farneback G, Westin CF. A bayesian approach for stochastic white matter tractography. *IEEE Trans Med Imaging.* 2006;25(8):965-978.
11. Mori S, van Zijl PC. Fiber tracking: principles and strategies: a technical review. *NMR Biomed.* 2002;15(7-8):468-480.
12. Stieltjes B, Kaufmann WE, van Zijl PC, et al. Diffusion tensor imaging and axonal tracking in the human brainstem. *Neuroimage*. 2001;14(3):723-735.
13. Frank LR. Anisotropy in high angular resolution diffusion-weighted MRI. *Magn Reson Med.* 2001;45(6):935-939.
14. Alexander DC, Barker GJ, Arridge SR. Detection and modeling of non-gaussian apparent diffusion coefficient profiles in human brain data. *Magn Reson Med.* 2002;48(2):331-340.
15. Descoteaux M, Deriche R, Knosche TR, Anwander A. Deterministic and probabilistic tractography based on complex fibre orientation distributions. *IEEE Trans Med Imaging.* 2009;28(2):269-286.

16. Behrens TE, Berg HJ, Jbabdi S, Rushworth MF, Woolrich MW. Probabilistic diffusion tractography with multiple fibre orientations: what can we gain? *Neuroimage*. 2007;34(1):144-155.
17. Tuch DS, Reese TG, Wiegell MR, Makris N, Belliveau JW, Wedeen VJ. High angular resolution diffusion imaging reveals intravoxel white matter fiber heterogeneity. *Magn Reson Med.* 2002;48(4):577-582.
18. Frank LR. Characterization of anisotropy in high angular resolution diffusion-weighted MRI. *Magn Reson Med.* 2002;47(6):1083-1099.
19. Anderson AW. Measurement of fiber orientation distributions using high angular resolution diffusion imaging. *Magn Reson Med.* 2005;54(5):1194-1206.
20. Descoteaux M, Angelino E, Fitzgibbons S, Deriche R. Apparent diffusion coefficients from high angular resolution diffusion imaging: estimation and applications. *Magn Reson Med.* 2006;56(2):395-410.
21. Candes E, Romberg J. Quantitative robust uncertainty principles and optimally sparse decompositions. *Foundations Computational Math.* 2006;6(2):227-254.
22. Candes E, Romberg J, Tao T. Robust uncertainty principles: exact signal reconstruction from highly incomplete frequency information. *IEEE Trans Inf Theory.* 2006;52(2):489-509.
23. Donoho D. Compressed sensing. *IEEE Trans Inf Theory.* 2006;52(4):1289-1306.
24. Michailovich O, Rathi Y. Fast and accurate reconstruction of HARDI data using compressed sensing. *Med Image Comput Comput Assist Interv.* 2010;13(pt 1):607-614.
25. Nimsky C, Ganslandt O, Fahlbusch R. Implementation of fiber tract navigation. *Neurosurgery*. 2007;61(1 suppl):306-317; discussion 317-318.
26. Gering DT, Nabavi A, Kikinis R, et al. An integrated visualization system for surgical planning and guidance using image fusion and interventional imaging. *Int Conf Med Image Comput Comput Assist Interv.* 1999;2:809-819.
27. Pieper S, Halle M, Kikinis R. 3D slicer. In: *Proceedings of the 1st IEEE International Symposium on Biomedical Imaging: From Nano to Macro 2004*. Vol 1. Arlington, VA: IEEE International Symposium on Biomedical Imaging; 2004:632-635.
28. Pieper S, Lorensen B, Schroeder W, Kikinis R. The NA-MIC Kit: ITK, VTK, pipelines, grids and 3D slicer as an open platform for the medical image computing community. Paper presented at: Proceedings of the 3rd IEEE International Symposium on Biomedical Imaging: From Nano to Macro 2006; April 6-9, 2006; Arlington, VA.
29. Merhof D. *Reconstruction and Visualization of Neuronal Pathways From Diffusion Tensor Data*. Erlangen, Germany: Department of Neuroscience, University of Erlangen-Nuremberg; 2007.
30. Biniek R. *Akute Aphasien*. Stuttgart, Germany: Thieme Verlag; 1997.
31. Jansen A, Menke R, Sommer J, et al. The assessment of hemispheric lateralization in functional MRI: robustness and reproducibility. *Neuroimage*. 2006;33(1):204-217.
32. Michailovich O, Rathi Y. On approximation of orientation distributions by means of spherical ridgelets. *IEEE Trans Image Process.* 2010;19(2):461-477.
33. Michailovich O, Rathi Y, Dolui S. Spatially regularized compressed sensing for high angular resolution diffusion imaging. *IEEE Trans Med Imaging.* 2011;30(5):1100-1115.
34. Landgraf P, Richter M, Merhof D. Anisotropy of HARDI diffusion profiles based on the L2-Norm. In: Handels H, Ehrhardt J, Deserno TM, eds. *Bildverarbeitung für die Medizin (BVM)*. Berlin, Germany: Springer; 2011.
35. Roberts DW, Strohbehn JW, Hatch JF, Murray W, Kettenberger H. A frameless stereotaxic integration of computerized tomographic imaging and the operating microscope. *J Neurosurg.* 1986;65(4):545-549.
36. Gasser T, Sandalcioglu E, Schoch B, et al. Functional magnetic resonance imaging in anesthetized patients: a relevant step toward real-time intraoperative functional neuroimaging. *Neurosurgery*. 2005;57(1 suppl):94-99; discussion 94-99.
37. Stadlbauer A, Prante O, Nimsky C, et al. Metabolic imaging of cerebral gliomas: spatial correlation of changes in O-(2-18F-fluoroethyl)-L-tyrosine PET and proton magnetic resonance spectroscopic imaging. *J Nucl Med.* 2008;49(5):721-729.
38. Assaf Y, Pasternak O. Diffusion tensor imaging (DTI)-based white matter mapping in brain research: a review. *J Mol Neurosci.* 2008;34(1):51-61.
39. Jones DK. The effect of gradient sampling schemes on measures derived from diffusion tensor MRI: a Monte Carlo study. *Magn Reson Med.* 2004;51(4):807-815.
40. Berger MS. Minimalism through intraoperative functional mapping. *Clin Neurosurg.* 1996;43:324-337.
41. Duffau H, Denvil D, Lopes M, et al. Intraoperative mapping of the cortical areas involved in multiplication and subtraction: an electrostimulation study in a patient with a left parietal glioma. *J Neurol Neurosurg Psychiatry.* 2002;73(6):733-738.
42. Merhof D, Richter M, Enders F, et al. Fast and accurate connectivity analysis between functional regions based on DT-MRI. *Med Image Comput Comput Assist Interv.* 2006;9(pt 2):225-233.
43. Merhof D, Meister M, Bingol E, Nimsky C, Greiner G. Isosurface-based generation of hulls encompassing neuronal pathways. *Stereotact Funct Neurosurg.* 2009;87(1):50-60.
44. Nimsky C, Ganslandt O, Hastreiter P, et al. Preoperative and intraoperative diffusion tensor imaging-based fiber tracking in glioma surgery. *Neurosurgery*. 2007;61(1 suppl):178-185; discussion 186.
45. Tuch DS. Q-ball imaging. *Magn Reson Med.* 2004;52(6):1358-1372.
46. Frey S, Campbell JS, Pike GB, Petrides M. Dissociating the human language pathways with high angular resolution diffusion fiber tractography. *J Neurosci.* 2008;28(45):11435-11444.
47. Prckovska V, Peeters TH, van Almsick M, Romeny B, Vilanova A. Fused DTI/HARDI visualization. *IEEE Trans Vis Comput Graph.* 2011;17(10):1407-1419.
48. Reisert M, Mader I, Anastasopoulos C, Weigel M, Schnell S, Kiselev V. Global fiber reconstruction becomes practical. *Neuroimage*. 2011;54(2):955-962.
49. Geschwind N. The organization of language and the brain. *Science*. 1970;170(3961):940-944.
50. Croxson PL, Johansen-Berg H, Behrens TE, et al. Quantitative investigation of connections of the prefrontal cortex in the human and macaque using probabilistic diffusion tractography. *J Neurosci.* 2005;25(39):8854-8866.
51. Catani M, Jones DK, ffytche DH. Perisylvian language networks of the human brain. *Ann Neurol.* 2005;57(1):8-16.
52. Powell HW, Parker GJ, Alexander DC, et al. Hemispheric asymmetries in language-related pathways: a combined functional MRI and tractography study. *Neuroimage*. 2006;32(1):388-399.
53. Pulvermuller F, Fadiga L. Active perception: sensorimotor circuits as a cortical basis for language. *Nat Rev Neurosci.* 2010;11(5):351-360.
54. Saur D, Kreher BW, Schnell S, et al. Ventral and dorsal pathways for language. *Proc Natl Acad Sci U S A.* 2008;105(46):18035-18040.
55. Archip N, Clatz O, Whalen S, et al. Non-rigid alignment of pre-operative MRI, fMRI, and DT-MRI with intra-operative MRI for enhanced visualization and navigation in image-guided neurosurgery. *Neuroimage*. 2007;35(2):609-624.
56. Cao A, Thompson RC, Dumpuri P, et al. Laser range scanning for image-guided neurosurgery: investigation of image-to-physical space registrations. *Med Phys.* 2008;35(4):1593-1605.
57. Miga MI, Sinha TK, Cash DM, Galloway RL, Weil RJ. Cortical surface registration for image-guided neurosurgery using laser-range scanning. *IEEE Trans Med Imaging.* 2003;22(8):973-985.

Acknowledgments

We would like to thank the members of the Slicer community for their contributions, especially Steve Pieper, PhD, and Demian Wassermann, PhD, (Department of Radiology, Brigham and Women's Hospital and Harvard Medical School, Boston, Massachusetts) for their support.

SCIENTIFIC REPORTS

OPEN

SUBJECT AREAS:
CANCER
COMPUTATIONAL SCIENCE
SOFTWARE
COMPUTATIONAL BIOLOGY AND BIOINFORMATICS

Received
31 May 2012

Accepted
15 February 2013

Published
4 March 2013

Correspondence and requests for materials should be addressed to J.E. (egger@bwh.harvard.edu)

GBM Volumetry using the 3D Slicer Medical Image Computing Platform

Jan Egger[1,2,3], Tina Kapur[1], Andriy Fedorov[1], Steve Pieper[1,4], James V. Miller[5], Harini Veeraraghavan[6], Bernd Freisleben[3], Alexandra J. Golby[1,7], Christopher Nimsky[2] & Ron Kikinis[1]

[1]Department of Radiology, Brigham and Women's Hospital, Harvard Medical School, Boston, MA, USA, [2]Department of Neurosurgery, University Hospital of Marburg, Marburg, Germany, [3]Department of Mathematics and Computer Science, The Philipps-University of Marburg, Marburg, Germany, [4]Isomics, Inc., Cambridge, MA, USA, [5]Interventional and Therapy Lab, GE Research, Niskayuna, NY, USA, [6]Biomedical Image Analysis Lab, GE Research, Niskayuna, NY, USA, [7]Department of Neurosurgery, Brigham and Women's Hospital, Harvard Medical School, Boston, MA, USA.

Volumetric change in glioblastoma multiforme (GBM) over time is a critical factor in treatment decisions. Typically, the tumor volume is computed on a slice-by-slice basis using MRI scans obtained at regular intervals. *(3D)Slicer* – a free platform for biomedical research – provides an alternative to this manual slice-by-slice segmentation process, which is significantly faster and requires less user interaction. In this study, 4 physicians segmented GBMs in 10 patients, once using the competitive region-growing based *GrowCut* segmentation module of *Slicer*, and once purely by drawing boundaries completely manually on a slice-by-slice basis. Furthermore, we provide a variability analysis for three physicians for 12 GBMs. The time required for *GrowCut* segmentation was on an average 61% of the time required for a pure manual segmentation. A comparison of *Slicer*-based segmentation with manual slice-by-slice segmentation resulted in a *Dice Similarity Coefficient* of 88.43 ± 5.23% and a *Hausdorff Distance* of 2.32 ± 5.23 mm.

Gliomas are the most common primary brain tumors, arising from the glial cells that support the cerebral nerve cells. The *World Health Organization (WHO)* grading system for gliomas defines grades I–IV, where grade I tumors are the least aggressive and IV are the most aggressive[1]. Of these, 70% are considered malignant gliomas (anaplastic astrocytoma *WHO* grade III and glioblastoma multiforme *WHO* grade IV). The glioblastoma multiforme, named for its histopathological appearance, is the most frequent malignant primary brain tumor and is one of the most highly malignant human neoplasms. The approach to the treatment of glioblastomas typically includes maximum safe resection, percutaneous radiation and chemotherapy. Despite new radiation strategies and the development of oral alcylating substances (e.g. Temozolomide), the life expectancy for GBM patients is still only about fifteen months[2]. Although in previous years the role of surgery was controversial, recent literature favors a maximum safe surgical resection as a positive predictor for extended patient survival[3]. Microsurgical resection can now be optimized with the technical development of neuronavigation based on data from diffusion tensor imaging (DTI), functional magnetic resonance imaging (fMRI), magnetoencephalography (MEG), magnetic resonance spectroscopy (MRS), or positron-emission-computed-tomography (PET). An early postoperative magnetic resonance imaging (MRI) with a contrast agent can be used to determine how much of the tumor mass has been removed and frequent MRI scans can help to monitor any new tumor growth.

For automatic glioma segmentation in general (*World Health Organization* grade I–IV), several algorithms have already been proposed that rely on magnetic resonance imaging. Szwarc et al.[4] have presented a segmentation approach that uses fuzzy clustering techniques. In their evaluation, the authors used six magnetic resonance (MR) studies of three subjects and the reported *Dice Similarity Coefficient (DSC)*[5,6] ranged from 67.21% to 75.63%. Angelini et al.[7] have presented an extensive overview of some deterministic and statistical approaches. Gibbs et al.[8] have introduced a combination of region growing and morphological edge detection for segmenting enhancing tumors in T1-weighted MRI data. The authors evaluated their method with one phantom data set and ten clinical data sets. An interactive method for segmentation of full-enhancing, ring-enhancing and non-enhancing tumors has been proposed by Letteboer et al.[9] and was evaluated on twenty clinical cases. Depending on intensity-based pixel probabilities for tumor tissue, Droske et al.[10] have presented a deformable model method, using a level set formulation, to divide the MRI data into regions of similar image properties for tumor segmentation. Clark et al.[11] have introduced a knowledge-based automated segmentation on multispectral data in order to partition

Table 1 | This table presents a comparison of a) the time it took for physicians to segment GBMs manually vs. using *3D Slicer*, b) the agreement between the two segmentations. The *MT* column shows the time (in minutes) it took a physician to segment each of ten GBMs on slice-by-slice basis. The *SlicerT* column shows the time (in minutes) it took a physician to segment it using *3D Slicer*. The *Slices* column shows the number of slices that the tumor spans in each case, as a rough approximation of the complexity of the segmentation task. Note that 9 out of 10 cases, *Slicer* < *MT*, and on an average, the time it took to segment with *3D Slicer* was 61% of the time it took to segment manually on a slice-by-slice basis. The columns *DSC* and *HD* show the agreement between the two segmentations using a *Dice Similarity Coefficient* and *Hausdorff Distance*, respectively

Case No.	MT (min)	SlicerT (min)	Slices	SlicerT/MT	DSC	HD (mm)	Manual Volume (mm^3)	Slicer Vol (mm^3)	Slicer/Manual Vol
1	9	4	36	0.44	0.85	2.80	33522	44694	1.33
2	19	7.5	51	0.39	0.91	3.68	28373	32383	1.14
3	6	4.5	42	0.75	0.92	1.71	42056	47752	1.14
4	16	6.5	60	0.41	0.91	3.00	69448	78776	1.13
5	3	2.5	10	0.83	0.81	2.00	1480	2016	1.36
6	14	6.25	43	0.45	0.94	2.00	39097	38905	1.00
7	13	8.5	36	0.65	0.87	2.23	22468	25331	1.13
8	7	9.25	42	1.32	0.92	2.12	27368	30648	1.12
9	5	3	11	0.60	0.79	2.39	2703	3908	1.45
10	11	2.5	16	0.23	0.92	0.31	10318	11720	1.14
Averages	10.30	5.45	34.70	0.61	0.88	2.32	27683	31613	1.19
		Time				**Agreement**			

glioblastomas. Direct comparison with a hand labeled segmentation 89 of 120 slices had a percent matching rate of 90% or higher. Segmentation based on outlier detection in T2-weighted MR data has been proposed by Prastawa et al.[12]. For each case, the time required for the automatic segmentation method was about ninety minutes. Sieg et al.[13] have introduced an approach to segment contrast-enhanced, intracranial tumors and anatomical structures of registered, multispectral MR data. The approach has been tested on twenty-two data sets, but no computation times were provided. Egger et al.[14,15] present a graph-based approach. After the graph has been constructed, the minimal cost closed set on the graph is computed via a polynomial time s-t cut[16]. The presented method has been evaluated with fifty glioblastoma multiforme yielding an average *Dice Similarity Coefficient* of 80.37 ± 8.93%.

Since fully automated segmentation often fails to match human judgments of tumor boundaries, a number interactive segmentation algorithms have been proposed. Vezhnevets and Konouchine[17] give an overview of methods for generic image editing and methods for editing medical images. An interactive segmentation technique called *Magic Wand*[17] is a common selection tool in image editing software applications. The tool gathers color statistics from the user specified image point (or region) and segments (connected) image regions with pixels whose color properties fall within some given tolerance of the gathered statistics. Reese[18] has presented a region-based interactive segmentation technique called *Intelligent Paint*, based on hierarchical image segmentation by tobogganing, with a connect-and-collect strategy to define an object's region. Mortensen and Barrett[19] have introduced a boundary-based method to compute a minimum-cost path between user-specified boundary points. The intelligent scissors method[20] treats each pixel as a graph node and uses shortest-path graph algorithms for boundary calculation and a faster variant of region-based intelligent scissors uses tobogganing for image over-segmentation and then treats homogenous regions as graph nodes. *GraphCut* is a combinatorial optimization technique applied to the task of image segmentation by Boykov and Jolly[21]. An extension of the *GraphCut* named *GrabCut* developed by Rother et al.[22], is an iterative segmentation scheme that uses a graph-cut for intermediate steps. A marker-based watershed transformation algorithm for medical image segmentation, developed by Moga and Gabbouj[23], uses user-specified markers for segmenting gray level images. The *Random Walker* algorithm of Grady and Funka-Lea[24] is a probabilistic approach using a small number of user-labeled pixels. Heimann et al.[25] have presented an interactive region growing method that is a descendant of one of the classic image segmentation techniques. A manual refinement system for graph-based approaches has recently been presented by Egger et al.[26,27]. The approach takes advantage of the basic design of graph-based image segmentation algorithms and restricts a graph-cut by using additional user-defined seed points to set up fixed nodes in the graph. Another resent publication by Zukić et al.[28] presents semi-automatic GBM segmentation with a *balloon inflation* approach[29]. The balloon inflation method has been evaluated with twenty-seven magnetic resonance imaging data sets with a reported average *DSC* of 80.46%. The *GrowCut* method, developed by Vezhnevets and Konouchine[17], is a cellular automaton-based algorithm for interactive multilabel segmentation of *N*-dimensional images. The *GrowCut* algorithm is freely available as a module[30] for the medical image computing platform *3D Slicer*[31] and has been used in a recent study to segment Pituitary Adenomas[32].

In this paper, we present a detailed study of the volumetric analysis of glioblastoma multiforme using the *GrowCut* tool *3D Slicer*. Our objective is to evaluate the utility of *3D Slicer* in simplifying the time-consuming manual slice-by-slice segmentation while achieving a comparable accuracy. Thus, 4 physicians segmented GBMs in 10 patients, once using the competitive region-growing based *GrowCut*

Table 2 | Manual intra- and inter-physician segmentation results (min, max, mean μ and standard deviation σ) for three neurosurgeons – *X*, *Y* and *Z* – for twelve glioblastoma multiforme (GBM) data sets. The first column represents the intra-physician segmentation result: within a time distance of two weeks Physician *X* segmented the twelve GBMs slice-by-slice twice. The second and third columns present the inter-physician segmentation results, whereby the manual slice-by-slice segmentations form Physician *Y* and Physician *Z* have been compared with the first manual segmentation of Physician *X*

	DSC for intra- and inter-physician segmentations		
	Physician X	Physician Y	Physician Z
Min	84.01%	78.68%	76.03%
Max	96.30%	94.86%	94.83%
$\mu \pm \sigma$	90.29 ± 4.48%	88 ± 6.08%	86.63 ± 6.87%

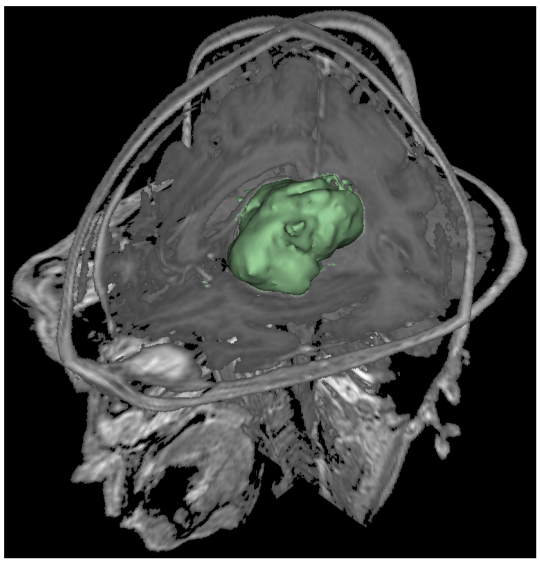

Figure 1 | This image presents the segmentation results of *GrowCut* (green) for the tumor and background initialization of Figure 3. After the initialization of the *GrowCut* algorithm under *Slicer* it took about ten seconds to get the segmentation result on an *Intel Core i7-990 CPU, 12 × 3.47 GHz, 12 GB RAM, Windows 7 Home Premium x64 Version, Service Pack 1.*

segmentation module of *3D Slicer*, and once by drawing boundaries manually on a slice-by-slice basis. The time required for *GrowCut* vs. manual segmentation were recorded. A comparison was performed of *3D Slicer* based segmentation with manual slice-by-slice segmentation using the *Dice Similarity Coefficient (DSC)* and the *Hausdorff Distance (HD)*[33–35].

Methods that use all slices to calculate the tumor boundaries have more information available to make accurate predictions of tumor volume. Simpler methods such as geometric models provide only a rough estimate of the tumor volume and may not be indicated for accurate determination of tumor burden. Geometric approximations use one or several user-defined diameters to estimate the tumor volume[36–38]. The Macdonald criteria[39] for measuring brain tumors adopts uniform, rigorous response criteria similar to those in general oncology where response is defined as a ≥50% reduction in tumor size and the usual measure of "size" is the largest cross-sectional area (the largest cross-sectional diameter multiplied by the largest diameter perpendicular to it). Accurate and repeatable methods to calculate tumor volume are therefore an important aspect of clinical care.

The rest of this article is organized as follows: *Section 2* presents the results of our experiments. *Section 3* discusses the performance of the proposed approach, concludes the contribution and outlines areas for future work. Finally, *Section 4* presents the material and the methods.

Results

The goal of this study was to evaluate the utility of *3D Slicer* for segmentation of GBMs compared to manual slice-by-slice segmentation. We used two metrics for this evaluation: a) the time it took for physicians to segment GBMs manually vs. using *3D Slicer*, b) the agreement between the two segmentations. In using these metrics to evaluate our results, our assumption is that if *3D Slicer* can be used to produce GBM segmentations that are statistically equivalent to what the physicians achieve manually, and in substantially less time, then the tool is useful for volumetric follow-ups of GBM patients. Overall, four physicians participated in our study: three physicians provided the manual slice-by-slice segmentations and one physician has been trained in a Slicer-based segmentation as described in the methods section. The results of our study are detailed in Table 1, the primary conclusion of which is that *3D Slicer* based GBM segmentation can be performed in about 60% of the time, and with acceptable agreement (DSC: 88.43 ± 5.23%, HD: 2.32 ± 5.23 mm) to manual segmentation by a qualified physician. In Table 1, The *MT* column shows the time (in minutes) it took a physician to segment each of ten GBMs on slice-by-slice basis. The *SlicerT* column shows the time (in minutes) it took a physician to segment it using *3D Slicer*. The *Slices* column shows the number of slices that the tumor spans in each case, as a rough approximation of the complexity of the segmentation task. Note that 9 out of 10 cases, *Slicer* < *MT*, and on an average, the time it took to segment with *3D Slicer* was **61%** of the time it took to segment manually on a slice-by-slice basis. The columns *DSC* and *HD* show the agreement between the two segmentations using a *Dice Similarity Coefficient* and *Hausdorff Distance*, respectively.

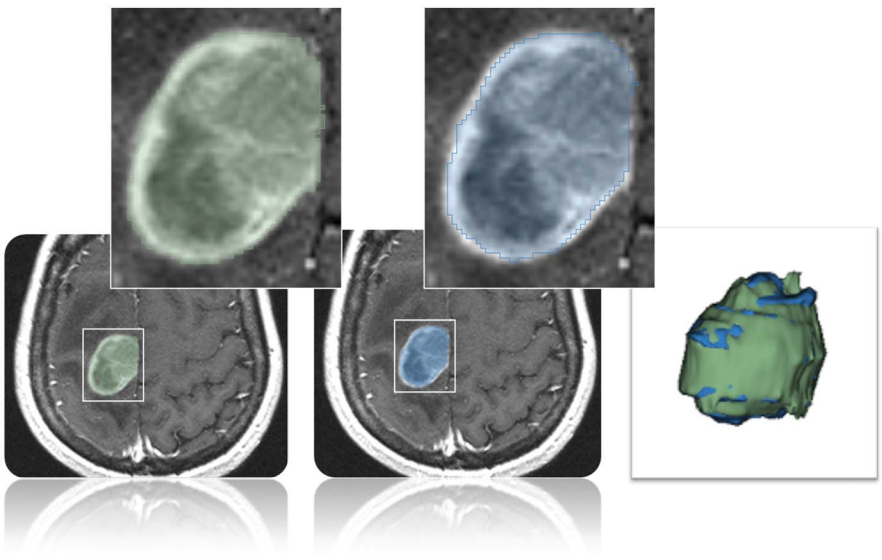

Figure 2 | Comparison of glioblastoma multiforme (GBM) segmentation results on an axial slice: semi-automatic segmentation under *Slicer* (green, left image) and pure manual segmentation (blue, middle image). Moreover, a fused visualization of the 3D masks of the manual and the *Slicer* segmentation is presented (rightmost image).

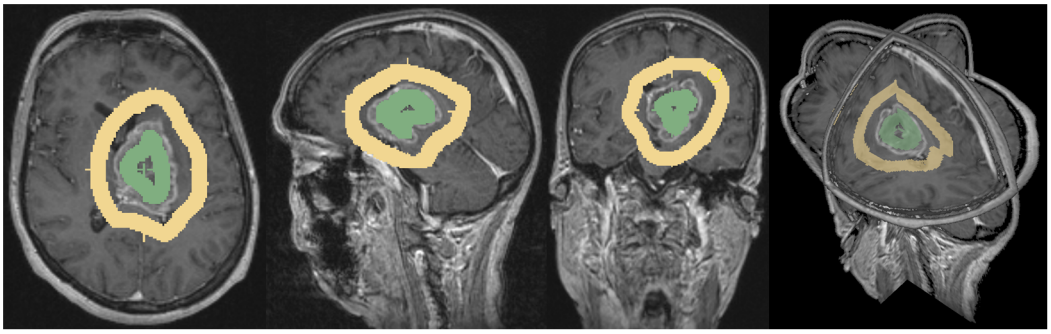

Figure 3 | These images present a typical user initialization for glioblastoma multiforme (GBM) segmentation under *Slicer* with *GrowCut*: axial (left image) sagittal (second image from the left), and coronal (third image from the left). Besides, a 3D visualization of all three slices is presented (rightmost image). Note: the tumor has been initialized in green and the background has been initialized in yellow.

To provide readers with a point of comparison on how *DSC* and *HD* computations vary between expert raters, we include in Table 2 some statistics that we published in another article where we analyzed the results of 12 manual slice-by-slice GBM segmentations by 3 neurosurgeons[40,41].

In addition to the quantitative results, we present sample GBM segmentation results in Figures 1 and 2 for visual inspection. Figure 1 shows the results of the *3D Slicer GrowCut* function (for the tumor and background initialization shown in Figure 3). The rendered 3D tumor segmentation is superimposed (green) on three orthogonal cross-sections of the data. Figure 2 presents the direct comparison of *3D Slicer* vs. manual segmentation on an axial slice: the semi-automatic segmentation under *3D Slicer* (green) is shown on the left side of the figure and the pure manual segmentation (blue) is shown in the middle of the figure. A fused visualization of the 3D masks of the manual and the *Slicer* segmentations are displayed on the right side of the figure.

Discussion

We observed that the automatic segmentation results produced by *3D Slicer* (*GrowCut*) typically required some additional editing on some slices to achieve the desired boundary and the time required for this manual correction is included in our measurements. Manual segmentation by neurosurgeons took three to nineteen minutes (mean: ten minutes), in contrast to the semi-automatic segmentation with the *GrowCut* implementation under *3D Slicer* that took about 60% of that time (mean: five minutes) including the time needed for editing the *GrowCut* results.

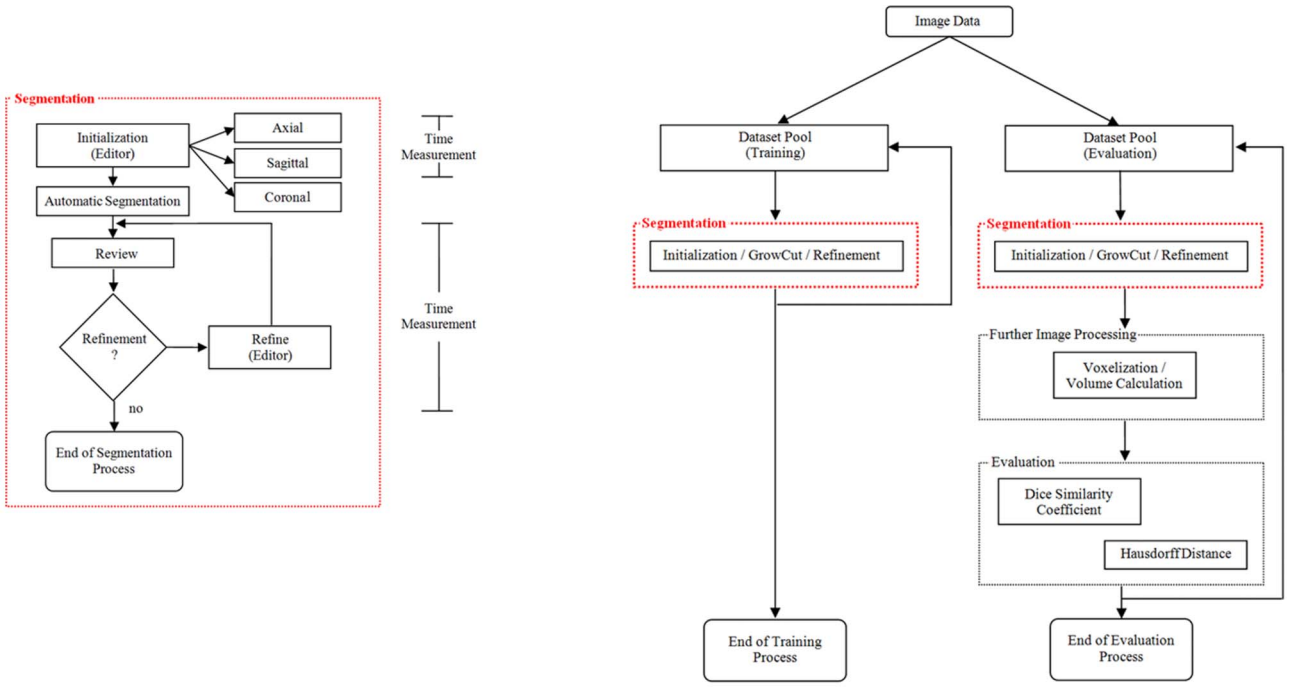

Figure 4 | Detailed workflow of the segmentation process that is used in the training and the evaluation phase (left). The segmentation process starts with the initialization of the *GrowCut* algorithm by the user on an axial, sagittal and coronal slice. Then, the automatic segmentation is started and afterwards reviewed by the user. This results into the refinement phase where the *Editor* tools under *Slicer* are used to correct the automatic segmentation result – mostly by navigating along the axial slices. During the evaluation phase the time for the initialization and the refinement has been measured. The overall workflow of the proposed study is presented on the right side; it starts with the image data and ends with the training or the evaluation process. Therefore, the data is divided into two pools of data sets: the training data set and the evaluation data set. The segmentation process is for both stages the same. However, for the evaluation phase further image processing (voxelization and volume calculation) is required to calculate the *Dice Similarity Coefficient (DSC)* and the *Hausdorff Distance (HD)* for a quantitative evaluation.

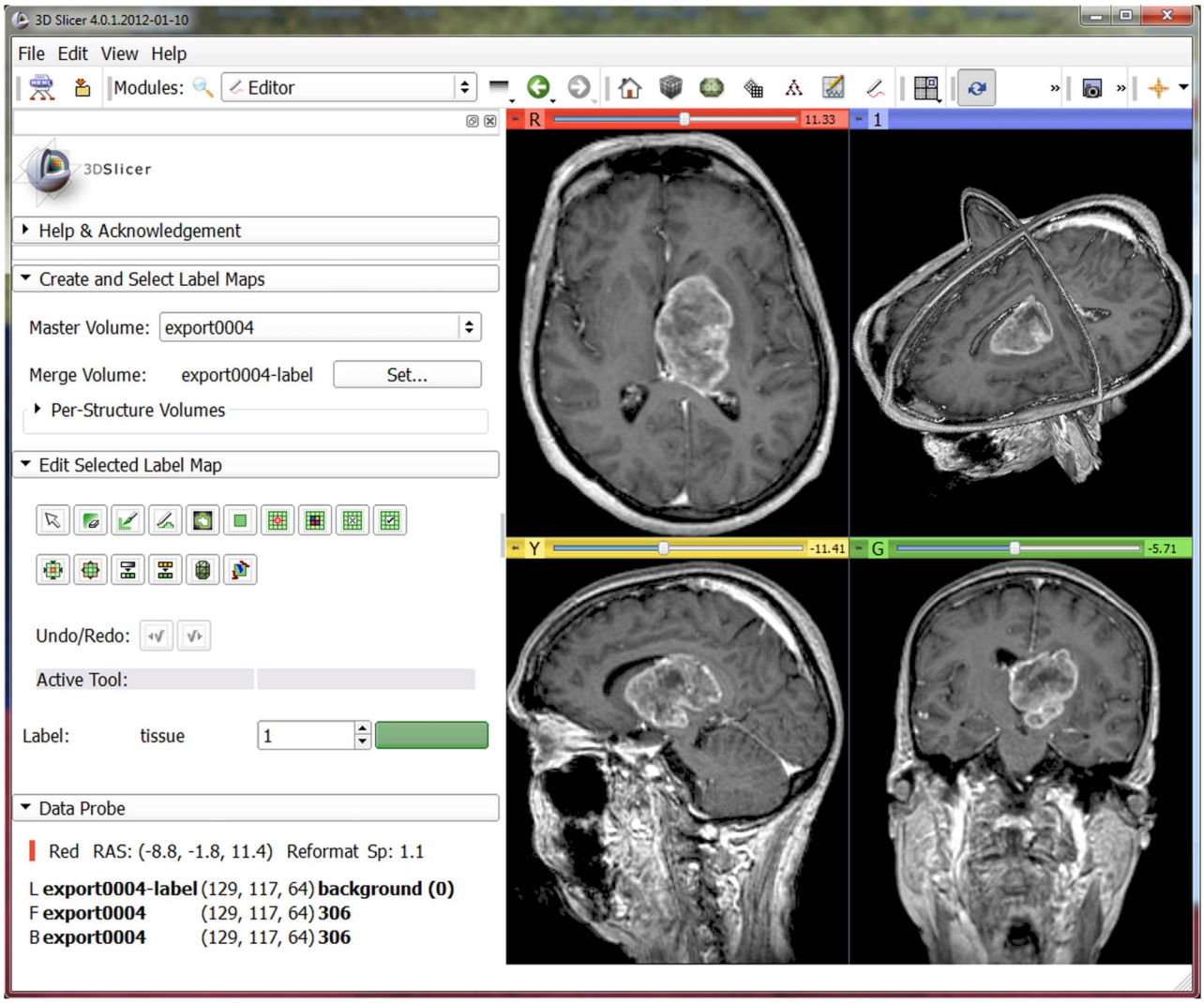

Figure 5 | ***Slicer*** **interface with the** ***Editor*** **on the left side and a loaded glioblastoma multiforme (GBM) data set on the right side: axial slice (upper left window), sagittal slice (lower left window), coronal slice (lower right window) and the three slices shown in a 3D visualization (upper right window).**

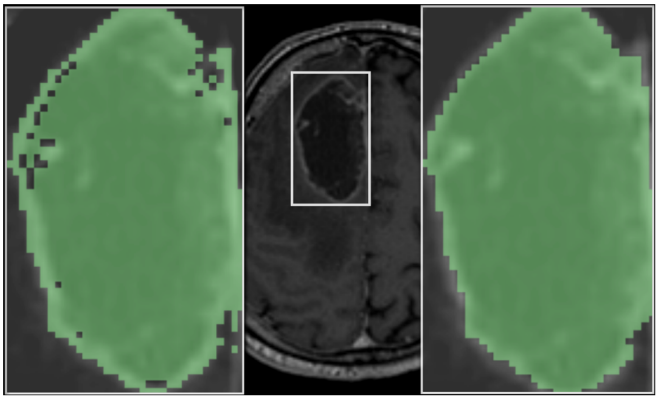

Figure 6 | **In these images the usage for the** ***Dilate*** **and** ***Erode*** **options under** ***Slicer*** **are presented.** The background shows an axial slice with a glioblastoma multiforme (white rectangle). The left white rectangle presents the zoomed segmentation result of *GrowCut* (green). As shown, the segmentation result is not very smooth at the tumor border. To get a smoother result the *Dilate* and *Erode* options under *Slicer* can be used. For this example *Dilate*, *Erode* and an additional *Erode* have been performed. The result of this operations is shown in the right white rectangle (green).

To quantify the quality of the *GrowCut* algorithm, we performed intra- and inter-physician segmentations[40,41]. The results also provided an upper segmentation threshold and therefore a quality measure for our algorithm. For the intra-physician segmentation, a neurosurgeon segmented twelve glioblastoma multiforme. After two weeks, the same neurosurgeon segmented these twelve cases again. The detailed results are presented in Table 2 and provide a mean value μ and a standard deviation σ of 90.29 $\pm$ 4.48% with a minimal *Dice Similarity Coefficient* of 84.01% and a maximal *Dice Similarity Coefficient* of 96.30% (see the first column). Finally, Table 2 also shows inter-physician segmentation results for the twelve glioblastoma multiforme (see the second and third columns). Therefore, the segmentation of the neurosurgeons Y and Z have been compared with the segmentations of neurosurgeon X. It is evident that there is an upper threshold with a *Dice Similarity Coefficient* of around ninety percent for the manual intra- and inter-physician segmentations (average *DSC* when compared with an automatic segmentation: 79.96 $\pm$ 8.06% (neurosurgeon X), 77.79 $\pm$ 8.49% (neurosurgeon Y) and 76.83 $\pm$ 13.67% (neurosurgeon Z)). The DSC of 90% can be thought of as a metric for estimating how well an automatic segmentation result is performing relative to the range of performance of experts, and perhaps also can serve as an indicator for how much

manual post-editing will be required after the automatic segmentation is performed.

In this paper, the evaluation of glioblastoma multiforme segmentation with the free and open source medical image analysis software *3D Slicer* has been presented. *Slicer* provides a semi-automatic, 3D segmentation algorithm, *GrowCut*, that is a viable alternative to the time-consuming process of volume determination during monitoring of a patient, for which slice-by-slice contouring has been the best demonstrated practice. Editing tools available in *3D Slicer* are used for manual editing of the results upon completion of the automatic *GrowCut* segmentation. The volume of the 3D tumor is then computed and stored as an aide for the surgeon in decision making for comparison with follow-up scans. This segmentation has been evaluated on 10 GBM data sets against manual expert segmentations using the *Dice Similarity Coefficient (DSC)* and the *Hausdorff Distance (HD)*. Additionally, intra-physician segmentations have been performed to provide a quality measure of the presented evaluation. In summary, the achieved research highlights of the presented work are:

- Manual slice-by-slice segmentations of glioblastoma multiforme (GBM) have been performed by clinical experts to obtain ground truth of tumor boundaries and estimates of rater variability.
- Physicians have been trained in segmenting glioblastoma multiforme with *GrowCut* and the *Editor* module of *3D Slicer*.
- Trained physicians used *Slicer* to segment a glioblastoma multiforme evaluation set.
- Semi-automatic segmentation times have been measured for *GrowCut* based segmentation in *3D Slicer*.
- *Dice Similarity Coefficient (DSC)* and *Hausdorff Distance (HD)* have been calculated to evaluate the quality of the segmentations.

There are several areas for future work. In particular, some steps of the segmentation workflow under *Slicer* can be automated. Instead of initializing the foreground on three single 2D slices, a single 3D initialization could be used by means of generating a sphere around the position of the user-defined seed point. Additionally, the algorithm can be enhanced with statistical information about the shape[42] and the texture of the desired object[43] to improve the automatic segmentation. Furthermore, we plan to evaluate the method on magnetic resonance imaging (MRI) data sets with *World Health Organization* grade I, II and III gliomas. As compared to high-grade gliomas, low-grade tumor MR images lack gadolinium enhancement. Thus, for these tumors, outlines cannot be expressed by contrast-enhancing T1-weighted images, but by surrounding edema in T2-weighted images. In addition, we want to study how *Slicer* can be used to enhance the segmentation process of vertebral bodies. Besides, we want to apply the scheme to segment other organs and pathologies. Moreover, we are considering improving the algorithm by performing the whole segmentation iteratively; that is, after the segmentation has been performed, the result of the segmentation can be used as a new initialization for a new segmentation run with the process repeated under user control. We anticipate that the iterative approach will result in more robustness with respect to initialization.

Methods

Data. Ten diagnostic T1-weighted MRI scans with gadolinium enhancement were used for segmentation. These were acquired on a 1.5 Tesla MRI scanner (Siemens MAGNETOM Sonata, Siemens Medical Solutions, Erlangen, Germany) using a standard head coil. Scan parameters were: TR/TE 2020/4.38 msec, isotropic matrix, 1 mm; FOV, 250 × 250 mm; 160 sections.

Software. For the semi-automatic segmentation work in this study we used *3D Slicer* 4.0, which is freely downloadable from the website http://www.slicer.org.

Manual segmentation of each data set was performed on a slice-by-slice basis by neurosurgeons at the *University Hospital of Marburg in Germany* (Chairman: Prof. Dr. Ch. Nimsky) with several years of experience in the resection of gliomas (note: if the tumor border was very similar between consecutive slices, the software allowed the user to skip manual segmentation in each slice, and instead interpolated the boundaries in these areas). The software used for this manual contouring provided simple contouring capabilities, and was created by us using the medical prototyping platform *MeVisLab* (see http://www.mevislab.de/). The hardware platform used was an *Intel Core i5-750 CPU, 4 × 2.66 GHz, 8 GB RAM, Windows XP Professional ×64 Version, Version 2003, Service Pack 2.*

***GrowCut* segmentation in 3D Slicer.** The *GrowCut* is an interactive segmentation algorithm based on the idea of cellular automaton. The algorithm achieves reliable and reasonably fast segmentation of moderately difficult objects in 2D and 3D using an iterative labeling procedure resembling competitive region growing. A user's interactions results in a set of seed pixels which in turn try to assign their labels to their pixel neighborhood. A pixel is assigned the label of its neighbor when the similarity measure of the two pixels weighted by the neighboring pixel's weight or "strength" exceeds its current weight. Label assignment also results in an update of the pixel's weight. The labeling procedure continues iteratively until a stable configuration is reached when modification of the pixel labels is no longer possible. The algorithm is simple to use requiring no additional inputs from the user besides the painted strokes on the apparent foreground and background. Furthermore, the user can modify the segmentation by adding additional labels in the image, thereby influencing the segmentation result.

Our implementation of the algorithm in *3D Slicer* consists of a GUI front-end to enable interactions of the user with the image and an algorithm back-end where the segmentation is computed. We employ a minimal interface, where the user interacts by painting on the image. The algorithm requires labeling with at least two different colors (for a foreground and a background label class). The naïve implementation of the algorithm would require every pixel to be visited in each iteration. Furthermore, a pixel will need to visit every one of its neighbors to update the pixel strengths and labels. Such an implementation would be computationally expensive especially for large 3D images. We implemented the following techniques for speeding up the segmentation. First, as the user may be interested only in segmenting out a small area in the image, the algorithm computes the segmentation only within a small *region of interest (ROI)*. The *ROI* is computed as a convex hull of all user labeled pixels with an additional margin of approximately 5% for our study. Second, the iterations involving the image are executed in multiple threads, such that several small regions of the image are updated simultaneously (note: the implementation is multithreaded and automatically makes use of all the cores of the computer). Finally, the similarity distance between the pixels are pre-computed once and reused. Also the algorithm keeps track of *saturated* pixels (those whose weights and therefore labels can no longer be updated) and avoids the expensive neighborhood computation on those pixels. Keeping track of such pixels also helps to determine when to terminate the algorithm.

GBM segmentation using 3D Slicer. After trials of the various segmentation facilities available in *Slicer*, we determined that the use of *GrowCut* followed by morphological operations such as *erosion*, *dilation*, and *island removal* provides the most efficient segmentation method for GBMs from gadolinium enhanced T1 images. As shown in Figure 4, we used the following workflow to perform GBM segmentation: 1) load the data set into *Slicer* 2) initialization of an area inside the tumor, and a stroke drawn outside the tumor with a brush size of about 1 cm 3) automatic competing region-growing using *GrowCut*, and 4) usage of Editing tools like *dilation*, *erosion*, and *island removal* or pure manual refinement after visual inspection of results (note: the users are responsible for qualitatively deciding how much dilation, erosion and island removal are required for the segmentation). Figure 5 shows the *Slicer Editor* module user interface on the left side and a loaded GBM data set on the right side. Figure 3 presents a typical user initialization for *GrowCut* on the axial, sagittal and coronal cross-sections. Figure 6 shows the results of subsequent *erosion* followed by a *dilation*, and Figure 1 shows the results of the *GrowCut* method.

The hardware platform used was an Apple MacBook Pro (4 Intel Core i7, 2.3 GHz, 8 GB RAM, AMD Radeon HD 6750 M, Mac OS × 10.6 Snow Leopard).

Measurement of segmentation time. We measured the time taken by the same physician to segment manually vs. the *3D Slicer* method. Within the *3D Slicer* segmentation, we separately measured the time taken by each of the three steps (initialization, *GrowCut*, refinement using morphological operations) of the *3D Slicer* method (see left chart of Figure 4).

Metrics for comparison between 3D Slicer and manual segmentation. The resulting segmentations from both methods were saved as binary volumes, and the agreement between the two was compared using the *Dice Similarity Coefficient* and the *Hausdorff Distance*.

The *Dice Similarity Coefficient (DSC)* of agreement between two binary volumes is calculated as follows:

$$DSC = \frac{2 \cdot V(A \cap R)}{V(A) + V(R)} \quad (1)$$

The *DSC* measures the relative volume overlap between A and R, where A and R are the binary masks from the automatic (A) and the reference (R) segmentation. $V(\cdot)$ is

the volume (in mm³) of voxels inside the binary mask, by means of counting the number of voxels, then multiplying with the voxel size.

The *Hausdorff Distance (HD)* between two binary volumes is defined in terms of the *Euclidean* distance between the boundary voxels of the masks. Given the sets *A* (of the automatic segmentation) and *R* (of the reference segmentation) that consist of the points that correspond to the centers of segmentation mask boundary voxels in the two images, the directed *HD h(A,R)* is defined as the minimum *Euclidean* distance from any of the points in the first set to the second set, and the *HD* between the two sets *H(A,R)* is the maximum of these distances:

$$h(A,R) = \max_{a \in A} (d(a,R)), \text{ where } d(a,R) = \min_{r \in R} \|a - r\|$$
$$H(A,R) = \max(h(A,R), h(R,A,)) \quad (2)$$

1. Kleihues, P. *et al.* The WHO classification of tumors of the nervous system. *Journal of Neuropathology & Experimental Neurology* **61**(3), 215–229 (2002).
2. Kortmann, R. D., Jeremic, B., Weller, M., Plasswilm, L. & Bamberg, M. Radiochemotherapy of malignant gliom in adults. Clinical experiences. *Strahlenther Onkol.* **179**(4), 219–232 (2003).
3. Lacroix, M. *et al.* A multivariate analysis of 416 patients with glioblastoma multiforme: Prognosis, extent of resection and survival. *Journal of Neurosurgery* **95**, 190–198 (2001).
4. Szwarc, P., Kawa, J., Bobek-Billewicz, B. & Pietka, E. Segmentation of Brain Tumours in MR Images Using Fuzzy Clustering Techniques. Proceedings of Computer Assisted Radiology and Surgery (CARS), Geneva, Switzerland (2010).
5. Zou, K. H. *et al.* Statistical Validation of Image Segmentation Quality Based on a Spatial Overlap Index: Scientific Reports. *Academic Radiology* **11**(2), 178–189 (2004).
6. Sampat, M. P. *et al.* Measuring intra- and inter-observer agreement in identifying and localizing structures in medical images. *IEEE Inter Conf Image Processing,* 4 pages (2006).
7. Angelini, E. D. *et al.* Glioma Dynamics and Computational Models: A Review of Segmentation, Registration, and In Silico Growth Algorithms and their Clinical Applications. *Current Med. Imaging Rev.* **3**, 262–76 (2007).
8. Gibbs, P. *et al.* Tumour volume determination from MR images by morphological segmentation. *Physics in Med. & Biology* **41**(11), 2437–46 (1996).
9. Letteboer, M. M. J. *et al.* Segmentation of tumors in magnetic resonance brain images using an interactive multiscale watershed algorithm. *Academic Radiology* **11**, 1125–1138 (2004).
10. Droske, M. *et al.* An adaptive level set method for interactive segmentation of intracranial tumors. *Neurol Res* **27**(4), 363–70 (2005).
11. Clark, M. *et al.* Automatic tumor segmentation using knowledge-based techniques. *IEEE Transactions on Medical Imaging (TMI)* **17**(2), 187–201 (1998).
12. Prastawa, M. *et al.* A brain tumor segmentation framework based on outlier detection. *Medical Image Analysis* **8**, 275–283 (2004).
13. Sieg, C., Handels, H. & Pöppl, S. J. Automatic Segmentation of Contrast-Enhanced Brain Tumors in Multispectral MR-Images with Backpropagation-Networks (in German). Bildverarbeitung für die Medizin (BVM), Springer Press, 347–351 (2001).
14. Egger, J. *et al.* Nugget-Cut: A Segmentation Scheme for Spherically- and Elliptically-Shaped 3D Objects. 32nd Annual Symposium of the German Association for Pattern Recognition (DAGM). *LNCS* **6376**, 383–392, Springer Press, Darmstadt, Germany (2010).
15. Egger, J., Kappus, C., Freisleben, B., & Nimsky, C. A Medical Software System for Volumetric Analysis of Cerebral Pathologies in Magnetic Resonance Imaging (MRI) Data. *J Med Syst. 2012 Aug* **36**(4), 2097–10 (2012).
16. Boykov, Y. & Kolmogorov, V. An Experimental Comparison of Min-Cut/Max-Flow Algorithms for Energy Minimization in Vision. *IEEE Transactions on Pattern Analysis and Machine Intelligence* **26**(9), 1124–1137 (2004).
17. Vezhnevets, V. & Konouchine, V. GrowCut-Interactive multi-label N-D image segmentation. *Proc. Graphicon*, 150–156 (2005).
18. Reese, L. Intelligent Paint: Region-Based Interactive Image Segmentation. Master's thesis, Department of Computer Science, Brigham Young University, Provo, UT (1999).
19. Mortensen, E. N. & Barrett, W. A. Interactive segmentation with intelligent scissors. *Graphical Models and Image Processing* **60**(5), 349–384 (1998).
20. Mortensen, E. N. & Barrett, W. A. Toboggan-based intelligent scissors with a four-parameter edge model. *IEEE Conference on Computer Vision and Pattern Recognition (CVPR),* pages 2452–2458 (1999).
21. Boykov, Y. & Jolly, M.-P. Interactive graph cuts for optimal boundary and region segmentation of objects in n-d images. *Proceedings of the International Conference on Computer Vision (ICCV),* volume **1**, pages 105–112 (2001).
22. Rother, C., Kolmogorov, V. & Blake, A. Grabcut-interactive foreground extraction using iterated graph cuts. *Proceedings of ACM Siggraph* (2004).
23. Moga, A. & Gabbouj, M. A parallel marker based watershed transformation. *In IEEE International Conference on Image Processing (ICIP),* **II**, 137–140 (1996).
24. Grady, L. & Funka-Lea, G. Multi-label image segmentation for medical applications based on graph-theoretic electrical potentials. *ECCV Workshops CVAMIA and MMBIA,* 230–245 (2004).
25. Heimann, T., Thorn, M., Kunert, T. & Meinzer, H.-P. New methods for leak detection and contour correction in seeded region growing segmentation. In 20th ISPRS Congress, Istanbul 2004. *International Archives of Photogrammetry and Remote Sensing,* vol. **XXXV**, 317–322 (2004).
26. Egger, J., Colen, R., Freisleben, B. & Nimsky, C. Manual Refinement System for Graph-Based Segmentation Results in the Medical Domain. *J Med Syst. 2012 Oct* **36**(5), 2829–39 (2011).
27. Egger, J. *et al.* A Flexible Semi-Automatic Approach for Glioblastoma multiforme Segmentation. Proceedings of International Biosignal Processing Conference, Charité, Berlin, Germany, 4 pages (2010).
28. Zukić, D. *et al.* Glioblastoma Multiforme Segmentation in MRI Data with a Balloon Inflation Approach. Proceedings of 6th RB Conference on Bio-Medical Engineering, State Technical University, Moscow, Russia, 4 pages (2010).
29. Cohen, L. D. On active contour models and balloons. *CVGIP: Image Understanding* **53**(2), 211–218 (1991).
30. Egger, J. *et al.* Square-Cut: A Segmentation Algorithm on the Basis of a Rectangle Shape. *PLoS One* **7**(2), e31064. Epub Feb 21 (2012).
31. Fedorov, A. *et al.* 3D Slicer as an Image Computing Platform for the Quantitative Imaging Network. *Magnetic Resonance Imaging 2012;* July PMID: 22770690 (2012).
32. Egger, J., Kapur, T., Nimsky, C. & Kikinis, R. Pituitary Adenoma Volumetry with 3D Slicer. *PLoS ONE* **7**(12), e51788 (2012).
33. Hausdorff, F. Grundzüge der Mengenlehre. Veit & Comp., Leipzig 1914 (rep. in Srishti D. Chatterji et al. (Hrsg.), Gesammelte Werke, Band II, Springer, Berlin, ISBN 3-540-42224-2 (2002).
34. Rockafellar, R. T. & Wets, R. J.-B. Variational Analysis. Springer, page 117, ISBN 3540627723, ISBN 978-3540627722 (2005).
35. Huttenlocher, D. P., Klanderman, G. A. & Rucklidge, W. J. Comparing images using the Hausdorff distance. *IEEE Transactions on Pattern Analysis and Machine Intelligence* **15**(9), 850–863 (1993).
36. Jimenez, C. *et al.* Follow-up of pituitary tumor volume in patients with acromegaly treated with pegvisomant in clinical trials. *European Journal of Endocrinology* **159**, 517–523 (2008).
37. Nobels, F. R. E. *et al.* Long-term treatment with the dopamine agonist quinagolide of patients with clinically non-functioning pituitary adenoma, in European. *Journal of Endocrinology* **143**, 615–621 (2000).
38. Korsisaari, N. *et al.* Blocking Vascular Endothelial Growth Factor-A Inhibits the Growth of Pituitary Adenomas and Lowers Serum Prolactin Level in a Mouse Model of Multiple Endocrine Neoplasia Type 1. *Clinical Cancer Research, January 1* **14**(1), 249–258 (2008).
39. Macdonald, D. R., Cascino, T. L., Schold, S. C. Jr. & Cairncross, J. G. Response criteria for phase II studies of supratentorial malignant glioma. *J Clin Oncol.* **8**(7), 1277–80 (1990).
40. Egger, J., Bauer, M. H. A., Kuhnt, D., Freisleben, B. & Nimsky, C. Min-Cut-Segmentation of WHO Grade IV Gliomas Evaluated against Manual Segmentation. XIX Congress of the European Society for Stereotactic and Functional Neurosurgery, Athens, Greece (2010).
41. Egger, J. *et al.* Evaluation of a Novel Approach for Automatic Volume Determination of Glioblastomas Based on Several Manual Expert Segmentations. Proceedings of 44. Jahrestagung der DGBMT, Rostock, Germany (2010).
42. Cootes, T. F. & Taylor, C. J. Active Shape Models-'Smart Snakes'. *Proceedings of the British Machine Vision Conference,* pages 266–275(1992).
43. Cootes, T. F. & Taylor, C. J. Statistical Models of Appearance for Computer Vision. Technical report, University of Manchester (2004).

Acknowledgements

The authors would like to thank the physicians: Dr. med. Barbara Carl, Rivka Colen, M.D., Christoph Kappus and Dr. med. Daniela Kuhnt for performing the manual segmentations of the medical images and participating in the study. The authors would also like to thank the members of the *Slicer Community* for their contributions. Furthermore, the authors would like to thank *Fraunhofer MeVis* in Bremen, Germany, for their collaboration and especially Prof. Dr. Horst K. Hahn for his support.

This project was supported by the National Center for Research Resources (P41RR019703) and the National Institute of Biomedical Imaging and Bioengineering (P41EB015898, U54EB005149, R03EB013792) of the National Institutes of Health. Its contents are solely the responsibility of the authors and do not necessarily represent the official views of the NIH.

Author contributions

Conceived and designed the experiments: J.E. & A.F. Performed the experiments: J.E. & A.F. Analyzed the data: J.E. & A.F. Contributed reagents/materials/analysis tools: J.E., T.K., A.F., S.P., J.V.M., H.V., B.F., A.J.G., C.N. & R.K. Wrote the paper: J.E., T.K. & S.P.

Additional information

Competing financial interests: The authors declare no competing financial interests.

How to cite this article: Egger, J. *et al.* GBM Volumetry using the 3D Slicer Medical Image Computing Platform. *Sci. Rep.* **3**, 1364; DOI:10.1038/srep01364 (2013).

Ein kubusbasierter Ansatz zur Segmentierung von Wirbeln in MRT-Aufnahmen

Robert Schwarzenberg[1,2], Bernd Freisleben[2], Ron Kikinis[1], Christopher Nimsky[3], Jan Egger[1,2,3]

[1]Surgical Planning Laboratory, Brigham and Women's Hospital, Harvard Medical School
[2]Dept. of Mathematics and Computer Science, University of Marburg
[3]Dept. of Neurosurgery, University of Marburg
rs@bwh.harvard.edu

Kurzfassung. In diesem Beitrag präsentieren wir ein graphbasiertes Verfahren zur volumetrischen Wirbelsegmentierung in MRT-Aufnahmen, das zur Segmentierung eine würfelförmige Vorlage nutzt. Dabei kann der Nutzer den Grad Δ (Smoothness-Term) der Abweichung von einem regulären Kubus bestimmen. Der Algorithmus generiert einen gerichteten zwei-terminalen Graphen (s-t-Netzwerk), wobei die Knoten des Graphen einer würfelförmigen Untermenge der Voxel entsprechen. Die Gewichtung der terminalen Kanten, die jeden Knoten mit einer virtuellen Quelle s und einer virtuellen Senke t verbinden, repräsentieren die Affinität eines Voxel zum Wirbel (Quelle) und zum Hintergrund (Senke); eine Menge unendlich gewichteter, nicht-terminaler Kanten realisiert den Smoothness-Term. Nach der Konstruktion wird in polynomialer Laufzeit ein minimaler s-t-Schnitt berechnet, der die Knoten in zwei disjunkte Mengen teilt, aus denen anschließend das Segmentierungsergebnis ermittelt wird. Die quantitative Auswertung einer C++ Implementierung des Algorithmus ergab einen durchschnittlichen Dice Similarity Coefficient von 81,33% bei einer maximalen Laufzeit von einer Minute.

1 Einleitung

Die demographische Entwicklung hat zu einem höheren Anteil älterer Patienten geführt, die einen operativen Eingriff an der Wirbelsäule benötigen [1, 2]. Dabei sind vor allem durch Veränderungen der ligamentären und ossären Strukturen degenerative Erkrankungen der Wirbelsäule weit verbreitet und die konsekutive Zunahme der Spinalkanalstenosen haben vermehrt Einschränkungen der Patienten im Alltag zur Folge. Zur präoperativen Evaluation der spinalen Knochenstruktur werden bevorzugt Computertomographie (CT)-Scans angefertigt, u.a. weil knöcherne Strukturen so besser erkennbar sind, als z.B. in Magnetresonanztomographie (MRT)-Aufnahmen [3].

In diesem Beitrag wird die Möglichkeit der MRT-Segmentierung im Hinblick auf die Rekonstruktion der Wirbelkörper vorgestellt. Potentiell wird so die Anzahl der CT-Scans zum Zweck der präoperativen Evaluierung von Wirbelkörpern

H.-P. Meinzer et al. (Hrsg.), *Bildverarbeitung für die Medizin 2013*, Informatik aktuell,
DOI: 10.1007/978-3-642-36480-8_14,

reduziert, da die Knochenstruktur durch die vorgestellte Methode auch in MRT-Aufnahmen gut erkennbar wird. Zudem wird der Zeitaufwand der präoperativen Maßnahmen durch eine automatische Segmentierung verringert.

In der Literatur finden sich mehrere Ansätze zur (semi-)automatischen Segmentierung von Wirbeln aus MRT-Aufnahmen. Bei dem Ansatz von Stern et al. [4] wird die Segmentierung durch eine Optimierung der Parameter eines dreidimensionalen deterministischen Modells der Wirbelsäule durchgeführt. Dabei wird nach der besten Übereinstimmung des deterministischen Modells mit der Wirbelsäule aus der Patientenaufnahme gesucht. Weese et al. [5] benutzen ein polygonales Modell der Wirbel und eine manuelle Initialisierung. Eine interne Energie entspricht der statistischen Form, eine externe Energie beruht auf den Bildgradienten. Der iterative Ansatz besteht aus zwei Schritten: Im ersten Schritt wird versucht, die Oberfläche zu erkennen, in einem zweiten Schritt wird das Modell angepasst. Das Verfahren von Ghebreab et al. [6] nutzt eine manuelle Initialisierung des ersten Wirbels und die Form der Wirbelsäule. Für die Repräsentation der Oberfläche wird eine B-Spline-Oberfläche mit 12x12 Kontrollpunkten genutzt, und zur Segmentierung benachbarter Wirbel wird ein statistisches Modell verwendet.

2 Material und Methoden

Der hier vorgestellte Algorithmus konstruiert in einem ersten Schritt ein zweiterminales Flussnetzwerk $F = ((V(G), E(G)), c, s, t)$, wobei $V(G)\backslash\{s, t\}$ eine Menge von Knoten bezeichnet, die wiederum einer Untermenge der Bildvoxel entspricht. $E(G)$ bezeichnet eine Menge von Kanten und c eine Funktion, die jeder Kante eine nicht-negative, reale Kapazität zuordnet. Außerdem besteht das Netzwerk aus einer Quelle $s \in V(G)$ und einer Senke $t \in V(G)$. Nach der Konstruktion des Netzwerks wird in polynomialer Zeit ein minimaler s-t-Schnitt (S, T) berechnet [7], aus dem anschließend das Segmentierungsergebnis wie folgt ermittelt wird:

- ein Knoten $v \in S$ wird dem Wirbelkörper zugeordnet und
- ein Knoten $v \in T$ wird dem Hintergrund zugeordnet.

Die betrachteten Voxel befinden sich entlang einer Menge von Strahlen, die ihren Ursprung alle in einem benutzerdefinierten Saatpunkt innerhalb des Wirbelkörpers haben. Hierbei besteht jeder Strahl aus der gleichen Menge von auf dem Strahl äquidistant verteilten Voxeln und alle Voxel der gleichen Ebene – z.B. die Menge der zweiten Voxel auf allen Strahlen – bilden eine Würfelform (Abb. 1, links).

Die terminalen Kanten des Netzwerks, die jeden Knoten mit s und t verbinden, repräsentieren die Grauwertunterschiede zwischen einem Voxel und seinem Vorgängervoxel auf demselben Strahl. Ist die Differenz klein (< 20), so wird davon ausgegangen, dass die beiden Voxel innerhalb einer homogenen Region des Bildes liegen (z.B. innerhalb des Wirbelkörpers), so dass die Kante, die den entsprechenden Knoten mit der Quelle verbindet, hoch gewichtet wird. Bei einer

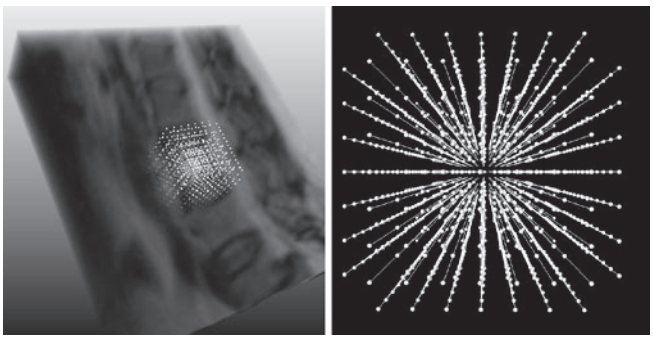

Abb. 1. Verteilung der Knoten eines Graphen (links) und Visualisierung der z-Kanten (rechts).

großen Differenz (> 20) kann von einem Objekt-Hintergrund-Übergang ausgegangen werden, so dass hier die entsprechende Kante zur Senke hoch gewichtet wird. Die terminalen Kantengewichtungen des ersten und des letzten Voxels auf jedem Strahl stellen außerdem sicher, dass der Saatpunkt dem Wirbelkörper und der letzte Voxel dem Hintergrund zugeordnet wird.

Um sicherzustellen, dass jeder Strahl nur genau einmal geschnitten wird, wird eine Menge von nicht-terminalen, ∞-gewichteten Kanten eingeführt, die jeden Knoten $v_{i_r} \in V(G)\backslash\{s,t,v_1\}$ mit seinem Vorgänger $v_{(i-1)_r} \in V(G)\backslash\{s,t\}$ auf einem Strahl r verbinden (Abb. 1, rechts) [8, 9]

$$A_z = \{(v_{i_r}, v_{(i-1)_r})\} \tag{1}$$

Einen Strahl r einmal zu schneiden verursacht, aufgrund von A_z, Kosten von mindestens ∞, da $(v_{i_r}, v_{(i+1)_r})$ geschnitten werden muss, gdw $v_{(j\leq i)_r} \in S$ und $v_{(j>i)_r} \in T$. Einen Strahl zweimal zu schneiden, würde Kosten von mindestens $2 \cdot \infty$ verursachen. Da jedoch der Saatpunkt v_1 in S liegt, während der letzte Knoten auf jedem Strahl T zugeordnet ist, muss ein Strahl von einem minimalen s-t-Schnitt genau einmal geschnitten werden. Im Fall eines scharfen Objekt/Hintergrund-Übergangs muss dieser Schnitt, aufgrund der hohen Gewichtung der terminalen Kante zur Senke, genau vor dem ersten Knoten im Hintergrund verlaufen.

Typische Herausforderungen im Kontext von graphbasierten Segmentierungen sind starke Abweichungen innerhalb der anatomischen Struktur, die einen zu frühen Schnitt zur Folge haben, sowie homogene Objekt/Hintergrund-Übergänge, die einen Überlauf des Segmentierungsergebnisses verursachen. Der Ansatz begegnet diesen Problemen, indem er dem Nutzer erlaubt, einen Smoothness-Term zu definieren, der die Objekt-Hintergrund Distanz $\Delta \in \mathbf{N_0}$ zweier benachbarter Strahlen beschränkt. Hierzu wird eine weitere Menge von nicht-terminalen, ∞-gewichteten Kanten eingeführt

$$A_{xy} = \{v_{i_r}, v_{\max\{i-\Delta,1\}_{r'}}\} \tag{2}$$

wobei r und r' aus einer Vierernachbarschaft stammen (Abb. 2). Ein Δ-Wert von Null hat somit eine reguläre Würfelform zur Folge, bei einem Δ-Wert $>$ Null sind entsprechende Abweichungen, abhängig von der Voxeldistanz auf den einzelnen Strahlen, möglich (Abb. 3).

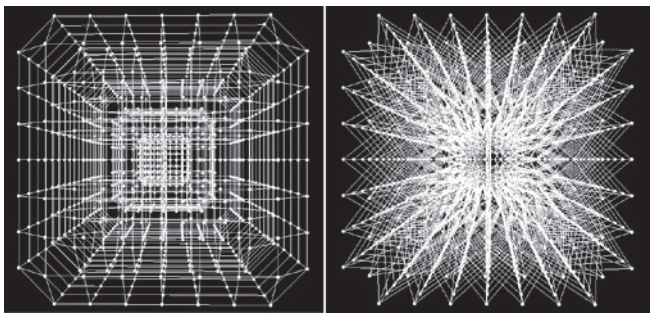

Abb. 2. Topologie der (x, y)-Kanten: $\Delta = 0$ (links) und $\Delta = 1$ (rechts).

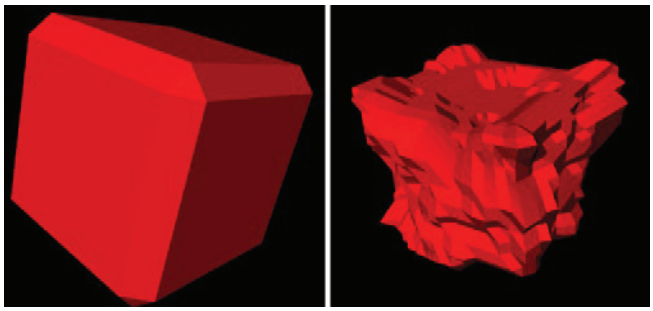

Abb. 3. Segmentierungsergebnis für $\Delta = 0$ (links) und $\Delta = 2$ (rechts).

3 Ergebnisse

Zur Evaluation des vorgestellten Segmentierungsverfahrens wurde eine C++ Implementierung innerhalb der medizinischen Bildverarbeitungsplattform MeVisLab (www.mevislab.de, Version 2.2.1) realisiert und anhand von zehn Wirbeln in zwei sagittalen, T2-gewichteten MRT-Datensätzen ($160 \times 160 \times 35$ und $160 \times 160 \times 23$) getestet. Die Tests lieferten bei einem direkten Vergleich mit manuell vorgenommen Schicht-für-Schicht-Segmentierungen einen durchschnittlichen Dice Similarity Coefficient (DSC) [10] von 81,33% (Tab. 1). Abb. 4 zeigt Segmentierungsergebnisse unseres Ansatzes (Cube-Cut).

Dabei hatten die rechenaufwendigsten Parametereinstellungen eine maximale Terminierungszeit von unter einer Minute (Netzwerkkonstruktion, s-t-Schnitt und Triangulierung des Segmentierungsergebnisses)[1]. Manuell erstellte Segmentierungen, für die ein Mediziner Schicht-für-Schicht die Außengrenzen eines Wirbelkörpers in den Aufnahmen einzeichnete, dauerten dagegen 6,65 bis 10 Minuten, so dass die automatische Segmentierung die präoperativen Evaluierungsmaßnahmen um 2,35 (min.) bis 15,65 Minuten (max.) verkürzte.

4 Diskussion

In diesem Beitrag wurde ein graphbasierter Ansatz zur Wirbelsegmentierung in MRT-Aufnahmen vorgestellt, wobei der Graph anhand einer würfelförmigen Vor-

[1] 2,1 GHz, 4 GB RAM x64 PC,Windows 7 Home Premium (SP1)

Tabelle 1. Evaluierungsergebnisse für zehn Wirbel. Die Abkürzungen man., aut., Vol., Vox. und DSC stehen für manuell, automatisch, Volumen in cm^3, Voxel und Dice Similarity Coefficient in %.

	man. Vol.	aut. Vol.	man. Vox.	aut. Vox.	DSC
min.	15,42	16,64	1892	2041	71,64
max.	33,83	28,78	5240	4320	86,69
$\mu \pm \sigma$	24,97 ± 6,15	23,48 ± 5,12	3750	3152	81,33 ± 5,07

lage konstruiert wird und die Knoten des Graphen nicht gleichverteilt und nicht äquidistant innerhalb der MRT-Aufnahme gesampelt werden. Dadurch liefert ein anschließender minimaler s-t-Schnitt - in Abhängigkeit von einem benutzerdefinierten Smoothness-Term (Abweichung) - auch eine würfelförmige Segmentierung zurück.

Unseren Wissens nach ist dies das erste Mal, dass bei einem graphbasierten Ansatz die Knoten anhand einer würfelförmigen Vorlage verteilt wurden und der minimale s-t-Schnitt somit auch ein würfelförmiges Segmentierungsergebnis bevorzugt. Das vorgestellte Verfahren kann auch zur Segmentierung anderer, vergleichbarer, kubusförmiger Zielstrukturen genutzt werden und eignet sich besonders um homogenen Objekt/Hintergrund-Übergängen zu begegnen, die eine automatische Segmentierung des Objektes erschweren. Es ist geplant das Verfahren in der Zukunft zu verfeinern, so bietet sich z.B. eine komplexere Kantendetektion an (gradient magnitude). Außerdem sollen die Segmentierungsergebnisse noch auf Formgleichheit untersucht werden.

Bei den aktuellen Parametereinstellungen kam es vor, dass Ecken der Wirbel nicht genau segmentiert wurden. Abb. 5 zeigt ein Beispiel, bei dem die Konturen zweier Ecken eines Wirbels (Kreise) „abgeschnitten“ wurden. Dieser Ungenauigkeit kann durch eine Verdichtung der Strahlen und dadurch auch einer Verdichtung der Knoten entgegengewirkt werden. Dies würde jedoch eine höhere Laufzeit zur Folge haben. Eine andere Möglichkeit wäre, anstatt eines Kubus

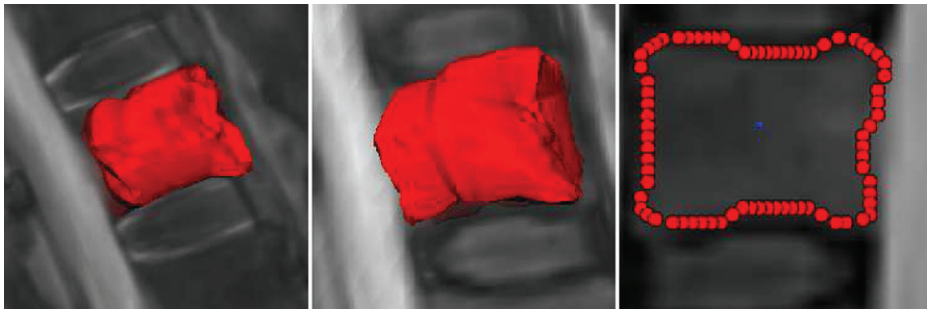

Abb. 4. 3D-Segmentierungsergebnisse (links und Mitte) und 2D-Perspektive auf ein Segmentierungsergebnis mit benutzerdefiniertem Saatpunkt in Blau (rechtes Bild).

eine dem Wirbel besser angepasste Vorlage für den Aufbau des Graphen zu verwenden, zum Beispiel mit Würfelseiten, die leicht nach innen gewölbt sind.

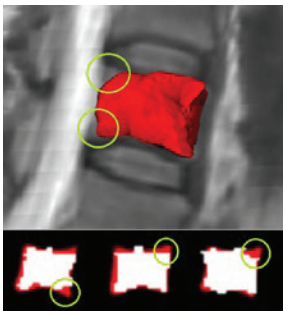

Abb. 5. Beispiel einer Segmentierung, bei der zwei Ecken des Wirbels (Kreise) nicht ausreichend segmentiert wurden. Im unteren Bildteil sind die manuellen Segmentierungen (rot) und die automatischen Segmentierungsergebnisse (weiß) in mehreren 2D-Schichten übereinandergelegt.

Danksagung. Wir danken Thomas Dukatz für sein Mitwirken an der Studie, Fraunhofer MeVis in Bremen für die Kollaboration und Horst-Karl Hahn für die Unterstützung und dem NIH (Grant 8P41EB015898-08).

Literaturverzeichnis

1. Joaquim AF, Sansur CA, Hamilton DK, et al. Degenerative lumbar stenosis: update. Arq Neuropsiquiatr. 2009;67(2B):553–8.
2. Hicks GE, Morone N, Weiner DK. Degenerative lumbar disc and facet disease in older adults: prevalence and clinical correlates. Spine (Phila Pa 1976). 2009;34(12):1301–6.
3. Richard PJ, George J, Metelko M, et al. Spine computed tomography doses and cancer induction. Spine (Phila Pa 1976). 2010;35(4):430–3.
4. Štern D, Vrtovec T, Pernuš F, et al. Segmentation of vertebral bodies in CT and MR images based on 3D deterministic models. Proc SPIE. 2011;7962.
5. Weese J, Kaus M, Lorenz C, et al. Shape constrained deformable models for 3D medical image segmentation. In: Insana M, Leahy R, editors. Information Processing in Medical Imaging. vol. 2082. Springer; 2001. p. 380–7.
6. Ghebreab S, Smeulders AW. Combining strings and necklaces for interactive three-dimensional segmentation of spinal images using an integral deformable spine model. IEEE Trans Biomed Eng. 2004;51(10):1821–9.
7. Boykov Y, Kolmogorov V. An experimental comparison of min-cut/max-flow algorithms for energy minimization in vision. IEEE Trans Pattern Anal Mach Intell. 2004;26(9):1124–37.
8. Li K, Wu X, Chen DZ, et al. Optimal surface segmentation in volumetric images: a graph-theoretic approach. IEEE Trans Pattern Anal Mach Intell. 2006;28(1):119–34.
9. Egger J, Kapur T, Dukatz T, et al. Square-cut: a segmentation algorithm on the basis of a rectangle shape. PLoS ONE. 2012;7(2):e31064.
10. Zou KH, Warfield SK, Bharatha A, et al. Statistical validation of image segmentation quality based on a spatial overlap index. Acad Radiol. 2004;2:178–89.

SpringerPlus
a SpringerOpen Journal

RESEARCH Open Access

Image-guided therapy system for interstitial gynecologic brachytherapy in a multimodality operating suite

Jan Egger

Abstract

In this contribution, an image-guided therapy system supporting gynecologic radiation therapy is introduced. The overall workflow of the presented system starts with the arrival of the patient and ends with follow-up examinations by imaging and a superimposed visualization of the modeled device from a PACS system. Thereby, the system covers all treatments stages (pre-, intra- and postoperative) and has been designed and constructed by a computer scientist with feedback from an interdisciplinary team of physicians and engineers. This integrated medical system enables dispatch of diagnostic images directly after acquisition to a processing workstation that has an on-board 3D Computer Aided Design model of a medical device. Thus, allowing precise identification of catheter location in the 3D imaging model which later provides rapid feedback to the clinician regarding device location. Moreover, the system enables the ability to perform patient-specific pre-implant evaluation by assessing the placement of interstitial needles prior to an intervention via virtual template matching with a diagnostic scan.

Introduction

With over eighty thousand new cases in 2010 and over Twenty-five Thousand deaths per year, gynecologic malignancies – including cervical, endometrial, and vaginal/vulvar cancers – are the 4th leading cause of death in women in the United States (Cancer Facts & Figures, American Cancer Society 2010). In general, therapy consists of three components: concurrent chemotherapy and external beam radiation followed by brachytherapy. During the external beam radiation stage a machine targets radiation beams at the pelvis from outside the body. In contrast to this, radioactive sources that deliver very high doses of radiation are placed directly inside the cancerous tissue during the brachytherapy stage. This is done by placing an applicator in the vaginal canal of the patient. In the past few years, several gynecologic cancer brachytherapy centers around the world have shown the benefit of using magnetic resonance imaging (MRI) scans to guide brachytherapy planning and incorporated it into their clinical practice. Viswanathan et al. (2007) was among the first to demonstrate that MRI significantly increased the coverage of the tumor by radiation dose as compared to computed tomography (CT).

Both, the European Society for Therapeutic Radiology and Oncology (ESTRO) and the American Brachytherapy Society (ABS) have recommended that T2-weighted MRI should be used for organs at risk (OARs) delineation and targeting in image-based cervical cancer brachytherapy. For a comprehensive explanation the reader is referred to a recent textbook on gynecologic radiation therapy and its references (Viswanathan et al. 2011) at this point, where the dosimetric and clinical gains from using MRI versus CT or ultrasound (US) are described in detail. Summarized, the ability to more accurately delineate the tumor and the surrounding normal tissue is the primary benefit in using MR compared to the more standard practice of CT. This leads to better dose escalation to the target volume while respecting dose constraints for the surrounding OARs. Studies have shown that CT may fail to distinguish cervical tumor from surrounding normal tissues such as small bowel, while MR determines the size, location, and paracervical involvement of the tumor and its relations to the applicator. The clinical practice of brachytherapy is well characterized using five components: 1) Applicator Choice and Insertion Techniques 2) Imaging Protocol

Correspondence: egger@uni-marburg.de
Department of Medicine, University Hospital of Giessen and Marburg (UKGM), Baldingerstraße, Marburg 35043, Germany

3) Contouring Protocol 4) Treatment Planning 5) Dose and Fractionation. Details of each step are also provided in the textbook of Viswanathan et al. (2011) and its references.

The purpose of this study is to introduce a system for supporting MR- and CT-guided gynecologic radiation therapy that covers all treatment stages (pre-, intra- and postoperative) with a focus on the five brachytherapy components introduced in the previous paragraph. To the best of the author's knowledge such a system has not yet been described. The system has been worked out hand-in-hand within an interdisciplinary team of physicians, computer scientists and engineers. Research highlights include linking a diagnostic imaging set in real-time to a 3D CAD model of a medical device and precise identification of catheter location in the 3D imaging model with real-time imaging feedback. Moreover, the system enables the ability to perform patient-specific pre-implant evaluation by virtually assessing the placement of interstitial needles prior to an intervention via template matching with a diagnostic scan.

The contribution is organized as follows: Materials and Methods section presents the materials and the methods, Results section presents the results, and Conclusions section concludes the contribution and outlines areas for future work.

Materials and methods

Equipment

The Brigham and Women's (BWH) Hospital in Boston has recently built an Advanced Multimodality Image-Guided Operating (AMIGO) suite, which enables 3 Tesla (3 T) MRI and PET/CT imaging during therapy (Egger et al. 2012a). AMIGO is an extension of the BWH's Image Guided Therapy (IGT) program, established in 1991 by Dr. Ferenc Jolesz. Launched in 2011 as the successor to the 0.5 Tesla "double-donut" Signa SP (General Electric Healthcare) interventional suite in which BWH teams performed over 3,000 surgical and interventional procedures, the charter of AMIGO is to continue these pioneering efforts with multimodal image guidance (Kapur et al. 2012) and intraoperative gynecological MRI data from AMIGO is freely available for download (Egger et al. 2012b).

System

The overall architecture of the medical system is shown in Figure 1 and has been preregistered as an invention disclosure (Egger et al. 2012c) and was adapted from a stent simulation system (Egger et al. 2009). The workflow starts with the arrival and imaging of the patient in the preoperative stage. The preoperative images are used to make a diagnosis and measure the relevant sizes for gynecologic radiation therapy. This also leads to the decision if the patient is eligible for an intervention or not. If the patient is eligible, an automatic request is send to the manufacturer and the inventory database and a first (medical) device selection is made. This selected device (e.g. Tandem and Ring/Ovoid +/−, interstitial needles or Vienna Applicator, interstitial needles alone) is modeled and visualized in the preoperative images from the patient and reviewed by a physician. Thereby, the system enables the virtual modeling and visualization of several instruments in the preoperative images of the patient, which allows a direct comparison of different devices to find the optimal one for treatment and dose delivery. Afterwards the selected device is ordered from the inventory and the modeled device (for example a 3D CAD model) is stored in a Picture Archiving Communication Software (PACS) system for the intra- and postoperative stage. In the intraoperative stage the patient is imaged with an intraoperative MRI (iMRI) and the modeled device from the PACS system is used for guidance during the intervention. Thus, the device is visualized in the patient's dataset to display the optimal position for dose delivery to the physician. The system ends in the postoperative stage with a follow-up examination by imaging and a superimposed visualization of the virtually modeled device from the PACS system.

The following sections describe the key components of the presented system in more detail, which include: the *Imaging* protocols that have been used to acquire the patient data, the *Linking* algorithm to register the 3D *Models* of the medical devices to the pre- and intraoperative patient datasets, the *Transfer* protocol to communicate between the different parts of the system, the *Contouring* of the patient's Organs at Risk and the *Planning* process for a precise dose distribution.

Imaging

After applicator placement, T1- and T2-weighted MR images are acquired with a 3 Tesla scanner. Therefore, T2-weighted sequences – Fast Spin Echo (FSE), Turbo Spin Echo (TSE) – are performed in the axial, sagittal and coronal orientation. Additionally, paraaxial, parasagittal, and paracoronal slices oriented orthogonal and parallel to the applicator axis are taken. Hereby, the axial images are obtained from above the uterine fundus down to the inferior border of the symphysis pubis, and in case of any vaginal tumor extension even below this. The sagittal images on the other side are obtained between internal obturator muscles. Finally, the (para) coronal and paraxial images are obtained so they cover the tumor, the entire cervix, the corpus uteri, the parametria, and the vagina. The slice thickness for the T1-weighted MR images is 3 mm with no gaps and the slice thickness for the T2-weighted MR images is 4-5 mm with 1 mm or no gaps (Viswanathan et al. 2011, Kapur 2012).

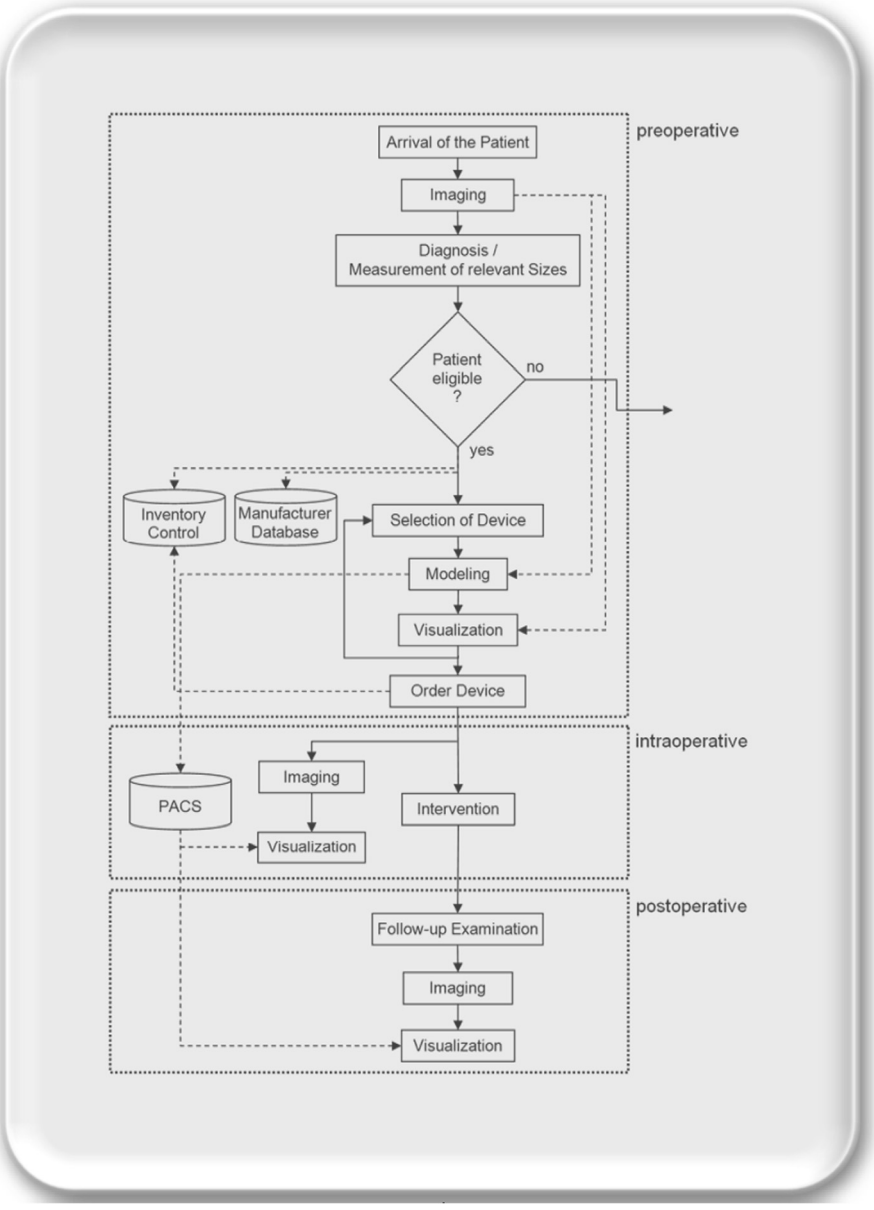

Figure 1 The overall end-to-end workflow of the presented system, starting with the arrival of the patient and finishing with follow-up examinations.

Linking

For linking a diagnostic and/or intraoperative imaging set to a 3D CAD model of a medical device a software prototype called iGyne has been developed, which allows identification of catheter location in the 3D imaging model with real-time imaging feedback. The first version of iGyne has been implemented in the medical platform MeVisLab (www.mevislab.de) as an own C++ module, end of 2011 (Egger et al. 2012a, Kapur et al. 2012). In the meantime there exist public available software modules for 3D Slicer (3DSlicer 2013, Pieper et al. 2004, Fedorov et al. 2012). 3D Slicer – or Slicer – is a free and open source software package for visualization and image analysis primarily used in the medical domain and has been developed by the Surgical Planning Laboratory (SPL) of the Brigham and Women's Hospital in Boston.

The intraoperative usage of iGyne in AMIGO consists of several steps (Chen et al. 2012): in a first step the CAD models of the medical devices are loaded into the software. Then, the patients MR scan with the template sutured to the perineum and the obturator placed in the vaginal canal is transferred via the DICOM protocol to iGyne. Next, an initial rigid registration is computed over three corresponding point pairs manually provided

by the user, which is afterwards refined using the Iterated Closest Point algorithm for rigid registration (Besl and McKay 1992, Xiaojun et al. 2007). Finally, iGyne enables the rendering of virtual needles in the 2D and 3D views which allows the visualization and observation of spatial relationships among the needles, tumors, and surrounding anatomical structures. Thus, supporting the determination of the amount of needles and their positions as well as their insertion depths for a patient.

Models

The 3D models of the medical devices like the interstitial template and vaginal obturator (Figure 2) were created in advance using CAD software (SolidWorks, Dassault Systèmes SolidWorks Corp., MA). All models were reveres-engineered by measuring the detailed dimensions from the clinically used devices. Afterwards, the models were converted to an industry standard format (STL).

Transfer

An important factor for a medical system using software and hardware from different manufactures is the data exchange. To have the intraoperative patient data immediately available in iGyne the DICOM listener from Slicer has been used. Thus, the patient acquisitions could be pushed automatically from the scanner to iGyne for further processing (e.g. *Linking* and *Contouring*). However, for an intraoperative navigation or guidance of catheter placement a more sophisticated solution is needed, where a navigation system or ultrasound is integrated into the whole system. This can be realized via the OpenIGTLink network protocol developed at the BWH (Tokuda et al. 2010). OpenIGTLink is a new, open, simple and extensible peer-to-peer network communication protocol for IGT which has already been used successfully for prostate interventions (Tokuda et al. 2008). The protocol provides a standardized mechanism to connect hardware and software by the transfer of coordinate transforms, images, and status messages. The advantage of OpenIGTLink is its simple specification, initially developed through a collaboration of academic, clinical and industrial partners for developing an integrated robotic system for MRI-guided prostate interventions (Fischer et al. 2008). It was designed for use in the application layer on the TCP/IP stack, allowing researchers to develop a prototype system that integrates multiple medical devices using the standard network infrastructure (Egger et al. 2012d). The OpenIGTLink protocol itself does not include mechanisms to establish and manage a session. It only defines a set of messages, which is the minimum data unit of this protocol. In Summary, an OpenIGTLink message contains all information necessary for interpretation by the receiver and begins with a 58-byte header section, which is common to all types of data, followed by a body section. The format of the body section varies by the data type that is specified in the header section. Since any compatible receiver can interpret the header section, which contains the size and the data type of the body, every receiver can gracefully

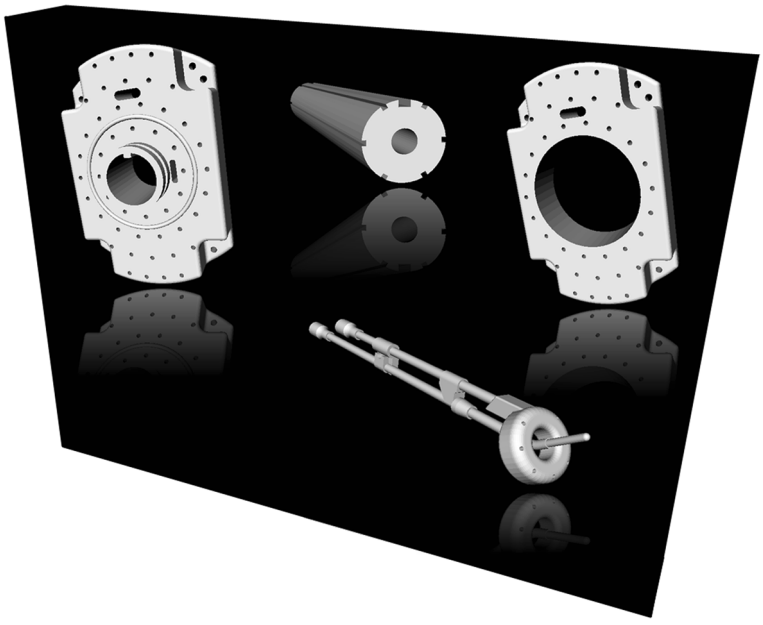

Figure 2 3D CAD models of an interstitial template (upper left), an obturator (upper middle) for Gynecologic Radiation Therapy, a modified interstitial template (upper right) and a tandem and ring (lower right) for Gynecologic Radiation Therapy.

handle any message, even those with an unknown data type, by ignoring incompatible messages without the system crashing.

Contouring

According to the GYN GEC ESTRO guidelines (Haie-Meder et al. 2005, Pötter et al. 2006), three types of structures are outlined in the patient data for the proposed system: the gross tumor volume (GTV), the clinical tumor volume (CTV) and the organs at risk (OAR). Hereby, the GTV is the tumor – as seen by the physician in the patient's images and clinical exams – which gets the maximum radiation dose for treatment. For the CTV two areas are defined: the intermediate risk clinical tumor volume (IR-CTV) and the high-risk clinical tumor volume (HR-CTV). Thereby, the HR-CTV is the GTV including the cervix and any suspicious areas where disease remains at the time of brachytherapy, like a uterine invasion or parametrial involved tissues. The IR-CTV is an extension of the HR-CTV by 1 cm and any disease extension at the time of diagnosis. Finally, the OARs consist of the bladder, the rectum, the sigmoid and the small bowel adjacent to the uterus which should get a minimal possible radiation dose (Viswanathan et al. 2011, Kapur 2012). For the segmentation of the pelvic structures for gynecologic brachytherapy we studied the capabilities available in Slicer. As a result, segmentation of the bladder could be achieved accurately using the implementation of the GrowCut algorithm in Slicer. But, manual segmentation was required to achieve segmentation results for the tumor and the rectosigmoid (Egger et al. 2012e).

Planning

The treatment planning of the presented system can be performed by using commercial software packages from Nucletron (Plato, OncentraGYN) and Varian (BrachyVision). These software applications work with different types of image modalities like MR, CT, X-ray, Ultrasound, and therefore a suitable for a multimodal operation suite like *AMIGO*. In a first step, the geometry of the inserted applicator is reconstructed, which is done by using its appearance in the images (Pernelle et al. 2013), followed by the generation of a treatment plan based on the prescribed doses to the contours GTV, CTV, and constraints on the OAR. Thereafter, manual refinement is performed to obtain optimal dose distribution covering the target (tumor). Thus, the isodose distribution is evaluated after each modification, which includes a detailed analysis of the dose-volume parameters (DVH) for CTVs and OARs (note: during the external beam radiation therapy (EBRT) the patients receive a dose of 40–50 Gy and the following brachytherapy provides an extra 3–5 fractions of 5.5-7 Gy each. The overall aim is to deliver a dose of 80–90 Gy to the high-risk clinical tumor volume and the dose to the OAR is assessed through measurement of dose rate. This measurement can be achieved with one of the following two methods: (1) the common ICRU 38 reference points, or more recently, (2) 3D volumes like the D2cc and D0.1 cc, which are defined for the bladder, the rectum/sigmoid, and small bowel. The D2cc tolerances are assumed to be approximately 90 Gy for the bladder, 70 Gy for rectum/sigmoid, and 55 Gy for the small bowel (Viswanathan et al. 2011, Kapur 2012).

Results

In this contribution an overall system for supporting Gynecologic Radiation Therapy with focus on a multimodality operating suite, like AMIGO, has been worked out. The Image-Guided Therapy system starts with the patient arrival and imaging. Then, diagnosis and measurement of relevant sizes for intervention in a multimodality operating suite are made leading to automatic inventory control and manufacturer request. Next, a first device is selected (e.g. Tandem and Ring/Ovoid +/– interstitial needles or interstitial needles alone) that is modeled in the preoperative images. Thereby, virtual modeling and visualization of several instruments for direct device comparison is enabled to find the optimal one. Afterwards, the device is ordered from the hospital inventory and the modeled device is stored (PACS). In the intraoperative stage the patient is imaged and the stored device allows guidance to an optimal position for the subsequent dose delivery. The system ends with follow-up examinations by imaging and a superimposed visualization of the modeled device from the PACS. In order to increase the physician's speed and monitor the consequences of inserting interstitial catheters in real-time a software prototype has been developed. The prototype has been realized as an own module called iGyne (interstitial Gynecologic Radiation) under the medical research platform 3D Slicer in C++:

https://github.com/xjchen/igyne

and Python:

https://github.com/gpernelle/iGynePy

http://www.slicer.org/slicerWiki/index.php/Documentation/Nightly/Extensions/iGyne

Figure 3 shows several screenshots of the iGyne module under Slicer. The screenshots show the 3D CAD model of the interstitial template that has been fitted to MRI scans. On the left side of the iGyne interface an interstitial planning sheet is provided which allows virtual preplanning of single needles (depth and length). The software also enables rendering of the planned interstitial needles in different 2D slices. The iGyne Slicer module could be performed the planning in *real-time* on a

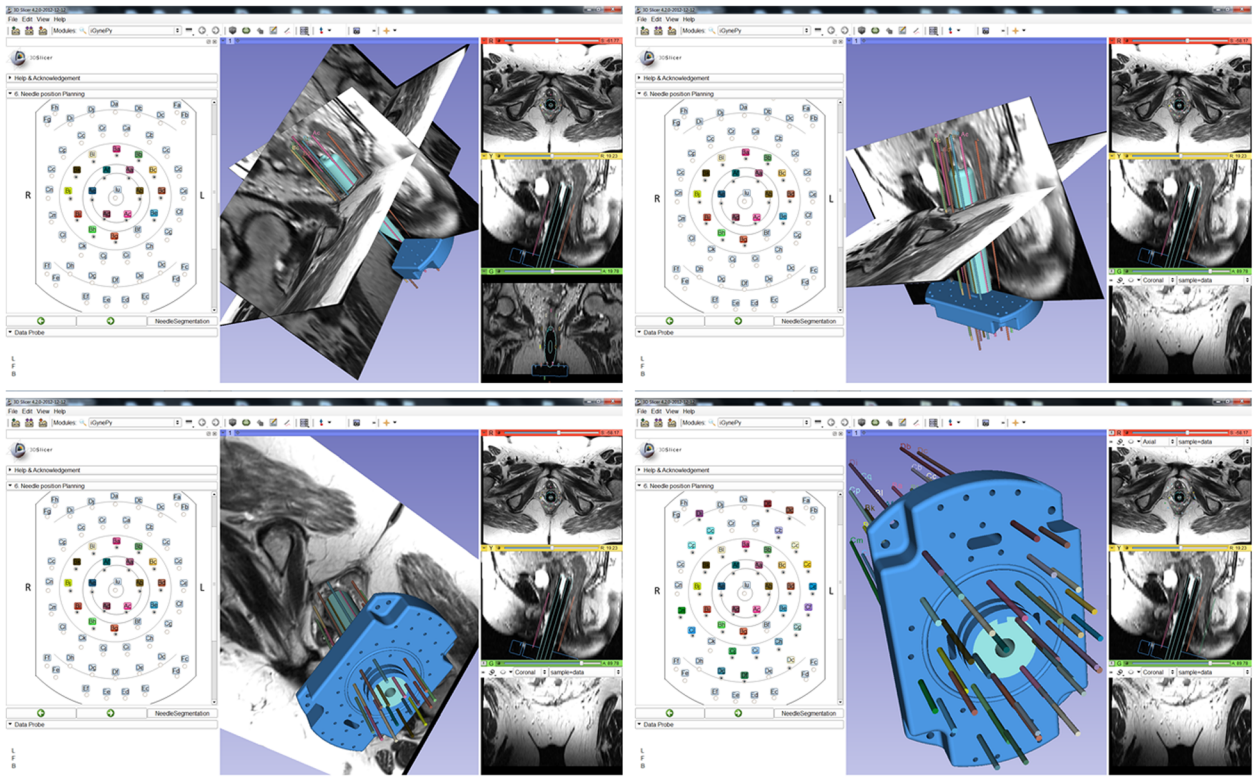

Figure 3 Screenshots of the research software (*iGyne*) that has been developed as an own module under the medical platform 3D Slicer (www.slicer.org). The dataset used for the screenshots is available from (accessed August 2013): https://github.com/xjchen/igyne/tree/master/Sample%20data/.

Laptop with Intel Core i5-2520 M CPU, 2 × 2.5 GHz, 4 GB RAM, Windows 7 Version, Service Pack 1, 32Bit.

Conclusions

In this contribution, an overall Image-Guided Therapy system for supporting Gynecologic Radiation Therapy has been introduced that covers all therapy stages from patient arrival/diagnosis (preoperative), intervention (intraoperative) to follow-up examinations (postoperative). To the best of the author's knowledge, this is the first time an overall medical system for Image-Guided Therapy supporting Gynecologic Radiation Therapy has been introduced. In summary, the achieved research highlights of the presented work include:

- linking a diagnostic imaging set in real-time to a 3D CAD model of a medical device;
- precise identification of catheter location in the 3D imaging model with real-time imaging feedback and
- ability to perform patient-specific pre-implant evaluation by assessing in the computer the placement of interstitial needles prior to an intervention via virtual template matching with a diagnostic scan.

The overall workflow of the designed system has been described in detail step-by-step: starting with the arrival of the patient and finishing with follow-up examinations.

However, there are several areas of future work, like the integration of intraoperative navigation (e.g. intraoperative ultrasound (iUS), electromagnetic (EM) tracking or optical navigation) into the system (Wang et al. 2013). In contrast to prostate interventions where navigation systems have been used (Tokuda et al. 2008, 2010) medical navigation systems have not yet found their way into gynecological interventions. However, there are other research studies that have influence on a medical navigation system for gynecologic radiation therapy, like the exploration of female patient positions undergoing gynecological surgeries (Power 2003). Moreover, a motion study between supine and lithotomy positions of the female pelvis should be performed by acquiring magnetic resonance imaging data in different stirrups adjustments. Critical is the deformation that has been studied for the prostate (Hirose et al. 2002, Bharatha et al. 2001) and also in particular for prostate brachytherapy (Bellon et al. 1999) but to the best of the author's knowledge not for the female pelvis.

Competing interests
The author in this paper has no potential competing interests.

Authors' information
egger@uni-marburg.de
egger@med.uni-marburg.de
egger@staff.uni-marburg.de

Acknowledgements
First of all, the author would like to acknowledge the *AMIGO* team in enabling this study and the members of the Slicer community for their support. In addition, the author wants to acknowledge Xiaojun Chen, Ph.D. and Guillaume Pernelle for implementing the C++ and Python versions of *iGyne* under *Slicer*. Moreover, the author wants to thank Sam Song, Ph.D. for generating the CAD models of gynecologic devices and Ehud Schmidt, Ph.D. for proofreading. Furthermore, the author thanks Professor Dr. Horst K. Hahn and Fraunhofer MeVis in Bremen, Germany, for their support by providing an academic license for the MeVisLab software.

Received: 31 May 2013 Accepted: 19 August 2013
Published: 21 August 2013

References

(2013) 3DSlicer – a free, open source software package for visualization and image analysis. Surgical Planning Laboratory (SPL), Brigham and Women's Hospital, Harvard Medical School, Boston, Massachusetts, USA, Available from: http://www.slicer.org/

Bellon J, Wallner K, Ellis W, Russell K, Cavanagh W, Blasko J (1999) Use of pelvic CT scanning to evaluate pubic arch interference of transperineal prostate brachytherapy. Int J Radiat Oncol Biol Phys 43(3):579–581

Besl P, McKay N (1992) A method for Registration of 3-D Shapes. IEEE Trans Pattern Anal Mach Intell 14(2):239–256

Bharatha A, Hirose M, Hata N, Warfield SK, Ferrant M, Zou KH, Suarez-Santana E, Ruiz-Alzola J, D'Amico A, Cormack RA, Kikinis R, Jolesz FA, Tempany CM (2001) Evaluation of three-dimensional finite element-based deformable registration of pre- and intraoperative prostate imaging. Med Phys 28(12):2551–2560

Cancer Facts & Figures, American Cancer Society (2010): http://www.cancer.org/acs/groups/content/@epidemiologysurveilance/documents/document/acspc-026238.pdf Accessed August, 2013

Chen X, Egger J, Viswanathan AN, Agrawal A, Wells W, Kikinis R, Tempany C, Jolesz F, Kapur T (2012) Image Processing for MR-guided Gynecologic Interstitial Brachytherapy in AMIGO. In: 9th Interventional MRI Symposium. , Boston, p 62, September 2012

Egger J, Großkopf S, O'Donnell T, Freisleben B (2009) A Software System for Stent Planning, Stent Simulation and Follow-Up Examinations in the Vascular Domain. In: 22nd IEEE International Symposium on Computer-Based Medical Systems. IEEE Press, ACM/SIGAPP, Albuquerque, New Mexico, USA, pp 1–7

Egger J, Chen X, Kapur T, Viswanathan AN (2012a) A novel computer program to support MR-guided gynecologic brachytherapy, vol 103, Supplement 2. World Congress of Brachytherapy, Barcelona, Spain, p S115, PO-288, May 2012

Egger J, Kapur T, Viswanathan AN (2012b) GYN Data Collection. The National Center for Image Guided Therapy (NCIGT), http://www.spl.harvard.edu/publications/item/view/2227

Egger J, Kapur T, Viswanathan AN (2012c) Medical System for Gynecologic Radiation Therapy. Technical Disclosure, Research Disclosure, ID 577033, Published in the Research Disclosure Journal 5/12, Published digitally 16 April, 2012

Egger J, Tokuda J, Chauvin L, Freisleben B, Nimsky C, Kapur T, Wells W (2012d) Integration of the OpenIGTLink Network Protocol for Image-Guided Therapy with the Medical Platform MeVisLab. Int J Med Robot 8(3):282–290. doi:10.1002/rcs.1415, Epub 2012 Feb 28

Egger J, Agrawal N, Blevins T, Farhat N, Pernelle G, Chen X, Gao Y, Wells W, Penzkofer T, Kapur T, Viswanathan AN (2012e) Segmentation of Pelvic Structures for Gynecologic Brachytherapy. In: 5th NCIGT and NIH Image Guided Therapy Workshop. NCIGT, NAC, Boston, p 45

Fedorov A, Beichel R, Kalpathy-Cramer J, Finet J, Fillion-Robin JC, Pujol S, Bauer C, Jennings D, Fennessy F, Sonka M, Buatti J, Aylward S, Miller JV, Pieper S, Kikinis R (2012) 3D Slicer as an Image Computing Platform for the Quantitative Imaging Network. Magn Reson Imaging 30(9):1323–1341. doi:10.1016/j.mri.2012.05.001, Epub 2012 Jul 6

Fischer GS, Iordachita I, Csoma C, Tokuda J, Dimaio SP, Tempany CM, Hata N, Fichtinger G (2008) MRI-compatible pneumatic robot for transperineal prostate needle placement. IEEE/ASME Trans Mechatronics 13(3):295–305

Haie-Meder C, Pötter R, Van Limbergen E, Briot E, De Brabandere M, Dimopoulos J, Dumas I, Hellebust TP, Kirisits C, Lang S, Muschitz S, Nevinson J, Nulens A, Petrow P, Wachter-Gerstner N (2005) Gynaecological (GYN) GEC-ESTRO Working Group. Recommendations from Gynaecological (GYN) GEC-ESTRO Working Group (I): concepts and terms in 3D image based 3D treatment planning in cervix cancer brachytherapy with emphasis on MRI assessment of GTV and CTV. Radiother Oncol 74(3):235–245, Review

Hirose M, Bharatha A, Hata N, Zou KH, Warfield SK, Cormack RA, D'Amico A, Kikinis R, Jolesz FA, Tempany CM (2002) Quantitative MR imaging assessment of prostate gland deformation before and during MR imaging-guided brachytherapy. Acad Radiol 9(8):906–912

Kapur T (2012) Joint Segmentation of MR and CT scans for Gynecologic Cancer Brachytherapy. National Institute of Biomedical Imaging and Bioengineering (NIBIB), 5R03EB013792-02

Kapur T, Egger J, Damato A, Schmidt EJ, Viswanathan AN (2012) 3-T MR-guided brachytherapy for gynecologic malignancies. Magn Reson Imaging 30(9):1279–1290. doi:10.1016/j.mri.2012.06.003, Epub 2012 Aug 13

Pernelle G, Egger J, Vale C, Chen X, Irlinger F, Lueth T, Wells W, Kikinis R, Viswanathan AN, Kapur T (2013) Robust Applicator Registration for Interstitial Gynecologic Brachytherapy. In: Brachytherapy, vol 12, Supplement 1., p S53

Pieper S, Halle M, Kikinis R (2004) 3D SLICER. Proceedings of the 1st IEEE International Symposium on Biomedical Imaging (ISBI): From Nano to Macro, 2004 1:632–635

Pötter R, Haie-Meder C, Van Limbergen E, Barillot I, De Brabandere M, Dimopoulos J, Dumas I, Erickson B, Lang S, Nulens A, Petrow P, Rownd J, Kirisits C (2006) GEC ESTRO Working Group. Recommendations from gynaecological (GYN) GEC ESTRO working group (II): concepts and terms in 3D image-based treatment planning in cervix cancer brachytherapy-3D dose volume parameters and aspects of 3D image-based anatomy, radiation physics, radiobiology. Radiother Oncol 78(1):67–77

Power H (2003) Patient positioning outcomes for women undergoing gynaecological surgeries. Can Oper Room Nurs J 20(3):7–10, 27–30

Tokuda J, Fischer GS, Csoma C, DiMaio SP, Gobbi DG, Fichtinger G, Tempany CM, Hata N (2008) Software strategy for robotic transperineal prostate therapy in closed-bore MRI. Med Image Comput Comput Assist Interv 11(Pt 2):701–709

Tokuda J, Fischer GS, DiMaio SP, Gobbi DG, Csoma C, Mewes PW, Fichtinger G, Tempany CM, Hata N (2010) Integrated navigation and control software system for MRI-guided robotic prostate interventions. Comput Med Imaging Graph 34(1):3–8, Epub 2009 Aug 20

Viswanathan AN, Dimopoulos J, Kirisits C, Berger D (2007) Pötter R (2007) Computed tomography versus magnetic resonance imaging-based contouring in cervical cancer brachytherapy: results of a prospective trial and preliminary guidelines for standardized contours. Int J Radiat Oncol Biol Phys 68(2):491–498

Viswanathan AN, Kirisits C, Erickson BE, Pötter R (2011) Gynecologic Radiation Therapy: Novel Approaches to Image-Guidance and Management. Springer, p 310. ISBN -13: 978–3540689546

Wang W, Mehrtash A, Tokuda J, Jayender J, Seethamraju RT, Kapur T, Viswanathan AN, Cormack RA, Schmidt EJ (2013) Real-time Catheter Tracking and Visualization in 3-T MR-Guided Brachytherapy. Sixth National Image Guided Therapy Workshop, Arlington, VA, p 21

Xiaojun C, Yanping L, Yiqun W, Chengtao W (2007) Computer-aided oral implantology: methods and applications. J Med Eng Technol 31(6):459–467

doi:10.1186/2193-1801-2-395
Cite this article as: Egger: **Image-guided therapy system for interstitial gynecologic brachytherapy in a multimodality operating suite.** *SpringerPlus* 2013 **2**:395.

OPEN ACCESS Freely available online

PLOS ONE

PCG-Cut: Graph Driven Segmentation of the Prostate Central Gland

Jan Egger*

Department of Medicine, University Hospital of Marburg (UKGM), Marburg, Hesse, Germany

Abstract

Prostate cancer is the most abundant cancer in men, with over 200,000 expected new cases and around 28,000 deaths in 2012 in the US alone. In this study, the segmentation results for the prostate central gland (PCG) in MR scans are presented. The aim of this research study is to apply a graph-based algorithm to automated segmentation (i.e. delineation) of organ limits for the prostate central gland. The ultimate goal is to apply automated segmentation approach to facilitate efficient MR-guided biopsy and radiation treatment planning. The automated segmentation algorithm used is graph-driven based on a spherical template. Therefore, rays are sent through the surface points of a polyhedron to sample the graph's nodes. After graph construction – which only requires the center of the polyhedron defined by the user and located inside the prostate center gland – the minimal cost closed set on the graph is computed via a polynomial time s-t-cut, which results in the segmentation of the prostate center gland's boundaries and volume. The algorithm has been realized as a C++ module within the medical research platform MeVisLab and the ground truth of the central gland boundaries were manually extracted by clinical experts (interventional radiologists) with several years of experience in prostate treatment. For evaluation the automated segmentations of the proposed scheme have been compared with the manual segmentations, yielding an average Dice Similarity Coefficient (DSC) of 78.94±10.85%.

Citation: Egger J (2013) PCG-Cut: Graph Driven Segmentation of the Prostate Central Gland. PLoS ONE 8(10): e76645. doi:10.1371/journal.pone.0076645

Editor: Zoran Culig, Innsbruck Medical University, Austria

Received July 25, 2013; **Accepted** August 30, 2013; **Published** October 11, 2013

Funding: This author has no support or funding to report.

Competing Interests: The author of this paper has no potential conflict of interests.

* E-mail: egger@med.uni-marburg.de

Introduction

Prostate cancer is the most abundant cancer in men, with over 200,000 expected new cases and around 28,000 deaths in 2012 in the US alone [1]. With many prostate cancers being of low aggressiveness and a high complication rate of radical prostatectomy (impotence, incontinence), accurate risk stratification for each individual cancer is central to a successful treatment strategy. To date prostate cancer diagnosis is widely based on prostate specific antigen (PSA) level testing and transrectal ultrasound (TRUS) guided biopsies, associated with a low specificity (PSA testing) or a low sensitivity (TRUS biopsies) resulting in high rates of rebiopsies. Diagnostic prostate magnetic resonance imaging (MRI) and MRI guided prostate biopsies were introduced clinically to resolve the shortcomings of the aforementioned methods, improving diagnostic discrimination rates [2]. The goal of this work is to enhance the state of the art in automated segmentation (i.e. delineation) of organ limits for the prostate, a step that has been shown to facilitate efficient MR-guided biopsy and radiation treatment planning.

Others working in the area of prostate segmentation are Ghose et al. [3], which introduced a graph cut based energy minimization [4] of the posterior probabilities obtained in a supervised learning schema for automatic 3D segmentation of the prostate in MRI data. Thus, the probabilistic classification of the prostate voxels is achieved with a probabilistic atlas and a random forest based learning framework. Furthermore, the posterior probabilities are combined to obtain the likelihood of a voxel belonging to the prostate and afterwards the 3D graph cut based energy minimization in the stochastic space provides segmentation of the prostate. Ghose et al. [5] also recently presented a comprehensive survey of prostate segmentation methodologies in ultrasound (US), magnetic resonance (MR) and computed tomography (CT) images. Amongst others, they discuss edge based [6–8], atlas based [9–11] and hybrid methods [12–14] for Prostate segmentation in MR images. For a detailed description of these approaches the reader is referred to the survey of Ghose. However, in the meantime there has been a prostate MR image segmentation challenge from the MICCAI society [15] and these (additional) approaches are presented in more detail in this section. Vincent et al. [16] introduce a fully automatic segmentation of the prostate using Active Appearance Models (AAM) [17]. Therefore, high quality correspondences for the model are generated using a Minimum Description Length (MDL) Groupwise Image Registration method [18] and a multi start optimisation scheme was used to robustly match the model to new images. Birkbecky et al. [19] present a region-specific hierarchical segmentation of MR Prostate images by using discriminative learning. After normalizing intra- and inter-image intensity variation, they used Marginal Space Learning (MSL) [20] to align a statistical mesh model on the image. Thus, the mesh is hierarchically refined to the image boundary using spatially varying surface classifiers. Malmberg et al. [21] introduce *Smart Paint*, which is an interactive segmentation method applied to MR prostate segmentation. Thereby, the user interaction is inspired by the way an airbrush is used and objects are segmented by *sweeping* with the mouse cursor in the image. The proposed segmentation tool allows the user to add or remove

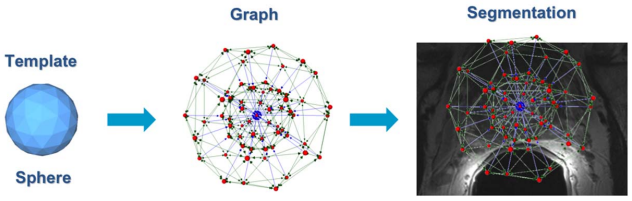

Figure 1. Principle of the Nugget-Cut Scheme: A spherical template (left) is used as a basic structure for the segmentation graph (middle), which is created inside the image (right).
doi:10.1371/journal.pone.0076645.g001

details in 3D and the user interface shows the segmentation result in 2D slices through the object. Ou et al. [22] present in their contribution a multi-atlas-based automatic pipeline for segmenting prostate in MR images. In a first step they register all atlases onto the target image to obtain an initial segmentation of the prostate. Afterwards, they *zoom-in* which means they re-run all atlas-to-target registrations. However, this time they restrict the registration to the vicinity of the prostate, ignoring compounding structures that are far away from the prostate and are largely variable. Kirschner et al. [23] used a probabilistic Active Shape Model (ASM) [24] and [25] for automatic prostate segmentation in MR images. However, first they employ a boosted prostate detector to locate the prostate in the images. Thus, they extend the Viola-Jones object detection algorithm [26] to 3D and afterwards they use the probabilistic ASM (PASM) for the delineation of the prostate contour. A convex optimization approach for 3D Prostate MRI Segmentation with generic Star shape prior has been proposed by Yuan et al. [27]. Thereby, the approach incorporates histogram-matching and a variational formulation of a generic star shape prior [28] and [29]. The presented generic star shape prior provides robustness to the segmentation when the images suffer from poor quality, noise, and artifacts. Gao et al. [30] introduce an automatic multi-atlas based prostate segmentation using local appearance-specific atlases and patch-based voxel weighting. Therefore, the atlases with the most similar global appearance are classified into the same categories and the sum-of-square local intensity difference after affine registration is used for an atlas selection. After the non-rigid registration, a local patch-based atlas fusion is performed using voxel weighting based on the local patch distance. Another contribution that uses Active Appearance Models in 3D for prostate MR image segmentation is presented by Maan and van der Heijden [31]. In a first step, the shape context based non-rigid surface registration of the manual segmented images was used to obtain the point correspondence between the given training cases. Thereby, their contribution builds on the work of Kroon et al. [32] where knee cartilages have been segmented. In the second step, the AAM was used to segment the prostate on 50 training cases. Litjens et al. [33] introduced a multi-atlas approach for prostate segmentation in MR images, where the atlases are registered using localized mutual information as a metric. Afterwards, the Selective and Iterative Method for Performance Level Estimation (SIMPLE)-algorithm [11] was used to merge the atlas labels and obtain the final segmentation. Ghose et al. [34] proposed a Random Forest based [35] classification approach for prostate segmentation in MR scans. Thus, they introduce a supervised learning framework of decision forest to achieve a probabilistic representation of the prostate voxels. Then, propagation of region based level-sets in the stochastic space provides [36] and [37] the segmentation of the prostate. Toth and Madabhushi [38] use deformable landmark-free Active Appearance Models to segment prostate MRI data. Therefore, a deformable registration framework was created to register a new image to the trained appearance model, which was subsequently applied to the prostate shape to yield a final segmentation. Yin et al. [39] proposed a fully automated 3D prostate central gland segmentation in MR images. Thus, they applied the Layered Optimal Graph Image Segmentation of Multiple Objects and Surfaces (LOGISMOS) approach. The LOGISMOS model contained both: shape and topology information during deformation and they generated the graph cost by training classifiers and they used coarse-to-fine search. Moreover, the authors want to point the reader at this point to a book chapter that includes a section about segmentation for prostate interventions [40].

The purpose of this contribution is to introduce the results of a graph based segmentation algorithm for the prostate central gland (PCG) in MR scans. The algorithm uses a spherical template and sends rays through the surface points of a polyhedron to sample the graph's nodes. Even if there exist graph-based segmentation methods in 2D for MR prostate images and some hybrid 3D methods for MR prostate images (like [41] and [42]), the author is not aware of a *pure* 3D graph-based method that has been applied to the PCG in MRI scans. For evaluation the Dice Similarity Coefficient (DSC) [43] and [44] a common evaluation metrics in

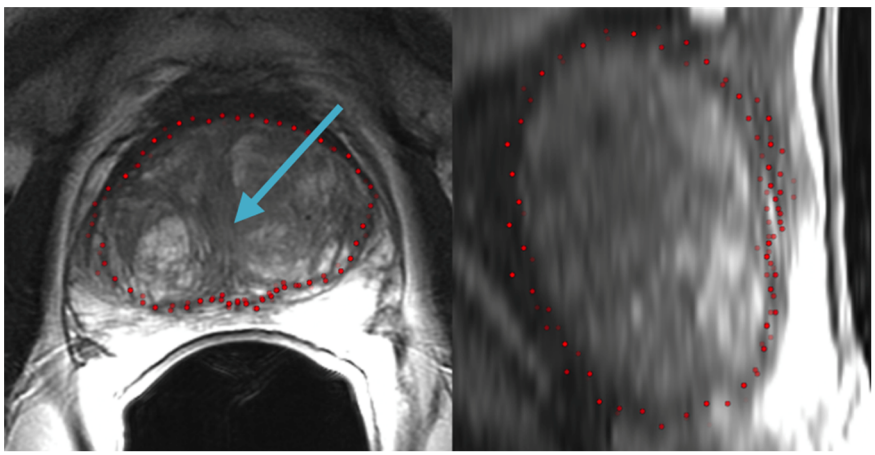

Figure 2. Segmentation results (red) in axial and sagittal reformatting (blue arrow: position of the seed point).
doi:10.1371/journal.pone.0076645.g002

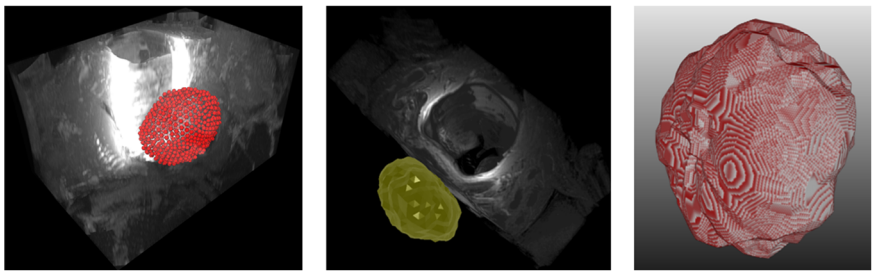

Figure 3. 3D visualizations of segmentation results: segmentation nodes and triangulated segmentation result with surrounding structures (left and middle), and voxelized mask of the segmented prostate (right).
doi:10.1371/journal.pone.0076645.g003

medical image processing was applied, which has also been used in the most of the existing contributions.

The contribution is organized as follows. Section 2 presents the materials and the methods. Section 3 presents the results of the experiments, and Section 4 concludes and discusses the contribution and outlines areas for future work.

Materials and Methods

Data

For testing the approach T2-weighted magnetic resonance imaging datasets from the clinical routine have been used. The datasets applied in the evaluation are freely available in the internet and can be used for research purposes [45]: http://www.na-mic.org/publications/item/view/2174.

Algorithm

The Nugget-Cut scheme [46] was applied for prostate center gland segmentation. It sets up a directed 3D-graph G(V,E) in two steps: (I) sending rays through the surface points of a polyhedron [47] and (II) sampling the graph's nodes n∈V along every ray. Additionally, a corresponding set of edges e∈E is generated, which consists of edges between the nodes and edges that connect the nodes to a source s and a sink t. After graph construction – the center of the polyhedron was defined by the user and located inside the prostate center gland – the minimal cost closed set on the graph is computed via a polynomial time s-t-cut [48], which results in the segmentation of the prostate center gland's boundaries and volume. The overall principle of the Nugget-Cut scheme that has been applied to the PCG segmentation is presented in Figure 1. As shown in the figure, a spherical template (left) is used as a basic structure for setting up the segmentation graph (middle). Finally, this graph is generated inside the image with its center at the position of the user-defined seed point (right).

By definition the edges/arcs $<v_i, v_j>\in E$ of the graph G connect two nodes v_i, v_j and there exist two types of ∞-weighted arcs: z-arcs A_z and r-arcs A_r, whereby $\mathcal{Z}$ is the number of sampled points along one ray $z = (0,\ldots,\mathcal{Z}\text{-}1)$ and R is the number of rays sent out to the surface points of a polyhedron $r = (0,\ldots,R\text{-}1)$. $V(x_n,y_n,z_n)$ is one neighbor of $V(x,y,z)$, or in other words $V(x_n,y_n,z_n)$ and $V(x,y,z)$ belong to the same triangle in case of a triangulation of the polyhedron:

$$A_z = \{\langle V(x,y,z), V(x,y,z-1)\rangle | z > 0\}$$

$$A_r = \{\langle V(x,y,z), V(x_n,y_n, \max(0, z-\Delta_r))\rangle\}$$

The ∞-weighted arcs between two nodes along a ray A_z ensure that all nodes below the polyhedron surface in the graph are included to form a closed set. According to this, the interior of the object is separated from the exterior in the data. On the other hand, arcs A_r between the nodes of different rays constrain the set of possible segmentations and enforce smoothness via a parameter Δ_r and the larger this parameter is, the larger is the number of possible segmentations. Finally, the s-t cut creates an optimal segmentation of the PCG under influence of the parameter Δ_r that controls the stiffness of the boundaries. For example, a Δ value of zero ($\Delta_r = 0$) ensures that the segmentation result is a sphere and the position of the sphere within the image is based on the edges to the source and sink (s-t-edges). The weights $w(x, y, z)$ for every s-t-edge are assigned in the following manner: weights are set to $c(x,y,z)$ when z is zero and otherwise to $c(x,y,z) - c(x,y,z\text{-}1)$. In doing so, $c(x,y,z)$ is the absolute value of the intensity difference between an average grey value of the PCG and the grey value of the voxel at position (x,y,z). Note that the average grey value of the PCG can

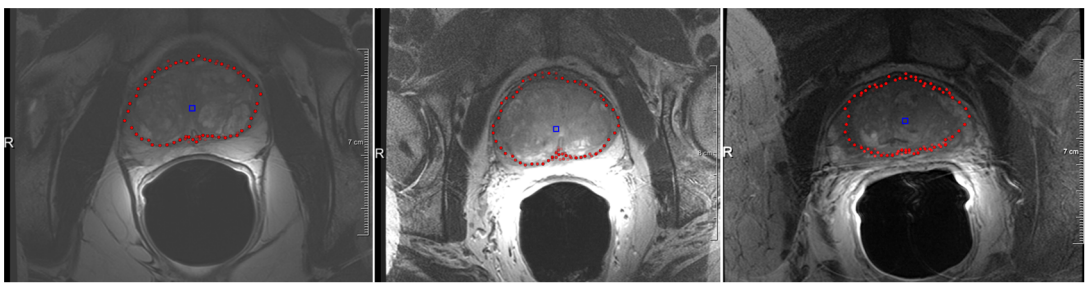

Figure 4. Segmentation results (red) for three different cases of proposed algorithm at the *axial* height of the user-defined seed point (blue).
doi:10.1371/journal.pone.0076645.g004

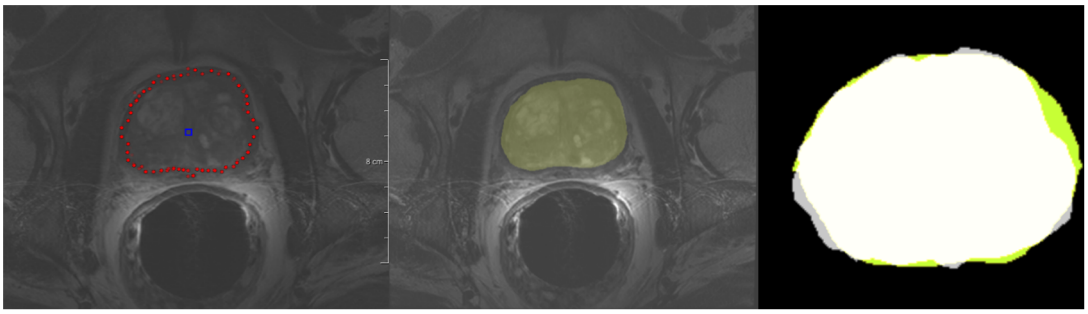

Figure 5. Direct comparison of automatic (red) and manual (yellow) segmentation results for the same case: automatic segmentation result (left), manual segmentation (middle) and superimposed visualization of both segmentations (right).
doi:10.1371/journal.pone.0076645.g005

automatically be estimated around the user-defined seed point inside the Prostate.

Results

A C++ module was implemented within the medical prototyping platform MeVisLab (see http://www.mevislab.de) for evaluation. In the C++ implementation the overall segmentation: (1) sending rays, (2) graph construction and (3) mincut computation, took about one second on a Macbook Pro laptop computer with an Intel Core i7-2860QM CPU, 4×2.50 GHz, 8 GB RAM, Windows 7 Professional ×64.

Figure 2 presents screenshots of an automated segmentation result (red) in axial (left) and sagittal reformatting (right) slices. The blue arrow in the left image points to the position of the user-defined seed point. Figure 3 shows several 3D visualizations of segmentation results of the PCG. On the left side of the segmentation nodes (red) of the mincut are presented. The image in the middle shows the corresponding triangulated segmentation result (green/yellow) with surrounding anatomical structures. Finally, the rightmost image presents the voxelized mask of the segmented prostate, which has been used to calculate the Dice Similarity Coefficient with the manual slice-by-slice segmented prostate. Segmentation results (red) for three different cases of the proposed algorithm at the *axial* height of the user-defined seed point (blue) are displayed in Figure 4. A direct comparison of an automated (red) and a manual (yellow) segmentation for the same case is presented in Figure 5. The automated segmentation result is shown on the left side of the figure, the manual segmentation in the middle and the superimposed visualization of both segmentations on the right. Finally, Figure 6 displays several axial slices containing the automated segmentation results (red) for a case. The fourth slice from the left includes also the user-defined seed point from which the segmentation graph has been created.

Table 1 presents the results for a direct comparison of manual slice-by-slice and PCG-Cut segmentation results for ten prostate central glands via the Dice Similarity Coefficient. Table 2 presents the summary of the results from Table 1, including the minimum (min), the maximum (max), mean μ and standard deviation σ for ten prostate central glands.

Conclusion and Discussion

In this study, the segmentation results for the prostate gland in MRI data using a recently developed method have been presented. Therefore, a graph driven method has been applied that bases on a spherical template. The algorithm prefers spherically- and elliptically-shaped 3D objects and has already been evaluated with glioblastoma multiforme (GBM), pituitary adenoma and cerebral aneurysm data [49]. To sample the graph's nodes rays are sent through the surface points of a polyhedron and afterwards the minimal cost closed set on the graph is computed via a polynomial time s-t-cut, which results in the segmentation of the prostate central gland boundaries and volume. Thereby, the

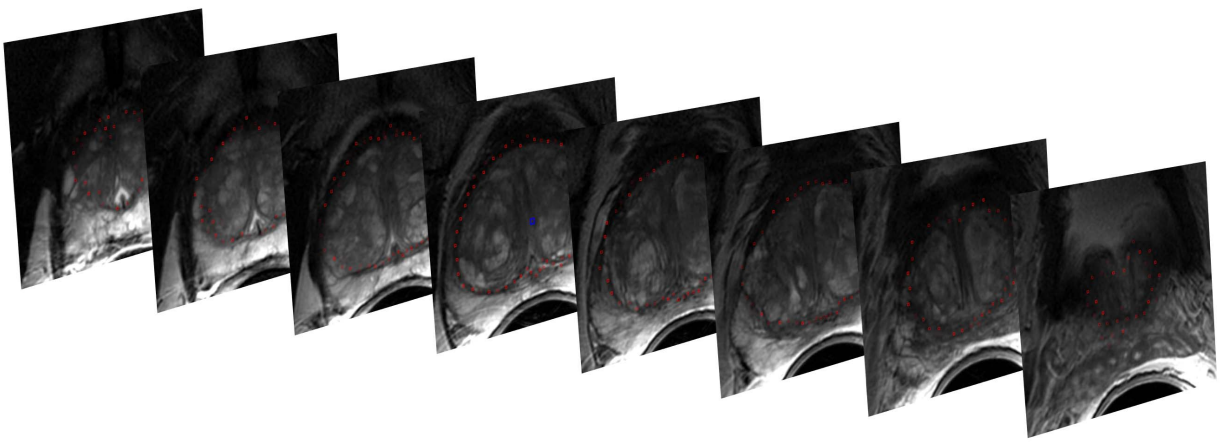

Figure 6. Several axial slices with automatic segmentation results (red). The fourth slice from the left contains also the user-defined seed point from which the segmentation graph has been created.
doi:10.1371/journal.pone.0076645.g006

Table 1. Direct comparison of manual slice-by-slice and PCG-Cut segmentation results for ten prostate central glands (PCG) via the Dice Similarity Coefficient (DSC).

Case No.	volume of PCG (mm^3)		number of voxels		DSC (%)
	manual	Automatic	manual	automatic	
1	20820.8	41692.1	682256	1366168	61.79
2	13670.3	16487.9	447949	540277	62.57
3	29006	31706.7	1419342	1551511	84.79
4	51418.2	56490.6	1684871	1851084	88.79
5	44258.4	40306	2165709	1972307	89.42
6	66161.6	67559.2	2167986	2213781	88.76
7	15317.8	13312.5	501932	436224	83.93
8	32826.1	38079.4	1075646	1247786	75
9	22047.6	13289.7	722456	435477	69.68
10	17718.1	16886	866648	825950	84.71

doi:10.1371/journal.pone.0076645.t001

approach requires only the center of the polyhedron defined by the user and located inside the prostate center gland and the algorithm has been realized as a C++ module within the medical research platform MeVisLab. As the reference for comparison, central gland boundaries manually extracted by interventional radiologists with several years of experience in prostate imaging have been used (see the details in Fedorov et al. [44]). Then, the segmentation results obtained using the proposed scheme have been compared with the manual segmentations, yielding an average Dice Similarity Coefficient around 80%. In summary, the research highlights are:

- A graph-based approach has been developed and applied to automatic PCG segmentation.
- Manual slice-by-slice segmentations of prostate central glands (PCG) have been performed by clinical experts resulting in ground truth of PCG boundaries.
- The quality of the automated segmentations have been evaluated with the Dice Similarity Coefficient.

The most existing approaches from the literature aim to automatic or even fully automatic process large amounts of prostate datasets to support time consuming manual slice-by-slice segmentations. In contrast, this is in general not possible with the presented approach because the user still needs to define a seed point for the graph inside the prostate central glad. In fact, the aim of the presented approach is to facilitate efficient MR-guided biopsy and radiation treatment planning during an intervention. And due to the specific graph construction, the segmentation result for the introduced approach can be calculated within one second (including graph construction and mincut calculation). Thus, a repositioning of the seed point and a recalculation of the segmentation result (in case of an unsatisfied segmentation) can be performed very fast, therefore making the approach eligible intraoperative MR-guidance (in general, a few replacements of the seed point had to be done for every case to achieve the presented results). Furthermore, most existing semi-automatic approaches need a more time-consuming initialization. Often areas inside and outside of the structure (e.g. the prostate) have to be defined by a user before the segmentation can be started.

Table 2. Summary of results: min, max, mean μ and standard deviation σ for ten prostate central glands (PCG).

	volume of PCG (cm^3)		number of voxels		DSC (%)
	manual	automatic	manual	automatic	
min	13.67	13.29	447949	435477	61.79
max	66.16	67.56	2167986	2213781	89.42
$\mu\pm\sigma$	31.32±17.45	33.58±18.88	1173479.5	1244056.5	78.94±10.85

doi:10.1371/journal.pone.0076645.t002

There are several areas of future work, including a direct comparison with other approaches on the same datasets and extensions of the automated segmentation to structures adjacent to the central zone of the prostate gland, such as the peripheral prostatic zone (Prostate-Cut). An immediate application for MR-guided biopsy is the generation of regions of interest as an aid to the automated registration of preoperative to intraprocedural images [44]. Moreover, the integration of a manual refinement method into the automatic algorithm [50] and [51] is planned and providing the approach as a module for 3D Slicer (http://www.slicer.org/) [52] to the community.

Acknowledgments

In the first place, the author would like to thank *Fraunhofer MeVis* in Bremen, Germany, for their collaboration and especially Horst K. Hahn for his support. Furthermore, the author thanks Drs. Fedorov, Tuncali, Fennessy and Tempany for sharing the prostate data collection and Dr. med. Tobias Penzkofer for his feedback and proofreading.

Author Contributions

Conceived and designed the experiments: JE. Performed the experiments: JE. Analyzed the data: JE. Contributed reagents/materials/analysis tools: JE. Wrote the paper: JE.

References

1. National Institutes of Health Cancer Topics: Prostate, http://www.cancer.gov/cancertopics/types/prostate, Last accessed: July 2013.
2. D'Amico AV, Cormack RA, Tempany CM (2001) MRI-Guided Diagnosis and Treatment of Prostate Cancer. N Engl J Med. 344: 776–777.
3. Ghose S, Mitra J, Oliver A, Martí R, Lladó X, et al. (2012) Graph Cut Energy Minimization in a Probabilistic Learning Framework for 3D Prostate Segmentation in MRI. International Conference on Pattern Recognition (ICPR), pp. 1–4, Tsukba, Japan.
4. Boykov Y, Funka-Lea G (2006) Graph cuts and efficient n-d image segmentation. International Journal of Computer Vision (IJCV), 70(2): 109–131.
5. Ghose S, Oliver A, Martí R, Lladó X, Vilanova JC, et al. (2012) A survey of prostate segmentation methodologies in ultrasound, magnetic resonance and computed tomography images. Comput Methods Programs Biomed. 2012 Oct; 108(1): 262–87. doi: 10.1016/j.cmpb.2012.04.006. Epub 2012 Jun 25.
6. Zwiggelaar R, Zhu Y, Williams S (2003) Semi-automatic segmentation of the prostate. Pattern Recognition and Image Analysis, F.J. Perales, A.J. Campilho, N.P. de la Blanca, A. Sanfeliu (Eds.), Proceedings of First Iberian Conference, IbPRIA, Springer, Berlin/Heidelberg/New York/Hong Kong/London/Milan/Paris/Tokyo, pp. 1108–1116.
7. Lindeberg T (1996) Edge detection and ridge detection with automatic scale selection. Proceedings of Computer Vision and Pattern Recognition, IEEE Computer Society Press, Los Alamitos/California/Washington/Brussels/Tokyo, pp. 465–470.
8. Samiee M, Thomas G, Fazel-Rezai R (2006) Semi-automatic prostate segmentation of MR images based on flow orientation. IEEE International Symposium on Signal Processing and Information Technology, IEEE Computer Society Press, USA, pp. 203–207.

9. Klein S, van der Heide UA, Lipps IM, Vulpen MV, Staring M, et al. (2008) Automatic segmentation of the prostate in 3D MR images by atlas matching using localized mutual information. Medical Physics 35, pp. 1407–1417.
10. Dowling J, Fripp J, Chandra S, Pluim JPW, Lambert J, et al. (2011) Fast automaticmulti-atlas segmentation of the prostate from 3d mr images. Prostate Cancer Imaging, A. Madabhushi, J. Dowling, H.J. Huisman, D.C. Barratt (Eds.), volume 6963 of Lecture Notes in Computer Science, Springer, pp. 10–21.
11. Langerak R, van der Heide UA, Kotte ANTJ, Viergever MA, van Vulpen M, et al. (2010) Label fusion in atlas-based segmentation using a selective and iterative method for performance level estimation (simple). IEEE Transactions on Medical Imaging 29, pp. 2000–2008.
12. Martin S, Daanen V, Troccaz J (2008) Atlas-based prostate segmentation using an hybrid registration, International Journal of Computer Assisted Radiology and Surgery 3, pp. 485–492.
13. Makni N, Puech P, Lopes R, Viard R, Colot O, et al. (2009) Combining a deformable model and a probabilistic framework for an automatic 3d segmentation of prostate on MRI. International Journal of Computer Assisted Radiology and Surgery 4, pp. 181–188.
14. Liu X, Langer DL, Haider MA, Yang Y, Wernick MN, et al. (2009) Prostate cancer segmentation with simultaneous estimation of markov random field parameters and class. IEEE Transactions on Medical Imaging 28, pp. 906–915.
15. Medical Image Computing and Computer Assisted Intervention (MICCAI) Grand Challenge: Prostate MR Image Segmentation 2012 (PROMISE12), Nice, France, October 2012, http://promise12.grand-challenge.org/, Last accessed: July 2013.
16. Vincent G, Guillard G, Bowes M (2012) Fully Automatic Segmentation of the Prostate using Active Appearance Models. Medical Image Computing and Computer Assisted Intervention (MICCAI) Grand Challenge: Prostate MR Image Segmentation 2012 (PROMISE12), 7 pages, Nice, France, October 2012.
17. Cootes TF, Edwards GJ, Taylor CJ (2001) Active appearance models. IEEE Trans Pattern Anal Mach Intell. 23(6): 681–5.
18. Cootes TF, Petrovi CV, Schestowitz R, Taylor C (2005) Groupwise construction of appearance models using piece-wise affine deformations. 16th British Machine Vision Conference, volume 2: 879–888.
19. Birkbecky N, Zhangy J, Requardtz M, Kieferz B, Gallz P, et al. (2012) Region-Specific Hierarchical Segmentation of MR Prostate Using Discriminative Learning. Medical Image Computing and Computer Assisted Intervention (MICCAI) Grand Challenge: Prostate MR Image Segmentation 2012 (PROMISE12), 8 pages, Nice, France, October 2012.
20. Zheng Y, Barbu A, Georgescu B, Scheuering M, Comaniciu D (2008) Four-chamber heart modeling and automatic segmentation for 3-D cardiac CT volumes using marginal space learning and steerable features. IEEE Trans. Med. Imag. 27(11), pp. 1668–1681.
21. Malmberg F, Strand R, Kullberg J, Nordenskjold R, Bengtsson E (2012) Smart Paint - A New Interactive Segmentation Method Applied to MR Prostate Segmentation. Medical Image Computing and Computer Assisted Intervention (MICCAI) Grand Challenge: Prostate MR Image Segmentation 2012 (PROMISE12), 8 pages, Nice, France, October 2012.
22. Ou Y, Doshi J, Erus G, Davatzikos C (2012) Multi-Atlas Segmentation of the Prostate: A Zooming Process with Robust Registration and Atlas Selection. Medical Image Computing and Computer Assisted Intervention (MICCAI) Grand Challenge: Prostate MR Image Segmentation 2012 (PROMISE12), 7 pages, Nice, France, October 2012.
23. Kirschner M, Jung F, Wesarg S (2012) Automatic Prostate Segmentation in MR Images with a Probabilistic Active Shape Model. Medical Image Computing and Computer Assisted Intervention (MICCAI) Grand Challenge: Prostate MR Image Segmentation 2012 (PROMISE12), 8 pages, Nice, France, October 2012.
24. Cootes TF, Taylor CJ, Cooper DH, Graham J (1995) Active shape models - their training and application. Computer Vision and Image Understanding 61(1), pp. 38–59.
25. Kirschner M, Wesarg S (2011) Active shape models unleashed. SPIE Medical Imaging: Image Processing Dawant, B.M., Haynor, D.R., eds., volume 7962.
26. Viola P, Jones M (2001) Robust real-time object detection. International Journal of Computer Vision 57(2), pp. 137–154.
27. Yuan J, Qiu W, Ukwatta E, Rajchl M, Sun Y, et al. (2012) An Efficient Convex Optimization Approach to 3D Prostate MRI Segmentation with Generic Star Shape Prior. Medical Image Computing and Computer Assisted Intervention (MICCAI) Grand Challenge: Prostate MR Image Segmentation 2012 (PROMISE12), 8 pages, Nice, France, October 2012.
28. Veksler O (2008) Star shape prior for graph-cut image segmentation. ECCV 2008, Forsyth, D., Torr, P., Zisserman, A., eds., volume 5304, pp. 454–467.
29. Strekalovskiy E, Cremers D (2011) Generalized ordering constraints for multilabel optimization. IEEE International Conference on Computer Vision (ICCV), pp. 2619–2626.
30. Gao Q, Rueckert D, Edwards P (2012) An automatic multi-atlas based prostate segmentation using local appearance-specific atlases and patch-based voxel weighting. Medical Image Computing and Computer Assisted Intervention (MICCAI) Grand Challenge: Prostate MR Image Segmentation 2012 (PROMISE12), 8 pages, Nice, France, October 2012.
31. Maan B, van der Heijden F (2012) Prostate MR image segmentation using 3D Active Appearance Models. Medical Image Computing and Computer Assisted Intervention (MICCAI) Grand Challenge: Prostate MR Image Segmentation 2012 (PROMISE12), 8 pages, Nice, France, October 2012.
32. Kroon DJ, Kowalski P, Tekieli W, Reeuwijk E, Saris D, et al. (2012) MRI based knee cartilage assessment. Proceedings of SPIE Medical Imaging: Computer-Aided Diagnosis 8315(0), pp. 83151V–83151V–10.
33. Litjens G, Karssemeijer N, Huisman H (2012) A multi-atlas approach for prostate segmentation in MR images. Medical Image Computing and Computer Assisted Intervention (MICCAI) Grand Challenge: Prostate MR Image Segmentation 2012 (PROMISE12), 8 pages, Nice, France, October 2012.
34. Ghose S, Mitra J, Oliver A, Marti R, Llado X, et al. (2012) A Random Forest Based Classification Approach to Prostate Segmentation in MRI. Medical Image Computing and Computer Assisted Intervention (MICCAI) Grand Challenge: Prostate MR Image Segmentation 2012 (PROMISE12), 8 pages, Nice, France, October 2012.
35. Geremia E, Menze BH, Clatz O, Konukoglu E, Criminisi A, et al. (2010) Spatial decision forests for ms lesion segmentation in multi-channel mr images. In: MICCAI. Volume 6361, pp. 111–118.
36. Chan TF, Vese LA (2001) Active Contours Without Edges. IEEE Transactions on Image Processing 10, pp. 266–277.
37. Li W, Liao S, Feng Q, Chen W, Shen D (2011) Learning image context for segmentation of prostate in ct-guided radiotherapy. In: MICCAI, Volume 6893, pp. 570–578.
38. Toth R, Madabhushi A (2012) Deformable Landmark-Free Active Appearance Models: Application to Segmentation of Multi-Institutional Prostate MRI Data. Medical Image Computing and Computer Assisted Intervention (MICCAI) Grand Challenge: Prostate MR Image Segmentation 2012 (PROMISE12), 8 pages, Nice, France, October 2012.
39. Yin Y, Fotin SV, Periaswamy S, Kunz J, Haldankar H, et al. (2012) Fully automated 3D prostate central gland segmentation in MR images: a LOGISMOS based approach. SPIE Medical Imaging: Image Processing. Edited by Haynor, David R.; Ourselin, Sébastien. volume 8314, pp. 83143B–83143B–9.
40. Kapur T, Egger J, Jagadeesan J, Toews M, Wells III WM (2014) Registration and Segmentation for Image Guided Therapy. Book chapter, Intraoperative Imaging and Image-Guided Therapy, Jolesz, Ferenc A. (Ed.), Springer, 920 pages, 504 illus., 386 illus. in color. *to appear*.
41. Artan Y, Haider MA, Yetik IS (2011) Graph-based active contours using shape priors for prostate segmentation with MRI. IEEE International Symposium on Biomedical Imaging (ISBI): From Nano to Macro, pp. 1459–1462.
42. Moschidis E, Graham J (2012) Automatic differential segmentation of the prostate in 3-D MRI using Random Forest classification and graph-cuts optimization. 9th IEEE International Symposium on Biomedical Imaging (ISBI): From Nano to Macro, pp. 1727–1730.
43. Zou KH, Warfield SK, Bharatha A, Tempany CMC, Kaus MR, et al. (2004) Statistical validation of image segmentation quality based on a spatial overlap index: scientific reports. Acad Radiol 11(2): 178–189.
44. Sampat MP, Wang Z, Markey MK, Whitman GJ, Stephens TW, et al. (2006) Measuring intra- and inter-observer Agreement in Identifying and Localizing Structures in Medical Images. IEEE Inter. Conf. Image Processing, pp. 81–84.
45. Fedorov A, Tuncali K, Fennessy F, Tokuda J, Hata N, et al. (2012) Image Registration for Targeted MRI-guided Prostate Transperineal Prostate Biopsy. J Magn Res Imag. doi:10.1002/jmri.23688.
46. Egger J, Bauer MHA, Kuhnt D, Carl B, Kappus C, et al. (2010) Nugget-Cut: A Segmentation Scheme for Spherically- and Elliptically-Shaped 3D Objects. In: 32nd Annual Symposium of the German Association for Pattern Recognition (DAGM), LNCS 6376, pp. 383–392, Springer Press, Darmstadt, Germany.
47. Egger J, Mostarkić Z, Großkopf S, Freisleben B (2007) A Fast Vessel Centerline Extraction Algorithm for Catheter Simulation. In: 20th IEEE International Symposium on Computer-Based Medical Systems (CBMS). Maribor, Slovenia, IEEE Press, pp. 177–182.
48. Boykov Y, Kolmogorov V (2004) An Experimental Comparison of Min-Cut/Max-Flow Algorithms for Energy Minimization in Vision. IEEE Transactions on Pattern Analysis and Machine Intelligence, 26(9), pp. 1124–1137.
49. Egger J, Kappus C, Freisleben B, Nimsky C (2011) A Medical Software System for Volumetric Analysis of Cerebral Pathologies in Magnetic Resonance Imaging (MRI) Data. In: Journal of Medical Systems, Springer, 6(4): 2097–109.
50. Egger J, Bauer MHA, Kuhnt D, Kappus C, Carl B, et a. (2010) A Flexible Semi-Automatic Approach for Glioblastoma multiforme Segmentation. In: Proceedings of International Biosignal Processing Conference, Kurths J, Penzel T, Malberg H, Wessel N (Hrsg), Berlin, Germany, Paper-ID: 060: 1–4, July 2010.
51. Egger J, Colen R, Freisleben B, Nimsky C (2012) Manual Refinement System for Graph-Based Segmentation Results in the Medical Domain. J Med Syst. 2012 Oct;36(5): 2829–39. Epub 2011 Aug 9.
52. Fedorov A, Beichel R, Kalpathy-Cramer J, Finet J, Fillion-Robin J-C, et al. (2012) 3D Slicer as an Image Computing Platform for the Quantitative Imaging Network. Magn Reson Imaging. 2012 Nov;30(9): 1323–41.

Computerized Medical Imaging and Graphics xxx (2014) xxx–xxx

Contents lists available at ScienceDirect

Computerized Medical Imaging and Graphics

journal homepage: www.elsevier.com/locate/compmedimag

Interactive-cut: Real-time feedback segmentation for translational research

Jan Egger[a,b,c,*,1], Tobias Lüddemann[d,1], Robert Schwarzenberg[a,1], Bernd Freisleben[a,2], Christopher Nimsky[b,2]

[a] Department of Mathematics and Computer Science, University of Marburg, Germany
[b] Clinic for Neurosurgery, University Hospital of Marburg, Germany
[c] Institute for Computer Graphics and Vision, Graz University of Technology, Graz, Austria
[d] Department of Mechatronics, Technical University of Munich (TUM), Munich, Germany

ARTICLE INFO

Article history:
Received 8 April 2013
Received in revised form 29 January 2014
Accepted 31 January 2014

Keywords:
Segmentation
Interactive
Real-time
Template-based
Predefined templates
Free drawing templates
Scale-invariant
Graph-cut
Translational research

ABSTRACT

In this contribution, a scale-invariant image segmentation algorithm is introduced that "wraps" the algorithm's parameters for the user by its interactive behavior, avoiding the definition of "arbitrary" numbers that the user cannot really understand. Therefore, we designed a specific graph-based segmentation method that only requires a single seed-point inside the target-structure from the user and is thus particularly suitable for immediate processing and interactive, real-time adjustments by the user. In addition, color or gray value information that is needed for the approach can be automatically extracted around the user-defined seed point. Furthermore, the graph is constructed in such a way, so that a polynomial-time mincut computation can provide the segmentation result within a second on an up-to-date computer. The algorithm presented here has been evaluated with fixed seed points on 2D and 3D medical image data, such as brain tumors, cerebral aneurysms and vertebral bodies. Direct comparison of the obtained automatic segmentation results with costlier, manual slice-by-slice segmentations performed by trained physicians, suggest a strong medical relevance of this interactive approach.

1. Introduction

Segmentation of digital imagery in general is a labeling problem in which the goal is to assign to each pixel in an input image a unique label that represents an object. In doing so, the input image can have an arbitrary dimension, like 1D, 2D or 3D, and the pixel values can be in color- or gray-level. An example for an object in digital imaging would be person in a video and an example for an object in medical imaging would be an anatomical structure in a patient scan. Finally, these labeled images are referred to as the "segmentation" of the input image or the "segmented" image [1]. In Computer Science several types of segmentation algorithms exist, like Active Contours [2,3], Active Appearance Models [4], graph-based approaches [5], fuzzy-based approaches [6], or neural network approaches [7]. However, in the medical field automatic segmentation methods are typically only suitable for a specific type of pathology in a specific imaging modality and still fail time-by-time, and moreover, most automatic approaches need precise parameter settings to provide good results. As a consequence, the state of the art or rather clinical practice in medical departments is still manual slice-by-slice segmentations which are very time consuming. Thus, interactive segmentation approaches like [8–12] get more and more popular, because they allow the user to support the algorithm with more information, especially in difficult segmentation tasks. However, in this contribution we introduce an interactive graph-based approach with a specific design of the graph which requires only one user-defined seed point inside an object for the segmentation process. The algorithm is therefore eligible for real-time segmentation by means of giving the user real-time feedback of the segmentation result. In addition, the specific graph construction enables to perform the mincut within a second on modern machines and the color value information that are needed for the approach can be automatically extracted around the user-defined seed point. For evaluation the focus of this contribution is on medical data and for the proof of concept, the presented scheme has been evaluated with fixed seed points mainly on medical image data in

* Corresponding author at: Clinic for Neurosurgery, University Hospital of Marburg, Germany. Tel.: +49 6421 58 66447.
E-mail addresses: egger@uni-marburg.de, egger@med.uni-marburg.de, egger@staff.uni-marburg.de, egger@icg.tugraz.at, egger@tugraz.at (J. Egger).
[1] Joint first authorship.
[2] Joint senior authorship.

http://dx.doi.org/10.1016/j.compmedimag.2014.01.006
0895-6111/

2D and 3D, like brain tumors, cerebral aneurysms and vertebral bodies. However, the segmentation approach can also be applied on arbitrary image data.

The paper is organized as follows. Section 2 presents the details of the proposed algorithm. Section 3 discusses the results of our experiments. Section 4 concludes the paper and outlines areas for future research.

2. Methods

Our interactive segmentation algorithm works in 2D and 3D and starts by setting up a directed graph from a user-defined seed point that is located inside the object to be segmented [13]. Therefore, points are sampled along rays cast through a contour (2D) or surface (3D) of an object template to create the graph. These sampled points are the nodes $n \in V$ of the graph $G(V, E)$. In addition, $e \in E$ is the corresponding set of edges which consists of edges between the nodes and edges that connect the nodes to a source s and a sink t to allow the computation of an s–t cut (note: the source $s \in V$ and the sink $t \in V$ are virtual nodes). In the style of the notation introduced by Li et al. [14], an arc $\langle v_i, v_j \rangle \in E$ connects two nodes v_i, v_j. Amongst the arcs are two types of ∞-weighted arcs: p-arcs A_p and r-arcs A_r – P is the number of sampled points along one ray $p = (0, ..., P-1)$ and R is the number of rays cast to the contour or surface of an object template $r = (0, ..., R-1)$. Furthermore, $V(x_n, y_n)$ is defined as a neighbor of $V(x, y)$ or in other words $V(x_n, y_n)$ and $V(x, y)$ belong to two adjacent rays:

$$\begin{aligned} A_p &= \{\langle V(x,y), V(x,y-1)\rangle \,|\, y > 0\} \\ A_r &= \{\langle V(x,y), V(x_n, \max(0, y - \Delta r))\rangle\} \end{aligned} \quad (1)$$

The ∞-weighted arcs for a surface in 3D are defined equivalent to the ∞-weighted arcs for a contour in 2D, except that there is an additional dimension for a node ($V(x, y, z)$):

$$\begin{aligned} A_p &= \{\langle V(x,y,z), V(x,y,z-1)\rangle \,|\, z > 0\} \\ A_r &= \{\langle V(x,y,z), V(x_n, y_n, \max(0, z - \Delta r))\rangle\} \end{aligned} \quad (2)$$

A_p – these arcs connect always two nodes along the same ray and ensure that all nodes below the contour or surface in the graph are included to form a closed set (correspondingly, the interior of the object is separated from the exterior in the data).A_r – these arcs connect nodes of different rays and therefore constrain the set of possible segmentations via the regularization parameter Δ_r (note: the larger this parameter is, the larger is the number of possible segmentations). Thus, Δ_r can be seen as a smoothness parameter that avoids outliers.

When the graph is constructed, the minimal cost closed set on the graph is computed via a polynomial time s–t cut [15] which results in an optimal segmentation of the object under the influence of the regularizing parameter Δ_r that controls the stiffness of the result. Hereby, a delta value of zero means that the segmentation result has exactly the form of the predefined template and the position and scale of the template depends on the best fit to the gray levels or appearance of the image. Finally, the weights $w(x, y)$ for every edge between $v \in V$ and the sink or the source are assigned in the following manner: weights are set to $c(x, y)$ if z is zero; otherwise they are set to $c(x, y) - c(x, y-1)$, where $c(x, y)$ is the absolute value of the difference between an average texture value of the desired object and the texture value of the pixel at position (x, y) [16]. It is obvious that this average texture value critically influences the segmentation result. However, due to the concept of our segmentation scheme the user-defined seed point is located somewhere inside the object and therefore the average texture value can be estimated automatically around it, e.g. by integrating over a small square S – in 2D – or cube C – in 3D – of dimension d centered on the user-defined seed point (s_x, s_y) or (s_x, s_y, s_z), respectively (note: we typically used a value of 1 cm for dimension d):

$$\int_{-d/2}^{d/2}\int_{-d/2}^{d/2} S(s_x + x, s_y + y)dxdy \quad (3)$$

$$\int_{-d/2}^{d/2}\int_{-d/2}^{d/2}\int_{-d/2}^{d/2} C(s_x + x, s_y + y, s_z + z)dxdydz \quad (4)$$

Fig. 1 presents examples of templates that have been used to construct graphs and segment different pathologies in 2D and 3D. In the upper row, a circle template has been used to set up a graph and segment the prostate. In the second row, a square template has been used to segment vertebrae in 2D. A sphere template has been used to segment Glioblastoma Multiforme in the third row. Finally, in the last row, a cube template has been used to segment a vertebral body in 3D. For all examples the graph is constructed at the seed point position defined by the user, optimally located close to the center of the pathology.

In contrast to the predefined templates, like circles or squares which work fine for certain pathologies, the user can also draw/define a (segmentation) template in a first step. This is particularly interesting for segmentation problems where the target object varies a lot. Examples are aortic aneurysms that arise at an arbitrary position along the aorta and can have different shapes and sizes for each patient. Here, an iterative approach along the aorta with a user-defined template for the graph in a first plane can make sense [17,18]. Fig. 2 shows how a user-defined template can be created for interactive segmentation of the rectum. Hereby, a graph's template is defined by manually outlining the rectum (yellow) on one 2D slice, like shown in the upper images from the left to the right. Afterwards, this manual contour is used to calculate the graph's center point (lower left image), sample the graph's nodes (second lower image) and finally construct the whole graph (third lower image).

3. Results

The interactive segmentation algorithms have been implemented within the medical prototyping platform MeVisLab (http://www.mevislab.de), whereby the algorithms have been implemented in C++ as additional MeVisLab-modules (note: although the foci of the prototyping platform MeVisLab are medical applications, it is also possible to process images from other fields). The special graph construction of the algorithm makes it eligible for real-time segmentation, because it only considers subsets of the whole image in the area of the pathology or object that the user wants to segment. However, even when the graph was set up with a few dozen rays and dozens of nodes where sampled along each ray, the overall segmentation (including the mincut computation besides the graph construction) took only around a second for our implementation – on an Intel Core i5-750 CPU, 4 × 2.66 GHz, 8 GB RAM, Windows XP Professional x64 Version, Version 2003, Service Pack 2. For evaluation of the proof of concept, the presented scheme has been evaluated with fixed seed points mainly on medical image data in 2D and 3D, like brain tumors, cerebral aneurysms and vertebral bodies. For evaluation we used a wide variety of datasets even within the single pathologies. The datasets of the spines for vertebral body segmentation ranged from 512 × 512 × 14 to 512 × 512 × 39 voxels, with voxel sizes from 0.391 mm^2 to 0.625 mm^2 and 4.4 mm slice thicknesses. The datasets for Glioblastoma Multiforme segmentations ranged from 256 × 256 × 66 to 512 × 512 × 160 voxels, with

Please cite this article in press as: Egger J, et al. Interactive-cut: Real-time feedback segmentation for translational research. Comput Med Imaging Graph (2014), http://dx.doi.org/10.1016/j.compmedimag.2014.01.006

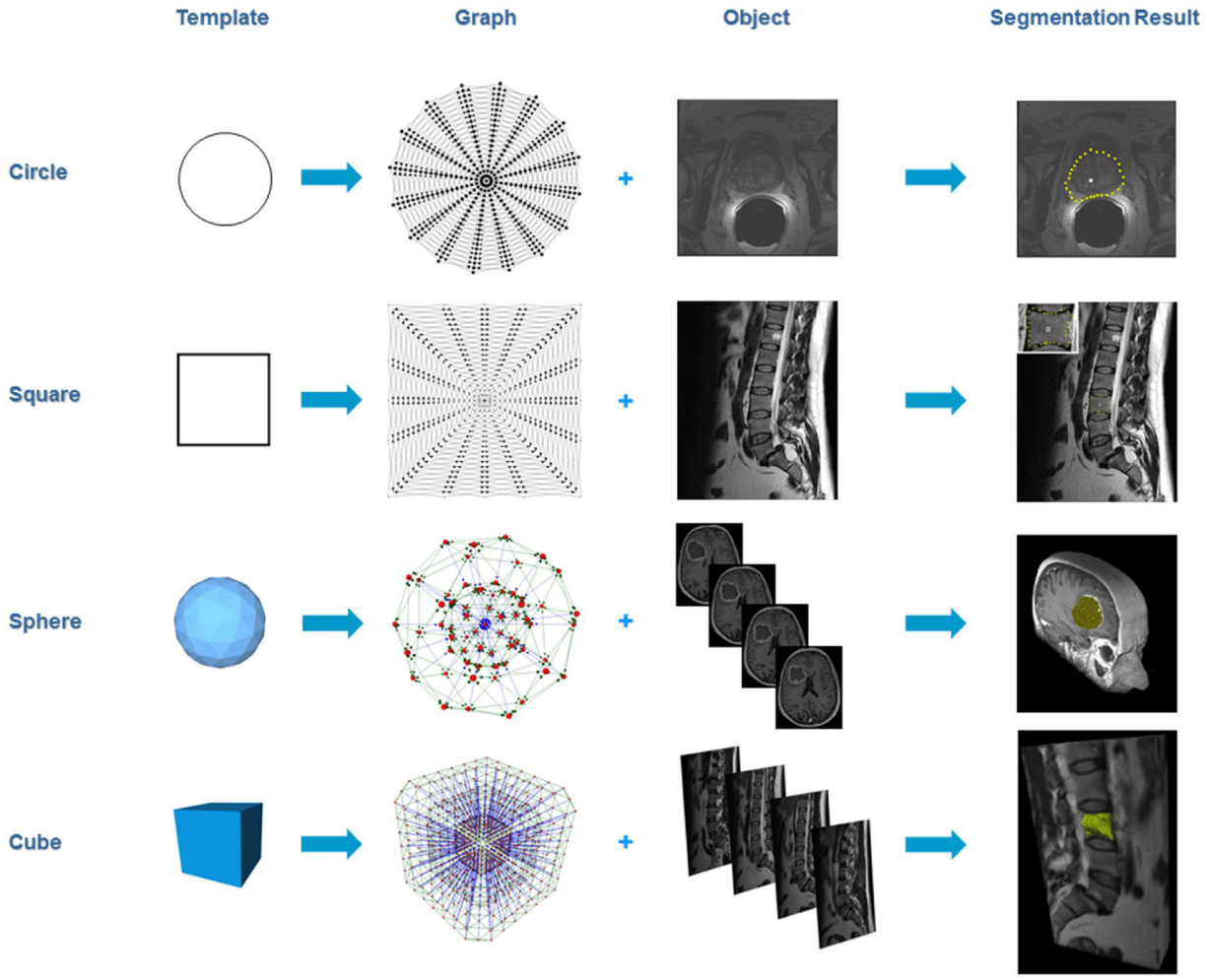

Fig. 1. Examples for templates that have been used to segmented different pathologies in 2D and 3D: a circle template has been used to set up a graph and segment the prostate (upper row), a square template has been used to segment vertebrae in 2D (second row), a sphere template has been used to segment Glioblastoma Multiforme (third row), and a cube template has been used to segment a vertebral body in 3D (lower row). For all examples the graph is constructed at the seed point position defined by the user, optimally located close to the center of the pathology.

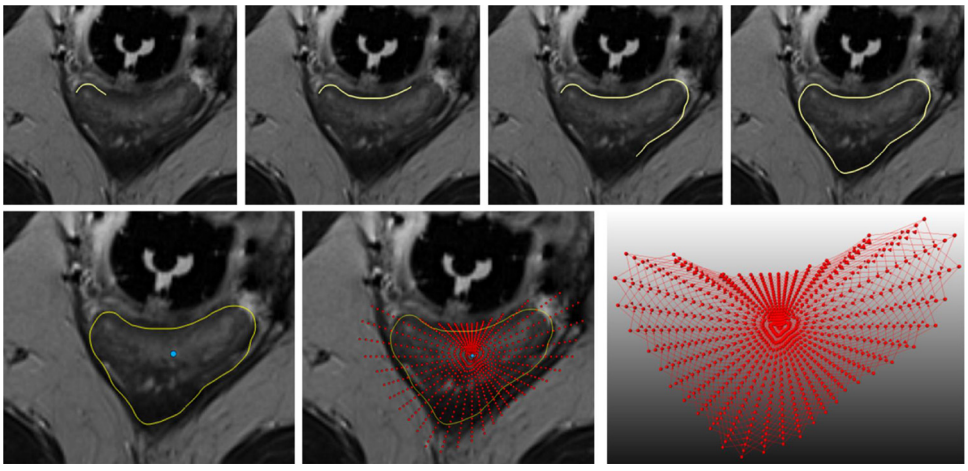

Fig. 2. Interactive segmentation of the rectum with a user-defined template: in this example a graph's template is defined by manually outlining the rectum (yellow) on one 2D slice, like shown in the upper images from the left to the right. Afterwards, this manual contour is used to calculate the graph's center point (lower left image), sample the graph's nodes (second lower image) and finally construct the whole graph (third lower image). (For interpretation of the references to color in this figure legend, the reader is referred to the web version of the article.)

Please cite this article in press as: Egger J, et al. Interactive-cut: Real-time feedback segmentation for translational research. Comput Med Imaging Graph (2014), http://dx.doi.org/10.1016/j.compmedimag.2014.01.006

Table 1
Summary of results: min, max, mean μ and standard deviation σ for the manual and automatic segmentation volumes (cm^3) of the pathologies, and mean μ and standard deviation σ for the Dice Similarity Coefficients (DSCs) between the manual and the automatic segmentations.

Pathology	Min/max of volumes (cm^3)		$\mu \pm \sigma$ of volumes (cm^3)		$\mu \pm \sigma$ of DSCs (%)
	Manual	Automatic	Manual	Automatic	
GBM	0.47/119.28	0.46/102.98	23.66 ± 24.89	21.02 ± 22.90	80.37 ± 8.93
PA	0.84/15.57	1.18/14.94	6.30 ± 4.07	6.22 ± 4.08	77.49 ± 4.52
CA	0.45/4.02	0.35/4.22	1.90 ± 1.88	2.02 ± 1.99	72.66 ± 10.71
PCG	13.67/66.16	13.29/67.56	31.32 ± 17.45	33.58 ± 18.88	78.94 ± 10.85
VB 2D	0.25/0.51	0.24/0.49	0.42 ± 0.072	0.40 ± 0.073	90.97 ± 2.2
VB 3D	15.42/33.83	16.64/28.78	24.97 ± 6.15	23.48 ± 5.12	81.33 ± 5.07

Abbreviations: Glioblastoma Multiforme (GBM), Pituitary Adenoma (PA), Cerebral Aneurysm (CA), Prostate Central Gland (PCG) and Vertebral Body (VB).

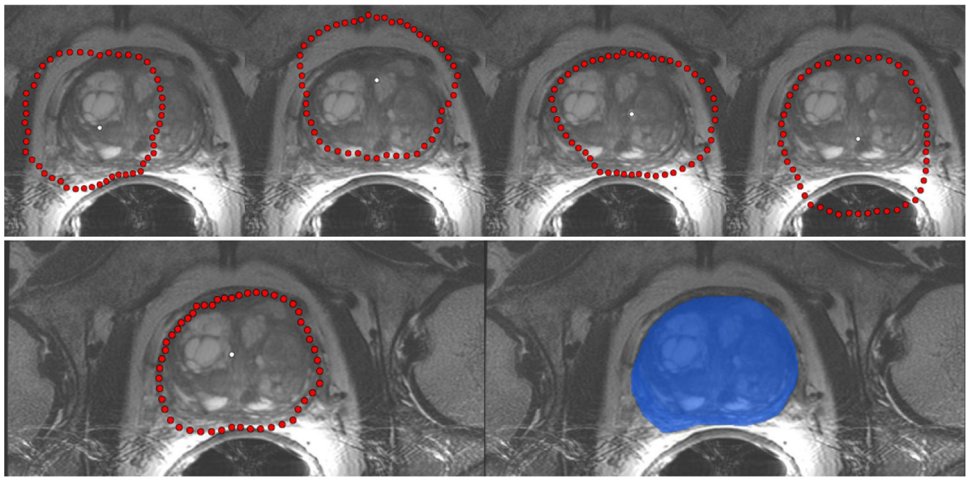

Fig. 3. Interactive prostate segmentation in a magnetic resonance imaging (MRI) scan with a circle template: the four images in the upper row present the resulting contour (red) for user-defined seed points (white) that have been moved closer to the border of the prostate. For example in the upper left image the seed point is located closer to the left border of the prostate and therefore the resulting contour (red) also tends to "leak" on the left side. However, the interactive behavior of the algorithm and the real-time feedback of the resulting contour enable the user to find quickly a satisfying contour of the prostate, like shown in the lower left image. For visual inspection of the segmentation result, the lower right image shows the corresponding manual segmented mask (blue) on the same 2D slice. (For interpretation of the references to color in this figure legend, the reader is referred to the web version of the article.)

voxel sizes from 0.449 mm^2 to 1.133 mm^2 and 1 mm to 6.5 mm slice thicknesses. The scans of the heads for Pituitary Adenoma segmentation ranged from $256 \times 256 \times 160$ to $512 \times 512 \times 80$ voxels, with voxel sizes from 0.449 mm^2 to 0.977 mm^2 and 1 mm to 6 mm slice thicknesses. The Cerebral Aneurysm datasets ranged from $440 \times 512 \times 30$ to $512 \times 512 \times 26$ voxels, with voxel sizes from 0.41 mm^2 to 0.467 mm^2 and 3.3 mm to 6.6 mm slice thicknesses. The images sizes for the prostate central Gland datasets ranged from $512 \times 512 \times 22$ to $512 \times 512 \times 30$ voxels, with voxel sizes from 0.273 mm^2 to 0.313 mm^2 and 3 mm to 4 mm slice thicknesses. For the gynecological data for rectum segmentation the image sizes ranged from $320 \times 256 \times 22$ to $384 \times 384 \times 72$ voxels, with voxel sizes from 0.625 mm^2 to 0.875 mm^2 and 3 mm slice thicknesses.

Direct comparison of the automatic segmentations with manual slice-by-slice segmentations from physicians resulted in acceptable Dice Similarity Coefficients (DSCs) and thus proofed that the interactive version is feasible. For evaluation we used fifty Glioblastoma Multiforme (GBM), ten Pituitary Adenoma (PA), three Cerebral Aneurysm (CA), ten Prostate Central Gland (PCG) and ten Vertebral Body (VB) datasets from the clinical routine. Thereby, the GBMs, the Pituitary Adenomas, the Cerebral Aneurysms and the PCGs have been segmented with the Nugget-Cut algorithm [19,20], the vertebral bodies in 2D with the Square-Cut algorithm [21,22], and the vertebral bodies in 3D with the Cube-Cut algorithm [23,24]. Table 1 presents the summary of the results including min, max, mean, μ and standard deviation σ for the manual and automatic segmentation volumes (cm^3) of the pathologies, and mean μ and standard deviation σ for the Dice Similarity Coefficients between the manual and the automatic segmentations (note: to calculate a volume for the vertebral bodies in 2D we used a slice thickness of 1 mm). In addition to the Dice Similarity results from Table 1 we evaluated an interactive rectum segmentation and calculated the Dice Similarity Coefficients and the Hausdorff Distances (HD) [25–27]. This resulted in an average DSC of 83.85 ± 4.08% (min. 79.04 and max.

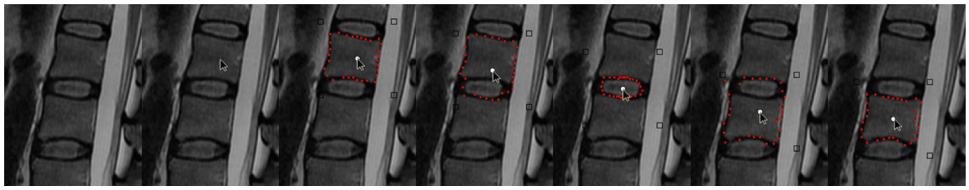

Fig. 4. Several screenshots from a video demonstrating the interactive real-time segmentation of vertebral bodies and intervertebral discs in a sagittal plane of a magnetic resonance imaging (MRI) scan from the left to the right. The graph's center point is the white dot from the third image on, the black boxes define the corners of the square template and the red dots are the segmentation outcomes.

Please cite this article in press as: Egger J, et al. Interactive-cut: Real-time feedback segmentation for translational research. Comput Med Imaging Graph (2014), http://dx.doi.org/10.1016/j.compmedimag.2014.01.006

89.54) and an average HD of 11.05 ± 6.81 mm (min. 4.36 and max. 25.47). For a better understanding of these results, we additionally compared two pure manual expert segmentations, which resulted in an average DSC of 83.97 ± 8.08% (min. 70.37 and max. 91.40) and a HD of 11.76 ± 7.54 mm (min. 4.03 and max. 22.29).

Based on our experience, the larger the segmentation volume of a pathology the easier it was to get higher Dice scores. For smaller volumes like the cerebral aneurysms it was harder to get high DSCs, because slight differences between the manual and automatic volumes already had a big influence on the Dice score. In contrast, for greater volumes like the GBMs or the vertebral bodies in 3D, deviations may not influence the resulting Dice score very much. However, in general it was also easier to get a high DSC in 2D than in 3D, as shown for the vertebral bodies. The reason for that is, that

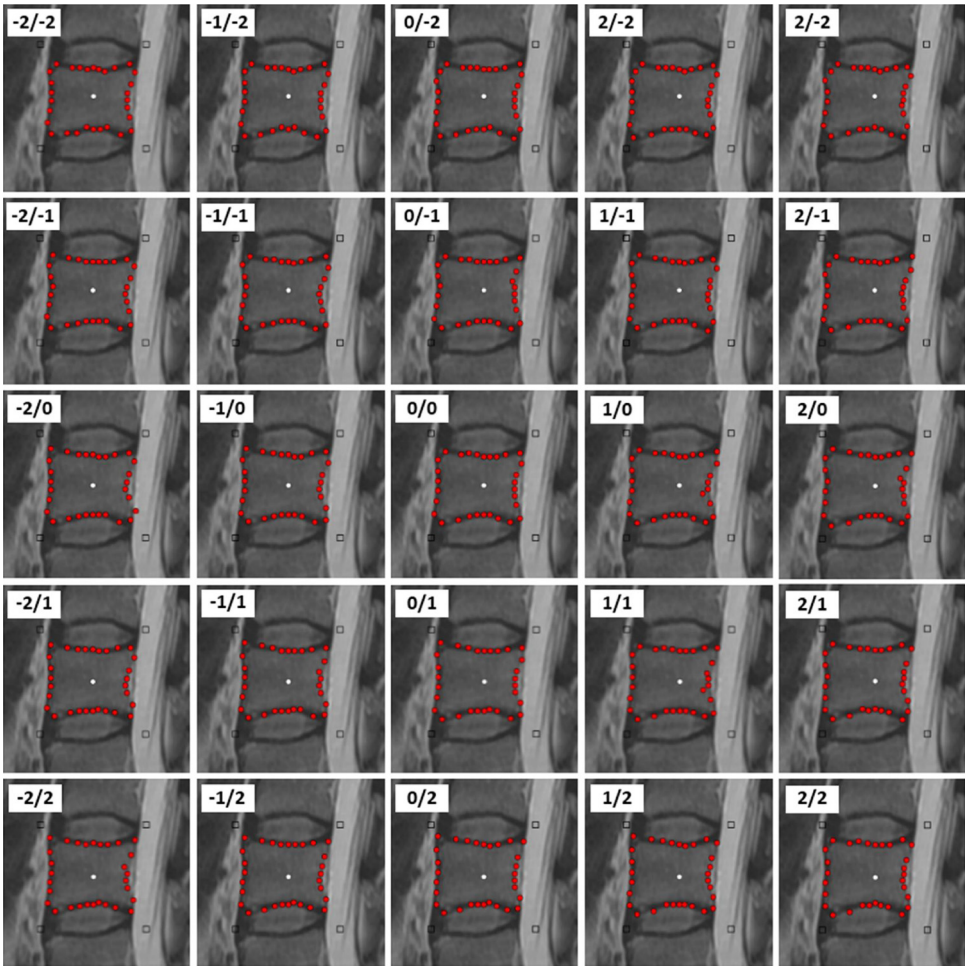

Fig. 5. Seed point analysis to demonstrate the variations of the segmentation results on a 4 × 4 grid. Initially a seed point has been placed near the center of the vertebra (0/0). Then, the seed point has been placed one voxel to the left (−1/0), two voxel to the left (−2/0), and so on. As shown in the segmentation is pretty stable within a small area close to the center of the vertebra. However, the more the see point is moved towards the border of the vertebra the segmentation result will leak, like shown in the upper images of Fig. 3.

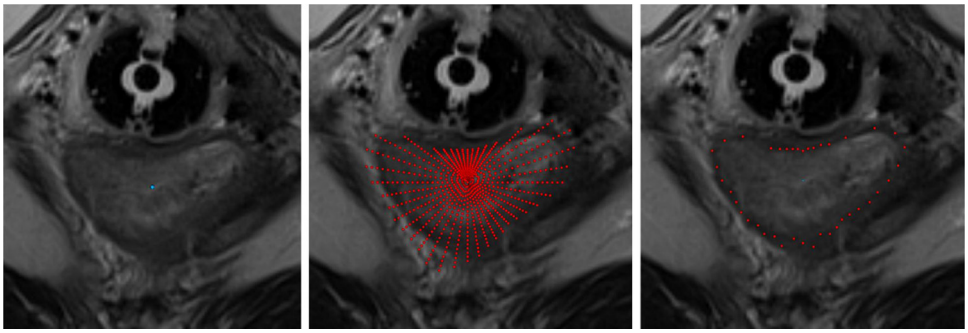

Fig. 6. Interactive rectum segmentation with a user-defined template: example how the individual graph from Fig. 2 can be used to segment adjacent rectum contours. Therefore, the user can scroll through the 2D slices of the patient dataset (in this case in *z* direction) and place a seed point (blue) inside the rectum (left image). Then, the graph's nodes are sampled based on the user-defined template from Fig. 2 (note: in general, the graph or the graph's nodes are not displayed to the user. This has only been done for demonstration purposes here). Finally, the segmentation result of the rectum is presented to the user depending on the user-defined seed point position (rightmost image). (For interpretation of the references to color in this figure legend, the reader is referred to the web version of the article.)

Please cite this article in press as: Egger J, et al. Interactive-cut: Real-time feedback segmentation for translational research. Comput Med Imaging Graph (2014), http://dx.doi.org/10.1016/j.compmedimag.2014.01.006

the segmentation result can be seen in one plane and the seed point can easily be (re-)placed in this plane. Finding a good seed point in 3D is much harder and in general the user has to navigate through the single 2D slicer to evaluate the overall segmentation result.

Fig. 3 presents the proposed approach for interactive prostate segmentation in MR images acquired during MR-guided prostate core needle biopsy [28] and the data is freely available for download [29]. For the interactive prostate segmentation a circle template has been applied and the four images in the upper row present the resulting contour (red) for user-defined seed points (white) that have been moved closer to the border of the prostate, e.g. in the upper left image the seed point is located closer to the left border of the prostate and therefore the resulting contour (red) also tends to "leak" on the left side. However, the interactive behavior of the algorithm and the real-time feedback of the resulting contour enable the user to find quickly a satisfying contour of the prostate, like shown in the lower left image. For visual inspection of the segmentation result, the lower right image shows the corresponding manual segmented mask (blue) on the same 2D slice. Fig. 4 presents several screenshots from a video demonstrating the interactive real-time segmentation of vertebral bodies and intervertebral discs in a sagittal plane of a magnetic resonance imaging (MRI) scan that provides real-time feedback to the user during the segmentation process [30,31]. The speed and the real-time behavior make this algorithm even suitable for MR-guided biopsies of vertebral bodies where several planes are used in planning and executing the interventions [32]. In Fig. 5 a seed point analysis is presented to demonstrate the variations of the segmentation results on a 4×4 grid. For the analysis, a seed point has been placed initially near the center of the vertebra (0/0). Then, the seed point has been replaced one voxel to the left (−1/0), two voxel to the left (−2/0), and so on. As shown the segmentation is pretty stable within a small area close to the center of the vertebra, but it will start leaking the more the seed point is moved towards the border of the vertebra similar to the Prostate Central Gland segmentation like shown in the upper images of Fig. 3. However, the interactive segmentation behavior of the approach makes it easy to find good segmentation results. Therefore, the approach was tested by several users (including physicians) who were all able to find satisfying segmentation result within seconds. Furthermore, it was easy to find sufficient segmentation results again by moving the seed point interactively over the image (repeatability). Fig. 6 presents the proposed approach for rectum segmentation in MR images acquired during gynecologic cancer brachytherapy [33–35] (note: the data is freely available for download [36–38]). In Fig. 6, the template from Fig. 2 is used for the interactive rectum segmentation process

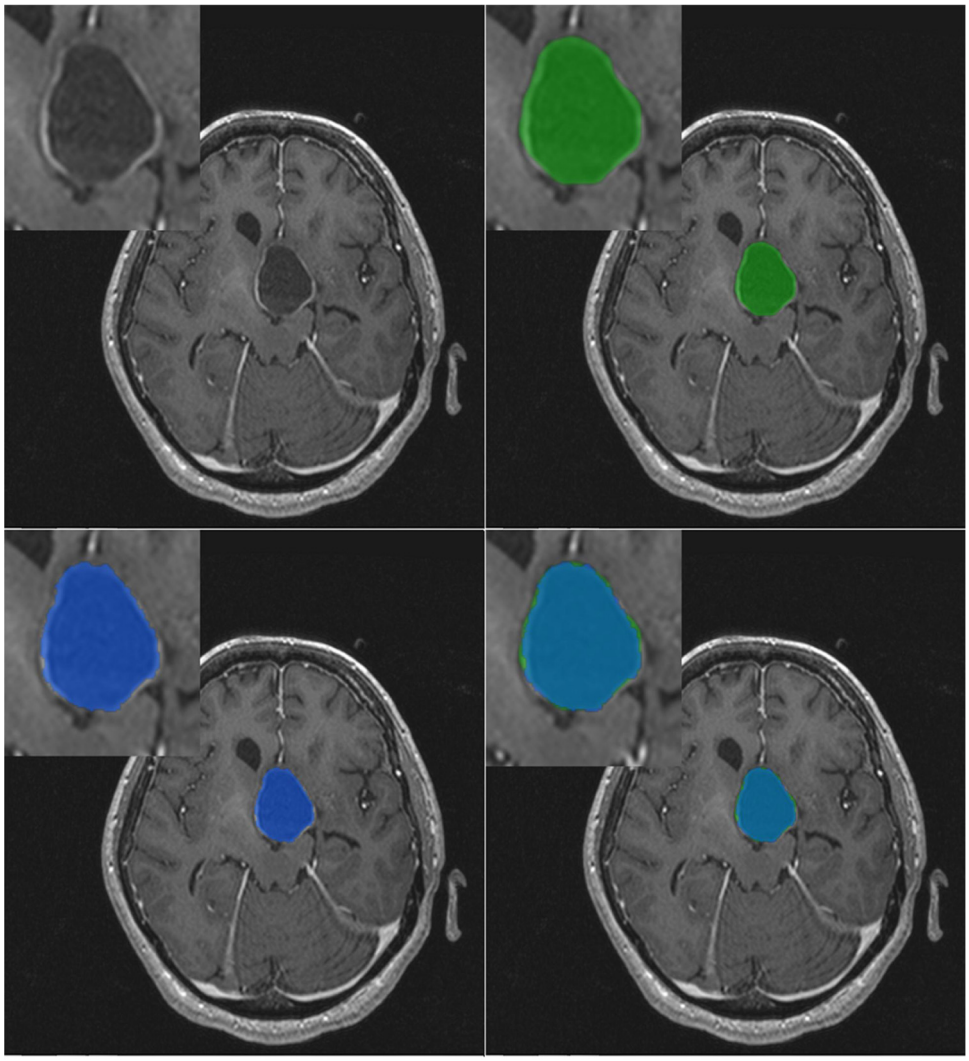

Fig. 7. Direct visual comparison of an automatic segmentation and a manual segmentation of a Glioblastoma Multiforme (GBM): native image (upper left), manual segmentation in green (upper right), automatic segmentation in blue (lower left) and superimposed segmentations (lower right). (For interpretation of the references to color in this figure legend, the reader is referred to the web version of the article.)

Please cite this article in press as: Egger J, et al. Interactive-cut: Real-time feedback segmentation for translational research. Comput Med Imaging Graph (2014), http://dx.doi.org/10.1016/j.compmedimag.2014.01.006

on an adjacent 2D slice. Therefore, the user can scroll through the 2D slices of the patient dataset (in this case in *z* direction) and place a seed point (blue) inside the rectum (left image). Then, the graph's nodes are sampled based on the user-defined template from Fig. 2 (note: in general, the graph or the graph's nodes are not displayed to the user. This has only been done for demonstration purposes here). Finally, the segmentation result of the rectum is presented to the user depending on the user-defined seed point position (rightmost image).

Figs. 7–9 present direct visual comparisons of automatic and manual segmentations of a Glioblastoma Multiforme (Fig. 7), a Pituitary Adenoma (Fig. 8) and a Cerebral Aneurysm (Fig. 9). Thereby, the native images are displayed in the upper left. The manual segmentations (green) and the automatic segmentations (blue) are presented in the upper right and lower left, respectively. In addition, superimposed images of the manual and automatic segmentations are shown in the lower right.

4. Discussion

In this contribution, a novel interactive image segmentation algorithm has been presented that provides the user with real-time feedback of the segmentation result during the segmentation process. Therefore, a specific graph-based segmentation scheme has been elaborated that needs only one user-defined seed point inside the object that has to be segmented. In contrast to other approaches, where a more intensive initialization is needed a single user-defined seed point makes the algorithm eligible for real-time segmentation. In addition, color or gray value information that is needed for the approach can be automatically extracted around the user-defined seed point. Thus, the algorithm's parameters are "wrapped" for the user by the interactive behavior of the approach, avoiding the definition of "arbitrary" numbers that the user cannot really understand.

For the proof of concept the introduced scheme has been evaluated within several studies mainly on medical image data in 2D and 3D, like prostates, brain tumors, cerebral aneurysms and vertebral bodies. Thereby, the automatic segmentations have been compared with manual slice-by-slice segmentations from physicians via the Dice Similarity Coefficient, proofing that an interactive version of the scheme is feasible. In summary, the achieved research highlights of the presented work are:

- A graph-based segmentation scheme has been designed that needs only one user-defined seed point for the segmentation process;

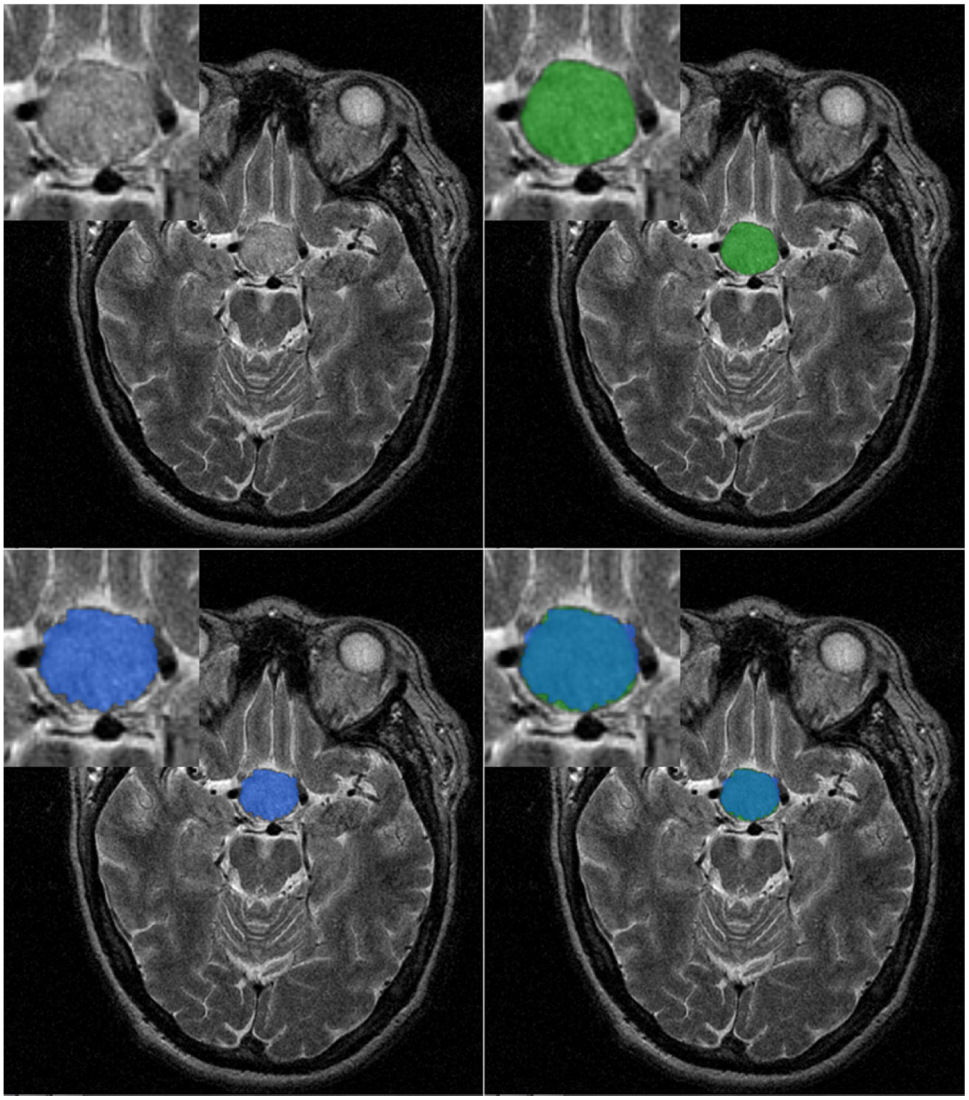

Fig. 8. Direct visual comparison of an automatic segmentation and a manual segmentation of a Pituitary Adenoma (PA): native image (upper left), manual segmentation in green (upper right), automatic segmentation in blue (lower left) and superimposed segmentations (lower right). (For interpretation of the references to color in this figure legend, the reader is referred to the web version of the article.)

Please cite this article in press as: Egger J, et al. Interactive-cut: Real-time feedback segmentation for translational research. Comput Med Imaging Graph (2014), http://dx.doi.org/10.1016/j.compmedimag.2014.01.006

- The specific design makes the scheme eligible for interactive real-time segmentation;
- Color or gray value information that is needed for the algorithm can automatically be extracted around the user-defined seed point;
- "Wrapping" the algorithm's parameters for the user by the interactive behavior of the approach;
- For the proof of concept the introduced scheme has been evaluated in several studies with fixed seed points;
- Manual slice-by-slice segmentations of medical data have been performed by clinical experts to obtain ground truth of pathology boundaries;
- Dice Similarity Coefficients (DSC) have been calculated to evaluate the quality of the segmentations.

There are several areas for future work: in particular, the scheme can also be extended to "Coupled Surfaces" to segment objects that consist of several borders, like the wall and lumen for the carotid [39] or the aorta [40]. Furthermore, the scheme can be extended by allowing the user to interactively specify an arbitrary number of additional points within the image. In case of the introduced graph-based approach, these points would support the algorithm with gray value information and geometrical constraints like presented in [41,42]. This principle can also be used to start with an interactive segmentation on several 2D slices, then switching to an interactive 3D segmentation where the segmentation results of the 2D slices are "fixed". This strategy would pre-restrict the 3D segmentation and thus support the user to find a satisfying segmentation result of the whole object in 3D (Fig. 10). The initial 2D segmentations could also be segmented in different oriented planes, for example a 2D segmentation in an axial plane, a 2D segmentation in a sagittal plane and a 2D segmentation in a coronal plane, similar to the initialization of the GrowCut algorithm [10] in recent studies for Pituitary Adenomas [43], Glioblastoma Multiforme [44] and vertebral bodies [45]. Moreover, we plan to study the segmentations with a larger number of "rays", especially in 3D. For 2D vertebra segmentation for example, we archived already satisfying results if the number of rays was set to 30 – but even with a larger number of rays the interactive segmentation in real-time was no issue at all. However, in 3D we had to restrict the number of rays to a few hundred to perform the segmentation still in a reasonable time. Depending on the current position of the seed

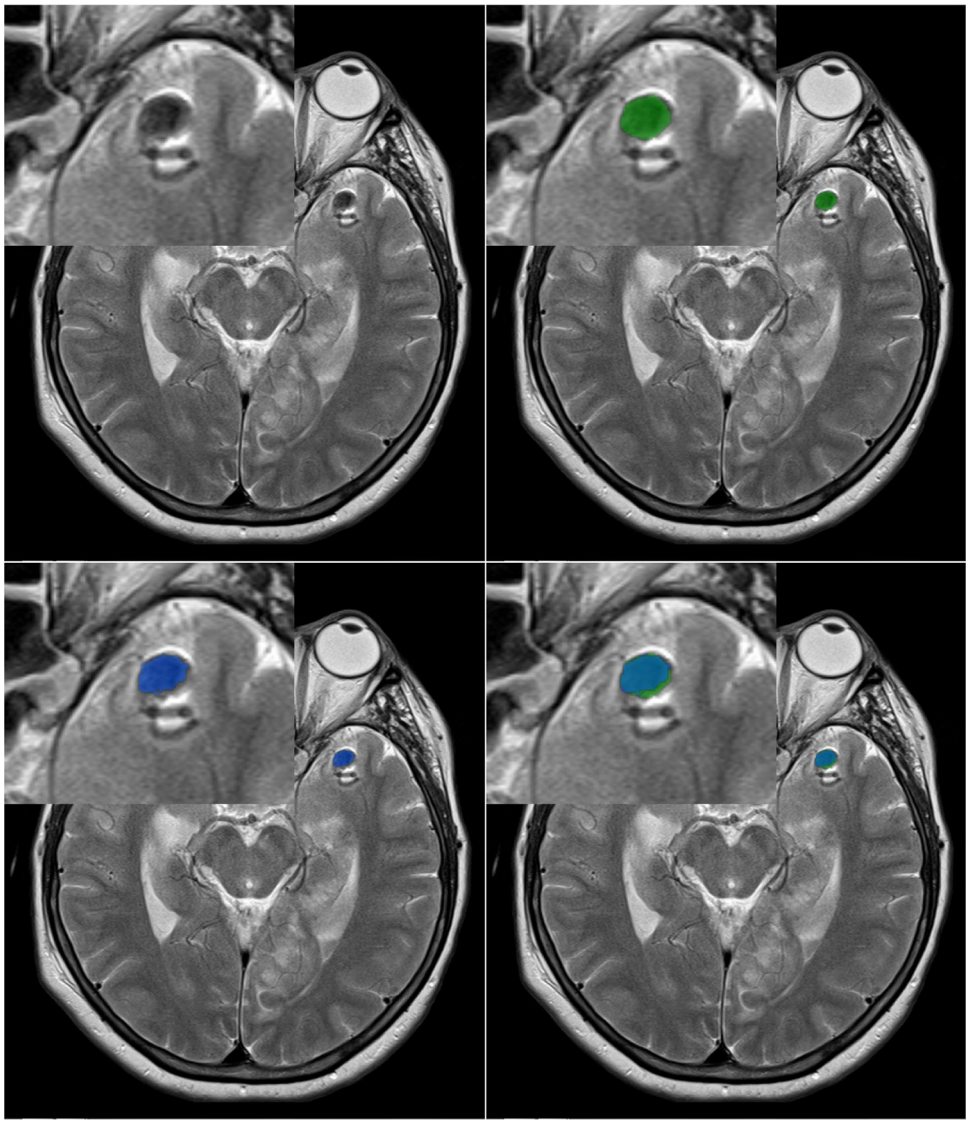

Fig. 9. Direct visual comparison of an automatic segmentation and a manual segmentation of a Cerebral Aneurysm (CA): native image (upper left), manual segmentation in green (upper right), automatic segmentation in blue (lower left) and superimposed segmentations (lower right). (For interpretation of the references to color in this figure legend, the reader is referred to the web version of the article.)

Please cite this article in press as: Egger J, et al. Interactive-cut: Real-time feedback segmentation for translational research. Comput Med Imaging Graph (2014), http://dx.doi.org/10.1016/j.compmedimag.2014.01.006

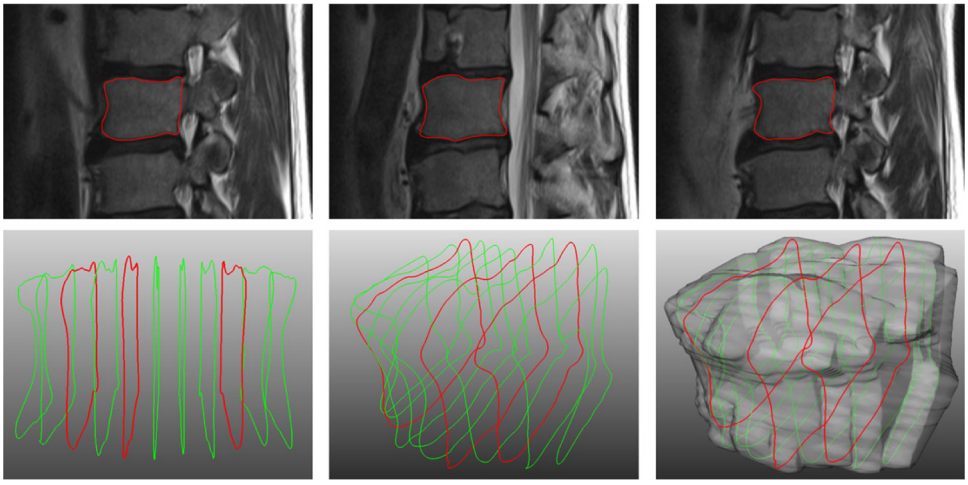

Fig. 10. Iterative segmentation: in a first step several vertebra contours (red, upper images) are segmented with an interactive 2D approach like presented in Fig. 4. In a second step a 3D graph for the whole vertebral body is generated where the three 2D slices from step one a fixed. Thus, restricting the 3D graph, and supporting and influencing the segmentation of the remaining contours (green, lower images). The red contours from the lower images correspond to the red contours from the upper images (from the left to the right). In addition, a voxelized mask is presented and superimposed in the lower rightmost image. (For interpretation of the references to color in this figure legend, the reader is referred to the web version of the article.)

point the vertices of the vertebral body's outer boundaries could sometimes be "missed". Fig. 11 presents an example where vertices of the vertebral body's outer boundaries have not be detected accurately (green circles). The upper part of Fig. 11 shows the 3D segmentation result and the lower part shows the 2D overlaps of manual (red) and automatic (white) segmentation results. But, this can be overcome with a more powerful PC that still can handle the segmentation calculation in real-time with a higher density of rays.

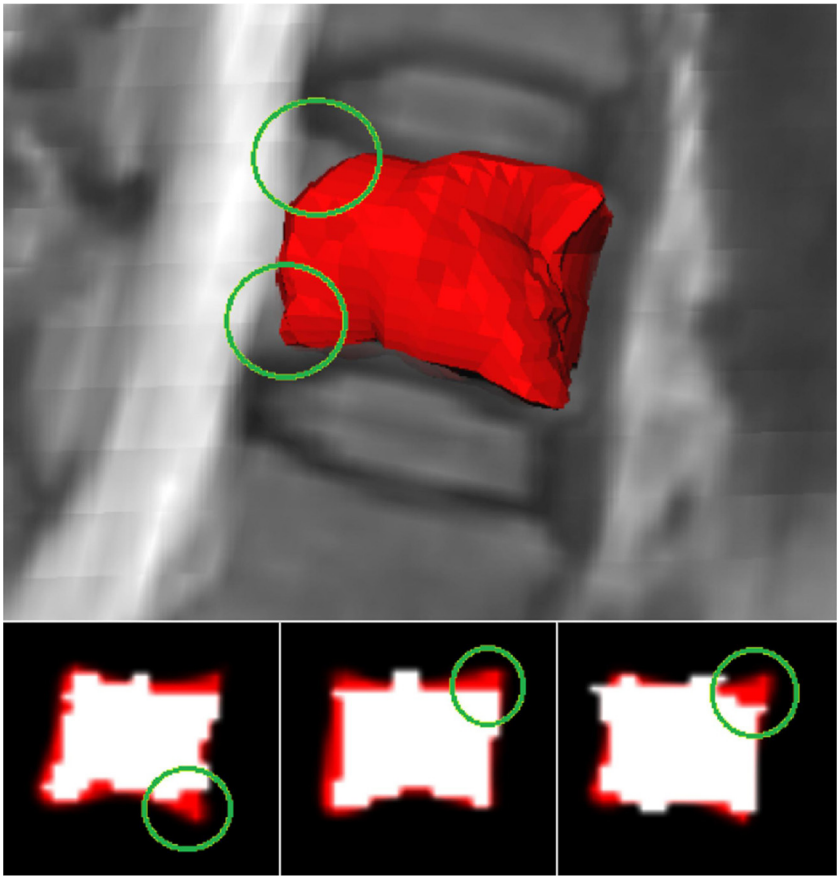

Fig. 11. Example where vertices of the vertebral body's outer boundaries have not be detected accurately (green circles). The upper part shows the 3D segmentation result, the lower part shows the 2D overlaps of manual (red) and automatic (white) segmentation results. (For interpretation of the references to color in this figure legend, the reader is referred to the web version of the article.)

Please cite this article in press as: Egger J, et al. Interactive-cut: Real-time feedback segmentation for translational research. Comput Med Imaging Graph (2014), http://dx.doi.org/10.1016/j.compmedimag.2014.01.006

Author contribution statement

Conceived and designed the experiments: JE, TL, RS. Performed the experiments: JE. TL, RS. Analyzed the data: JE, TL, RS. Contributed reagents/materials/analysis tools: JE, TL, RS, BF, CN. Wrote the paper: JE.

Conflict of interest statement

The authors of this paper have no potential conflict of interests.

Acknowledgements

First of all, the authors would like to thank the physicians Neha Agrawal, M.B.B.S., Dr. med. Barbara Carl, Thomas Dukatz, Christoph Kappus, Dr. med. Malgorzata Kolodziej and Dr. med. Daniela Kuhnt for performing the manual slice-by-slice segmentations of the medical images and therefore providing the 2D and 3D masks for the evaluation. Furthermore, the authors are thanking Drs. Fedorov, Tuncali, Fennessy and Tempany, for sharing the prostate data collection. Finally, the authors would like to thank Fraunhofer MeVis in Bremen, Germany, for their support by providing an academic license for the MeVisLab software.

References

[1] Kapur T, Egger J, Jayender J, Toews M, Wells III WM. Registration and segmentation for image guided therapy. In: Jolesz Ferenc A, editor. Book chapter, intraoperative imaging and image-guided therapy. New York: Springer; 2014. p. 79–91. ISBN: 978-1-4614-7656-6 (Print) 978-1-4614-7657-3 (Online).
[2] Kass M, Witkin A, Terzopoulos D. Snakes – active contour models. International Journal of Computer Vision 1987;1:321–31.
[3] McInerney T, Terzopoulos D. Deformable models in medical image analysis: a survey. Medical Image Analysis 1996;1:91–108.
[4] Cootes TF, Edwards GJ, Taylor CJ. Active appearance models. In: Proceedings of the European Conference on Computer Vision, vol. 2, Springer, 1998. 1998. p. 484–98.
[5] Shi J, Malik J. Normalized cuts and image segmentation. IEEE Transactions on Pattern Analysis and Machine Intelligence 2000;22:888–905.
[6] Ji ZX, Sun QS, Xia DS. A modified possibilistic fuzzy c-means clustering algorithm for bias field estimation and segmentation of brain MR image. Computerized Medical Imaging and Graphics 2011;35(July (5)):383–97, http://dx.doi.org/10.1016/j.compmedimag.2010.12.001.
[7] Fu JC, Chen CC, Chai JW, Wong ST, Li IC. Image segmentation by EM-based adaptive pulse coupled neural networks in brain magnetic resonance imaging. Computerized Medical Imaging and Graphics 2009;34(June (4)):308–20, http://dx.doi.org/10.1016/j.compmedimag.2009.12.002.
[8] Boykov Y, Jolly M-P. Interactive graph cuts for optimal boundary and region segmentation of objects in N–D images. IEEE International Conference on Computer Vision (ICCV) 2001;1:105–12.
[9] Steger S, Sakas G. FIST: Fast interactive segmentation of tumors. Abdominal Imaging 2011;7029:125–32.
[10] Vezhnevets V, Konouchine V. GrowCut-interactive multi-label N-D image segmentation. In: Proc. Graphicon. 2005. p. 150–6.
[11] Heckel F, Moltz JH, Tietjen C, Hahn HK. Sketch-based editing tools for tumour segmentation in 3D medical images. Computer Graphics Forum 2013:1–14, http://dx.doi.org/10.1111/cgf.12193.
[12] Barbosa D, Heyde B, Cikes M, Dietenbeck T, Claus P, Friboulet D, et al. Real-time 3D interactive segmentation of echocardiographic data through user-based deformation of B-spline explicit active surfaces. Computerized Medical Imaging and Graphics 2013;38(January (1)):57–67, http://dx.doi.org/10.1016/j.compmedimag.2013.10.002.
[13] Egger J, Freisleben B, Nimsky C, Kapur T. Template-cut: a pattern-based segmentation paradigm. Scientific Reports, Nature Publishing Group (NPG) 2012;2:420.
[14] Li K, Wu X, Chen DZ, Sonka M. Optimal surface segmentation in volumetric images – a graph-theoretic approach. IEEE Transactions on Pattern Analysis and Machine Intelligence 2006;28(1):119–34.
[15] Boykov Y, Kolmogorov V. An experimental comparison of min-cut/max-flow algorithms for energy minimization in vision. IEEE Transactions on Pattern Analysis and Machine Intelligence 2004;26(9):1124–37.
[16] Bauer MHA, Egger J, O'Donnell T, Freisleben B, Barbieri S, Klein J, et al. A fast and robust graph-based approach for boundary estimation of fiber bundles relying on fractional anisotropy maps. In: 20th International Conference on Pattern Recognition (ICPR). 2010. p. 4016–9.
[17] Egger J, O'Donnell T, Hopfgartner C, Freisleben B. Graph-based tracking method for aortic thrombus segmentation. In: Proceedings of 4th European Congress for Medical and Biomedical Engineering, Engineering for Health. 2008. p. 584–7.
[18] Egger J, Freisleben B, Setser R, Renapuraar R, Biermann C, O'Donnell T. Aorta segmentation for stent simulation. In: 12th International Conference on Medical Image Computing and Computer Assisted Intervention (MICCAI), Cardiovascular Interventional Imaging and Biophysical Modelling Workshop. 2009. p. 1–10.
[19] Egger J, Bauer MHA, Kuhnt D, Carl B, Kappus C, Freisleben B, et al. Nugget-cut: a segmentation scheme for spherically- and elliptically-shaped 3D objects. In: 32nd Annual Symposium of the German Association for Pattern Recognition (DAGM). 2010. p. 383–92.
[20] Egger J. PCG-cut: graph driven segmentation of the prostate central gland. PLoS ONE 2013;8(10):e76645.
[21] Egger J, Kapur T, Dukatz T, Kolodziej M, Zukić D, Freisleben B, et al. Square-cut: a segmentation algorithm on the basis of a rectangle shape. PLoS ONE 2012;7(2):e31064.
[22] Egger J, Dukatz T, Freisleben B, Nimsky C. A semi-automatic approach to calculate the area of vertebrae in MRI scans. In: Proceedings of Bildverarbeitung für die Medizin (BVM). 2012. p. 274–9.
[23] Schwarzenberg R [Bachelor Thesis] Semi-Automatic, Graph-Based Vertebra Segmentation in MRI Data. Germany: Department of Mathematics and Computer Science, University of Marburg; October 2012. p. 1–68.
[24] Schwarzenberg R, Freisleben B, Kikinis R, Nimsky C, Egger J. A cube-based approach to segment vertebrae in MRI-acquisitions. In: Proceedings of Bildverarbeitung für die Medizin (BVM). 2013. p. 69–74.
[25] Hausdorff F. Grundzüge der Mengenlehre. Veit & Comp., Leipzig 1914 (rep. in Srishti D. Chatterji et al. (Hrsg.)), Gesammelte Werke, Band II. Berlin: Springer; 2002, ISBN 3-540-42224-2.
[26] Rockafellar RT, Wets RJ-B. Variational Analysis. New York: Springer; 2005. p. 117. ISBN 3540627723, ISBN 978-3540627722.
[27] Huttenlocher DP, Klanderman GA, Rucklidge WJ. Comparing images using the Hausdorff distance. IEEE Transactions on Pattern Analysis and Machine Intelligence 1993;15(9):850–63.
[28] Fedorov A, Tuncali K, Fennessy F, Tokuda J, Hata N, Wells WM, et al. Image registration for targeted mri-guided prostate transperineal prostate biopsy. Journal of Magnetic Resonance Imaging 2012, http://dx.doi.org/10.1002/jmri.23688.
[29] Fedorov A, Tuncali K, Fennessy FM, Tempany CM. MR-guided prostate biopsy pre- and intra-procedural MRI registration evaluation dataset. The National Center for Image Guided Therapy (NCIGT); 2012. http://www.spl.harvard.edu/publications/item/view/2147
[30] Egger J, Kapur T. Interactive technique for image segmentation. Research Disclosure 2012;1/13(December) [ID 585025, Published digitally].
[31] Egger J, Kapur T, Freisleben B, Nimsky C. Interactive real-time segmentation for vertebral bodies and intervertebral discs in sagittal planes. In: 6th NCIGT and NIH Image Guided Therapy Workshop. 2013.
[32] Salomonowitz E. MR imaging-guided biopsy and therapeutic intervention in a closed-configuration magnet: single-center series of 361 punctures. American Journal of Roentgenology 2001;177(July (1)):159–63.
[33] Kapur T, Egger J, Damato A, Schmidt EJ, Viswanathan AN. 3-T MR-guided brachytherapy for gynecologic malignancies. Magnetic Resonance Imaging 2012;30(9):1279–90.
[34] Lüddemann T [Diploma Thesis] Interactive graph-based segmentation of the rectosigmoid colon in MRI data for image guided gynecological brachytherapy. Munich, Germany: Department of Mechatronics, Technical University of Munich (TUM); May 2013. p. 1–102.
[35] Lüddemann T, Egger J. Rectum segmentation in MR-guided gynecologic brachytherapy data. In: Proceedings of The British Gynaecological Cancer Society Annual Scientific Meeting in conjunction with the Irish Gynaecological Cancer Society. 2013. p. 162–3 [Abstract topic: Cervix, PO97].
[36] Egger J, Kapur T, Viswanathan A. GYN data collection. The National Center for Image Guided Therapy (NCIGT); August 2012. http://www.spl.harvard.edu/publications/item/view/2227
[37] Egger J. Image-guided therapy system for interstitial gynecologic brachytherapy in a multimodality operating suite. SpringerPlus 2013;2:395, http://dx.doi.org/10.1186/2193-1801-2-395.
[38] Pernelle G, Mehrtash A, Barber L, Damato A, Wang W, Seethamraju RT, et al. Validation of catheter segmentation for MR-guided gynecologic cancer brachytherapy. Medical Image Computing and Computer-Assisted Intervention (MICCAI). Lecture Notes in Computer Science, vol. 8151. Berlin Heidelberg: Springer; 2013. p. 380–7.
[39] Ukwatta E, Yuan J, Rajchl M, Qiu W, Tessier D, Fenster A. 3D carotid multi-region MRI segmentation by globally optimal evolution of coupled surfaces. IEEE Transactions on Medical Imaging (TMI) 2013:1–16.
[40] Renapurkar RD, Setser RM, O'Donnell TP, Egger J, Lieber ML, Desai MY, et al. Aortic volume as an indicator of disease progression in patients with untreated infrarenal abdominal aneurysm. European Journal of Radiology 2011;81(February (2)):e87–93, http://dx.doi.org/10.1016/j.ejrad.2011.01.077.
[41] Egger J, Colen R, Freisleben B, Nimsky C. Manual refinement system for graph-based segmentation results in the medical domain. Journal of Medical Systems 2012;36(October (5)):2829–39.
[42] Egger J, Bauer MHA, Kuhnt D, Kappus C, Carl B, Freisleben B, et al. A flexible semi-automatic approach for glioblastoma multiforme segmentation. In: Kurths J, Penzel T, Malberg H, Wessel N(Hrsg), editors. Proceedings of International Biosignal Processing Conference. 2010.
[43] Egger J, Kapur T, Nimsky C, Kikinis R. Pituitary adenoma volumetry with 3D Slicer. PLoS ONE 2012;7(12):e51788.

Please cite this article in press as: Egger J, et al. Interactive-cut: Real-time feedback segmentation for translational research. Comput Med Imaging Graph (2014), http://dx.doi.org/10.1016/j.compmedimag.2014.01.006

[44] Egger J, Kapur T, Fedorov A, Pieper S, Miller JV, Veeraraghavan H, et al. GBM volumetry using the 3D slicer medical image computing platform. Scientific Reports, Nature Publishing Group (NPG) 2013;3:1364.
[45] Egger J, Kappus C, Carl B, Nimsky C. GrowCut-based vertebral body segmentation with 3D slicer. In: Jahrestagung der Sektion Wirbelsäule der Deutschen Gesellschaft für Neurochirurgie (DGNC). 2013.

Jan Egger is currently a Senior Researcher at the Institute for Computer Graphics and Vision of the Graz University of Technology in Austria. He received his German pre-diploma and diploma degree in Computer Science from the University of Wiesbaden, Germany in 2001 and 2004, respectively, his Master's degree in Computer Science from the University of Applied Sciences, Darmstadt, Germany in 2006, his first Ph.D. in Computer Science from the University of Marburg, Germany, in 2009, and his second interdisciplinary Ph.D. in Human Biology from the University Hospital of Marburg, Germany, in 2012. His research interests are Medical Image Analysis and Computer Vision, and Image-Guided Therapy, and he is currently working towards his German Habilitation in Computer Science.

Tobias Lüddemann received his diploma in Mechanical Engineering with majors in Medical Engineering and Information Technology from the Technical University of Munich, Germany, in 2013. His current research interests include biomedical image processing and medical device networks.

Robert Schwarzenberg received his Bachelor's degree in computer science from the University of Marburg, Germany, in 2012. Currently he is studying towards a dual degree in chemistry and English linguistics and literature.

Bernd Freisleben is a full professor of computer science in the Department of Mathematics and Computer Science at the University of Marburg, Germany. He received his Master's degree in computer science from the Pennsylvania State University, USA, in 1981, and his Ph.D. degree in computer science from the Darmstadt University of Technology, Germany, in 1985. His research interests include computational intelligence, scientific computing, multimedia computing, and medical image processing.

Christopher Nimsky is a professor and chairman of the Department of Neurosurgery at the University of Marburg, Germany. After medical school at the University Heidelberg he received his neurosurgical training at the Department of Neurosurgery at the University Erlangen-Nuremberg and became staff member in 1999. He became associate professor in 2001 after finishing his Ph.D. thesis on "intraoperative magnetic resonance imaging" and was vice chairman from 2005 to 2008 at the Department of Neurosurgery in Erlangen. His research focus is on medical technologies in neurosurgery, like intraoperative imaging and multimodal navigation, as well as molecular biology in neurooncology.

Please cite this article in press as: Egger J, et al. Interactive-cut: Real-time feedback segmentation for translational research. Comput Med Imaging Graph (2014), http://dx.doi.org/10.1016/j.compmedimag.2014.01.006

Semi-automatische Echtzeit-Konturierung
Ein vorlagenbasierter skalierungsinvarianter Ansatz

Jan Egger

Fachbereich Medizin, Universitätsklinikum Gießen und Marburg (UKGM)
egger@med.uni-marburg.de

Kurzfassung. In diesem Beitrag wird ein semi-automatischer und skalierungsinvarianter Segmentierungsalgorithmus zur Echtzeit-Konturierung vorgestellt. Dabei „verpackt" der Ansatz Parameter des Algorithmus in seiner Interaktivität für den Anwender. Dadurch wird vermieden, dass ein Anwender, um ein akzeptables Segmentierungsergebnis zu erzielen, ihm unbekannte Parametereinstellungen finden muss, die er im Gegensatz zum Entwickler des Algorithmus nicht ohne weiteres verstehen kann. Für die interaktive Segmentierung wurde ein spezieller graphbasierter Ansatz entwickelt, der sich insbesondere für eine interaktive Echtzeit-Konturierung eignet, da nur ein benutzerdefinierter Saatpunkt innerhalb der Zielstruktur benötigt wird und sich das Segmentierungsergebnis durch die besondere geometrische Konstruktion des Graphen sehr schnell berechnen lässt. Außerdem lassen sich die Grauwertinformationen, die für den Ansatz benötigt werden, automatisch aus dem Bereich um den benutzerdefinierten Saatpunkt herum extrahieren. Der Ansatz wurde über feste Saatpunkte in medizinischen 2D- und 3D-Daten evaluiert. Ein direkter Vergleich mit wesentlich zeitintensiveren manuellen Segmentierungen soll die praktische Anwendbarkeit des Ansatzes verdeutlichen.

1 Einleitung

Segmentierungsalgorithmen in der medizinischen Bildverarbeitung werden im Allgemeinen für eine ganz bestimmte Pathologie in einer ganz bestimmten Aufnahmemodalität entwickelt. Dennoch versagen (voll)automatische Segmentierungsalgorithmen bei neuen Daten immer wieder. Ganz wesentlich sind präzise Parametereinstellungen, um gute Ergebnisse zu liefern. Deshalb werden Konturierungen in der klinischen Routine immer noch rein manuell und Schicht für Schicht vorgenommen. Interaktive Segmentierungsansätze [1, 2], bei denen der Benutzer den Algorithmus mit intuitiven Informationen beim Segmentierungsprozess unterstützt, werden immer interessanter für die klinische Routine, insbesondere bei schwierigen Segmentierungsproblemen. In diesem Beitrag wird ein interaktiver graphbasierter Segmentierungsalgorithmus zur Konturierung von medizinischen Strukturen vorgestellt. Aufgrund der speziellen Graphkonstruktion benötigt der Ansatz nur einen Saatpunkt und eine Segmentierung kann sehr schnell berechnet werden. Dadurch eignet sich der Ansatz auch für eine interaktive Konturierung in Echtzeit.

T. M. Deserno et al. (Hrsg.), *Bildverarbeitung für die Medizin 2014,* Informatik aktuell,
DOI 10.1007/978-3-642-54111-7_67,

2 Material und Methoden

Der Segmentierungsansatz funktioniert mit 2D- und 3D-Daten und beginnt mit der Graphkonstruktion, ausgehend von einem benutzerdefinierten Saatpunkt innerhalb der zu segmentierenden Struktur. Die Knoten $n \in V$ des Graphen $G(V, E)$ werden entlang von Strahlen abgetastet, die radial vom Saatpunkt ausgesandt werden. Zusätzlich ist $e \in E$ eine Menge von Kanten, die aus Kanten zwischen den Knoten bestehen und aus Kanten, die die Knoten mit einer Quelle s und einer Senke t verbinden, um die Berechnung eines minimalen s-t-Schnitts [3] zu ermöglichen. In Anlehnung an die Notation von Li et al. [4] verbindet eine Kante $< v_\mathrm{i}, v_\mathrm{j} > \in E$ zwei Knoten v_i, v_j. In der Kantenmenge gibt es zwei Arten von ∞-gewichteten Kanten: p-Kanten A_p und r-Kanten A_r. P ist die Anzahl der Knoten, die entlang eines Strahles $p = (0, \ldots, P-1)$ abgetastet wurden, und R ist die Anzahl der Strahlen, die radial ausgesandt wurden, mit $r = (0, \ldots, R-1)$. $V(x_\mathrm{n}, y_\mathrm{n})$ ist als der Nachbar von $V(x, y)$ definiert (für weitergehende Details zur Graphkonstruktion wird an dieser Stelle auf [5, 6] verwiesen)

$$\begin{aligned} A_\mathrm{p} &= \{\langle V(x,y), V(x,y-1)\rangle \mid y > 0\} \\ A_\mathrm{r} &= \{\langle V(x,y), V(x_\mathrm{n}, \max(0, y - \Delta_\mathrm{r}))\rangle\} \end{aligned} \tag{1}$$

Die ∞-gewichteten Kanten für eine Oberfläche in 3D werden äquivalent zu den ∞-gewichteten Kanten für eine Kontur in 2D definiert

$$\begin{aligned} A_\mathrm{p} &= \{\langle V(x,y,z), V(x,y,z-1)\rangle \mid z > 0\} \\ A_\mathrm{r} &= \{\langle V(x,y,z), V(x_\mathrm{n}, y_\mathrm{n}, \max(0, z - \Delta_\mathrm{r}))\rangle\} \end{aligned} \tag{2}$$

Ist der Graph konstruiert, wird der minimale s-t-Schnitt für den Graphen berechnet [3], der wiederum dem Segmentierungsergebnis entspricht. In Abb. 1 findet man verschiedene Beispiele für Vorlagen, mit denen unterschiedliche Pathologien in 2D und 3D segmentiert wurden. Bei allen Beispielen wurde der Graph von einem benutzerdefinierten Saatpunkt aus konstruiert, der innerhalb der Pathologie lag. Für die Segmentierung benötigt der Ansatz auch einen mittleren Grauwert der zu segmentierenden Struktur. Dieser mittlere Grauwert wird im Bereich des Saatpunktes automatisch bestimmt und jedes Mal neu berechnet, wenn der Benutzer ihn interaktiv auf dem Bild verschiebt. Das macht den Ansatz robuster gegen Segmentierungsfehler, wenn der Saatpunkt kurzfristig über Bereiche verschoben wird, die zwar innerhalb der zu segmentierenden Struktur liegen, aber nicht dem mittleren Grauwert der zu segmentierenden Struktur entsprechen, wie z.B. bei sehr hellen Kalzifikationen.

3 Ergebnisse

Der vorgestellte Ansatz wurde innerhalb der Plattform MeVisLab realisiert. Der spezielle Aufbau der Graphen ermöglichte eine Echtzeit-Konturierung auf einem Rechner mit Intel Core i5-750 CPU, 4x2.66 GHz, 8 GB RAM. Die Evaluierung erfolgte über feste Saatpunkte in medizinischen 2D- und 3D-Daten (Tab. 1). Abb. 2

gibt mehrere Screenshots aus einem Video wider, die die interaktive Echtzeit-Konturierung von Wirbelkörpern und Bandscheiben in einer sagittalen Schicht einer MRT-Aufnahme zeigen. Der Mittelpunkt des Graphen ist in Weiß dargestellt und kann vom Benutzer interaktiv auf dem Bild verschoben werden, die roten Punkte stellen das Ergebnis der Segmentierung dar. In Abb. 3 sieht man eine interaktive Prostata-Segmentierung mit einer Kreisvorlage in einer MRT-Aufnahme. Die oberen vier Bilder zeigen die resultierende Kontur (rot), wenn der benutzerdefinierte Saatpunkt näher an den Rand der Prostata verschoben wurde. Im oberen linken Bild zum Beispiel befindet sich der Saatpunkt näher am linken Rand der Prostata, daher tendiert das Segmentierungsergebnis auch zu einer Übersegmentierung im linken Bereich der Prostata. Allerdings ermög-

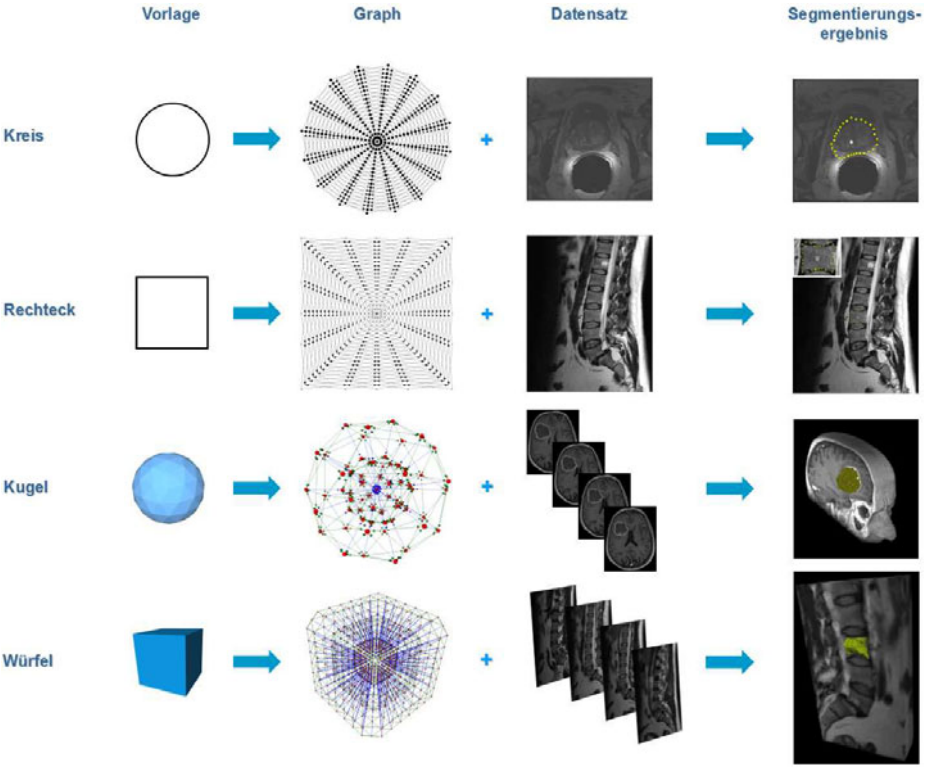

Abb. 1. Verschiedene Beispiele für Vorlagen, mit denen unterschiedliche Pathologien in 2D und 3D segmentiert wurden: Eine Kreisvorlage wurde dazu genutzt, einen Graphen aufzubauen und die Prostata zu segmentieren (erste Zeile), eine Rechteckvorlage wurde verwendet, um Wirbelkonturen in einzelnen 2D-Schichten zu bestimmen (zweite Zeile), eine Kugelvorlage diente dazu, Glioblastoma Multiforme (GBM) zu segmentieren (dritte Zeile), und für die Bestimmung ganzer Wirbelkörper in 3D kam eine Würfelvorlage zum Einsatz (untere Zeile). Bei allen Beispielen wurde der Graph vom benutzerdefinierten Saatpunkt innerhalb der Pathologie aus konstruiert.

Abb. 2. Mehrere Screenshots aus einem Video, die die interaktive Echtzeit-Konturierung von Wirbelkörpern und Bandscheiben in einer sagittalen Schicht einer Magnetresonanztomographie (MRT)-Aufnahme zeigen (von links nach rechts). Der Mittelpunkt des Graphen ist in Weiß dargestellt und kann vom Benutzer interaktiv auf dem Bild verschoben werden, die kleinen schwarzen Boxen zeigen die Ecken der Rechteckvorlage an, und die roten Punkte stellen das Ergebnis der Segmentierung da.

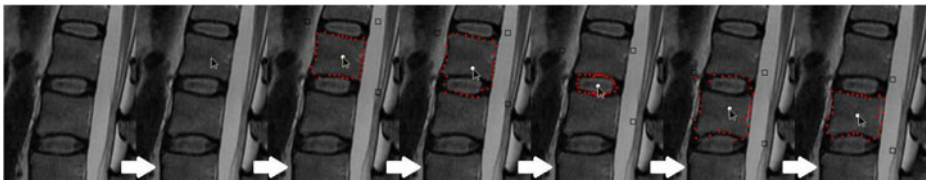

lichen das interaktive Verhalten und die Echtzeit-Rückmeldung des Ansatzes es dem Benutzer, schnell ein zufriedenstellendes Segmentierungsergebnis zu finden (linkes unteres Bild). Zum visuellen Vergleich des Segmentierungsergebnisses aus dem linken unteren Bild ist im rechten unteren Bild die Maske (blau) einer rein manuellen Segmentierung auf derselben 2D-Schicht dargestellt.

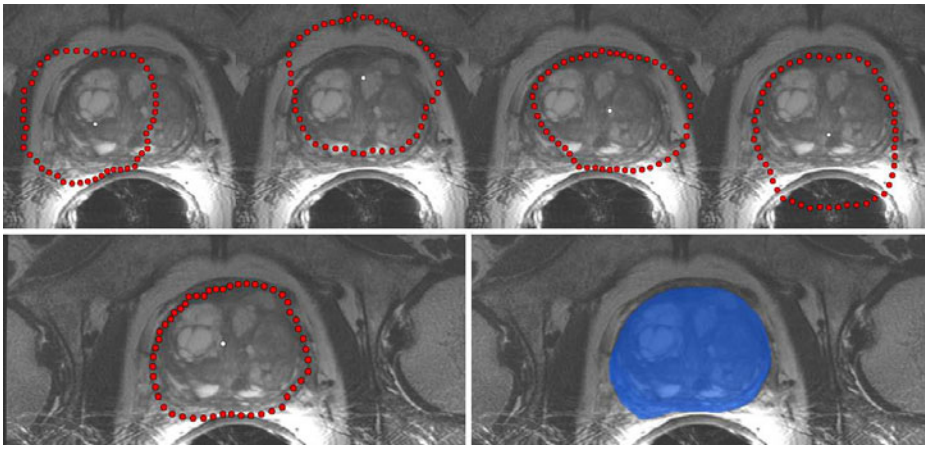

Abb. 3. Interaktive Prostata-Segmentierung mit einer Kreisvorlage in einer MRT-Aufnahme: Die oberen vier Bilder zeigen die resultierende Kontur (rot), wenn der benutzerdefinierte Saatpunkt näher an den Rand der Prostata verschoben wurde. Im oberen linken Bild z.B. befindet sich der Saatpunkt näher am linken Rand der Prostata, daher tendiert das Segmentierungsergebnis auch zu einer Übersegmentierung im linken Bereich der Prostata. Allerdings ermöglicht es die interaktive Echtzeit-Rückmeldung des Ansatzes dem Benutzer, schnell ein zufriedenstellendes Segmentierungsergebnis zu finden (linkes unteres Bild). Zum visuellen Vergleich des Segmentierungsergebnisses aus dem linken unteren Bild ist im rechten unteren Bild die Maske (blau) einer rein manuellen Segmentierung auf derselben 2D-Schicht dargestellt.

Tabelle 1. Ergebnisse: Mittelwert μ und Standardabweichung σ sind für manuell und automatisch segmentierte Volumina (cm^3) der Pathologien und für die Dice Similarity Koeffizienten (DSC) [7] zwischen den manuellen und automatischen Segmentierungen angegeben. Abkürzungen: Glioblastoma Multiforme (GBM), Hypophysenadenome (HA), Zerebrale Aneurysmen (ZA), Prostatadrüsen (PD) und Wirbelkörper (WK).

Pathologie	min./max. [cm^3]		$\mu \pm \sigma$ [cm^3]		$\mu \pm \sigma$
(Anzahl)	manuell	automatisch	manuell	automatisch	DSCs [%]
GBM (50)	0,47/119,28	0,46/102,98	23,66 ± 24,89	21,02 ± 22,90	80,37 ± 8,93
HA (10)	0,84/15,57	1,18/14,94	6,30 ± 4,07	6,22 ± 4,08	77,49 ± 4,52
ZA (3)	0,45/4,02	0,35/4,22	1,90 ± 1,88	2,02 ± 1,99	72,66 ± 10,71
PD (10)	13,67/66,16	13,29/67,56	31,32 ± 17,45	33,58 ± 18,88	78,94 ± 10,85
WK 2D (9)	0,25/0,51	0,24/0,49	0,42 ± 0,072	0,40 ± 0,073	90,97 ± 2,20
WK 3D (10)	15,42/33,83	16,64/28,78	24,97 ± 6,15	23,48 ± 5,12	81,33 ± 5,07

4 Diskussion

Der Fortschritt in diesem Beitrag besteht darin, dass Algorithmen (wie der Square-Cut) in einen echtzeitfähigen Ansatz transformiert und getestet wurden. Im Gegensatz zu anderen interaktiven Ansätzen [8, 9], die meistens eine aufwändige Initialisierung benötigen, wird durch diesen Ansatz eine interaktive Echtzeit-Segmentierung ermöglicht, da nur ein benutzerdefinierter Saatpunkt innerhalb des zu segmentierenden Objektes benötigt wird. Außerdem kann durch die spezielle geometrische Konstruktion des Graphen die Echtzeitfähigkeit (insbesondere in 3D) je nach Rechnerausstattung sichergestellt werden, z.B. durch eine geringere Strahlen- und Knotendichte. Darüber hinaus können Grauwertinformationen im Bereich des Saatpunktes automatisch analysiert und für die Segmentierung genutzt werden. Damit „verpackt“ der Ansatz in seinem interaktiven Verhalten Parameter und verhindert dadurch, dass der Benutzer diese definieren muss. Auch wenn die Evaluation gezeigt hat, dass der Ansatz mit (festen) Saatpunkten gute Ergebnisse liefert, ist es (im Gegensatz zu einer interaktiven Segmentierung in 2D) recht schwierig, ein Objekt in 3D interaktiv zu segmentieren. Das liegt daran, dass der Saatpunkt im Raum verschoben wird und dabei die Seiten eines 3D-Objekts für eine zufriedenstellende Segmentierung überwacht werden müssen. Das Verfahren soll daher als nächstes zu einer Art iterativem Ansatz erweitert werden. Dabei segmentiert der Benutzer (interaktiv) zuerst mehrere Konturen in 2D. Anschließend wird ein 3D-Graph zur interaktiven Segmentierung aufgebaut, der allerdings in den drei vorher segmentierten 2D-Schichten bereits fixiert ist (Abb. 4). Diese 2D-Fixierungen schränken die Anzahl der möglichen s-t-Schnitte massiv ein [10] und unterstützen den Benutzer, auch in 3D einen geeigneten Saatpunkt interaktiv zu finden.

Danksagung. Ich danke den Neurochirurgen des UKGM in Marburg für ihr Mitwirken an der Studie, Robert Schwarzenberg für die Implementierung des Cube-Cut-Algorithmus, Fraunhofer MeVis in Bremen für die MeVisLab-Lizenz,

Abb. 4. Iterative Segmentierung: Zuerst werden mehrere Wirbelkonturen (obere Reihe, rot) mit einem interaktiven 2D-Ansatz wie aus Abb. 2 segmentiert. Danach wird ein 3D-Graph zur Segmentierung des Wirbelkörpers in 3D konstruiert, bei dem die drei schon segmentierten 2D-Konturen im 3D-Graphen fixiert sind. Diese Restriktionen des 3D-Graphen beeinflussen und unterstützen die Segmentierung der restlichen Konturen des Wirbelkörpers (grüne Konturen in der unteren Reihe). Die roten Konturen aus den Bildern der unteren Reihe korrespondieren mit den Konturen der Bilder der oberen Reihe. Rechts unten ist die voxelisierte Maske des Wirbelkörpers eingeblendet.

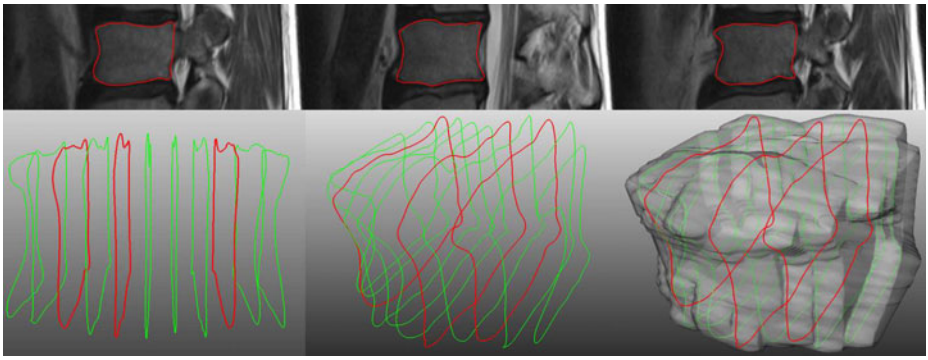

Edith Egger-Mertin für das Korrekturlesen und Fedorov et al. für die Prostatadatensätze: `http://www.spl.harvard.edu/publications/item/view/2174`

Literaturverzeichnis

1. Steger S, Sakas G. FIST: fast interactive segmentation of tumors. Abdom Imaging. 2011;7029:125–32.
2. Heckel F, Moltz JH, Tietjen J, et al. Sketch-based editing tools for tumor segmentation in 3D medical images. Comput Graph Forum. 2013.
3. Boykov Y, Kolmogorov V. An experimental comparison of min-cut/max-flow algorithms for energy minimization in vision. IEEE PAMI. 2004;26(9):1124–37.
4. Li K, Wu X, Chen DZ, et al. Optimal surface segmentation in volumetric images: a graphtheoretic approach. IEEE PAMI. 2006;28(1):119–34.
5. Egger J, Kapur T, Dukatz T, et al. Square-cut: a segmentation algorithm on the basis of a rectangle shape. PLoS One. 2012;7(2):e31064.
6. Egger J, Freisleben B, Nimsky C, et al. Template-cut: a pattern-based segmentation paradigm. Sci Rep. 2012;2(420).
7. Zou KH, Warfield SK, Bharatha A, et al. Statistical validation of image segmentation quality based on a spatial overlap index. Acad Radiol. 2004;2:178–89.
8. Boykov Y, Jolly MP. Interactive graph cuts for optimal boundary and region segmentation of objects in N-D images. Proc IEEE ICCV. 2001;1:105–22.
9. Vezhnevets V, Konouchine V. GrowCut-interactive multi-label N-D image segmentation. Proc Graphicon. 2005; p. 150–6.
10. Egger J, Bauer MHA, Kuhnt D, et al. A flexible semi-automatic approach for glioblastoma multiforme segmentation. Biosignal. 2010;60:1–4.

SpringerPlus
a SpringerOpen Journal

RESEARCH Open Access

Development of an open source software module for enhanced visualization during MR-guided interstitial gynecologic brachytherapy

Xiaojun Chen[1] and Jan Egger[2*]

Abstract

In 2010, gynecologic malignancies were the 4th leading cause of death in U.S. women and for patients with extensive primary or recurrent disease, treatment with interstitial brachytherapy may be an option. However, brachytherapy requires precise insertion of hollow catheters with introducers into the tumor in order to eradicate the cancer. In this study, a software solution to assist interstitial gynecologic brachytherapy has been investigated and the software has been realized as an own module under (3D) Slicer, which is a free open source software platform for (translational) biomedical research. The developed research module allows on-time processing of intra-operative magnetic resonance imaging (iMRI) data over a direct DICOM connection to a MR scanner. Afterwards follows a multi-stage registration of CAD models of the medical brachytherapy devices (template, obturator) to the patient's MR images, enabling the virtual placement of interstitial needles to assist the physician during the intervention.

Introduction

In 2010, gynecologic cancer – including cervical, endometrial, and vaginal/vulvar types – is with over 80,000 new cases and over 25,000 deaths the 4th leading cause of death in women in the United States (American Cancer Society 2010). However, depending on the type and stage of the cancer, different treatment approaches may be performed, like radiation including a course of brachytherapy for patients with extensive locally advanced or recurrent pelvic disease. Hereby, brachytherapy enables the placement of radioactive sources direct inside the cancerous tissue that deliver very high doses of radiation and for interstitial gynecologic brachytherapy, catheters are guided into place through holes in a so called template (Figure 1, left) sutured to the patient's perineum. Viswanathan et al. conducted a first prospective trial of real-time magnetic resonance image (MRI)-guided catheter placement in gynecologic brachytherapy in a 0.5T unit (Viswanathan et al. 2006, 2013), and Lee et al. in a computed tomography (CT) brachytherapy suite (Lee and Viswanathan 2012; Lee et al. 2013). In the meantime, the benefit of using magnetic resonance imaging scans to guide brachytherapy planning has been shown in other gynecologic cancer brachytherapy centers around the world and a CT/MR comparison showed that MR contoured volumes are narrower than CT (Viswanathan et al. 2007). As a result of this, the highest dose regions (D90 and D100) and the tumor volume that receives 100% dose (V100) can be increased and a T2-weighted MRI is therefore considered the gold standard for target delineation in image-based cervical cancer brachytherapy (Viswanathan et al. 2011). In Viswanathan et al. the dosimetric and clinical gains from using MRI, CT or ultrasound (US) have also been described in detail and in summary the ability to more accurately delineate tumor and surrounding normal tissue is the primary benefit in using 3D compared to the more standard practice of x-ray. Subsequent, this leads to a more precise dose escalation to the target volume while at the same time respecting dose constraints for the surrounding organs at risk (OAR). Furthermore, CT may not be possible to distinguish the cervical tumor from the surrounding normal tissues such as small bowel in CT acquisitions. In contrast, MR can determine in such

* Correspondence: egger@uni-marburg.de
[2]Department of Medicine, University Hospital of Giessen and Marburg (UKGM), Baldingerstraße, Marburg 35043, Germany
Full list of author information is available at the end of the article

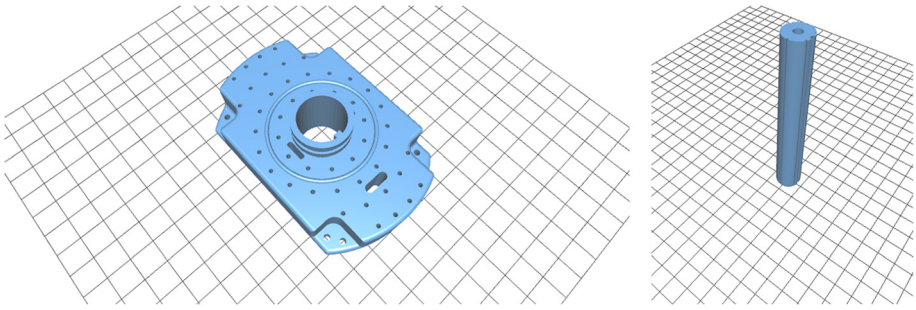

Figure 1 Two medical devices used for interstitial gynecologic brachytherapy: the template (left) is sutured to the patient's perineum and afterwards catheters are guided into place through template's holes. The obturator (right) is inserted through the large hole in the middle of the template into the vaginal canal (amongst others for better template stabilization). The 3D CAD models in STL format are freely available for download: https://github.com/xjchen/igyne/tree/master/scene for template and obturator for template and obturator. Last accessed on March 2014.

cases the size, location, and paracervical involvement of the tumor and its relations to the applicator.

Other working in the field of radiation therapy to support cervical cancer treatment are Staring et al. (2009). Staring et al. addressed the registration of cervical data using mutual information (MI) of not only image intensity, but also features that describe local image structure. The presented algorithm was compared to a standard approach, based on the mutual information of image intensity only showing that the registration error can be improved at important tissue interfaces, like the bladder with the clinical target volume (CTV), and the interface of the rectum with the uterus and cervix. Krishnan and Sujatha (2010) worked on the segmentation of cervical cancer images using Active Contour Models (ACM) (Kass et al. 1987, 1988), and introduced a method for automatic extraction of object region and boundary from the background for cell nucleus segmentation of cervical cancer images. Therefore, the method starts computing a threshold based on the clusters automatically calculated by a K-means clustering algorithm, whereby the cluster center of this threshold region, acts as a seed for further processing. Ultimately, the object region is extracted from the object boundary and a gray scale cluster. A method for simultaneous non-rigid registration, segmentation, and tumor detection in MRI-guided cervical cancer radiation therapy using a unified Bayesian framework has recently been introduced by Lu et al. (2012). The presented framework can generate a tumor probability map while progressively identifying the boundary of an organ of interest based on the achieved non-rigid transformation. In addition, the framework is able to handle the challenges of significant tumor regression and its effect on surrounding tissues and the proposed methods help with the delineation of the target volume and other structures of interest during the treatment of cervical cancer with external beam radiation therapy (EBRT). However, the purpose of this contribution is to investigate a research software to support 3D-guided interstitial gynecologic brachytherapy during the intra-operative stage and to the best of our knowledge such a tool has not yet been described and there is no commercial software currently available. The software exists as a free module available under 3D Slicer, which is an open source software platform for biomedical research and research highlights include linking a diagnostic imaging set in *real-time* to a 3D CAD model of the template (Figure 1, left) and the obturator (Figure 1, right), which enables the identification of catheter location in the 3D imaging model with *real-time* imaging feedback. Furthermore, the introduced software allows patient-specific pre-implant evaluation by assessing the placement of interstitial needles prior to an intervention via virtual template matching with a diagnostic scan (note: this contribution relates to a previously published work in *SpringerPlus* (Egger 2013). There, an overall image-guided therapy system for interstitial gynecologic brachytherapy in a multimodality operating suite was introduced).

The rest of this article is organized as follows: Section 2 presents the material and the methods. Section 3 presents the results of our experiments, and Section 4 concludes and discusses the paper and outlines areas for future work.

Materials and methods

This section describes the Material and Methods that have been used for this study, resulting in an open source software module for enhanced visualization during MR-guided interstitial gynecologic brachytherapy. Thereby, this section starts with a paragraph about the *Equipment, Data and CAD Models* that have been used for this study. Afterwards, the software platform *3D Slicer* (Slicer) is introduced, within the new software module has been realized. In the next paragraph the *Software Design* for the module is presented. Finally, the last paragraph of this section describes the detailed *Application Workflow* for the presented software module.

Equipment, data and CAD models

The Advanced Multimodality Image-Guided Operating (AMIGO) suite at Brigham and Women's hospital (BWH) allows intraoperative 3 Tesla MR imaging and has been used to develop and test the introduced software module for enhanced visualization during MR-guided interstitial gynecologic brachytherapy. Moreover, the intraoperative MRI (iMRI) data used for this study (acquired in AMIGO) is freely available for download (Egger J, Kapur T, Viswanathan AN, GYN Data Collection, The National Center for Image Guided Therapy) (Kapur et al. 2012):

http://www.spl.harvard.edu/publications/item/view/2227. Last accessed on March 2014.

The CAD models like the interstitial template and the vaginal obturator (Figure 1) needed for the software module (see section *Application workflow*) have been generated using a CAD software from SolidWorks (Dassault Systèmes SolidWorks Corp., MA). Therefore, the gynecological CAD models have been reverse-engineered by measuring the precise dimensions from the clinically devices and afterwards converted to an industry standard format (STL). These models are also available online:

https://github.com/xjchen/igyne/tree/master/scene for template and obturator. Last accessed on March 2014

3D Slicer

The introduced software of this contribution has been developed within 3D Slicer or Slicer (http://www.slicer.org/), which is a free and open source software platform for visualization and image analysis (Pieper et al. 2004, 2006; Surgical Planning Laboratory (SPL) 2014) and a detailed review of the current capabilities of Slicer has been recently been published by Fedorov et al. (2012). Slicer is a cross-platform software, which can be used for different biomedical research tasks like visualization, segmentation, registration, volume measurements and network communications via DICOM (e.g. direct to a scanner or PACS systems). Several of these tasks are implemented within Slicer as own modules, like the Volume Rendering module, the DICOM module, the Change Tracker module (Konukoglu et al. 2008) and the EM Segmentation module (Rannou et al. 2009; Pohl et al. 2007). This modular concept allows researchers and programmers to develop software modules for new tasks and provide them to the community. Slicer realizes the *Model-View-Controller* (MVC) design pattern and therefore the classes which implement the core of 3D Slicer, as well as loadable modules, are organized into three main groups (Fedorov et al. 2012). As common for the MVC pattern, the data organization and serialization is handled by the *Model*. Thereby the *Model* is supported by the Medical Reality Markup Language (MRML), which defines the hierarchies of the data elements and the APIs for accessing and serializing the individual nodes. Furthermore, a C++ class library is used to instantiate the MRML nodes and organize them into a coherent internal data structure called the *MRML scene*, which maintains the links between the individual data items, their visualization and any other persistent state of the application and modules. The visual elements of the application are provided by the *View* to the user. The functionality consists of the Graphical User Interface (GUI) and *displayable manager* classes of the Slicer core, which maintain consistency between the internal MRML state of the Model and the visual appearance of the GUI. The processing and analysis functionality of the application core is encapsulates by the *Controller* and does not depend on the existence of GUI. However, it is fully aware of the MRML data structures, and the communication between the *View* and the *Controller* takes indirectly place through changes in MRML data structures. In addition, the *Controller* uses the MRML nodes for storing the computation results and the *View* receives event updates from the MRML scene and individual nodes, which then update the visualization elements.

Software design

This research software module has been developed as a first step for assisting in MR-guided gynecologic brachytherapy in a multi-modal operating suite like AMIGO. The high level design of the software module is shown in Figure 2; two components (GUI and Logic) are created for observing changes in the MRML scene and for processing events (Fedorov et al. 2012; slicer.org/slicerWiki/index.php/Documentation/4.1/Developers/MRML 2012). Thereby, the software module for MR-Guided Interstitial Gynecologic Brachytherapy, has been developed as an own *loadable module* for Slicer (note: details on different mechanisms of writing Slicer extension modules, including loadable modules are available in (Fedorov et al. 2012)).

Application workflow

Figure 3 shows the diagram of the presented module consisting of the workflow and functions for the enhanced visualization during MR-guided interstitial gynecologic brachytherapy (green), the relevant modules that have been used from Slicer4 (blue) and the supporting algorithms and techniques (orange). The workflow starts with loading of the MR image data and the CAD models, and ends with the selection of the interstitial needles and is described in detail as follows:

1. Loading of Applicator CAD models and MR images: The CAD models for the template and obturator are loaded from disk while the patient is imaged in the

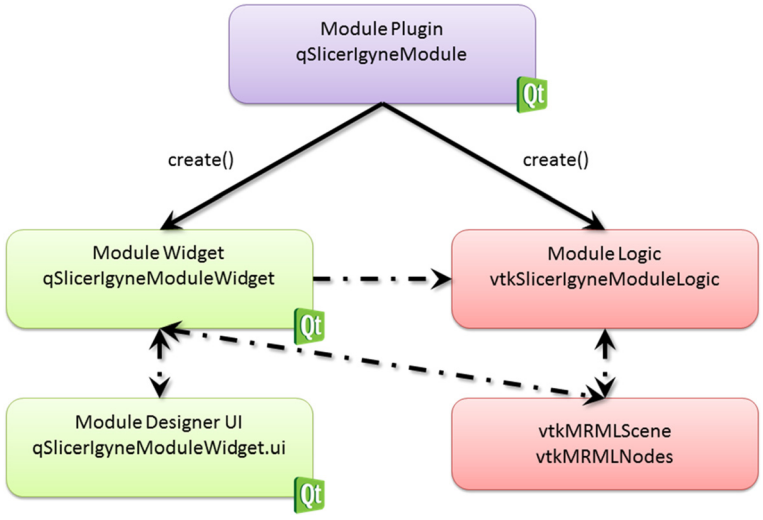

Figure 2 The overall infrastructure of the software module: two components (GUI and Logic) are created for observing changes in the Medical Reality Markup Language (MRML) scene and for processing events.

MR scanner. When imaging is complete (with the template sutured to the perineum and the obturator placed in the vaginal canal), the acquired images are automatically transferred to this module via the Slicer DICOM module.

2. Initial registration of CAD model of the Template to MR images: A rigid registration (or transformation) between the CAD model of the template and its appearance in the MRI is computed in two steps. First, the user uses the mouse to identify three clearly visible landmarks in the template in the MRI scan (as shown in Figure 4). The registration transformation is computed using the closed form solution to the absolute orientation problem (Horn 1987). This step is accomplished using the following three modules in 3D Slicer: the "Annotations" module for manual marking of landmarks by user, and the "Fiducial Registration" and "Transforms" modules for obtaining the rigid registration between corresponding sets of points.
3. Registration Refinement: The initial registration obtained above is refined using additional points on the superior surface of the template (the surface that is in contact with the patient perineum). The points on this surface of the CAD model are computed using the locations of the holes. The points on this surface in the MRI scan are obtained interactively from the user; the user is first prompted to create a rough region of interest that encompasses the template, and then to provide a threshold that highlights (approximately) the very bright surgical lubricant filled template holes in the MRI. This set of points is also overlaid as a 3D surface on top of the CAD model, to allow the user to visualize the agreement between the two. The registration refinement method is the Iterative Closest Point (ICP) algorithm (Besl and McKay 1992), which computes the least-squares distance between two sets of point clouds. The ICP algorithm is described as follows (Xiaojun et al. 2007).

ICP Registration: Suppose the two point sets under the CAD template model and MR image coordinate system are respectively $P = \{p_i,\ i = 0,1,2,\ldots,k\}$, and $U = \{u_i,\ i = 0,1,2,\ldots,n\}$, then:

- Compute the closest points: For each point in U, compute the corresponding closest point in P that yields the minimum distance. Let Q denote the resulting set of closest points, $P = \{q_i,\ i = 0,1,2,\ldots,n\}$.
- Compute the registration between U and Q via the quaternion-based least squares method so that $\min_{R,T} \sum \|q_i - (Ru_i + T)\|^2$, where R is 3×3 rotation matrix, and T is 3×1 translation matrix.
- Apply the registration, i.e. let $U_1 = RU + T$.
- Compute the mean square error between U_1 and Q, and terminate the process if it falls below a preset threshold $\varepsilon > 0$ specifying the desired precision of the registration, otherwise, perform the iteration with the substitution of U_1 for U.

The modules of 3D Slicer used in this step are: "Model Maker" to create a 3D surface model from the thresholded image using the Marching Cubes algorithm (Lorensen and Cline 1987).

4. Visualization of Registration: The registration results are provided for easy visual inspection by displaying

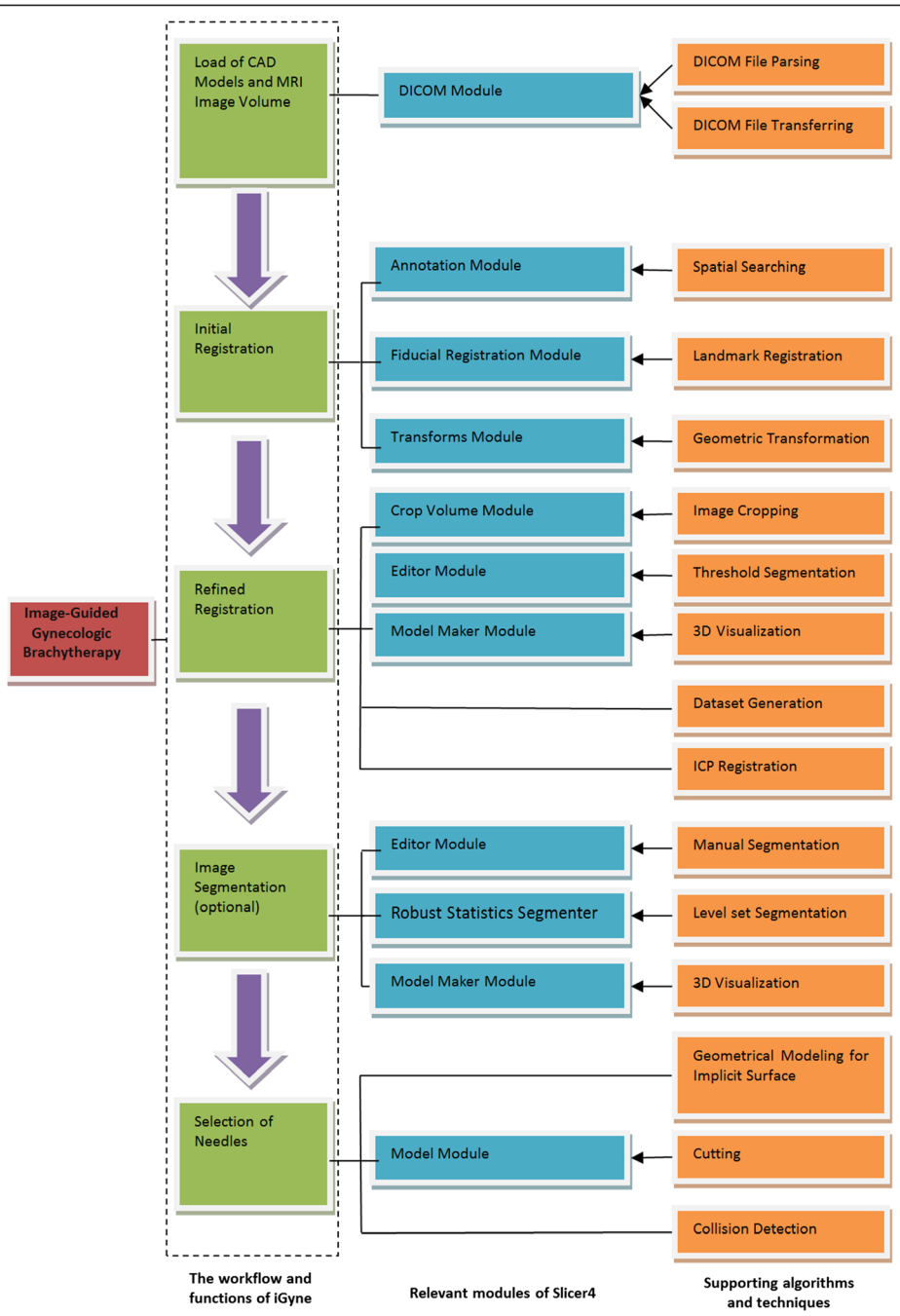

Figure 3 Diagram of the presented module consisting of the workflow and functions for the enhanced visualization during MR-guided interstitial gynecologic brachytherapy (green), the relevant modules that have been used from Slicer4 (blue) and the supporting algorithms and techniques (orange). The workflow starts with loading of the MR image data and the CAD models, and ends with the selection of the interstitial needles.

the intersections of the template and the obturator with the 2D axial, sagittal, and coronal planes. If this result is not visually satisfactory, the capability of manual refinement is also available.
These steps are accomplished using the "Model" and "Transforms" module in 3D Slicer.

5. Image Segmentation: To allow the user to visualize the 3D renderings of the applicator in the context of the tumor and organs of interest, the tumor, bladder, and rectosigmoid can be manually or semi-automatically segmented in the MR scan using the Slicer modules: "Editor", "Robust Statistics

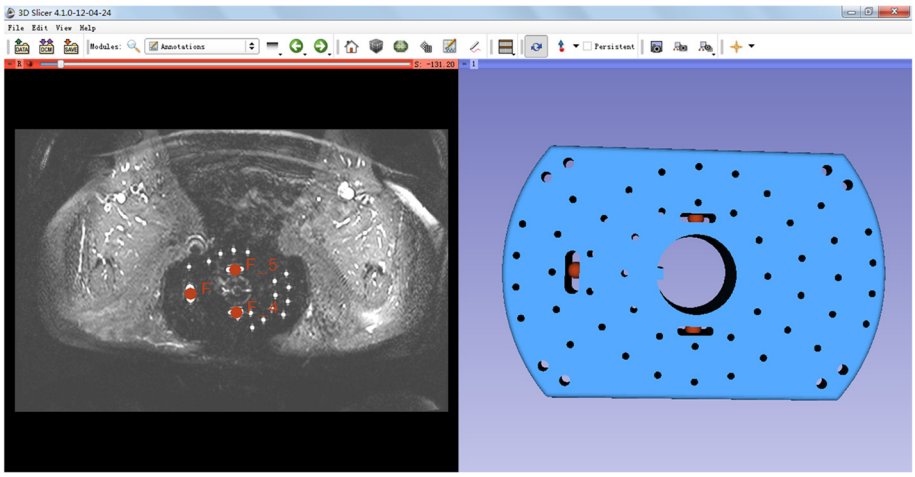

Figure 4 The three corresponding point pairs (red) used for an initial registration: the left image shows the user-defined landmarks in the MR image, the right image shows corresponding landmark positions in the CAD model of the template.

Segmenter" (Gao et al. 2012) or "Grow Cut Segmenter" (Vezhnevets and Konouchine 2005).

6. Needle Selection and Display of Virtual Needles relative to Applicator CAD models and Tumor Segmentation: After the reconstruction of the 3D model of the tumor, virtual needles that originate from the template and penetrate the tumor can be automatically selected by the module using a collision detection algorithm based on OBB (Oriented Bounding Box) trees (Gottschalk et al. 1996). For the triangular mesh of each needle model and the tumor model, OBB trees are constructed top-down, by recursive subdivision, and each leaf node of the OBB tree corresponds to a single triangle in the mesh. Effectively an OBB of the tumor model is compared against an OBB of each needle model. If the two OBBs intersect, then the children of the second OBB are compared against the current OBB of the first tree recursively, until the contacting cells are found. This process is conducted for each virtual needle, and the needles whose trajectory intersects with the tumor are selected. Finally, the selected virtual needles are automatically annotated on a schematic of the template (that is displayed in the user interface) and rendered in the 2D and 3D views, with the insertion depth independently adjustable for each needle. This allows for ease of visualization of spatial relationships among the needles, tumors, and surrounding anatomical structures.

Results

During this study, a first free and open source research software module for the 3D Slicer platform supporting MR-guided interstitial brachytherapy of gynecologic cancer has been investigated. The principle of the module has been pre-published in a recent research disclosure (Egger et al. 2012a), however, algorithmic details are presented in this publication. The software module and the interface is illustrated in the screenshots of Figures 5 and 6. The two screenshots show the CAD models of the interstitial template (blue) and the obturator (green) which have been fitted to intraoperative MRI scans of AMIGO patients. In more detail, Figure 5 presents a refined registration result of the template and the obturator, in an axial (upper left window), a sagittal (lower left window), a coronal (lower right window) and a 3D view (upper right window). In Figure 6, the manual segmented tumor is also visualized (brown) and on the left side of the interface the interstitial planning sheet is provided that allows virtual pre-planning of the depth and length of single interstitial needles. In this case, several needles (pink and green) around the obturator have been pre-planned to target the tumor. Furthermore, the software module enables rendering of the pre-planned interstitial needles in different 2D slices (right side of Figure 6). The software module has been developed in C++ under Visual Studio (Version 9) and in our implementation the planning could be performed within a few minutes on a Laptop with Intel Core i5-2520M CPU, 2 × 2.5 GHz, 4 GB RAM, Windows 7 Version, Service Pack 1, 32Bit. Moreover, the module is open source and public available as a loadable module for Slicer:

https://github.com/xjchen/igyne. Last accessed on March 2014

Note: in the meantime there has been a study about catheter segmentation for MR-Guided gynecologic cancer brachytherapy which uses the successor of our software module (Pernelle et al. 2013):

https://github.com/gpernelle/iGyne. Last accessed on March 2014

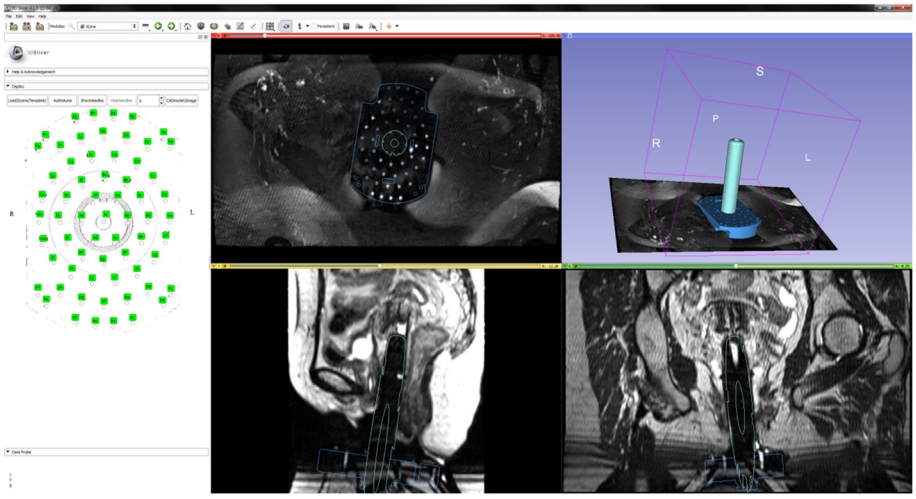

Figure 5 A screenshot of the refined registration result of the template (blue) and the obturator (green), in an axial (upper left window), a sagittal (lower left window), a coronal (lower right window) and a 3D view (upper right window).

The dataset used for the screenshots of Figures 4, 5 and 6 is available from:

https://github.com/xjchen/igyne/tree/master/Sample%20data. Last accessed on March 2014

Conclusions

In this contribution, we introduced a research software module to support interstitial gynecologic brachytherapy. The module has been implemented and tested within the free open source software platform for biomedical research, called 3D Slicer (or just Slicer). The implementation and workflow of the designed Slicer module has been described in detail and research highlights include:

- on-time processing of intra-operative MRI data,
- a multi-stage registration of a template
- and the virtual placement of interstitial needles.

The presented software module allows on-time processing of the intra-operative MRI data realized via a DICOM connection to the scanner. Afterwards, a multi-stage registration of the template and the obturator to the patient's dataset enables a virtual placement of

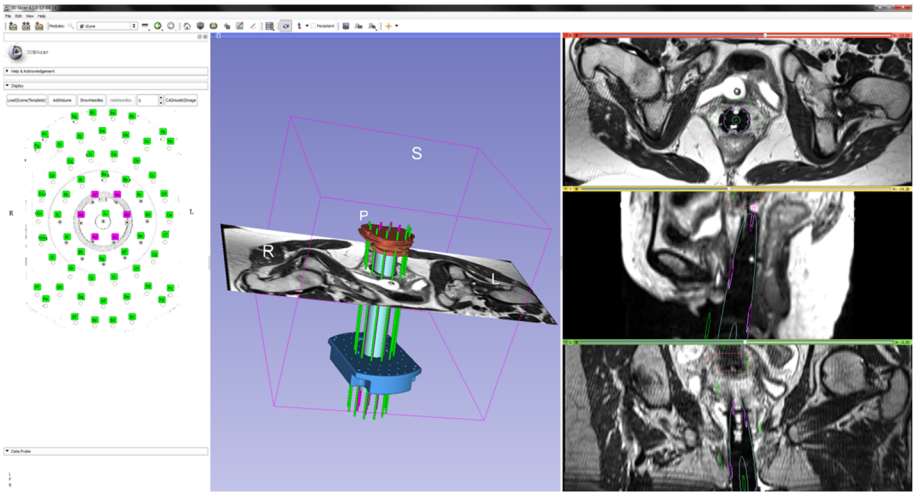

Figure 6 A screenshot of the visualization of the segmented tumor (brown) and selected needles (pink and green) in a 3D view. Moreover, it enables rendering of the planned interstitial needles in different 2D slices (right windows).

interstitial needles to assist the physician during the intervention.

Areas for future work include the enhancement of the registration method by using the obturator as well as additional physical markers that can be (semi-)automatically detected by image processing. Another area of future work includes the integration of intra-operative navigation, like intraoperative ultrasound (iUS), electromagnetic (EM) tracking or optical navigation via the OpenIGTLink network protocol (Tokuda et al. 2009; Egger et al. 2012b) to support applicator guidance (note: in contrast to interventions in the male pelvis where navigation systems have been used (Tokuda et al. 2008; Fischer et al. 2008) medical navigation systems have not yet been successfully introduced for gynecological interventions). Furthermore, we plan a (semi-)automatic segmentation of the organs at risk (OAR) with a graph-based approach (Egger et al. 2011a, 2012c) that we have already applied to the bladder (Egger et al. 2010, 2011b), and the integration of a real-time dose calculation engine (Cormack et al. 2000; Haie-Meder et al. 2005; Pötter et al. 2006).

Competing interest

All authors in this paper have no potential conflict of interests.

Authors' contributions

Conceived and designed the experiments: XC. Performed the experiments: XC. Analyzed the data: XC. Contributed reagents/materials/analysis tools: XC JE. Wrote the paper: XC JE. Both authors read and approved the final manuscript.

Acknowledgements

The authors would like to acknowledge the support of the *AMIGO* team in enabling this study, Kanokpis Townamchai, M.D. for performing the manual segmentations of the medical images, Sam Song, Ph.D. for generating the CAD models of gynecologic devices and the members of the *Slicer Community* for creating a platform that enabled the software module. Dr. Xiaojun Chen receives support from NSFC (National Natural Science Foundation of China) grants 51005156 and 81171429.

Author details

[1]Institute of Biomedical Manufacturing and Life Quality Engineering, School of Mechanical engineering, Shanghai Jiao Tong University, Dong Chuan Road 800, Shanghai Post Code: 200240, China. [2]Department of Medicine, University Hospital of Giessen and Marburg (UKGM), Baldingerstraße, Marburg 35043, Germany.

Received: 11 September 2013 Accepted: 2 January 2014
Published: 31 March 2014

References

(2012) Slicer MRML Overview., http://www.slicer.org/slicerWiki/index.php/Documentation/4.1/Developers/MRML. Last accessed on March, 2014

American Cancer Society (2010) Cancer statistics., http://www.cancer.org/acs/groups/content/@epidemiologysurveilance/documents/document/acspc-026238.pdf. Last accessed on March, 2014

Besl P, McKay N (1992) A method for registration of 3-D shapes. IEEE Trans Pattern Anal Mach Intell 14(2):239–256

Cormack RA, Kooy H, Tempany CM, D'Amico AV (2000) A clinical method for real-time dosimetric guidance of transperineal 125I prostate implants using interventional magnetic resonance imaging. Int J Radiat Oncol Biol Phys 46(1):207–214

Egger J (2013) Image-guided therapy system for interstitial gynecologic brachytherapy in a multimodality operating suite. SpringerPlus 2:395

Egger J, Bauer MHA, Kuhnt D, Carl B, Kappus C, Freisleben B, Nimsky C (2010) Nugget-cut: a segmentation scheme for spherically- and elliptically-shaped 3D objects, 32nd Annual Symposium of the German Association for Pattern Recognition (DAGM), LNCS 6376. Springer Press, Darmstadt, Germany, pp 383–392

Egger J, Colen R, Freisleben B, Nimsky C (2011a) Manual refinement system for graphbased segmentation results in the medical domain. J Med Syst, 2012 Oct;36(5):2829-39, Epub 2011 Aug 9

Egger J, Viswanathan A, Kapur T (2011b) Bladder segmentation for interstitial gynecologic brachytherapy with the nugget-Cut approach, 4th NCIGT and NIH Image Guided Therapy Workshop, Arlington, Virginia, USA

Egger J, Kapur T, Viswanathan AN (2012a) Medical system for gynecologic radiation therapy., Technical Disclosure, Research Disclosure, ID 577033, Published in the Research Disclosure Journal 5/12

Egger J, Tokuda J, Chauvin L, Freisleben B, Nimsky C, Kapur T, Wells WM III (2012b) Integration of the OpenIGTLink network protocol for image-guided therapy with the medical platform MeVisLab. Int J Med Robot 8(3):282–290, doi:10.1002/rcs.1415. Epub 2012 Feb 28

Egger J, Freisleben B, Nimsky C, Kapur T (2012c) Template-cut: a pattern-based segmentation paradigm. Sci Rep 2(420)

Fedorov A, Beichel R, Kalpathy-Cramer J, Finet J, Fillion-Robin J-C, Pujol S, Bauer C, Jennings D, Fennessy F, Sonka M, Buatti J, Aylward SR, Miller JV, Pieper S, Kikinis R (2012) 3D slicer as an image computing platform for the quantitative imaging network. Magn Reson Imaging 30(9):1323–1341, PMID: 22770690

Fischer GS, Iordachita I, Csoma C, Tokuda J, Dimaio SP, Tempany CM, Hata N, Fichtinger G (2008) MRI-compatible pneumatic robot for transperineal prostate needle placement. IEEE ASME Trans Mechatron 13(3):295–305

Gao Y, Kikinis R, Bouix S, Shenton M, Tannenbaum A (2012) A 3D interactive multi-object segmentation tool using local robust statistics driven active contours. Med Image Anal 16(6):1216–1227, doi:10.1016/j.media.2012.06.002. Epub 2012 Jul 6

Gottschalk S, Lin M, Manocha D (1996) OBB-tree: a hierarchical structure for rapid interference detection, Proc. of ACM Siggraph

Haie-Meder C, Pötter R, Van Limbergen E, Briot E, De Brabandere M, Dimopoulos J, Dumas I, Hellebust TP, Kirisits C, Lang S, Muschitz S, Nevinson J, Nulens A, Petrow P, Wachter-Gerstner N, Gynaecological (GYN) GEC-ESTRO Working Group (2005) Recommendations from Gynaecological (GYN) GEC-ESTRO Working Group (I): concepts and terms in 3D image based 3D treatment planning in cervix cancer brachytherapy with emphasis on MRI assessment of GTV and CTV. Radiother Oncol 74(3):235–245, Review

Horn BKP (1987) Closed-form solution of absolute orientation using unit quaternions. J Opt Soc Am A 4:629–642

Kapur T, Egger J, Damato A, Schmidt EJ, Viswanathan AN (2012) 3-T MR-guided brachytherapy for gynecologic malignancies. Magn Reson Imaging 30 (9):1279–1290, doi:10.1016/j.mri.2012.06.003, Epub 2012 Aug 13

Kass M, Witkin A, Terzopoulos D (1987) Snakes-active contour models. Int J Comput Vis 1(4):321–331

Kass M, Witkin A, Terzopoulos D (1988) Constraints on deformable models: recovering 3D shape and nongrid motion. Artif Intell 36:91–123

Konukoglu E, Wells WM, Novellas S, Ayache N, Kikinis R, Black PM, Pohl KM (2008) Monitoring slowly evolving tumors, Proc. of 5th IEEE International Symposium on Biomedical Imaging: From Nano to Macro., pp 812–815

Krishnan N, Sujatha SNN (2010) Segmentation of cervical cancer images using active contour models, IEEE International Conference on Computational Intelligence and Computing Research (ICCIC)., pp 1–8

Lee LJ, Viswanathan AN (2012) Predictors of toxicity after image-guided high-dose-rate interstitial brachytherapy for gynecologic cancer. Int J Radiat Oncol Biol Phys, epub Jan 2012

Lee LJ, Damato A, Viswanathan AN (2013) Clinical outcomes of high-dose-rate interstitial gynecologic brachytherapy using real-time CT guidance. Brachytherapy 12(4):303–310, doi:10.1016/j.brachy.2012.11.002. Epub 2013 Mar 13

Lorensen WE, Cline HE (1987) Marching cubes: a high resolution 3D surface construction algorithm. Comput Graph 21:4

Lu C, Chelikani S, Jaffray DA, Milosevic MF, Staib LH, Duncan JS (2012) Simultaneous nonrigid registration, segmentation, and tumor detection in MRI guided cervical cancer radiation therapy. IEEE Trans Med Imaging 31(6):1213–1227

Pernelle G, Mehrtash A, Barber L, Damato A, Wang W, Seethamraju RT, Schmidt E, Cormack RA, Wells W, Viswanathan A, Kapur T (2013) Validation of catheter

segmentation for MR-guided gynecologic cancer brachytherapy. Med Image Comput Comput Assist Interv 16(Pt 3):380–387
Pieper S, Halle M, Kikinis R (2004) 3D slicer. Proceedings of the 1st IEEE International Symposium on Biomedical Imaging: From Nano to Macro 1:632–635
Pieper S, Lorensen B, Schroeder W, Kikinis R (2006) The NA-MIC Kit: ITK, VTK, pipelines, grids and 3D slicer as an open platform for the medical image computing community. Proceedings of the 3rd IEEE International Symposium on Biomedical Imaging: From Nano to Macro 1:698–701
Pohl K, Bouix S, Nakamura M, Rohlfing T, McCarley R, Kikinis R, Grimson W, Shenton M, Wells WM (2007) A hierarchical algorithm for MR brain image parcellation. IEEE Trans Med Imaging 26(9):1201–1212
Pötter R, Haie-Meder C, Van Limbergen E, Barillot I, De Brabandere M, Dimopoulos J, Dumas I, Erickson B, Lang S, Nulens A, Petrow P, Rownd J, Kirisits C, GEC ESTRO Working Group (2006) Recommendations from gynaecological (GYN) GEC ESTRO working group (II): concepts and terms in 3D image-based treatment planning in cervix cancer brachytherapy-3D dose volume parameters and aspects of 3D image-based anatomy, radiation physics, radiobiology. Radiother Oncol 78(1):67–77
Rannou N, Jaume S, Pieper S, Kikinis R (2009) New expectation maximization segmentation pipeline in slicer 3. Insight J 2009:1–47
Staring M, van der Heide UA, Klein S, Viergever MA, Pluim JPW (2009) Registration of cervical MRI using multifeature mutual information. IEEE Trans Med Imaging 28(9):1412–1421, Epub 2009 Mar 10
Surgical Planning Laboratory (SPL) (2014) 3DSlicer – a free, open source software package for visualization and image analysis., Brigham and Women's Hospital, Harvard Medical School, Boston, Massachusetts, USA. Available from: http://www.slicer.org/
Tokuda J, Fischer GS, Csoma C, DiMaio SP, Gobbi DG, Fichtinger G, Tempany CM, Hata N (2008) Software strategy for robotic transperineal prostate therapy in closed-bore MRI. Med Image Comput Comput Assist Interv 11(Pt 2):701–709
Tokuda J, Fischer GS, Papademetris X, Yaniv Z, Ibanez L, Cheng P, Liu H, Blevins J, Arata J, Golby AJ, Kapur T, Pieper S, Burdette EC, Fichtinger G, Tempany CM, Hata N (2009) OpenIGTLink: an open network protocol for image-guided therapy environment. Int J Med Robot 5(4):423–434, doi:10.1002/rcs.274
Vezhnevets V, Konouchine V (2005) Grow-cut - interactive multi-label N-D image segmentation, Proc. Graphicon., pp 150–156
Viswanathan AN, Cormack R, Holloway CL, Tanaka C, O'Farrell D, Devlin PM, Tempany C (2006) Magnetic resonance-guided interstitial therapy for vaginal recurrence of endometrial cancer. Int J Radiat Oncol Biol Phys 66:91–99
Viswanathan AN, Dimopoulos J, Kirisits C, Berger D, Pötter R (2007) Computed tomography versus magnetic resonance imaging-based contouring in cervical cancer brachytherapy: results of a prospective trial and preliminary guidelines for standardized contours. Int J Radiat Oncol Biol Phys 68(2):491–498
Viswanathan AN, Syzmonifka J, Tempany-Afdhal C, O'Farrell D, Cormack R (2013) A prospective trial of real-time magnetic resonance image-guided catheter placement in gynecologic brachytherapy. Brachytherapy 12(3):240–247, doi: 10.1016/j.brachy.2012.08.006. Epub 2013 Feb 12
Viswanathan AN, Kirisits C, Erickson BE, Pötter R (2011) Gynecologic radiation therapy: novel approaches to image-guidance and management. Springer, Berlin Heidelberg, ISBN-13: 978-3540689546
Xiaojun C, Yanping L, Yiqun W, Chengtao W (2007) Computer-aided oral implantology: methods and applications. J Med Eng Technol 31(6):459–467

doi:10.1186/2193-1801-3-167
Cite this article as: Chen and Egger: **Development of an open source software module for enhanced visualization during MR-guided interstitial gynecologic brachytherapy.** *SpringerPlus* 2014 **3**:167.

OPEN ACCESS Freely available online

PLOS ONE

Cube-Cut: Vertebral Body Segmentation in MRI-Data through Cubic-Shaped Divergences

Robert Schwarzenberg[1], Bernd Freisleben[1], Christopher Nimsky[2], Jan Egger[1,2]*

1 Department of Mathematics and Computer Science, University of Marburg, Marburg, Germany, **2** Department of Neurosurgery, University Hospital of Marburg, Marburg, Germany

Abstract

In this article, we present a graph-based method using a cubic template for volumetric segmentation of vertebrae in magnetic resonance imaging (MRI) acquisitions. The user can define the degree of deviation from a regular cube via a smoothness value Δ. The Cube-Cut algorithm generates a directed graph with two terminal nodes (s-t-network), where the nodes of the graph correspond to a cubic-shaped subset of the image's voxels. The weightings of the graph's terminal edges, which connect every node with a virtual source s or a virtual sink t, represent the affinity of a voxel to the vertebra (source) and to the background (sink). Furthermore, a set of infinite weighted and non-terminal edges implements the smoothness term. After graph construction, a minimal s-t-cut is calculated within polynomial computation time, which splits the nodes into two disjoint units. Subsequently, the segmentation result is determined out of the source-set. A quantitative evaluation of a C++ implementation of the algorithm resulted in an average Dice Similarity Coefficient (DSC) of 81.33% and a running time of less than a minute.

Citation: Schwarzenberg R, Freisleben B, Nimsky C, Egger J (2014) Cube-Cut: Vertebral Body Segmentation in MRI-Data through Cubic-Shaped Divergences. PLoS ONE 9(4): e93389. doi:10.1371/journal.pone.0093389

Editor: Yong Fan, Institution of Automation, CAS, China

Received September 26, 2013; **Accepted** March 4, 2014; **Published** April 4, 2014

Funding: The authors have no support or funding to report.

Competing Interests: The authors have declared that no competing interests exist.

* E-mail: egger@med.uni-marburg.de

Introduction

Lumbar stenosis (LS), a narrowing of any part of the lumbar spinal canal with encroachment on the neural structures by surrounding bone and soft tissue [1,2] is the most frequent reason for surgery in patients over 65 years of age [1]. While MR imaging (MRI) is considered particularly purposive for the visualization of the soft tissue, X-ray computer tomography (CT) is seen as the method of choice for preoperatively evaluating bone anatomy [3]. CT, however, exposes the patient to carcinogenic radiation while the magnetic field in MR imaging is harmless.

Sometimes, degenerative spondylolisthesis, an asymptomatic slipping forward of one lumbar vertebra on another one with an intact neural arch, can be linked to LS [1] (Figure 1). Similar to LS, degenerative spondylolisthesis primarily occurs in elderly patients, and a combination of MRI and CT is also applied for preoperative evaluations in this case. A shift towards a more frequent application of MRI, even for morphological evaluations of the bone structure, would result in less radiation exposure [3], which is also what motivates this work.

Several features of the spinal anatomy can be distinguished by their different grey values in an MR image. In most T1- and T2-weighted image slices, normal adult vertebral body bone marrow can be differentiated from the outer boundaries of the vertebral body by a homogeneously lighter grey value [4]. This is because the outer, compact cortical bone, which coats the vertebral body, results in a much darker color/lower grey value than the cancellous, spongy inner part. Thus, the grey-value difference between a voxel in the vertebral body and a voxel on the outer boundaries (e.g. cortical bone) is higher than the difference between two voxels inside the vertebral body.

This, however, does not apply to slices that depict the pedicles. Figure 2 shows that the pedicles of the vertebral arch are not considered part of the vertebral body. Nevertheless, since they are connected to the vertebral body, they belong to its outer boundaries. However, unlike the cortical bone, they define a weak, homogeneous object-background transition region. Furthermore, in Figure 3, instead of the cortical bone, the cerebrospinal fluid (CSF, surrounding the red arrow), which causes the high grey value of the spinal canal in T2-weighted images [4], defines parts of the outer boundary of the vertebral body. This is due to noise and signal distortion, resulting in an overlapping. Due to signal distortion and noise, as well as anatomical structures like the pedicles and occasional voxel outliers, the vertebral body cannot be defined by sharp boundaries in all MR image slices - a challenge every segmentation algorithm has to address.

Several approaches for vertebra segmentation have been proposed in the literature [6–21]. Some of them [6–11] belong to the 2D approaches and others [12–21] belong to the 3D approaches. As we present a novel volumetric approach in this contribution, the following state-of-the-art paragraphs introduce the 3D approaches in greater detail. [12–18] all use some kind of shape constraints and the shapes in [12,15,18] rely on training data. In contrast, [19] is a free-form segmentation approach which uses balloon forces. At the end of this background section, we discuss a training-based model which detects and labels intervertebral disks in MR images [21].

Figure 1. T2-weighted MR image showing a degenerative spondylolisthesis (red arrow) and a lumbar stenosis (green arrow).
doi:10.1371/journal.pone.0093389.g001

Klinder et al. [12] use articulated shape models for spine segmentation. Their approach considers not only individual objects (vertebrae) one at a time, but also object constellations from a more global perspective. A constellation is presented as a consecution of local vertebra coordinate systems, whereas the individual morphology of a vertebra is encoded into a triangulated surface model. Performing non-rigid deformations, the processing of an individual object happens simultaneously to the processing of all other objects, allowing different deformation processes to interact. Klinder et al. explain that in the course of this, the model is attracted to image features but that the attraction is also constrained by a former learned shape. For their method, the authors report a segmentation accuracy of 1.0 mm in average for ten thoracic CT images.

Hoad and Martel [13] describe a three-step algorithm, which segments bone from soft tissue in MR images of the spine. In the first step, the vertebral bodies are segmented, in the second step the posterior structures are segmented, and in the third step, manual corrections are made. The authors explain that in the three different stages, they combine thresholded region growing with morphological filtering and masking using set shapes. For evaluation, they registered the segmented data to a physical model of a spine which they obtained using CT scans. Hoad and Martel report that their method produces segmentation results equally suitable for registration as the *gold standard* CT data and they regard their algorithm as robust. Furthermore, they point out that different threshold levels, within visually acceptable intervals, had very little effect on the registration results. The authors conclude that in general, the accuracy of the registration relies on the similarity between actual and automatically generated surfaces as well as the precision of the digitized points used for the registration.

Štern et al. [14] make use of superquadrics to deterministically model volumetric shapes of vertebral bodies which they then align with vertebrae in 3D CT scans and MR images, for segmentation. All in all, they introduce 29 parameters to the superquadric function to obtain a vertebral-shaped geometrical model. In case the user wants to incorporate certain pathological deformations, further parameters have to be introduced. The parameters are then automatically optimized in order to achieve the most accurate alignment of the model with the vertebral body in the CT or MRI data. The optimization is driven by a combination of intensity gradient information with image intensity appearance of the bone structures and surrounding soft tissues. The method is initialized with a single point inside the vertebral body and was tested on 75 vertebrae from CT scans and 75 vertebrae in MR images. Štern et al. performed 100 segmentation experiments per vertebra by randomly displacing the initial 3D model from the ground truth pose and considered the subsequent segmentation successful if the mean radial Euclidian distance of the final 3D model from the ground truth points was less than 3 mm. For their experiments, they report an overall mean radial Euclidian distance ($\pm$standard deviation) between the final 3D models and the ground truth points of 1.17 ± 0.33 mm for CT images (success rate 94.5%) and 1.85 ± 0.47 mm for MR images (success rate 88.6%).

Aslan et al. [15] describe a graph-based method for the volumetric segmentation of vertebral bodies which incorporates shape priors. The authors obtain the required shape information from a training set of manually segmented vertebral bodies in CT data: After aligning the manual segmentation results, they determine an object region that describes the cross section of all vertebral bodies, a variability volume, consisting of the remaining

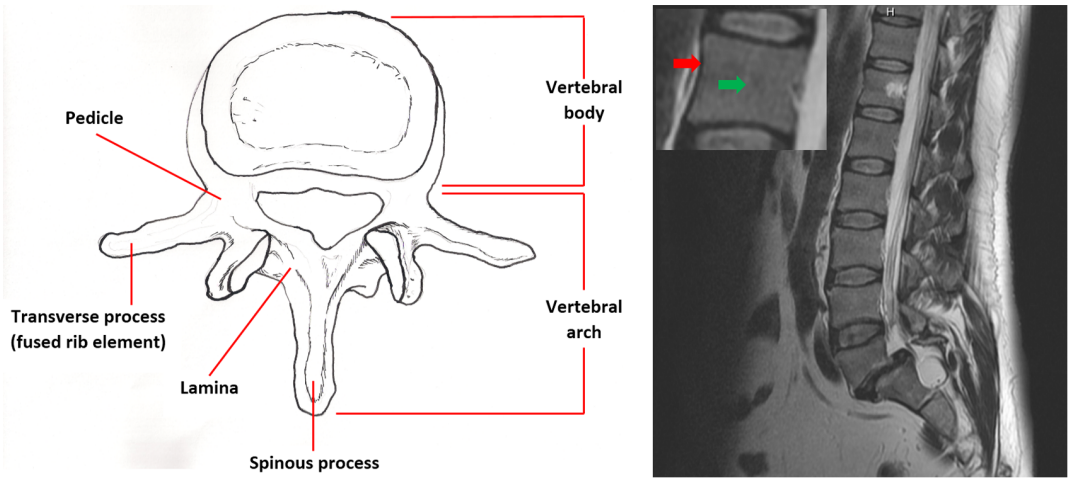

Figure 2. Vertebral anatomy: (a) illustrates the anatomy of a vertebra from a coronal view (adopted from [5]), (b) shows a sagittal T2-weighted MRI slice. The green arrow in the enlargement points to an area inside the vertebral body, whereas the red arrow points to the cortical bone, the outer boundary.
doi:10.1371/journal.pone.0093389.g002

Figure 3. Object/background transition regions (red arrows). (a) shows a homogenous object/background transition. In (b), the spinal canal (CSF) makes up parts of the vertebral body's outer boundaries.
doi:10.1371/journal.pone.0093389.g003

target-structure voxels, and a background region. To detect shape variations in the variability zone, Aslan et al. apply a distance probabilistic model. Then, they construct an undirected, weighted graph, implementing the 3D-shape prior through the edges' capacities. In a final step, a minimum cost cut is performed, partitioning the image's voxel set into two disjoint units, namely the target structure and the background.

Weese et al. [16] present shape constrained deformable models for 3D medical image segmentation, which they apply to vertebra CT acquisitions. Their hybrid approach combines the advantages of an active shape model and an elastically deformable surface model. The latter one is implemented as a surface mesh, whereby its flexibility is constrained by the shape model, which also ensures an optimal distribution of mesh vertices. In order to increase their approach's robustness against false object boundaries, Weese et al. attract the deformable model to locally detected surfaces, using an external energy. For validation, they compared the semi-automatic segmentation results of their algorithm to manually segmented vertebrae. In case of a proper manual placement of the mean vertebra model, Weese et al. report a mean segmentation error of 0.93 mm with deviations around 4.5–7 mm in problematic areas.

Yao et al. [17] describe a method for the automatic segmentation and partitioning of the spinal column. Their approach starts with a simple thresholding to mask out bone voxels and subsequently, it applies blob extraction, identifying the largest connected blob as the initial spine segmentation. Yao et al. explain that afterwards, a hybrid method based on the watershed algorithm and directed graph search is employed to obtain the spinal canal. They then use the spinal canal to position a vertebra model which consists of four parts, namely the vertebral body, spinous process, and left and right transverse processes. In the next step, the initial model is deformed in a way such that a maximum model-to-image match is achieved. In the last step they generate curved planar reformations (CPRs) in sagittal and coronal directions as well as they analyze aggregated intensity profiles along the spinal cord in order to partition the spinal column into the different vertebrae. For evaluation, the approach was tested on 71 CT scans and the authors state that the algorithm successfully extracted and partitioned 69 spinal columns, with only 2 cases that had one missed partition at the T1-T2 level.

Ghebreab and Smeulders [18] present an integral deformable spine model for three-dimensional segmentation of spinal images. They explain that their approach learns the representation of vertebrae in CT scans from multiple continuous features registered along vertebra boundaries in a given training set. Statistics are encoded into a necklace model, which is coupled by string models that provide detailed information on morphological variations in the appearance of spinal structures from multiple continuous features registered in the training set. Ghebreab and Smeulders further state that on the necklace model, landmarks are differentiated on their free dimensions and that, in order to reduce complexity, the landmarks are used within a priority segmentation scheme. For segmentation of new image data, the necklace and the string models are employed to detect vertebral structures interactively by means of elastic deformations. Ghebreab and Smeulder remark that this bears an analogy to a marionette with strings constraining the deformations in a way such that only movements within feasible solutions are allowed.

Zukić et al. [19], [20] present a fast and semi-automatic approach for spine segmentation in routine clinical MR images. A single vertebra is segmented based on multiple-feature boundary classification and mesh inflation, and it starts with a simple point-in-vertebra initialization. To prevent self-intersections, the inflation retains a star-shaped geometry and the smoothness is controlled via a constrained subdivision hierarchy. The main spine direction is deduced by analyzing the shape of the first vertebra and the locations of neighboring vertebral bodies are estimated for further segmentation. Against manual reference segmentations, the average Dice Similarity Coefficient (DSC) [22,23] was 78% and a detection rate of 93%. The approach was tested on eleven routine lumbar datasets with 92 segmented vertebrae.

Kelm et al. [21] use iterated marginal space learning (MSL) to detect and label intervertebral disks in MR images. Furthermore,

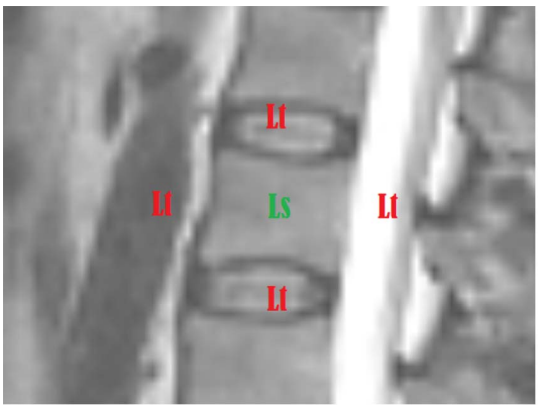

Figure 4. Illustration of voxel labeling for the foreground (L_s) and the background (L_t).
doi:10.1371/journal.pone.0093389.g004

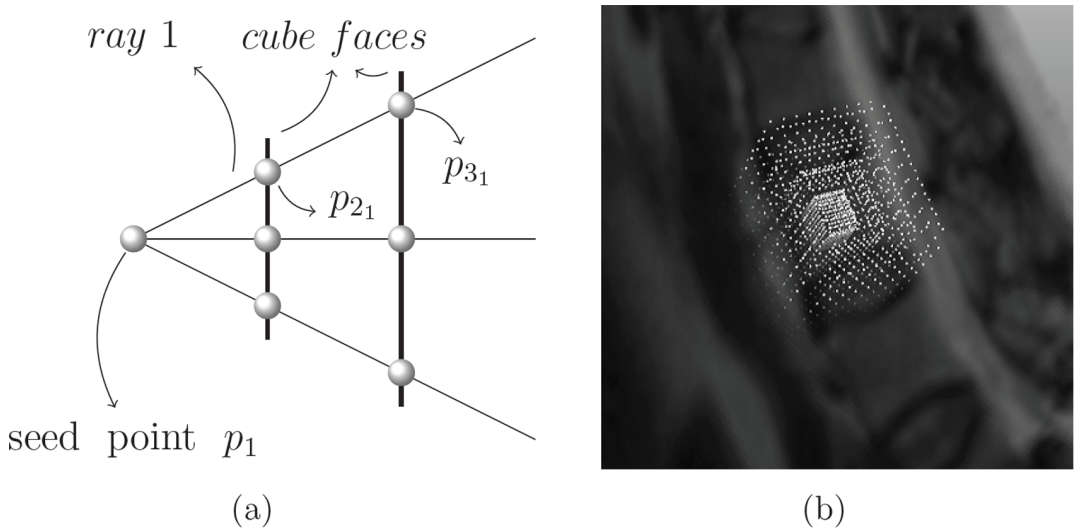

Figure 5. Profile of two cube faces intersected by three rays (a) and a cubic voxel subset (b).
doi:10.1371/journal.pone.0093389.g005

they claim that since their approach is learning-based, it can be applied to CT scans, as well. In a first step (after roughly locating the spine), their method uses an iterative extension of the MSL method to determine candidate regions including the potential targets' positions, orientations, and scales. In a second step, Kelm et al. use a global probabilistic spine model to detect the most probable candidates among them. They report that experimental validations of their method revealed 98.6% sensitivity, 7.3% false positive detections, an average position error of 2.4 mm, an angular error of 3.9°, and an overall processing time of 11.5 seconds.

Our approach to solve the problem of three-dimensional vertebral body segmentation is a non-trivial enhancement of the previously introduced two-dimensional graph-based segmentation strategy *Square-Cut* [11], which uses a rectangle template to segment vertebral bodies on single MRI-slices. Consequently, we now use a cubic-shaped distribution of the graph's nodes in the three-dimensional case. Moreover, we developed, implemented and evaluated far more complex three-dimensional neighborhood relations which can be easily altered as they are implemented as a function of a user-defined smoothness-term.

The rest of this contribution is organized as follows: *Section 2* presents the methods behind the introduced algorithm, *Section 3* presents the results of our experiments and *Section 4* concludes the paper and outlines areas for future work.

Methods

The new vertebral body segmentation algorithm presented here will be referred to as *Cube-Cut*. Cube-Cut extends a two-dimensional approach, previously introduced by Egger et al. [11] to a third dimension (Note: initial results of *Cube-Cut* have been presented on a workshop [24] and a German conference [25]). This extension allows the volumetric segmentation of a vertebral body with only one click, instead of just a two-dimensional segmentation on a single slice. The introductory paragraphs of this section first give a conceptual overview of the basic features and the behavior of Cube-Cut. This conceptual overview serves as a frame of reference for the more detailed discussion of the actual implementation that follows at a later stage and which introduces the reader to the concepts of a cubic-shaped graph and the related smoothness-constraint. To keep it consistent, the notation for the graph construction follows the notations of previous graph-based publications [26–35], where possible.

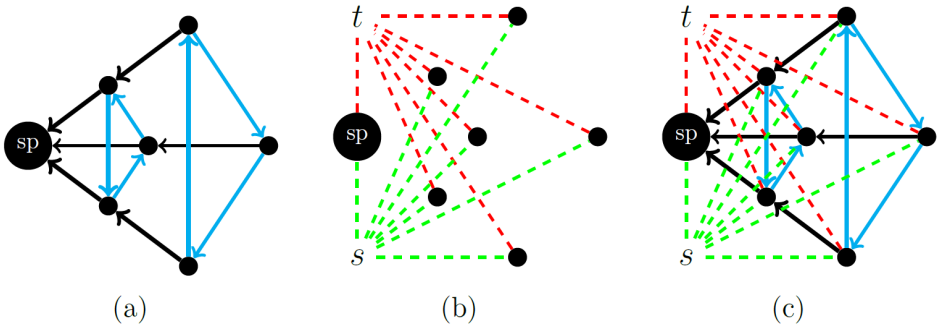

Figure 6. Illustration of the different kinds of edges. (a) i-links: z-edges (black), xy-edges (blue). (b) o-links: s-links(green), t-links(red). (c) whole graph.
doi:10.1371/journal.pone.0093389.g006

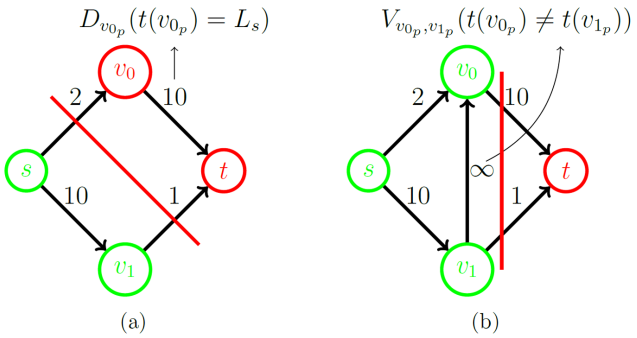

Figure 7. Illustration of the penalty effect. (a) shows a network without i-links. (b) shows a network with an i-link. The red line depicts a minimal cut.
doi:10.1371/journal.pone.0093389.g007

2.1 Conceptual Overview

2.1.1 Labeling. Given a volumetric MR image P, Cube-Cut first selects a subset $P' \subseteq P$ of the image's voxels and in a last step it tags each voxel $p \in P'$ with either one of the labels L_s or L_t [36]:

$$t : P' \rightarrow \{L_s, L_t\} \quad (1)$$

2.1.2 Penalties. The labeling of a voxel $p \in P'$ involves two penalties [36]:

- $D_p(t(p)) \in \mathbb{R}_{\geq 0}$ is the penalty for assigning the label t(p) to p and
- $V_{p,p'}(t(p),t(p')) \in \mathbb{R}_{\geq 0}$ is the penalty for assigning t(p) to p when t(p') is the label of the voxel p'∈P'.

D describes a voxel's affinities to the labels L_s and L_t. For example, the higher $D_p(t(p) = L_t)$, the more p is affiliated with L_s. V on the other hand reflects a voxel's affiliation to another voxel. In practice, $V_{p,p'}(t(p), t(p'))$ is greater than zero only if $t(p) \neq t(p')$. Thus, V indirectly describes p's affiliation with p' by awarding a penalty for tagging the two voxels with different labels: The higher $V_{p,p'}$, the more p is affiliated with p'. Nevertheless, note that $V_{p,p'}(t(p), t(p')) = 0$ *for* $t(p) \neq t(p')$ does not necessarily mean that the two voxels p and p' can be tagged differently without penalty costs. If, for instance, $V_{p,p''}(t(p), t(p'')) > 0$, for $t(p) \neq t(p'')$ and $p'' \in P'$ and if $V_{p'',p'}(t(p''), t(p')) > 0$ for $t(p'') \neq t(p')$, then the penalty cost for assigning different labels to p and p' is at least $min\{V_{p,p''}, V_{p'',p'}\}$.

2.1.3 Return value. Cube-Cut tags the voxels in a way such that the overall penalty cost is minimized. The overall cost is described by (2). Cube-Cut thus returns the argument L which minimizes.

$$E(L) = \sum_{\substack{p \in P' \\ t(p) \in L}} D_p(t(p)) + \sum_{\substack{p,p' \in P' \\ t(p),t(p') \in L}} V_{p,p'}(t(p),t(p')) \quad (2)$$

where $L = \{t(p) \mid p \in P'\}$ is a labeling of the subset P' [36,37]. However, until now, the features above have been discussed detached from the context of vertebral segmentation. The next section will make the connection.

2.1.4 Object and background separation. Cube-Cut selects P' and implements D and V (on the basis of the predetermined subset P') in a way such that the returned labeling is to be interpreted in the following manner (Figure 4):

- Cube-Cut assumes all voxels $p \in P'$ for which $t(p) = L_s$ inside the vertebral body and

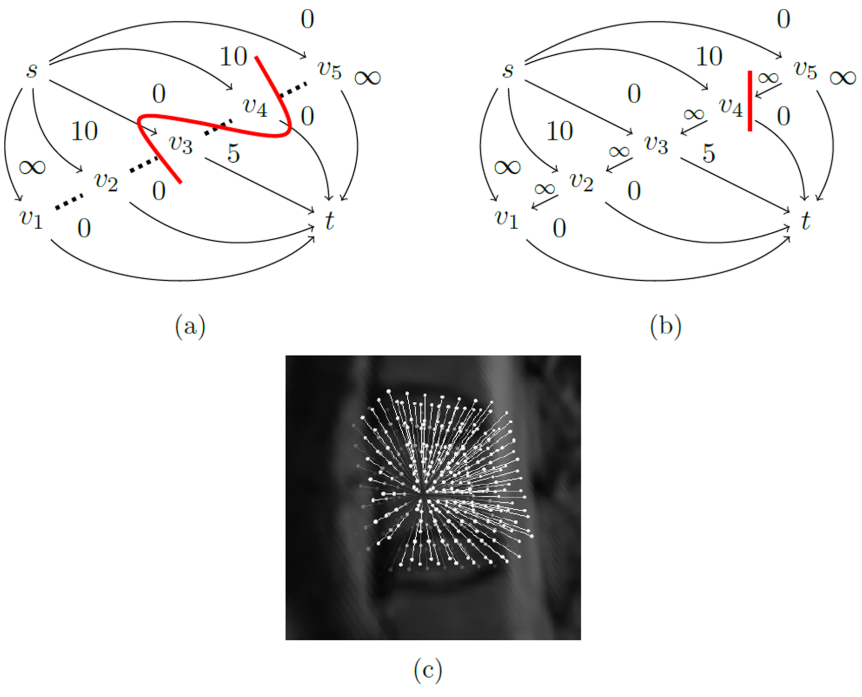

Figure 8. Illustration of the z-edges principle. (a) shows a ray without z-edges: The minimal s-t-cut (red) cuts the ray twice with a capacity of 0. (b) shows the same ray with z-edges. The ray is only cut once. The capacity of the minimal s-t-cut is ∞ +5. (c) shows z-edges, embedded into an MR image.
doi:10.1371/journal.pone.0093389.g008

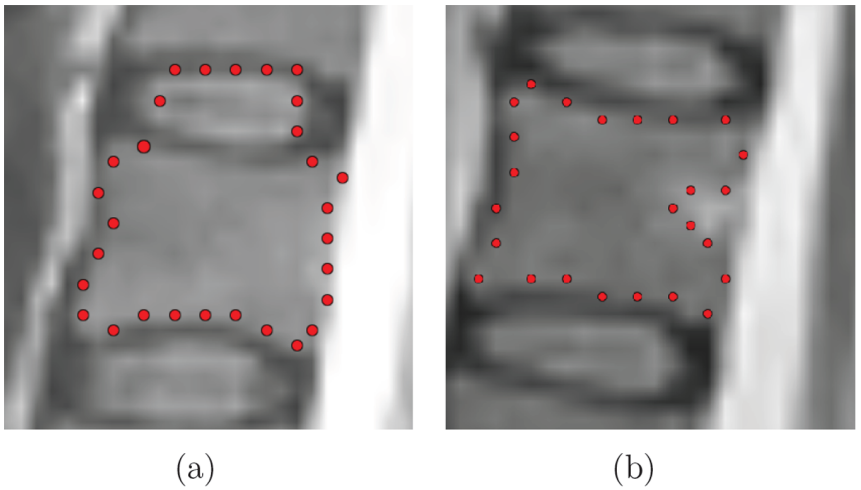

Figure 9. Adverse effects on segmentation results (2-dimensional view). (a) shows an overrun in the upper part due to a violation of condition (3). (b) shows a segmentation result affected by an outlier which causes a violation of condition (4). The cut happens too close to the seed point (not shown) in the middle of the vertebra because there is a light area similar to the spinal canal.
doi:10.1371/journal.pone.0093389.g009

- all voxels $p \in P'$ for which $t(p) = L_t$ can be assumed outside the vertebral body.

Hence, in a first step Cube-Cut selects a subset of voxels, and on the basis of this subset, implements two penalty functions which then determine a clustering of the subset into two disjoint units of voxels. One unit describes the vertebral body while the other describes the background (which may include other vertebrae). The following paragraphs will describe the implementation of the algorithm.

2.2 Implementation

2.2.1 Voxel subset. The voxels $p \in P'$ are distributed along n rays that expand from a user-defined seed point in the MR image. Each ray consists of k equidistantly spread voxels, where for all rays, the first voxel is always the user-defined seed point, so that $|P'| = n * (k - 1) + 1$. As the seed point, the number and the length of the rays as well as the number of voxels per ray can be determined by the user. It is assumed that each ray exceeds the vertebral body. In the following, let $p_{i_r} \in P'$ denotes a voxel on ray r, where $1 \leq r \leq n$ and where the voxel p_{i_r} is closer to the seed point (p_1 or p_{1_r}) than p_{j_r}, if $1 \leq i < j \leq k$ (Note: If only one ray is being discussed, the indexing r might be omitted. Furthermore, from now on, k will always denote the number of voxels per ray and n the number of rays).

2.2.2 Cubic distribution. The rays expand in a way such that all voxels of the same layer form a cube shape, so that if $i = j \neq 1$ and $m \neq n$, then the voxels p_{i_m} and p_{j_m} lie on the surface of one cube, which has the user-defined seed point as its center. Since there are k voxels on each ray, there are $k-1$ different sized cubes for which p_1 is the center (Figure 5). On a cube's face, the voxels are distributed equidistantly and the volumes of the cubes increase evenly. However, note that due to the theorem of intersecting lines, the distance between two voxels on a cube's face is less than the distance of the corresponding voxels on a bigger cube.

2.2.3 Implementation of penalties and labeling. Cube-Cut generates a network $N = ((G = (V(G), E(G))), c, s, t)$, where G is a directed, two-terminal graph and $|V(G)| = |P'| + 2$. Each vertex $v \in V(G) \setminus \{s,t\}$ corresponds to exactly one voxel $p \in P'$ and no two vertices correspond to the same voxel. In the following, v_p will denote a mapping of the vertex $v \in V(G) \setminus \{s,t\}$ onto its corresponding voxel $p \in P'$ and p_v will describe the reverse mapping. The source s and the sink t have no counterparts in P' and thus they are referred to as *virtual* nodes. In $E(G)$, there exist two types of edges [36], [38] (Figure 6):

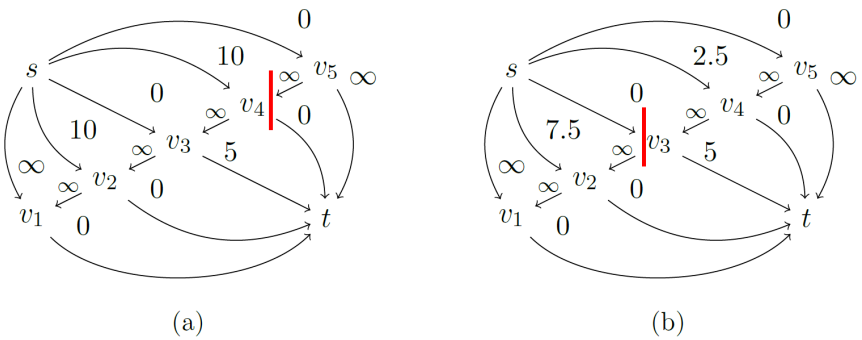

Figure 10. Effect of the coefficient *w*. In (b), w is applied on the s-weights in (a): The cut, with a capacity of $\infty + 2.5$, now happens closer to the seed point. Note that the same cut in (b) would have cost $\infty + 10$ whereas the cut depicted in (b) has a capacity of only $\infty + 5$.
doi:10.1371/journal.pone.0093389.g010

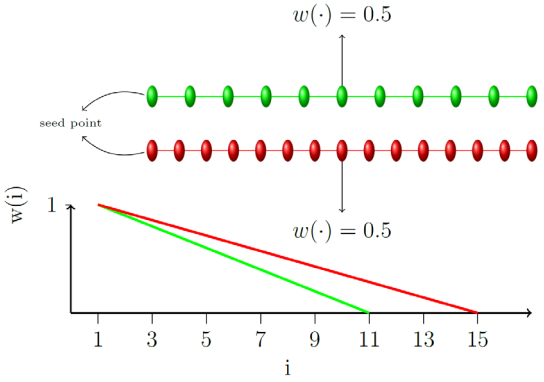

Figure 11. Courses of *w(i,11)* (green) and *w(i,15)* (red). The upper part illustrates that *w(i,k)* reflects the position of the voxel p_i on a ray consisting of *k* uniformly distributed voxels. Note that that w is only partially defined for the natural numbers but that Cube-Cut never calls w with an argument in the undefined scope.
doi:10.1371/journal.pone.0093389.g011

- *i-links* (inter-links) connect vertices $v \in V(G)\backslash\{s,t\}$ with each other. The *i-links* are further subdivided into *z-edges* and *xy-edges*, where *z-edges* connect vertices corresponding to neighboring voxels of the same ray (e.g. $(v_{i_n}, v_{(i+1)_n})$, while *xy-edges* connect vertices corresponding to voxels of different rays (e.g. (v_{i_n}, v_{j_m})).
- *o-links* (outward-links) connect all vertices $v \in V(G)\backslash\{s,t\}$ with the source *s* (*s-links*) and the sink *t* (*t-links*). Hence, there are two *o-links* for each vertex.

The capacities of the *i-* and *o-links* reflect the penalty functions *D* and *V* in the following manner (Figure 7):

$$\begin{aligned} &\forall v \in V(G)\backslash\{s,t\} : c(s,v) = D_p((t(v_p) = L_t)), \\ &\forall v \in V(G)\backslash\{s,t\} : c(v,t) = D_p((t(v_p) = L_s)), \\ &\forall (v,v') \in E(G) : c(v,v') = V_{p,p'}(t(v_p), t(v'_p)). \end{aligned} \tag{3}$$

Note that the skew symmetry constraint does not have an effect since by convention $c(v, v') = 0$ is assumed, if $(v, v') \notin E(G)$. After the graph has been set up, Cube-Cut determines a minimal s-t-cut (S, T) by deploying the Boykov-Kolmogorov algorithm [36] (http://vision.csd.uwo.ca/code/, accessed: March 2014) and then it labels P' as follows:

$$\forall v_p \in P' : t(v_p) \begin{cases} L_s & if\ v \in S; \\ L_t & else. \end{cases} \tag{4}$$

Since by definition, the capacity of a minimal s-t-cut is minimal among all possible s-t-cuts, the labeling above minimizes (2).

2.2.4 Z-Edges: onetime cut per ray. Since each ray intersects with the outer boundaries of the vertebral body only once, a set of *z-edges* is introduced that ensures that each ray is exactly cut one time by a minimal s-t-cut [38,39]:

$$A_z = \{(v_{i_r}, v_{(i-1)_r}) | 1 < i \leq k \wedge 1 \leq r \leq n\}, \tag{5}$$

where *n* is the user-defined number of rays and *k* the total number of voxels per ray, again (note: in what follows, v_{i_r} will denote the corresponding vertex of the i^{th} voxel on ray *r*. Furthermore, if only one ray is being discussed, the indexing *r* might be omitted). The set of *z-edges* connects each vertex v_i with its predecessor $v_{(i-1)}$ on the same ray (Figure 8). The capacities of all *z-edges* are initialized to ∞. Therefore, it costs ∞ each time a *z-edge* is cut.

By making sure that the seed point is in *S* and that the last voxel on each ray is in *T* (see next section), a minimal s-t-cut (*S, T*) has to cut each ray at least once. Yet, it does not cut any ray more than once because that would cost at least $2 \cdot \infty$. This is why a ray is cut exactly one time. The next section explains how Cube-Cut encourages this cut to happen close in front of the vertebral body's outer boundaries.

2.2.5 O-links: marking the outer boundaries. A voxel p_{i_r} is characterized by $(x_{i_r}, y_{i_r}, z_{i_r}, g_{i_r})$ where $x_{i_r}, y_{i_r}, z_{i_r} \in \mathbb{N}_0$ denote the voxel's position in the image and $g_{i_r} \in R_{\geq 0}$ denotes its grey value (note: simplified, voxel coordinates assumed). Cube-Cut investigates a small cube *((x1, y1, z1), (x2, y2, z2))* around the user-defined seed point (inside the vertebra) and determines its interval of grey values $I = [min(GV), max(GV)]$, where.

$$GV = \{\pi_4(x,y,z,g) | x_1 \leq x \leq x_2, y_1 \leq y \leq y_2, z_1 \leq z \leq z_2\} \tag{6}$$

is the multi-set of all grey values within the cube and $\pi_i(\cdot)$ is a projection onto the i^{th} element of a tuple. Furthermore, Cube-Cut also iterates over the cube to determine an average grey value g_{avg} by

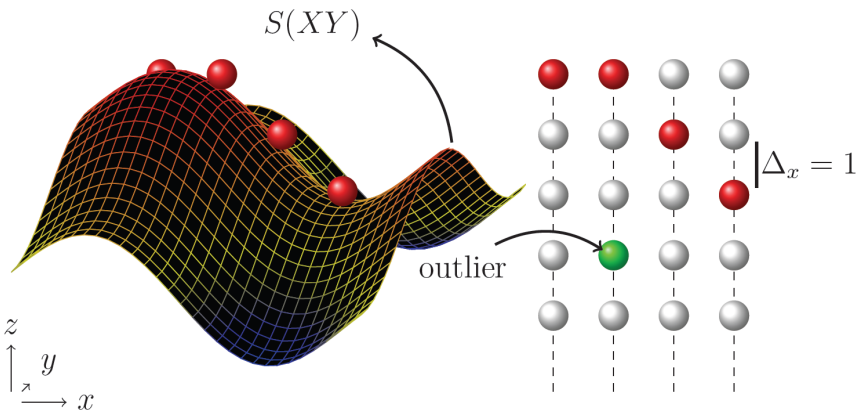

Figure 12. A feasible surface and intersecting rays (transformed in x-direction for a better visibility). The green node depicts an outlier as it would violate the smoothness constraint $\Delta_x = 1$ if classed with the surface voxels.
doi:10.1371/journal.pone.0093389.g012

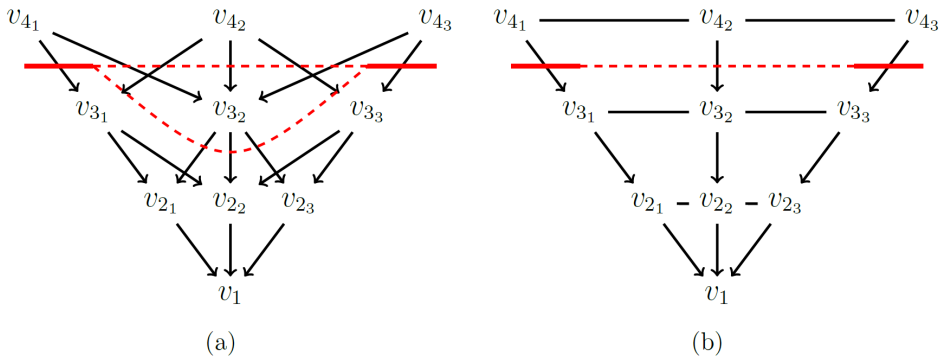

Figure 13. Illustration of the xy-edges principle. (a) shows a minimal cut (thick lines) and the two possible continuations (dashed lines) within the boundaries of a smoothness constraint $\Delta = 1$. All other cuts would have a capacity greater than $7 \cdot \infty$. (b) shows the only possible continuation within the boundaries of a Δ-value of 0, where the cut has a capacity of $3 \cdot \infty$.
doi:10.1371/journal.pone.0093389.g013

$$g_{avg} = \frac{1}{|GV|} \cdot \int_{x_1}^{x_2} \int_{y_1}^{y_2} \int_{z_1}^{z_2} \pi_4(x,y,z,g)\,dx\,dy\,dz. \qquad (7)$$

In the course of weighting the *o-links*, the interval I and the average grey value g_{avg} are used as frames of reference.

The following Pseudo-Code depicts the fundamental principle of how Cube-Cut assigns capacities to the *o-links* (note: Each ray r consists of k voxels):

0 $c(s,v_1) \leftarrow \infty$
1 $c(v_1,t) \leftarrow 0$
2 *assign*(*ray r*)
3 $\forall p_{i_r} = (x_i,y_i,z_i,g_i) \in r \setminus \{p_{1_r}\}$
4 *if* $i == k$
5 $c(s,v_{i_r}) \leftarrow 0$
6 $c(v_{i_r},t) \leftarrow \infty$
7 *else if* $g_i \in I$ *or* $abs(g_{avg} - g_i) \leq abs(g_{avg} - g_{i-1})$
8 $c(s,v_{i_r}) \leftarrow abs(abs(g_{avg} - g_i) - abs(g_{avg} - g_{i-1}))$
9 $c(v_{i_r},t) \leftarrow 0$
10 *else*
11 $c(s,v_{i_r}) \leftarrow 0$
12 $c(v_{i_r},t) \leftarrow abs(abs(g_{avg} - g_i) - abs(g_{avg} - g_{i-1}))$

The ∞-weighting in line 0 ensures that the seed point is tagged with L_s. The premise on which this is based is that the user defines the seed point within the vertebral body (in the center).

Furthermore, it is assumed that the last voxel on each ray (p_{k_r}) lies outside the vertebra (since the user is supposed to define a ray length that exceeds the vertebral body). To ensure that the last voxels are tagged with L_t, the *t-links* (v_{k_r},t) are also ∞-weighted while for all rays $c(s,v_{k_r})$ is consequently initialized to zero (line 4 - 6)

The capacities of all of the other, intermediate *o-links* reflect the value difference between a voxel and its predecessor on the ray (lines 8,9,11 & 12). This is in order to "mark" the outer boundaries.

As already mentioned above, the rays expand from the user-defined seed point in the center of the vertebral body and they eventually intersect with the outer boundaries. Ignoring occasional outliers and homogeneous object/background transition regions for now, the inner vertebral body is characterized by a homogeneous set of voxel grey values, which are all higher or lower than the grey values that make up the outer boundaries (e.g. cortical bone, spinal canal, compare *Introduction*). Thus, on each ray, the difference in value between the last voxel in the vertebral body and the first voxel on the outer boundaries can be assumed high.

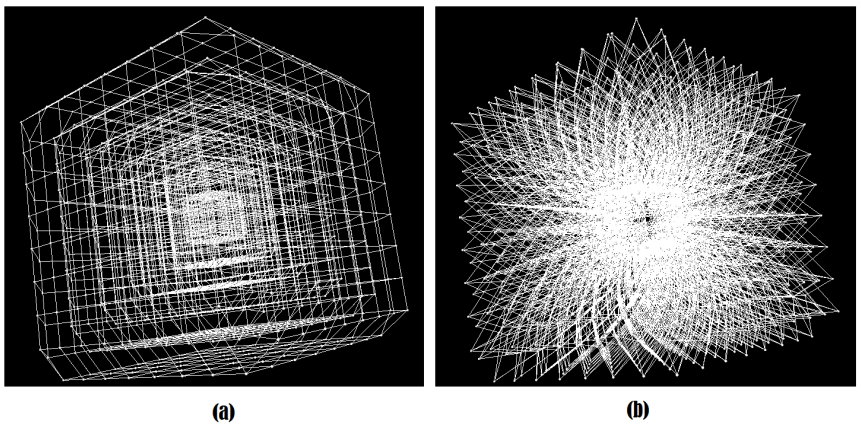

Figure 14. Topology of xy-edges for $\Delta = 0$ (a) and $\Delta = 1$ (b).
doi:10.1371/journal.pone.0093389.g014

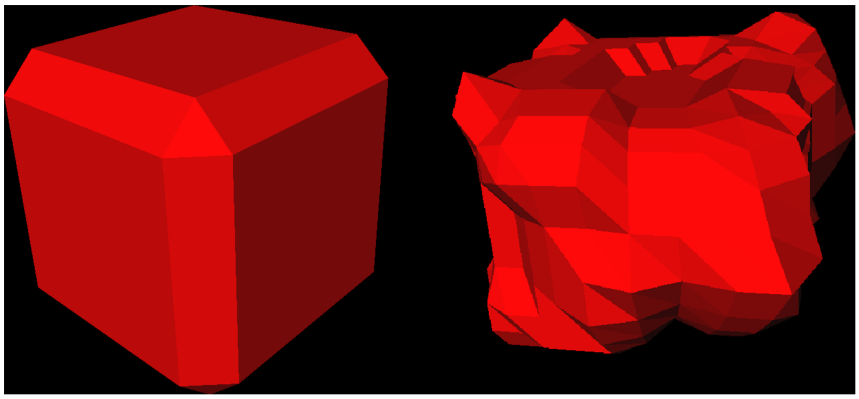

Figure 15. Segmentation result for $\Delta = 0$ (left) and $\Delta = 2$ (right).
doi:10.1371/journal.pone.0093389.g015

Taking the condition in line 7 into account, the outer boundaries therefore implement high *t-link* capacities (line 12). Note that this makes a cut right in front of the corresponding vertices very probable. The next sections explain how peculiarities and anomalies in vertebral MRI data sometimes prevent a cut from happening right in front of the outer boundaries and how Cube-Cut addresses these adverse effects.

2.2.6 Adverse effects on the segmentation result. A cut right in front of the outer boundaries is a cut that separates the last vertex that corresponds to a voxel which is still located inside the vertebral body from the subsequent ones on the same ray. If, for each ray, the cut takes place right in front of the outer boundaries of the vertebral body, then Cube-Cut returns a satisfactory segmentation result.

Let v_{i_r} be the first vertex on a ray r that corresponds to a voxel on the outer boundaries/background. If a minimal s-t-cut (S, T) cuts the ray right in front of v_{i_r}, so that $v_{(i-1)_r} \in S$ and $v_{i_r} \in T$, then.

$$\sum_{j=i}^{k-1} c(s, v_{j_r}) < \sum_{j=i}^{k-1} c(v_{j_r}, t) \tag{8}$$

and

$$\forall h < i : h > 1 \Rightarrow \sum_{j=h}^{i-1} c(v_{j_r}, t) \leq \sum_{j=h}^{i-1} c(s, v_{j_r}) \tag{9}$$

For most rays, the two (minimum) conditions hold true and thus, the cut takes place right in front of the outer boundaries. Equation (8) usually holds true because the value difference between p_{i_r} and $p_{(i-1)_r}$ is greater than the sum of the subsequent *s-weights* since behind the outer boundaries, the rays mostly penetrate homogeneous areas dissimilar from the vertebral body (compare lines 7 & 8 of the pseudo code). Equation (9) holds true for most rays because of the homogeneity of voxel grey values in the vertebral body and their similarity to the close environment of the seed point (compare lines 7, 8 & 12 of the pseudo code).

Nevertheless, there are exceptions. Figure 9 depicts such exceptions. (a) clearly shows a 2-dimensional view of a segmentation result that overruns the vertebral body in the upper part. For the corresponding rays, equation (3) does not hold true. The similarity between the vertebral and the intervertebral voxels, in terms of their grey values, can easily be recognized. Furthermore, there are minor variations of grey values in the intervertebral disc.

As a consequence, the condition in line 7 of the pseudo code holds true for a sufficient number of background voxels on each of the affected rays, which is why condition (8) is not satisfied. Thus, the overrun occurs. Observe that the same applies to homogeneous object/background transition regions. Among others, Cube-Cut tackles this problem by introducing a coefficient w, which loads the *s-weights* according to their distance from the seed point (see next section). Line 8 of the pseudo code is extended to:

$$c(s, v_{i_r}) \leftarrow w(i,k) \cdot abs\left(abs\left(g_{avg} - g_i\right) - abs\left(g_{avg} - g_{i-1}\right)\right).$$

Another phenomenon that negatively affects the segmentation result is outliers. Outliers share all relevant properties (grey values) that distinguish the vertebra's boundaries except that they are part of the inner vertebral body.

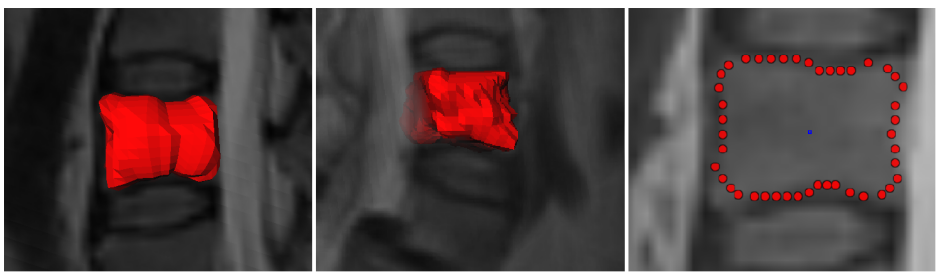

Figure 16. 3D segmentation result (left and middle image) and 2D segmentation result with the user-defined seed point in blue (rightmost image).
doi:10.1371/journal.pone.0093389.g016

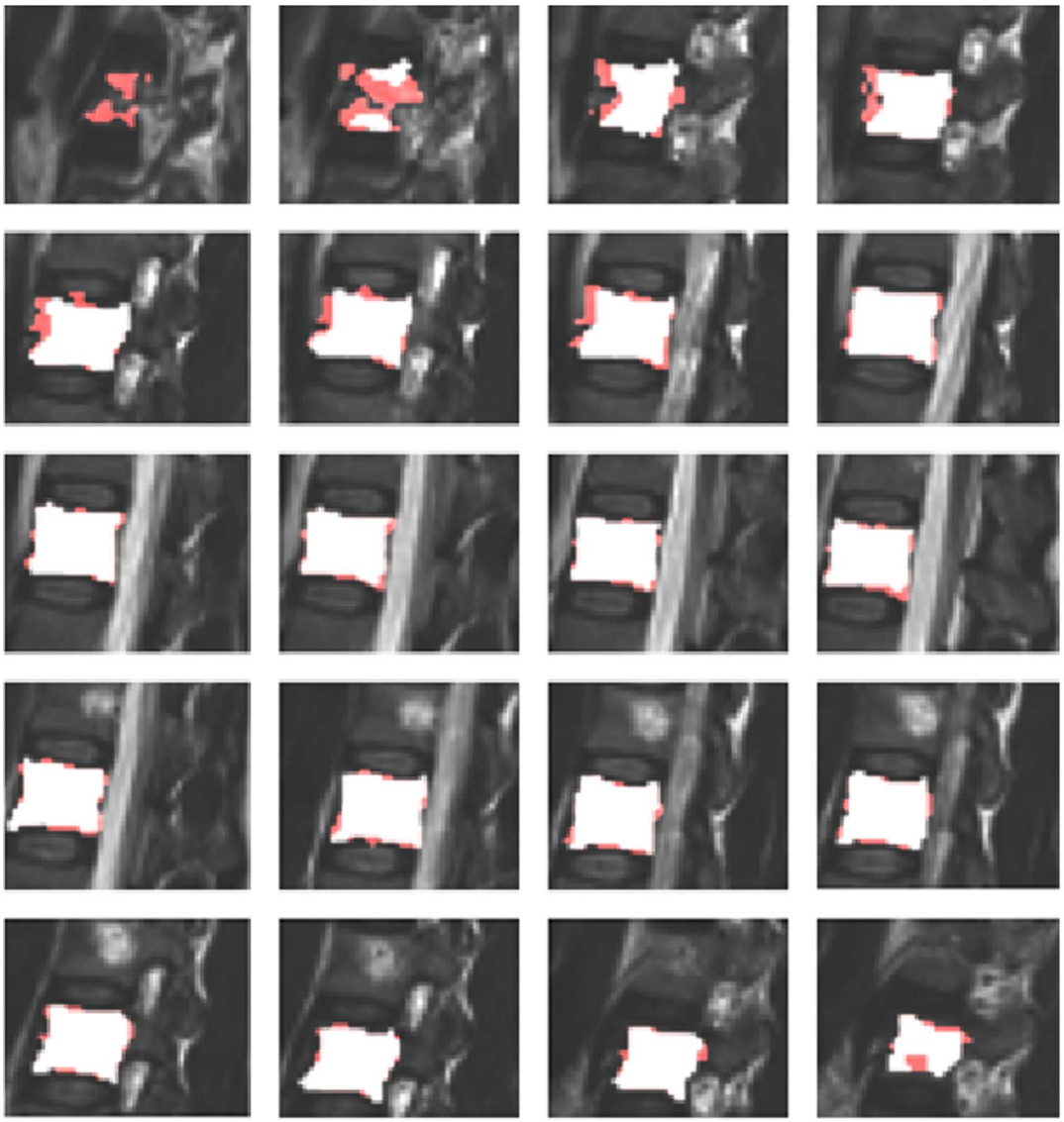

Figure 17. Superimposition of a manual segmentation result and a Cube-Cut segmentation result.
doi:10.1371/journal.pone.0093389.g017

To be specific, an outlier causes the violation of equation (9). On the corresponding ray, the cut then happens too close to the seed point (Figure 9 (b)). Cube-Cut decreases the possible adverse effects due to outliers by imposing a smoothness constraint on the segmentation result. In addition, the smoothness constraint also addresses the problem of a violation of equation (8), as discussed above. The next two sections present Cube-Cut's problem-solving approaches in detail. The first matter to be addressed will be the loading of the *s-capacities* and then the smoothness constraint will be discussed.

2.2.7 Loading the s-Capacities. The coefficient $w(\cdot)$ loads an *s-capacity* according to the corresponding voxel's (p_{i_r}) position on the ray (Figure 10). For a ray r, consisting of k voxels, it is defined as $w(i,k) = mi+b$, where $k \geq i \in \mathbb{N}_{>0}$ and $m = -\frac{1}{k-1}$ and $b = 1-m$.

Observe that since the voxels are distributed uniformly on each ray, $w(i, k) = 1$ for the seed point ($p_{i=1}$), $w(\cdot, k) = 0.5$ for a voxel that is half way on a ray (Figure 11) and $w(\cdot, k) = 0$ for the last voxel on each ray. A voxel far away from the seed point is more likely to be outside the vertebral body.

Cube-Cut takes this into account by decreasing its *s-capacity* accordingly, thereby reducing the risk of a cut being located behind the outer boundaries of the vertebral body because.

$$\sum_{j=i}^{k-1} c(s,v_{j_r}) > \sum_{j=i}^{k-1} w(j,k)\cdot c(s,v_{j_r}) \qquad (10)$$

As already mentioned above, the coefficient is not the only measure Cube-Cut takes in order to counteract a violation of condition (8): The smoothness constraint, which also addresses a violation of condition (9), will be the subject matter in the next section.

2.2.8 XY-edges: imposing a smoothness constraint. The smoothness constraint is based on the optimal surface segmentation algorithm developed by Li et al. [38]. It is useful to first

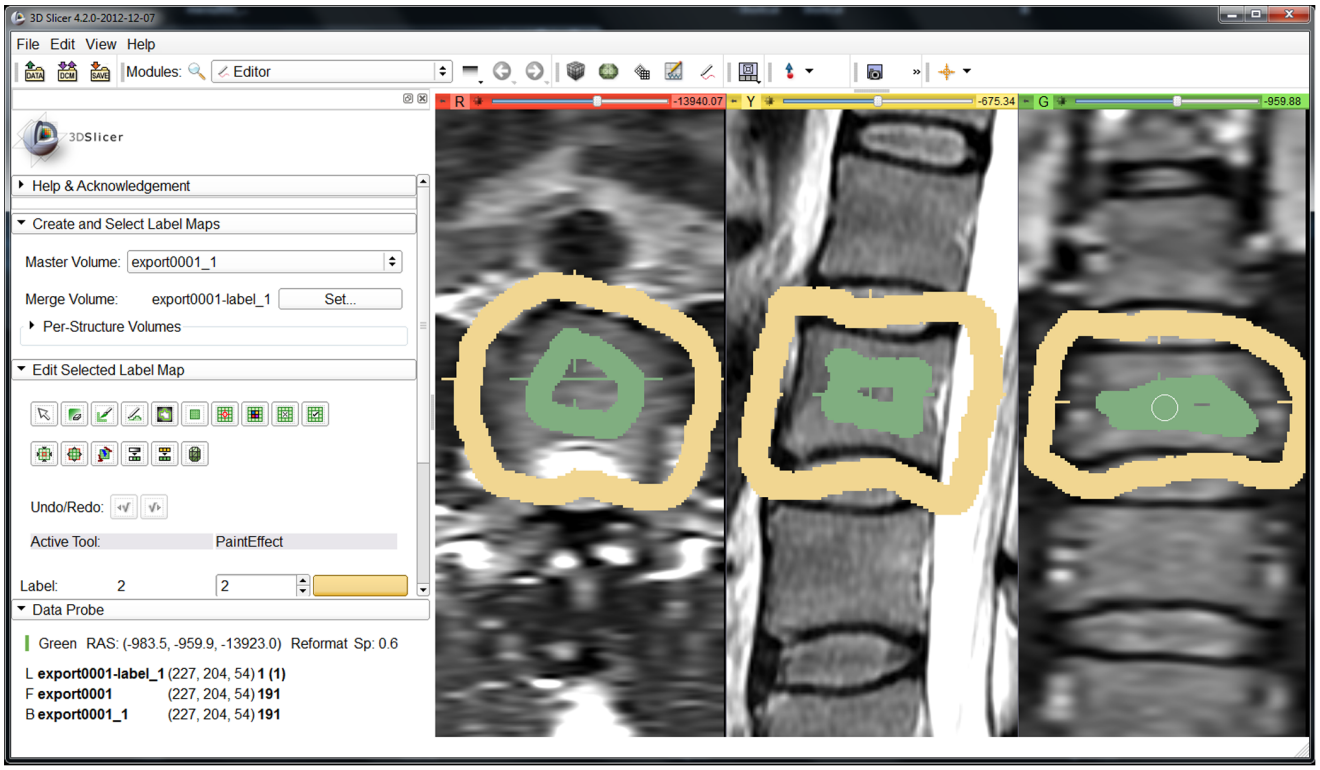

Figure 18. Typical user initialization of GrowCut for this study. The Editor module is used to mark parts of the vertebra (green) and the background (yellow) in an axial, sagittal and coronal plane.
doi:10.1371/journal.pone.0093389.g018

discuss it conceptually, slightly detached from the context of vertebral segmentation. A single, feasible surface in a volumetric Image $I=(X, Y, Z)$, where $X, Y, Z \subset N_0$, can be characterized by a bijection $S : XY \rightarrow Z$, where $XY \subseteq X \times Y$ is a cohesive area. Li et al. refer to a surface as feasible if two smoothness constraints are satisfied:

$$\forall (x,y),(x+1,y) \in XY : |S(x,y) - S(x+1,y)| \leq \Delta_x \qquad (11)$$

and

$$\forall (x,y),(x,y+1) \in XY : |S(x,y) - S(x,y+1)| \leq \Delta_y \qquad (12)$$

Δ_x and Δ_y constrain the degree to which the surface "moves" upwards or downwards in x- or y-direction within an interval of one: *S(x, y)* and *S(x+1, y)* as well as *S(x, y)* and *S(x, y+1)* are neighboring x- and y-positions. Thus, two neighbors on a feasible surface cannot be arbitrarily distant from each other. Hereby, the smoothness constraints assure what Li et al. refer to as "surface connectivity". Observe that for a plane $\Delta_x = \Delta_y = 0$.

Now consider a number of equidistant rays that consist of the same number of uniformly spread voxels and which all extend parallel to the *z-axis*. The voxels that make up a ray do not necessarily have to lie on neighboring positions in the image. Furthermore, for convenience, assume that I is a binary image with only two possible values for each voxel: "colored" *xor* "white". In addition, let all rays intersect with a colored surface *S(XY)* in *I*, which means that each ray extends from *XY* and shares exactly one colored voxel with the surface.

In this context, in which only a subset of the image's voxels is observed, the smoothness constraint has to be defined via the neighborhood relations of the rays. Figure 12 shows four neighboring rays in *x-direction* (same *y-value* for each voxel), which extend parallel to the *z-axis*, as described above. Here, a smoothness parameter $\Delta_x = 1$ means that for a "colored" voxel that is considered part of the surface, all voxels on adjacent rays that are also classed with the surface voxels must lie on the same "z-layer" or the next upper or lower one. An outlier in this context is a colored voxel that exceeds the prescribed maximum distance.

Cube-Cut allows the user to impose a smoothness constraint on the segmentation result. It interprets each of the six sides of a vertebral body's outer boundaries (from a sagittal view: front, back, top, bottom, right, and left) as a feasible surface. Furthermore, it takes into account that the six surfaces are anatomically connected, which is why the neighborhood relations overlap at the "edges" of the boundaries.

Cube-Cut implements the smoothness constraint $\Delta \in N_0$ by introducing a set of infinity-weighted *xy-edges* [38]:

$$A_{xy} = \{(v_{ir}, v_{(\max\{(i-\Delta),1\})_{r'}})\} | (r,r') \in N_4\} \qquad (13)$$

N_4 denotes a 4-neighborhood and as already mentioned above, the neighborhood relations overlap at the "edges" of the cubic voxel subset that the algorithm observes.

The infinity-weighting of the *xy-edges* ensures that a minimal s-t-cut cuts the rays in a way such that the vertebra is segmented within the boundaries of the user-defined smoothness constraint Δ (Figure 13). Note that for a given Δ-value, an 8-neighborhood would increase the "stiffness" of the segmentation result.

For a smoothness constraint $\Delta = 0$, any minimal s-t-cut results in a regular, cubic segmentation result, whereas a Δ-value greater

Table 1. Direct comparison of manual slice-by-slice and Cube-Cut segmentation results for ten vertebrae via the Dice Similarity Coefficient (DSC).

No.	volume of vertebrae (mm^3)		number of voxels		DSC (%)
	manual	automatic	manual	automatic	
1	23860.6	26314.3	2927	3228	86.69
2	27423	27431.1	3364	3365	84.17
3	33830.4	28776.2	4150	3530	82.06
4	27121.4	23901	3327	2932	82.57
5	22165	17795.4	2719	2138	71.64
6	15423	16638	1892	2041	84.16
7	42658.9	33194.5	5233	4072	82.85
8	42715.9	35216.2	5240	4320	85.54
9	39903.5	29909.3	4895	3669	80.71
10	30594.1	18105.4	3753	2221	72.95
min	15.42	16.64	1892	2041	71.64
max	33.83	28.78	5240	4320	86.69
$\mu \pm \sigma$	24.97±6.15	23.48±5.12	3750	3152	81.33±5.07

doi:10.1371/journal.pone.0093389.t001

zero allows a corresponding deviation. Figure 14 shows the topology of the *xy-edges* for a Δ-value of zero and a Δ-value of one and Figure 15 shows corresponding segmentation results, illustrating the purpose of the cubic shaped voxel subset.

Results

A C++ implementation of Cube-Cut was tested within the medical image processing platform MeVisLab 2.2.1 (www.mevislab.de). We used two T2-weighted, volumetric, pathological MR-images (512×512×16 and 512×512×10), both of which had an anisotropic voxel spacing in x- and y-directions of 0.63 millimeters and 4.4 millimeters along the z-axis. We obtained isotropic voxel sizing (2.01258 millimeters in all directions) by resampling the two images, using the MeVisLab Resample3D-module, which resulted in resolutions of 159×159×35 and 159×159×22 respectively. The first image contained a stenosis and a spondylolisthesis; the second image showed a slipped disc.

In order to place the seed-point roughly in the center of the vertebra, we scrolled through two-dimensional, sagittal image slices. After Cube-Cut terminated, the triangulation was visually evaluated. If overruns occurred, we decremented the smoothness-constraint and/or replaced the seed-point accordingly, e.g. we moved it in x-direction if the overrun occurred in y-direction. We learned that once parameter settings were found for one vertebra in a data set, these settings could also be successfully applied to most of the other vertebrae in the same image. Figure 16 shows volumetric and two-dimensional segmentation results.

The obtained segmentation results were then compared to ten segmentation results obtained in a slice-by-slice manner, performed by trained physicians. Table 1 presents the detailed results for all ten cases and in addition the summary of results, with min, max, mean μ and standard deviation σ. For visual inspection, Figure 17 shows a superimposition of a pure manually segmented and an automatically obtained (Cube-Cut) segmentation result. Furthermore, the manual slice-by-slice segmentations have been compared to segmentation results obtained using the GrowCut-algorithm [40] (Table 2). For testing GrowCut with our datasets we used an implementation that is freely available in the medical platform (3D) Slicer (www.slicer.org). For initialization of the GrowCut algorithm, strokes have been drawn inside and outside the vertebral body on a two-dimensional, sagittal image, a two-dimensional axial image and a two-dimensional coronal image (Figure 18), as it has been done in [41], [42] and [43]. Table 2 presents the direct comparison of the manual slice-by-slice and a GrowCut segmentation for the ten vertebrae from Table 1 with a mean DSC-value of 80.61%.

It was found that it takes a trained physician 10±6.65 minutes to manually segment a vertebra in a slice-by-slice manner. On a 2.1 GHz ×64-based PC with 4 GB RAM running the Microsoft Windows 7 Home Premium (SP1) operating system, version 6.1.7601, the most expensive parameter settings took Cube-Cut less than a minute (graph-construction, mincut computation and triangulation) to terminate. The settings that resulted in a maximum DSC of over 86% only took 19 seconds to execute. Overall, we achieved a mean DSC-value of 81.33%.

Table 2. Direct comparison of manual slice-by-slice and GrowCut segmentation results for ten vertebrae via the Dice Similarity Coefficient (note: the cases 1–10 correspond to Table 1).

Case	1	2	3	4	5	6	7	8	9	10
DSC (%)	78.55	81.34	83.90	71.33	71.34	70.65	88.58	91.95	85.13	83.30

doi:10.1371/journal.pone.0093389.t002

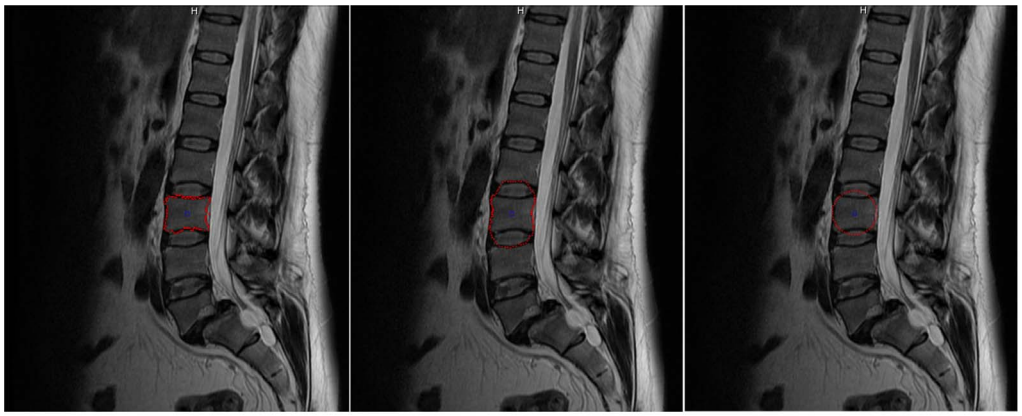

Figure 19. Vertebra segmentation results (red) for a graph that has been constructed with a spherical template from a user-defined seed point (blue). The left image shows the segmentation result when the density of the rays/sampled nodes and the delta value are set to very large values. When these values are smaller the graph cut prefers a more spherical/elliptical segmentation result (middle). The rightmost image shows the extreme case where the delta value was set to zero. There the graph cut has to come back with a perfect sphere and the only variation is the size of the sphere which depends on the gray values.
doi:10.1371/journal.pone.0093389.g019

Conclusion

A novel approach towards the volumetric segmentation of vertebral bodies was presented. Cube-Cut is a non-trivial, three-dimensional extension of the previously introduced two-dimensional segmentation strategy Square-Cut [11] and a proof of concept implementation of the optimal surface segmentation approach by Li et al. [38]. The introduced method is the first one using a 3D-graph that is based on a cubic-shaped subset of non-equidistant image voxels as well as a smoothness-constraint in order to segment volumetric, cubic-like target-structures. The possibility to approach a cubic template by changing the graph's topology as a function of the user-defined smoothness-term in real-time effectively allows overcoming homogeneous object-background transition regions. In summary, the research highlights are:

- development of a specific graph-based algorithm for vertebral body segmentation;
- algorithm bases on a cubic template which is a novelty in the segmentation domain;
- scale-invariant segmentation by an optimal mincut through cubic-shaped divergences;
- physicians performed slice-by-slice segmentations to obtain ground truth boundaries;
- segmentation quality of the algorithm has been evaluated via the Dice Coefficient.

The proposed method only requires a single user seed, while other approaches [13,18] require multiple user-inputs to achieve comparable results. On the other hand, the easily alterable smoothness term seemingly provides more flexibility than the

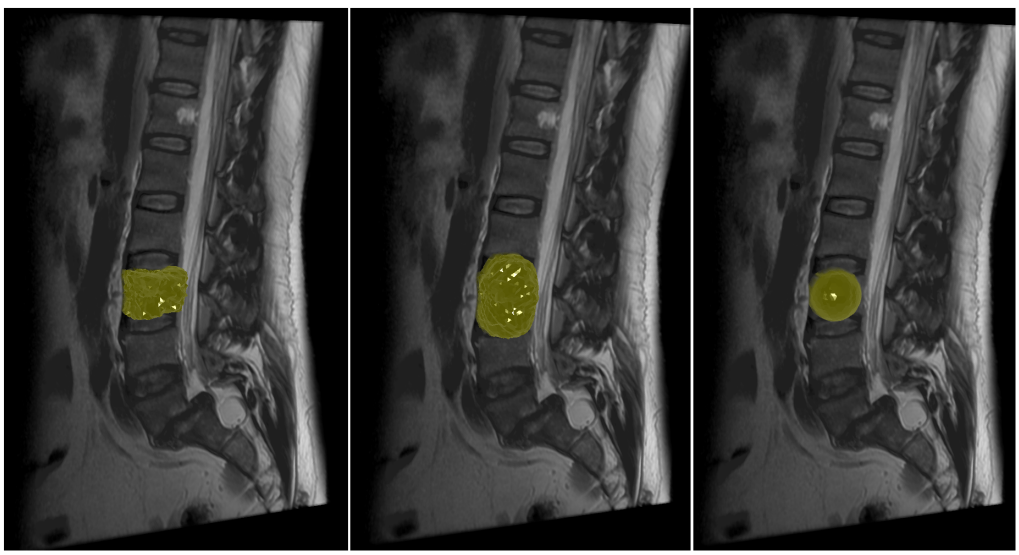

Figure 20. Corresponding 3D results of Figure 19, where a graph has been constructed with a spherical template for vertebra segmentation. The left image shows the 3D segmentation result (yellow) when the density of the rays/sampled nodes and the delta value are set to very large values. When these values are smaller the graph cut prefers a more spherical/elliptical segmentation result (middle). The rightmost image shows the extreme case where the delta value was set to zero, which resulted into a perfect sphere.
doi:10.1371/journal.pone.0093389.g020

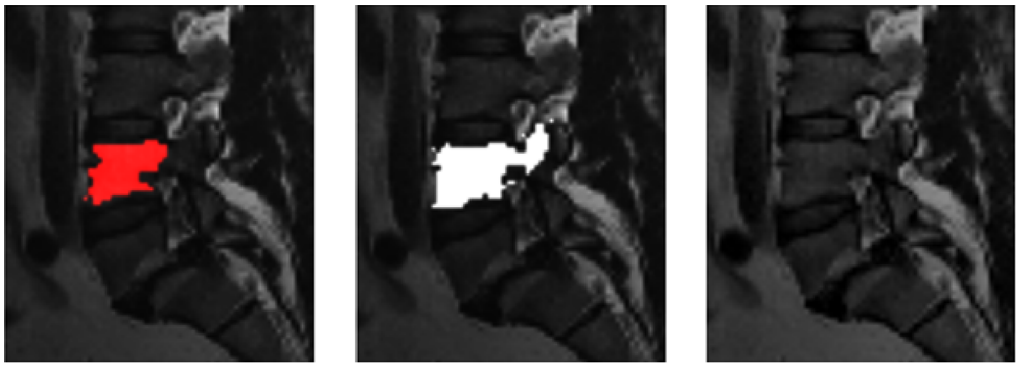

Figure 21. Sagittal 2D-view on Cube-Cut segmentation result (left, red), GrowCut segmentation result (center, white) and reference image (right). The GrowCut algorithm detects false boundaries in the pedicles-region.
doi:10.1371/journal.pone.0093389.g021

approach proposed by Štern et al. [14], since the authors state that they might have to introduce new parameters to their deterministic model when confronted with not yet considered pathologies or deformations.

In addition, contrary to most of the alternative approaches [12,15,18], our proposed method does not rely on training data and is thus not constrained to the variations, deformations and pathologies covered in the data set. This also means that Cube-Cut needs a far less expensive initialization phase. Furthermore, the graph-based approach presented by Aslan et al. [15] observes the whole set of the image's voxels, while Cube-Cut only requires a subset. Both algorithms compute the mincut in polynomial time and thus our approach outperforms the approach of Aslan et al. in terms of theoretical runtime.

Furthermore, whereas other approaches [12,15,16,17,18] have tested their algorithms only on CT datasets, we show that our approach is suitable for MR-image processing, and contrary to several other approaches [13,14], we have tested our algorithm on pathological spine data, achieving a better mean DSC than Zukić et al. [19]. A shift towards a more frequent application of MRI in the preoperative evaluation of surgical patients would result in less radiation exposure compared to the more frequent application of CT.

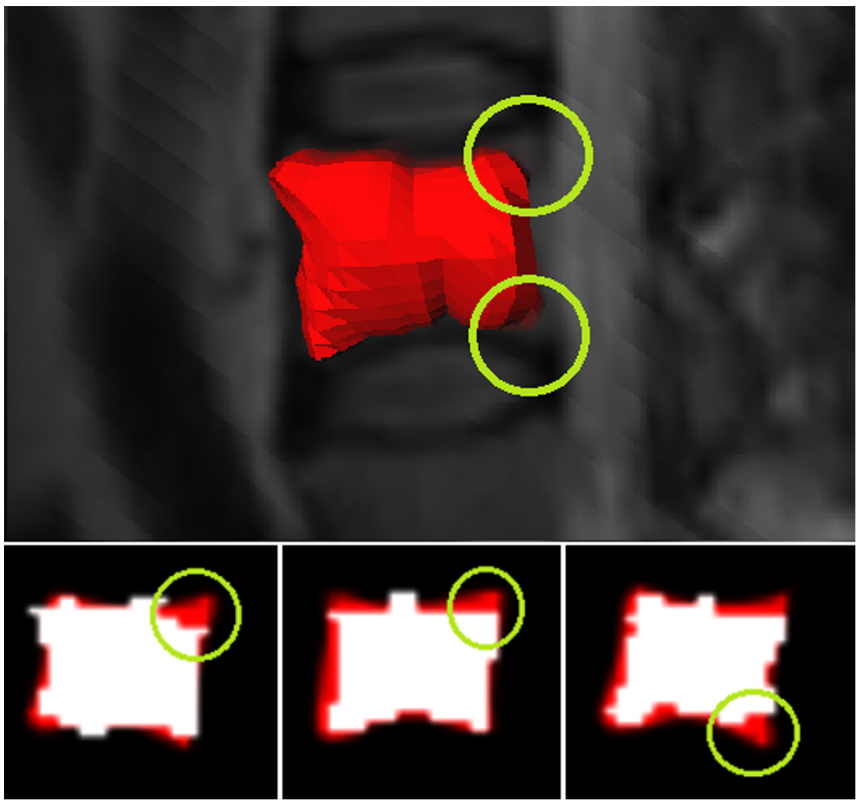

Figure 22. "Vertices" of the vertebral body's outer boundaries were not detected accurately (green circles). The upper image shows a 3D segmentation result, the lower images show 2D overlaps of manual (red) and automatic (white) segmentation results.
doi:10.1371/journal.pone.0093389.g022

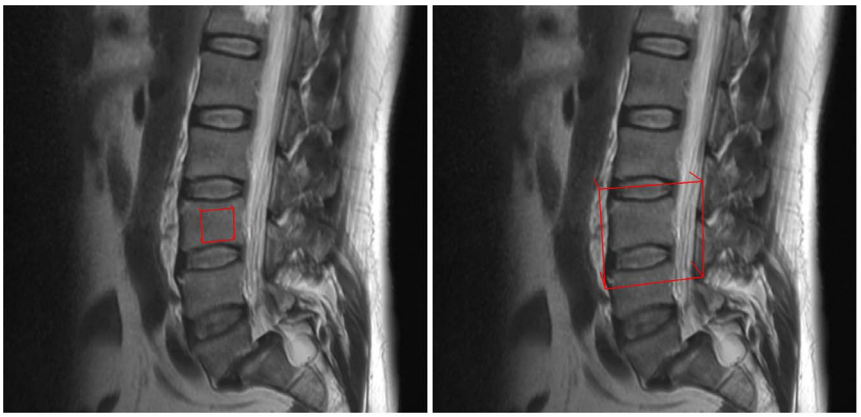

Figure 23. The size of the cube (red) in the left image is too small to segment the vertebra, because a graph that is constructed inside this cube does not cover the border of the vertebra and the s-t-cut will lie inside the vertebra. In contrast, the size of the cube in the right image is sufficient, because a graph that is constructed inside this cube will also cover the vertebra's border and thus is able to segment it.
doi:10.1371/journal.pone.0093389.g023

To summarize, Cube-Cut generates a two-terminal s-t-network where the vertices correspond to a cubic shaped subset of the image's voxels. By only observing a subset of the image's voxels, the algorithm improves the theoretical runtime in comparison to other graph-based approaches that consult the whole voxel set. The capacities of the terminal edges reflect a voxel's affiliation with the object (vertebral body) and the background, while the topology of non-terminal ∞-weighted edges implements the smoothness-constraint. After network construction, a minimal s-t-cut, computed in polynomial time, determines the segmentation result. For the mincut computation, the Boykov-Kolmogorov algorithm is applied, since it was demonstrated [36], that despite a worst case complexity of $O(v(G)^2e(G)\ |C_{min}|)$, where $v(G)$ is the number of vertices, $e(G)$ the number of edges and $|C_{min}|$ the capacity of a minimal cut, the algorithm is most effective for networks of low complexity, like the one Cube-Cut generates. In addition, we want to point out here that Boykov's graph cut model can support high dimensional data in its own settings.

For evaluation, Cube-Cut 3D-masks were compared to manual vertebral body segmentation results, obtained in a time-costly slice-by-slice manner, performed by trained physicians, achieving a promising mean DSC of 81.33%, which is on par with the state of the art (comparable to [19]). The computation (graph construction, mincut computation and triangulation) that led to the maximum DSC value of 86.69% terminated in 19 seconds on a customary PC. All other parameter settings took no more than a minute to execute. It was found that a slice-by-slice segmentation of a vertebra took trained physicians 10 ± 6.65 minutes on average, and a subsequent conversion into a 3D-mask was also still needed. This illustrates the practicability of the novel approach in terms of preoperative time management, since its employment could save up to nine minutes per vertebra.

Moreover, we also used a spherical template instead of the cubic shaped one, to set up a graph and applied it to vertebra segmentation. As shown in Figure 19 and 20 on the left side, a vertebra can roughly be segmented this way if the density of the rays/sampled nodes and the delta value are set to very large values. However, as soon as these values are smaller, the graph cut prefers a more spherical/elliptical segmentation result, as shown in the middle images of Figure 19 and Figure 20. In the extreme case where the delta value is set to zero, the graph cut has to come back with a perfect sphere and the only variation is the size of the sphere which depends on the gray values (rightmost images of Figure 19 and 20). Hence, the above illustrates the superiority of cubic-shaped templates when it comes to vertebra segmentation.

Furthermore, we also compared the Cube-Cut masks with GrowCut results and found that Cube-Cut clearly outperformed GrowCut in this setup, regardless of the similar DSC values. Besides others, GrowCut regularly did not recognize the vertebral body's outer boundaries in the pedicle-regions, which led to false boundary detections as shown in Figure 21. This strongly illustrates the convenience of the alterable smoothness-term. Furthermore, manual adjustments of the results obtained with Cube-Cut, which at this stage would still be necessary in a clinical context, would take less user effort, since the cubic characteristics of a vertebral body are already incorporated into the calculations. A re-initialization of GrowCut – in case of an unsatisfying segmentation result – can be very time-consuming, because strokes have to be drawn all over again in several 2D slices. The initialization of GrowCut on three 2D slices took an experienced user around one minute and the run time of GrowCut – after the initialization – was around 1–3 minutes. The re-initialization of Cube-Cut however, usually only required the replacement of the one seed.

Nevertheless, visual evaluations of Cube-Cut's segmentation results indicate that the algorithm frequently segments the same specific areas of a vertebral body inaccurately. Recognizing the rectangle shape of a vertebral body, on sagittal slices, these areas could be referred to as the vertebral body's "vertices" (Figure 22). Although the present version of Cube-Cut already allows an arbitrary increase of precision in terms of number of rays and points per ray, future versions of the algorithm could overcome this problem by a densification of rays only in the corresponding spaces or by allowing the user to adjust the segmentation result manually.

Regarding the robustness of Cube-Cut in general, we can report that the method only performs satisfactory if the cube's volume is larger than the vertebral body's (Figure 23, right side), since in case the cube is smaller (Figure 23, left) side, the graph does not penetrate the background which results in an s-t-cut that lies somewhere inside the vertebral body. Thus, a cube larger than the vertebra is desirable. Right now, we estimate the volume of the largest vertebral body in a data set visually and choose the cube's volume accordingly. Future versions of Cube-Cut could provide the user with the possibility of defining the size of the cube interactively, e.g. by drawing a stroke through the vertebra at its

largest measurement. The length of the stroke would then be used to define the cube's size automatically, with an additional safety margin.

Furthermore, as already mentioned above, the seed has to be placed roughly around the center region of the vertebral body in order to obtain satisfactory segmentation results. Nevertheless, the algorithm proved itself relatively stable against small deviations and moreover, the replacement of the seed only takes a second which is one of the distinguishing advantages of Cube-Cut.

Acknowledgments

We want to acknowledge the physicians Thomas Dukatz and Dr. med. Malgorzata Kolodziej from the neurosurgery department of the university hospital in Marburg, Germany, for performing the manual slice-by-slice segmentations of the vertebrae and thus providing the ground truth for the evaluation. Moreover, the authors would like to thank Fraunhofer MeVis in Bremen, Germany, for providing an academic license for MeVisLab. Furthermore, the authors want to thank Bernd Egger for drawing the image on the left side of Figure 2.

Author Contributions

Conceived and designed the experiments: RS JE. Performed the experiments: RS. Analyzed the data: RS JE. Contributed reagents/materials/analysis tools: RS BF CN JE. Wrote the paper: RS JE BF.

References

1. Joaquim AF, Sansur CA, Hamilton DK, Shaffrey CI (2009) Degenerative lumbar stenosis:update. Arquivos de Neuro-Psiquiatria, vol. 67(2B), 553–558.
2. Weinstein JN, Lurie JD, Tosteson TD, Hanscom B, Tosteson AN, et al. (2007) Surgical versus nonsurgical treatment for lumbar degenerative spondylolisthesis. N Engl J Med. 2007 May 31;356(22):2257–70.
3. Miao J, Wang S, Wan Z, Park WM, Xia Q, et al. (2012) Motion characteristics of the vertebral segments with lumbar degenerative spondylolisthesis in elderly patients. Eur Spine J. 2013 Feb;22(2):425–31. doi: 10.1007/s00586–012–2428–3. Epub 2012 Aug 15.
4. Chen MYM, Pope TL, Ott DJ (2010) Basic Radiology. Trade paperback, McGraw-Hill Medical Publishing 2nd ed. 396 pages, ISBN-13: 9780071627085.
5. Drake R, Vogl AW, Mitchell AWM (2009) Gray's Anatomy for Students. Churchill Livingstone, 2nd ed. 1136 pages, ISBN 9780443069529.
6. Michopoulou SK, Costaridou L, Panagiotopoulos E, Speller R, Panayiotakis G, et al. (2009) Atlas-based segmentation of degenerated lumbar intervertebral discs from MR images of the spine. IEEE Trans Biomed Eng 56(9): 2225–31.
7. Shi R, Sun D, Qiu Z, Weiss KL (2007) An efficient method for segmentation of MRI spine images. IEEE/ICME International Conference on Complex Medical Engineering, CME, IEEE Press. 713–717.
8. Huang SH, Chu YH, Lai SH, Novak CL (2009) Learning-based vertebra detection and iterative normalized-cut segmentation for spinal MRI. IEEE Trans Med Imaging 28(10): 1595–605.
9. Peng Z, Zhong J, Wee W, Lee JH (2005) Automated Vertebra Detection and Segmentation from the Whole Spine MR Images. Conf Proc IEEE Eng Med Biol Soc 3: 2527–30.
10. Carballido-Gamio J, Belongie SJ, Majumdar S (2004) Normalized cuts in 3-D for spinal MRI segmentation. IEEE Trans Med Imaging 23(1): 36–44.
11. Egger J, Kapur T, Dukatz T, Kolodziej M, Zukić D, et al. (2012) Square-Cut: A Segmentation Algorithm on the Basis of a Rectangle Shape. PLoS ONE 7(2): e31064. doi:10.1371/journal.pone.0031064
12. Klinder T, Wolz R, Lorenz C, Franz A, Ostermann J (2008) Spine segmentation using articulated shape models. Medical Image Computing and Computer-Assisted Intervention (MICCAI), Metaxas D, Axel L, Fichtinger G, Szekely G, eds. vol. 5241 of Lecture Notes in Computer Science, Springer Press. 227–234.
13. Hoad CL, Martel AL (2002) Segmentation of MR images for computer-assisted surgery of the lumbar spine. Physics in Medicine and Biology 47(19): 3503.
14. Štern D, Vrtovec T, Pernus F, Likar B (2011) Segmentation of vertebral bodies in CT and MR images based on 3D deterministic models. Proc SPIE Medical Imaging, Summers RM, van Ginneken B, eds. volume 7963.
15. Aslan MS, Ali A, Farag AA, Rara H, Arnold B, et al. (2010) 3D Vertebral Body Segmentation Using Shape Based Graph Cuts. Pattern Recognition (ICPR), 2010 20th International Conference on, 3951–3954.
16. Weese J, Kaus M, Lorenz C, Lobregt S, Truye R, et al. (2001) Shape constrained deformable models for 3D medical image segmentation. Information Processing in Medical Imaging, Insana M, Leahy R, eds. vol. 2082 of Lecture Notes in Computer Science, Springer Press. 380–387.
17. Yao J, O'Connor SD, Summers RM (2006) Automated spinal column extraction and partitioning. 3rd IEEE International Symposium on Biomedical Imaging: Nano to Macro, IEEE Press. 390–393.
18. Ghebreab S, Smeulders AW (2004) Combining strings and necklaces for interactive three-dimensional segmentation of spinal images using an integral deformable spine model. IEEE Transactions on Biomedical Engineering 51(10): 1821–1829.
19. Zukić D, Vlasák A, Dukatz T, Egger J, Horinek D, et al. (2012) Segmentation of Vertebral Bodies in MR Images. 17th International Workshop on Vision, Modeling and Visualization (VMV), The Eurographics Association, 135–142.
20. Zukić D, Vlasák A, Egger J, Hořínek D, Nimsky C, et al. (2014) Robust Detection and Segmentation for Diagnosis of Vertebral Diseases using Routine MR Images. Computer Graphics Forum, March 2014.
21. Kelm BM, Zhou SK, Suehling M, Zheng Y, Wels M, et al. (2010) Detection of 3D spinal geometry using iterated marginal space learning. MCV'10 Proceedings of the 2010 international MICCAI conference on Medical computer vision: recognition techniques and applications in medical imaging, Springer, ACM, 96–105.
22. Zou KH, Warfield SK, Bharatha A, Tempany CMC, Kaus MR, et al. (2004) Statistical Validation of Image Segmentation Quality Based on a Spatial Overlap Index: Scientific Reports. Academic Radiology 11(2): 178–189.
23. Sampat MP, Wang Z, Markey MK, Whitman GJ, Stephens TW, et al. (2006) Measuring intra- and inter-observer agreement in identifying and localizing structures in medical images. IEEE Inter Conf Image Processing, 4 pages.
24. Schwarzenberg R, Kapur T, Wells W, Nimsky C, Freisleben B, et al. (2012) Graph-Based Vertebra Segmentation Using a Cubic Template. In: 5th NCIGT and NIH Image Guided Therapy Workshop, Boston, page 44.
25. Schwarzenberg R, Freisleben B, Kikinis R, Nimsky C, Egger J (2013) [A Cube-Based Approach to Segment Vertebrae in MRI-Acquisitions]. In: Proceedings of Bildverarbeitung für die Medizin (BVM), Springer Press, 69–74, Heidelberg, Germany, March 2013.
26. Egger J, Freisleben B, Nimsky C, Kapur T (2012) Template cut: A Pattern-based Segmentation Paradigm. Scientic Reports, Nature Publishing Group (NPG), vol. 2(420), 1–8.
27. Egger J, Bauer MHA, Kuhnt D, Carl B, Kappus C, et al. (2010) Nugget-Cut: A Segmentation Scheme for Spherically- and Elliptically-Shaped 3D Objects. 32nd Annual Symposium of the German Association for Pattern Recognition (DAGM), LNCS 6376, Springer Press. 383–392.
28. Egger J, Freisleben B, Setser R, Renapuraar R, Biermann C, et al. (2009) Aorta Segmentation for Stent Simulation. 12th International Conference on Medical Image Computing and Computer Assisted Intervention (MICCAI), Cardiovascular Interventional Imaging and Biophysical Modelling Workshop, 10 pages.
29. Egger J, O'Donnell T, Hopfgartner C, Freisleben B (2008) Graph-Based Tracking Method for Aortic Thrombus Segmentation. Proceedings of 4th European Congress for Medical and Biomedical Engineering, Engineering for Health, Springer Press. 584–587.
30. Bauer MHA, Egger J, O'Donnell T, Freisleben B, Barbieri S, et al. (2010) A Fast and Robust Graph-based Approach for Boundary Estimation of Fiber Bundles Relying on Fractional Anisotropy Maps. In: 20th International Conference on Pattern Recognition (ICPR), Istanbul, Turkey, IEEE Computer Society, 4016–4019, August 2010.
31. Egger J, Penzkofer T, Kapur T, Tempany C (2012) Prostate Central Gland Segmentation Using a Spherical Template Driven Graph Approach. In: 5th NCIGT and NIH Image Guided Therapy Workshop, Boston, Page 43, September 2012.
32. Egger J (2013) PCG-Cut: Graph Driven Segmentation of the Prostate Central Gland. PLoS One. 2013; 8(10): e76645. Epub 2013 Oct 11.
33. Egger J, Lüddemann T, Schwarzenberg R, Freisleben B, Nimsky C (2014) Interactive-Cut: Real-Time Feedback Segmentation for Translational Research. Comput Med Imaging Graph. Available online 11 February 2014.
34. Egger J, Colen R, Freisleben B, Nimsky C (2011) Manual Refinement System for Graph-Based Segmentation Results in the Medical Domain. J Med Syst. 2012 Oct; 36(5):2829–39. Epub 2011 Aug 9.
35. Egger J, Kappus C, Freisleben B, Nimsky C (2011) A Medical Software System for Volumetric Analysis of Cerebral Pathologies in Magnetic Resonance Imaging (MRI) Data. J Med Syst. 2012 Aug; 36(4):2097–109. Epub 2011 Mar 8.
36. Boykov Y, Kolmogorov V (2004) An Experimental Comparison of Min-Cut/Max-Flow Algorithms for Energy Minimization in Vision. IEEE Transactions on Pattern Analysis and Machine Intelligence 26(9): 1124–1137.
37. Greig D, Porteous B, Seheult A (1989) Exact maximum a posteriori estimation for binary images. Journal of the Royal Statistical Society, Series B, vol. 51(2), 271–279.
38. Li K, Wu X, Chen DZ, Sonka M (2006) Optimal surface segmentation in volumetric images – a graph-theoretic approach. IEEE Transactions on Pattern Analysis and Machine Intelligence (PAMI), 28, 119–134.
39. Veksler O (2008) Star Shape Prior for Graph-Cut Image Segmentation: European Conference on Computer Vision 2008, (ECCV'08).
40. Vezhnevets V, Konouchine V (2005) GrowCut - Interactive Multi-Label N-D Image Segmentation. Proc. Graphicon. 150–156.

41. Egger J, Kapur T, Nimsky C, Kikinis R (2012) Pituitary adenoma volumetry with 3DSlicer. PLoS ONE 2012; 7(12): e51788.
42. Egger J, Kapur T, Fedorov A, Pieper S, Miller JV, et al. (2013) GBM Volumetry using the 3D Slicer Medical Image Computing Platform. Sci Rep., Nature Publishing Group (NPG), 2013; 3:1364. Epub 2013 March 4.
43. Egger J, Kappus C, Carl B, Nimsky C (2013) GrowCut-Based Vertebral Body Segmentation with 3D Slicer. In: Jahrestagung der Sektion Wirbelsäule der Deutschen Gesellschaft für Neurochirurgie (DGNC), Frankfurt am Main, Germany, Poster 24, September 2013.

SCIENTIFIC REPORTS

OPEN

SUBJECT AREAS:
TRANSLATIONAL RESEARCH
MEDICAL RESEARCH

Received
19 March 2014

Accepted
12 May 2014

Published
4 June 2014

Correspondence and requests for materials should be addressed to J.E. (egger@tugraz.at)

Refinement-Cut: User-Guided Segmentation Algorithm for Translational Science

Jan Egger

Faculty of Computer Science and Biomedical Engineering, Institute for Computer Graphics and Vision, Graz University of Technology, Graz, Styria, Austria.

In this contribution, a semi-automatic segmentation algorithm for (medical) image analysis is presented. More precise, the approach belongs to the category of interactive contouring algorithms, which provide real-time feedback of the segmentation result. However, even with interactive real-time contouring approaches there are always cases where the user cannot find a satisfying segmentation, e.g. due to homogeneous appearances between the object and the background, or noise inside the object. For these difficult cases the algorithm still needs additional user support. However, this additional user support should be intuitive and rapid integrated into the segmentation process, without breaking the interactive real-time segmentation feedback. I propose a solution where the user can support the algorithm by an easy and fast placement of one or more seed points to guide the algorithm to a satisfying segmentation result also in difficult cases. These additional seed(s) restrict(s) the calculation of the segmentation for the algorithm, but at the same time, still enable to continue with the interactive real-time feedback segmentation. For a practical and genuine application in translational science, the approach has been tested on medical data from the clinical routine in 2D and 3D.

Nowadays, the most clinics – at least in the western world – have in general several medical scanners, like computed tomography (CT) or magnetic resonance imaging (MRI), which produce every day a massive amount of medical patient data. In addition, new scanner generations get more and more precise, and thus produce more and more data. However, there is by far not the time and manpower for a precise manual analysis of this important and critical data. Therefore, approximations are often used, like the estimated calculation of a tumor volume via its maximal diameter in a 2D view, which may not very accurate and can lead to inaccurate treatment decisions[1]. A solution could be to support and automate medical image analysis with segmentation algorithms, like Active Contours in 2D[2] or 3D[3], Active Appearance Models[4], graph-based approaches[5], fuzzy-based approaches[6], or neural networks[7]. But after observing dozen of interventions in several clinics and different departments, I never met a physician who used any segmentation algorithm. The main reason was, that the segmentation approaches are not stable enough and fail far too often, especially for fully automatic algorithms. This may also be the reason that major manufacturers of medical imaging equipment don't really offer sophisticated segmentation options within their workstations and software packages. Additionally, the existing approaches are often not user friendly and intuitive implemented, e.g. they need a precise definition of "mystic" parameters for an accurate segmentation result. A temporal solution to speed-up a segmentation task, until (fully) automatic algorithms provide reliable results, are semi-automatic methods, like interactive segmentation approaches. Thereby, the user supports and guides the algorithm by interactive input. This can be carried out by marking parts of the pathology and the surrounding background with a simple brush[8]. Thus providing the segmentation algorithm with information about the pathology's location in the image and information about the texture of the pathology and background[9,10]. An overview about several interactive medical image segmentation approaches has recently been published by Zhao and Xie X[11], where they also classify the approaches by their type of interactions:

- Pictorial input on an image grid, like Seeds for region growing[12],
- Parameter tuning using slider, dial, or similar interface, like the maximum size of segmented regions[13], or
- Menu option selection by mouse clicking, like Accept/reject the segmentation results[14].

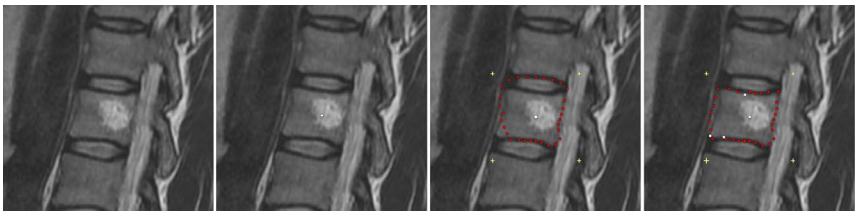

Figure 1 | Interactive refinement segmentation of a vertebral body contour in 2D from a magnetic resonance imaging (MRI) acquisition. The leftmost image presents the native scan and the second image from the left shows the initial user-defined seed point (white) that has been placed inside the vertebral body for the interactive segmentation. The third image from the left presents the segmentation outcome for the current position of the user-defined seed. However, due to the bright region inside the vertebral body, the average gray value – which is automatically calculated from the region around the user-defined seed – is not calculated "correctly", and thus the resulting contour (red) leaks in the upper area and misses an edge in the lower left (note: for the interactive segmentation of the vertebral body, a rectangle was used as template to construct the graph. Thereby, the center of the rectangle is the user-defined seed point and the yellow crosses in the two rightmost images display the four corners of the rectangle). Finally, the rightmost image presents the result of the refined segmentation. Therefore, the user simply placed three additional seeds (white dots on the contour of the vertebral body), and thus forced the algorithm to perform the min-cut at these positions – which also influences the cuts along the neighboring rays. Furthermore, additional gray value information can be extracted around these extra seeds that the user placed on the contour of the vertebral body.

An exciting (new) class of interactive segmentation algorithms – which are not discussed to detailed within the review – are real-time approaches, which are able to calculate a segmentation result within a fraction of a second. In the meantime, this is possible because hardware becomes faster and faster and therefore allows the execution of high level segmentation approaches in an extremely short time, even on up-to-date laptops. This opens up completely new possibilities, where the user gets immediate feedback, instead of waiting for the segmentation result to come back and then re-initialize and start over again, which can be very frustrating. A real-time interactive image segmentation approach that uses user indicated real-world seeds has been presented by Gomes et al.[15]. The approach can be used for videos or still images and because the seeds are indicated by a user, e.g. via a laser pointer, it is possible to segment objects without any computer interface. Armstrong et al.[16] introduce interactive segmentation of image volumes with live surface. In summary, Live Surface does for 3D volumes what Intelligent Scissors[17,18] did for 2D images, and allows the user to segment volumes continuously with immediate visual feedback in the refinement of the selected surface. A variational model for interactive shape prior segmentation and real-time tracking has been proposed by Werlberger et al.[19]. The semi-automated segmentation approach is based on minimizing the Geodesic Active Contour[20] energy incorporating a shape prior that represents the desired structure. Additionally, the user has the possibility to make corrective during the segmentation and adapt the shape prior position. To achieve a real-time behavior the method was implemented on the GPU. A computer-aided design system for refinement of segmentation errors has been introduced by Jackowski and Goshtasby[21], where a surface is interactively revised until the desired segmentation has been achieved. Therefore, the surface is revised by moving certain control points and the user sees the changes in the surface in real-time. Mory et al.[22] propose a real-time 3D image segmentation method based on user-constrained template deformation. The interactive image segmentation algorithm incorporates in a first step user input as inside/outside labeled points to drive the deformation and improve both robustness and accuracy. In a second step, a fast implementation of non-rigid template-to-image registration enables interactions with a real-time visual feedback.

In this contribution, an interactive real-time segmentation algorithm is introduced. The algorithm is scale-invariant and keeps its interactive real-time segmentation behavior even if the user refines the segmentation result with additional seeds. Thus, in principle, the algorithm combines some basic characteristics from existing segmentation methods into a novel segmentation approach which can also handle difficult segmentation task; and to the best of the author's knowledge such an approach has not yet been described.

The paper is organized as follows: The Materials and Methods section presents the details of the proposed algorithm and online resources where medical data can be found; the Results section displays the outcomes of my experiments; and the Discussion section concludes the paper and outlines areas for future research.

Results

Figure 1 presents the interactive refinement segmentation of a vertebral body contour in 2D from a MRI acquisition. The leftmost image shows the native scan and the second image from the left displays the initial user-defined seed point (white) that has been placed inside the vertebral body for the interactive segmentation. The third image from the left presents the segmentation outcome for the current position of the user-defined seed. However, due to the bright region inside the vertebral body, the average gray value – which is automatically calculated from a region around the user-defined seed – is not detected "correctly", and thus the resulting contour (red) leaks in the upper area and misses an edge in the lower left (note: for the interactive segmentation of the vertebral body, a rectangle was used as template to construct the graph. Thereby, the center of the rectangle is at the position of the user-defined seed point and the yellow crosses in the two rightmost images display the four corners of the rectangle). Nevertheless, the rightmost image presents the result of a refined segmentation. Therefore, the user simply placed three additional seeds (white dots on the contour of the vertebral body), and thus forced the algorithm to perform the min-cut at these positions – which also influences the cuts along the neighboring rays. Furthermore, additional gray value information can be extracted around these extra seeds that the user placed on the contour of the vertebral body.

Figure 2 presents the interactive refinement segmentation of the rectum from an intraoperative gynecological 3-Tesla magnetic resonance imaging dataset. The leftmost image shows the native scan and the second image from the left presents the initial seed point (white) for the interactive segmentation placed by the user inside the rectum. The red dots present the segmentation outcome with regard to the current seed point position (note: for the interactive segmentation of the rectum, a triangle was used as template to construct the graph. Thereby, the center of the rectangle is located at the user-defined seed point and the yellow crosses display the three corners of the triangle). In the third image from the left an additional seed point (white) has been placed in the upper left contour of the rectum. This additional seed forces the algorithm to perform the min-cut at this position. In the fourth image from the left, the user has interactively repositioned the initial seed point inside the rectum to find a better segmentation outcome. However, the additional seed at the contour stays fixed during the interactive repositioning of the initial

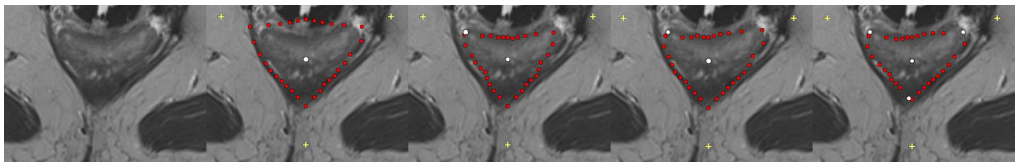

Figure 2 | Interactive refinement segmentation of the rectum from an intraoperative gynecological 3-Tesla magnetic resonance imaging dataset. The leftmost image shows the native scan and the second image from the left presents the initial seed point (white) for the interactive segmentation placed by the user inside the rectum. The red dots present the segmentation outcome with regard to the current seed point position (note: for the interactive segmentation of the rectum, a triangle was used as template to construct the graph. Thereby, the center of the rectangle is the user-defined seed point and the yellow crosses display the three corners of the triangle). In the third image from the left, an additional seed point (white) has been placed in the upper left contour of the rectum. This additional seed forces the algorithm to perform the min-cut at this position. In the fourth image from the left, the user has interactively repositioned the initial seed point inside the rectum to find a better segmentation outcome. However, the additional seed at the contour stays fixed during the interactive repositioning of the initial seed and still forces the algorithm to perform the min-cut at its position in the upper left contour of the rectum. In the rightmost image, the user further refined the segmentation outcome with two additional seed points.

seed and still forces the algorithm to perform the min-cut at its position in the upper left contour of the rectum. In the rightmost image, the user further refined the segmentation outcome with two additional seed points.

Figure 3 presents the interactive segmentation of a stented lumen and the thrombus from a postoperative computed tomography angiography (CTA) scan from a patient with an abdominal aortic aneurysm (AAA)[23,24]. The leftmost image shows the original scan and the second image from the left presents the segmentation of the stented lumen (red) with the initial user-defined seed point (green) placed inside the lumen (note: for the interactive segmentation a circle was used as template to construct the graph). The following three images show how the user places a second seed point and interactively drags it to the contour of the thrombus. However, the graph is still constructed from the initial seed point that has been placed at first inside the lumen. The second seed point forces the algorithm to perform the min-cut at its position and therefore also influences the positions of the min-cut in the neighboring rays. During the interactive dragging of the second seed inside the thrombus (images three and four from the left), the algorithm tries to adapt to other structures appearing in the thrombus. In this example, contrast enhanced blood from an endoleak[25] is visible (elongated bright area inside the thrombus), and the resulting contour partly fits to this endoleak in the third and the fourth image in the lower right area: once to the left contour of the endoleak (third image) and once to the right contour of the endoleak (fourth image). In the rightmost image, the segmentation outcome has furthermore been refined by an additional seed point placed by the user on the contour of the thrombus in the lower left.

Figure 4 presents the interactive segmentation of the prostate central gland (PCG) in 3D with a spherical template. The leftmost images show the original scan in axial (top), coronal (middle) and sagittal (bottom) views. The second image from the left presents the segmentation outcome (red) for a user-defined seed point (blue) placed inside the prostate (note: the seed point has been placed in the axial view, even if it is also displayed in the coronal and sagittal views). For comparison, the green masks display the outcome of a manual slice-by-slice segmentation from an expert. However, as the initial seed point is placed close to the right border of the prostate, the algorithm missed the contours on the left side of the PCG (axial and coronal views). Though, the interactive real-time behavior of the approach makes a repositioning easy, and thus it is also easy to find a good segmentation outcome for the axial, coronal and sagittal views (third image from the left). In the rightmost image, the segmentation result has been further refined with an additional seed that has been placed by the user in the lower right within the sagittal view.

Figure 5 presents different views – axial (top), coronal (middle) and sagittal (bottom) – of the 3D segmentation outcome from Figure 4. The left images show the last nodes (red) that still belong to the foreground (PCG) after the min-cut, and therefore defining the prostate central gland. In the images displayed in the middle column, the segmentation result has been superimposed with the manual mask (green) from the slice-by-slice expert segmentation. Finally, the rightmost images present a closed surface form the graph's nodes, which can be used to generate a solid mask of the segmentation outcome for further processing.

In addition, performance tests have been carried out with a square template for vertebral body segmentation[26] on a laptop with Intel Core i5-750 CPU, 4 × 2.66 GHz, 8 GB RAM running Windows 7 Professional x64 Version. Thereby, the computation time included the graph construction (sending out the rays from the user-defined seed point, sampling the nodes along these rays and constructing the

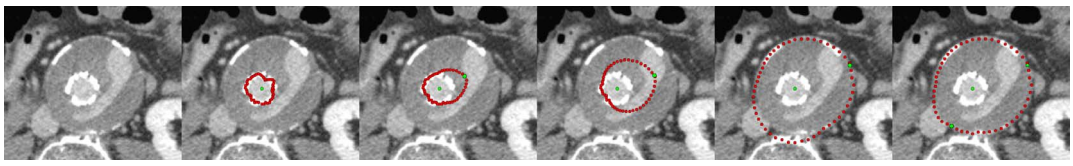

Figure 3 | Interactive segmentation of a stented lumen and the thrombus from a postoperative computed tomography angiography (CTA) scan from a patient with an abdominal aortic aneurysm (AAA). The leftmost image shows the original scan and the second image from the left presents the segmentation of the stented lumen (red) with the initial user-defined seed point (green) that has been placed inside the lumen (note: for the interactive segmentation a circle was used as template to construct the graph). The following three images show how the user places a second seed point and interactively drags it to the contour of the thrombus. However, the graph is still constructed from the initial seed point that has been placed inside the lumen. In addition, the second seed point forces the algorithm to perform the min-cut at its position and therefore also influences the positions of the min-cut in the neighboring rays. During the interactive dragging of the second seed point inside the thrombus (image three and image four from the left), the algorithm tries to adapt to other structures visible in the thrombus. In this example, contrast enhanced blood from an endoleak is visible (elongated bright area inside the thrombus), and the resulting contour adapts to this endoleak in the third and the fourth image in the lower right area: once to the left contour of the endoleak (third image) and once to the right contour of the endoleak (fourth image). In the rightmost image, the segmentation outcome has been furthermore refined by an additional seed point placed on the contour of the thrombus in the lower left.

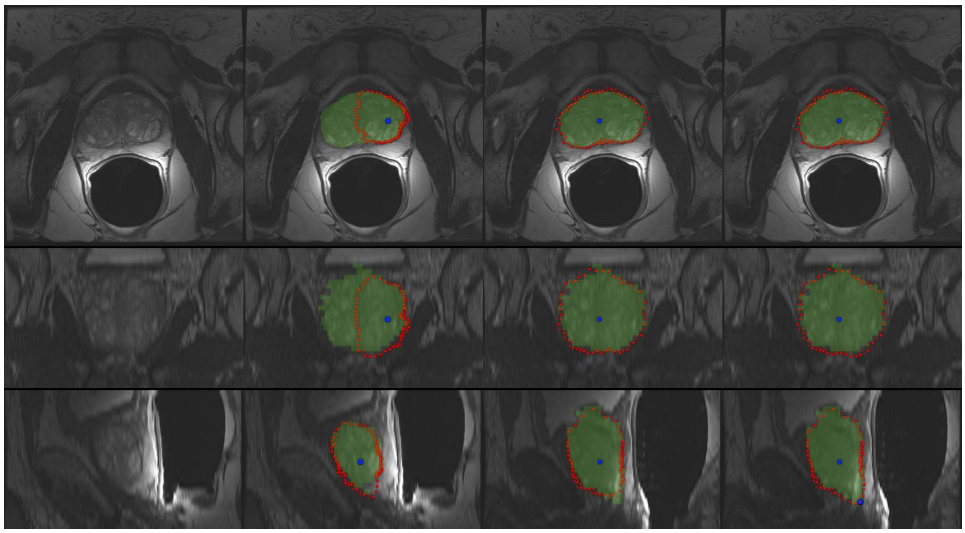

Figure 4 | Interactive segmentation of the prostate central gland (PCG) in 3D with a spherical template. The leftmost images show the original scan in axial (top), coronal (middle) and sagittal (bottom) views. The second image from the left presents the segmentation outcome (red) for a user-defined seed point (blue) that has been placed inside the prostate (note: the seed point has been placed in the axial view, but it is also displayed in the coronal and sagittal views). For comparison, the green masks display the outcome of a manual slice-by-slice segmentation from an expert. However, as the initial seed point is placed close to the right border of the prostate, the algorithm missed the contours of the PCG on the left (axial and coronal views). Though, the interactive real-time behavior of the approach makes a repositioning easy, and thus it is also easy finding a good segmentation outcome for the axial, coronal and sagittal views (third image from the left). In the rightmost image, the segmentation result has been further refined with an additional seed that has been placed in the lower right within the sagittal view.

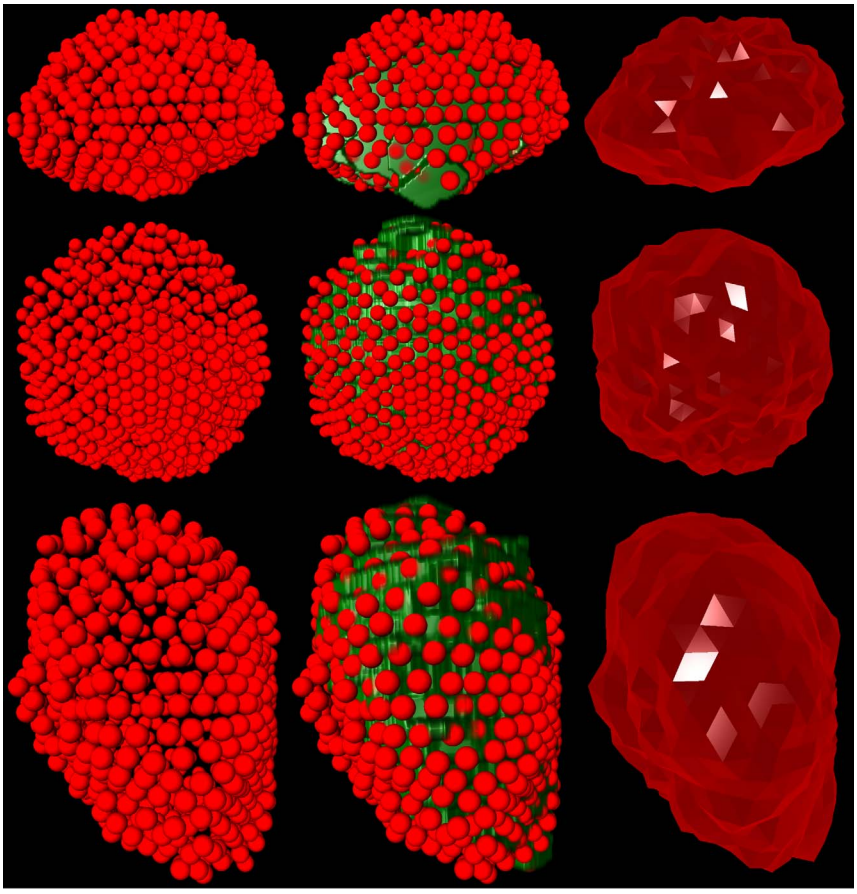

Figure 5 | Different views – axial (top), coronal (middle) and sagittal (bottom) – of the 3D segmentation outcome from Figure 4. The left images present the last nodes (red) that still belong to the foreground after the min-cut, and therefore they define the segmented prostate central gland contour. In the images of the middle column, the segmentation result has been superimposed with the manual mask (green) from the slice-by-slice expert segmentation. Finally, the rightmost images present a closed surface form the graph's nodes, which can be used to generate a solid mask of the segmentation outcome for further processing.

edges), analyzing the average gray value around the user-defined seed point (which is incorporated into weights of the graph's edges) and the optimal mincut calculation to separate the background from the foreground. The diameter of the square template was set to 80 mm and the delta value was set to 2. For 900 nodes (coming from 30 rays and 30 nodes per ray), an average interactive segmentation time of 30 ms could be achieved. For 9.000 nodes (300 rays, 30 nodes per ray), the segmentation time was in general still under 100 ms, which is still acceptable and within the time range from current smartphone touchscreens[27].

However, for 90.000 nodes (3.000 rays and 30 nodes per ray, or 300 rays and 300 nodes per ray) the average time was around 130 ms, where a minor latency time could already been recognized. That would mean the approach is not real-time anymore, but from a user point of view this is still acceptable for an interactive segmentation process. In contrast, 900.000 nodes (30.000 rays, 30 nodes per ray) were too slow for a convenient interactive segmentation, because the computation time went up to one second.

The outcome of the final segmentations for the presented interactive approach is heavily dependent on the manually placed seed points. However, in previous publications the segmentation of medical pathologies (like Glioblastoma Multiforme, Pituitary Adenomas, Cerebral Aneurysms, Prostate Central Glands and Vertebral Bodies) have already been evaluated via one fixed user-defined seed point, and the summary of these results have been presented here[28]. There, it could already show that a DSC around 80% is possible with only one seed point. However, in principle a user can get very close to the ground truth (manual segmentation) if enough manual seed points are added. Figure 6 presents an example of the prostate where several seed points (white) have been placed to get a segmentation result (red) that matches almost perfect with the manual segmentation (green).

Discussion

In this study, an interactive contouring algorithm for image segmentation, with a strong focus on medical data, has been introduced. More specific, the presented algorithm belongs to the class of interactive contouring approaches, which provide immediate feedback of the segmentation result to the user. Thus, allowing the user to interfere easily and intuitive into the algorithms calculation of the segmentation result. Nevertheless, there are always cases where the user cannot find a satisfying segmentation, when an algorithm has to detect the majority of the objects contour. This can have several reasons, the most frequent are in general homogeneous appearances between the object and the background, noise within the object to segment, or "complex" shapes of the object. For these difficult cases an algorithm requires additional support. This support should be intuitive and fast accomplishable by the user, and furthermore allows to continue the interactive segmentation. The proposed solution in this contribution is an easy and fast interactive placement of additional seed points in case of an unsatisfying segmentation outcome. Moreover, the approach allows to come back to an interactive refinement of the initial seed point, even under the new restrictions of the additional seeds. Furthermore, the additional seeds can provide the algorithm with broader geometrical and textural information and therefore restrict the possible segmentation calculation even more. For an initial feasibility evaluation, the approach has been implemented within a medical prototyping platform and tested mainly two- and three-dimensional medical data from the clinical routine, with the ultimate goal to assist pure manual slice-by-slice outlining.

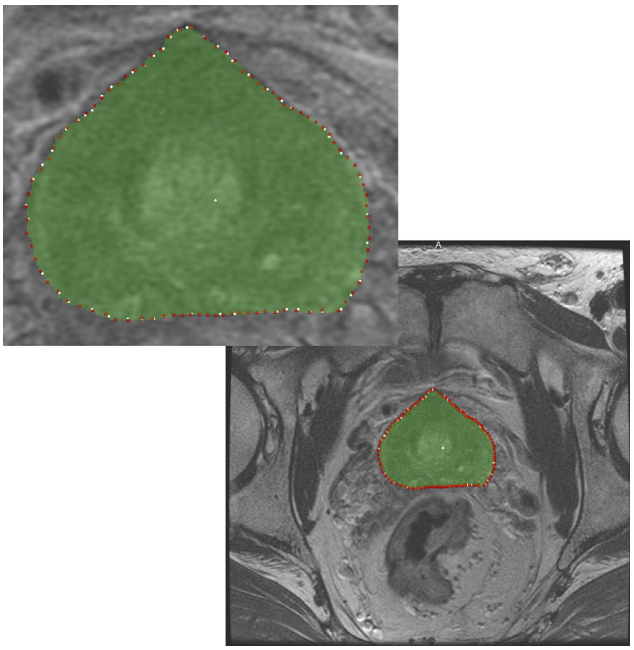

Figure 6 | Semi-automatic segmentation of the prostate where several seed points (white) have been placed to get a segmentation result (red) that matches almost perfect with a pure manual segmentation (green).

The novelty within this study lies in the combination of several pre-developed segmentation techniques[26,28–32], resulting in an advanced interactive *real-time* contouring algorithm for (medical) data. More specific, the presented work extends and incorporates a refinement option[29,30] – introduced only for fixed seed points and a spherical shape[31] – into the recently published Interactive-Cut[28] algorithm that can handle arbitrary shapes[32], but had no refinement option. In sum, the achieved research highlights of the study are:

- An novel interactive contouring algorithm has been designed;
- The algorithm combines shape-based segmentation with user refinement;
- The user refinement is intuitive and fast, with immediate feedback;
- The segmentation works on 2D and 3D image data;
- The evaluation has been performed on medical data from the clinical routine.

There are several areas for future work: in particular, supporting manual strokes from the user which have been drawn along the border of the object to segment – instead of "only" single seed points. Albeit, this may "break" the real-time feedback you get from single seed points even if these are dragged on the image. As shown in the result section, a single seed point can still be moved around to find a better segmentation result, this is not so easy and intuitive anymore if the user has once drawn a stroke. Though, a solution may be an iterative adaption to the manually sketched parts of the user[33].

Furthermore, a detailed study for the end user (which are primarily physicians in case of medical data) is necessary. Even if several physicians from different fields already tested the approach and responded positively, it's of course not certain that they will use it for own research (e.g. for a time-consuming analysis of medical data for own research purpose) or even in the clinical routine. However, after carrying out several studies with a typical stroke-based approach[9,10,34], it is clear that they would only accept such a course of action (the initialization) if the segmentation outcome is afterwards always satisfying (note: for the automatic segmentation the participating physicians had only to mark parts of the fore- and background with a simple brush; no other settings or parameters had to be defined). However, a long-term end user study regarding the presented approach already has been started within two European funded projects ClinicIMPPACT (www.clinicimppact.eu/) and GoSmart (www.gosmart-project.eu), where post-interventional radiofrequency ablation (RFA) zones are segmented[35].

Methods

Data. For a practical and genuine application in translational science, the elaborated approach has been tested with two-dimensional and three-dimensional medical data from the clinical routine. Intraoperative gynecological 3-Tesla magnetic resonance imaging datasets that have been used for this study can be found here[36,37,38]. MRI datasets of the spine, which are public available for research purposes, can be downloaded here[39,40,41]. Pre- and intra-procedural MR-guided prostate biopsy datasets with manual segmentations are freely available here[42,43,44].

Software. The presented approach has been implemented as own C++ module within the medical prototyping platform MeVisLab (www.mevislab.de, Version 2.3, Date of access: 28/04/2014) under the 64-bit version of Windows 7 Professional. Thereby, basic functionalities provided by MeVisLab, like loading medical data, e.g. in the DICOM format (OpenImage module), viewing and navigating through 2D slices (View2D module), displaying data and results in 3D (View3D module) and placing seed points (SoView2DMarkerEditor module) have been used. To calculate the max-flow/min-cut on graphs, the public available source code from Yuri Boykov and Vladimir Kolmogorov has been used (http://vision.csd.uwo.ca/code/, Version 3, Date of access: 28/04/2014)[45]:

Algorithm. The core algorithm has been implemented as own MeVisLab C++ module and is a combination and extension of the Template-Cut[32] and the Interactive-Cut[28] approaches, and the refinement method introduced in[29,30]. The new algorithm (Refinement-Cut), as well as the predecessor methods it builds up, belong to the graph-based approaches. Here, an image is interpreted as graph $G(V,E)$ which consists of nodes $n \in V$ sampled in the image and edges $e \in E$ establishing connections between nodes. After graph construction a minimal s-t-cut[45] is calculated on the graph, dividing the nodes into two disjoint sets, whereby one set the segmented objects and one set the background represents – note: for the calculation of the minimal s-t-cut, two additional virtual nodes $s \in V$ (called *source*) and $t \in V$ (called *sink*) are used. The minimal s-t-cut returns the global optimum on a constructed graph, in contrast to iterative approaches, like the Active Contours, which in general find a solution stepwise, and thus can get stuck during this process in a local minimum. However, the immediate calculation of a global optimum, like the minimal s-t-cut, makes graph-based approaches in particular eligible for an interactive real-time application. First of all, for the graph construction, the nodes $n \in V$ are sampled along rays which are sent out from one single seed point and with regards to a certain template. This template represents the basic shape of the segmented object, like described in the Template-Cut approach. Examples are

- A rectangle shape for vertebra segmentation in 2D[26];
- A circle template for prostate central gland segmentation in 2D[28];
- A cubic shape for vertebral body segmentation in 3D[46,47];
- A spherical shape for prostate central gland or brain tumor segmentation in 3D[31,43];
- Or even a user-defined shape for objects that vary too much to be predefined by a simple shape[48].

After the nodes and the underlying texture values within the image have been sampled, the graph's edges E are generated, that establish the connections between the (virtual) nodes, and an edge $\langle v_i, v_j \rangle \in E$ defines the connection between the two nodes v_i, v_j. Taking over the notation of Li et al.[49], there are two types of ∞-weighted edges:

- Intra-edges which connect nodes along the same ray to ensure that the minimal s-t-cut runs through only one edge within this ray;
- Inter-edges which connect nodes from different rays under a smoothness value delta Δ_r, which influences the number of possible s-t-cuts and therefore the flexibility of the resulting segmentation.

Furthermore, there are edges between the sampled nodes and the virtual nodes (s and t) for the graph construction established, and the weights of these edges depend on the sampled texture values within the image and a cost function. For more detail about the graph construction the reader is referred at this point to the previous Template-Cut publication[32]. However, the specific graph construction, which basically starts from one single seed point inside the segmentation object, is particularly suitable for an interactive real-time segmentation, because the user has only to drag this one single seed point over the image – in contrast, to approaches where more input like information about fore- and background or strokes are needed. Moreover, the user can easily add more seed points on the object's contour, which modify the graph and force the minimal s-t-cut to go through this additional seeds. Thereto, the algorithm search for the graph's node that is closest to the additional seed point provided by the user (note: In general, the additional seed's position will not match 100% with the position of a sample node, especially for a low density of rays and sampled nodes, rather the closest graph's node c is chosen). In a next step, the minimal s-t-cut has to be forced to be at this position. In order to ensure that, the graph's node c and all its predecessors within the same ray are connected via ∞-weighted edges to the source s, and all successor of c within the same ray are connected via ∞-weighted edges to the sink t. Furthermore, the intra-edge between c and its direct successor node within the same ray is removed. That this course of action works, has already been shown in an initial study with fixed seeds point for the segmentation of glioblastoma multiforme (GBM)[30], where the Dice Similarity Score (DSC)[50] could be improved from 77.72% to 83.91%. However, the possibility to drag an additional seed around an image and at the same time getting the updated segmentation result, makes this approach much more powerful and therefore the finding of a satisfying segmentation result much more convenient. Nevertheless, during dragging the closest graph's node c will most likely change, and has to be re-calculated as soon as the graph is re-constructed. But this allows the user to drag the additional seed points to arbitrary positions on the image and even works if a seed point is outside the predefined template. The additional user-defined seed points also influence the position of the minimal s-t-cuts on the neighboring rays. This influence gets even stronger for lower delta values, which restricts the flexibility of the resulting segmentation. Hence, there are many things going on "under the hood" (and hidden for the user) but still have to be handled in real-time during the interactive dragging of the seeds on the image.

1. Iliadis, G. *et al.* The importance of tumor volume in the prognosis of patients with glioblastoma: comparison of computerized volumetry and geometric models. *Strahlenther Onkol.* **185**, 743–750 (2009).
2. Kass, M., Witkin, A. & Terzopoulos, D. Snakes - Active Contour Models. *Int J Comput Vision* **1**, 321–331 (1987).
3. McInerney, T. & Terzopoulos, D. Deformable models in medical image analysis: a survey. *Me Image Anal* **1**, 91–108 (1996).
4. Cootes, T. F., Edwards, G. J. & Taylor, C. J. Active Appearance Models. *ECCV* **2**, 484–498 (1998).
5. Shi, J. & Malik, J. Normalized cuts and image segmentation. *IEEE Trans Pattern Anal and Mach Intell* **22**, 888–905 (2000).
6. Ji, Z. X., Sun, Q. S. & Xia, D. S. A modified possibilistic fuzzy c-means clustering algorithm for bias field estimation and segmentation of brain MR image. *Comput Med Imaging Graph.* **35**, 383–397 (2011).
7. Fu, J. C., Chen, C. C., Chai, J. W., Wong, S. T. & Li, I. C. Image segmentation by EM-based adaptive pulse coupled neural networks in brain magnetic resonance imaging. *Comput Med Imaging Graph.* **34**, 308–320 (2010).
8. Vezhnevets, V. & Konouchine, V. GrowCut-Interactive multi-label N-D image segmentation. *Graphicon* 150–156 (2005).
9. Egger, J., Kapur, T., Nimsky, C. & Kikinis, R. Pituitary Adenoma Volumetry with 3D Slicer. *PLoS ONE* **7**, e51788 (2012).
10. Egger, J. *et al.* GBM Volumetry using the 3D Slicer Medical Image Computing Platform. *Sci Rep.* **3**, 1364 (2013).
11. Zhao, F. & Xie, X. An Overview of Interactive Medical Image Segmentation. *Annals of the BMVA* **2013**, 1–22 (2013).
12. Adams, R. & Bischof, L. Seeded region growing. *IEEE Trans. Pattern Anal. Mach. Intell.* **16**, 641–647 (1994).
13. Sivewright, G. J. & Elliot, P. J. Interactive region and volume growing for segmenting volumes in MR and CT images. *Med. Inform.* **19**, 71–80 (1994).
14. Udupa, J. K. *et al.* Multiple sclerosis lesion quantification using fuzzy-connectedness principles. *IEEE Trans. Med. Imag.* **16**, 598–609 (1997).
15. Gomes, R. B., Aroca, R. V., Carvalho, B. M. & Goncalves, L. M. G. Real time Interactive Image Segmentation Using User Indicated Real-world Seeds. *SIBGRAPI.* 182–189 (2012).
16. Armstrong, C. J., Price, B. L. & Barrett, W. A. Interactive segmentation of image volumes with Live Surface. *Comp. Graph.* **31**, 212–229 (2007).
17. Mortensen, E. N. & Barrett, W. A. Intelligent scissors for image composition. *ACM TOG.* 191–198 (1995).
18. Mortensen, E. N. & Barrett, W. A. Toboggan-based intelligent scissors with a four-parameter edge model. *CVPR.* 2452–2458 (1999).
19. Werlberger, M., Pock, T., Unger, M. & Bischof, H. A Variational Model for Interactive Shape Prior Segmentation and Real-Time Tracking. *SSVM* **5567**, 200–211 (2009).
20. Caselles, V., Kimmel, R. & Sapiro, G. Geodesic active contours. *Int J of Comput Vis* **22**, 61–79 (1997).
21. Jackowski, M. & Goshtasby, A. A Computer-Aided Design System for Refinement of Segmentation Errors. *Med Image Comput Comput Assist Interv (MICCAI)* **3750**, 717–724 (2005).
22. Mory, B., Somphone, O., Prevost, R. & Ardon, R. Real-Time 3D Image Segmentation by User-Constrained Template Deformation. *Med Image Comput Comput Assist Interv (MICCAI)* **15**, 561–568 (2012).
23. Egger, J., Großkopf, S. & Freisleben, B. Simulation of Bifurcated Stent Grafts to Treat Abdominal Aortic Aneurysms (AAA). *SPIE Med Img* **6509**, 65091N(1–6) (2007).
24. Renapurkar, R. D. *et al.* Aortic volume as an indicator of disease progression in patients with untreated infrarenal abdominal aneurysm. *Eur J Radiol.* **81**, e87–93 (2011).
25. Lu, J. *et al.* Detection and Visualization of Endoleaks in CT Data for Monitoring of Thoracic and Abdominal Aortic Aneurysm Stents. *SPIE Med Img* **6918**, 69181F(1–7) (2008).
26. Egger, J. *et al.* Square-Cut: A Segmentation Algorithm on the Basis of a Rectangle Shape. *PLoS ONE* **7**, e31064 (2012).
27. Agawi. TouchMarks I: Smartphone Touchscreen Latencies (2013) http://appglimpse.com/blog/touchmarks-i-smart-phone-touch-screen-latencies/ (Date of access: 28/04/2014).
28. Egger, J., Lüddemann, T., Schwarzenberg, R., Freisleben, B. & Nimsky, C. Interactive-Cut: Real-Time Feedback Segmentation for Translational Research. *Comput Med Imaging Graph.* 1–11 (2014).
29. Egger, J. *et al.* A Flexible Semi-Automatic Approach for Glioblastoma multiforme Segmentation. *Inter Biosignal Proc Conf* **060**, 1–4 (2010).

30. Egger, J., Colen, R., Freisleben, B. & Nimsky, C. Manual Refinement System for Graph-Based Segmentation Results in the Medical Domain. *J Med Syst.* **36**, 2829–2839 (2012).
31. Egger, J. *et al.* Nugget-Cut: A Segmentation Scheme for Spherically- and Elliptically-Shaped 3D Objects. *32nd DAGM* **6376**, 383–392 (2010).
32. Egger, J., Freisleben, B., Nimsky, C. & Kapur, T. Template-Cut: A Pattern-Based Segmentation Paradigm. *Sci Rep.* **2**, 420 (2012).
33. Steger, S. & Sakas, G. FIST: Fast interactive segmentation of tumors. *Abdom Imaging* **7029**, 125–132 (2011).
34. Egger, J., Kappus, C., Carl, B. & Nimsky, C. GrowCut-Based Vertebral Body Segmentation with 3D Slicer. *DGNC,* Poster 24, Frankfurt am Main, Germany (2013).
35. Kainz, B. *et al.* High-Resolution Contrast Enhanced Multi-Phase Hepatic Computed Tomography Data from a Porcine Radio-Frequency Ablation Study. *IEEE ISBI,* Bejing, China, (2014)
36. Kapur, T. *et al.* 3-T MR-guided brachytherapy for gynecologic malignancies. *Magn Reson Imaging* **30**, 1279–1290 (2012).
37. Egger, J. Image-guided therapy system for interstitial gynecologic brachytherapy in a multimodality operating suite. *SpringerPlus* **2**, 395 (2013).
38. Egger, J., Kapur, T. & Viswanathan, A. GYN Data Collection, NCIGT (2012) http://www.spl.harvard.edu/publications/item/view/2227 (Date of access: 28/04/2014).
39. Zukić, D. *et al.* Segmentation of Vertebral Bodies in MR Images. *VMV.* 135–142 (2012).
40. Zukić, D. *et al.* Robust Detection and Segmentation for Diagnosis of Vertebral Diseases using Routine MR Images. *Comput Graph Forum.* 1–15 (2014).
41. Zukić, D. Spine segmentation and analysis (2013) http://www.cg.informatik.uni-siegen.de/en/spine-segmentation-and-analysis (Date of access: 28/04/2014).
42. Fedorov, A. *et al.* Image Registration for Targeted MRI-guided Prostate Transperineal Prostate Biopsy. *J Magn Res Imag.* **36**, 987–992 (2012).
43. Egger, J. PCG-Cut: Graph Driven Segmentation of the Prostate Central Gland. *PLoS One* **8**, e76645 (2011).
44. Fedorov, A., Tuncali, K., Fennessy, F. M. & Tempany, C. M. MR-guided Prostate Biopsy pre- and intra-procedural MRI Registration Evaluation Dataset (2012) http://www.spl.harvard.edu/publications/item/view/2147 (Date of access: 28/04/2014).
45. Boykov, Y. & Kolmogorov, V. An Experimental Comparison of Min-Cut/Max-Flow Algorithms for Energy Minimization in Vision. *IEEE Trans Pattern Anal Mach Intell* **26**, 1124–1137 (2004).
46. Schwarzenberg, R. *et al.* A Cube-Based Approach to Segment Vertebrae in MRI-Acquisitions. *BVM*, 69–74 (2013).
47. Schwarzenberg, R. *et al.* Cube-Cut: Vertebral Body Segmentation in MRI-Data through Cubic-Shaped Divergences. *PLoS ONE* **9**, e93389 (2014).
48. Lüddemann, T. & Egger, J. Rectum Segmentation in MR-guided Gynecologic Brachytherapy Data. *Proc. British Gynaecological Cancer Society Annual Scientific Meeting in conjunction with the Irish Gynaecological Cancer Society* **PO97**, 162–163 (2013).
49. Li, K., Wu, X., Chen, D. Z. & Sonka, M. Optimal surface segmentation in volumetric images - a graph-theoretic approach. *IEEE Trans Pattern Anal Mach Intell (PAMI)* **28**, 119–113 (2006).
50. Sampat, M. P. *et al.* Measuring intra- and inter-observer Agreement in Identifying and Localizing Structures in Medical Images. *IEEE Inter. Conf. Image Processing.* 81–84 (2006).

Acknowledgments

Primarily, the author thanks the physicians Dr. med. Barbara Carl, Thomas Dukatz, Christoph Kappus, Dr. med. Malgorzata Kolodziej, Dr. med. Daniela Kuhnt and Professor Dr. med. Christopher Nimsky for providing the neurosurgical datasets, and performing manual slice-by-slice segmentations for the evaluation of the algorithm. The author also thanks Drs. Fedorov, Tuncali, Fennessy and Tempany, for sharing the prostate data collection plus manual segmentations, and Fraunhofer MeVis for providing an academic MeVisLab license. The work received funding from the European Union in FP7: Clinical Intervention Modelling, Planning and Proof for Ablation Cancer Treatment (ClinicIMPPACT, grant agreement no. 610886) and Generic Open-end Simulation Environment for Minimally Invasive Cancer Treatment (GoSmart, grant agreement no. 600641).

Author contributions

Conceived and designed the experiments: J.E. Performed the experiments: J.E. Analyzed the data: J.E. Contributed reagents/materials/analysis tools: J.E. Wrote the paper: J.E.

Additional information

Competing financial interests: The authors declare no competing financial interests.

How to cite this article: Egger, J. Refinement-Cut: User-Guided Segmentation Algorithm for Translational Science. *Sci. Rep.* **4**, 5164; DOI:10.1038/srep05164 (2014).